Computational Investigation of the Structure and Reactivity of Metal-Nitrogen-Carbons for Electrocatalysis

Inaugural-Dissertation

to obtain the academic degree
Doctor rerum naturalium (Dr. rer. nat.)

submitted to
The Department of Biology, Chemistry, Pharmacy
of Freie Universität Berlin

By

Jian Liang Low
from Singapore, Singapore

2024

This work was conducted under the supervision of
Prof. Dr. Beate Paulus (Freie Universität Berlin)
from May 2020 until February 2024

First reviewer:	Prof. Dr. Beate Paulus
Second reviewer:	Prof. Dr.-Ing. Christina Roth
Date of defense:	19th April 2024

I hereby declare that this dissertation was written independently by me. I used no other sources than the ones marked and acknowledged as such. This work has not yet been submitted or published as a dissertation to any other university.

Abstract

The development of metal-nitrogen-carbons (M-N-Cs) has gained significant momentum in the 21st century, driven by their potential as sustainable alternatives to precious metals for electrocatalytic applications. However, as the pyrolytic synthesis often produces highly disordered carbonized materials, it can be challenging to accurately characterize the active sites and their involvement in the catalytic reactions. In this regard, quantum chemical methodologies like density functional theory (DFT) could provide crucial atomic-level information to guide the characterization and optimization of M-N-Cs. In this thesis, I present computational studies related to the synthesis of M-N-Cs in the first part, followed by their electrocatalytic applications in the second part. In parallel to these studies, potential factors for the material degradation during the synthesis and applications are also identified, especially for the generally active but unstable Fe-N-Cs.

Inspired by the recent success of the templating-transmetallation strategy in producing M-N-Cs with dense active sites, the first part of the thesis features a computational investigation on the chemical properties of metals at the MN_4 sites. By constructing and optimizing structural models for the incorporation of MN_4 motifs in conductive carbon matrices, we determined several advantages of using molecular DFT methods for modeling the active sites, especially the structurally complex pyrrolic MN_4 motifs. Using these models, we further examined the trends among the first-row transition metals pertaining their binding within the MN_4 site as well as their relative affinity to the pyrrolic or pyridinic motifs. It could be shown that metals with more significant ionic binding character, such as Zn and Mg, are more likely to form the pyrrolic MN_4 sites than the catalytically active metals like Fe and Co, leading to the successful characterization of the pyrrolic MN_4 sites from synthesis strategies which utilized Zn^{2+} or Mg^{2+} as the sacrificial templating ions. In addition, the binding of Zn was determined to be the weakest among the transition metals, making it an optimal choice for the subsequent transmetallation.

As the transmetallation step generally retains the original structure of the active site, in addition to its morphological properties and active site densities, it became a crucial starting point for intrinsic activity comparisons among metals in the

M-N-Cs. In the second part of this thesis, the electrocatalytic mechanisms for the oxygen reduction reaction (ORR) and the carbon dioxide reduction reaction (CO_2RR) on the previously identified pyrrolic MN_4 sites are presented along with corresponding side reactions including the Fenton reaction and the hydrogen evolution reaction (HER). The combined efforts of theory and experiment led to the identification of inconspicuous species at the interface, such as hydroxides for alkaline ORR, water for the Fenton reaction, and cations for the CO_2RR, which in fact play an active role in the mechanisms of the respective reactions. For the ORR, we determined the involvement of the outer-sphere electron transfer in the reaction mechanism, especially in the alkaline medium, leading to the formation of H_2O_2 whose subsequent reactions could depend on specific interactions with the MN_4 site. For the CO_2RR, a theory-experiment contradiction in the activity and selectivity of Ni-N-Cs could be resolved with the inclusion of alkali metal ions in the mechanism, whose adsorption was made favorable by the pyrrolic N atoms at the MN_4 site. Overall, these insights derived with DFT provide strong theoretical support for the knowledge-based optimization of the activity, selectivity and stability of M-N-Cs for sustainable energy conversion applications.

Kurzzusammenfassung

Die Entwicklung vom metall- und stickstoff-codotierten Kohlenstoff (M-N-C) hat im 21. Jahrhundert erheblichen Auftrieb erhalten, angetrieben durch ihr Potenzial als nachhaltige Alternativen zu Edelmetallen für elektrokatalytische Anwendungen. Da jedoch die pyrolytische Synthese oft stark ungeordnete karbonisierte Materialien erzeugt, kann es herausfordernd sein, die aktiven Zentren genau zu charakterisieren und ihre Beteiligung an den katalytischen Reaktionen zu verstehen. In diesem Zusammenhang können quantenchemische Methoden wie die Dichtefunktionaltheorie (DFT) entscheidende atomare Informationen liefern, um die Charakterisierung und Optimierung von M-N-Cs zu unterstützen. In dieser Arbeit präsentiere ich im ersten Teil theoretische Studien zur Synthese von M-N-Cs, gefolgt von deren elektrokatalytischen Anwendungen im zweiten Teil. Parallel zu diesen Erkenntnissen werden potenzielle Faktoren für die Materialdegradierung während der Synthese und Anwendungen identifiziert, insbesondere für die im Allgemeinen aktiven, aber instabilen Fe-N-Cs.

Inspiriert von dem Erfolg der Templating-Transmetallation-Strategie bei der Herstellung von M-N-Cs mit erhöhten Dichten der aktiven Zentren, beinhaltet der erste Teil dieser Arbeit eine theoretische Untersuchung der chemischen Eigenschaften von Metallatomen an den aktiven Zentren. Durch den Aufbau sowie die Optimierung von Strukturmodellen für die Integration von MN_4-Motiven in leitfähigen Kohlenstoffe haben wir mehrere Vorteile der Verwendung von molekularen DFT-Methoden zur Modellierung der aktiven Zentren festgestellt, besonders für die strukturell komplexen pyrrolischen MN_4-Motive. Unter Verwendung dieser Modelle haben wir weiterhin die Trends unter den Übergangsmetallen der ersten Reihe in Bezug auf ihre Bindung innerhalb der MN_4-Zentren sowie ihre relative Affinität zu den pyrrolischen oder pyridinischen Motiven untersucht. Es konnte gezeigt werden, dass Metalle mit stärker ionischem Bindungscharakter, wie Zn und Mg, eher dazu neigen, die pyrrolischen MN_4-Zentren zu bilden als die katalytisch aktiven Metalle wie Fe und Co, was zur erfolgreichen Charakterisierung der pyrrolischen MN_4-Zentren aus Synthesestrategien führte, die Zn^{2+} oder Mg^{2+} als Templating-Ionen verwendeten. Zusätzlich wurde festgestellt, dass die Bindung von Zn zu den schwächsten unter den untersuchten Metallen gehört, weshalb es sich ideal für die anschließende Transmetallation eignet.

Da die Transmetallationsstrategie im Allgemeinen die ursprüngliche Struktur der aktiven Zentren beibehält und zudem deren morphologische Eigenschaften sowie Dichten der aktiven Zentren, wird sie zu einem entscheidenden Ausgangspunkt für intrinsische Aktivitätsvergleiche zwischen den Metallen in den M-N-Cs. Im zweiten Teil dieser Arbeit werden die elektrokatalytischen Mechanismen für die Sauerstoffreduktionsreaktion (ORR) und die Kohlendioxidreduktionsreaktion (CO_2RR) zusammen mit entsprechenden Nebenreaktionen wie der Fenton-Reaktion und der Wasserstoffentwicklungsreaktion (HER) vorgestellt. Die ausführliche Analyse von theoretischen und experimentellen Daten führte zur Identifizierung unauffälliger Spezies an den Grenzflächen, wie Hydroxide für die alkalische ORR, Wasser für die Fenton-Reaktion und Kationen für die CO_2RR, die eigentlich eine aktive Rolle bei der Mechanismen der jeweiligen Reaktionen spielen. Für die ORR bestimmten wir die Beteiligung des Outer-Sphere-Elektronentransfers im Reaktionsmechanismus, insbesondere im alkalischen Medium, was zur Bildung von H_2O_2 führte, dessen folgende Reaktionen von spezifischen Wechselwirkungen mit den MN_4-Zentren abhängen könnte. Bei der CO_2RR konnte ein Widerspruch zwischen Theorie und Experiment hinsichtlich der Aktivität und Selektivität von Ni-N-Cs durch die Einbeziehung von Alkalimetallionen im Mechanismus gelöst werden, deren Adsorption durch die pyrrolischen Stickstoffatome an den MN_4-Zentren begünstigt wurde. Insgesamt bieten diese Erkenntnisse aus der Dichtefunktionaltheorie (DFT) eine solide theoretische Grundlage für die wissensbasierte Optimierung der Aktivität, Selektivität und Stabilität von M-N-Cs für nachhaltige Energieumwandlungsanwendungen.

List of Publications

Main Publications

[M1] **Resolving the Dilemma of Fe–N–C Catalysts by the Selective Synthesis of Tetrapyrrolic Active Sites via an Imprinting Strategy**
D. Menga, J. L. Low, Y.-S. Li, I. Arčon, B. Koyutürk, F. Wagner, F. Ruiz-Zepeda, M. Gaberšček, B. Paulus, and T.-P. Fellinger, *J. Am. Chem. Soc.* **2021**, *143*, 18010-18019.
DOI: https://doi.org/10.1021/jacs.1c04884

[M2] **Computational Modelling of Pyrrolic MN_4 Motifs Embedded in Graphene for Catalyst Design**
J. L. Low, B. Paulus, *Catalysts* **2023**, *13(3)*, 566.
DOI: https://doi.org/10.3390/catal13030566

[M3] **Elucidating the Intrinsic Activity of Tetrapyrrolic Fe-N-C Electrocatalysts for the Oxygen Reduction Reaction in Alkaline Medium**
D. Menga, J. L. Low, A. G. Buzanich, B. Paulus and T.-P. Fellinger, *submitted to Adv. Energy Mater.*

[M4] **Exploring the inner- and outer-sphere mechanistic pathways of ORR on M-N-Cs with pyrrolic MN_4 motifs**
J. L. Low, C. Roth and B. Paulus, *submitted to J. Phys. Chem. C*

[M5] **On the Intrinsic CO_2 Reduction Activity of Atomically-Dispersed Ni-N-C and Co-N-C Electrocatalysts**
A. Mehmood, S. A. Abbas, J. L. Low, S. Dietzmann, G. Ali, B. Paulus, K. H. Chae, K. M. Nam, K.-D. Jung and T.-P. Fellinger, *submitted to ACS Catal.*

Supporting Publications

[S1] **A Copper Single-Atom Cascade Bionanocatalyst for Treating Multidrug-Resistant Bacterial Diabetic Ulcer**
X. Fan, Y. Gao, F. Yang, J. L. Low, L. Wang, B. Paulus, Y. Wang, A. Trampuz, C. Cheng, R. Haag, *Adv. Funct. Mater.* **2023**, *33*, 2301986.
DOI: https://doi.org/10.1002/adfm.202301986

Contents

1 Introduction

"In the midst of chaos, there is also opportunity."

-Sun Tzu

In the drive towards a sustainable economy, there is a surging interest in the utilization of carbon for numerous energy-related applications, justified by its huge natural abundance and diversity in structural and electronic properties [1]. In particular, conductive carbon matrices based on graphitic materials are relevant to electrocatalysis due to their ability to host foreign elements that promote electron transfers [2, 3]. These materials can potentially substitute precious metal-based catalysts for the oxygen reduction reaction (ORR) and carbon dioxide reduction reaction (CO_2RR), among other electrochemical processes, severely reducing their economic and environmental burden [3, 4]. Despite its advantages, the huge structural variability of carbon often translates to structural disorder within the materials, making it particularly challenging to characterize active sites and perform mechanistic studies. In that regard, computational approaches like density functional theory (DFT) can be strategically invoked to derive atomic-level insights on the coordination structures and catalytic mechanisms, complementing the experimental optimization of the carbon-based catalysts [5].

Among the plethora of doped carbon materials, the most important ones with regards to electrocatalytic applications are the metal- and nitrogen-doped carbons (M-N-Cs), especially those hosting the transition metals (TMs). For instance, Fe-N-Cs and Co-N-Cs are promising materials for alkaline ORR, achieving initial performances that can match or even exceed state-of-the-art catalysts derived from platinum group metals (PGMs) [6–8]. For CO_2RR, Ni-N-Cs and Cu-N-Cs can be highly selective towards the production of CO [9, 10], potentially substituting noble metals like Ag and Au. Besides electrocatalysis, certain M-N-Cs have also been shown to catalyze the Fenton reaction, dissociating hydrogen peroxide to produce reactive oxygen species (ROS). Although such reactions are detrimental to the stability of the electrochemical cell, recent crossovers to the biomedical discipline exploited the Fenton reactivity of certain M-N-Cs for killing pathogens and cancer cells, providing a cheaper and possibly safer alternative to the enzyme-based biocatalysts [11].

1.1 M-N-C Synthesis

The study of M-N-Cs for electrochemical applications dates back to 1964, when Jasinski *et al.* showed that certain metal phthalocyanine complexes were able to catalyze ORR [12, 13]. Later, Jahnke *et al.* reported a significant improvement of ORR performance upon pyrolysis of such complexes supported on carbon, possibly integrating the MN_4 macrocycles into the support [14]. More than a decade later, Gupta *et al.* reported the synthesis of pyrolyzed materials with similar ORR activities, but without the MN_4 macrocycle as precursors, showcasing the inherent ability of metals to template the MN_4 sites during pyrolysis [15]. Since then, a variety of precursors have been proposed for the pyrolytic synthesis of M-N-Cs, including nitrogen-rich organic molecules [7, 16], polymers [15, 17, 18], ionic liquids [19, 20] and metal-organic frameworks (MOFs) [8, 21–24].

Although increasing the sheer quantity of active sites should intuitively lead to better catalytic performances, attempts to introduce more TM dopants into the material are often faced with a synthetic dilemma [25]. TMs that confer the best ORR activity to M-N-Cs, such as Fe and Co, are also known to catalyze the graphitization of the carbon framework at the pyrolysis temperatures [26], leading to the expulsion of the TM dopants to form inorganic side phases such as metallic nanoparticles, metal carbides, and metal nitrides that cannot be removed by acid washing [27–29]. The collective process, known as carbothermal reduction, not only limits the electrochemical activity through the morphological destruction of the catalyst, but also complicates the characterization and mechanistic studies due to the presence of side phases [25]. In order to eliminate carbothermal reduction from the picture, Mehmood *et al.* proposed a templating-transmetallation strategy that used Mg^{2+} to template the MgN_4 sites during pyrolysis, followed by an ion exchange with Fe^{2+} [30]. Following its success in eliminating side phases in M-N-Cs, the templating-transmetallation strategy was further optimized in recent years to produce M-N-Cs with dense active sites, with the majority of successful strategies employing Zn^{2+} as the sacrificial templating ion [8, 24, 25, 31].

Throughout the optimization of the templating-transmetallation procedures, it became increasingly evident that metals like Zn and Mg are not merely placeholders for the active TMs, but are actively involved in the formation and stabilization of the single atom sites [25, 30]. Furthermore, the absence of side phases from such synthesis procedures facilitated an accurate characterization of the coordination structure, for example in **Paper M1** and **Paper M5**, potentially resolving a long-standing controversy in the coordination chemistry at the MN_4 site. On the

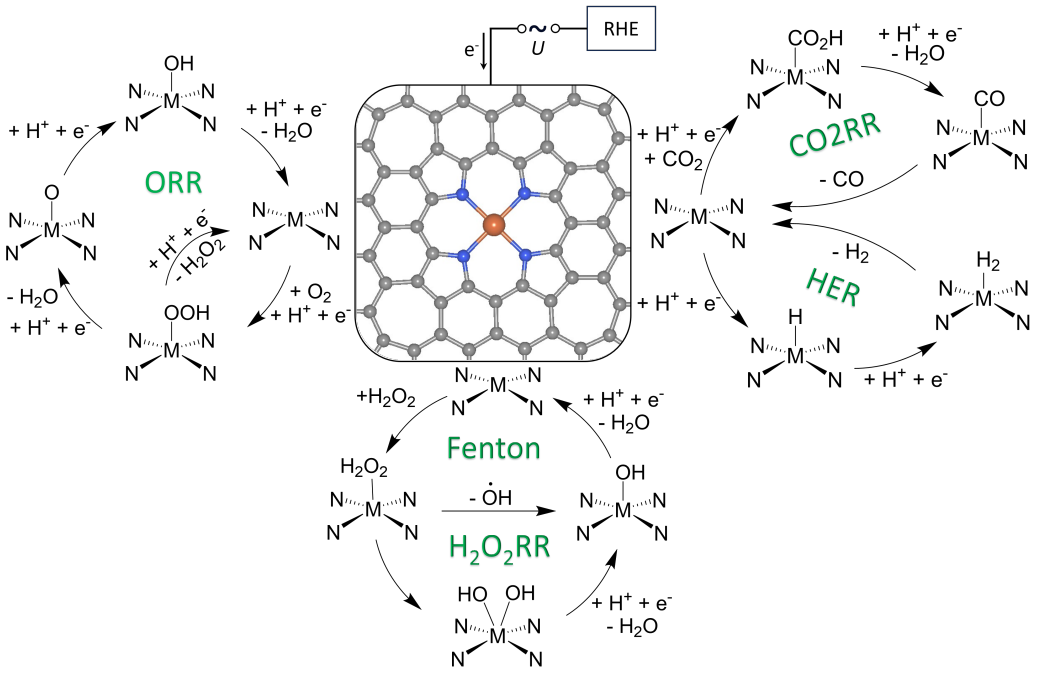

Figure 1.1: Magnified view of the planar pyrrolic MN_4 structure (middle) and the inner sphere mechanisms for ORR (left), parallel H_2O_2RR and Fenton reaction (bottom), competing CO_2RR and HER (right).

one hand of the controversy, the structural resemblance of the pyridinic MN_4C_{10} coordination to graphene (Figure 2.5a) is proposed to confer thermodynamic stability to the active site [32–34]. On the other hand, several recent studies have correlated the electrochemical activities to the pyrrolic MN_4C_{12} coordination shown in Figure 1.1 [35–38], mirroring nature's preference in forming pyrrolic MN_4 complexes. **Paper M1** and **Paper M2** feature the discussions on the templating effect of different metal ions in relation to their respective affinity to the pyrrolic or pyridinic MN_4 motifs, along with the thermodynamics and kinetics of the transmetallation process.

1.2 Catalytic Properties of M-N-Cs

1.2.1 Oxygen Reduction Reaction

With a relatively long historical development as discussed in Section 1.1, the ORR is the most widely studied electrocatalytic application of M-N-Cs. The process is fundamental to fuel cells and metal-air batteries, utilizing atmospheric oxygen instead of a stored oxidant for the energy conversion. Consequently, these energy

storage devices are able to achieve some of the highest energy densities (energy per unit volume) or specific energies (energy per unit mass) [39, 40], making them desirable for applications that require minimal weight or volume (*e.g.* portable and wearable electronics [40, 41], aviation [42, 43] and marine mobility [44, 45]). Unfortunately, the exceptional energy storage capacities come at the cost of Faradaic losses and diminished power densities, as a result of the sluggish kinetics for the activation of O_2 [46]. As the ORR kinetics is often current-limiting for the overall energy conversion, power densities can be boosted by introducing an ORR electrocatalyst, conventionally derived from the scarce and expensive platinum group metals (PGMs) like Pt and Pd. However, major development in the past two decades contributed to the rise of M-N-Cs, especially Fe-N-Cs and Co-N-Cs, as potential economically and environmentally sustainable alternatives to the PGMs [6, 7].

For electrocatalytic processes like the ORR, an understanding of the underlying reaction mechanisms is crucial for the knowledge-based design of the catalysts. The most commonly proposed mechanism for ORR involves consecutive reductive protonation to an O_2 directly adsorbed at an active site (Figure 1.1, left). The so-called inner-sphere mechanism is deeply rooted in the conventional understanding of heterogeneous catalysis, where surface adsorption would intuitively precede any form of reaction. However, one critical difference between electrocatalysis and thermal catalysis is often overlooked, namely the increased emphasis on interfacial electron transfers compared to the surface-induced collisions. Alternative to the inner-sphere mechanism is the outer-sphere mechanism, described by a long-range electron transfer to species at the outer-Helmholtz planes. Such a mechanism is especially relevant in the alkaline environment, as the inner-sphere activity could be restricted by the specific adsorption of hydroxides [47–49]. Experimentally, the relative contributions from either the inner-sphere or the outer-sphere electron transfers could be determined through poisoning the active sites. Malko *et al.* reported that poisoning a Fe-N-C with nitrite (NO_2^-) and nitric oxide (NO) led to a reduction in acidic ORR activity, but surprisingly negligible influence on alkaline ORR [50]. The difference in poisoning behavior suggested that a free Fe-site indeed contributes to acidic ORR, consistent with an inner-sphere mechanism, while the alkaline ORR does not necessarily involve the Fe-site. In a subsequent study, Malko *et al.* further determined a smaller kinetic isotope effect in the alkaline environment than in acid, suggesting the existence of a proton-free rate-determining step (RDS) as another hint towards an outer-sphere electron transfer [51]. In **Paper M3**, we

provide further evidence for the outer-sphere electron transfer through correlations between the experimental onset potentials and the calculated valence electronic properties at the MN_4 site. **Paper M4** extends the theoretical study to other metals, with a supplementary analysis of the electronic distributions, thereby elucidating the influence of the metal dopant on the valence electronic properties of the carbon host.

1.2.2 Hydrogen Peroxide Reduction and Fenton Reaction

Among the ORR-active M-N-Cs, those containing the mid-TMs like Cr-N-Cs, Mn-N-Cs and Fe-N-Cs are often reported to catalyze the full 4-electron reduction to water [3, 7, 52–55], while late TMs like Co-N-Cs generally favor partial 2-electron reduction (2e-ORR) to H_2O_2 [55, 56]. Mechanistically, the full reduction can be further categorized into direct mechanisms which do not involve a H_2O_2 intermediate (4e-ORR), or indirect ones involving the production and consumption of H_2O_2 at the same active site (2e+2e-ORR) or at different active sites (2e×2e-ORR) [3].[1] For the in-situ quantification of H_2O_2 yield using macroscopic techniques like the rotating ring-disk electrode (RRDE), the distinction between the direct and indirect mechanisms can be convoluted by the thickness of the porous materials, as a thicker catalyst would trap the H_2O_2 intermediates longer and promote their subsequent reduction, making it seem like a direct 4e-ORR process. In fact, several studies reported lower electron transfer numbers and larger H_2O_2 yields as the catalyst loading decreased [52, 57, 58], implying that the apparent 4e-selectivity of certain M-N-Cs could be better represented with a 2e+2e-ORR mechanism.

Since H_2O_2 appears to be involved in ORR, either as an intermediate (2e+2e-ORR) or a product (2e-ORR), an understanding of its origin as well as how it interacts with the materials can provide crucial guidance in improving the selectivity and stability of catalysts during ORR. Notably, the formation of H_2O_2 is highly consistent with the adsorption-free nature of the outer-sphere mechanism as introduced in Section 1.2.1. While an outer-sphere electron transfer to a H_2O_2 at the OHP is also possible, and in fact very likely to occur, a fully outer-sphere mechanism cannot explain differences in the ORR selectivities. In addition to the elucidation of the outer-sphere mechanism for the RDS, **Paper M3** further illustrates that the ORR selectivity, especially pertaining to the differences among

1 I assume the former definition for indirect processes, but note that an ”active-site” for the outer-sphere electron transfer is subject to interpretations.

M-N-Cs, cannot be fully explained with an outer-sphere process. This inspired a computational study of the specific interactions between MN_4 sites and H_2O_2, which will be presented in **Paper M4**.

For materials that exhibit high inner-sphere activity like Fe-N-Cs, the strong interactions between H_2O_2 and the active sites can be both a blessing and a curse. On the one hand, promoting the dissociation of H_2O_2 would ultimately lead to its subsequent reduction to water, increasing the overall current densities and preventing it from corroding other parts of the electrochemical cell. On the other hand, side reactions with H_2O_2 tend to produce reactive oxygen species (ROS) that accelerate the degradation of the catalyst via demetallation [18, 59] and oxidative destruction of the carbon matrix [60, 61], leading to highly active Fe-N-Cs losing their activities within hours of operation [21, 62]. While the degradation mechanism of Fe-N-Cs is not fully understood so far, the Fenton reaction is commonly identified as the culprit [63]. In an ideal H_2O_2RR mechanism, a H_2O_2 molecule would dissociate into OH ligands that would later desorb as hydroxide or water (Figure 1.1, bottom). The Fenton reaction is mechanistically similar, also involving the dissociation of a H_2O_2, but with one ·OH desorbing as a radical instead (Figure 1.1, bottom). Despite its rare occurrence relative to the desired H_2O_2RR, the occasional ROS generated by the Fenton reaction would gradually destroy the catalyst. In a recent work by Eigler *et al.*, the Fenton reaction has been reported, and even exploited, to enlarge defects in graphene for other applications, showcasing its significant morphological influence on carbon-based materials [64]. In **Paper M4**, we examine the specific interactions between the MN_4 site and H_2O_2 to provide a clearer understanding on how these interactions could correlate to the selectivity and stability of M-N-Cs during ORR.

Although the Fenton reaction is effectively a disease for 4e-ORR catalysis, it can be advantageous in situations where ·OH radicals are desired. In biochemistry, the targeted production of ROS from H_2O_2, for example with the peroxidase enzyme [65, 66], is relevant for the elimination of harmful bacteria and tumor cells [11, 67]. Recently, the Fenton-like activity of certain M-N-Cs has been exploited for the treatment of various medical conditions [11], including cancer [68–70], bacteria-infected wounds [71, 72] and diabetic ulcers [73]. Due to their higher Fenton activities compared to biocatalysts based on the peroxidase enzyme, they not only reduce the material cost for the treatment, but also the required H_2O_2 dosage, potentially lowering the toxicity of the treatment. **Paper S1** features a mechanistic study of the Fenton reaction on a trivalent Cu-N-C which is used in combination with gold nanoparticles to treat diabetic ulcers.

Although the study has little to do with electrochemistry, the conclusions derived from the mechanistic studies are expected to be relevant for the Fenton-induced degradation of Fe-N-Cs during ORR.

1.2.3 Carbon Dioxide Reduction Reaction

In the context of carbon capture and utilization (CCU), the CO_2RR (Figure 1.1, right) encompasses a promising class of reactions that convert the greenhouse gas CO_2 to useful chemical products through an input of electrical energy, ideally from a renewable source. The products of CO_2RR are extremely diverse, ranging from 2-electron products like carbon monoxide (CO) and formic acid (HCOOH) to higher carbon "C_{2+}" products [74]. Universally, CO_2RR electrocatalysts have to overcome the hurdle of suppressing the competing hydrogen evolution reaction (HER, Figure 1.1, right), requiring active sites that interact selectively with CO_2 instead of the huge reservoir of protons in the aqueous medium.

For M-N-Cs featuring atomically dispersed active sites, the CO_2RR selectivity is generally confined to 2-electron C_1 products CO [10, 75, 76] and HCOOH [77] due to the inability of a single atom site to promote C-C coupling. In particular, high Faradaic efficiencies for CO ($FE_{CO} > 90\%$) have been reported for Ni-N-Cs [9, 78–80]. This pronounced reactivity towards CO_2RR brings joy to experimentalists, but simultaneously presents a conundrum for computational chemists, as DFT studies often predict a highly unstable *COOH intermediate at the NiN_4 sites [10, 16, 81, 82], presenting a large electrochemical barrier to the reaction. In order to explain the discrepancy between theory and experiment, modified NiN_x sites were proposed, including those with broken symmetries [83], N-unsaturated NiN_xC_{4-x} sites [84, 85] and trivalent NiN_3 sites [81, 82]. Although these sites would theoretically lower the electrochemical barrier for *COOH, they generally do not explain how CO_2RR would be preferentially enhanced compared to HER. Furthermore, in **Paper M5**, the modified Ni sites are even less justifiable since the materials were obtained after transmetallation from a templated MgN_4 site, with an excellent structural fit to the pyrrolic NiN_4 coordination.

Since the high CO_2RR activity and selectivity were observed even on a defined NiN_4 site in **Paper M5**, there has to be a mechanistic explanation for the theory-experiment discrepancy that does not involve structural modifications to the active sites. In a study by Asset *et al.*, the reactivity of Ni-N-Cs seems to be correlated to the weak binding of CO on the NiN_4 site [75]. Despite the irony, it should be noted that Ni-N-Cs are just another addition to the catalog of CO_2RR

catalysts that are historically poor in reactivity, including the noble metals Cu [86, 87], Ag [88] and Au [89]. Recently, studies of CO_2RR on these metal surfaces elucidated the involvement of cations in the CO_2RR mechanisms, suggesting that they are not mere spectators, but rather decisive enablers for the CO_2RR mechanisms [90–97]. In these studies, the cations' involvement appears to be transient in nature, as the metal surfaces did not seem to favor the adsorption of cations. In **Paper M5**, we examine the influence of cations on the CO_2RR mechanism at the NiN_4 site, as well as the role of pyrrolic N atoms in promoting their adsorption.

As a whole, the thesis is structured to cover many aspects of M-N-C catalysis, ranging from its synthetic birth to potential causes of its death by morphological destruction. **Paper M1** and **Paper M2** focus on the synthesis aspect of these materials, especially in relation to the templating effect of the metals for the templating-transmetallation strategy. **Paper M3**, **Paper M4** and **Paper M5** and **Paper S1** feature the studies of (electro)catalytic mechanisms, corresponding to their potential careers as electrocatalysts and biocatalysts. Finally, factors influencing the morphological destruction of the catalysts are also discussed briefly, particularly in relation to the carbothermal reduction in **Paper M1** and **Paper M2** as well as the Fenton-induced degradation of the catalyst in **Paper M4**, supported by the mechanistic study of this reaction in **Paper S1**.

2 Theory and Methods

"Experience without theory is blind, but theory without experience is mere intellectual play."

-Immanuel Kant

This chapter introduces the theory for the ab-initio modeling of chemical properties based on electronic structure methods. Section 2.1 introduces the principles of quantum mechanics, linking the fundamental Schrödinger equation to DFT, the main workhorse of quantum chemistry today. In Section 2.2, a connection between virtual simulations and the physical reality is established through the concepts of physical chemistry, providing the foundation for interdisciplinary research between computational and experimental chemists.

2.1 Quantum Mechanics

Due to significant advancements in computing efficiencies over the past decades, quantum chemistry has become a relatively low-cost, low-risk, high-output method for understanding chemical interactions at the atomic-level, enabling the predictions of material properties and guiding the design of molecules and materials for numerous applications. Sections 2.1.1 and 2.1.2 introduce the fundamental Schrödinger equation and approximations required to reduce its dimensionality. Section 2.1.3 highlights the variational principle, which centrally serves as a guide towards the quantum mechanical ground state in the hunt for approximate solutions. Founded on this principle, two main approaches to calculate the electronic ground state are introduced, namely the Hartree-Fock method (Section 2.1.4) and the Kohn-Sham DFT (Section 2.1.5). In Section 2.1.6, we examine further practical aspects regarding the DFT calculations specific to this study. This section is written with reference to textbooks by Szabo and Ostlund for general quantum chemistry [98], Koch and Holthausen for the application of DFT to chemical problems [99], and Kittel for the discussion of periodic electronic structures [100]. Unless specified otherwise, the equations and quantities in this section are expressed in the computationally convenient atomic units [101].

2.1.1 Schrödinger equation

The Schrödinger equation [102] (SE) lays the theoretical foundation for quantum chemistry calculations

$$\hat{H}\Phi(\boldsymbol{x}, \boldsymbol{R}, t) = i\frac{\delta}{\delta t}\Phi(\boldsymbol{x}, \boldsymbol{R}, t) \tag{2.1}$$

where Φ is the full wave function described by the spatial and spin coordinates of all electrons $\boldsymbol{x}$, nuclear coordinates $\boldsymbol{R}$ and time t. For a molecular system with M atomic nuclei and N electrons in the absence of potential energy perturbation, the non-relativistic Hamiltonian can be written, in atomic units, as

$$\hat{H} = \hat{T}_\mathrm{e} + \hat{T}_\mathrm{n} + \hat{V}_\mathrm{ne} + \hat{V}_\mathrm{ee} + \hat{V}_\mathrm{nn} \tag{2.2}$$

$$= -\frac{1}{2}\sum_{i=1}^{N}\nabla_i^2 - \frac{1}{2}\sum_{A=1}^{M}\frac{1}{M_A}\nabla_A^2 - \sum_{i=1}^{N}\sum_{A=1}^{M}\frac{Z_A}{r_{iA}} + \sum_{i=1}^{N}\sum_{j>i}^{N}\frac{1}{r_{ij}} + \sum_{A=1}^{M}\sum_{B>A}^{M}\frac{Z_A Z_B}{R_{AB}} \tag{2.3}$$

where $\hat{T}_\mathrm{e}$ and $\hat{T}_\mathrm{n}$ are operators for the kinetic energy of the electrons and nuclei respectively whereas $\hat{V}_\mathrm{ne}$, $\hat{V}_\mathrm{ee}$ and $\hat{V}_\mathrm{nn}$ describe the Coulomb interactions between each pair of charged particles. $\{\nabla_i^2\}$ and $\{\nabla_A^2\}$ are the respective Laplacians of the spatial coordinates of electrons and nuclei.[2] $\{M_A\}$ and $\{Z_A\}$ are the masses and charges of the nuclei relative to an electron. $\{r_{iA}\}$, $\{r_{ij}\}$ and $\{R_{AB}\}$ are the distances between respective charged particles.

Due to the time-independence of the molecular Hamiltonian, the full wave function Φ can be separated into a position-dependent wave function $\Psi(\boldsymbol{x}, \boldsymbol{R})$ and a relatively trivial time-dependent phase function, leading to the famous time-independent SE

$$\hat{H}\Psi(\boldsymbol{x}, \boldsymbol{R}) = E\Psi(\boldsymbol{x}, \boldsymbol{R}) \tag{2.4}$$

$$\Phi(\boldsymbol{x}, \boldsymbol{R}, t) = \Psi(\boldsymbol{x}, \boldsymbol{R})\exp(-iEt) \tag{2.5}$$

Without any approximation, the time-independent SE is a differential equation which depends on $4N$ electronic (spatial and spin) coordinates and $3M$ nuclear coordinates and is incredibly difficult to solve. Exact solutions to the time-independent SE are only known for one-particle systems (*e.g.* particle in a box, rigid rotors, harmonic oscillators) and some multi-particle systems in which all but one particle can be treated as immobile (*e.g.* hydrogen-like atoms, diatomic

2 Braces { } are used to define a set of quantities in this thesis.

harmonic oscillators). For most chemically relevant systems, however, an exact solution does not exist, and numerous approximations are required to approach a chemically interpretable solution.

2.1.2 Born Oppenheimer Approximation

The first major simplification is achieved through the Born-Oppenheimer approximation [103], exploiting the fact that electrons are much lighter than nuclei and can be assumed to adjust their distributions instantaneously to the nuclear coordinates. This allows us to define, from the perspective of an electron, the electronic Hamiltonian which is independent of nuclear motion ($T_\mathrm{n} = 0$, $V_\mathrm{nn} = \mathrm{constant}$) but parametrically dependent on nuclear positions through $\hat{V}_\mathrm{ne}$

$$\hat{H}_\mathrm{el} = \hat{T}_\mathrm{e} + \hat{V}_\mathrm{ee} + \hat{V}_\mathrm{ne} \tag{2.6}$$

with its own eigenfunctions Ψ_el defined by the electronic SE

$$\hat{H}_\mathrm{el}\Psi_\mathrm{el}(\boldsymbol{x};\boldsymbol{R}) = E_\mathrm{el}\Psi_\mathrm{el}(\boldsymbol{x};\boldsymbol{R}) \tag{2.7}$$

where E_el is the energy of the electrons in an electronic state defined by Ψ_el. The electronic energy E_el combines with the inter-nuclear repulsion term V_nn to an effective potential energy surface V_PES

$$V_\mathrm{PES}(\boldsymbol{R}) = E_\mathrm{el}(\boldsymbol{R}) + V_\mathrm{nn}(\boldsymbol{R}) \tag{2.8}$$

leading to the definition of the nuclear SE to describe nuclear motions (translation, rotation, vibration).

$$\hat{H}_\mathrm{n}\Phi_\mathrm{n}(\boldsymbol{R}) = \left(\hat{T}_\mathrm{n} + V_\mathrm{PES}\right)\Phi_\mathrm{n}(\boldsymbol{R}) = E_\mathrm{BO}\Phi_\mathrm{n}(\boldsymbol{R}) \tag{2.9}$$

where Φ_n is the nuclear wave function and E_BO is the total energy of the system within the Born-Oppenheimer approximation.[3] However, since nuclear motions are relatively slow and the non-analytical form of the PES makes the nuclear SE rather challenging to solve, the nuclear motions are typically either treated classically (*e.g.* force-based propagation during geometry optimization) or approximated using analytical models like the particle in a box, the rigid rotor and the

3 The Born Oppenheimer approximation assumes no diabatic coupling between electronic and nuclear motion, and breaks down at nuclear coordinates where the PES of two electronic states intersect.

harmonic oscillator to describe translation, rotations and vibrations respectively. We will discuss the use of analytical models to approximate thermodynamic state functions arising from nuclear motions in Section 2.2.1, and focus solely on obtaining approximate solutions to the electronic SE in this chapter.

2.1.3 Variational Principle

In theory, solving any SE exactly would give all possible eigenstates defined by the Hamiltonian, as in the case of the hydrogen atom. However, in practice, further approximations to the solution of the electronic SE limit the numerical solution to the electronic ground state and low-lying excited states. A central idea to obtain an approximate ground-state solution to any time-independent SE is the variational principle. Considering that the eigenfunctions to a Hamiltonian form a complete orthogonal basis, any other functions Ψ_{trial} in the same functional space can be described as a linear expansion of these eigenfunctions.

$$\Psi_{\text{trial}} = \sum_{i=0}^{\infty} c_i \Psi_i \tag{2.10}$$

where $\{c_i\}$ is the set of expansion coefficients for eigenfunctions $\{\Psi_i\}$. If the eigenfunctions are normalized, the squared expansion coefficients have to sum to unity,

$$\sum_{i=0}^{\infty} c_i^2 = 1 \tag{2.11}$$

in which case the energy can be written as the expectation value of the Hamiltonian

$$E_{\text{trial}} = \left\langle \Psi_{\text{trial}} \middle| \hat{H} \middle| \Psi_{\text{trial}} \right\rangle = \sum_{i=0}^{\infty} c_i^2 E_i \leq E_0. \tag{2.12}$$

Since the energy expectation value E_{trial} is effectively a $\{c_i^2\}$-weighted average of the energy eigenvalues $\{E_i\}$, the energy of a trial wave function can never be lower than the ground state energy E_0. If the trial wave function is parametrized with $\{C_k\}$, the set of parameters that give the lowest energy would be the closest we get to the true ground state based on the parametrization ansatz. Mathematically, the energy minimum in the entire parameter space is defined where the total differential is zero

$$dE_{\text{trial}} = \sum_k \left(\frac{\delta E_{\text{trial}}}{\delta C_k} \right) \mathrm{d}C_k = 0 \tag{2.13}$$

which implies for independent parameters that each individual partial derivative is 0

$$\frac{\delta E_{\text{trial}}}{\delta C_k} = 0 \tag{2.14}$$

For electronic structure calculations, electronic wave functions are often expanded as a linear combination of basis functions, such as atom-centered basis functions (inspired by atomic orbitals) for molecular DFT and plane-wave basis functions for periodic DFT calculations. As such, the parameters to be optimized within the variational framework are often the respective coefficients of the basis function. The basis set expansion will be further discussed in Section 2.1.6

2.1.4 Hartree Fock Theory

Even considering the Born-Oppenheimer approximation, a single differential equation of $4N$ electronic coordinates is still impossible to solve analytically for $N > 1$. Fortunately, with the aid of high performance computing, approximate numerical solutions are increasingly accessible. One of the most fundamental numerical methods for approximately solving the electronic SE is the Hartree Fock (HF) method. Although the HF method is not explicitly used in this work, the approximations and insights obtained from this approach are applicable to other orbital-based quantum chemistry calculations like Kohn-Sham DFT. In the HF approach, the N-electron wave function is approximated as the Slater determinant of N single-electron wave functions [104, 105],

$$\Psi_{\text{el}} \approx \Psi_{\text{SD}} = \frac{1}{\sqrt{N!}} \begin{vmatrix} \chi_1(\boldsymbol{x}_1) & \chi_2(\boldsymbol{x}_1) & \dots & \chi_N(\boldsymbol{x}_1) \\ \chi_1(\boldsymbol{x}_2) & \chi_2(\boldsymbol{x}_2) & \dots & \chi_N(\boldsymbol{x}_2) \\ \vdots & \vdots & & \vdots \\ \chi_1(\boldsymbol{x}_N) & \chi_2(\boldsymbol{x}_N) & \dots & \chi_N(\boldsymbol{x}_N) \end{vmatrix} \tag{2.15}$$

where each spin-orbital χ_a is a product of the spatial orbital ψ_a and a spin function σ_a

$$\chi_a(\boldsymbol{x_i}) = \psi_a(\boldsymbol{r_i})\sigma_a(m_{\text{s,i}}) \tag{2.16}$$

where $\{a\}$ numbers the orbitals and $\{i\}$ numbers the electrons. This ansatz is designed to obey the Pauli principle, which states that a wave function describing multiple electrons (or fermions in general) should be anti-symmetric with respect to an exchange of coordinates between two electrons [106]. Inserting the Slater determinant into the electronic SE (Equation 2.7) and integrating over all

coordinates, we obtain the expression for the HF energy

$$E_{\mathrm{HF}} = \left\langle \Psi_{\mathrm{SD}} \middle| \hat{H}_{\mathrm{el}} \middle| \Psi_{\mathrm{SD}} \right\rangle \tag{2.17}$$

$$= \sum_a h_a + \frac{1}{2} \sum_a \sum_b (J_{ab} - K_{ab}) \tag{2.18}$$

where $\{h_a\}$ are the hypothetical orbital energies for a fictitious system of non-interacting electrons

$$h_a = \int \mathrm{d}\boldsymbol{x}_i \left[\chi_a^*(\boldsymbol{x}_i) \left(-\frac{1}{2} \boldsymbol{\nabla}_i^2 - \sum_{A=1}^{N} \frac{Z_A}{r_{iA}} \right) \chi_a(\boldsymbol{x}_i) \right] = \left\langle \chi_a \middle| \hat{h} \middle| \chi_a \right\rangle \tag{2.19}$$

while $\{J_{ab}\}$ and $\{K_{ab}\}$ are the two-electron integrals capturing the electron-electron interactions $\hat{V}_{\mathrm{ee}}$

$$\left\langle \hat{J}_{ab} \right\rangle = \int \int \left[\chi_a^*(\boldsymbol{x}_i) \chi_b^*(\boldsymbol{x}_j) \left(\frac{1}{r_{ij}} \right) \chi_a(\boldsymbol{x}_i) \chi_b(\boldsymbol{x}_j) \right] \mathrm{d}\boldsymbol{x}_i \mathrm{d}\boldsymbol{x}_j \tag{2.20}$$

$$= \left\langle \chi_a(\boldsymbol{x}_i) \chi_b(\boldsymbol{x}_j) \middle| \frac{1}{r_{ij}} \middle| \chi_a(\boldsymbol{x}_i) \chi_b(\boldsymbol{x}_j) \right\rangle \tag{2.21}$$

$$\left\langle \hat{K}_{ab} \right\rangle = \int \int \left[\chi_a^*(\boldsymbol{x}_i) \chi_b^*(\boldsymbol{x}_j) \left(\frac{1}{r_{ij}} \right) \chi_b(\boldsymbol{x}_i) \chi_a(\boldsymbol{x}_j) \right] \mathrm{d}\boldsymbol{x}_i \mathrm{d}\boldsymbol{x}_j \tag{2.22}$$

$$= \left\langle \chi_a(\boldsymbol{x}_i) \chi_b(\boldsymbol{x}_j) \middle| \frac{1}{r_{ij}} \middle| \chi_b(\boldsymbol{x}_i) \chi_a(\boldsymbol{x}_j) \right\rangle \tag{2.23}$$

The Coulomb term $\left\langle \hat{J}_{ab} \right\rangle$ can be interpreted classically as the mean field Coulomb repulsion term between the electron density of orbital a ($\rho_a = \chi_a^* \chi_a$) and that of orbital b ($\rho_b = \chi_b^* \chi_b$). In contrast, the exchange term $\left\langle \hat{K}_{ab} \right\rangle$ does not have a classical interpretation, but simply arises from the antisymmetry of the electronic wave function.

The Slater determinant is essentially a trial wave function (Equation 2.10) containing parameters within the definition of the spin-orbitals. Applying the variation principle to Equation 2.18 ($\mathrm{d}E_{\mathrm{HF}} = 0$) under the constraint that the spin-orbitals are orthonormal, we obtain a series of Fock equations that optimize the occupied spin-orbitals $\{\chi_a\}$

$$\hat{f} \chi_a(\boldsymbol{x}_i) = \left[\hat{h} + \frac{1}{2} \sum_b \left(\hat{J}_{ab} - \hat{K}_{ab} \right) \right] \chi_a(\boldsymbol{x}_i) = \epsilon_a \chi_a(\boldsymbol{x}_i) \tag{2.24}$$

where $\hat{h}$ is the one electron operator defined in Equation 2.19. Each Coulomb

operator $\hat{J}_{ab}$ and exchange operator $\hat{K}_{ab}$ captures the interactions between two electrons in the spin-orbital to be solved χ_a and another spin-orbital χ_b

$$\hat{J}_{ab}\chi_a(\boldsymbol{x}_i) = \left[\int \chi_b^*(\boldsymbol{x}_j)\left(\frac{1}{r_{ij}}\right)\chi_b(\boldsymbol{x}_j)\mathrm{d}\boldsymbol{x}_j\right]\chi_a(\boldsymbol{x}_i) \tag{2.25}$$

$$\hat{K}_{ab}\chi_a(\boldsymbol{x}_i) = \left[\int \chi_b^*(\boldsymbol{x}_j)\left(\frac{1}{r_{ij}}\right)\chi_a(\boldsymbol{x}_j)\mathrm{d}\boldsymbol{x}_j\right]\chi_b(\boldsymbol{x}_i) \tag{2.26}$$

such that projection of each term onto $\langle\chi_a(\boldsymbol{x}_i)|$ returns Equations 2.21 and 2.23. It should be mentioned that for $b = a$, the so-called self-interaction terms $\hat{J}_{aa} = \hat{K}_{aa}$ cancel out in Equation 2.24. Thus, there is no need to uniquely define the Fock operator with "$b \neq a$" for each spin-orbital in Equation 2.24 (*i.e.* the Fock operator $\hat{f}$ is universal for all spin-orbitals in the system).

Based on the Fock equations, we can now introduce a parametrized definition of the spin-orbitals to be optimized. For molecular systems, the most chemically intuitive form of the definition is the MO-LCAO (molecular orbitals - linear combination of atomic orbitals) theory

$$\psi_a = \sum_{\nu=1}^{L} c_{\nu a}\phi_\nu \tag{2.27}$$

where $\{\phi_\nu\}$ are basis functions which closely resemble atomic orbitals (AO) and $\{c_{\nu a}\}$ are the respective coefficients of each basis function in molecular orbital (MO) ψ_a. Inserting Equation 2.27 into the Fock Equation 2.24, and projecting onto each basis function $\langle\phi_\mu|$ yields the Roothan-Hall matrix equation [107, 108]

$$\boldsymbol{FC} = \boldsymbol{\epsilon SC} \tag{2.28}$$

with the coefficient matrix $\boldsymbol{C}$ mapping each MO to its constituent basis functions, the Fock matrix elements $F_{\mu\nu} = \left\langle\phi_\mu\middle|\hat{f}\middle|\phi_\nu\right\rangle$ and overlap integral $S_{\mu\nu} = \langle\phi_\mu|\phi_\nu\rangle$ and a diagonal matrix of the orbital energy eigenvalue $\boldsymbol{\epsilon}$.

In essence, the HF method decomposes the N-electron problem into a series of N one-electron eigenvalue problems defined by the Fock equations (Equation 2.24). However, it can be seen in Equations 2.25 and 2.26 that the definition of the Fock operator $\hat{f}$ already requires an input of the orbitals. Consequently, the Fock equations have to be solved iteratively in a self-consistent field (SCF) procedure. Starting from an initial guess of the coefficient matrix $\boldsymbol{C}_0$, the Fock operator $\hat{f}_0$ is defined and the Fock matrix $\boldsymbol{F}_0$ can be constructed. Solving the

Roothan-Hall equation gives a new coefficient matrix $\boldsymbol{C}_1$ which can be used to construct a new Fock matrix $\boldsymbol{F}_1$. This procedure is iterated until self-consistency, such that solving the Roothan-Hall equation using $\boldsymbol{F}_{\text{iter}-1}$ and $\boldsymbol{C}_{\text{iter}-1}$ gives back the same coefficient matrix ($\boldsymbol{C}_{\text{iter}} \approx \boldsymbol{C}_{\text{iter}-1}$). Computationally, the SCF convergence is defined when the change in E_{HF} is smaller than a given energy threshold. Additional criteria can also be given, such as the change in the individual orbital energies $\{\epsilon_a\}$.

As seen in Equation 2.21, each Coulomb term J_{ab} represents the mean-field repulsion between the density of an electron in orbital χ_a and another in orbital χ_b, implicitly assuming that electron distributions are independent. In reality, due to their repulsive interactions, electrons tend to avoid one another and the electron coordinates are thus not mutually independent variables. This leads to a single, but significant error in the HF description of Coulomb interaction called the correlation energy E_{corr}, which is defined as

$$E_{\text{corr}} = E_0 - E_{\text{HF}} \tag{2.29}$$

where E_0 is the true ground state energy and E_{HF} is the HF limit of the single Slater-determinant ansatz. While the HF method itself does not generally give accurate results due to the negligence of the correlation energy, the optimized Slater determinant becomes a crucial starting point for constructing better wave functions that capture such effects. For example, the Møller-Plessets perturbation theory [109] (MP2, MP3,...) treats the correlation operator $\hat{V}_{\text{corr}} = \hat{H} - \hat{F}$ as a perturbation to the Fock operator $\hat{F}$ in order to apply progressive corrections to the HF wave function. Alternatively, the extensive class of truncated configuration interaction (CI) methods construct excited Slater determinants from the Fock orbitals, each representing an electronic configuration and given a coefficient (weight) to be optimized within the variational principle. While the post-HF methods have the advantage of being systematically improvable, the major drawback of these methods is their enormous computational costs, for example with the cheapest member MP2 scaling to $O(N^5)$ and the ”gold standard” CCSD(T) calculations scaling to $O(N^7)$.

2.1.5 Density Functional Theory

An alternative approach to wave function based methods is to shift the perspective from the full 4N-dimensional wave function to a combined 3-dimensional electron density distribution. Considering that electrons are indistinguishable, it is only

necessary to track the spatial distribution of a single electron to obtain the (spin-free) 3-dimensional electron density of a molecule

$$\rho(\boldsymbol{r}_1) = N \sum_{m_{s1}} \int \ldots \int |\Psi_{\mathrm{el}}(\boldsymbol{x}_1, \boldsymbol{x}_2, \ldots, \boldsymbol{x}_n)|^2 \, \mathrm{d}\boldsymbol{x}_2 \ldots \mathrm{d}\boldsymbol{x}_N \tag{2.30}$$

The first attempt at using the electron density to derive system observables was made by Thomas and Fermi in their description of the free-electron gas [110, 111]. However, the validity of such a simplification could not be justified until decades later, when Hohenberg and Kohn introduced two groundbreaking theorems founded on the variational principle [112]. The first Hohenberg-Kohn theorem states that electronic Hamiltonians $\hat{H} = \hat{T}_{\mathrm{e}} + \hat{V}_{\mathrm{ee}} + \hat{V}_{\mathrm{ext}}$ that differ only in the external potential $\hat{V}_{\mathrm{ext}}$ by more than a constant cannot have the same ground state density. Consequently, any physically meaningful electron density could be directly mapped to (the non-constant part of) the external potential V_{ext}, and by extension the Hamiltonian, of which it is the ground state density. Any ground state property of a system defined by this unique Hamiltonian could be expressed as a functional of the ground state density ρ_0. In particular, the ground state energy can be expressed as

$$E_0 = E_0[\rho_0] = T[\rho_0] + E_{\mathrm{ee}}[\rho_0] + E_{\mathrm{ext}}[\rho_0] \tag{2.31}$$

$$= F_{\mathrm{HK}}[\rho_0] + \int \rho_0(\boldsymbol{r}) V_{\mathrm{ext}} \, \mathrm{d}\boldsymbol{r} \tag{2.32}$$

where we split the ground state energy functional into a system dependent external potential energy functional E_{ext} and a universally valid, but universally unknown, Hohenberg-Kohn functional $F_{\mathrm{HK}}[\rho_0] = T[\rho_0] + E_{\mathrm{ee}}[\rho_0]$. For a chemical system, since we are only interested in a pre-determined external potential V_{ne} (*e.g.* a molecule in a certain structure), it is desirable to find the ground state density that determines this specific Hamiltonian ($V_{\mathrm{ext}} = V_{\mathrm{ne}}$). This brings us to the second Hohenberg-Kohn theorem. With an arbitrary trial density $\tilde{\rho}$ defining its own Hamiltonian with the corresponding ground state wave function $\tilde{\Psi}$, we apply the variational principle using $\tilde{\Psi}$ as a trial wave function for the true Hamiltonian $\hat{H}$

$$E[\tilde{\rho}] = \left\langle \tilde{\Psi} \middle| \hat{H} \middle| \tilde{\Psi} \right\rangle \geq \left\langle \Psi_0 \middle| \hat{H} \middle| \Psi_0 \right\rangle = E[\rho_0] \tag{2.33}$$

leading to the conclusion that the ground state energy functional is at its minimum if and only if the trial density is the ground state density. Although the Hohenberg-Kohn theorems fundamentally prove that the ground state density is sufficient

to determine the ground state properties of a system and has an equivalent variational framework for approaching the solution, they do not contain any information of how to map a ground state density to its Hamiltonian and *vice versa*. In particular, without the exact form of the Hohenberg-Kohn functional F_{HK} in Equation 2.32, there is no way tell whether an electron density is indeed the ground state density of our desired system, or that of some other system.

A common scientific framework to approach an unknown function is to assume a theoretical model as a starting point and correct for the errors associated with this model. This can be done for each term in the Hohenberg-Kohn functional. The electron-electron repulsion term E_{ee} can be expressed as

$$E_{\mathrm{ee}}[\rho] = J[\rho] + E_{\mathrm{ncl}}[\rho] = \frac{1}{2}\int\int \frac{\rho(\boldsymbol{r}_1)\rho(\boldsymbol{r}_2)}{r_{12}}\mathrm{d}\boldsymbol{r}_1\mathrm{d}\boldsymbol{r}_2 + E_{\mathrm{ncl}}[\rho]. \tag{2.34}$$

where J is the classical mean-field electron-electron repulsion term and E_{ncl} is the error arising from non-classical contributions. Noting that the densities here refer to the N-electron densities instead of orbitals in HF (Equation 2.21), there is no equivalent expression for the exchange energy of Equation 2.23. Therefore, the non-classical contribution E_{ncl} contains not only the correlation energy neglected by the mean-field treatment, but also the exchange energy and self-interaction energy. The kinetic energy term in the Hohenberg Kohn functional, while relatively straightforward in the orbital picture, cannot easily be expressed in terms of the N-electron density. In order to provide a reasonable starting point, Kohn and Sham reintroduced the concept of orbitals by defining a fictitious reference system of non-interacting electrons where the Hamiltonian can be separated into one-electron Kohn-Sham (KS) operators $\hat{f}^{\mathrm{KS}}$ [113]

$$\hat{H}_{\mathrm{ref}} = -\frac{1}{2}\sum_i^N \nabla_i^2 + \sum_i^N V_{\mathrm{eff}}(\boldsymbol{r}_i) = \sum_i^N \hat{f}_i^{\mathrm{KS}} \tag{2.35}$$

with V_{eff} as the effective potential for this non-interacting system. The KS operators f^{KS} have its own set of eigenfunctions known as the KS orbitals ϕ_a

$$\hat{f}_1^{\mathrm{KS}}\phi_a(\boldsymbol{r}_1) = \left(-\frac{1}{2}\nabla_1^2 + V_{\mathrm{eff}}(\boldsymbol{r}_1)\right)\phi_a(\boldsymbol{r}_1) = \epsilon_a\phi_a(\boldsymbol{r}_1) \tag{2.36}$$

Since the electrons are indistinguishable, solving the KS equations for $\boldsymbol{r}_1$ is as good as solving it for any other electron. Just like the HF method (Section 2.1.4),

the orbitals combine into the total KS wave function with a Slater determinant

$$\Psi_{\mathrm{KS}} = \frac{1}{\sqrt{N!}} \begin{vmatrix} \phi_1(\boldsymbol{r}_1)\sigma_1(m_{s1}) & \phi_2(\boldsymbol{r}_1)\sigma_2(m_{s1}) & \dots & \phi_N(\boldsymbol{r}_1)\sigma_N(m_{s1}) \\ \phi_1(\boldsymbol{r}_2)\sigma_1(m_{s2}) & \phi_2(\boldsymbol{r}_2)\sigma_2(m_{s2}) & \dots & \phi_N(\boldsymbol{r}_2)\sigma_N(m_{s2}) \\ \vdots & \vdots & & \vdots \\ \phi_1(\boldsymbol{r}_N)\sigma_1(m_{sN}) & \phi_2(\boldsymbol{r}_N)\sigma_2(m_{sN}) & \dots & \phi_N(\boldsymbol{r}_N)\sigma_N(m_{sN}) \end{vmatrix} \tag{2.37}$$

where $\{\sigma_i\}$ are the spin function for the KS spin orbitals. The ansatz of an anti-symmetrized product of the orbitals allows the total density to be written as a sum of individual spatial orbital densities

$$\rho_{\mathrm{ref}}(\boldsymbol{r}_1) = \sum_{a=1}^{N} |\phi_a(\boldsymbol{r}_1)|^2 \tag{2.38}$$

with the density of this reference system defined to be identical to that of the real system ($\rho_0(\boldsymbol{r}_1) = \rho_{\mathrm{ref}}(\boldsymbol{r}_1)$). The KS method extracts the kinetic energy of the reference system T_{S} from the individual KS orbitals

$$T_{\mathrm{ref}}[\rho] = -\frac{1}{2}\sum_a \langle \phi_a | \nabla^2 | \phi_a \rangle = T[\rho] - \Delta T[\rho]. \tag{2.39}$$

However, since the orbitals are not the orbitals of the true system, there is an associated error for the kinetic energy ΔT. Combining equations 2.34, 2.39 into Equation 2.32, the true energy functional can be expressed as

$$\begin{aligned} E_0[\rho(\boldsymbol{r}_1)] &= E_{\mathrm{ne}}[\rho] + T_{\mathrm{e}}[\rho] + E_{\mathrm{ee}}[\rho] && (2.40)\\ &= E_{\mathrm{ne}}[\rho] + (T_{\mathrm{S}}[\rho] + \Delta T[\rho]) + (J[\rho] + E_{\mathrm{ncl}}[\rho]) && (2.41)\\ &= -\int \sum_A^M \rho(\boldsymbol{r}_1)\frac{Z_{\mathrm{A}}}{r_{1A}}\,\mathrm{d}\boldsymbol{r}_1 + \sum_a^N \langle \phi_a | \nabla^2 | \phi_a \rangle && (2.42)\\ &\quad + \frac{1}{2}\int\int \frac{\rho(\boldsymbol{r}_1)\rho(\boldsymbol{r}_2)}{r_{12}}\mathrm{d}\boldsymbol{r}_1\mathrm{d}\boldsymbol{r}_2 + E_{\mathrm{XC}}[\rho] && (2.43) \end{aligned}$$

where we define the exchange-correlation functional E_{XC} to capture every source of error that cannot be described by the model systems. In addition to the exchange energy and correlation energy, E_{XC} also contains the kinetic energy correction and self-interaction correction terms. Applying the variational principle in accordance with the second Hohenberg-Kohn theorem, under the constraint that the KS orbitals are orthonormal, we obtain an expression for the effective

potential V_{eff} in the Equation 2.36

$$V_{\text{eff}}(\boldsymbol{r}_1) = \int \frac{\rho(\boldsymbol{r}_2)}{r_{12}} \mathrm{d}\boldsymbol{r}_2 + V_{\text{XC}}(\boldsymbol{r}_1) - \sum_A^M \frac{Z_A}{r_{1A}} \tag{2.44}$$

where the exchange correlation potential V_{XC} is defined as

$$V_{\text{XC}} = \frac{\delta E_{\text{XC}}}{\delta \rho}. \tag{2.45}$$

Similar to the HF method (Equation 2.24), the definition of the KS operator $\hat{f}^{\text{KS}}$ already demands an input density, and Equation 2.36 thus requires an iterative self-consistent solution. In principle, the entirety of the KS formalism is exact and does not involve any approximation beyond those of electronic SE. However, it also does not bring us any closer to the exact solution, since everything we do not know about the Hohenberg-Kohn functional is merely transferred to definition of the exchange-correlation functional. In order to exploit the computational efficiency of using a 3-dimensional density description, it is necessary to find, calibrate and improve approximate forms of the exchange correlation functional E_{XC}, which is still an ongoing effort decades after the original implementation of KS-DFT.

The Exchange-Correlation Functional

The most fundamental approximation to the exchange-correlation functional is the local density approximation (LDA) based on a hypothetical system of uniform electron gas. For this model system, an exact analytical form of the exchange energy is known [114] while a highly accurate correlation energy could be obtained from quantum Monte Carlo sampling [115, 116].

$$E_{\text{XC}}^{\text{LDA}}[\rho] = \int \rho(\boldsymbol{r}) \epsilon_{\text{XC}}(\rho(\boldsymbol{r}))\, \mathrm{d}\boldsymbol{r} \tag{2.46}$$

where ϵ_{XC} is the exchange-correlation energy per particle of a uniform electron gas. For spin-unrestricted calculations, an analogous expression is defined by splitting the density based on their spin-orientations $\rho = \rho_\alpha + \rho_\beta$, leading to the local spin-density approximation (LSDA)

$$E_{\text{XC}}^{\text{LSDA}}[\rho_\alpha, \rho_\beta] = \int \rho(\boldsymbol{r}) \epsilon_{\text{XC}}\big(\rho_\alpha(\boldsymbol{r}), \rho_\beta(\boldsymbol{r})\big)\, \mathrm{d}\boldsymbol{r} \tag{2.47}$$

for which highly accurate exchange and correlation functionals are also known for a spin-polarized uniform electron gas. Within the LDA or LSDA approximation, each infinitesimal volume of the electron density is treated as if it were in a uniform electron gas of the same density. Thus, information about electron densities elsewhere are not factored into ϵ_{XC}, thereby making it a "local" approximation. Clearly, such a description is inherently flawed in molecular systems with non-uniform electron densities.

A major improvement to account for the inhomogeneity of the electron density could be achieved by incorporating the (local) gradient of the density $\nabla\rho$, and subsequently (local) curvatures of the density $\nabla^2\rho$, in the description of the exchange-correlation energy, leading to functionals in the generalized gradient approximation (GGA) or meta-GGA (mGGA) respectively

$$E_{\mathrm{XC}}^{\mathrm{GGA}}[\rho] = \int f(\rho, \nabla\rho)\, \mathrm{d}\boldsymbol{r} \tag{2.48}$$

$$E_{\mathrm{XC}}^{\mathrm{mGGA}}[\rho] = \int f(\rho, \nabla\rho, \nabla^2\rho)\, \mathrm{d}\boldsymbol{r} \tag{2.49}$$

where the respective integrand f does not have a universal expression, but is either calibrated to theoretically expected properties of the densities (*e.g.* PBE [116], TPSS [117]) or to reference values obtained from physical experiments or high-level wave function-based calculations (*e.g.* BLYP [118, 119], BP86 [118, 120]).

In Equation 2.34, the expression of the classical mean-field interaction J with the product of two N-electron densities effectively describes $\frac{1}{2}N \cdot N$ pairs of interactions instead of the expected $\binom{N}{2} = \frac{1}{2}N \cdot (N-1)$ pairs, leading to an unphysical picture of each electron interacting with itself. The self-interaction error is a persistent problem in LDA, GGA and mGGA functionals, often leading to an over-delocalization of electronic distributions, *i.e.* the delocalization error which will be discussed in Section 2.1.6. However, recall that in the Hartree Fock method (Section 2.1.4), the condition of $b \neq a$ was also not enforced in the Fock equations (Equation 2.24), such that it should also imply the erroneous $\frac{1}{2}N \cdot N$ pairs of interactions, but the self-interaction error could be elegantly eliminated through the cancellation of Coulomb and exchange interaction for $J_{\mathrm{aa}} - K_{\mathrm{aa}} = 0$. Thus, we apply the concept of the orbital-based exact exchange energy from the HF method to the DFT functionals

$$E_{\mathrm{X}}^{\mathrm{HF}} = \int\int \phi_a^*(\boldsymbol{r}_1)\phi_b^*(\boldsymbol{r}_2)\frac{1}{r_{12}}\phi_b(\boldsymbol{r}_1)\phi_a(\boldsymbol{r}_2)\, \mathrm{d}\boldsymbol{r}_1\, \mathrm{d}\boldsymbol{r}_2 \tag{2.50}$$

which should ideally address the self-interaction error using the KS orbitals $\{\phi_a, \phi_b\}$. However, this non-local description of the exchange interaction does not generally combine well with standard semi-local correlation functionals, leading to an erroneous description of the exchange-correlation hole if the exchange interaction was solely described with Equation 2.50 [99]. In order to achieve an optimal balance, the exact exchange is fractionally mixed with other (semi-local) GGA or mGGA exchange functionals, leading to a class of hybrid functionals

$$E_{XC} = aE_X^{HF} + (1-a)E_X^{(m)GGA} + E_C^{(m)GGA} \tag{2.51}$$

where the mixing parameter a is either determined empirically or deduced with theoretical reasonings. For the PBE0 functional applied in the majority of my work, a 25% exact exchange is mixed into the PBE functional

$$E_{XC}^{PBE0} = 0.25E_X^{HF} + 0.75E_X^{PBE} + E_C^{PBE} \tag{2.52}$$

as theoretically justified through a perturbative approach, and is thus free of empirical parameters [121]. Contrastingly, the B3LYP functional [122, 123] used in **Paper M5** incorporates 20% exact exchange in the functional

$$E_X^{B3LYP} = aE_X^{HF} + (1-a)E_X^{LDA} + b\Delta E_X^{B88} \tag{2.53}$$

$$E_C^{B3LYP} = cE_C^{VWN} + (1-c)E_C^{LYP} \tag{2.54}$$

where the parameters $a = 0.2$, $b = 0.72$ and $c = 0.19$ were optimized through empirical fitting to the atomization energies, ionization energies and proton affinities in the G2 data base [122]. E_X^{HF} is the exact exchange energy, E_X^{LDA} is the LDA exchange energy [114], ΔE_X^{B88} is the Becke's 1988 gradient-correction to the LDA exchange [118], E_C^{VWN} is the LDA correlation energy [115], and E_C^{LYP} is the GGA correlation functional by Lee, Yang and Parr [119]. While the use of hybrid functionals can reduce errors associated with self-interaction, it is not always feasible in practice. Since the exact exchange requires the explicit calculation of the four-centered integrals in Equation 2.50, the implementation of hybrid functionals incurs significantly higher computational costs than the GGA and mGGA functionals, making its implementation particular challenging for larger systems including crystalline materials discussed in the following section.

Periodic Systems

In the previous sections, it was emphasized that the computational cost of quantum chemical calculations generally exhibits polynomial dependence to the size of the chemical system. However, crystalline materials can be considered an exception, as they are theoretically infinite in size, but could still be described with a finite computational cost. This is achieved by exploiting the translational symmetry of these materials, such that translational vector $\boldsymbol{T}$ can be defined

$$\boldsymbol{T} = T_1\boldsymbol{a}_1 + T_2\boldsymbol{a}_2 + T_3\boldsymbol{a}_3 \tag{2.55}$$

where $\boldsymbol{a}_1$, $\boldsymbol{a}_2$ and $\boldsymbol{a}_3$ are the lattice vectors defining the unit cell (UC) and T_1, T_2 and T_3 are integers. The translational symmetry of a lattice dictates that the observable magnitude of any local property has to be exactly the same at a position displaced by the translation vector $\boldsymbol{T}$ (*i.e.* translational invariance). In a crystalline material, the periodic potential set up by the nuclei and electrons can be described with a Fourier expansion into plane waves

$$V(\boldsymbol{r}) = \sum_{\boldsymbol{G}} V_{\boldsymbol{G}} \exp(i\boldsymbol{G}\boldsymbol{r}) \tag{2.56}$$

where $\boldsymbol{G}$ is a 3-dimensional vector of Fourier modes in the reciprocal space (also known as momentum space or k-space). For each real-space direction $\boldsymbol{a}_i$, only plane waves with wavelengths $\lambda = \frac{|\boldsymbol{a}_i|}{n}$ for $n \in \mathbb{Z}$ satisfy the periodicity of the lattice. Consequently, for the discussion of the Fourier components, the continuous reciprocal space can be reduced to discrete points defined by the reciprocal space lattice vectors $\boldsymbol{b}_1$, $\boldsymbol{b}_2$ and $\boldsymbol{b}_3$ such that

$$\boldsymbol{b}_i \cdot \boldsymbol{a}_j = 2\pi\delta_{ij} \tag{2.57}$$

and the vector of Fourier modes $\boldsymbol{G}$ can be written as an integer sum of the reciprocal lattice parameters, analogous to the translational vector $\boldsymbol{T}$ in the real space

$$\boldsymbol{G} = G_1\boldsymbol{b}_1 + G_2\boldsymbol{b}_2 + G_3\boldsymbol{b}_3 \tag{2.58}$$

Similar to Equation 2.56, a periodic one-electron wave function ϕ can also described with a Fourier-expansion

$$\phi(\boldsymbol{r}) = \sum_{\boldsymbol{G}'} C_{\boldsymbol{G}'} \exp\left(i\boldsymbol{G}'\boldsymbol{r}\right) \tag{2.59}$$

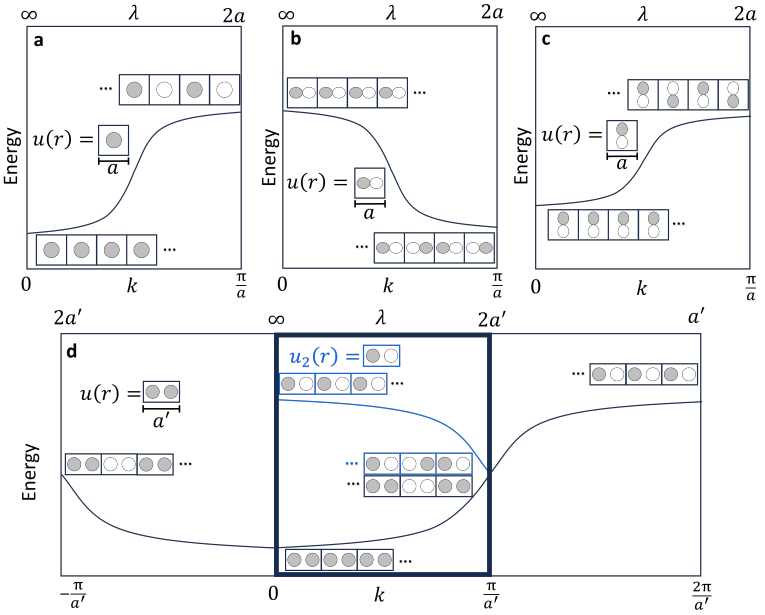

Figure 2.1: Illustration of the Bloch theorem for a linear chain of hydrogen atoms with lattice constant a for a (a) s-band, (b) p-band parallel to bonding axis and (c) p-band perpendicular to bonding axis. (d) Illustration of the redundancy of sampling beyond the irreducible Brillouin zone based on a diatomic unit cell. The blue band with a different $u_2(r)$ contains the same electronic states of $u(r)$ from $\frac{\pi}{a'} \leq k \leq \frac{2\pi}{a'}$.

where $\boldsymbol{G'}$ is, just like $\boldsymbol{G}$, a 3-dimensional vector of Fourier modes which can be defined in the reciprocal space lattice (Equation 2.58).

Just like in molecular calculations, $V_{\boldsymbol{G}}$ and $C_{\boldsymbol{G'}}$ are mutually dependent and thus require a self-consistent solution. For periodic DFT studies, this is achieved by inserting Equations 2.56 and 2.59 into the KS equations. The electronic states obtained upon solution of the KS equations generally obey Bloch's theorem [124], which states that a periodic wave function can be written as a product of a translational invariant unit-cell function $u(\boldsymbol{r})$ and a sinusoidal function $\exp(i\boldsymbol{kr})$ which describes the phase difference among unit cells

$$\phi_{\mathrm{k}}(\boldsymbol{r}) = u(\boldsymbol{r}) \exp(i\boldsymbol{kr}) \tag{2.60}$$

where $\boldsymbol{k}$ is the wave vector which relates to the wavelength in each lattice direction ($k_{1,2,3} = \frac{2\pi}{\lambda_{1,2,3}}$). Electronic states containing the same $u(\boldsymbol{r})$ are thus grouped together to define an electronic band, with variations in inter-UC phase difference described by $\boldsymbol{k}$.

The implications of Bloch's theorem can be understood by a didactic model of a 1-dimensional lattice of hydrogen atoms with lattice constant a (Figure 2.1). Each

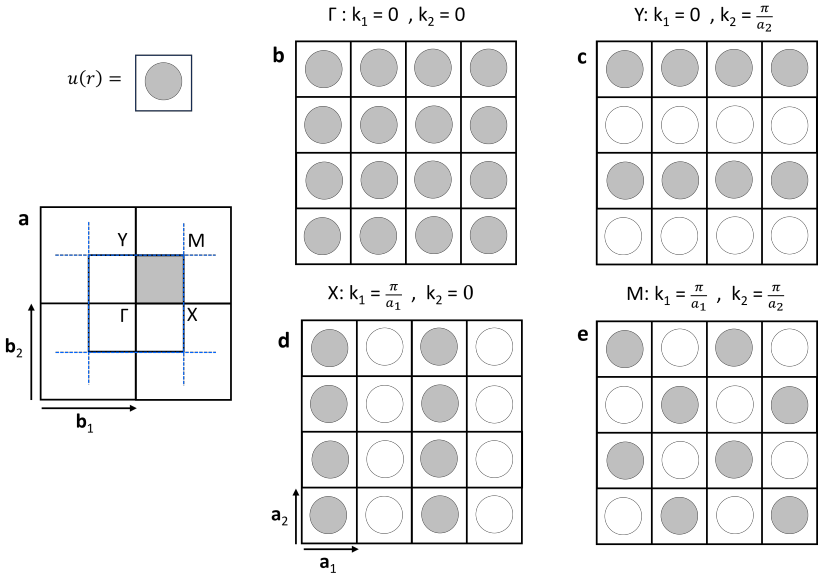

Figure 2.2: (a) Construction of the Brillouin zone in a rectangular lattice and the corresponding high symmetry points. The blue dotted lines which bisect the lattice vectors combine to form the reducible Brillouin zone. The grey shaded area represents the irreducible Brillouin zone in which k-points are sampled. (b-e) Illustration of the phase difference between each unit cell at each of the high symmetry points shown in (a).

point on the pseudo-continuous band represents a single electronic wave function. At $k = 0$ (Γ-point), the phase function simplifies to unity and all unit cells are in phase. In contrast, at $k = \frac{\pi}{a}$, the wavelength of $\lambda = 2a$ implies antiphase between any 2 adjacent unit cells. In the case of s-orbitals (Figure 2.1a) and p-orbitals oriented perpendicular to the bonding axis (Figure 2.1c), it can be deduced that constructive interference leading to bonding interactions occurs at $k = 0$, whereas destructive interference leading to antibonding interactions occurs at $k = \frac{\pi}{a}$. The situation is reversed for p-orbitals oriented along the bonding axis (Figure 2.1b) with destructive interference at $k = 0$ and constructive interference at $k = \frac{\pi}{a}$. In addition to the mirror symmetry about the Γ-point ($\phi(-k) = \phi(k)$), any point beyond $k > \frac{\pi}{a}$ involves phase variations within a unit cell, which can be equally described with a separate electronic band within $0 \leq k \leq \frac{\pi}{a}$ (blue band in Figure 2.1d). Therefore, discussions on electronic band structure are generally focused on this specific range of k defining the irreducible Brillouin zone (IBZ) in the reciprocal space.

Moving beyond the 1D lattice, more physically relevant 2D or 3D lattices are significantly more challenging in terms of spatial complexity. Analogous to the 1D lattice, the first Brillouin zone ($-\frac{\pi}{a} \leq k \leq \frac{\pi}{a}$ in Figure 2.1) can be defined in 2D

and 3D lattices through the spatial region that is closer to the Γ-point ($\boldsymbol{k} = \mathbf{0}$) than any other lattice points. Geometrically, this is constructed using perpendicular bisectors (*e.g.* blue lines in Figure 2.2a)[4] of the lines between the Γ-point and its nearest lattice points, which intersect to form the boundaries of the reducible first Brillouin zone. For a rectangular lattice, considering the mirror symmetry of the band structure along the axes ΓX and ΓY, the sampling of the Brillouin zone could be further confined to the IBZ (*e.g.* □ΓXMY in Figure 2.2a).[5] The corresponding electronic states at the high symmetry points of the IBZ are depicted in Figure 2.2b-e, in the example of a band of s-orbitals. Similar to the 1D lattice in Figure 2.1a, the Γ-point in Figure 2.2b captures a fully constructive interference and is the energy minimum in the IBZ. The other extreme is represented by the M-point in Figure 2.2e, which has the highest energy due to anti-bonding interactions in both directions. In principle, a complete description of a band structure requires information from a theoretically infinite number of k-points within the IBZ. However, due to computational constraints, only a limited number of k-points can practically be sampled, and the electronic bands are interpolated from these sampled k-points. Thus, during the initial calibration of a periodic DFT study, it is necessary to test the sensitivity of the electronic energy towards the number of sampled k-points in order to minimize the associated computational artefacts.

2.1.6 Computational Considerations

Basis Functions

When solving the one-electron HF or KS equations, the unknown wave functions are generally expanded into a linear combination of basis functions (Equations 2.27 and 2.59). If the basis expansion was infinite, any complete set of basis functions would give the exact solution to the respective equations. In reality, however, only a finite number of basis functions can be included in the calculation. Therefore, basis sets have to be designed to capture the most crucial parts of the electronic distribution within the limited number of basis functions.

For molecular calculations, the most intuitive choice of basis functions are the atomic orbitals as supported by the MO-LCAO theory (Equation 2.27). Based on the exact solution to the hydrogen atoms, atomic-orbitals are best described as Slater-type orbitals (STOs) where the radial part generally follows an exponential

4 In 3D lattices, the Brillouin zone is constructed with bisecting planes.

5 Note that for a square lattice with $a_1 = a_2$, the sampled Brillouin zone could be further reduced to △ΓXM due to additional rotational symmetry.

decay

$$R_{\mathrm{STO}}(r) \propto r^{l} \exp(-\zeta r) \tag{2.61}$$

where r is the distance from the nucleus, l is the angular momentum and ζ is the orbital-dependent decay coefficient. However, modern quantum chemistry calculations typically employ the Gaussian-type orbitals (GTOs) due to computational convenience [125]. The radial part of a primitive Gaussian function R_{PG} follows the form

$$R_{\mathrm{PG}}(r) \propto r^{l} \exp\left(-\zeta r^{2}\right). \tag{2.62}$$

Obviously, a primitive Gaussian function is not exactly an STO and cannot reproduce specific features such as the cusp-like radial distribution near the nuclei. In order to recover the STO-form of the atomic orbitals, multiple primitive Gaussian functions are combined linearly to form the contracted GTOs

$$R_{\mathrm{GTO}}(r) = r^{l} \sum_{f}^{n} C_{f} \exp\left(-\zeta_{f} r^{2}\right) \tag{2.63}$$

where n is the number of primitive Gaussian functions used for the contraction and $\{C_f\}$ are fixed contraction coefficients. The main motivation behind using GTOs in place of STOs originates from the Gaussian product theorem, which states that the product of two Gaussian functions centered on two different atoms can be written as a single Gaussian function centered at a point between the atoms. This allows the four-centered integrals in Equations 2.21, 2.23 and 2.50 to be reduced to two-centered integrals, tremendously reducing computational costs.

If the MO-LCAO ansatz is rigidly followed and only occupied orbitals of the free atom are considered in the basis set, one speaks of a minimal basis such as STO-nG basis sets ($n \in \mathbb{N}$). The minimal basis performs poorly for the description of chemical bonding, as valence AOs are forced to retain their spherical distributions and cannot redistribute along the bonding axis. The accuracy is significantly improved by introducing additional basis functions containing primitive Gaussians with larger decay coefficients ζ to accommodate electron distributions away from the nuclei, leading to the library of split-valence basis sets which are classified based on how many GTOs are used to represent each valence AO (double-ζ, triple-ζ *etc.*). Furthermore, in order to capture the asymmetric (non-radial) electronic redistributions (*e.g.* the polarization of bonding orbitals towards the bond center), GTOs of a higher angular momentum quantum number than

the valence electrons (polarization functions) can also be added to the basis set. Molecular calculations in this work are mainly performed with the Karlsruhe def2- basis sets, particularly the def2-SVP (split valence polarized) and def2-TZVP (triple-ζ valence polarized) basis sets [126–128]. These basis sets are designed to give consistent errors across the periodic table (except lanthanides) if the same basis is used for all elements [128].

For periodic calculations, atomic basis functions are less popular as they are tricky to reproduce in the reciprocal space. Fortunately, as emphasized in Section 2.1.5, periodic wave functions can be alternatively expressed with a Fourier expansion (Equation 2.59) which naturally serves as a basis set expansion. The Fourier transform of a plane wave is simply a point in the reciprocal space. The truncation of plane wave basis functions is numerically defined with the kinetic energy of the plane waves,

$$E_{\mathrm{kin,PW}} = \frac{|\boldsymbol{G} + \boldsymbol{G'}|^2}{2} \leq E_{\mathrm{cut}} \tag{2.64}$$

allowing for a better systematic improvability in contrast to atom-centered basis functions. However, the plane wave basis functions suffer tremendously when describing highly localized electronic distributions such as the core electrons. Therefore, periodic calculations almost always have to be performed with pseudopotentials to substitute core electrons. However, without the explicit core orbitals for the orthogonality constraint (*e.g.* the radial node of a 2s orbital makes it orthogonal to the 1s orbital), the pseudo wave functions $\tilde{\phi}$ (*i.e.* expanded as plane waves in the pseudopotential) do not correctly describe the oscillatory and nodal features near the nuclei. In order to recover these oscillatory features, pseudopotentials are commonly implemented in the projector augmented wave (PAW) formalism [129]. The method defines an augmentation sphere of radius r_{aug} around each atom

$$\phi = \begin{cases} \tilde{\phi} & \text{for } r \geq r_{\mathrm{aug}} \\ \hat{P}\tilde{\phi} & \text{for } r < r_{\mathrm{aug}} \end{cases} \tag{2.65}$$

where $\tilde{\phi}$ is the pseudo wave function from the plane wave expansion, ϕ is the augmented wave function and $\hat{P}$ is the projector function which maps the pseudo-wave function in the nuclear-region to radial orbital-like functions that contain the correct oscillatory features.

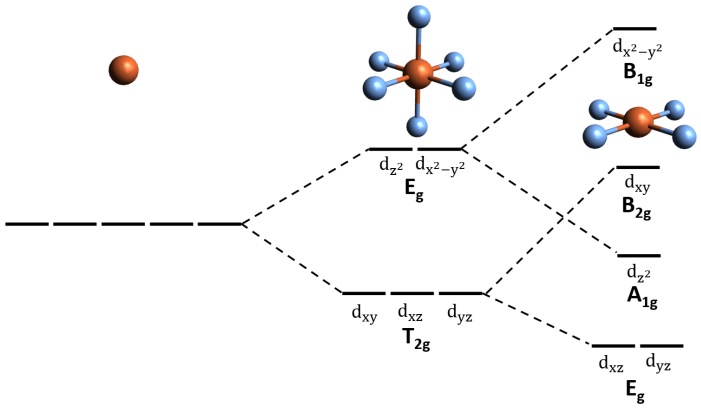

Figure 2.3: Illustration of the CFT in the context of d-orbital splitting for an octahedral complex (middle) and a square planar complex (right).

Transition Metals

In contrast to main-group chemistry which generally gravitates towards the noble gas atomic configurations, TM chemistry is highly intricate due to complexities in their d-orbital interactions and spin states. The splitting of the 5-fold degenerate d-orbitals of a TM atom in the presence of ligands is frequently discussed in the context of the crystal field theory (CFT) [130]. Figure 2.3 depicts the d-orbital splitting of a TM complex in the presence of the octahedral (O_h point group) and the square planar (D_{4h} point group) crystal field. Upon interaction with the ligands' σ-donating orbitals, electrons located in the d-orbitals oriented along the bonding axes are repelled more strongly than others and are thus destabilized. For an octahedral complex, since the E_g orbitals ($d_{x^2-y^2}$ and d_{z^2}) are oriented along the bonding axes, they become destabilized relative to the T_{2g} orbitals (d_{xy}, d_{xz} and d_{yz}). The d-orbital splitting of a square planar complex can be further deduced based on that of the octahedral complex. As ligands on the z-axis are removed from an octahedral complex, the repulsive effect in the z-direction is lifted, causing orbitals with a z-component (d_{xz}, d_{yz}, d_{z^2}) to become stabilized relative to those without ($d_{x^2-y^2}$, d_{xy}).

The CFT is successful in predicting d-orbital splitting and occupation in many TM-containing complexes and crystals. Nevertheless, a more comprehensive, quantum chemically relevant picture is portrayed by the ligand field theory (LFT) which combines insights from CFT with the MO-LCAO ansatz (Equation 2.27) [131]. For illustrating the similarities and differences between CFT and LFT, Figure 2.4 depicts the LFT applied to a square planar complex that is predominantly σ-bonding [132]. From the MO-LCAO ansatz, the interaction

between a d-orbital and symmetry-adapted linear combinations (SALCs) of the σ-bonding orbitals generates corresponding bonding and anti-bonding orbitals. The SALCs are generally lower in energy due to the higher electronegativity of the heteroatoms, resulting in bonding orbitals that are polarized towards the ligands. Therefore, for the effective d-orbital occupation of TMs, only non-bonding and the anti-bonding orbitals are of relevance (boxed region in Figure 2.4), thereby illuminating the origin of the "repulsive" effect portrayed by CFT. In contrast to the CFT which considers only direct σ-interactions, the LFT is able to capture more intricate influences such as hyperconjugation and π-bonding. These effects were examined in a study by Börgel *et al.* [132], for example with the σ-bonding square-planar $[Pd(NH_3)_4]^{2+}$ complex already exhibiting hyperconjugative effects in the E_g (predominantly d_{xz} and d_{yz}) orbitals (Figure 2.4), leading to the slight destabilization of the (anti-bonding) d_{xz} and d_{yz} orbitals compared to the CFT prediction (Figure 2.3). A second example relevant to my studies is illustrated in Figure 2.5, based on the pyridinic MN_4 site hosted in a graphene-like unit cell. From Figure 2.5b,c, the smeared-out energy distribution of the d_{xz} and d_{yz} orbitals could be traced to their hybridization with the π-system, thus bringing them energetically closer to the d_{xy} and d_{z^2} orbitals. In addition to the energetic ordering, the d-orbital occupation of TM complexes is further influenced by the magnitude of the d-orbital splitting. In general, if the orbital splitting is small enough to compensate the spin-pairing energy, a high spin complex is expected, and vice versa. For square planar complexes, the interplay between σ- and π-bonding can lead to the d-orbitals except $d_{x^2-y^2}$ being relatively close in energy, such that "high-spin" configurations with up to 4 unpaired electrons can be achieved (**Paper M4**).

For the modeling of TM chemistry, d-orbitals are often victims to the self-interaction error of standard GGA functionals like PBE (Section 2.1.5), leading to artefacts that tend to exaggerate their reactivity. This can be illustrated by the projected density of state (PDOS) plots showing the d-orbital energies for the Fe atom in a graphene-hosted pyridinic FeN_4 unit cell modeled with the PBE and PBE0 functionals shown in Figure 2.5. For the PBE functional (Figure 2.5b), the bands of the β d-electrons saturate at the Fermi level, correlating to extremely high reactivity at the Fe-center. However, after accounting for self-interaction error with hybrid functionals like PBE0 (Figure 2.5c), the d-orbitals are evidently shifted further away from the Fermi-level, correlating to lower reactivity at the Fe-site. In spite of the self-interaction error, many computational studies still resort to the GGA functionals due to the high computational cost of hybrid

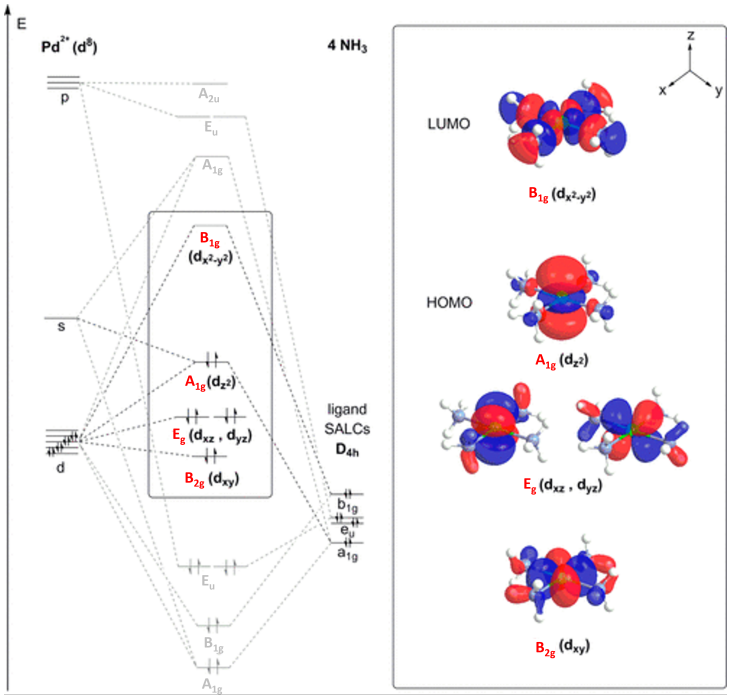

Figure 2.4: MO-diagram illustrating the LFT for the square planar $[Pd(NH_3)_4]^{2+}$ complex adapted from reference [132].

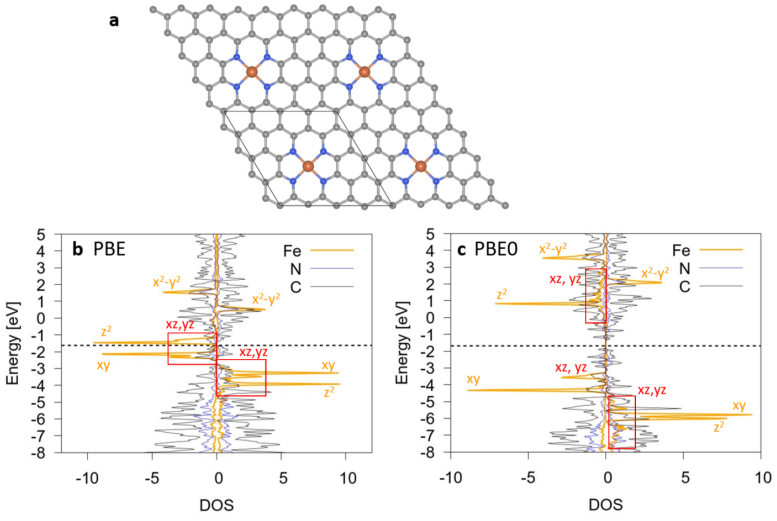

Figure 2.5: (a) Structural model of the pyridinic FeN_4 unit cell derived from a 4x4 supercell of graphene. Projected density of state plots for each element in this unit cell using the (b) PBE and (c) PBE0 functional. The positive DOS represents α electrons while negative DOS represent β electrons. The dotted line is the calculated Fermi energy. The red boxes are the delocalized contributions from the d_{xz} and d_{yz} due to hybridization with the π-bands of graphene.

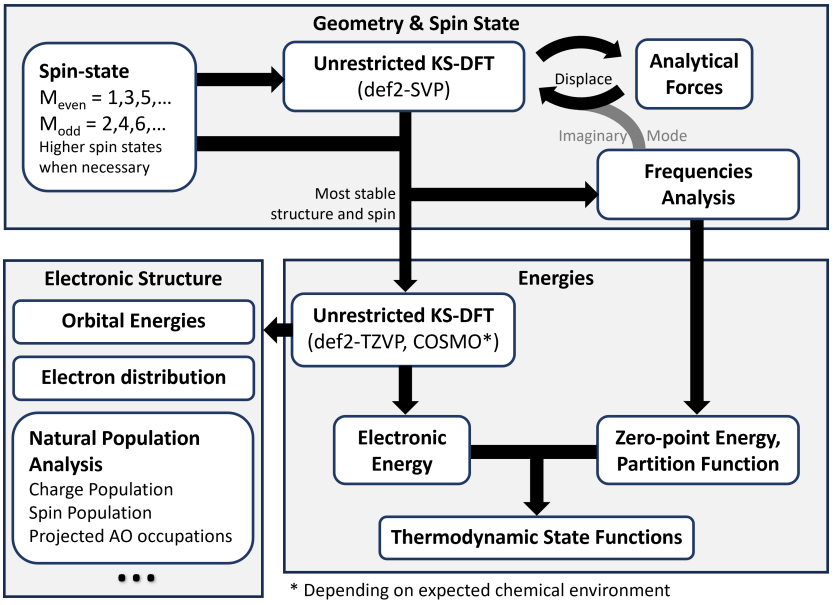

Figure 2.6: General computational setup for the DFT of a TM complex in a molecular model.

functionals in periodic DFT. Since the self-interaction error ultimately enhances the electrochemical reactivities, the validity of the GGA functionals is rarely questioned [5]. Nevertheless, a benchmarking study by Patel *et al.* highlighted the necessity of a hybrid functional in describing single atom catalysts containing TMs [5, 133, 134], which became an important consideration for most of my work.

Computational Setup

The general computational setup for the molecular DFT calculations is shown in Figure 2.6. The initial geometry optimization served not only to obtain a minimum in the PES, but also to determine the stable spin states of the cluster. Open-shell systems (including open shell singlets) were generally modeled with the unrestricted KS-DFT ($\phi_i^\alpha \neq \phi_i^\beta$). For the singlet state, an additional restricted closed-shell calculation ($\phi_i^\alpha = \phi_i^\beta$) was performed for energetic comparison. In order to capture high-spin and low-spin d-electron configurations of the TM, the initial geometry optimization was performed independently in various spin-states, using the def2-SVP basis [128]. For mid-TMs (Cr, Mn, Fe, Co), even higher spin states may be required in order to drive the metals towards the high spin configuration. In these cases, the optimized KS orbitals were used for the re-

optimization of the lower spin states by moving an electron from the α-HOMO to the β-LUMO (*i.e.* with creation and annihilation operators).

Among all the spin-states, the one that gave the lowest energy was chosen for further analysis. Firstly, an analytical frequency calculation was performed at the optimized geometry with the same parameters as the optimization step. If an imaginary frequency was obtained, the structure was displaced along the imaginary mode (one in each direction) and re-optimized in the same spin state. Once a geometric minimum could be confirmed with the absence of imaginary frequencies, a more accurate single point calculation was performed with the def2-TZVP basis [128]. In order to account for the aqueous environment during electrochemical and biochemical reactions, the COnductor-like Screening MOdel (COSMO) was applied during the single point calculations for studies that involved the aqueous environment [135]. In **Paper M5**, COSMO was additionally applied during geometry optimization due to the higher sensitivity of cations' adsorption geometries to the solvation environment. In the COSMO approach, the solvent is generally approximated as an ideal electrical conductor that is polarized by the intrinsic charge distribution of the molecule or cluster. Solvents with high electric permittivity like water ($\epsilon_r \approx 80$) are generally well approximated by the ideal conductor ($\epsilon \rightarrow \infty$) [135].

Finally, the electronic energy from the (solvated) single point calculation combined with the vibrational frequencies from frequency analysis to approximate the Gibbs' free energy at 298 K based on principles of statistical thermodynamics, which will be further discussed in Section 2.2.1. Additionally, the converged electronic structures were further analyzed to obtain chemically intuitive details, for example by partitioning the electron density to specific atoms through a natural population analysis [136], or by analyzing the frontier molecular orbitals to access electron-donating and -accepting capabilities.

2.2 Physical Chemistry of (Electro)Catalysis

"Let's get physical!"

-Dua Lipa

Physical chemistry plays a central role in all chemical processes. In this section, fundamental principles governing catalytic processes are illustrated along with the corresponding considerations for quantum chemical modeling. Sections 2.2.1 and 2.2.3 respectively introduce general thermodynamic and kinetic principles for understanding chemical stability and reactivity, while Sections 2.2.2 and 2.2.4 extend these concepts to electrochemical processes. Finally, in Section 2.2.5, we discuss the structure of the electrode-electrolyte interface and its role in facilitating electron transfers to and from redox species. The general physical chemistry concepts are written with reference to the textbook by Engel and Reid [137] while concepts related to electrochemical reactions are based on that of Bard and Faukner [138]. Starting from this section, equations are written in S.I. units instead of atomic units. Unless otherwise defined, quantities are expressed per species (atom/molecule) instead of the molar quantities.

2.2.1 Statistical Thermodynamics

In quantum chemistry calculations, the electronic energies obtained are generally without any form of thermodynamic contribution (*i.e.* at $T = 0\ K$ excluding zero-point energies). In order to connect these energies to the physical world, we apply the concepts of statistical thermodynamics to approximate the state functions from the population of various energy levels in a system. The fundamental relation which governs the relative population among energy levels (microstates) at a high temperature T is the Boltzmann distribution [139]

$$\frac{N_i}{N_j} = \exp\left(-\frac{\epsilon_i - \epsilon_j}{k_\mathrm{B} T}\right) \tag{2.66}$$

where ϵ_i is the energy of the microstate i.[6] Defining an arbitrary reference point for the energy (conventionally but not necessarily the ground state) and summing over the population of all energy levels ϵ_j, we obtain the proportion p_i of particles

6 The Boltzmann distribution is the high-temperature limit for the even more fundamental Bose-Einstein distribution [140] for bosons or Fermi-Dirac distribution [141] for fermions which consider effects based on the quantum state symmetry of the wave function.

in the microstate i

$$p_i = \frac{N_i}{N} = \frac{\exp\left(-\frac{\epsilon_i}{k_B T}\right)}{\sum_j \exp\left(-\frac{\epsilon_j}{k_B T}\right)} = \frac{1}{q}\exp\left(-\frac{\epsilon_i}{k_B T}\right) \tag{2.67}$$

where we define the partition function q to capture the sum over all microstates. A higher value of the partition function q correlates to a higher statistical population of the excited states, relative to the ground state. If the ground state is chosen as the energy reference ($\epsilon_0 = 0$), a system that is dominated by a non-degenerate ground state would have a partition function close to 1, which is the case for most electronic partition functions. Multiplying the partition functions from the geometric degrees of freedom (DOF) in a molecular system (translational, rotational, vibrational), we define the overall partition function Q

$$Q = q_{\text{trans}} \cdot q_{\text{rot}} \cdot q_{\text{vib}} = \sum_i \exp\left(-\frac{E_i}{k_B T}\right) \tag{2.68}$$

where E_i is the total internal energy of a molecule in the microstate defined by a quantum number for each geometric DOF

$$E_i = \epsilon_{\text{trans}} + \epsilon_{\text{rot}} + \epsilon_{\text{vib}} \tag{2.69}$$

The internal energy U can be calculated as the population-weighted mean of the energy levels

$$U = \sum_i p_i E_i \tag{2.70}$$

Similarly, a statistical formulation of the Gibbs entropy is given by

$$S = -k_B \sum_i p_i \ln(p_i) \tag{2.71}$$

$$= -k_B \sum_i p_i \ln\left(\frac{\exp\left(-\frac{E_i}{k_B T}\right)}{Q}\right) \tag{2.72}$$

$$= \frac{\sum_i p_i E_i}{T} + \sum_i p_i k_B \ln Q \tag{2.73}$$

$$= \frac{U}{T} + k_B \ln Q \tag{2.74}$$

where Equation 2.70 is applied in the last step. Combining Equations 2.70 and 2.74, we obtain a relatively simple expression for the Helmholtz free energy F

$$F = U - TS = U - T\left(\frac{U}{T} + k_{\mathrm{B}} \ln Q\right) = -k_{\mathrm{B}} T \ln Q \tag{2.75}$$

which illustrates that knowledge of the partition function is sufficient to obtain a central thermodynamic quantity with reference to its absolute ground state. For the condensed phase, since volume changes are often negligible, the Helmholtz free energy F is a good approximation to the Gibbs free energy G. In addition, the translational and rotational partition functions become trivial relative to the vibrational DOFs. Thus, with reference to the absolute ground state (including the zero-point energy), the Gibbs free energy of a condensed system simplifies to

$$G \approx F \approx -k_{\mathrm{B}} T \ln q_{\mathrm{vib}} \approx -k_{\mathrm{B}} T \sum_{\mathrm{i}} \ln\left(1 - \exp\left(-\frac{hc\nu_{\mathrm{i}}}{k_{\mathrm{B}} T}\right)\right)^{-1} \tag{2.76}$$

where the final expression is derived by approximating the vibrational partition function q_{vib} with energy levels of a harmonic oscillator for each normal mode i. For the following discussions, since most electrochemical measurements are performed in isobaric conditions, I will use the term "free energy" to imply Gibbs free energy by default, but note that in most condensed systems the distinction is not significant due to Equation 2.76. Shifting the reference from the system-specific ground state to a universal zero, the free energy of a condensed system can be obtained through quantum chemical calculations

$$G = E_{\mathrm{el}} + \frac{1}{2}\sum_{i}(hc\nu_i) - k_{\mathrm{B}} T \sum_{i} \ln\left(1 - \exp\left(-\frac{hc\nu_i}{k_{\mathrm{B}} T}\right)\right)^{-1} \tag{2.77}$$

where E_{el} is the electronic ground state energy and the second term contains the zero-point energy correction to the electronic energy at $T = 0$ K. Both the zero-point energy and free energy correction are calculated from the vibrational frequencies ν_i which are obtained with a frequency analysis. This definition of the free energy is now comparable across chemical systems, allowing for a description of the reaction thermodynamics. For a chemical reaction, the change in free energy ΔG is a central quantity that determines its feasibility under isothermal and isobaric conditions. In a reaction mixture, the concentration dependence

of the free energy G_X of species X[7] is conventionally expressed relative to a reference state

$$G_X = G_X^0 + k_B T \ln a_X \tag{2.78}$$

where the reference state corresponding to G_X^0 is typically defined at convenient standard concentrations. The dimensionless activity a_X is the concentration of the species c_X relative to this standard concentration c_X^0.[8]

$$a_X = \frac{c_X}{c_X^0} \tag{2.79}$$

For solids and liquids (including the solvent of a dilute solution), the standard condition is the respective pure forms and the activity is generally close to unity. For ideal gases whose concentration is directly proportional to the partial pressure p_X, the reference state is defined at atmospheric pressure $p^0 = 1\ \text{atm}$

$$a_X^{\text{gas}} = \frac{p_X}{1\ \text{atm}} = p_X(\text{atm}) \tag{2.80}$$

whereas for dissolved species in an ideal dilute solution, the reference state is a concentration of $c^0 = 1\ \frac{\text{mol}}{\text{L}}$

$$a_X^{\text{solute}} = \frac{c_X}{1\ 1\ \frac{\text{mol}}{\text{L}}} = c_X(1\ \frac{\text{mol}}{\text{L}}) = [\text{X}](1\ \frac{\text{mol}}{\text{L}}) \tag{2.81}$$

where [X] is a chemists' notation for denoting the concentration of species X. For a chemical reaction, we sum over the absolute Gibbs energies of each species, based on the stoichiometry of the reaction, to get the reaction free energy ΔG

$$\Delta G = G_{\text{products}} - G_{\text{reactants}} = \sum_X \kappa_X G_X \tag{2.82}$$

where κ_X is the stoichiometric coefficient of species X in the reaction equation (reactants get negative values). Substituting G_X in Equation 2.82 with Equation 2.78,

7 To be exact, the Gibbs free energy is a term reserved for an **extensive** property of an entire system. The species-specific term G_X is more correctly, but less relatably, referred to as an **intensive** property, the chemical potential $\mu_X = \left(\frac{\delta G}{\delta N_X}\right)_{P,T,N_{Y\neq X}}$.

8 For non-ideal gases and solutions, correction terms such as the fugacity coefficient and activity coefficients are necessary to capture the non-linear dependence of the activity w.r.t. concentrations, but they lie beyond the scope of this work.

we obtain

$$\Delta G = \sum_{\mathrm{X}} \left(\kappa_{\mathrm{X}} G^0_{\mathrm{X}} \right) + k_{\mathrm{B}} T \ln \left(\prod_{\mathrm{X}} a_{\mathrm{X}}^{\kappa_{\mathrm{X}}} \right) \tag{2.83}$$

$$= \Delta G^0 + k_{\mathrm{B}} T \ln Q_{\mathrm{R}} \tag{2.84}$$

where ΔG^0 is the standard reaction free energy if all species are at their respectively defined reference state ($a_{\mathrm{X}} = 1$ for all X). Q_{R} is the reaction quotient containing the activities of each species a_{X} raised to the power of its stoichiometric coefficient κ_{X}

$$Q_{\mathrm{R}} = \prod_{\mathrm{X}} a_{\mathrm{X}}^{\kappa_{\mathrm{X}}} \tag{2.85}$$

Defining an equilibrium condition of $\Delta G = 0$ in Equation 2.84, the standard reaction free energy ΔG^0 can be expressed as

$$\Delta G^0 = -k_{\mathrm{B}} T \ln K_{\mathrm{eq}}. \tag{2.86}$$

with K_{eq} as the reaction quotient at equilibrium, commonly known as the equilibrium constant. This enables the determination of the standard reaction free energy ΔG^0 from the experimentally measurable concentrations at equilibrium.

2.2.2 Electrochemical Thermodynamics

The free energy of a reaction was originally termed the ”available energy” by Gibbs [142], as it quantifies the energy that is available for, or required by, external work when the reaction occurs. If $\Delta G > 0$, the reaction has an energy debt that needs to be paid for by external sources. If $\Delta G < 0$, the excess free energy can be harvested to fund other energy-consuming processes, such as the production of a thesis. In an electrochemical cell, the currency for the energy conversion takes the form of electrical energy, such that the measured potential difference describes the change in free energy ΔG per unit charge transported between electrodes

$$E_{\mathrm{cell}} = -\frac{\Delta G}{ze} \tag{2.87}$$

with e as the charge of an electron and z as the number of transferred electron(s) per reaction. Combining equations Equations 2.84 and 2.87, we obtain the overall

Nernst equation for an electrochemical cell

$$E_{\text{cell}} = E^0_{\text{cell}} - \frac{k_B T}{ze} \ln Q_R \tag{2.88}$$

with $E^0_{\text{cell}} = -\frac{\Delta G^0}{ze}$ as the thermodynamic limit to the potential difference under standard conditions. A unique aspect of electrochemical reactions is that the species at the cathode do not directly interact with those at the anode, making it possible to define a potential scale by decoupling the reactions

$$E_{\text{cell}} = E_{\text{cat}} - E_{\text{an}} \tag{2.89}$$

where E_{cat} and E_{an} are the potentials of the cathode and anode respectively. Conventionally, the half-cell potentials $E_{\text{cat/an}}$ are defined in the direction of reduction (*i.e.* reduction potentials)

$$\text{Ox} + ze^- \rightleftharpoons \text{Red} \tag{2.90}$$

$$E_{\text{cat/an}} = E^0 - \frac{k_B T}{ze} \ln\left(\frac{[\text{Red}]}{[\text{Ox}]}\right) \tag{2.91}$$

where E^0 is the reduction potential under standard conditions and concentrations. The standard reduction potentials are conventionally reported with reference to standard hydrogen electrode (SHE) which is defined as the zero-point on the potential scale

$$2\,H^+ + 2\,e^- \longrightarrow H_2(g) \qquad\qquad E^0(H^+/H_2) = 0V \tag{2.92}$$

For the computational modeling of electrochemical reactions, the SHE forms the basis of the computational hydrogen electrode (CHE) method by Nørskov *et al.* [143] which connects the free energy of the $(H^+ + e^-)$ to the free energy of H_2 under standard conditions, which is more accessible from quantum chemistry calculations

$$G^0_{H^+ + e^-} = \frac{1}{2} G^0_{H_2(g)} - eU_{\text{SHE}} \tag{2.93}$$

where U_{SHE} is the potential of the working electrode with reference to the SHE. With the CHE method, the free energy of any elementary reaction step of the form

$$X + (H^+ + e-) \xrightarrow{U_{\text{SHE}}} XH \tag{2.94}$$

can be approximated with the free energy of the oxidized species X and reduced species XH with reference to the standard hydrogen electrode

$$\Delta G^0_{\mathrm{X}\to\mathrm{XH}} = G^0_{\mathrm{XH}} - G^0_{\mathrm{X}} - \left(\frac{1}{2}G^0_{\mathrm{H_2(g)}} - eU_{\mathrm{SHE}}\right). \tag{2.95}$$

The definition of the CHE in Equation 2.93 assumes standard concentrations ($pH = 0$, $P_{\mathrm{H_2}} = 1\ \mathrm{atm}$). If the pH of the solution is non-zero, it is advantageous to use the reversible hydrogen electrode (RHE) instead, which is measured at the same pH as the working electrode. The potential of the RHE is derived from the Nernst equation (Equation 2.91) and the reaction half-equations for the SHE (Equation 2.92)

$$E_{\mathrm{RHE}}(pH) = E^0_{\mathrm{SHE}} - \frac{k_{\mathrm{B}}T}{2e}\ln\left(\frac{P_{\mathrm{H_2(g)}}}{[\mathrm{H^+}]^2}\right) \tag{2.96}$$

$$= \frac{k_{\mathrm{B}}T}{e}\ln[\mathrm{H^+}] \tag{2.97}$$

$$= -\frac{k_{\mathrm{B}}T\ln 10}{e}pH \approx -0.059\ \mathrm{V}\cdot pH. \tag{2.98}$$

where we define $pH = -\log[\mathrm{H^+}]$. If the reaction follows the form of Equation 2.94 and the potential is measured vs RHE, both electrode potentials are shifted by this value, which then cancels out in Equation 2.89. The overall cell potential thus remains independent of the pH (if the mechanism itself is pH-independent) and is almost identical to the SHE definition in Equation 2.95

$$\Delta G^{\mathrm{RHE}}_{\mathrm{X}\to\mathrm{XH}} = G^0_{\mathrm{XH}} - G^0_{\mathrm{X}} - \left(\frac{1}{2}G^0_{\mathrm{H_2(g)}} - eU_{\mathrm{RHE}}\right) \tag{2.99}$$

This equation serves as the foundation for the study of the potential dependent free energies of the ORR and CO_2RR intermediates in **Paper M4** and **Paper M5** respectively.

While the CHE is generally sufficient for most electrochemical reactions in the aqueous phase, it is only applicable to reactions involving proton transfers. Instead of H^+, the concept can be generalized to other ions M^+, provided that the free energy of $(M^+ + e^-)$ can be analogously inferred from a reference material through the standard reduction potential. Modifications of the CHE have already been applied to study the adsorption of anions on metal surfaces [144, 145]. **Paper M5** involved studying the potential-dependent adsorption of alkali metal

ion(s) M^+ at the active site X

$$X + (M^+ + e-) \xrightarrow{U_{RHE}} XM \tag{2.100}$$

For alkali metal ions, the standard reduction potentials $E^0_{M^+/M(s)}$ are known with respect to the solid metal whose free energy can be in principle be calculated with periodic DFT

$$G^0_{M^+ + e^-} = G^0_{M(s)} - e\left(U_{SHE} - E^0_{M^+/M(s)}\right). \tag{2.101}$$

However, when using a molecular model, the electronic energy of solid M is not readily accessible. However, we can extrapolate it from the free energy of the metal atom treated as an ideal gas and the free energy of atomization $\Delta_{at}G^0$ of the metal, defined as the free energy required to fully atomize the metal (note that the reverse process is involved when using the gaseous free energy to derive the solid free energy)

$$G^0_{M(s)} = G^0_{M(g)} - \Delta_{at}G^0 \tag{2.102}$$

Since Equation 2.100 is not a proton transfer process, the ion concentrations do not cancel out even when referenced to RHE unlike in Equation 2.99. Thus, the concentrations of ions involved have to be explicitly included in the free energy changes when the potential is referenced to the RHE

$$G_{M^+ + e^-} = G^0_{M^+ + e^-} + k_B T \ln\left(\frac{[H^+]}{[M^+]}\right) \tag{2.103}$$

Inserting Equation 2.104 into Equation 2.103, the overall change in free energy for the potential-dependent adsorption of M^+ with reference to RHE is

$$\Delta G^{RHE}_{X \to XM} = G^0_{M(g)} - \Delta_{at}G^0 - e\left(U_{RHE} - E^0_{M^+/M(s)}\right) + k_B T \ln \frac{[H^+]}{[M^+]} \tag{2.104}$$

which was used to approximate the potential-dependent adsorption of alkali metal ions in **Paper M5**.

2.2.3 Reaction Kinetics

Studies of chemical processes like catalytic reactions almost always require an understanding of the reaction dynamics, particularly of reaction mechanisms at the atomic level. Nevertheless, especially for reactions in the condensed phase,

the experimental elucidation of reaction kinetics is largely macroscopic in nature, averaging over time, the numerous paths on the potential energy surface, and the different types of active sites in the material. Based on principles of reaction kinetics discussed in this section, computational methods like DFT are able to extract intrinsic kinetic parameters of a reaction on a particular active site in order to identify possible mechanistic pathways and compare the kinetics across materials and active sites.

The rate of most chemical reactions increases with the concentration of a reactant. For example, for a one-step unimolecular reaction of the kind

$$\mathrm{R} \underset{k_\mathrm{b}}{\overset{k_\mathrm{f}}{\rightleftharpoons}} \mathrm{P} \tag{2.105}$$

the overall reaction rate v can be expressed as the difference between the rates of the forward reaction v_f and the backward reaction v_b

$$v = v_\mathrm{f} - v_\mathrm{b} \tag{2.106}$$

which is respectively dependent on by the concentrations $[\mathrm{R}]$ and $[\mathrm{P}]$

$$v_\mathrm{f} = k_\mathrm{f}[\mathrm{R}] \tag{2.107}$$

$$v_\mathrm{b} = k_\mathrm{b}[\mathrm{P}] \tag{2.108}$$

where k_f and k_b are the rate constants. For simplicity, we assume for our discussion that the reaction is irreversible, such that $k_\mathrm{b} = 0$ and $k_\mathrm{f} = k$. In 1889, Arrhenius empirically determined an exponential relation between the reaction rate and the temperature, establishing the Arrhenius equation for the rate constant [146]

$$k = A \exp\left(-\frac{E_\mathrm{a}}{k_\mathrm{B} T}\right) \tag{2.109}$$

where A is the pre-exponential factor and E_a is the activation barrier of the reaction. Based on the deprecated collision theory, E_a can be loosely understood as an energy barrier between the reactant and product, while A is the frequency at which the reactant "attempts" to cross the barrier. Computational studies on reaction kinetics typically rely on a more refined connection between the activation energy and an activated complex established by the transition state theory of Eyring, Evans and Polanyi [147, 148]. Since any physically quantifiable reactant, intermediate or product is a (meta)stable configuration represented by a

minimum on the PES, the interconversion among them must involve a geometric rearrangement along a reaction path, on which the most unstable configuration is defined to be the transition state (TS). Inspired by thermodynamic principles (Section 2.2.1), the transition state theory assumes a quasi-equilibrium between the reactant R and the TS

$$\mathrm{R} \overset{K^{\ddagger}}{\rightleftharpoons} \mathrm{TS} \xrightarrow{k^{\ddagger}} \mathrm{P} \tag{2.110}$$

where a quasi-equilibrium constant $K^{\ddagger}$ can be defined as

$$K^{\ddagger} = \frac{[\mathrm{TS}]}{[\mathrm{R}]} \tag{2.111}$$

with $[\mathrm{TS}]$ as the hypothetical concentration of the TS. The quasi-equilibrium constant $K^{\ddagger}$ is subsequently used to define the Gibbs free energy of the transition state relative to the reactants, $\Delta G^{\ddagger}$, as though it were an equilibrium property (Equation 2.86)

$$\Delta G^{\ddagger} = -k_{\mathrm{B}} T \ln K^{\ddagger} \tag{2.112}$$

Based on Equation 2.110, the rate of product formation can be expressed in relation to the transition state "concentration" $[\mathrm{TS}]$, and subsequently to the reactant concentration through Equation 2.111

$$v = k^{\ddagger}[\mathrm{TS}] = k^{\ddagger} K^{\ddagger}[\mathrm{R}] = k[\mathrm{R}]. \tag{2.113}$$

This allows the experimentally measurable rate constant to be alternatively defined as a product of the two conceptual parameters $K^{\ddagger}$ and $k^{\ddagger}$, and finally to the free energy of the transition state $G^{\ddagger}$ through Equation 2.112

$$k = k^{\ddagger} K^{\ddagger} = k^{\ddagger} \exp\left(-\frac{\Delta G^{\ddagger}}{k_{\mathrm{B}} T}\right) \tag{2.114}$$

resulting in a similar expression to the originally empirical Arrhenius relation (Equation 2.109). Therefore, the activation barrier E_{a} in the Arrhenius equation can be interpreted as the free energy of the transition state, thereby connecting the computationally (partially) accessible PES (Section 2.1.2) to the physically observable reaction kinetics. While a theoretically infinite number of paths could exist between any two minima on the PES, the exponential relation in Equation 2.114 asserts the statistical dominance of the reaction path(s) with the lowest transition state free energy $\Delta G^{\ddagger}$, also known as the minimum energy

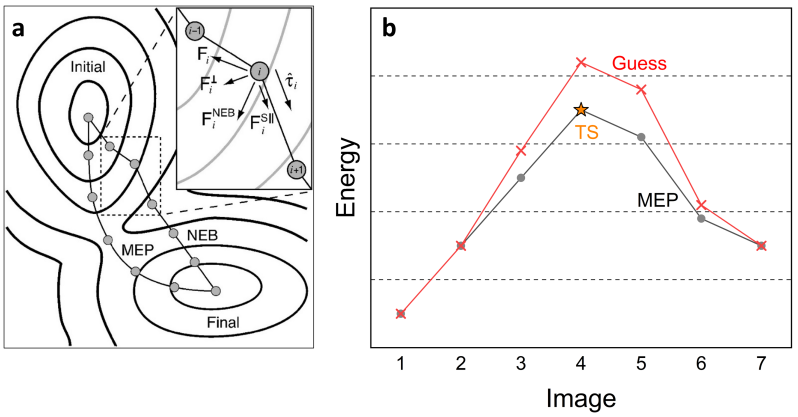

Figure 2.7: (a) Illustration of the NEB method on a 2D-PES adapted from reference [149]. (b) Corresponding reaction energy profile before (red) and after (black) the optimization of the reaction path. The grid lines in (b) correspond to the contour lines in (a). The transition state is marked with a star. Figures are not drawn to scale.

path(s) (MEP). Consequently, computational approaches to study reaction kinetics typically involve searching for the TS on the PES to quantify the activation barrier.

Unlike the geometry optimization of (meta)stable species which simply requires a downhill propagation in energy ($\boldsymbol{F}_i = -\boldsymbol{\nabla} E_i$ in Figure 2.7), a transition state is defined by a first-order saddle point on the PES, requiring the identification and uphill optimization of one (out of $3M - 6$) normal mode as the reactive mode. If the structure of the transition state can be guessed based on intuitively similar reactions, a direct transition state optimization can be performed by going uphill in the direction of the reactive normal mode, determined by the imaginary frequency upon frequency analysis, but downhill for all other modes [150, 151]. In most cases where the structure of the transition state is not as intuitive, one would have to perform a guided exploration of the PES to find the TS.

A common approach for finding transition states with quantum chemical calculations is the nudged elastic band (NEB) method [149, 152, 153]. With reference to Figure 2.7(a), a path containing a series of structures (images) is guessed, typically with linear interpolation, from the coordinates of R and P and subsequently optimized. Obviously, simply relying on the natural force $\boldsymbol{F}_i$ would cause every image to converge to a minimum. Instead, the NEB method extracts only the perpendicular component from this force relative to the displacement from the neighboring image

$$\boldsymbol{F}_i^{\perp} = \boldsymbol{F}_i - (\boldsymbol{F}_i \cdot \boldsymbol{\tau}_i)\boldsymbol{\tau}_i \tag{2.115}$$

where $\boldsymbol{\tau}_i$ is a unit vector describing the structural displacement between image i and image $i+1$. In addition to the perpendicular component, the NEB method introduces spring forces $\boldsymbol{F}_i^{S\parallel}$ to equalize the spacing between adjacent images

$$\boldsymbol{F}_i^{S\parallel} = k_{\text{spring}}(|\boldsymbol{R}_{i+1} - \boldsymbol{R}_i| - |\boldsymbol{R}_i - \boldsymbol{R}_{i-1}|)\boldsymbol{\tau}_i \tag{2.116}$$

where k_{spring} is an artificially defined spring constant and $\boldsymbol{R}_i$ is the vector of nuclear coordinates for image i. This spring force is a crucial aspect of NEB, as it prevents the images from collapsing to a minimum. In the example shown in Figure 2.7(a), $\boldsymbol{R}_i$ is closer to $\boldsymbol{R}_{i-1}$ than $\boldsymbol{R}_{i+1}$, so image i is "nudged" towards the latter by the spring force $\boldsymbol{F}_i^{S\parallel}$. The perpendicular component derived from the natural force $\boldsymbol{F}_i^{\perp}$ combines with the artificial spring force $\boldsymbol{F}_i^{S\parallel}$ to the final NEB force $\boldsymbol{F}_i^{\text{NEB}}$

$$\boldsymbol{F}_i^{\text{NEB}} = \boldsymbol{F}_i^{\perp} + \boldsymbol{F}_i^{S\parallel} \tag{2.117}$$

that displaces the image towards the MEP. The force calculation is performed for all images except the reactant and product for each NEB cycle, and the cycle is repeated until all forces approach a convergence criteria, with the TS being the image with the highest energy. This algorithm was applied in **Paper M1** and **Paper S1** for finding the transition states for non-electrochemical reactions.

2.2.4 Electrokinetics

Since the electrode and the redox species generally exist in separate phases, electrocatalysis can be classified as a form of heterogeneous catalysis. However, it is also important to consider its uniqueness beyond conventional heterogeneous catalysis, including the influence of the applied potential on the kinetics of the redox half-reactions (Faradaic processes) and on the transport and distribution of species to the interface (non-Faradaic processes). This section focuses on the former, while the latter is discussed in Section 2.2.5.

With the net current being zero by definition for an electrochemical cell at equilibrium, it is useful to define an overpotential η relative to the equilibrium potential for studying the kinetics of Faradaic processes

$$\eta = E - E_{\text{eq}} \tag{2.118}$$

where E_{eq} is the thermodynamic limit for the reaction determined by the Nernst equation (Equation 2.88). Consider the model half-reaction as defined in Equation 2.90. For the forward (cathodic) or the backward (anodic) direction of the

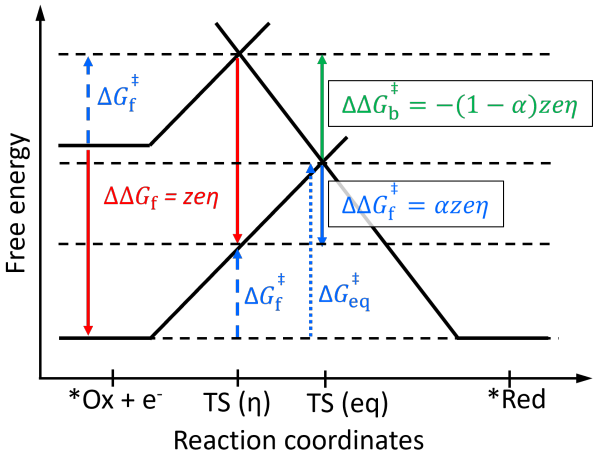

Figure 2.8: Illustration of the linear reaction energy profile for the derivation of the Butler-Volmer equation.

reversible reaction, a partial current i can be defined by the respective rate of reaction at the electrode surface

$$|i_{(\mathrm{cat/an})}| = \frac{\mathrm{d}Q}{\mathrm{d}t} = e\frac{\mathrm{d}n_\mathrm{e}}{\mathrm{d}t} = ze\frac{\mathrm{d}N_{(^*\mathrm{Ox}/^*\mathrm{Red})}}{\mathrm{d}t} = zeA\frac{\mathrm{d}[(^*\mathrm{Ox}/^*\mathrm{Red})]}{\mathrm{d}t} = zeAv \tag{2.119}$$

where Q is the amount of transferred charges, n_e is number of transferred electrons, $N_{(^*\mathrm{Ox}/^*\mathrm{Red})}$ is the number of adsorbed reacting species (*Ox for cathodic and or *Red for anodic current), $[(^*\mathrm{Ox}/^*\mathrm{Red})]$ is the surface concentration of the reacting species and v is the rate of reaction per unit surface area A. Defining the cathodic current as positive, the cathodic and anodic current combine to the total current I

$$I = i_\mathrm{cat} - i_\mathrm{an} = zeA(v_\mathrm{f} - v_\mathrm{b}) = zeA(k_\mathrm{f}[^*\mathrm{Ox}] - k_\mathrm{b}[^*\mathrm{Red}]) \tag{2.120}$$

where we applied Equation 2.107 and Equation 2.108 in the last step with $[^*\mathrm{Ox}]$ and $[^*\mathrm{Red}]$ as the surface concentrations of the oxidized and reduced form respectively. Just as in Equation 2.114, the rate constants could in principle be defined with the free energy of the transition state. However, an additional consideration in electrokinetics is that the energy of the transferred electron, and by extension the thermodynamic stability of (*Ox + ze$^-$) relative to *Red, depends on the applied potential (Equation 2.88). Consequently, the activation barriers for the forward and the backward reaction also change with potential, corresponding to the changes in the measured current. A model for describing the

potential dependence of the activation barrier is expressed by the Butler-Volmer kinetics [154–157]. For simplicity, we assume for a particular equilibrium potential that the oxidized form is in isomolar equilibrium with the reduced species ($[^*\mathrm{Ox}]_{eq} = [^*\mathrm{Red}]_{eq}$), such that the two species are at the same energy level and thus share the same activation barrier $\Delta G^{\ddagger}_{eq}$ (Figure 2.8). Upon polarization with a negative overpotential ($\eta < 0$), the oxidized form becomes higher in energy and the forward reaction becomes more exergonic by $\Delta\Delta G_f = ze\eta$ (Figure 2.8, red). The Butler-Volmer approach assumes a linear reaction energy profile in order to estimate the changes in the activation barrier relative to the change in the reaction free energy. Based on geometric considerations shown in Figure 2.8, the magnitudes of the change in activation barriers for the forward reaction (blue) and for the backward reaction (green) have to sum to the change in reaction free energy (red)

$$|\Delta\Delta G^{\ddagger}_b| + |\Delta\Delta G^{\ddagger}_f| = |\Delta\Delta G_f| \tag{2.121}$$

such that the complementary fractions α and $(1-\alpha)$ can be assigned to the forward and backward reaction respectively. Thus, the non-equilibrium activation barriers can be written as

$$\Delta G^{\ddagger}_f = \Delta G^{\ddagger}_{f(eq)} + \alpha ze\eta \tag{2.122}$$

$$\Delta G^{\ddagger}_b = \Delta G^{\ddagger}_{b(eq)} - (1-\alpha)ze\eta \tag{2.123}$$

where $\Delta G^{\ddagger}_{f(eq)}$ and $\Delta G^{\ddagger}_{b(eq)}$ are the respective activation barriers for the forward and backward reaction at equilibrium potential ($\Delta G^{\ddagger}_{f(eq)} = \Delta G^{\ddagger}_{b(eq)} = \Delta G^{\ddagger}_{eq}$ in the example of Figure 2.8). The fractional transfer coefficient α can be interpreted as the proportion of the electrons that are involved in shifting the barrier of the reaction. For a hypothetical barrier-free process, the free energy of the "transition state" is effectively that of the higher-energy species (*i.e.* either *Ox or *Red), and the transfer coefficient becomes unity for an endergonic process (*i.e.* all electrons are involved in shifting the barrier), or zero for an exergonic process (*i.e.* no electrons are involved in shifting the "barrier" of zero). Based on transition state theory (Section 2.2.3), the activation barrier is defined by the free energy of the transition state in Equation 2.114, which combines with Equation 2.122 and Equation 2.123 to expressions for the potential dependence of the rate constants

$$k_f = A_f \exp\left(-\frac{\Delta G^{\ddagger}_f}{k_B T}\right) = A_f \exp\left(-\frac{\Delta G^{\ddagger}_{f(eq)}}{k_B T}\right)\exp[-\alpha z f \eta] \tag{2.124}$$

$$k_b = A_b \exp\left(-\frac{\Delta G_b^{\ddagger}}{k_B T}\right) = A_b \exp\left(-\frac{\Delta G_{b(eq)}^{\ddagger}}{k_B T}\right) \exp[(1-\alpha) z f \eta] \tag{2.125}$$

where $f = \frac{e}{k_B T}$. Inserting a boundary condition that the net current should be zero at equilibium potential ($\eta = 0$) and thus $i_{cat} = i_{an}$, it follows from Equations 2.120, 2.124 and 2.125 that

$$k_{f(eq)}[^*\mathrm{Ox}] = k_{b(eq)}[^*\mathrm{Red}] = v_{eq} \tag{2.126}$$

$$A_f \exp\left(-\frac{\Delta G_{f(eq)}^{\ddagger}}{k_B T}\right)[^*\mathrm{Ox}] = A_b \exp\left(-\frac{\Delta G_{b(eq)}^{\ddagger}}{k_B T}\right)[^*\mathrm{Red}] = v_{eq} \tag{2.127}$$

where we define v_{eq} to be the hypothetical rate of the forward or backward reaction in the context of a dynamic equilibrium. Combining Equations 2.124, 2.125 and 2.127 into Equation 2.120, we obtain the Butler-Volmer equation [156, 157] for electrode kinetics relating the measured current to the overpotential

$$I = zeAv_{eq}[\exp(-\alpha z f \eta) - \exp((1-\alpha) z f \eta)] \tag{2.128}$$

This equation holds for a straightforward one-step reaction with a single reaction barrier as described by Equation 2.90. For a reaction with multiple elementary steps, the description of the overall kinetics can become convoluted with the reaction rates of each elementary step. In the simplest assumption that a single rate-determining step (RDS) is significantly slower than the others, the Butler Volmer equation is still applicable, but the kinetic parameters of interest in Equations 2.122 and 2.123 are those of the RDS and the concentrations $[^*\mathrm{Ox}]$ and $[^*\mathrm{Red}]$ refer to the intermediates involved at the RDS, which are assumed to be in rapid equilibrium with the fully-oxidized and fully-reduced species respectively. From Equation 2.128, we further distinguish between the number of electrons transferred at the RDS z_{RDS} and that of the entire reaction z

$$I = zeAv_{eq}\left[\exp\left(-\alpha z_{RDS} f \eta\right) - \exp\left((1-\alpha) z_{RDS} f \eta\right)\right] \tag{2.129}$$

$$= i_{eq}\left[\exp\left(-\alpha z_{RDS} f \eta\right) - \exp\left((1-\alpha) z_{RDS} f \eta\right)\right] \tag{2.130}$$

where $i_{eq} = zeAv_{eq}$ is the hypothetical current in either direction in the context of a dynamic equilibrium, commonly known as the exchange current. Due to the exponential dependence of the current on the overpotentials, applying an oxidizing ($\eta > 0$) or a reducing ($\eta < 0$) potential quickly leads to one exponent

in Equation 2.128 becoming significantly larger than the other. Since this work only deals with reduction reactions, we focus on the cathodic current produced at negative overpotentials ($\eta < 0$). At a sufficiently negative overpotential, the total current is dominated by the cathodic current

$$I = i_{\mathrm{eq}} \exp\left(-\alpha z_{\mathrm{RDS}} f \eta\right) \tag{2.131}$$

Taking the logarithm on both sides yields the originally empirical Tafel relation [158]

$$\log I = \log i_{\mathrm{eq}} - \left(\frac{\alpha z_{\mathrm{RDS}} f}{\ln 10}\right) \cdot \eta \tag{2.132}$$

which describes a quasi-linear dependence between the overpotential and the logarithm of current I. A plot of $\log I$ against overpotential η (or vice versa) is called a Tafel plot. The plot is approximately linear in a very specific region of the overpotential which (i) should be large enough such that the anodic current is negligible but (ii) should not be too large as the surface concentration [*Ox], which factors into i_{eq}, would otherwise be potential-dependent due to mass transport limitations.[9] In this linear overpotential region, the gradient of the Tafel plot, known as the Tafel slope, depends on both the transfer coefficient α and the number of electrons transferred at the RDS, z_{RDS}. Since the transfer coefficient α in turn depends on the PES of the reaction (symmetry of the intersections in Figure 2.8), reactions of the same type (*e.g.* ORR in **Paper M3**) with the same Tafel slope are very likely to have the same RDS. The exchange current i_{eq}, obtained by extrapolating the linear part of the Tafel plot to $\eta = 0$, is a descriptor for the overall electrode kinetics, which depends on the surface concentrations of redox species, the intrinsic catalytic properties of the active site, as well as quantitative aspects like the surface area, porosity and active site density of the material.

2.2.5 The Electric Double Layer

Following the discussion of the Faradaic process in the previous section, electrocatalysts are often designed to optimize these processes so as to produce higher currents. However, we cannot neglect the role of the non-Faradaic processes in preparing the interface for electron transfer. Universally, when a solid is immersed into a solution or electrolyte, mobile species in this medium undergo rearrangement at the surface of the solid depending on their respective interac-

9 At low overpotentials, we assume that the mass transport is much faster than the elementary redox step, such that the equilibrium surface concentration is maintained.

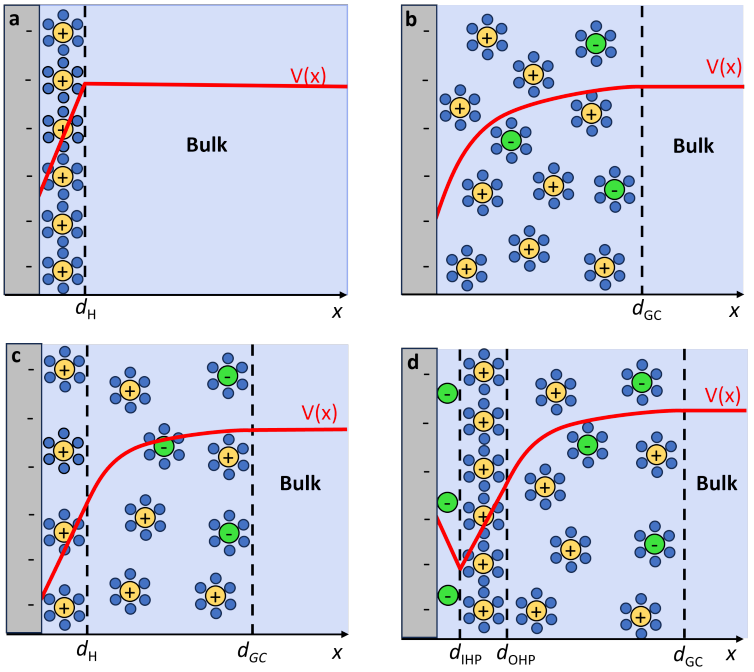

Figure 2.9: Illustration of ion distribution at the solid-electrolyte interface according to (a) the Helmholtz model, (b) the Gouy-Chapman model, (c) the Stern model and (d) the Graham model.

tions with the surface atoms, leading to an inherently heterogeneous interfacial layer.

For electrochemical processes, the influence of surface charges becomes especially important in shaping the heterogeneous interface. Even without coupling to an electron source or sink, the surface of a conductive material immersed in solution can still be charged due to dipoles induced by interactions with the electrolyte. Each combination of electrode/electrolyte has a unique potential, known as the point of zero charge (PZC)[10], at which the externally applied potential cancels out the inherent charge of the surface and the material effectively behaves as charge-neutral. At the PZC, the potential at the surface V_0 is equal to the potential of the bulk solution V_∞. Relative to the PZC, polarizing the electrode with positive or negative potentials introduces corresponding charges at the electrode surface, leading to a redistribution of the ionic species at the interface (Figure 2.9).

In 1879, Helmholtz introduced a simplified model to describe the interface

10 A distinction should be made from a related definition of PZC in colloidal chemistry, which often refers to the **pH** at which the material surface becomes charge-neutral.

by assuming that the electrified surface is covered by a single layer of solvated counter-ions [159], forming an ideal capacitor in which the potential increases or decreases linearly with distance from the surface x (Figure 2.9a). The capacitance within the Helmholtz layer C_{H} is a constant given by

$$C_{\mathrm{H}} = \frac{\epsilon_{\mathrm{r}}\epsilon_0}{d_{\mathrm{HL}}} \tag{2.133}$$

where ϵ_0 is the absolute permittivity of vacuum and ϵ_{r} is the permittivity of the electrolyte relative to vacuum. d_{HL} is the thickness of the Helmholtz layer which measures the distance between the electrode surface and the layer of counter-ions. The Helmholtz model did not account for the rearrangement of electrolyte species away from the electrode and assumed that everything beyond the single layer of counter-ions was immediately the homogeneous bulk solution. In 1910-1913, Gouy and Chapman proposed a conceptually different model to account for mutual screening effects of counter-ions which determine their spatial distribution (Figure 2.9b) [160, 161], bearing some similarities to modern pictures of how core electrons screen the valence electrons from the nuclear charges in atoms. With reference to the bulk solution, the position-dependent concentration of each ionic species [X] can be defined with Boltzmann statistics

$$[\mathrm{X}] = [\mathrm{X}]_\infty \exp\left(\frac{-z_{\mathrm{X}} e(V - V_\infty)}{k_{\mathrm{B}} T}\right) \tag{2.134}$$

where $[\mathrm{X}]_\infty$ is the concentration of species X in the bulk solution and V is the position-dependent electric potential and V_∞ is the potential of the bulk solution. In an electrolyte where various cations and anions coexist, the charges $\{z_{\mathrm{X}} e\}$ and the concentration profiles $\{[\mathrm{X}]\}$ of all charged species combine to describe the net charge density

$$\rho(x) = \sum_{\mathrm{X}} z_{\mathrm{X}} e[\mathrm{X}] = \sum_{X} z_{\mathrm{X}} e[\mathrm{X}]_\infty \exp\left(\frac{-z_{\mathrm{X}} e(V - V_\infty)}{k_{\mathrm{B}} T}\right) \tag{2.135}$$

where we applied Equation 2.134 in the final step. The net charge density $\rho(x)$ is related to the potential $V(x)$ through the Poisson equation

$$\rho(x) = -\epsilon_{\mathrm{r}}\epsilon_0 \frac{\delta^2 V}{\delta x^2} \tag{2.136}$$

which combines with Equation 2.135 to the Poisson-Boltzmann equation

$$\frac{\delta^2 V}{\delta x^2} = -\frac{e}{\epsilon_r \epsilon_0} \sum_X z_X [X]_\infty \exp\left(\frac{-z_X e(V - V_\infty)}{k_B T}\right). \tag{2.137}$$

For a z:z electrolyte (*i.e.* z_-=$-z_+$, *e.g.* K^+Cl^-, $Mg^{2+}SO_4^{2-}$), solving the Poisson-Boltzmann equation under the constraint that the potential asymptotically approaches the bulk solution potential ($V \to V_\infty$ and $\frac{dV}{dx} \to 0$ as $x \to \infty$), it can be shown that the potential $V(x)$ follows a pseudo-exponential decay with increasing distance from the electrode surface

$$\frac{\tanh[ze(V - V_\infty)]}{\tanh[ze(V_0 - V_\infty)]} = \exp\left(-\frac{x}{d_{GC}}\right) \tag{2.138}$$

where V^0 is the potential at the electrode surface and d_{GC} is the thickness of diffuse layer, which is defined by

$$d_{GC} = \sqrt{\frac{\epsilon_r \epsilon_0 k_B T}{2 c_\infty z^2 e^2}} \tag{2.139}$$

and depends only on properties of the electrolyte, including its permittivity ϵ_r, bulk ionic concentration c_∞ and ion charges z. The capacitance of this diffuse layer is given by

$$C_{GC} = \sqrt{\frac{2z^2 e^2 \epsilon_r \epsilon_0 c_\infty}{k_B T}} \cosh\left(\frac{ze(V^0 - V_\infty)}{2k_B T}\right). \tag{2.140}$$

While the Gouy-Chapman model is successful for reproducing the capacitance near the PZC, it predicts an unrealistically large capacitance at higher polarization vs PZC due to the exponential term in Equation 2.140 ($\cosh x \approx 0.5e^{|x|}$ for large $|x|$). The discrepancy of this model traces back to the use of charge density to derive the Poisson-Boltzmann Equation 2.137, implicitly treating the ions as point charges which could approach the electrode arbitrarily closely. At high polarization vs PZC, this erroneous picture results in an unrealistically high capacitance compared to observed values (recall in Equation 2.133 that $C \propto \frac{1}{d}$ for an ideal capacitor). Recognizing the deficiencies of both models, Stern proposed a combined double-layer model where the electrode surface is covered by a compact Helmholtz layer, followed by a diffuse layer described by the Poisson-Boltzmann distribution (Figure 2.9c) [162]. The two layers are individually treated

as capacitors which are connected in series

$$\frac{1}{C_S} = \frac{1}{C_H} + \frac{1}{C_{GC}} \tag{2.141}$$

where C_S is the total capacitance of the Stern double-layer, C_H is the capacitance of the compact Helmholtz layer and C_{GC} is the capacitance of the diffuse layer. At high polarization vs PZC, the inclusion of the Helmholtz layer imposes a limit to the maximum overall capacitance of the double layer $\left(\frac{1}{C_{GC}} << \frac{1}{C_H}\right)$, thereby circumventing the exponential surge in capacitance predicted by the Gouy-Chapman model. Since the Stern model and the preceding models are derived based on electrical concepts such as Coulomb-interactions between the electrode and the electrolyte species, they did not fully account for material-specific chemical interactions at the electrode surface. In 1947, Grahame further refined the Stern model by factoring in these specific interactions [163] by separating the Helmholtz layer into an inner Helmholtz plane (IHP) which contains the specifically adsorbed species, and an outer Helmholtz plane (OHP) as a layer of solvated counter-ions (Figure 2.9d).

For the study of electrocatalysis, the distinction between processes at the IHP and the OHP is especially crucial. It is commonly assumed that reacting species would diffuse into the IHP as a direct contact with the electrode would facilitate electron transfers, whereas spectator species like the cations would reside at the OHP. These assumptions will be challenged in **Paper M3** and **Paper M5**, with the former featuring the outer-sphere electron transfer as an alternative pathway to circumvent the formation of unstable *OOH intermediates for ORR and the latter describing the necessary involvement of cations in stabilizing the *COOH intermediates at the IHP during CO_2RR.

3 Publications

Paper M1

Resolving the Dilemma of Fe–N–C Catalysts by the Selective Synthesis of Tetrapyrrolic Active Sites via an Imprinting Strategy

D. Menga, J. L. Low, Y.-S. Li, I. Arčon, B. Koyutürk, F. Wagner, F. Ruiz-Zepeda, M. Gaberšček, B. Paulus, and T.-P. Fellinger, *J. Am. Chem. Soc.* **2021**, *143*, 18010-18019.

DOI: https://doi.org/10.1021/jacs.1c04884

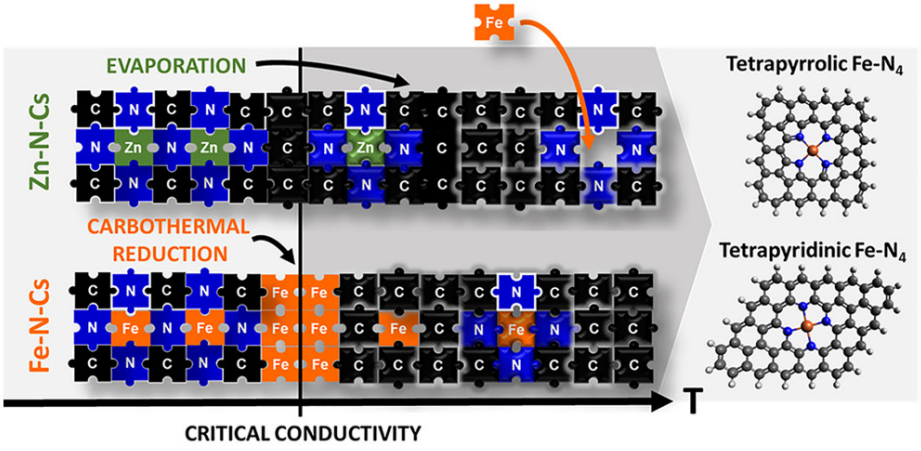

Figure 3.1: Graphical abstract of paper M1.

Computational Highlights

This paper featured the templating-transmetallation strategy for the synthesis of Fe-N-Cs, using a Zn-salt as templating agent in the initial pyrolysis step to prevent the carbothermal reduction and achieve high dopant concentrations. Assisting in the elucidation of local geometry with EXAFS, we designed and optimized geometric models incorporating the planar pyrrolic and pyridinic MN_4 motifs with various types and quantities of oxygen ligands. Upon successful fitting of EXAFS data to the pyrrolic models, we subsequently studied and confirmed the higher affinity of Zn towards forming the pyrrolic MN_4 structures, based

on comparisons in conformational energy (pyrrolic vs pyridinic) and atomic structures. We further concluded that Fe is bound much more strongly at the N_4 site than Zn due to its covalent interaction with the π-system, rationalizing the transmetallation procedure with a small activation barrier determined with nudged-elastic band calculations.

Author Contributions

Davide Menga and Tim-Patrick Fellinger planned and designed the experiments. Davide Menga synthesized and characterized the catalysts and performed the electrochemical measurements. Jian Liang Low constructed the structural models and performed the DFT calculations. Jian Liang Low designed the computational study, analyzed the DFT results and drafted the computational parts of the manuscript under the guidance of Beate Paulus. Yan-Sheng Li performed the single-cell PEMFC measurements. Iztok Arčon performed and analyzed the XAS measurements with structural models from Jian Liang Low. Burak Koyutürk measured and analyzed the XPS data. Friedrich Wagner performed and analyzed the Mössbauer spectroscopy measurements. Francisco Ruiz-Zepeda performed the TEM imaging. Davide Menga and Tim-Patrick Fellinger wrote the manuscript with contributions from Miran Gaberšček. All authors contributed to the final version of the manuscript.

JACS
JOURNAL OF THE AMERICAN CHEMICAL SOCIETY
pubs.acs.org/JACS
Article

Resolving the Dilemma of Fe−N−C Catalysts by the Selective Synthesis of Tetrapyrrolic Active Sites via an Imprinting Strategy

Davide Menga, Jian Liang Low, Yan-Sheng Li, Iztok Arčon, Burak Koyutürk, Friedrich Wagner, Francisco Ruiz-Zepeda, Miran Gaberšček, Beate Paulus, and Tim-Patrick Fellinger*

Cite This: J. Am. Chem. Soc. 2021, 143, 18010−18019

ABSTRACT: Combining the abundance and inexpensiveness of their constituent elements with their atomic dispersion, atomically dispersed Fe−N−C catalysts represent the most promising alternative to precious-metal-based materials in proton exchange membrane (PEM) fuel cells. Due to the high temperatures involved in their synthesis and the sensitivity of Fe ions toward carbothermal reduction, current synthetic methods are intrinsically limited in type and amount of the desired, catalytically active Fe−N_4 sites, and high active site densities have been out of reach (dilemma of Fe−N−C catalysts). We herein identify a paradigm change in the synthesis of Fe−N−C catalysts arising from the developments of other M−N−C single-atom catalysts. Supported by DFT calculations we propose fundamental principles for the synthesis of M−N−C materials. We further exploit the proposed principles in a novel synthetic strategy to surpass the dilemma of Fe−N−C catalysts. The selective formation of tetrapyrrolic Zn−N_4 sites in a tailor-made Zn−N−C material is utilized as an active-site imprint for the preparation of a corresponding Fe−N−C catalyst. By successive low- and high-temperature ion exchange reactions, we obtain a phase-pure Fe−N−C catalyst, with a high loading of atomically dispersed Fe (>3 wt %). Moreover, the catalyst is entirely composed of tetrapyrrolic Fe−N_4 sites. The density of tetrapyrrolic Fe−N_4 sites is more than six times as high as for previously reported tetrapyrrolic single-site Fe−N−C fuel cell catalysts.

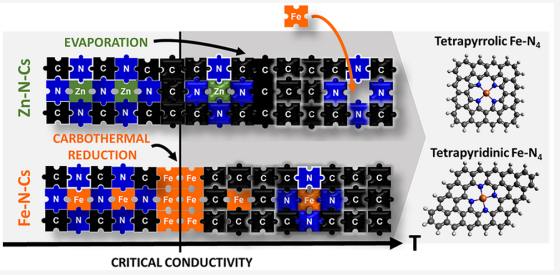

INTRODUCTION

In order to move from the burning of fossil fuels to clean and sustainable energy conversion and storage, electrochemical systems represent a central future technology, and reactions such as CO_2- and O_2-reduction reaction (CO2RR and ORR, respectively) as well as the O_2 evolution reaction (OER) play a pivotal role.[1] To be sustainable and yet economically advantageous, the materials employed to catalyze electrochemical reactions should be preferably composed of abundant and inexpensive elements.[2] Maximizing the atomic efficiency of metals, single-atom catalysts (SACs) have attracted the interest of many scientists in the field of catalysis, both heterogeneous and electrochemical.[3,4] Undoubtedly, the most promising class of such electrocatalysts, regarding activity and range of applications, is the family of metal and nitrogen co-doped carbons (M−N−Cs). In particular, Fe−N−C catalysts are among the best candidates to replace Pt-based materials for fuel cell applications due to their promising ORR activity.[5,6] While the desirable composition of Fe−N−C catalysts was debated for decades, in recent times the community vastly agrees that atomically dispersed square-planar Fe−N_4 sites, embedded into the conductive and supporting nitrogen-doped carbon (NDC) scaffold, are the desirable catalytically active motif. Therefore, Fe−N−C SACs are currently the subject of numerous research activities, fueled by the need for electrification of the transport sector.

Although the activity of Fe−N−C catalysts was impressively optimized in the past ∼30 years, further substantial improvements were hampered by limitations in the preparation of the catalysts. The formation of Fe−N−C SACs having concentrations above 0.5 wt % of Fe results in the formation of inorganic side phases such as metallic Fe, iron carbides, or iron nitrides.[7,8] The atomically dispersed Fe−N_4 active sites decompose at the temperature of their pyrolytic formation. This phenomenon is commonly described as the dilemma of Fe−N−C catalysts. There have been tremendous efforts in the last years to optimize the synthetic conditions in order to improve the activity by increasing the active site density for Fe−N−C catalysts.[9] Multistep syntheses are employed, comprising pyrolysis, leaching of soluble side-phases, and additional thermal processing steps.[10,11] The employment of

Received: May 18, 2021
Published: October 24, 2021

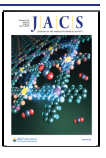

https://doi.org/10.1021/jacs.1c04884
J. Am. Chem. Soc. 2021, 143, 18010−18019

metal−organic framework precursors led to a significant increase in activity.[12] Reducing the mobility of Fe atoms throughout the pyrolytic synthesis can also reduce side-phase formation, leading to higher Fe loadings. The success of the mostly quite advanced synthetic protocols proves the possibility for further performance gain, although generally Fe contents still do not exceed 3 wt %.[12−14] Furthermore, there has been a long-standing debate and uncertainty about the surrounding structure of the Fe−N_4 sites. It is commonly believed that the active site exists mainly in a pyridinic Fe−N_4 environment. Such an environment has indeed been visualized in atomic resolution,[15] and, recently, for the first time a tetrapyridinic macrocycle (Cl-coordinated or O-bridged) has been employed as a model for Fe−N−Cs.[16] On the other end, Zitolo and Jaouen et al. developed a single-site Fe−N−C catalyst with minute amounts of Fe and proved the active sites therein to be of square-planar pyrrolic nature.[8] Supported by DFT calculations, pyrrolic M−N_4 sites with different metals in M−N−Cs are supposed to have superior activity compared to pyridinic ones in many catalytic applications.[17−19] Nonetheless, a comprehensive understanding on the formation of Fe−N−Cs, resulting in a rational synthesis of specific active sites, is still lacking. The uncontrolled nature of pyrolysis and the endless number of possible precursor systems obscure a clear view on the chemistry of Fe−N−Cs.

Herein, we identify a paradigm change for the synthesis of Fe−N−Cs arising from recent developments of other M−N−C single-atom catalysts. Supported by DFT calculations we propose ground-breaking principles for the synthesis of Fe−N−C catalysts, and M−N−C materials in general. On the basis of an abstract view on the formation pathway of different active sites, we came up with a synthesis strategy toward atomically dispersed, iron-rich Fe−N−C SACs hosting tetrapyrrolic Fe−N_4 complexes as single active sites and solve the long-standing dilemma of Fe−N−C catalysts.

RESULTS AND DISCUSSION

Today, there is evidence for pyrrolic and pyridinic (better tetrapyrrolic and tetrapyridinic) Fe−N_4 sites as active sites in Fe−N−C SACs. Density functional theory (DFT) calculations on isomeric model structures with the chemical formula of $[FeN_4]C_{52}H_{20}$ reveal that the square-planar tetrapyridinic motifs (Figure 1a) are thermodynamically more stable compared to the square-planar tetrapyrrolic motif (Figure 1b and c). The total energy difference of 3.02 eV for the pyrrolic-D_{4h} structure and 3.05 eV for the pyrrolic-C_{4h} structure (Table 1) arises by the necessity for defects within the carbon honeycomb structure in order to embrace the tetrapyrrolic site,

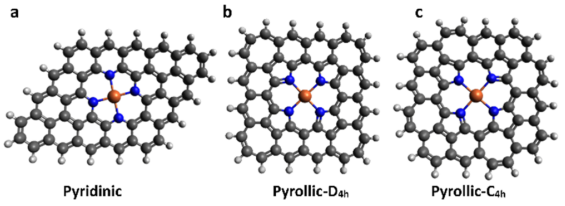

Figure 1. Chemical structure of planar tetrapyridinic (a) and two planar tetrapyrrolic (with two different symmetries, D_{4h} (b) and C_{4h} (c)) $[FeN_4]C_{52}H_{20}$ isomers. The seven-membered-ring defects are necessary to introduce the tetrapyrrolic motif into the planar graphene lattice.

Table 1. Comparison of Calculated M Binding Energy and Calculated Conformational Stability for Different $MN_4C_{52}H_{20}$ Clusters (M = Zn, Fe)[a]

stability	empty	Zn	Fe	Zn binding energy	Fe binding energy
pyridinic	0 (ref)	0 (ref)	0 (ref)	−4.2 eV	−7.9 eV
pyrrolic-D_{4h}	4.79 eV	2.97 eV	3.04 eV	−6.1 eV	−9.7 eV
pyrrolic-C_{4h}	3.45 eV	2.29 eV	3.01 eV	−5.4 eV	−8.3 eV

[a]Stability values are presented with reference to the energy of the pyridinic structure.

while the tetrapyridinic site perfectly fits into the graphene lattice, entirely made of C6 units. The tetrapyrrolic motif only fits the honeycomb lattice if the misalignment caused by five-membered pyrrolic rings is compensated by seven-membered-ring defects as in the case of Stone−Wales defects.

The thermodynamically more stable tetrapyridinic Fe−N_4 structure is interestingly incompatible with findings in organic coordination chemistry, in which pyridinic complexes of Fe^{2+} usually have an octahedral structure, e.g., in $[Fe(bipy)_3]X_2$ or $[Fe(terpy)_2]X_2$ (X = monovalent anion). Only recently was one tetrapyridinic macrocycle presented as an Fe−N_4 model, although the square-planar geometry seems to only arises in the case of an axial Cl ligand or for oxygen-bridged dimers.[16,20] The tetrapyrrolic M−N_4 structure, in contrast, is ubiquitously present in organic coordination chemistry[21,22] and in natural compounds, with the most prominent heme molecules for the case of Fe−N_4 motifs in mammal's blood. Hence, although the tetrapyridinic form is thermodynamically favored, the kinetically preferred tetrapyrollic FeN_4 is the abundant form. The realization of the graphene lattice entirely made of C6 units via preparative wet-chemical bottom-up synthesis is a highly complex discipline, typically involving many synthetic steps and requiring extraordinary synthetic control.[23]

How are tetrapyridinic Fe−N_4 sites formed? To facilitate discrimination from the tetrapyrrolic motif, the tetrapyridinic motif is simply called "pyridinic" in the following. The pyridinic Fe−N_4 site is thermodynamically favorable; however, the rearrangement of the carbon backbone into the honeycomb structure requires temperatures above 1300 °C, as known from graphitization. M−N−Cs are typically prepared between 750 and 1050 °C, where the critical conductivity of electrocatalysts is obtained along with electrocatalytic activity. Hence, the formation of pyridinic M−N_4 sites is actually surprising in common M−N−C syntheses.

Some metals, including iron, are catalysts for graphitization though.[24] At elevated temperature, metallic iron is able to dissolve carbon (formation of iron carbide) and reprecipitate it, allowing for dissociative reaction mechanisms, such as the formation of pyridinic Fe−N_4 sites, as well as further enhancement in conductivity. At the same time, the carbon structure is essentially recrystallized, going along with the destruction of the catalyst morphology, the loss of heteroatoms, and the formation of harmful inorganic side phases (metallic iron, iron carbide, and iron nitride). This process is very common for Fe−N−C syntheses, where metallic iron is formed via carbothermal reduction at elevated temperatures.

With this in mind, we can propose general principles for all conventional M−N−C preparations, which are bottom-up, comprising the heating of the metal, carbon, and nitrogen

https://doi.org/10.1021/jacs.1c04884
J. Am. Chem. Soc. 2021, 143, 18010−18019

Scheme 1. Representation of the Synthetic Route Adopted to Obtain NDC-Fe-HT Containing Exclusively Atomically Dispersed Fe from the Starting Zn−N−C Material Employing Low- and High-Temperature Ion Exchange Reactions

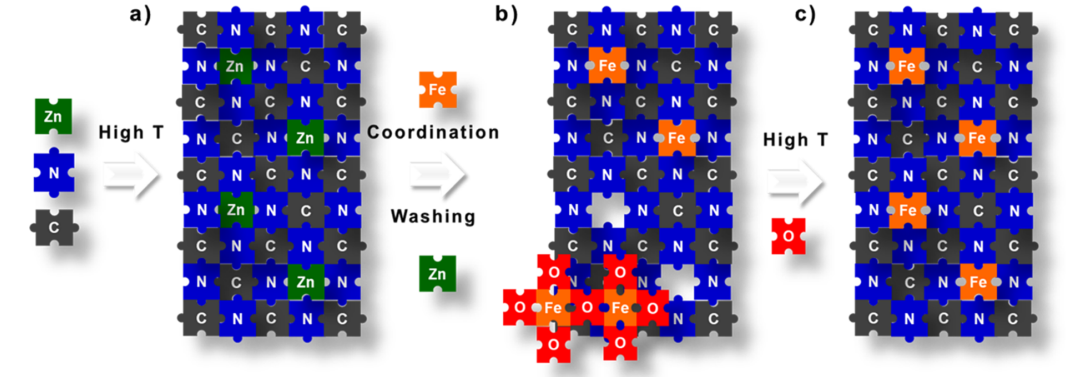

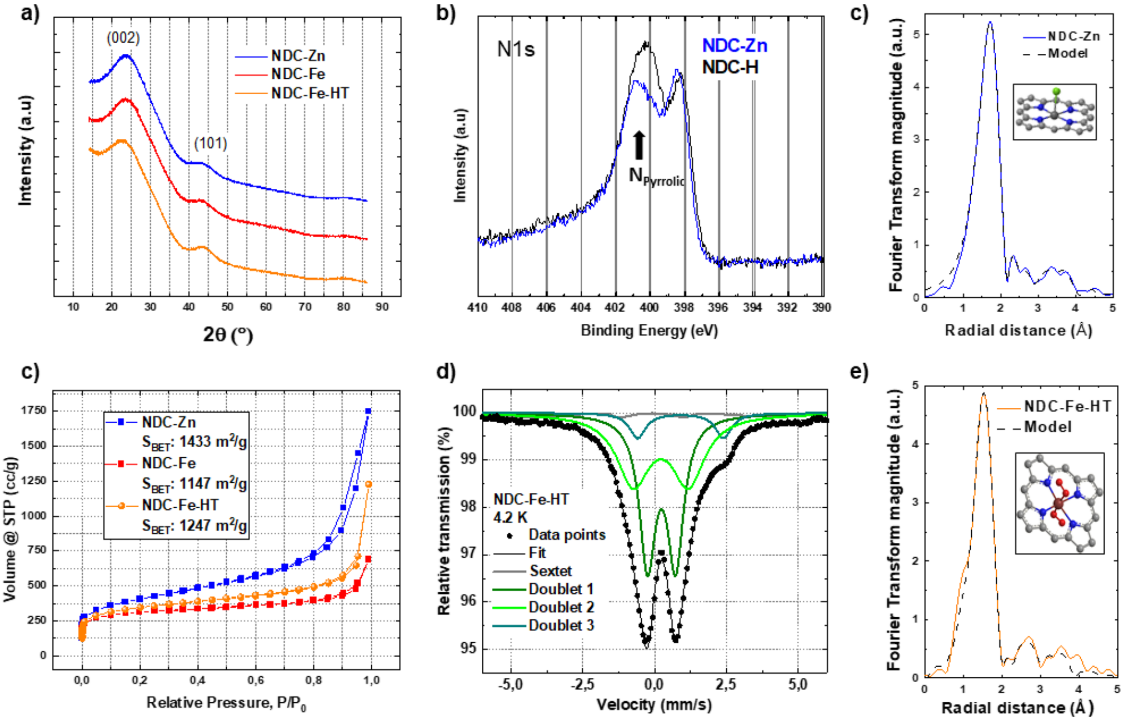

Figure 2. XRD of the NDC-M is characteristic for highly disordered carbons (a). XPS of the N 1s showing the increase of pyrrolic nitrogen after replacing Zn^{2+} with H^+ (b). Fourier transform magnitude of k^3-weighted Zn EXAFS spectra of an NDC-Zn sample, calculated in the k range of 3.0−12 $Å^{-1}$ and R range of 1−4 Å. Experiment (solid blue line); best fit EXAFS model (dashed black line). The structure used as model for the EXAFS analysis is displayed in the inset: the Zn atom (dark gray sphere) is bound axially with one Cl atom (green sphere) and in plane to four nitrogen atoms (blue spheres) in the porphyrin complex, where carbon atoms are presented as light gray spheres (c). Isotherms of the NDC-M obtained from N_2 sorption measurement (d). Mössbauer spectra of NDC-Fe-HT recorded at 4.2 K with the corresponding fitting (e). Fourier transform magnitude of k^3-weighted Fe K-edge EXAFS spectra of an NDC-Fe-HT sample, calculated in the k range of 3.0−11.5 $Å^{-1}$ and R range of 1−3.8 Å. Experiment (solid orange line); best fit EXAFS model (dashed black line). The structure used as a model for the EXAFS analysis is displayed in the inset: the Fe atom (brown sphere) is bound axially with two O_2 molecules (red spheres) and in plane to four nitrogen atoms (blue spheres) in the porphyrin complex, where carbon atoms are presented as gray spheres (f).

precursors in an inert atmosphere to temperatures between ∼750 and ∼1300 °C.

1. Throughout heating, tetrapyrrolic $M-N_4$ sites are formed within defective carbon scaffolds.
2. Pyrolytic reactions generate the critical conductivity for electrocatalysts at ∼750 °C.
3. Pyridinic $M-N_4$ sites are formed in the case of catalytic graphitization.

https://doi.org/10.1021/jacs.1c04884
J. Am. Chem. Soc. 2021, 143, 18010−18019

According to this description of the formation of Fe−N−Cs, the dilemma of limited Fe−N_4 site concentration is only valid for pyridinic Fe−N_4 sites, since only their formation is connected to the pyrolytic decomposition of the Fe−N−C structure arising from carbothermal reduction. Indeed, Fe−N_4 sites were shown to be formed already slightly above 400 °C, where it is extremely unlikely that pyridinic Fe−N_4 sites will form.[25]

The stability of $Fe^{2+/3+}$ toward carbothermal reduction depends on their chemical environment, their concentration, and the chosen gas atmosphere.[26] If the carbothermal reduction is avoided until a sufficiently conductive Fe−N−C is obtained, only tetrapyrrolic Fe−N_4 sites should be present. This is consistent with the finding of a tetrapyrrolic model Fe−N−C by Zitolo and Jaouen et al., which was obtained with Fe concentrations as low as 0.5 wt %.[8]

In contrast to Fe, less precious metals, such as Zn, are also less sensitive toward carbothermal reduction.[26,27] Therefore, the selective synthesis of tetrapyrrolic M−N_4 sites should allow for higher concentrations. In fact, M−N_4 complexes for M−N−Cs with metals other than Fe were recently also subjected to intense research.[28,29] For example Zn−N−Cs were previously reported, and Zn is also present in the popular Fe−N−C preparation protocols involving specific metal−organic frameworks.[30,31]

We carried out DFT calculations on the Zn-coordinated isomers of the above presented tetrapyrrolic and pyridinic Fe−N_4 structures. Like in the case of the iron-based structures, the pyridinic structures have higher thermodynamic stability.

Curiously, the difference in energy is lower for Zn compared to Fe, indicating a higher stability of the kinetically favored tetrapyrrolic Zn−N_4 toward transformation to pyridinic sites. Due to back-bonding effects of the Fe d-orbitals, the Zn−N binding energy is however smaller compared to the Fe−N binding energy (Table 1). We recently discovered that Fe−N_4 active sites can be prepared by ion exchange from other M−N−C materials.[32,33] A relatively high concentration of atomically dispersed Fe−N_4 sites, corresponding to an Fe loading of 1.34 wt %, was obtained from Zn−N−Cs. This can be explained by our DFT calculations showing that the Zn−N bond is weaker than the Fe−N bond. The exchange of $Fe^{2+/3+}$ with Zn^{2+} ions consequently results in the more stable Fe−N−C SACs. However, after aqueous workup, insoluble Fe(III) oxide remained as an inorganic side phase, impeding proper determination of the resulting Fe−N_4 active site structure. Therefore, herein we attempt successive ion exchange reactions, at low temperature and at high temperature, targeting Fe−N−Cs with very high total Fe contents. The summarized synthetic strategy is illustrated in Scheme 1.

Preparation of Fe−N−C SACs. The catalysts are named as NDC-M, where M indicates the metal ions coordinated to the NDC solid-state ligand (here either Zn^{2+} or $Fe^{2+/3+}$) or NDC-M-HT when the high-temperature ion exchange treatment is performed. NDC-Zn was prepared by pyrolysis of a mixture of 1,2-dicyanobenzene and a binary $ZnCl_2$/LiCl (60 mol % LiCl) mixture in an Ar atmosphere at 800 °C for 1 h, followed by washing with 0.1 M hydrochloric acid and aqueous workup.[33] NDC-Zn was converted into NDC-Fe via a low-temperature ion exchange reaction at 170 °C (slightly above T_m) by stirring in an excess eutectic $FeCl_3$/LiCl salt melt for 5 h, with a workup as described before. NDC-Fe-HT was obtained subjecting NDC-Fe to a flash pyrolysis at 1000 °C in an Ar atmosphere for 20 min.

Materials Characterization. NDC-Zn is a hierarchically porous carbon material with a high specific surface area of 1433 m^2/g. X-ray powder diffraction (XRD) data are characteristic for amorphous carbons, which are highly defective in their structure (Figure 2a). The possibility to form a high concentration of defects is a consequence of the precursor choice. In our case, the surface stabilization provided by the $ZnCl_2$-based molten salt route provides structural versatility.[27,34]

Although a fraction of Zn^{2+} coordinated to N_4 sites might be removed by washing (ion exchange with protons), a residual Zn content of 2.95 wt % and a total N content of 13.61 wt % are prospective for a high concentration of N_4 coordination sites for the formation of Fe−N_4 sites (Table S3). Zn K-edge EXAFS analysis of an NDC-Zn sample was used to determine the local Zn structure in the pristine NDC-Zn (Figure 2c).

Structural parameters of the local Zn neighborhood (type and average number of neighbor atoms; the radii and the Debye−Waller factor of neighbor shells) are quantitatively resolved from the EXAFS spectra by comparing the measured EXAFS signal with the model signal, constructed *ab initio* using the FEFF6 program code,[35] based on Zn-porphyrin as a model structure, where Zn is bound to four pyrrolic nitrogen atoms and surrounded by respective carbon atoms with one additional Cl atom placed at an axial position (model parameters are given in Table S1).

An almost perfect fit is found (best fit parameters are given in Table S1), which shows that the Zn cations in NDC-Zn are indeed embedded into the carbon matrix in a macrocyclic tetrapyrrolic motif with the four pyrrolic N neighbors detected at 2.05 Å, similar to the Zn-porphyrin structure. The axial Cl atom is reasonably explained by the synthesis using $ZnCl_2$ or from the washing with HCl.

To further prove the pyrrolic nature of the Zn-imprinted N_4 cavities, NDC-Zn has been treated in strong, but not oxidizing 2.4 M aqueous HCl at 150 °C, in a closed vessel to replace Zn^{2+} ions with protons. XPS comparison of the pristine NDC-Zn and the obtained NDC-H sample shows a drastic drop in Zn content, while the N 1s spectra reveal that the N−Zn signal fully turns into pyrrolic N when Zn^{2+} ions are replaced by H^+ (Figure 2b, Figure S1 and Table S2), whereas the content of the other nitrogen species (i.e., graphitic, oxidized, and pyridinic) remains constant.

The finding of a single-site Zn−N−C being entirely composed of tetrapyrrolic Zn−N_4 embedded in the amorphous carbon structure allows for first conclusions on the proposed general principles of M−N−C syntheses. In fact, Zn ions undergo carbothermal reduction at higher temperature compared to Fe ions.[26] However, metallic Zn does not catalyze graphitization and already evaporates in the relevant temperature range (T_b = 907 °C). Hence the dissociative reorganization of the carbon structure in the present synthesis is obviously limited to the development of conductivity. The formation of pyridinic Zn−N_4 sites or transformation of tetrapyrrolic Zn−N_4 sites via dissociation of multiple bonds is expected to require much higher temperatures. The finding agrees well with our herein proposed M−N−C formation mechanism.

After the first ion exchange reaction, Zn^{2+} ions are partly removed and replaced by $Fe^{2+/3+}$ ions, which additionally occupy previously empty (i.e., protonated) tetrapyrrolic cavities. Due to the low temperature employed, it is reasonable to assume that the nitrogen content remains stable. The

https://doi.org/10.1021/jacs.1c04884
J. Am. Chem. Soc. 2021, 143, 18010−18019

decrease in wt % N is therefore an indication for the increased density of the material. This is also reflected in the N_2-sorption isotherm of NDC-Fe, which presents a downshift compared to NDC-Zn and consequently lower surface area and cumulative pore volume, but with an unchanged pore size distribution (Figure S2). This indicates that once the NDC solid-state ligand has been formed, its properties are retained throughout the ion exchange. The increased density of NDC-Fe is explained by the coordination of $Fe^{2+/3+}$ to protonated N_4 cavities as well as by the formation of iron oxide. XRD, like in case of NDC-Zn, reveals no indication of graphitization at the low temperature of 170 °C (Figure 2a). In order to study the kinetics of the substitution reaction at the N_4 site, we conducted a DFT study on the adsorption of an Fe atom on the various ZnN_4 motifs (Fe@ZnN_4) and *vice versa* (Zn@FeN_4) as well as the transition state between these states (Figure S4). For all tetrapyrrolic and pyridinic motifs, Fe@ZnN_4 exhibits a unique geometry with Fe anchored to two of the N atoms instead of the Zn center, resulting in a relatively strong adsorption. In contrast, Zn prefers a direct coordination to the Fe center in Zn@FeN_4 and exhibits weaker binding. The activation barriers between the two intermediates are relatively low (0.4−0.9 eV), suggesting that the ion exchange is kinetically feasible. Residual amounts of Zn after the ion exchange reaction may be explained by incomplete ion exchange caused by steric hindrance, e.g., accessibility from only one site of the active site. Furthermore, the adsorption of Zn to the Fe−N_4 sites is stable and explains the importance of the acidic workup.

The atomically dispersed nature of the iron species after ion exchange can nicely be observed by aberration-corrected annular-dark-field scanning transmission electron microscopy (ADF-STEM) shown in Figure S5. No crystalline phases are observed; however due to the folded nature of the carbon, the atomic Fe species may appear in some cases as clusters, if the carbon layers are overlapping. Low-temperature Mössbauer spectra more accurately reveal the Fe species present in the Fe−N−C catalyst than room-temperature spectra, since nanosized Fe(III) oxide can only be distinguished from the Fe−N_4 site doublets by the magnetic hyperfine splitting they exhibit at low temperatures.[36] We recorded the Mössbauer spectrum at 4.2 K for NDC-Fe (Figure S6) and find two doublets, characteristic for atomically dispersed Fe, as well as a sextet, indicative of nanosized oxidic Fe(III), which is tentatively assigned to ferrihydrite, a poorly crystalline hydrous ferric oxyhydroxide ($Fe_{10}O_{14}(OH)_2$).[37] Based on these results, the Fe−N_4 sites correspond to ∼1.34 wt % of the total Fe, indicating that the ion exchange at lower temperature is kinetically hampered.[38] Despite the presence of the oxidic iron, the structure of the Fe−N_4 formed should still be entirely of tetrapyrrolic nature.

It has been recently shown that nanosized oxidic iron can decompose and release Fe atoms, which can coordinate to NC defects in ZIF-based carbons.[39] Accordingly, a thermal treatment may similarly decompose the ferrihydrite and activate the oxidic iron for a successive ion exchange reaction to form more Fe−N_4 sites. Indeed, based on investigation of the thermal treatment of NDC-Fe at 1000 °C in Ar in TGA-MS experiments (described in the SI), the following mechanism for the coordination of Fe to empty (protonated) N_4 cavities is proposed:

Step 1: Dehydration of ferrihydrite:

$$Fe_{10}O_{14}(OH)_2 \rightarrow Fe_{10}O_{15} + H_2O$$

Step 2: Carbothermal reduction:

$$2\ Fe_{10}O_{15} + 5\ C \rightarrow 20\ FeO + 5\ CO_2$$

Step 3: Coordination of iron:

$$FeO + H_2{-}N_4 \rightarrow Fe{-}N_4 + H_2O$$

In fact, the decomposition of the inorganic particles is indicated by a lower gravimetric density of NDC-Fe-HT compared to NDC-Fe, which is reflected in the N_2-soprtion isotherms and subsequent increase of surface area to 1247 m^2/g. Moreover, in the pore size distribution plot, a 61% increase in porosity can be assigned to pores larger than 5 nm (Figure S2). This further points to ferrihydrite decomposition and the related disclosure of previously blocked porosity as well as the reactive activation of the carbon scaffold (step 2). Both phenomena are desirable to further improve the mass transport and the accessibility of active sites. Overall, the final NDC-Fe-HT catalyst shows hierarchical porosity, including microporosity, high external surface area, mesoporosity (with negligible hysteresis), and macroporosity, which is advantageous for catalytic applications in general. We have previously reported the impact of the pore design on the ORR performance for morphologically related nitrogen-doped carbons.[40]

Intriguingly, the XRD pattern of NDC-Fe-HT still shows no sign of graphitization, with a characteristic diffractogram for amorphous carbon, essentially unchanged compared to NDC-Zn (Figure 2a). This is the case despite the high pyrolytic temperature and the presence of a large quantity of Fe. Mössbauer spectroscopy (Figure 2e) reveals that the ferrihydrite phase of NDC-Fe (sextet signal) is almost quantitatively removed after the second heat treatment, while a second doublet (often referred to as D2), characteristic for atomically dispersed Fe−N_4 sites, arose. Indeed, 90% of the iron previously present as an oxidic side phase is converted into atomically dispersed Fe−N_4 sites in the high-temperature ion exchange (step 3), while no other side phases are formed. The synthetic strategy of N_4-site imprinting by means of Zn^{2+} ions and successive low- and high-temperature ion exchange successfully results in Fe−N−C SACs with a very high Fe loading of 3.46 wt % (according to ICP-MS, Table S3). The Mössbauer spectrum comprises three doublets, D1, D2, and D3, with relative intensities of 44% (D1), 42% (D2), and 8% (D3), which are characteristic of atomically dispersed Fe−N_4 sites. The doublets do not allow the assignment of pyrrolic or pyridinic Fe−N_4 sites.[16,41,42] However, the absence of side phases such as metallic iron, iron carbide, or iron nitride confirms that no graphitization has occurred, despite the high temperature of 1000 °C and the high total Fe content. Obviously, the stability of pyrrolic Fe−N bonds (at least in the tetrapyrrolic Fe−N_4 sites originating from Zn^{2+} imprinting) is high enough to overcome temperatures of 1000 °C, at least for some time, without undergoing carbothermal reduction, although the quantity and quality of the nitrogen doping is still affected by the heating (Table S3, Figure S3). Also, the mobile Fe species formed by the thermolysis of the ferrihydrite (step 2) do not lead to the formation of condensed metallic iron and hence no initiation of catalytic graphitization. This may be explained by fast trapping in preformed N_4 cavities.

Fe K-edge XANES spectroscopy was employed to determine the average Fe valence state in NDC-Fe-HT, deduced from the energy position of the Fe K-edge. The energy position of the absorption edge is correlated with the valence state of the

https://doi.org/10.1021/jacs.1c04884
J. Am. Chem. Soc. 2021, 143, 18010−18019

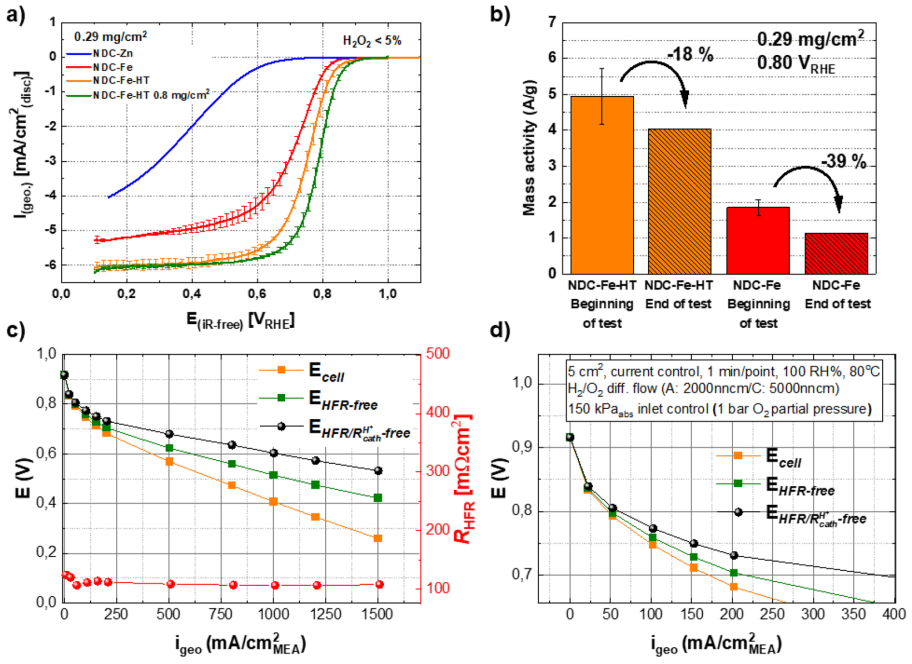

Figure 3. ORR curves of the three NDC-M recorded with an RDE setup at room temperature in O_2-saturated 0.1 M $HClO_4$ at 1600 rpm, 5 mV/s (anodic scans). All curves were corrected for capacitance contributions (a). Kinetic mass activity at 0.8 V calculated from RDE measurement of NDC-Fe (red) and NDC-Fe-HT (orange) before (full color) and after (line pattern) the stability test (b). Polarization curve of NDC-Fe-HT with a catalyst loading of 2 mg/cm^2 recorded in current-control mode (1 min-hold/point) at 80 °C, 150 kPa_{abs} inlet-controlled pressure, 100% RH for both reactants, and constant flows of 2000 nccm of H_2 on the anode and 5000 nccm of O_2 on the cathode. Anode and cathode were operated in counter flow mode. Measured cell voltage curve (orange), cell voltage corrected by the HFR (green), and corrected by the HFR and the effective proton conduction resistance (black) (c). Zoom-in of the low current density region of the polarization curve of NDC-Fe-HT (d).

absorbing atom in the sample. With increasing oxidation state the absorption edge is shifted to higher energies for about 4.5 eV per valence from Fe^{2+} to Fe^{3+}.[43−45] Comparing the XANES spectrum of NDC-Fe-HT with spectra of reference Fe compounds we found that the energy position of the Fe K-edge in NDC-Fe-HT is between the edge position of Fe^{3+} compounds and the edge position of $Fe^{2.67+}$ compound Fe_3O_4 (Figure S7), indicating that iron in the sample is predominantly in a trivalent state with about 20% of Fe^{2+} in the mixture. Fe K-edge EXAFS analysis was used to directly probe the local structure around Fe cations in an NDC-Fe-HT sample in the same way as for NDC-Zn. The results based on the tetrapyrrolic Fe-porphyrin molecule as model structure (Figure 2f) show that the Fe cations in NDC-Fe-HT are embedded into the carbon matrix in a macrocyclic, tetrapyrrolic motif, almost perfectly resembling the Fe-porphyrin structure (even the more distant coordination shell of carbon atoms is characteristic for Fe-porphyrin). In addition, each Fe cation is bound to oxygen on both axial positions (oxygen molecules according to the Fe−O distance), suggesting that the atomically dispersed Fe atoms, embedded into the high-surface-area, nongraphitized carbon scaffold, are accessible to the gas phase. This is not surprising, since formation of $Fe-N_4$ sites already required the accessibility to Fe ions/atoms. N_4-imprinted Zn−N−C SACs are indeed resulting in entirely tetrapyrrolic and entirely dispersed Fe−N−C SACs, with 3.46 wt % iron content, which is almost seven times as high as that for previously proven tetrapyrrolic single-site Fe−N−C SACs.[8]

Electrocatalytic Activity toward the ORR. The electrocatalytic activity of the catalysts was preliminarily evaluated using rotating disc electrode (RDE) testing in O_2-saturated 0.1 M $HClO_4$ (Figure 3a). NDC-Zn is not particularly active toward the ORR, showing a high overpotential and slow kinetics. However, the voltammetry results show sufficient conductivity due to the pyrolytic synthesis at 800 °C. The related blue curve in Figure 3a can be considered as background activity of the nitrogen-doped carbon scaffold.

After low-temperature ion exchange from Zn to Fe, the catalyst (NDC-Fe) becomes active toward the ORR by the formation of active sites showing a half-wave potential, $E_{1/2}$, already above 0.7 vs RHE. This implies a low ORR activity of $Zn-N_4$ sites in acid. After high-temperature treatment the catalyst gains even more activity, which is attributed to the increased active site density and accessibility derived from the decomposition of the iron oxide. The increased active site density is apparent from the upshift of the onset potential by ~50 mV. The improved mass transport characteristics within the complex pore system are reflected in the increased slope in the mixed transport- and kinetically limited region.[40] With a high loading of 800 $\mu g/cm^2$, the catalyst exhibits an $E_{1/2}$ of about 0.8 V and an onset above 0.9 V. Since the half-wave potential is loading dependent and higher loadings come with a high film thickness and increased capacitive current, the mass activity is reported as a more reliable activity descriptor.[46] An intermediate loading of 290 $\mu g/cm^2$ is selected for all the experiments shown in continuation. NDC-Fe-HT shows a mass activity of 0.91 ± 0.16 A/g at 0.85 V and 4.95 ± 0.77 A/g

https://doi.org/10.1021/jacs.1c04884
J. Am. Chem. Soc. 2021, 143, 18010−18019

at 0.80 V, with a Tafel slope of 66 mV/dec (Figure S8), representing state-of-the-art performance for Fe−N−C electrocatalysts (Table S4). However, when compared with a reference catalyst prepared like NDC-Fe-HT but with the Fe source already present during the carbonization step (i.e., conventional synthetic method), the catalyst prepared via an active site imprinting strategy shows much higher activity, i.e., more than 20 times higher mass activity at 0.8 V and more than 100 mV in $E_{1/2}$. Comparative RDE tests corroborate that the activity gain is strictly connected to a high-temperature ion exchange, i.e., to the ferrihydrite decomposition within active site imprinted NDC-Zn (Figure S9).

The stability of NDC-Fe and NDC-Fe-HT was evaluated by cycling in O_2-saturated 0.1 M $HClO_4$ between 0.4 and 0.8 V with a relatively slow scan rate of 50 mV/s. The increased active site density after the second ion exchange shows a positive impact not only on the activity but also on the stability of the catalyst, with NDC-Fe-HT showing only 18% loss in mass activity at 0.8 V vs 39% loss for NDC-Fe after 500 cycles at 50 mV/s (Figure 3b). This corresponds to downshifts in half-wave potentials $E_{1/2}$ of 20 mV for NDC-Fe-HT and 40 mV for NDC-Fe. This effect may be understood with the additional activity of $Fe-N_4$ sites toward the reduction of peroxide, which is a harmful reaction intermediate of the ORR, especially in an acidic electrolyte.[47] NDC-Fe-HT, indeed, shows a very high selectivity toward a $4e^-$ reduction. Rotating ring disc electrode (RRDE) experiments with different catalyst loading were employed to quantify the H_2O_2 production. For the Fe−N−C catalyst, a substantial increase in the fraction of H_2O_2 produced is usually observed when the catalyst loading is decreased.[48] NDC-Fe-HT shows only ∼3% H_2O_2 even with a low catalyst loading of 0.095 mg/cm^2, which is about seven times less compared to the commercial Fe−N−C benchmark catalyst (Pajarito Powder) measured with similar loading (Figure S10). The high selectivity, which approaches the ones observed for Pt/C catalysts, may intuitively be explained with the single-site nature of the catalyst. If tetrapyrrolic sites are more selective compared to pyridinic $Fe-N_4$ sites remains speculative until Fe−N−Cs with similar morphology are developed with entirely pyridinic $Fe-N_4$ sites.[49] Our results indicate that this may be hardly possible with bottom-up synthesis approaches. Additional stability measurements with a faster scan rate (250 mV/s) confirm the high stability of NDC-Fe-HT, only losing 31 mV in half-wave potential $E_{1/2}$ after 10k cycles in O_2-saturated 0.1 M $HClO_4$, (Figure S11a). At the same time the selectivity toward a $4e^-$ reduction is fully retained (Figure S11b). Upon cycling, no degradation is observed in an Ar-saturated electrolyte, respectively (Figure S11a).

Single-cell (5 cm^2) proton exchange membrane fuel cell (PEMFC) testing of NDC-Fe-HT with a loading of 2 mg/cm^2 was performed in H_2/O_2 under the DOE proposed conditions to determine the ORR activity and in H_2/air to examine the stability in conditions relevant to commercial application.[50] The single-site tetrapyrrolic Fe−N−C SAC shows state-of-the-art ORR activity in H_2/O_2 (Figure 3c and d and Table S5), with a high mass activity of 2.3 A/g already at 0.9 V HFR-free cell voltage, where only the onset of activity is observed in the RDE activity test.

Compared to thin catalyst layers in the range of 10 μm for Pt/C catalysts, the thicker Fe−N−C catalyst layers (∼50 μm for NDC-Fe-HT) go along with larger high-frequency resistances (HFRs) and related voltage losses (Figure 3, E_{cell}). Even though the packing factor f for NDC-Fe-HT is smaller than for the commercial Fe−N−C standard ($f_{NDC\text{-}Fe\text{-}HT} \approx 22-25$ μm mg^{-1} cm^{-2} vs $f_{Pajarito} \approx 30$ μm mg^{-1} cm^{-2}), further reduction may be a promising target for future catalyst development.

Furthermore, the stability of Fe−N−C catalysts is a key issue for the practical PEMFC application and has been addressed in recent research.[51] Similar to the testing protocol proposed by Banham et al. for the first commercial PGM-free based PEMFC system,[52] the durability of NDC-Fe-HT was investigated in single-cell tests in H_2/air at 80 °C and 100% RH by applying constant current at 140 mA/cm^2 and cell voltage at 0.6 V under this condition. A similar result to the report on the commercial system was obtained,[52] with a fast degradation step observed in the initial ∼10 min of testing, before the cell voltage reaches a relatively stable, slowly decreasing trend. After 12 h of operation, the cell voltage only decreased by ∼12%, suggesting a very promising stability of atomically dispersed Fe−N−C SACs based on tetrapyrrolic $Fe-N_4$ sites (Figure S11c).

CONCLUSION

Herein we utilized a Zn−N−C synthesis as a pyrolytic Zn^{2+} template ion reaction to imprint a high concentration of tetrapyrrolic N_4 coordination sites into a conductive carbon. Consecutive Zn to Fe ion exchange reactions result in a very high concentration of tetrapyrrolic $Fe-N_4$ sites, the motif of the heme molecule, that originally inspired the development of M−N-C catalysts.[53] The $Fe-N_4$ site density, with an Fe loading of 3.46 wt % or 0.72 at. %, of the very selective and stable catalyst surpasses the typical limit for Fe−N−Cs, and higher values seem to be a matter of optimization only.

General principles of M−N−C syntheses are revealed and explain the structural complexity of Fe−N−C/Co−N−C materials, their challenging assignment of active sites, and the previously complicated structure−performance relation. The formation of kinetically preferred tetrapyrrolic Fe−N−C electrocatalysts is interfered by the carbothermal reduction of Fe before critical conductivity is reached. The carbothermal reduction catalyzes the formation of the thermodynamically more stable pyridinic sites, however also leading to morphological destruction (the dilemma). Kinetically preferred tetrapyrrolic Zn−N−Cs can be heated above 900 °C, reaching critical conductivity. Consecutive ion exchange leads to selective formation of tetrapyrrolic Fe−N−Cs, even in high concentrations.

The herein obtained iron loading outmatches the maximum loading of current tetrapyrrolic single-site Fe−N−Cs by more than six times. The possibility to direct the synthesis toward specific active site geometries further unlocks the tool of increasing the specific activity of M−N−C catalysts in general and Fe−N−C SACs in particular. This iron-rich and entirely tetrapyrrolic Fe−N−C SAC, not yet optimized regarding mass transport and electrode design, already reaches state-of-the-art Fe−N−C performance in RDE and single-cell PEMFC tests, additionally showing very promising durability throughout fuel cell operation.

ASSOCIATED CONTENT

Supporting Information

The Supporting Information is available free of charge at https://pubs.acs.org/doi/10.1021/jacs.1c04884.

https://doi.org/10.1021/jacs.1c04884
J. Am. Chem. Soc. 2021, 143, 18010−18019

Experimental section; materials characterization; DFT tables; activity comparison with literature; and TGA-MS analysis (PDF)

AUTHOR INFORMATION

Corresponding Author

Tim-Patrick Fellinger − *Chair of Technical Electrochemistry, Department of Chemistry and Catalysis Research Center, Technische Universität München (TUM), 85748 Garching, Germany; Bundesanstalt für Materialforschung und -prüfung (BAM), 12203 Berlin, Germany;* orcid.org/0000-0001-6332-2347; Email: tim-patrick.fellinger@bam.de

Authors

Davide Menga − *Chair of Technical Electrochemistry, Department of Chemistry and Catalysis Research Center, Technische Universität München (TUM), 85748 Garching, Germany*

Jian Liang Low − *Chair for Theoretical Chemistry, Institut für Chemie und Biochemie, Freie Universität Berlin, 14195 Berlin, Germany*

Yan-Sheng Li − *Chair of Technical Electrochemistry, Department of Chemistry and Catalysis Research Center, Technische Universität München (TUM), 85748 Garching, Germany*

Iztok Arčon − *Laboratory of Quantum Optics, University of Nova Gorica, SI-5001 Nova Gorica, Slovenia; Department of Low and Medium Energy Physics, Jožef Stefan Institute, SI-1001 Ljubljana, Slovenia*

Burak Koyutürk − *Chair of Technical Electrochemistry, Department of Chemistry and Catalysis Research Center, Technische Universität München (TUM), 85748 Garching, Germany*

Friedrich Wagner − *Department of Physics, Technische Universität München (TUM), 85748 Garching, Germany*

Francisco Ruiz-Zepeda − *Department of Materials Chemistry, National Institute of Chemistry, SI-1000 Ljubljana, Slovenia*

Miran Gaberšček − *Department of Materials Chemistry, National Institute of Chemistry, SI-1000 Ljubljana, Slovenia*

Beate Paulus − *Chair for Theoretical Chemistry, Institut für Chemie und Biochemie, Freie Universität Berlin, 14195 Berlin, Germany*

Complete contact information is available at: https://pubs.acs.org/10.1021/jacs.1c04884

Author Contributions

All authors have given approval to the final version of the manuscript.

Notes

The authors declare no competing financial interest.

ACKNOWLEDGMENTS

The German Federal Ministry of Economic Affairs and Energy (BMWi) is acknowledged for funding within the Verbundproject innoKA (Project No. 03ET6096A) and Dr. Gilleßen from PTJ for constructive supervision of the project. Prof. Hubert Gasteiger is acknowledged for hosting the group and for providing an educative and supportive atmosphere. Part of this research was supported by the Slovenian Research Agency (P1-0112) and by the project CALIPSOplus under the Grant Agreement 730872 from the EU Framework Programme for Research and Innovation HORIZON 2020. Access to the synchrotron radiation facilities of ELETTRA (beamline XAFS, project 20185092) is acknowledged. We would like to thank Giuliana Aquilanti, Luca Olivi, and Simone Pollastri of ELETTRA, for support and expert advice on beamline operation.

REFERENCES

(1) Qiao, S.; Liu, J.; Kawi, S. Editorial: Electrocatalysis - From Batteries to Clean Energy Conversion. *ChemCatChem* **2019**, *11* (24), 5835−5837.

(2) Anastas, P.; Eghbali, N. Green Chemistry: Principles and Practice. *Chem. Soc. Rev.* **2010**, *39* (1), 301−312.

(3) Wang, A.; Li, J.; Zhang, T. Heterogeneous single-atom catalysis. *Nature Reviews Chemistry* **2018**, *2* (6), 65−81.

(4) Cheng, N.; Zhang, L.; Doyle-Davis, K.; Sun, X. Single-Atom Catalysts: From Design to Application. *Electrochemical Energy Reviews* **2019**, *2* (4), 539−573.

(5) Gasteiger, H. A.; Kocha, S. S.; Sompalli, B.; Wagner, F. T. Activity benchmarks and requirements for Pt, Pt-alloy, and non-Pt oxygen reduction catalysts for PEMFCs. *Appl. Catal., B* **2005**, *56* (1−2), 9−35.

(6) Lefèvre, M.; Proietti, E.; Jaouen, F.; Dodelet, J.-P. Iron-Based Catalysts with Improved Oxygen Reduction Activity in Polymer Electrolyte Fuel Cells. *Science* **2009**, *324* (5923), 71−74.

(7) Kramm, U. I.; Herrmann-Geppert, I.; Fiechter, S.; Zehl, G.; Zizak, I.; Dorbandt, I.; Schmeißer, D.; Bogdanoff, P. Effect of iron-carbide formation on the number of active sites in Fe-N-C catalysts for the oxygen reduction reaction in acidic media. *J. Mater. Chem. A* **2014**, *2* (8), 2663−2670.

(8) Zitolo, A.; Goellner, V.; Armel, V.; Sougrati, M.-T.; Mineva, T.; Stievano, L.; Fonda, E.; Jaouen, F. Identification of catalytic sites for oxygen reduction in iron- and nitrogen-doped graphene materials. *Nat. Mater.* **2015**, *14* (9), 937−942.

(9) Huang, X.; Shen, T.; Zhang, T.; Qiu, H.; Gu, X.; Ali, Z.; Hou, Y. Efficient Oxygen Reduction Catalysts of Porous Carbon Nanostructures Decorated with Transition Metal Species. *Adv. Energy Mater.* **2020**, *10*, 1900375.

(10) Artyushkova, K.; Rojas-Carbonell, S.; Santoro, C.; Weiler, E.; Serov, A.; Awais, R.; Gokhale, R. R.; Atanassov, P. Correlations between Synthesis and Performance of Fe-Based PGM-Free Catalysts in Acidic and Alkaline Media: Evolution of Surface Chemistry and Morphology. *ACS Applied Energy Materials* **2019**, *2* (8), 5406−5418.

(11) Sahraie, N. R.; Kramm, U. I.; Steinberg, J.; Zhang, Y.; Thomas, A.; Reier, T.; Paraknowitsch, J.-P.; Strasser, P. Quantifying the density and utilization of active sites in non-precious metal oxygen electroreduction catalysts. *Nat. Commun.* **2015**, *6*, 8618.

(12) Wan, X.; Liu, X.; Li, Y.; Yu, R.; Zheng, L.; Yan, W.; Wang, H.; Xu, M.; Shui, J. Fe-N-C electrocatalyst with dense active sites and efficient mass transport for high-performance proton exchange membrane fuel cells. *Nature Catalysis* **2019**, *2* (3), 259−268.

(13) Liu, Q.; Liu, X.; Zheng, L.; Shui, J. The Solid-Phase Synthesis of an Fe-N-C Electrocatalyst for High-Power Proton-Exchange Membrane Fuel Cells. *Angew. Chem., Int. Ed.* **2018**, *57* (5), 1204−1208.

(14) Wan, X.; Chen, W.; Yang, J.; Liu, M.; Liu, X.; Shui, J. Synthesis and Active Site Identification of Fe-N-C Single-Atom Catalysts for the Oxygen Reduction Reaction. *ChemElectroChem* **2019**, *6* (2), 304−315.

(15) Chung, H. T.; Cullen, D. A.; Higgins, D.; Sneed, B. T.; Holby, E. F.; More, K. L.; Zelenay, P. Direct atomic-level insight into the active sites of a high-performance PGM-free ORR catalyst. *Science (Washington, DC, U. S.)* **2017**, *357* (6350), 479−484.

(16) Marshall-Roth, T.; Libretto, N. J.; Wrobel, A. T.; Anderton, K. J.; Pegis, M. L.; Ricke, N. D.; Voorhis, T. V.; Miller, J. T.; Surendranath, Y. A pyridinic Fe-N4 macrocycle models the active sites in Fe/N-doped carbon electrocatalysts. *Nat. Commun.* **2020**, *11* (1), No. 5283.

(17) Zhang, N.; Zhou, T.; Chen, M.; Feng, H.; Yuan, R.; Zhong, C. A.; Yan, W.; Tian, Y.; Wu, X.; Chu, W.; Wu, C.; Xie, Y. High-purity pyrrole-type FeN4 sites as a superior oxygen reduction electrocatalyst. *Energy Environ. Sci.* **2020**, *13* (1), 111−118.
(18) Zhang, J.; Zheng, C.; Zhang, M.; Qiu, Y.; Xu, Q.; Cheong, W.-C.; Chen, W.; Zheng, L.; Gu, L.; Hu, Z.; Wang, D.; Li, Y. Controlling N-doping type in carbon to boost single-atom site Cu catalyzed transfer hydrogenation of quinoline. *Nano Res.* **2020**, *13* (11), 3082−3087.
(19) Zhao, K.; Nie, X.; Wang, H.; Chen, S.; Quan, X.; Yu, H.; Choi, W.; Zhang, G.; Kim, B.; Chen, J. G. Selective electroreduction of CO_2 to acetone by single copper atoms anchored on N-doped porous carbon. *Nat. Commun.* **2020**, *11* (1), No. 2455.
(20) Ogawa, S.; Yamaguchi, T.; Gotoh, N. Preparation of a conjugated tautomer of 1,14:7,8-diethenotetrapyrido-[2,1,6-de:2',1',6'-gh:2,1,6-kl:2,1,6na][1,3,5,8,10,12]hexa-azacyclotetradecine and its metal derivatives. *J. Chem. Soc., Perkin Trans. 1* **1974**, No. 0, 976−978.
(21) Peng, P.; Shi, L.; Huo, F.; Mi, C.; Wu, X.; Zhang, S.; Xiang, Z. A pyrolysis-free path toward superiorly catalytic nitrogen-coordinated single atom. *Science Advances* **2019**, *5* (8), No. eaaw2322.
(22) Peng, P.; Shi, L.; Huo, F.; Zhang, S.; Mi, C.; Cheng, Y.; Xiang, Z. In Situ Charge Exfoliated Soluble Covalent Organic Framework Directly Used for Zn-Air Flow Battery. *ACS Nano* **2019**, *13* (1), 878−884.
(23) Narita, A.; Wang, X.-Y.; Feng, X.; Müllen, K. New advances in nanographene chemistry. *Chem. Soc. Rev.* **2015**, *44* (18), 6616−6643.
(24) Glatzel, S.; Schnepp, Z.; Giordano, C. From Paper to Structured Carbon Electrodes by Inkjet Printing. *Angew. Chem., Int. Ed.* **2013**, *52* (8), 2355−2358.
(25) Li, J.; Zhang, H.; Samarakoon, W.; Shan, W.; Cullen, D. A.; Karakalos, S.; Chen, M.; Gu, D.; More, K. L.; Wang, G.; Feng, Z.; Wang, Z.; Wu, G. Thermally Driven Structure and Performance Evolution of Atomically Dispersed FeN4 Sites for Oxygen Reduction. *Angew. Chem., Int. Ed.* **2019**, *58* (52), 18971−18980.
(26) Ellingham, H. J. T. Transactions and Communications. *J. Soc. Chem. Ind., London* **1944**, *63* (5), 125−160.
(27) Graglia, M.; Pampel, J.; Hantke, T.; Fellinger, T.-P.; Esposito, D. Nitro Lignin-Derived Nitrogen-Doped Carbon as an Efficient and Sustainable Electrocatalyst for Oxygen Reduction. *ACS Nano* **2016**, *10* (4), 4364−4371.
(28) Luo, F.; Roy, A.; Silvioli, L.; Cullen, D. A.; Zitolo, A.; Sougrati, M. T.; Oguz, I. C.; Mineva, T.; Teschner, D.; Wagner, S.; Wen, J.; Dionigi, F.; Kramm, U. I.; Rossmeisl, J.; Jaouen, F.; Strasser, P. P-block single-metal-site tin/nitrogen-doped carbon fuel cell cathode catalyst for oxygen reduction reaction. *Nat. Mater.* **2020**, *19* (11), 1215−1223.
(29) Xie, X.; He, C.; Li, B.; He, Y.; Cullen, D. A.; Wegener, E. C.; Kropf, A. J.; Martinez, U.; Cheng, Y.; Engelhard, M. H.; Bowden, M. E.; Song, M.; Lemmon, T.; Li, X. S.; Nie, Z.; Liu, J.; Myers, D. J.; Zelenay, P.; Wang, G.; Wu, G.; Ramani, V.; Shao, Y. Performance enhancement and degradation mechanism identification of a single-atom Co-N-C catalyst for proton exchange membrane fuel cells. *Nature Catalysis* **2020**, *3* (12), 1044−1054.
(30) Wang, Q.; Ina, T.; Chen, W.-T.; Shang, L.; Sun, F.; Wei, S.; Sun-Waterhouse, D.; Telfer, S. G.; Zhang, T.; Waterhouse, G. I. N. Evolution of Zn(II) single atom catalyst sites during the pyrolysis-induced transformation of ZIF-8 to N-doped carbons. *Sci. Bull.* **2020**, *65*, 1743.
(31) Proietti, E.; Jaouen, F.; Lefèvre, M.; Larouche, N.; Tian, J.; Herranz, J.; Dodelet, J.-P. Iron-based cathode catalyst with enhanced power density in polymer electrolyte membrane fuel cells. *Nat. Commun.* **2011**, *2* (1), 416.
(32) Mehmood, A.; Pampel, J.; Ali, G.; Ha, H. Y.; Ruiz-Zepeda, F.; Fellinger, T.-P. Facile Metal Coordination of Active Site Imprinted Nitrogen Doped Carbons for the Conservative Preparation of Non-Noble Metal Oxygen Reduction Electrocatalysts. *Adv. Energy Mater.* **2018**, *8* (9), No. 1701771.
(33) Menga, D.; Ruiz-Zepeda, F.; Moriau, L.; Šala, M.; Wagner, F.; Koyutürk, B.; Bele, M.; Petek, U.; Hodnik, N.; Gaberšček, M.; Fellinger, T.-P. Active-Site Imprinting: Preparation of Fe-N-C Catalysts from Zinc Ion-Templated Ionothermal Nitrogen-Doped Carbons. *Adv. Energy Mater.* **2019**, *9* (43), 1902412.
(34) Chang, Y.; Antonietti, M.; Fellinger, T.-P. Synthesis of Nanostructured Carbon through Ionothermal Carbonization of Common Organic Solvents and Solutions. *Angew. Chem., Int. Ed.* **2015**, *54* (18), 5507−5512.
(35) Rehr, J. J.; Albers, R. C.; Zabinsky, S. I. High-order multiple-scattering calculations of x-ray-absorption fine structure. *Phys. Rev. Lett.* **1992**, *69* (23), 3397−3400.
(36) Sougrati, M. T.; Goellner, V.; Schuppert, A. K.; Stievano, L.; Jaouen, F. Probing active sites in iron-based catalysts for oxygen electro-reduction: A temperature-dependent 57Fe Mössbauer spectroscopy study. *Catal. Today* **2016**, *262*, 110−120.
(37) Bishop, J. L.; Pieters, C.; Burns, R. G. Reflectance and Mössbauer spectroscopy of ferrihydrite-montmorillonite assemblages as Mars soil analog materials. *Geochim. Cosmochim. Acta* **1993**, *57* (19), 4583−4595.
(38) Baker, H.; Hambright, P.; Wagner, L.; Ross, L. Metal ion interactions with porphyrins. I. Exchange and substitution reactions. *Inorg. Chem.* **1973**, *12* (9), 2200−2202.
(39) Li, J.; Jiao, L.; Wegener, E.; Richard, L. L.; Liu, E.; Zitolo, A.; Sougrati, M. T.; Mukerjee, S.; Zhao, Z.; Huang, Y.; Yang, F.; Zhong, S.; Xu, H.; Kropf, A. J.; Jaouen, F.; Myers, D. J.; Jia, Q. Evolution Pathway from Iron Compounds to Fe1(II)-N4 Sites through Gas-Phase Iron during Pyrolysis. *J. Am. Chem. Soc.* **2020**, *142* (3), 1417−1423.
(40) Pampel, J.; Fellinger, T.-P. Opening of Bottleneck Pores for the Improvementof Nitrogen Doped Carbon Electrocatalysts. *Adv. Energy Mater.* **2016**, *6* (8), No. 1502389.
(41) Wagner, S.; Auerbach, H.; Tait, C. E.; Martinaiou, I.; Kumar, S. C. N.; Kübel, C.; Sergeev, I.; Wille, H.-C.; Behrends, J.; Wolny, J. A.; Schünemann, V.; Kramm, U. I. Elucidating the Structural Composition of an Fe-N-C Catalyst by Nuclear- and Electron-Resonance Techniques. *Angew. Chem., Int. Ed.* **2019**, *58* (31), 10486−10492.
(42) Mineva, T.; Matanovic, I.; Atanassov, P.; Sougrati, M.-T.; Stievano, L.; Clémancey, M.; Kochem, A.; Latour, J.-M.; Jaouen, F. Understanding Active Sites in Pyrolyzed Fe-N-C Catalysts for Fuel Cell Cathodes by Bridging Density Functional Theory Calculations and 57Fe Mössbauer Spectroscopy. *ACS Catal.* **2019**, *9* (10), 9359−9371.
(43) Arčon, I.; Piccolo, O.; Paganelli, S.; Baldi, F. *BioMetals* **2012**, *25* (5), 875−881.
(44) Arčon, I.; Kolar, J.; Kodre, A.; Hanžel, D.; Strlič, M. XANES analysis of Fe valence in iron gall inks. *X-Ray Spectrom.* **2007**, *36* (3), 199−205.
(45) Kuezma, M.; Dominko, R.; Hanžel, D.; Kodre, A.; Arčon, I.; Meden, A.; Gaberšček, M. Detailed In Situ Investigation of the Electrochemical Processes in Li_2FeTiO_4 Cathodes. *J. Electrochem. Soc.* **2009**, *156* (10), A809.
(46) Beltrán, D. E.; Litster, S. Half-Wave Potential or Mass Activity? Characterizing Platinum Group Metal-Free Fuel Cell Catalysts by Rotating Disk Electrodes. *ACS Energy Letters* **2019**, *4* (5), 1158−1161.
(47) Bae, G.; Chung, M. W.; Ji, S. G.; Jaouen, F.; Choi, C. H. pH Effect on the H2O2-Induced Deactivation of Fe-N-C Catalysts. *ACS Catal.* **2020**, *10* (15), 8485−8495.
(48) Bonakdarpour, A.; Lefevre, M.; Yang, R.; Jaouen, F.; Dahn, T.; Dodelet, J.-P.; Dahn, J. R. Impact of Loading in RRDE Experiments on Fe-N-C Catalysts: Two- or Four-Electron Oxygen Reduction? *Electrochem. Solid-State Lett.* **2008**, *11* (6), B105−B108.
(49) Paulus, U. A.; Schmidt, T. J.; Gasteiger, H. A.; Behm, R. J. Oxygen reduction on a high-surface area Pt/Vulcan carbon catalyst: a thin-film rotating ring-disk electrode study. *J. Electroanal. Chem.* **2001**, *495* (2), 134−145.

(50) US Department of Energy. *Multi-Year Research, Development, and Demonstration Plan*; Fuel Cell Technologies Office. Multi-Year Research, D., and Demonstration Plan, 2017.
(51) Shao, Y.; Dodelet, J.-P.; Wu, G.; Zelenay, P. PGM-Free Cathode Catalysts for PEM Fuel Cells: A Mini-Review on Stability Challenges. *Adv. Mater.* **2019**, *31* (31), 1807615.
(52) Banham, D.; Kishimoto, T.; Zhou, Y.; Sato, T.; Bai, K.; Ozaki, J.-i.; Imashiro, Y.; Ye, S. Critical advancements in achieving high power and stable nonprecious metal catalyst-based MEAs for real-world proton exchange membrane fuel cell applications. *Sci. Adv.* **2018**, *4* (3), eaar7180.
(53) Cook, A. Catalytic properties of the phthalocyanines. Part I. Catalase properties. *J. Chem. Soc.* **1938**, *0*, 1761−1769.

https://doi.org/10.1021/jacs.1c04884
J. Am. Chem. Soc. 2021, 143, 18010−18019

Supporting Information

Resolving the Dilemma of Fe-N-C Catalysts by the Selective Synthesis of Tetrapyrrolic Active Sites via Imprinting Strategy

Davide Menga, Jian Liang Low, Yan-Sheng Li, Iztok Arčon, Burak Koyutürk, Friedrich Wagner, Francisco Ruiz-Zepeda, Miran Gaberšček, Beate Paulus and Tim-Patrick Fellinger[*]

Experimental Section

Synthesis of NDC-Zn and conventional Fe-N-C:

In a typical synthesis, 0.7 g of 1,2-dicyanobenzene was mixed with 7 g of a 60 mol% LiCl/$ZnCl_2$ mixture in a Ar-filled glovebox. The resulting powder was placed in an alumina crucible and heated with a heating rate of 10 K/min to 800 °C in a tube furnace with a constant Ar flow. After 1 h at 800 °C, the sample was let to cool down to room temperature. The obtain material was ground, washed with 0.1 M HCl for several hours and dried. The synthesis of the conventional Fe-N-C is analogous but with the addition of 16 mg of $FeCl_3$ to the mixture.

Synthesis of NDC-Fe:

NDC-Zn was employed as starting material in the ion exchange reaction from Zn to Fe. Typically, NDC-Zn was degassed in a Büchi oven at 250 °C under vacuum and afterwards mixed with a eutectic mixture of LiCl/$FeCl_3$ in a Schlenk tube in a Ar-filled glovebox. The closed tube was heated up to 175 °C to melt the salt mixture and the sample was stirred for 5 h to ensure complete ion exchange. Once at room temperature, the sample was washed with H_2O to remove the salt mixture and afterwards washed with 0.1 M HCl for several hours and dried.

Synthesis of NDC-Fe-HT:

For the high temperature treatment, 1 g of NDC-Fe was placed in an alumina crucible and pushed inside a tube furnace pre-heated at 1000 °C under Ar atmosphere. After 20 minutes the furnace was turned off and opened to quickly cool down the sample to room temperature.

Characterization:

Mössbauer spectra were recorded with a standard transmission spectrometer using a sinusoidal velocity waveform. The measurements at 4.2 K were performed with both the source of 57Co in rhodium and the absorber in the liquid He bath of a cryostat. The spectra were fitted with suitable Lorentzian lines grouped into electric quadrupole doublets and sextets arising from magnetic hyperfine splitting. MOSFIT software package version 2.2 (FAST-COMTEC GmbH) was used for the fitting of the spectra. Isomer shifts measured in this way are relative to the source at 4.2 K. In order to refer them to α-Fe at ambient temperature, 0.245 mm s^{-1} was added to the measured shifts.

XRD data were recorded with a StadiP diffractometer with Cu Kα radiation (λ = 1.54060, 50 kV, 30 mA, germanium (111)).

Fe and Zn K-edge absorption spectra of NDC-Fe-HT and NDC-Zn sample, respectively, were measured at room temperature in transmission detection mode at the XAFS beamline of the ELETTRA synchrotron radiation facility in Trieste, Italy. A Si (111) double crystal monochromator was used with 0.8 eV resolution at 8 keV. Higher-order harmonics were effectively eliminated by detuning the monochromator crystals to 60% of the rocking curve maximum. The intensity of the monochromatic X-ray beam was measured by three consecutive 30 cm long ionization detectors respectively filled with the following gas mixtures: 580 mbar N2 and 1420 mbar He; 1000 mbar N2, 90 mbar Ar and 910 mbar He; 350 mbar Ar, 1000 mbar N2 and 650 mbar He. In the XANES region equidistant energy steps of 0.25 eV were used, while for the EXAFS region equidistant k steps of 0.03 $Å^{-1}$ were adopted with an integration time of 1 s/step. The exact energy calibration was established with simultaneous absorption measurement on a 5-micron thick Fe or Zn metal foil placed between the second and the third ionization chamber. Absolute energy reproducibility of the measured spectra was ±0.03 eV. The analysis of XANES and EXAFS spectra was performed with the IFEFFIT program package.[1]

TGA-MS was performed on a Mettler Toledo TGA/DSC 1 instrument connected to a Pfeiffer Vacuum Thermostar mass spectrometer in Ar atmosphere with a heating rate of 10 K/min and two

isothermal steps at 150 °C and 250 °C for 20 and 45 minutes respectively to ensure the complete outgas of the samples.

N_2 sorption measurements were performed using a Quantachrome Autosorb iQ2 after outgassing the samples overnight at 250 °C under vacuum. Specific surface areas were determined using Micropore BET Assistant supplied by Quantachrome ASiQwin software. Pore size distributions were calculated with the quenched-solid density functional theory (QSDFT) method (slit/cylindrical pores) with an error ~ 0.2 %.

XPS measurements were performed using a Kratos Axis Supra spectrometer with monochromatized Al Kα radiation. Spectra were acquired with 0.1 eV step size and corrected with respect to C 1s peak at 284.7 eV. Data analysis was performed with ESCAA software.

Aberration corrected scanning transmission electron microscopy (AC-STEM) was performed in a JEOL ARM 200CF microscope imaging with a probe current of ~14 pA and operated at 80 kV.

RDE tests:

Electrochemical measurements were performed in a three-electrode glass cell using 0.1 M $HClO_4$ as electrolyte, diluted with deionized ultrapure water (Milli-Q Integral 5, 18.2 MΩ cm) from a 60% solution (Guaranteed Reagent, Kanto Chemical). Autolab PGSTAT302N (Metrohm) potentiostat was employed for the measurements. Au wire was used as the counter electrode and a freshly calibrated RHE was used as the reference electrode. The solution resistance was determined by electrochemical impedance spectroscopy. The reported polarization curves for ORR were corrected for capacitive currents by subtracting from the curves recorded in O_2-saturated electrolyte the ones recorded in Ar-saturated electrolyte. The catalyst inks were prepared by dispersing 5 mg of catalyst powder in 840 μL of N,N-dimethylformamide (≥99.8, Fisher Scientific) and 50 μL of 5 wt% Nafion suspension (Sigma-Aldrich), followed by sonication for 30 min. 10 μL of ink was drop-cast onto a well-polished glassy carbon electrode (Ø = 5 mm, obtained from Pine Research Instrumentation) and dried under an infrared heater for 60 min. The resulting catalyst loading was 290 μg/cm^2. The accelerated stress

tests were conducted by cycling between 0.4 and 0.8 V at 400 rpm and with a scan rate of 50 mV/s for the short test and 250 mV/s for the long one.

RRDE technique was employed to quantify the H_2O_2 production with different catalyst loading. The platinum ring was held at 1.2 V_{RHE} and a value of -0.255 was used for the collection efficiency.[2]

MEA preparation and PEMFC tests:

Catalyst inks were prepared by dispersing the catalyst powder in a mixture of water, 1-propanol, and ionomer solution, with an I/C ratio of 0.67 g/g, ca. 40 wt% ionomer loading in the catalyst layer. The ink with PGM-free catalyst was coated onto PTFE substrates (50 µm) by applying a bar-coating technique, targeting a final catalyst loading of 2 mg/cm^2 with 5 cm^2 active area of catalyst layer. The anode electrodes were prepared analogously, but using a 20 wt% Pt/C catalyst (TKK) with a final Pt loading of 0.1 mg/cm^2 and an I/C ratio of 0.65 g/g. Through a hot-pressing-based decal procedure (130-160^{o}C with applied pressure 2.2 kN for 12 min), the catalyst layers (both anode and cathode) were directly transferred onto the membrane and subsequently the PTFE substrates are peeled off, yielding the final catalyst coated membranes (CCMs) or membrane electrode assemblies (MEAs). The membrane used was Nafion® 212 with 50 µm thickness, and the gas diffusion layers (GDLs) used was Freundenberg H14C10 with an uncompressed thickness of ≈150 µm and assembled into the single-cell at a compressive strain of 13%. H_2/O_2 polarization curve was recorded under differential-flow conditions (*i.e.*, with H_2/O_2 feed flows of 2000/5000 nccm) at 80^{o}C and 100% relative humidity (RH). The fuel cell inlet pressure was set to 150 kPa_{abs}, which corresponds to H_2 and O_2 partial pressures of approximately 1 bar at given operating condition. The polarization curve was recorded in the current-control mode, holding at each current for 1 minute and averaging the corresponding voltage over the last 30 seconds. The stability testing was performed by applying constant current for 12 hours (140 mA/cm^2, corresponding to uncorrected cell voltage of 0.6 V) at 100% RH, 80^{o}C, and 150 kPa_{abs} H_2/Air by inlet control.

For determining the ORR kinetics in typical PEMFC, the cell voltage was corrected by using equation 1[3]

$$E_{iR-\mathrm{free}} = E_{\mathrm{cell}} + i \cdot R_{\mathrm{HFR}} + i \cdot R^{\mathrm{eff}}_{\mathrm{H+,cath}}$$

Where R_{HFR} represents the high frequency resistance, which is the contribution of electrical contact resistance across the flow field and GDLs as well as the proton conduction resistance of the membrane. $R^{\mathrm{eff}}_{\mathrm{H+,cath}}$ represents the effective proton sheet resistance across the thickness of the cathode catalyst layer, $R_{\mathrm{H+,cath}}$, (in unit of mΩ·cm^2) which can be calculated by equation 2

$$R^{\mathrm{eff}}_{\mathrm{H+,cath}} = \frac{R_{\mathrm{H+,cath}}}{3 + \zeta}$$

Where $R_{\mathrm{H+,cath}}$ is further determined from AC impedance spectra recorded with H_2/N_2 feeds (anode/cathode) at 0.2 V, using a peak-to-peak perturbation of 3.5 mV between 500 kHz and 0.2 Hz (20 points per decade). For the determination of $R_{\mathrm{H+,cath}}$ was applied the same approach as reported in ref [4], assuming negligible electronic resistance compared to proton resistance of catalyst layer. ζ represent the correction factor, which is a function of kinetic resistance and can be expressed a function of Tafel slope.[3] The Tafel slope was assumed 140 mV/dec which corresponds to one electron process at 80 °C.[5] The approach of equation 2 enables to determine ORR activity in absence of O_2 diffusion resistances for any given values of current density.

DFT:

Ab-initio calculations were performed using density functional theory (DFT) as implemented in TURBOMOLE.[6] All calculations were performed on finite-sized graphene clusters with H-termination on boundary carbons to reduce boundary effects.[7] After initial geometry optimization using the TPSS-D3(BJ) functional and def2-SVP basis set, a single point calculation was performed with the PBE-D3(BJ) functional and def2-TZVP basis set.[8-12]

The SCF convergence criteria were 10^{-6} E_h in the total energy and 10^{-3} E_h in the orbital energies. The geometry optimization condition was 10^{-3} a.u. in the maximum norm of the Cartesian gradient. All calculations were performed with various pre-assigned multiplicities among which the system with the lowest total energy was determined to be the ground state.

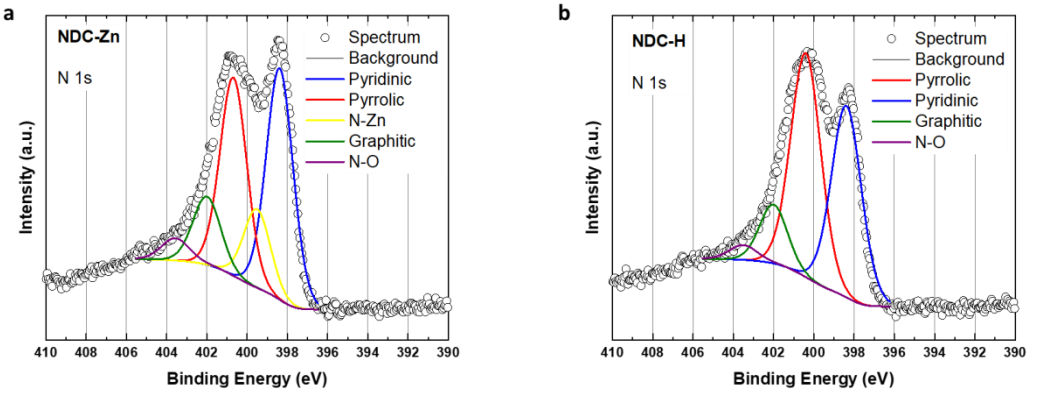

Figure S1: XPS of the N 1s of NDC-Zn (a) and NDC-H (b) with the corresponding peak fitting.

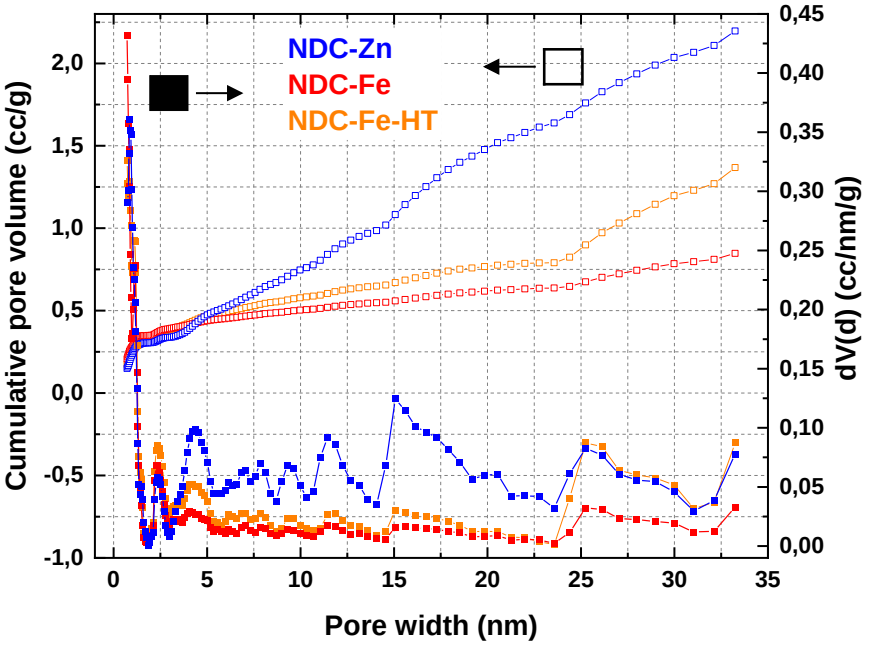

Figure S2: Pore size distributions and cumulative pore volumes calculated from N_2-sorption measurment of NDC-M. QSDFT model for carbon with slit/cylindrical pores was employed. For all three samples the error was ~ 0.2 %.

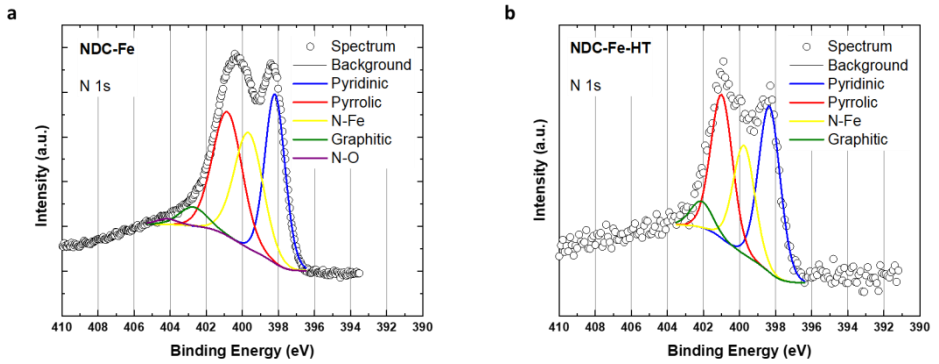

Figure S3: XPS of the N 1s of NDC-Fe (a) and NDC-Fe-HT (b) with the corresponding peak fitting.

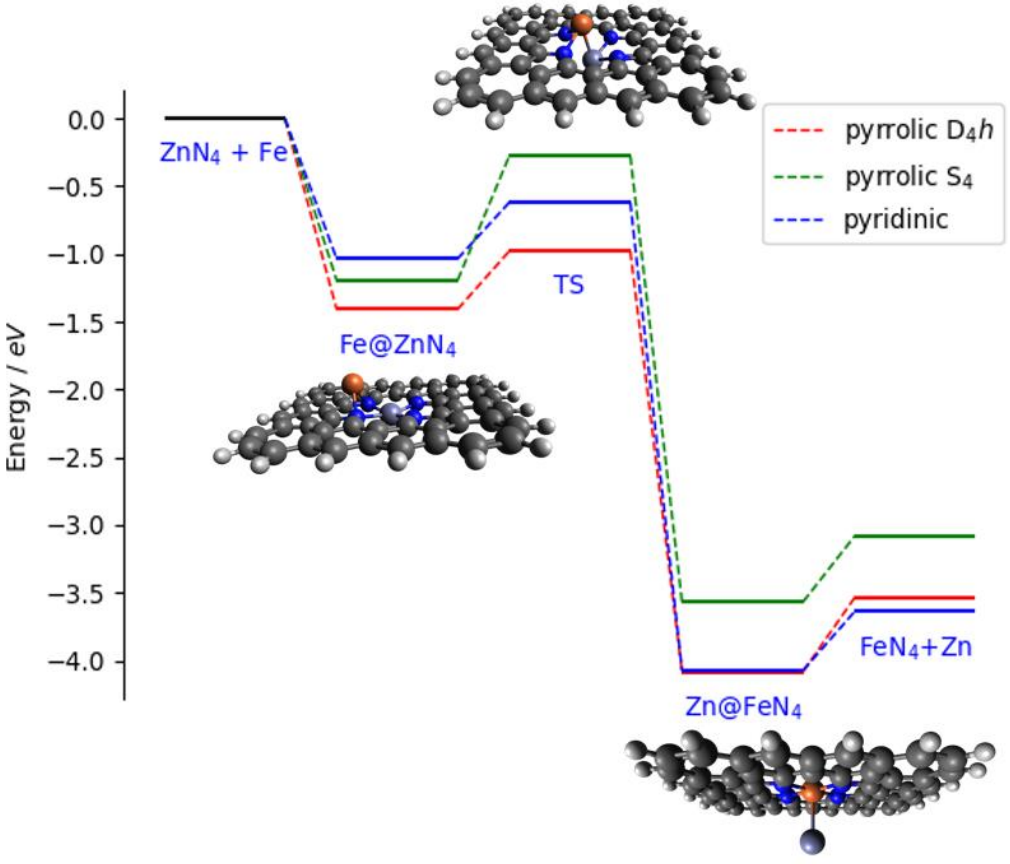

Figure S4. Energy diagram for the Zn-to-Fe exchange reac-tion including the transition states (TS) calculated using the PBE functional. Adsorption geometries for the Pyrrolic-D_{4h} motifs are shown.

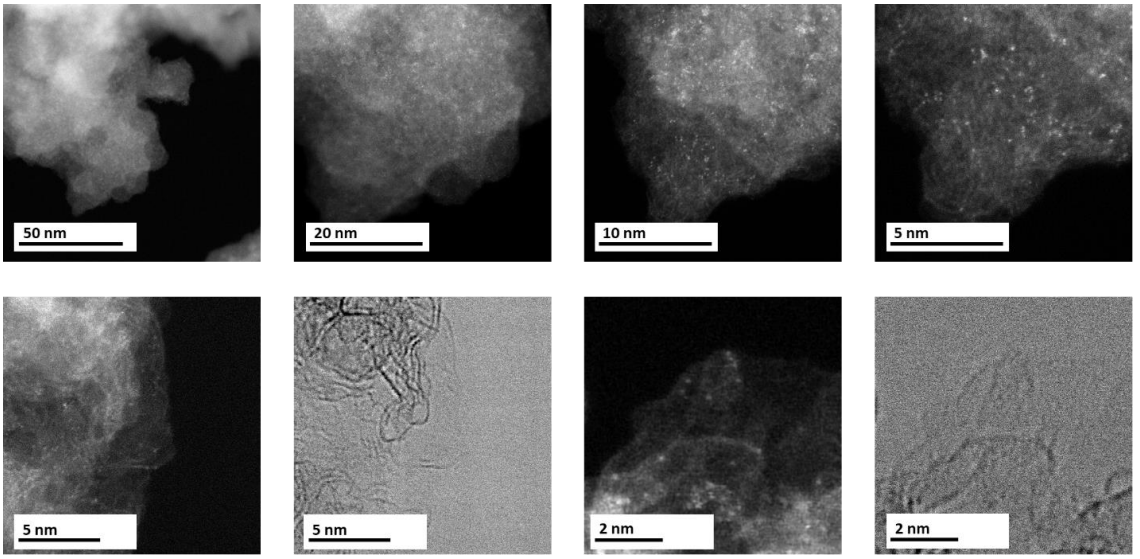

Figure S5: Annular-dark-field and bright-field scanning transmission electron microscopy (ADF- and BF-STEM) and images of NDC-Fe (top) and NDC-Fe-HT (bottom) showing the atomically dispersed Fe atoms.

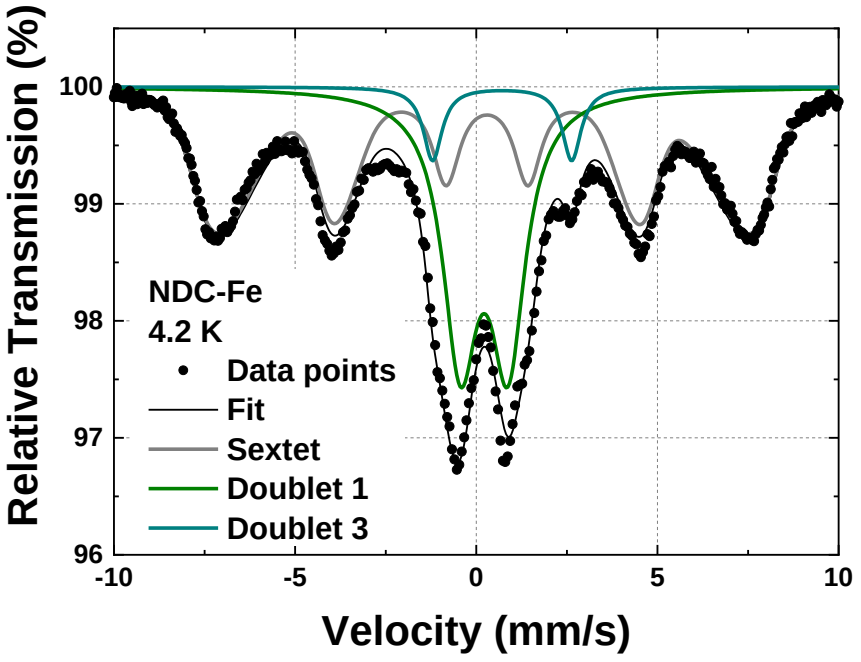

Figure S6: Mössbauer spectra of NDC-Fe recorded at 4.2 K with the corresponding fitting.

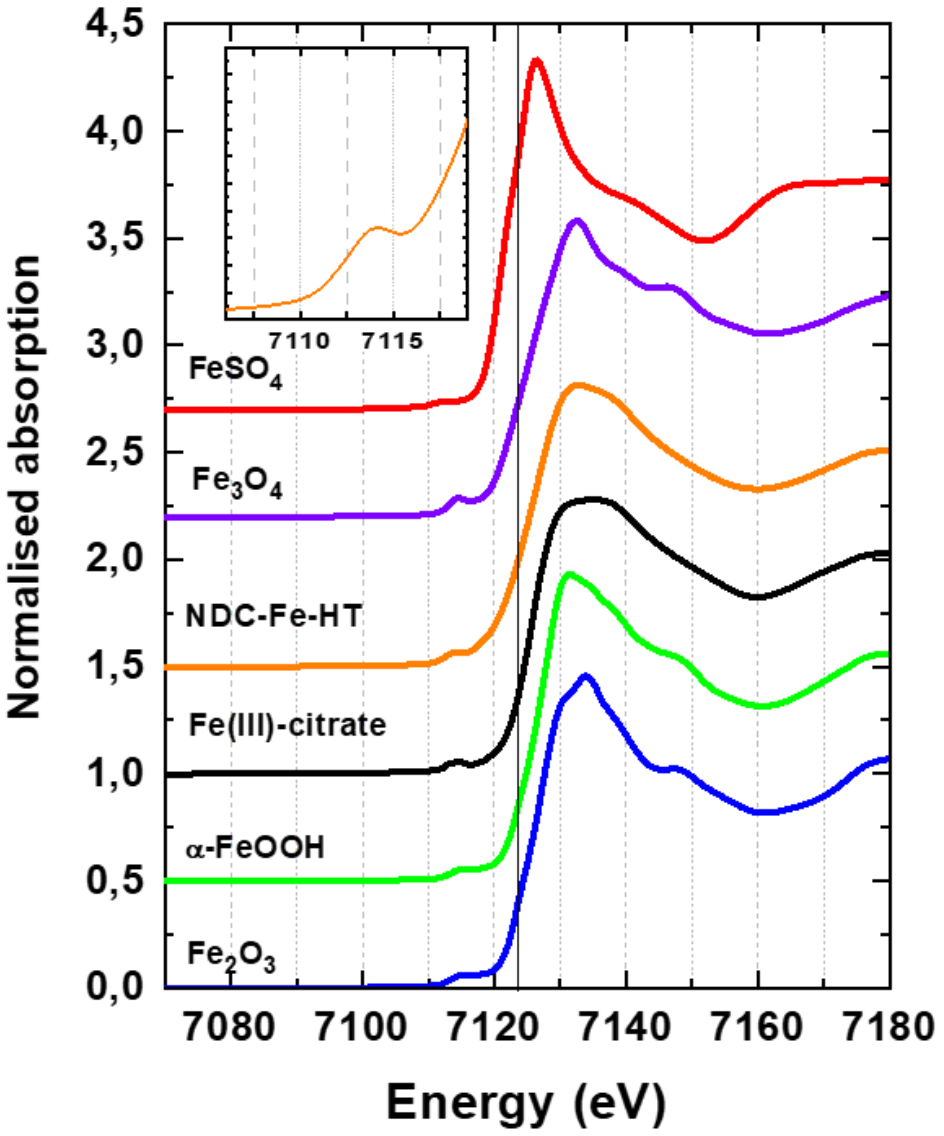

Figure S7: Fe K-edge XANES spectra of NDC-Fe-HT and reference iron compounds with different iron valence states between Fe^{2+} and Fe^{3+} ($FeSO_4 \cdot 7\ H_2O$, Fe_3O_4, Fe(III)-citrate, α-FeOOH and Fe_2O_3). The inset shows the pre-edge peak of NDC-Fe-HT, typical for M-N_4 structures with square-planar coordination.

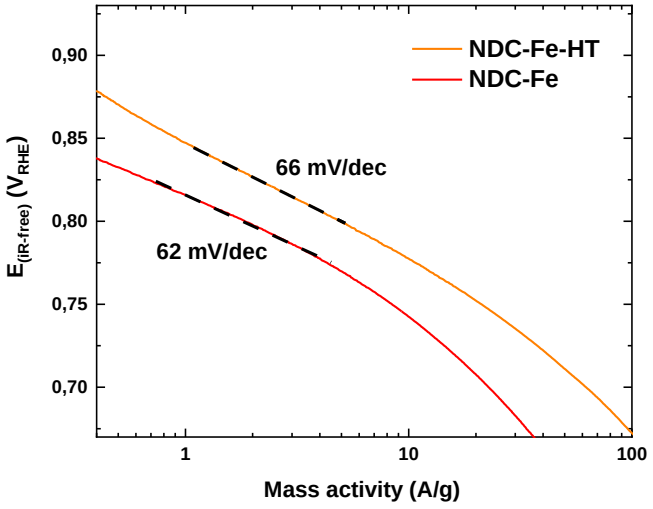

Figure S8: Tafel plot of NDC-Fe (red) and NDC-Fe-HT (orange). Dotted lines represent the Tafel slope.

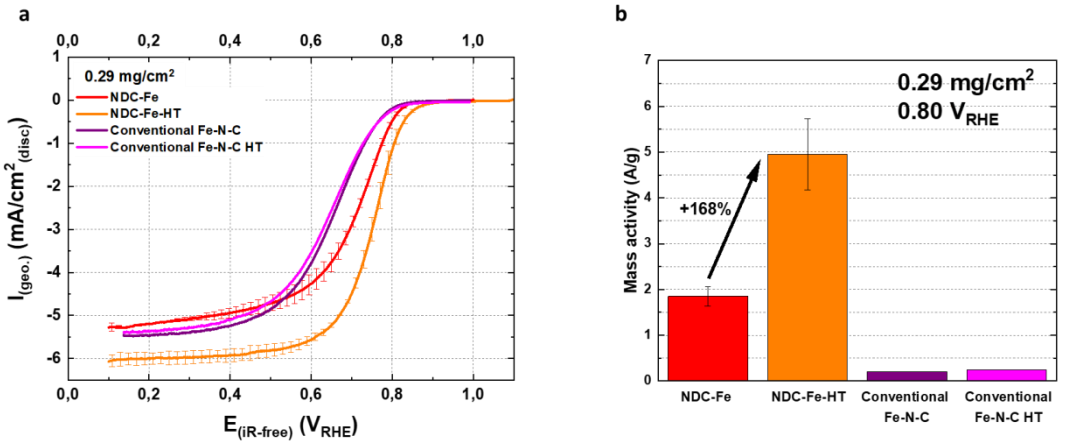

Figure S9: ORR curves of NDC-Fe, NDC-Fe-HT in comparison with a conventional Fe-N-C with and without high temperature treatment recorded with an RDE setup at room temperature in O_2-saturated 0.1 M HClO4 at 1600 rpm, 5 mV/s (anodic scans) (a) and their corresponding kinetic mass activity at 0.8 V (b). All curves were corrected for capacitance contributions.

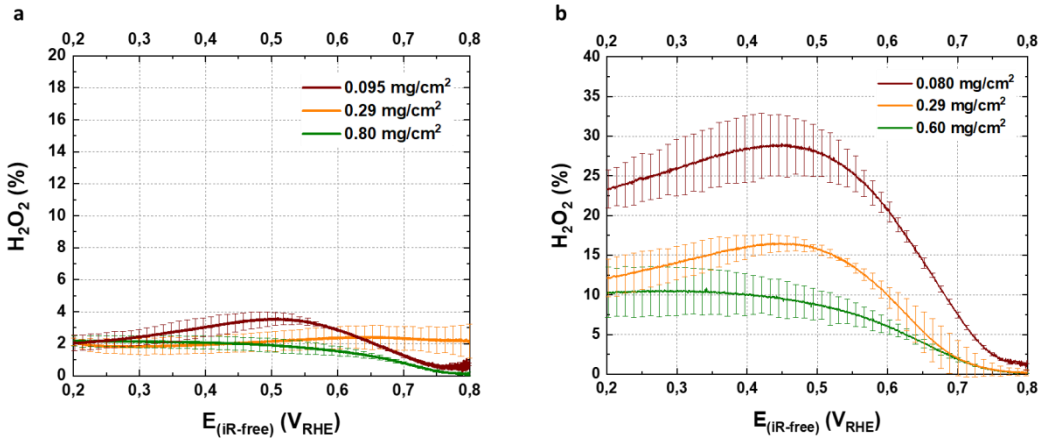

Figure S10: H_2O_2 yield obtained via RRDE experiments for NDC-Fe-HT (a) and a commercially available Fe-N-C catalyst (Pajarito Powder) (b). Measurements were performed at room temperature in O_2-saturated 0.1 M $HClO_4$ at 1600 rpm, 5 mV/s (anodic scans).

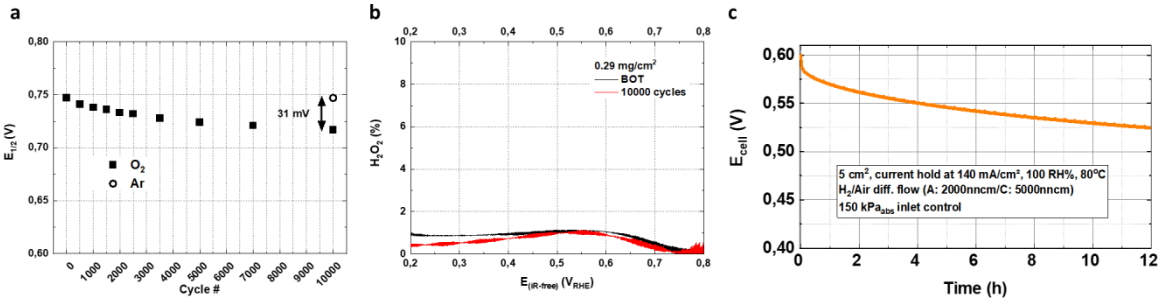

Figure S11: Change in half-wave potential over accelerated stress test (AST) cycle number for NDC-Fe-HT in O_2- or Ar-saturated electrolyte. Activity measurements were performed at room temperature in O_2-saturated 0.1 M $HClO_4$ at 1600 rpm, 5 mV/s (anodic scans) (a). H_2O_2 yield obtained via RRDE experiments for NDC-Fe-HT before and after AST (b). Measured cell voltage curve of NDC-Fe-HT with a catalyst loading of 2 mg/cm^2 recorded with a 140 mA/cm^2 current hold at 80 °C, 150 kPa_{abs} inlet-controlled pressure, 100% RH for both reactants, and constant flows of 2000 nccm of H_2 on the anode and 5000 nccm of air on the cathode. Anode and cathode were operated in counter flow mode (c).

Zn neighbour	*N*	*R* (Å)	σ^2 (Å^2)	*R*-factor
N	4	2.05(1)	0.008(1)	
Cl	1	2.28(1)	0.006(2)	
C	6	2.99(3)	0.030(5)	0.00009
C	4	3.38(3)	0.013(2)	
C	8	4.44(3)	0.014(3)	

Table S1: Parameters of the nearest coordination shells around Zn atoms in the NDC-Zn sample: average number of neighbor atoms (*N*), distance (*R*), and Debye-Waller factor (σ^2). Uncertainty of the last digit is given in parentheses. A best fit is obtained with the amplitude reduction factor S_0^2 = 0.76 and the shift of the energy origin $\Delta E_o = 4 \pm 2$ eV. The goodness-of-fit parameter, *R*-factor, is given in the last column.

The atomic species of neighbours are identified in the fit by their specific scattering factor and phase shift. We constructed the FEFF model for Zn K-edge EXAFS analysis, based on Zn-porphyrin as model structure, where Zn is bound to four pyrrolic nitrogen atoms atoms at 2.05 Å, and surrounded by respective carbon atoms (8 C at 3.07 Å, 4 C at 3.46 Å and 8 C at 4.29 Å), with one additional Cl atom placed at axial position.at the distance of 2.30 Å. Two variable parameters for each shell of neighbours are introduced in each EXAFS model: the distance (*R*) and the Debye-Waller factor (σ^2). The shell coordination numbers (*N*) are kept fixed. A common shift of energy origin ΔE_o in each scattering path is allowed to vary. The amplitude-reduction factor S_0^2 is kept fixed. The EXAFS modelling is performed in the reciprocal k-space, with a k range of 3 Å^{-1} to 12 Å^{-1} and the R range of 1.0 Å to 3.8 Å.

XPS N 1s	NDC-Zn	NDC-H
Total N (wt.%)	8.17	7.95
Npyrrolic/Ntotal (%)	32.93	46.29
Npyridinic/Ntotal (%)	38.43	39.61
N-Zn/Ntotal (%)	13.10	0
Ngraphitic/Ntotal (%)	11.75	11.32
N-O/Ntotal (%)	3.79	2.78

Table S2: Total N content and relative amount of different N species in NDC-Zn and NDC-H (i.e. before and after Zn^{2+} extraction). The amount of $N_{pyrrolic}$ after Zn^{2+} extraction matches the sum of $N_{pyrrolic}$ and N-Zn in the pristine sample, indicating the pyrrolic nature of the Zn-coordinating N atoms.

	Fe wt. %			Zn wt. %		N wt. %	
	XPS	**ICP-MS**	**Mössbauer**	**XPS**	**ICP-MS**	**CHNS**	**XPS**
NDC-Zn	0	0	-	1.26	2.95	13.61	8.17
NDC-Fe	0.54	3.12	4.63	0.39	0.56	10.35	7.92
NDC-Fe-HT	2.31	3.46	3.53	0	-	6.81	5.84

Table S3: Iron, zinc and nitrogen content for NDC-M obtained from different techniques. All values are corrected for the water content in the samples except the ones from XPS.

	i_{mass} at 0.85 VRHE (A/g)	i_{mass} at 0.80 VRHE (A/g)	Ref.
NDC-Fe	0.25 ± 0.02	1.85 ± 0.21	This work
NDC-Fe-HT	0.91 ± 0.16	4.95 ± 0.77	This work
PAJ	0.50	2.33	13
CNRS	0.60	2.00	13
ICL	0.25	1.20	13
UNM	0.50	2.40	13
FeCl2-/NC-1000	1.5	6.6	14
TPI@Z8(SiO2)-650-C	4.04	36.7	15
(CM+PANI)-Fe-C	0.56	5	16
FeNx/GM	1.17	6.37	17
HP-FeN4	0.92	7	18
FeNC-S-MSUFC-2	-	0.53	19
FeSA-N-C	0.92	10.71	20
SA-Fe-N-1.5-800	1.08	7.5	21

Table S4: Literature comparison of mass activity of Fe-N-C catalysts obtained in RDE experiment in acidic electrolyte. When not directly reported by the authors, the values have been extracted from the plots.

	i_{geo} at 0.9 $V_{HFR\text{-}free}$ (mA/cm^2)	i_{geo} at 0.8 $V_{HFR\text{-}free}$ (mA/cm^2)	Loading (mg/cm^2)	i_{mass} at 0.9 $V_{HFR\text{-}free}$ (A/g)	i_{mass} at 0.8 $V_{HFR\text{-}free}$ (A/g)	Ref.
NDC-Fe-HT	4.5	56	2	2.3	28	This work
$FeCl_2$-/NC-1000	1.5	105	4	0.38	26.3	14
TPI@Z8(SiO_2)-650-C	22	300	2.7	8.1	111	15
FeNx/GM	13*	184*	4	3.3	46	17
HP-FeN4	30.4*	169*	4	7.6	42.3	18
PFeTTPP-700	3	158	4	0.75	39.5	22
LANL 2019	34.4**	485**	6.8	5.06	71.3	23

* Not HFR-free

**Data from the first polarization curve

Table S5 Literature comparison of mass activity obtained from H_2-O_2 PEMFC measurements under DOE reference conditions. When not directly reported by the authors, the values have been extracted from the plots.

Sample	D1 (IS; QS; %)	D2 (IS; QS; %)	D3 (IS; QS; %)	Sextet (IS; H; %)
NDC-Fe	0.22; 1.32; 37.1	-	0.71; 3.84; 5.7	0.25; 44; 57.2
NDC-Fe-HT	0.24; 0.98; 44.4	0.22; 1.92; 41.6	0.90; 2.99; 7.6	-0.08; 40; 6.4

Table S6: Isomer shift (IS), quadrupole splitting (QS), magnetic field (H) and percentage (%) values extracted from the Mössbauer measurement of NDC-Fe and NDC-Fe-HT.

Fe neighbour	*N*	*R* (Å)	σ^2 (Å^2)	*R*-factor
O	2.3(5)	1.94(4)	0.008(1)	
N	4	2.05(2)	0.008(1)	
C	8	3.05(2)	0.018(4)	0.006
C	4	3.41(5)	0.013(4)	
C	8	4.29(5)	0.026(7)	

Table S7: Parameters of the nearest coordination shells around Fe atoms in the NDC-Fe-HT sample: average number of neighbor atoms (*N*), distance (*R*), and Debye-Waller factor (σ^2). Uncertainty of the last digit is given in parentheses. A best fit is obtained with the amplitude reduction factor S_0^2 = 0.80 and the shift of the energy origin ΔE_o = -4 ± 2 eV. The goodness-of-fit parameter, *R*-factor, is given in the last column.

The atomic species of neighbours are identified in the fit by their specific scattering factor and phase shift. We constructed the FEFF model for Fe K-edge EXAFS analysis, based on the Fe-porphyrin structure, with two additional oxygen molecules in axial positions Two variable parameters for each shell of neighbours are introduced in each EXAFS model: the distance (*R*) and the Debye-Waller factor (σ^2). The shell coordination numbers (*N*) are kept fixed. A common shift of energy origin ΔE_o in each scattering path is allowed to vary. The amplitude-reduction factor S_0^2 is kept fixed. The EXAFS modelling is performed in the reciprocal k-space, with a k range of 3 Å^{-1} to 12 Å^{-1} and the R range of 1.0 Å to 3.8 Å.

	Empty (½ diagonal N-N)	**Zn**	**Fe**
Pyridine	1.92 Å	1.97 Å	1.90 Å
Pyrollic-D_{4h}-2	1.99 Å	2.02 Å	1.96 Å
Pyrollic- C_{4h}-2	2.09 Å	2.08 Å	2.02 Å

Table S8: Average M-N bond length for M = Zn, Fe compared to half-diagonal N-N distance in the metal-free structure. Geometry optimization was performed in the TPSS functional and def2-SVP basis set.

	Fe-N	Fe-C1	Fe-C2	Fe-C3		Zn-N	Zn-C1	Zn-C2	Zn-C3
Pyrollic-1	2.00	3.05	3.43	4.28		2.06	3.08	3.45	4.32
Pyrollic-D4h-2	1.96	3.01	3.45	4.24		2.02	3.05	3.47	4.28
Pyrollic-C4h-2	2.02	3.03, 3.12	3.53	4.25, 4.33		2.08	3.06, 3.15	3.54	4.28, 4.37
Pyrollic-D4h-3	1.96	3.01	3.45	4.24		2.02	3.05	3.46	4.28
Pyrollic-C4h-2	2.00	3.00, 3.10	3.50	4.20. 4.32		2.05	3.02, 3.13	3.51	4.23. 4.36

Table S9: Comparison of average M-X distances in Å for different pyrrolic clusters (M = Fe, Zn; X = N, C) obtained with DFT geometry optimization with the TPSS functional and def2-SVP basis set.

Fe-N distance	Fe-C distances	Zn-N distance	Zn-C distances
1.90	2.72, 2.98, 3.35, 4.10, 4.28	1.98	2.74, 3.01, 3.37, 4.10, 4.29

Table S10: Comparison of calculated M-X distances in Å for the pyridinic $MN_4C_{52}H_{20}$ clusters (M = Fe, Zn; X = N, C)

NDC-Zn	N wt. %
800	13.61
900	6.66
1000	4.67

Table S11: Nitrogen content obtained from CHNS analysis of NDC-Zn prepared at different temperature.

XPS N 1s	NDC-Fe	NDC-Fe-HT
Total N (wt.%)	7.92	5.84
Npyrrolic/Ntotal (%)	33.21	32.39
Npyridinic/Ntotal (%)	30.81	37.34
N-Fe/Ntotal (%)	30.30	24.49
Ngraphitic/Ntotal (%)	4.67	5.88
N-O/Ntotal (%)	1.01	-

TGA-MS analysis:

TGA-MS was employed to gain a better understanding of the second ion exchange and the relative stability of Zn-N_4 *vs.* Fe-N_4 sites. In the experiment, the selected high surface area samples were degassed twice, first at 150 °C and then at 250 °C in Ar atmosphere. Afterwards, the temperature was raised to 1000 °C, also in Ar atmosphere, with a heating rate of 10 K/minute. The ferrihydrite and the formed Fe-N_4 sites are the only differences between the pristine NDC-Zn and the ion exchanged NDC-Fe. Functional groups on the surface, arising from the aqueous work-up, are expected to be similar for both materials. For both samples, a weight loss of ≈ 15 % attributed to H_2O and air is observed in the first degassing step, as expected for high surface area carbon (**Figure S10**). When comparing the weight loss at temperatures above 250 °C (**Figure S11**), NDC-Fe clearly shows a steeper loss, which is also initiated at lower temperature compared to NDC-Zn. In the MS analysis of NDC-Fe a clear event can be noted at temperature close to 400 °C involving CO_2 and H_2O (**Figure S12**). Since it does not happen in NDC-Zn, we can connect this to the ferrihydrite decomposition. Consequently, the coordination of Fe to empty (protonated) N_4 cavities, in the presence of oxygen, could act in accordance with the following mechanism:

1) Dehydration of ferrihydrite: $Fe_{10}O_{14}(OH)_2 \rightarrow Fe_{10}O_{15} + H_2O$
2) Carbothermal reduction: $2\ Fe_{10}O_{15} + 5\ C \rightarrow 20\ FeO + 5\ CO_2$
3) Coordination of iron: $FeO + H_2\text{-}N_4 \rightarrow Fe\text{-}N_4 + H_2O$

At temperatures around preliminary synthesis temperature of 800 °C, pyrolytic reorganization is observed for both NDC-Fe and NDC-Zn, visible by evolution of CO_2, H_2O and NO (**Figure S13**). When comparing the N_2 signal in the two samples (**Figure S14**) it is worth noticing that for NDC-Fe two different events are visible, one centered at ≈815 °C and another at ≈950 °C, whereas for NDC-Zn only one event centered at ≈985 °C is visible, indicating that the N_2 loss is initiated at ~170 °C lower temperature for NDC-Fe compared to NDC-Zn. This N_2 loss may be attributed to the decomposition of the Fe-N_4 sites. For NDC-Zn the evolution of NO is an obvious difference compared to the NDC-Fe sample. NO may be involved in the decomposition of Zn-N_4 sites.

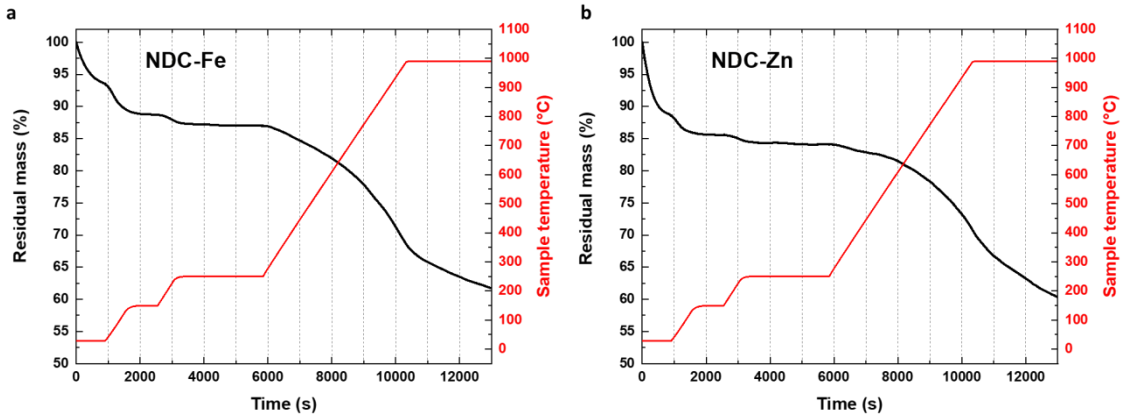

Figure S12: TGA curves for NDC-Fe (a) and NDC-Zn (b). Sample mass in percentage is shown in black and sample temperature in red.

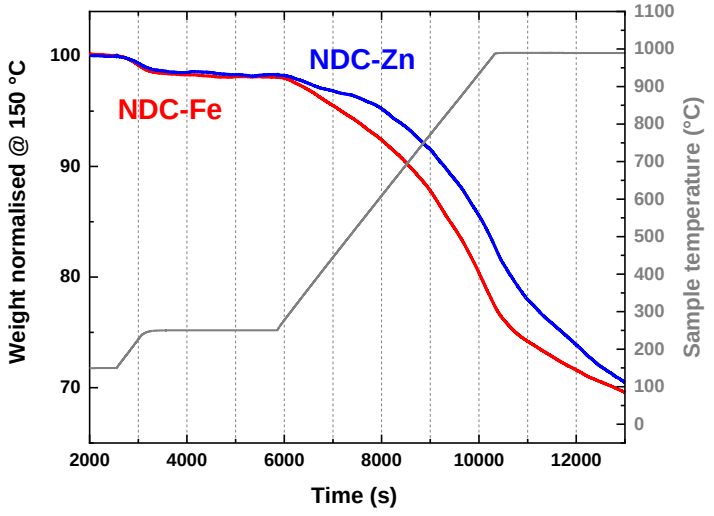

Figure S13: TGA curves for NDC-Fe (red) and NDC-Zn (blue). Sample mass has been normalised to the value after the first degassing step at 150 °C. Sample temperature is displayed in grey.

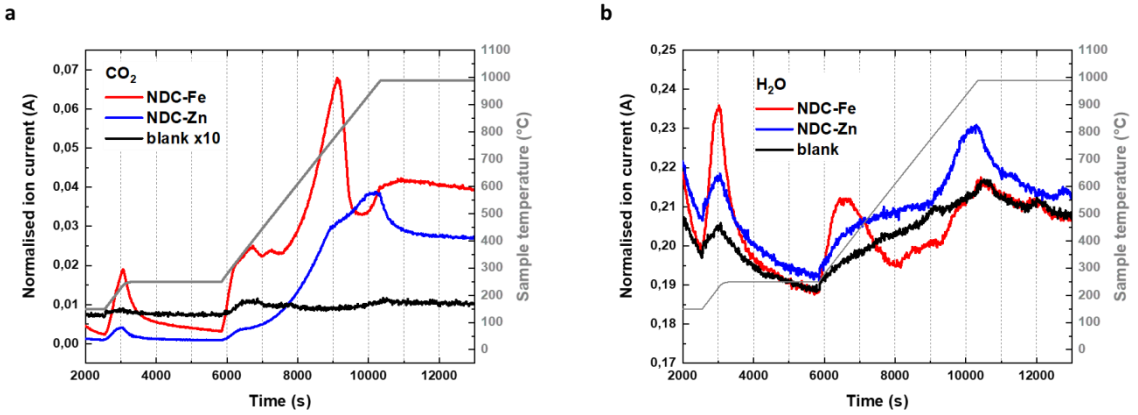

Figure S14: CO_2 (a) and H_2O (b) MS signal for NDC-Fe (red), NDC-Zn (blue) and the blank measurement where no sample is present (black). Sample temperature is displayed in grey.

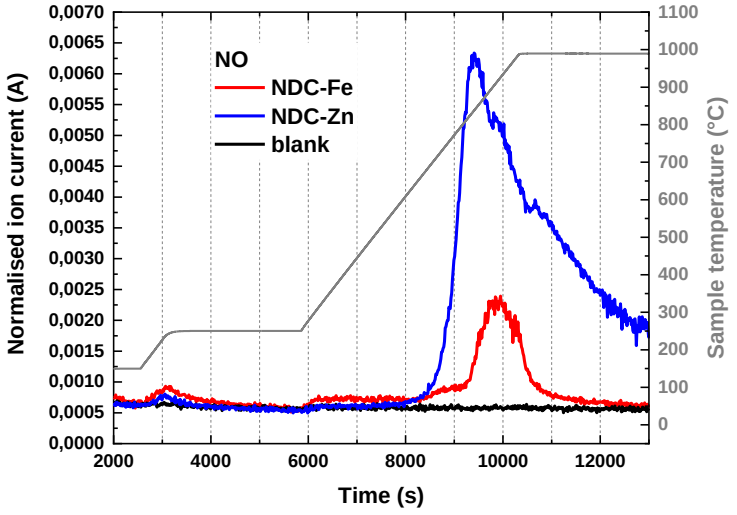

Figure S15: Nitric oxide MS signal for NDC-Fe (red), NDC-Zn (blue) and the blank measurement where no sample is present (black). Sample temperature is displayed in grey.

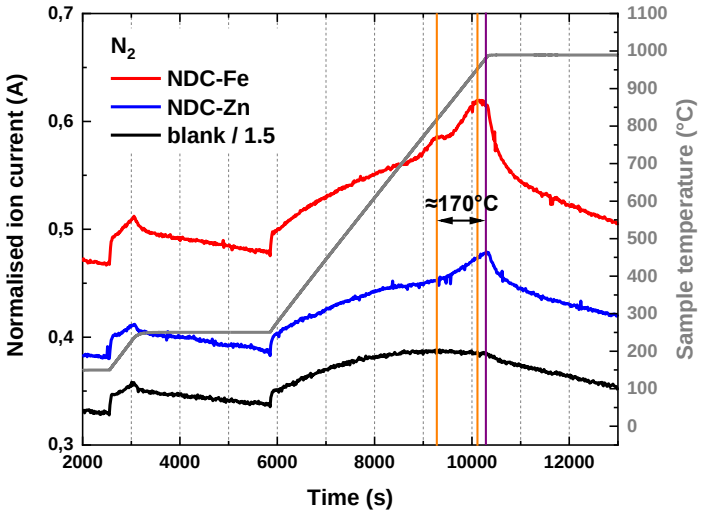

Figure S16: N_2 MS signal for NDC-Fe (red), NDC-Zn (blue) and the blank measurement where no sample is present (black). Sample temperature is displayed in grey. The orange vertical lines are centered with the NDC-Fe related peaks and the purple vertical line is centered with the NDC-Zn related peak.

References:

1. Ravel, B.; Newville, M., ATHENA, ARTEMIS, HEPHAESTUS: data analysis for X-ray absorption spectroscopy using IFEFFIT. *J Synchrotron Radiat* **2005,** *12* (Pt 4), 537-41.
2. Madkikar, P.; Menga, D.; Harzer, G. S.; Mittermeier, T.; Siebel, A.; Wagner, F. E.; Merz, M.; Schuppler, S.; Nagel, P.; Muñoz-García, A. B.; Pavone, M.; Gasteiger, H. A.; Piana, M., Nanometric Fe-Substituted ZrO2on Carbon Black as PGM-Free ORR Catalyst for PEMFCs. *Journal of The Electrochemical Society* **2019,** *166* (7), F3032-F3043.
3. Neyerlin, K. C.; Gu, W.; Jorne, J.; Clark, A.; Gasteiger, H. A., Cathode Catalyst Utilization for the ORR in a PEMFC. *Journal of The Electrochemical Society* **2007,** *154* (2), B279.
4. Liu, Y.; Murphy, M.; Baker, D.; Gu, W.; Ji, C.; Jorne, J.; Gasteiger, H. A., Determination of Electrode Sheet Resistance in Cathode Catalyst Layer by AC Impedance. *ECS Transactions* **2007,** *11* (1), 473-484.
5. Osmieri, L.; Ahluwalia, R. K.; Wang, X.; Chung, H. T.; Yin, X.; Kropf, A. J.; Park, J.; Cullen, D. A.; More, K. L.; Zelenay, P.; Myers, D. J.; Neyerlin, K. C., Elucidation of Fe-N-C electrocatalyst active site functionality via in-situ X-ray absorption and operando determination of oxygen reduction reaction kinetics in a PEFC. *Applied Catalysis B: Environmental* **2019,** *257*, 117929.
6. Ahlrichs, R.; Bär, M.; Häser, M.; Horn, H.; Kölmel, C., Electronic structure calculations on workstation computers: The program system turbomole. *Chemical Physics Letters* **1989,** *162* (3), 165-169.
7. Khosravi, A.; Vessally, E.; Oftadeh, M.; Behjatmanesh-Ardakani, R., Ammonia capture by MN4 (M = Fe and Ni) clusters embedded in graphene. *Journal of Coordination Chemistry* **2018,** *71* (21), 3476-3486.
8. Weigend, F.; Ahlrichs, R., Balanced basis sets of split valence, triple zeta valence and quadruple zeta valence quality for H to Rn: Design and assessment of accuracy. *Physical Chemistry Chemical Physics* **2005,** *7* (18), 3297.
9. Tao, J.; Perdew, J. P.; Staroverov, V. N.; Scuseria, G. E., Climbing the Density Functional Ladder: Nonempirical Meta–Generalized Gradient Approximation Designed for Molecules and Solids. *Physical Review Letters* **2003,** *91* (14).
10. Perdew, J. P.; Burke, K.; Ernzerhof, M., Generalized Gradient Approximation Made Simple. *Physical Review Letters* **1996,** *77* (18), 3865-3868.
11. Grimme, S.; Antony, J.; Ehrlich, S.; Krieg, H., A consistent and accurate ab initio parametrization of density functional dispersion correction (DFT-D) for the 94 elements H-Pu. *The Journal of Chemical Physics* **2010,** *132* (15), 154104.
12. Grimme, S.; Ehrlich, S.; Goerigk, L., Effect of the damping function in dispersion corrected density functional theory. *Journal of Computational Chemistry* **2011,** *32* (7), 1456-1465.
13. Primbs, M.; Sun, Y.; Roy, A.; Malko, D.; Mehmood, A.; Sougrati, M.-T.; Blanchard, P.-Y.; Granozzi, G.; Kosmala, T.; Daniel, G.; Atanassov, P.; Sharman, J.; Durante, C.; Kucernak, A.; Jones, D.; Jaouen, F.; Strasser, P., Establishing reactivity descriptors for platinum group metal (PGM)-free Fe–N–C catalysts for PEM fuel cells. *Energy & Environmental Science* **2020**.
14. Li, J.; Jiao, L.; Wegener, E.; Richard, L. L.; Liu, E.; Zitolo, A.; Sougrati, M. T.; Mukerjee, S.; Zhao, Z.; Huang, Y.; Yang, F.; Zhong, S.; Xu, H.; Kropf, A. J.; Jaouen, F.; Myers, D. J.; Jia, Q., Evolution Pathway from Iron Compounds to Fe1(II)–N4 Sites through Gas-Phase Iron during Pyrolysis. *Journal of the American Chemical Society* **2020,** *142* (3), 1417-1423.
15. Wan, X.; Liu, X.; Li, Y.; Yu, R.; Zheng, L.; Yan, W.; Wang, H.; Xu, M.; Shui, J., Fe–N–C electrocatalyst with dense active sites and efficient mass transport for high-performance proton exchange membrane fuel cells. *Nature Catalysis* **2019,** *2* (3), 259-268.
16. Chung, H. T.; Higgins, D.; Zelenay, P.; Cullen, D. A.; Sneed, B. T.; More, K. L.; Holby, E. F., Direct atomic-level insight into the active sites of a high-performance PGM-free ORR catalyst. *Science* **2017,** *357* (6350), 479-484.
17. Fu, X.; Li, N.; Ren, B.; Jiang, G.; Liu, Y.; Hassan, F. M.; Su, D.; Zhu, J.; Yang, L.; Bai, Z.; Cano, Z. P.; Yu, A.; Chen, Z., Tailoring FeN 4 Sites with Edge Enrichment for Boosted Oxygen Reduction Performance in Proton Exchange Membrane Fuel Cell. *Advanced Energy Materials* **2019,** *9* (11), 1803737.
18. Zhang, N.; Zhou, T.; Chen, M.; Feng, H.; Yuan, R.; Zhong, C. A.; Yan, W.; Tian, Y.; Wu, X.; Chu, W.; Wu, C.; Xie, Y., High-purity pyrrole-type FeN4 sites as a superior oxygen reduction electrocatalyst. *Energy & Environmental Science* **2020,** *13* (1), 111-118.
19. Mun, Y.; Lee, S.; Kim, K.; Kim, S.; Lee, S.; Han, J. W.; Lee, J., Versatile Strategy for Tuning ORR Activity of a Single Fe-N4 Site by Controlling Electron-Withdrawing/Donating Properties of a Carbon Plane. *Journal of the American Chemical Society* **2019,** *141* (15), 6254-6262.

20. Jiao, L.; Wan, G.; Zhang, R.; Zhou, H.; Yu, S.-H.; Jiang, H.-L., From Metal-Organic Frameworks to Single-Atom Fe Implanted N-doped Porous Carbons: Efficient Oxygen Reduction in Both Alkaline and Acidic Media. *Angewandte Chemie International Edition* **2018,** *57* (28), 8525-8529.
21. Miao, Z.; Wang, X.; Tsai, M.-C.; Jin, Q.; Liang, J.; Ma, F.; Wang, T.; Zheng, S.; Hwang, B.-J.; Huang, Y.; Guo, S.; Li, Q., Atomically Dispersed Fe-N x /C Electrocatalyst Boosts Oxygen Catalysis via a New Metal-Organic Polymer Supramolecule Strategy. *Advanced Energy Materials* **2018,** *8* (24), 1801226.
22. Yuan, S.; Shui, J.-L.; Grabstanowicz, L.; Chen, C.; Commet, S.; Reprogle, B.; Xu, T.; Yu, L.; Liu, D.-J., A Highly Active and Support-Free Oxygen Reduction Catalyst Prepared from Ultrahigh-Surface-Area Porous Polyporphyrin. *Angewandte Chemie International Edition* **2013,** *52* (32), 8349-8353.
23. Zelenay, P, ElectroCat, 2020 Hydrogen and Fuel Cells Program Annual Merit Review.

Paper M2

Computational Modelling of Pyrrolic MN_4 Motifs Embedded in Graphene for Catalyst Design

J. L. Low, B. Paulus, *Catalysts* **2023**, *13(3)*, 566.
DOI: https://doi.org/10.3390/catal13030566

Computational Highlights

This paper provided the initial testing for the design of geometric models in the study of MN_4 sites in M-N-Cs as used in all other publications. By comparing the metal binding energy and geometries of MN_4 sites (M = Zn, Fe) between the cluster and periodic models, we determined that the chemical properties do not differ significantly for MN_4 sites with similar atomic structures, justifying a switch to the cluster model for easier implementation of hybrid functionals and pyrrolic MN_4 site. We subsequently studied the isomeric pyrrolic and pyridinic MN_4 clusters and determined trends in the conformational energies (pyrrolic vs pyridinic), metal binding energies and M-N bond lengths in relation to the NBO charge population, allowing us to understand the nature of binding, especially among the first-row transition metals which are relevant for catalytic applications.

Author Contributions

The project was conceived by Jian Liang Low under the guidance of Beate Paulus and inspired by experimental results from Davide Menga and Tim-Patrick Fellinger. Jian Liang Low designed the computational study and performed the DFT calculations. Jian Liang Low analyzed the data and wrote the manuscript under the guidance of Beate Paulus.

catalysts

IMPACT FACTOR 3.9

CITESCORE 6.3

Article

Computational Modelling of Pyrrolic MN_4 Motifs Embedded in Graphene for Catalyst Design

Jian Liang Low and Beate Paulus

Special Issue

Computational Design of Solid Catalysts for Electrocatalysis and Photocatalysis

Edited by

Prof. Dr. Huilong Dong

MDPI

https://doi.org/10.3390/catal13030566

catalysts

MDPI

Article

Computational Modelling of Pyrrolic MN_4 Motifs Embedded in Graphene for Catalyst Design

Jian Liang Low * and Beate Paulus *

Institute of Chemistry and Biochemistry, Freie Universität Berlin, Arnimallee 22, 14195 Berlin, Germany
* Correspondence: low.jian.liang@fu-berlin.de (J.L.L.); b.paulus@fu-berlin.de (B.P.)

Abstract: Carbon-based materials doped with metal and nitrogen (M-N-Cs) have promising potential in electrocatalytic applications with the advantage of material sustainability. MN_4 motifs incorporated into a carbon lattice are generally known to be responsible for the activity of these materials. While many computational studies assume the tetrapyridinic MN_4 motifs, recent studies have elucidated the role of tetrapyrrolic MN_4 motifs in electrocatalysis. Using density functional theory, we constructed and compared various structural models to study the incorporation of tetrapyrrolic and tetrapyridinic MN_4 motifs in 2D carbon materials and analyzed the type of interactions between each metal species and the N_4 site. We further quantified the relative affinity of various metal species to the two types of N_4 site. Upon analysis of energies, bond lengths, electronic population and charges, we found that metals that exhibit highly ionic binding characters have a greater affinity towards tetrapyrrolic MN_4 motifs compared to species that participate in covalent interactions with the π-system. Furthermore, the binding strength of each species in the N_4 site depend on the electronegativity as well as the availability of orbitals for accepting electrons from the π-system.

Keywords: single-atom catalyst; carbon material; density functional theory; pyrrolic and pyridinic MN_4

check for updates

Citation: Low, J.L.; Paulus, B. Computational Modelling of Pyrrolic MN_4 Motifs Embedded in Graphene for Catalyst Design. *Catalysts* **2023**, *13*, 566. https://doi.org/10.3390/catal13030566

Academic Editor: Huilong Dong

Received: 15 February 2023
Revised: 6 March 2023
Accepted: 9 March 2023
Published: 10 March 2023

1. Introduction

As humanity strives towards a sustainable economy with minimal fossil fuel combustion and carbon footprint, increasing political and economic attention has been directed towards optimizing electrochemical processes for efficient energy conversion and storage. Some of the key electrochemical processes include the oxygen reduction reaction (ORR) and carbon dioxide reduction reaction (CO_2RR). The former is a crucial cathodic process for energy conversion in emission-free fuel cell vehicles while the latter serves a dual purpose to control CO_2 emission by converting it into useful chemical products. State-of-the-art electrocatalysts for these processes are generally derived from relatively sparse elements such as the platinum group metals (PGMs) [1,2] and coinage metals [3,4], thereby posing a limit to the sustainability of these processes. Recently, electrocatalysts based on earth-abundant materials have been developed as low-cost substitutes [5–7], especially metal- and nitrogen-codoped carbon materials (M-N-Cs) which have attracted widespread attention as promising and sustainable alternatives to the PGMs [5,6].

M-N-Cs are often synthesized by pyrolyzing a combination of organic and inorganic precursors, including aromatic compounds, metal–organic frameworks, and metal salts. Due to the great degree of disorder present in the pyrolyzed materials, it is often challenging to determine the identity of active sites responsible for the catalysis, much less to understand the mechanisms behind the reactions. While there is a general agreement that the planar MN_4 site is the catalytically active site for most electrochemical applications [7,8], there are diverging views on how these MN_4 sites are incorporated into the carbon backbone. The pyridinic MN_4 sites are generally believed to be ideal, as their formation induces the least number of defects on the carbon backbone. However, naturally abundant MN_4 complexes such as haem and chlorophylls exhibit an almost exclusively tetrapyrrolic

coordination. Furthermore, various in-situ reaction studies have identified the tetrapyrrolic FeN_4 sites as the active site responsible for the high ORR activity of Fe-N-Cs [9–12].

In recent years, there have been several reports on the successful synthesis and characterization of M-N-Cs containing phase-pure tetrapyrrolic MN_4 sites [8,13]. For the synthesis of Fe-N-Cs, transmetallation strategies employing Zn as a sacrificial templating ion during pyrolysis have been developed in order to avoid side phases of iron oxides and carbides, with the identification of exclusively tetrapyrrolic sites in the synthesized material [8,14–16]. It is also worthy to note that Mg has also been employed as sacrificial templating ion [17], suggesting that the templating pathway is not exclusive to Zn. With the successful implementation of the transmetallation strategies, it is now possible to incorporate a certain level of control in the unpredictable pyrolytic synthesis. As the morphology and site density remain relatively unchanged after transmetallation, quantitative studies on the intrinsic activities of MN_4 sites could potentially be performed [18]. In addition, less conventional choices of metal dopants could in principle be introduced into the system, leading to a wide range of unexplored M-N-C catalysts. In this study, we apply density functional theory (DFT) to compare the affinity of various metals towards tetrapyrrolic and tetrapyridinic MN_4 motifs. For simplicity, since this study deals exclusively with tetracoordinated MN_4 sites, the terms tetrapyrrolic and tetrapyridinic will be shortened to pyrrolic and pyridinic, respectively.

2. Computational Details

In general, the density functional theory (DFT) calculations were performed in the unrestricted/spin-polarized Kohn–Sham formalism. The PBE functional was used for the initial comparisons between the cluster and periodic calculations [19]. For the extended study involving different metals in the MN_4 clusters, we switched to the hybrid PBE0 functional in order to reduce the delocalization error associated with the d-orbitals of transition metals [20–22]. For both functionals, the Grimme D3 dispersion correction was applied with the Becke–Johnson damping function [23,24] to account for dispersion interactions.

Cluster calculations were performed using the program package TURBOMOLE with finite-sized clusters terminated with H-atoms [25,26]. Geometry optimizations were performed with the def2-SVP basis while a larger def2-TZVP basis was applied for single-point calculations [27]. Electronic steps were converged to 10^{-6} a.u. in the total energy and 10^{-3} a.u. in the orbital energies, while geometric steps were converged to 10^{-3} a.u. in the maximum norm of the Cartesian gradient. Each cluster was calculated with various preassigned multiplicities until the most stable spin state was found and determined as the ground state. Atomic charges were obtained with the natural bond orbital (NBO) population analysis [28] and abbreviated as NBO charges.

Periodic calculations were performed with the Vienna Ab initio Simulation Package (VASP) using the projector augmented-wave (PAW) method with an energy cutoff $E_{cut} = 600$ eV [29–32]. The RMM-DIIS algorithm was applied for electronic relaxation and the electronic convergence criterion was set to 10^{-5} eV. The Gaussian smearing approach with a smearing width of $\sigma = 0.05$ eV was applied. K-points were sampled using a $3 \times 3 \times 1$ Γ-centered mesh grid for the geometry optimization and $6 \times 6 \times 1$ grid for single-point calculations. Ionic relaxation steps were performed with the conjugate gradient algorithm with a force convergence of 10^{-2} $\frac{eV}{Å}$. During geometry optimization, all atomic positions and lattice constants were relaxed under the constraint of constant unit cell volume (ISIF = 4), with an initial vacuum width of 15 Å perpendicular to the 2D material. All atomic structures were visualized with VESTA [33].

3. Results and Discussion

3.1. Structural Model Comparison

For the purpose of the comparison between pyrrolic and pyridinic MN_4 sites embedded in a graphene layer, we constructed several clusters and unit cell models of different shapes and sizes as shown in Figure 1. Extending a basic pyrrolic MN_4C_{20} unit with purely

hexagonal carbon rings generally led to huge distortions in the planarity of the cluster, indicative of a high lattice strain in an extended environment. In order to minimize the lattice strain and keep the clusters planar, seven-membered rings were introduced next to the pyrrole units.

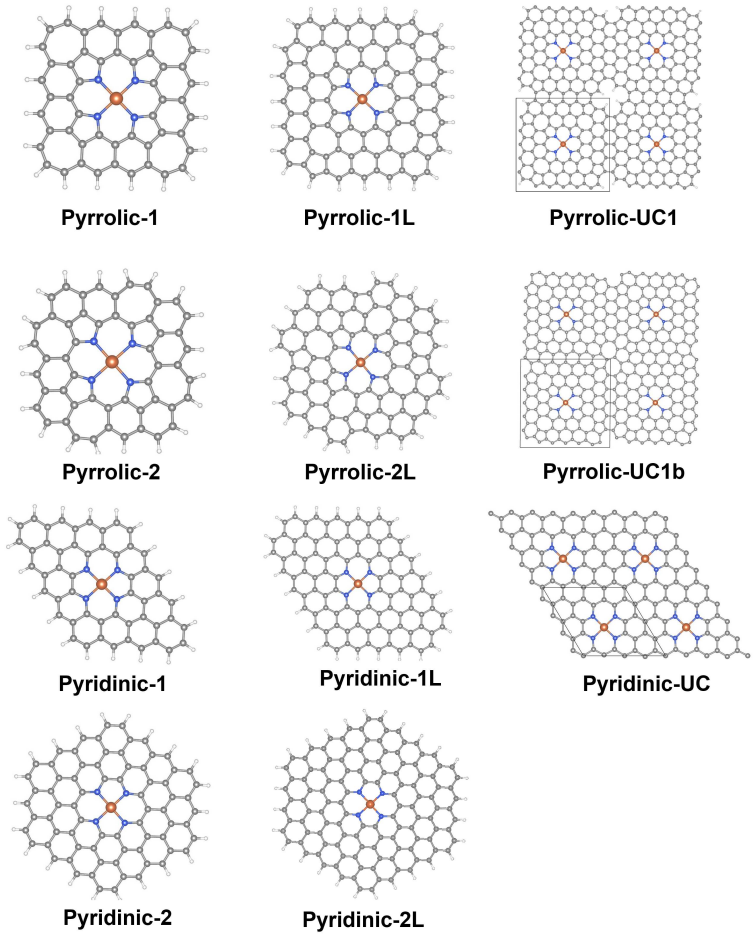

Figure 1. Structural models used for the comparison of binding energies and bond lengths in Table 1, including small cluster models (**left**), corresponding larger cluster models (**middle**), and unit cell models (**right**).

Considering the success of the Zn-Fe transmetallation strategy in producing Fe-N-Cs with high dopant concentrations [8,16], Zn and Fe are ideal candidates as reference for constructing the model used in the DFT calculations. Based on the NBO charges (Table 2) and frontier molecular orbital (FMO) analysis (Figures S3–S6 in Supplementary Materials), Zn and Fe represent two different types of binding in the N_4 site, with Zn exhibiting highly ionic binding character while Fe contains covalent contributions from the d-orbitals. In constructing a cluster model, the finite-size of the π-system compared to an extended graphene can potentially influence its chemical properties. We thus studied the binding of Fe and Zn in the N_4 sites of different shapes and sizes and compared them to a periodic model (Table 1). The binding energy of species M is defined as

$$E_b = E_{MN_4} - E_{N_4} - E_M \quad (1)$$

where E_{N_4} and E_M are the charge-neutral DFT ground state energies of the empty N_4 site and the metal atom, respectively. For the cluster models, a plot of the binding energies

against the M-N bond lengths is shown in Figure 2. Due to the additional inner-shell carbon atoms, the pyrrolic MN_4C_{12} sites were larger than the pyridinic MN_4C_{10} sites. In addition, the size of the pyrrolic N_4 site was further influenced by the arrangement of carbon atoms surrounding the MN_4 unit, with the pyrrolic-2(L) motifs exhibiting longer bond lengths than pyrrolic-1(L). We first examined the deviations between values obtained from the cluster model and periodic model (pyrrolic-1/1L/UC1 and pyridinic-1/1L/UC1). Fortunately, considering methodological differences in the basis set, pseudopotentials, and extensiveness of the models, only slight differences between the cluster and the unit cell models were observed. For Fe, the smaller pyrrolic-1 and pyridinic-1 cluster had a deviation of up to 0.23 eV compared to the unit cell model, but the larger clusters (pyrrolic-1L, pyridinic-1L) almost exactly reproduced the binding energies and bond lengths of the respective unit cell models (pyrrolic-UC1, pyridinic-UC). For Zn, the cluster models consistently predicted a stronger binding than the unit cell model for both pyrrolic and pyridinic models. Surprisingly, it was the pyridinic motif that deviated relatively strongly between the cluster model and unit cell model. The reason for the deviation seems to lie in the geometric distortion of the Zn-N bond lengths to compensate for the unfavorably short Zn-N bond lengths at pyridinic sites which only occurred on the pyridinic-1(L) clusters where the D_{2h} symmetry of the pyridinic ZnN_4 site was not retained.

Table 1. M-N bond lengths and binding energies of Fe and Zn in various N_4 models obtained with PBE-D3(BJ) functional.

Species	Model	E_b (eV)	d_{M-N} (Å)
Fe	Pyrrolic-1	−9.64	1.95
	Pyrrolic-1L	−9.89	1.95
	Pyrrolic-UC1	−9.87	1.95
	Pyrrolic-UC1b	−10.11	1.93, 1.96
	Pyrrolic-2	−8.53	1.97
	Pyrrolic-2L	−9.45	2.00
	Pyridinic-1	−7.86	1.90, 1.91
	Pyridinic-1L	−7.77	1.90, 1.91
	Pyridinic-UC	−7.74	1.89
	Pyridinic-2	−7.57	1.90
	Pyridinic-2L	−7.36	1.90
Zn	Pyrrolic-1	−6.01	2.02
	Pyrrolic-1L	−6.15	2.03
	Pyrrolic-UC1	−5.94	2.02
	Pyrrolic-UC1b	−6.11	1.99, 2.03
	Pyrrolic-2	−5.43	2.06
	Pyrrolic-2L	−6.34	2.06
	Pyridinic-1	−4.14	1.96, 2.00
	Pyridinic-1L	−4.11	1.96, 1.99
	Pyridinic-UC	−3.79	1.96
	Pyridinic-2	−3.92	1.97
	Pyridinic-2L	−3.62	1.97

Another important aspect to consider when constructing clusters to model N_4 embedded in graphene is the shape of the cluster, as influences arising from the boundary carbons should be avoided when describing catalytic activity at the MN_4 site. We thus compared two different pyrrolic clusters with different placement of the seven-membered rings (pyrrolic-1,2) as well as their respective extension of the carbon backbone (pyrrolic-1L,2L). The pyrrolic-2 model exhibited a large deviation of about 1 eV in the binding energy compared to the pyrrolic-1 and pyrrolic-UC values in Table 1. The anomaly can be explained by the saddle-like curvature of the pyrrolic-2 model in contrast to the other planar pyrrolic models. Increasing the size of the pyrrolic-2 cluster reduced the deviation as the cluster became more planar. Nevertheless, some deviations still remained due to the inherently

larger size of the N_4 cavity in the pyrrolic-2L model along with a slight residual curvature. For the pyridinic model, a cluster model with a different shape was constructed to examine the influence of the cluster shape (pyridinic-2, pyridinic-2L). Due to these models retaining the D_{2h} symmetry of the MN_4 site, the geometric distortion apparent in the pyridinic-1(L) clusters was not observed, and the respective binding energies were closer to that of the unit cell. However, these models seemed to underestimate the binding strength of Fe in pyridinic N_4 sites, especially the pyridinic-2L cluster with a deviation of 0.4 eV to the unit cell model.

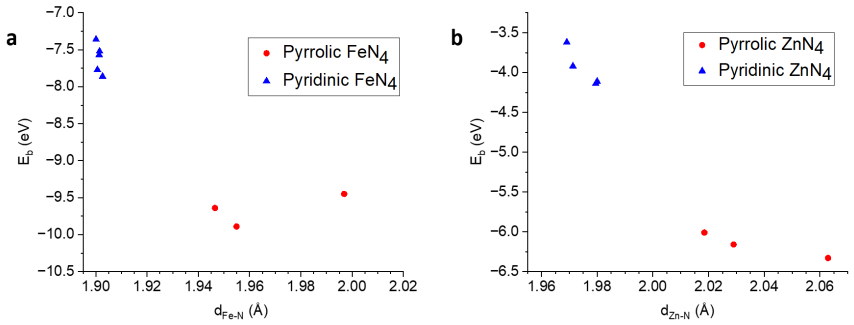

Figure 2. Plot of binding energy E_b against M-N bond length d_{M-N} for (**a**) Fe and (**b**) Zn in respective clusters.

For the pyrrolic MN_4 unit cell, an alternative model was constructed whereby the four hydrogen atoms at the unit cell boundary of the pyrrolic-UC1 model were replaced by two carbon atoms, producing a cavity-free carbon lattice (pyrrolic-UC1b). The closing of the lattice in this manner led to some ring strain in the system, evident in the presence of some distorted hexagons along the unit cell boundary (Figure 1). As a result, the breaking of the unit cell symmetry could even be observed in the inequivalent M-N bond lengths of the pyrrolic-UC1b model and the binding energies obtained (Fe: −10.11 eV; Zn: −6.11 eV) were slightly higher in magnitude than the pyrrolic-UC1 model (Fe: −9.87 eV; Zn: −5.94 eV). Due to the presence of ring strain, the pyrrolic-UC1b model may not be suitable for reaction studies as the introduction of adsorbates can produce incomparable structures in attempts to relieve the ring strains. However, since the energy deviations were relatively small at 0.2 eV (<3% of the calculated binding energies), we do not expect significant anomalies in the intrinsic chemical properties of the MN_4 sites. Furthermore, since the pyrrolic-UC1 model contains a cavity which introduces an artificial band gap in the system, the pyrrolic-UC1b model would be better suited for studying the electrical and electronic properties in an extended system, including band gaps, Fermi energies and conductivities.

Finally, we examined the relationship between the M-N bond length and the binding energy for planar models (i.e., excluding pyrrolic-2). From Figure 2b, it can be observed that the binding energy of Zn has a strong dependence on the size of the N_4 cavity with a longer Zn-N bond length generally corresponding to a stronger binding. It is thus evident that Zn has a higher affinity towards larger cavities, possibly explaining the dominance of pyrrolic ZnN_4 site observed when Zn was introduced during pyrolysis [8]. The geometric distortion observed in the unequal Zn-N bond lengths (Table 1) leading to a stronger Zn binding in the pyridinic-1(L) clusters was further evidence that the small pyridinic motifs were not ideal for Zn. In contrast, Fe exhibited highly consistent bond lengths around 1.90 Å among the pyridinic motifs and much smaller distortion at the pyridinic-1(L) site, hinting towards its geometric affinity for the smaller pyridinic site. The relative affinity of each metal towards pyrrolic and pyridinic MN_4 sites is further discussed in Section 3.2.3.

3.2. Binding of Metals in N_4

In order to identify possible candidates for templating and substitution, we studied the binding of metals from the first three periods of the periodic table in the pyrrolic and pyridinic N_4 pockets. Table 2 displays information on the binding of various metals in the pyrrolic N_4 sites. In order to reduce the effects of the delocalization errors associated with the GGA functionals, we used the hybrid PBE0 functional in this study. The binding energies and M-N bond lengths shown in Table 2 can be compared with those in Table 1 to illustrate the differences between PBE and PBE0. It was observed that the inclusion of a 25% exact exchange in the PBE0 functional led to a weakening of the binding energy of Fe by 0.5–0.8 eV while the Zn binding was strengthened by 0.3–1.2 eV. The difference in behavior could be explained by the degree of ionic and covalent binding characters within the MN_4 sites. The NBO charge of Zn was very close to +2, suggesting an almost fully ionic binding character in the formally N_4^{2-} pocket. Contrastingly, Fe and many other transition metals exhibited NBO charges that were significantly smaller than +2, implying electron donation from the π-system to Fe and thus a certain extent of covalent binding character involving electron delocalization. Evidently, the delocalization error associated with the GGA functionals favored the latter binding situation (with additional delocalization of the d-electrons with the π-system) and thus overestimated the binding strength in these cases, whereas ionic binding strengths were conversely underestimated. The advantage of using cluster models is highlighted here, since the implementation of hybrid functionals in periodic calculations can be computationally expensive, especially for pyrrolic MN_4 motifs which require relatively large unit cells due to the defects in the carbon lattice.

Table 2. Binding energies E_b obtained with Equation (1), M-N bond length d_{M-N}, NBO charge of metal Q_M in the pyrrolic-1 and pyridinic-1 clusters and the energy difference between the pyrrolic-1 and pyridinic-1 isomers ΔE_{isomer} obtained with Equation (3). The geometry was optimized with PBE0-D3(BJ)/def2-SVP, followed by a single-point calculation with PBE0-D3(BJ)/def2-TZVP to obtain energies and charges. Species that are not coplanar to both N_4 pocket are marked with *, while species that are not coplanar only with the pyridinic motif are marked with $*^{pyri}$. Nonplanar binding motifs are shown in Figures S1 and S2 of the Supplementary Materials.

Metal	E_b (eV)		d_{M-N} (Å)		Q_M (e)		ΔE_{isomer}
	Pyrrolic	Pyridinic	Pyrrolic	Pyridinic	Pyrrolic	Pyridinic	(eV)
empty	-	-	2.01 **	1.92 **	-	-	6.19
Li	−7.27	−5.31	2.00	1.94	+0.86	+0.86	4.23
Na *	−5.66	−3.49	2.25	2.27	+0.91	+0.93	4.03
K *	−5.14	−3.16	2.63	2.66	+0.95	+0.97	4.21
Be	−10.31	−8.35	1.91	1.84	+1.67	+1.67	4.24
Mg	−9.13	−6.09	2.02	1.97	+1.78	+1.77	3.15
Ca *	−9.25	−6.20	2.28	2.27	+1.79	+1.78	3.15
Sc *	−12.51	−8.51	2.08	2.08	+2.02	+1.89	2.19
Ti $*^{pyri}$	−12.15	−8.04	2.01	2.02	+1.68	+1.59	2.09
V $*^{pyri}$	−11.18	−7.61	1.99	1.99	+1.45	+1.22	2.62
Cr	−10.02	−6.84	2.00	1.96	+1.20	+1.14	3.02
Mn	−9.35	−5.97	1.96	1.94	+1.58	+1.24	2.81
Fe	−9.12	−7.05	1.96	1.91	+1.18	+1.09	4.12
Co	−9.61	−7.33	1.95	1.90	+1.08	+1.07	3.92
Ni	−9.49	−7.24	1.95	1.88	+1.03	+0.97	3.94
Cu	−7.95	−5.47	1.98	1.93	+1.35	+1.31	3.71
Zn	−7.17	−4.40	2.01	1.97	+1.66	+1.64	3.42
Al	−11.89	−8.46	1.94	1.89	+1.97	+1.88	2.76
Ga	−9.45	−6.03	1.97	1.93	+1.88	+1.79	2.78

*: not planar in pyrrolic and pyridinic MN_4 ; $*^{pyri}$: not planar in pyridinic MN_4; **: fictitious bond length taken as half the diagonal N-N distance.

3.2.1. Binding Geometry

In Table 2, metal atoms marked with * and ^{*pyri} are not coplanar with the nitrogen atoms in which the perpendicular distances from M to the N_4 plane were measured to be greater than 0.2 Å. Their relatively long M-N bond lengths suggest that they were too large to fit into the respective N_4 site. Interestingly, the longest M-N bond length among the planar MN_4 sites were generally exhibited by Mg and Zn, two of the most commonly used templating agents [8,14,16,17]. It is further noteworthy that the M-N bond lengths of these metals closely matched the size of the relaxed metal-free pyrrolic-1 cluster, suggesting excellent geometric fit to the pyrrolic motifs. Contrastingly, mid-to-late transition metals (Mn-Cu) and group 13 metals bound in the pyridinic motifs were shown to fit geometrically to the naturally smaller pyridinic-1 sites. Comparing the optimized geometries of the first-row transition metals in the N_4 sites, it can be observed that most first-row transition metals remained bound within the N_4 site with the exception of early transition metals (Sc, Ti, and V). Ti and V were particularly unique as they fitted into the pyrrolic MN_4 clusters, but were slightly displaced from the pyridinic one, suggesting a relatively high geometric affinity to the pyrrolic motif.

3.2.2. Binding Energy

The binding energies shown in Table 2 were calculated with Equation (1). In the framework of the transmetallation strategy, we could identify metals with smaller binding energies as ideal templating agents that could be substituted with relative ease. Transmetallation should then be carried out using species with a stronger binding energy.

Among the main-group elements, there was a clear trend between the strength of the binding and the valency of the metals (group 1 < group 2 < group 13). The increasing strength of the ionic binding was also reflected in the increasing NBO charges. Nevertheless, we further observed that the NBO charge of group-13 metals and early transition metals were closer to +2 despite their preference for an oxidation state of +3, indicating that the N_4^{2-} site could not be further reduced. The mismatch in the oxidation state suggests that these metals would be readily oxidized and possibly poisoned by anionic ligands.

Due to the varying participation of d-orbitals and preferences for oxidation states among the first-row transition metals, their corresponding binding energies spanned a wide range from −7.17 eV for Zn to −12.51 eV for Sc. The progression of the binding energy and NBO charge across the first-row transition metals are illustrated in Figure 3a,b. Among the early transition metals (Sc–Cr), the binding became weaker with an increasing atomic number accompanied by a decreasing NBO charge. This trend reflected the increasing electronegativity and thus ionization energy of the transition metals with an increasing atomic number, leading to weaker ionic interactions and thus smaller binding energies. It is also noteworthy that the trend-breaking low electronegativity of Mn in the Pauling electronegativity scale was reproduced in the calculated NBO charges. Compared to the early transition metals, the late transition metals (Fe–Zn) showed a contradicting trend whereby an increase in NBO charge was instead correlated to a weaker binding. We attribute this deviation to the covalent contribution which arises from the relatively high electronegativities of the late transition metals, especially Fe, Co, and Ni. As the NBO charges deviated significantly from the expected oxidation state of +2, there was some electron donation from the π-system into the d-orbitals of the transition metals. This was further confirmed by a FMO analysis from which orbitals indicating π-d interactions were observed in the FeN_4 but not in the ZnN_4 clusters (Figures S3–S6 of Supplementary Materials). We quantified the degree of electron donation $n_{\pi \to d}$ by comparing the net NBO population of the d-orbitals with the expected occupancy of an M^{2+} ion (e.g., d^6 for Fe^{2+}).

$$n_{\pi \to d} = n_d - (Z - 20) \quad (2)$$

where n_d is the d-orbital population obtained with the NBO population analysis, and $(Z - 20)$ is the expected d-orbital population for a first-row transition metal with nuclear

charge Z in the oxidation state of +2. The separation in trends between the early and late transition metal is reproduced in Figure 3c,d, whereby late transition metals Fe-Zn exhibited a positive correlation between the $\pi \rightarrow d$ electron transfer and the magnitude of the binding energy. This further confirmed that the deviation of the NBO charge from the ideal oxidation state of +2 for transition metals originated from the electron-accepting properties of the d-orbitals. From Ni to Zn, as the availability of unoccupied d-orbitals decayed to 0, a sharp decrease in binding strength was also observed. As a result of its relatively high electronegativity and lack of unoccupied d-orbitals for accepting electrons, Zn exhibited the weakest binding energy among the elements studied and is thus an ideal candidate for subsequent substitution in a templating synthesis strategy.

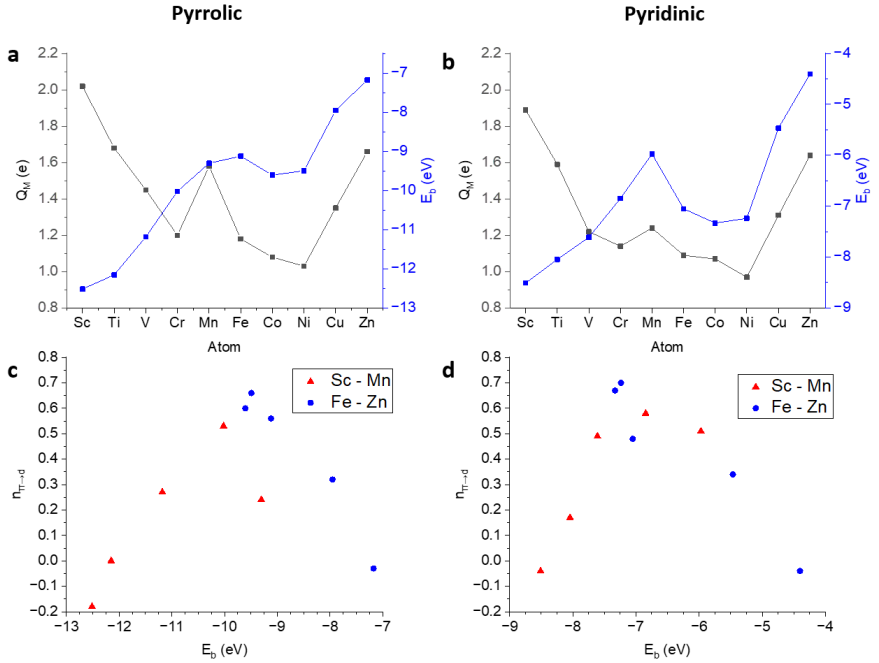

Figure 3. NBO charge (black) and corresponding binding energies (blue) of first-row transition metals in (**a**) pyrrolic-1 and (**b**) pyridinic-1 clusters. Plot of net $\pi \rightarrow d$ electron transfer against metal binding energies for (**c**) pyrrolic-1 and (**d**) pyridinic-1 clusters.

3.2.3. Affinity towards Pyrrolic Motifs

Since the pyrrolic-1 and pyridinic-1 clusters are isomers, the difference in total energy ΔE_{isomer} shown in Table 2 provides insights on the respective metals' affinity towards pyrrolic and pyridinic MN_4 motifs. The energy difference between isomeric pyrrolic-1 and pyridinic-1 MN_4 cluster is obtained with

$$\Delta E_{\text{isomer}} = E_{\text{pyrrolic-1}} - E_{\text{pyridinic-1}} \quad (3)$$

where $E_{\text{pyrrolic-1}}$ and $E_{\text{pyridinic-1}}$ are the total electronic energies of metal-bound pyrrolic-1 and pyridinic-1 clusters, respectively. From this definition, the lower the ΔE_{isomer}, the higher its affinity towards pyrrolic MN_4 motifs. In general, due to the presence of defects, pyrrolic motifs are still thermodynamically less stable than pyridinic motifs. However, since it has been proven that Zn forms pyrrolic MN_4 motifs [8] and several recent studies have independently arrived to the conclusion that it is the pyrrolic MN_4 sites that are responsible for the high ORR activity of Fe-N-Cs [10,11] as well as the CO_2RR activity of Ni-N-Cs [12], it is clear that thermodynamics is not the deciding factor on the type of MN_4 sites that are formed during pyrolysis. In addition, it is also worthy to note that Sc,

Ti, and V exhibited some of the smallest ΔE_{isomer} due to significant geometry differences between the pyrrolic and pyridinic MN_4 clusters as discussed in Section 3.2.1.

Since Zn is known to form pyrrolic motifs, metals with lower ΔE_{isomer} than Zn are also likely to do so. Referring to the values shown in Table 2 and Figure 4, the affinity of Zn towards pyrrolic motifs was actually relatively high compared with many other metals, including group-2 metals (Mg, Ca), group-13 metals (Al, Ga) as well as early transition metals (Sc, Ti, V, Cr, Mn). According to Figure 4a, a general negative trend could be observed between the ΔE_{isomer} and the average NBO charge, further confirming that the pyrrolic motif has a higher preference towards ionic binding than the pyridinic motif. Conversely, late-transition metals which formed covalent binding with the π-system (Fe-Cu) had higher ΔE_{isomer} and thus a lower affinity towards forming pyrrolic motifs. This difference in affinity towards ionic and covalent binding further explains an anomaly of Mn, in which two very different binding characters were observed in the pyrrolic and pyridinic motifs. Highly ionic binding was preferred for pyrrolic MnN_4 with a large NBO charge (+1.58 e) whereas indications of $\pi \rightarrow$ d donation were reflected in the significantly lower NBO charge in pyridinic MnN_4 (+1.24 e).

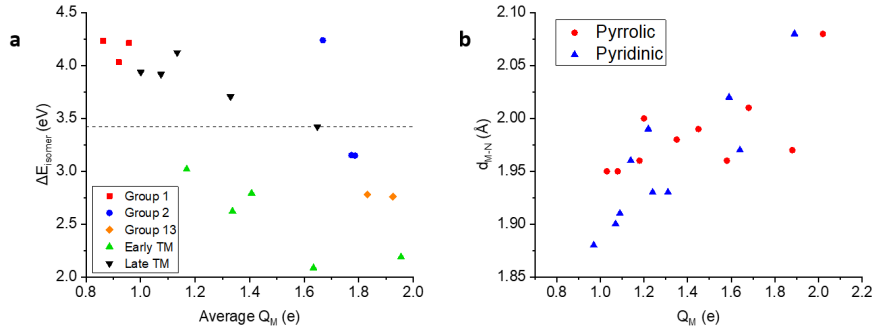

Figure 4. (**a**) Plot of ΔE_{isomer} against the average NBO charge of metal M in pyrrolic and pyridinic N_4 sites. The ΔE_{isomer} for Zn is marked with a dashed line. (**b**) Plot of M-N distance against the NBO charge of transition metal M.

Coincidentally, the direct synthesis of M-N-Cs containing late transition metals, especially Fe, Co, and Ni, generally face challenges involving graphitization and inorganic side phases [12,18,34,35]. A possible explanation for their graphitization tendency could be their higher affinity towards pyridinic motifs which exhibit a closer structural resemblance to graphene due to the absence of defective carbon rings. Conversely, the structural defects in the carbon lattice of pyrrolic MN_4 can be crucial in preventing graphitization as significant carbon rearrangement involving the breaking and formation of multiple C-C bonds is required to recover the honeycomb graphite structure. Thus, although Zn has the weakest binding energy and is thus possibly the easiest to remove for a transmetallation strategy, other metals such as Mg and early transition metals have a higher affinity towards pyrrolic motifs, which can be optimal for their survivability in the graphene lattice, possibly leading to higher single-atomic dopant concentrations. Nevertheless, removing these metals from the N_4 sites is likely to require harsher transmetallation conditions due to their stronger binding energies.

4. Conclusions

In conclusion, we constructed and compared several cluster models of pyrrolic and pyridinic MN_4 sites based on the binding energy and geometry of Zn and Fe. Zn was shown to bind stronger on larger N_4 sites and thus had a higher preference towards pyrrolic motifs in contrast to Fe, which had a higher preference for smaller N_4 sites. The study was further extended to other metals and it was shown based on binding energies, M-N bond lengths, and an NBO charge analysis that the pyrrolic N_4 site is ideal for ionic binding of

main-group metals and early transition metals, while the smaller pyridinic N_4 site is more suitable for covalent binding, especially of late-transition metals, where $\pi \rightarrow$ d electron donation plays a significant role in binding. Knowledge of the metals' affinity towards the types and sizes of the N_4 site, as well as their binding strength relative to other metals, is likely to be critical in formulating a templating strategy for synthesizing carbon materials with the desired MN_4 motifs.

Supplementary Materials: The following supporting information can be downloaded at: https://www.mdpi.com/article/10.3390/catal13030566/s1, atomics coordinates for structural models containing Fe; Figures S1 and S2: top and side-view of non-planar MN_4 sites in pyrrolic-1 and pyridinic-1 clusters; Figures S3–S6: frontier molecular orbital diagram of FeN_4 and ZnN_4 in the pyrrolic-1 and pyridinic-1 clusters obtained with the program Molden [36,37].

Author Contributions: Conceptualization, J.L.L.; methodology, J.L.L.; validation, J.L.L. and B.P.; formal analysis, J.L.L.; investigation, J.L.L.; resources, J.L.L. and B.P.; data curation, J.L.L.; writing—original draft preparation, J.L.L.; writing—review and editing, J.L.L. and B.P.; visualization, J.L.L.; supervision, B.P.; project administration, B.P.; funding acquisition, J.L.L. and B.P. All authors have read and agreed to the published version of the manuscript.

Funding: This research received no external funding. The publication of this article was funded by Freie Universität Berlin.

Data Availability Statement: See Supplementary Materials. Further data can be requested from the authors.

Acknowledgments: J.L. Low acknowledges the Elsa-Neumann Scholarship for funding and support. The computations were performed with resources provided by the North-German Supercomputing Alliance (HLRN) and computer facilities of the Freie Universität Berlin (ZEDAT).

Conflicts of Interest: The authors declare no conflict of interest.

Abbreviations

The following abbreviations are used in this manuscript:

M-N-Cs	Metal- and nitrogen-doped carbons
ORR	Oxygen reduction reaction
CO_2RR	CO_2 reduction reaction
DFT	Density functional theory
GGA	Generalized gradient approximation
RMM-DIIS	Residual minimization–direct inversion in the iterative subspace
NBO	Natural bond orbital
FMO	Frontier molecular orbitals

References

1. Gasteiger, H.A.; Kocha, S.S.; Sompalli, B.; Wagner, F.T. Activity benchmarks and requirements for Pt, Pt-alloy, and non-Pt oxygen reduction catalysts for PEMFCs. *Appl. Catal. B Environ.* **2005**, *56*, 9–35. [CrossRef]
2. Shao, M.; Chang, Q.; Dodelet, J.P.; Chenitz, R. Recent advances in electrocatalysts for oxygen reduction reaction. *Chem. Rev.* **2016**, *116*, 3594–3657. [CrossRef] [PubMed]
3. Hori, Y. Electrochemical CO2 reduction on metal electrodes. *Mod. Asp. Electrochem.* **2008**, 89–189. [CrossRef]
4. Kortlever, R.; Shen, J.; Schouten, K.J.P.; Calle-Vallejo, F.; Koper, M.T. Catalysts and reaction pathways for the electrochemical reduction of carbon dioxide. *J. Phys. Chem. Lett.* **2015**, *6*, 4073–4082. [CrossRef]
5. Lefèvre, M.; Proietti, E.; Jaouen, F.; Dodelet, J.P. Iron-based catalysts with improved oxygen reduction activity in polymer electrolyte fuel cells. *Science* **2009**, *324*, 71–74. [CrossRef]
6. Wang, Y.; Cui, X.; Peng, L.; Li, L.; Qiao, J.; Huang, H.; Shi, J. Metal–nitrogen–carbon catalysts of specifically coordinated configurations toward typical electrochemical redox reactions. *Adv. Mater.* **2021**, *33*, 2100997. [CrossRef]
7. Jaouen, F.; Jones, D.; Coutard, N.; Artero, V.; Strasser, P.; Kucernak, A. Toward platinum group metal-free catalysts for hydrogen/air proton-exchange membrane fuel cells. *Johns. Matthey Technol. Rev.* **2018**, *62*, 231–255. [CrossRef]
8. Menga, D.; Low, J.L.; Li, Y.S.; Arčon, I.; Koyutürk, B.; Wagner, F.; Ruiz-Zepeda, F.; Gaberšček, M.; Paulus, B.; Fellinger, T.P. Resolving the dilemma of Fe–N–C catalysts by the selective synthesis of tetrapyrrolic active sites via an imprinting strategy. *J. Am. Chem. Soc.* **2021**, *143*, 18010–18019. [CrossRef]

9. Zitolo, A.; Goellner, V.; Armel, V.; Sougrati, M.T.; Mineva, T.; Stievano, L.; Fonda, E.; Jaouen, F. Identification of catalytic sites for oxygen reduction in iron-and nitrogen-doped graphene materials. *Nat. Mater.* **2015**, *14*, 937–942. [CrossRef]
10. Ni, L.; Gallenkamp, C.; Wagner, S.; Bill, E.; Krewald, V.; Kramm, U.I. Identification of the catalytically dominant iron environment in iron-and nitrogen-doped carbon catalysts for the oxygen reduction reaction. *J. Am. Chem. Soc.* **2022**, *144*, 16827–16840. [CrossRef]
11. Hu, X.; Chen, S.; Chen, L.; Tian, Y.; Yao, S.; Lu, Z.; Zhang, X.; Zhou, Z. What is the Real Origin of the Activity of Fe–N–C Electrocatalysts in the O2 Reduction Reaction? Critical Roles of Coordinating Pyrrolic N and Axially Adsorbing Species. *J. Am. Chem. Soc.* **2022**, *144*, 18144–18152. [CrossRef]
12. Koshy, D.M.; Chen, S.; Lee, D.U.; Stevens, M.B.; Abdellah, A.M.; Dull, S.M.; Chen, G.; Nordlund, D.; Gallo, A.; Hahn, C.; et al. Understanding the origin of highly selective CO2 electroreduction to CO on Ni, N-doped carbon catalysts. *Angew. Chem. Int. Ed.* **2020**, *59*, 4043–4050. [CrossRef] [PubMed]
13. Zhang, N.; Zhou, T.; Chen, M.; Feng, H.; Yuan, R.; Yan, W.; Tian, Y.; Wu, X.; Chu, W.; Wu, C.; et al. High-purity pyrrole-type FeN 4 sites as a superior oxygen reduction electrocatalyst. *Energy Environ. Sci.* **2020**, *13*, 111–118. [CrossRef]
14. Menga, D.; Ruiz-Zepeda, F.; Moriau, L.; Šala, M.; Wagner, F.; Koyutürk, B.; Bele, M.; Petek, U.; Hodnik, N.; Gaberšček, M.; et al. Active-site imprinting: Preparation of Fe–N–C catalysts from zinc ion–templated ionothermal nitrogen-doped carbons. *Adv. Energy Mater.* **2019**, *9*, 1902412. [CrossRef]
15. Jiao, L.; Li, J.; Richard, L.L.; Sun, Q.; Stracensky, T.; Liu, E.; Sougrati, M.T.; Zhao, Z.; Yang, F.; Zhong, S.; et al. Chemical vapour deposition of Fe–N–C oxygen reduction catalysts with full utilization of dense Fe–N4 sites. *Nat. Mater.* **2021**, *20*, 1385–1391. [CrossRef] [PubMed]
16. Mehmood, A.; Gong, M.; Jaouen, F.; Roy, A.; Zitolo, A.; Khan, A.; Sougrati, M.T.; Primbs, M.; Bonastre, A.M.; Fongalland, D.; et al. High loading of single atomic iron sites in Fe–NC oxygen reduction catalysts for proton exchange membrane fuel cells. *Nat. Catal.* **2022**, *5*, 311–323. [CrossRef]
17. Mehmood, A.; Pampel, J.; Ali, G.; Ha, H.Y.; Ruiz-Zepeda, F.; Fellinger, T.P. Facile metal coordination of active site imprinted nitrogen doped carbons for the conservative preparation of non-noble metal oxygen reduction electrocatalysts. *Adv. Energy Mater.* **2018**, *8*, 1701771. [CrossRef]
18. Fellinger, T.P.; Menga, D.; Buzanich, A.G.; Wagner, F. Evaluation of the Specific Activity of M-N-Cs and the Intrinsic Activity of Tetrapyrrolic Fe-N4 Sites for the Oxygen Reduction Reaction. *Angew. Chem.* **2022**, e202207089.
19. Perdew, J.P.; Burke, K.; Ernzerhof, M. Generalized gradient approximation made simple. *Phys. Rev. Lett.* **1996**, *77*, 3865. [CrossRef]
20. Perdew, J.P.; Ernzerhof, M.; Burke, K. Rationale for mixing exact exchange with density functional approximations. *J. Chem. Phys.* **1996**, *105*, 9982–9985. [CrossRef]
21. Ernzerhof, M.; Scuseria, G.E. Assessment of the Perdew–Burke–Ernzerhof exchange-correlation functional. *J. Chem. Phys.* **1999**, *110*, 5029–5036. [CrossRef]
22. Tolba, S.A.; Gameel, K.M.; Ali, B.A.; Almossalami, H.A.; Allam, N.K. The DFT+U: Approaches, Accuracy, and Applications. In *Density Functional Calculations*; Yang, G., Ed.; IntechOpen: Rijeka, Croatia, 2018; Chapter 1. [CrossRef]
23. Grimme, S.; Antony, J.; Ehrlich, S.; Krieg, H. A consistent and accurate ab initio parametrization of density functional dispersion correction (DFT-D) for the 94 elements H-Pu. *J. Chem. Phys.* **2010**, *132*, 154104. [CrossRef] [PubMed]
24. Grimme, S.; Ehrlich, S.; Goerigk, L. Effect of the damping function in dispersion corrected density functional theory. *J. Comput. Chem.* **2011**, *32*, 1456–1465. [CrossRef] [PubMed]
25. Ahlrichs, R.; Bär, M.; Häser, M.; Horn, H.; Kölmel, C. Electronic structure calculations on workstation computers: The program system turbomole. *Chem. Phys. Lett.* **1989**, *162*, 165–169. [CrossRef]
26. Khosravi, A.; Vessally, E.; Oftadeh, M.; Behjatmanesh-Ardakani, R. Ammonia capture by MN4 (M= Fe and Ni) clusters embedded in graphene. *J. Coord. Chem.* **2018**, *71*, 3476–3486. [CrossRef]
27. Weigend, F.; Ahlrichs, R. Balanced basis sets of split valence, triple zeta valence and quadruple zeta valence quality for H to Rn: Design and assessment of accuracy. *Phys. Chem. Chem. Phys.* **2005**, *7*, 3297–3305. [CrossRef]
28. Reed, A.E.; Weinstock, R.B.; Weinhold, F. Natural population analysis. *J. Chem. Phys.* **1985**, *83*, 735–746. [CrossRef]
29. Kresse, G.; Hafner, J. Ab initio molecular dynamics for liquid metals. *Phys. Rev. B* **1993**, *47*, 558. [CrossRef] [PubMed]
30. Kresse, G.; Furthmüller, J. Efficiency of ab-initio total energy calculations for metals and semiconductors using a plane-wave basis set. *Comput. Mater. Sci.* **1996**, *6*, 15–50. [CrossRef]
31. Kresse, G.; Furthmüller, J. Efficient iterative schemes for ab initio total-energy calculations using a plane-wave basis set. *Phys. Rev. B* **1996**, *54*, 11169. [CrossRef]
32. Kresse, G.; Joubert, D. From ultrasoft pseudopotentials to the projector augmented-wave method. *Phys. Rev. B* **1999**, *59*, 1758. [CrossRef]
33. Momma, K.; Izumi, F. VESTA 3 for three-dimensional visualization of crystal, volumetric and morphology data. *J. Appl. Crystallogr.* **2011**, *44*, 1272–1276. [CrossRef]
34. Iwase, K.; Ebner, K.; Diercks, J.S.; Saveleva, V.A.; Unsal, S.; Krumeich, F.; Harada, T.; Honma, I.; Nakanishi, S.; Kamiya, K.; et al. Effect of cobalt speciation and the graphitization of the carbon matrix on the CO2 electroreduction activity of Co/N-doped carbon materials. *ACS Appl. Mater. Interfaces* **2021**, *13*, 15122–15131. [CrossRef] [PubMed]
35. Yudasaka, M.; Kikuchi, R. Graphitization of carbonaceous materials by Ni, Co and Fe. In *Supercarbon*; Springer: Berlin/Heidelberg, Germany, 1998; pp. 99–105.

36. Schaftenaar, G.; Noordik, J.H. Molden: A pre-and post-processing program for molecular and electronic structures. *J. Comput. Aided Mol. Des.* **2000**, *14*, 123–134. [CrossRef] [PubMed]
37. Schaftenaar, G.; Vlieg, E.; Vriend, G. Molden 2.0: Quantum chemistry meets proteins. *J. Comput. Aided Mol. Des.* **2017**, *31*, 789–800.

Supplementary Materials: Computational Modelling of Pyrrolic MN_4 Motifs Embedded in Graphene for Catalyst Design

Jian Liang Low * and Beate Paulus *

Contents

1. Structural Data

The structural data for FeN_4 clusters and unit cells. For each cluster, the top and side views are shown. Cluster geometries are given in xyz format and unit cell geometries are given in VASP POSCAR format.

1.1. FeN_4, Pyrrolic-1

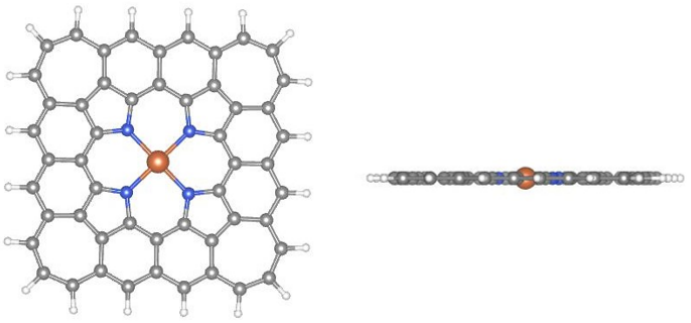

```
77

Fe     0.0000003    0.0000000   -0.0028854
N      1.5297301    1.2304290   -0.0027044
N      1.2306124   -1.5289339   -0.0024921
N     -1.5297294   -1.2304290   -0.0029250
N     -1.2306118    1.5289339   -0.0027329
C      1.5028481    2.5894089   -0.0024796
C      2.8087827    3.1520664   -0.0020020
```

C	3.6841437	2.0637356	-0.0018571
C	2.8587782	0.9113956	-0.0022247
C	-0.9130634	2.8533393	-0.0023483
C	-2.5989855	1.5026596	-0.0022713
C	-2.0597321	3.6797925	-0.0017644
C	-3.1577317	2.7962824	-0.0017267
C	-2.8587777	-0.9113956	-0.0027054
C	-1.5028475	-2.5894089	-0.0026320
C	-2.8087822	-3.1520665	-0.0025435
C	-3.6841432	-2.0637356	-0.0025231
C	2.5989861	-1.5026596	-0.0019140
C	0.9130639	-2.8533393	-0.0021286
C	3.1577322	-2.7962824	-0.0013457
C	2.0597326	-3.6797925	-0.0014799
C	3.4146497	-0.3639964	-0.0017202
C	0.3752701	3.4114333	-0.0021929
C	-3.4146491	0.3639964	-0.0021592
C	-0.3752696	-3.4114332	-0.0020532
C	-1.9389067	5.1015690	-0.0010318
C	0.5293651	4.8409117	-0.0015776
C	-0.6452399	5.6462346	-0.0011366
C	5.1167800	1.9437166	-0.0011989
C	4.8554901	-0.5212571	-0.0009962
C	4.5750120	-2.9876381	-0.0005519
C	5.3869581	-1.8380684	-0.0004473
C	5.6616022	0.6448728	-0.0008699
C	1.9389071	-5.1015690	-0.0008578
C	-0.5293647	-4.8409117	-0.0015350
C	-5.1167796	-1.9437167	-0.0020096
C	-4.8554897	0.5212571	-0.0017239
C	-5.6616016	-0.6448729	-0.0018496
C	-5.3869576	1.8380685	-0.0014058
C	-4.5750116	2.9876381	-0.0011366
C	-2.9937186	-4.5747255	-0.0019580
C	-1.8451505	-5.3820948	-0.0016999
C	1.8451509	5.3820948	-0.0014046
C	2.9937190	4.5747254	-0.0014875
C	0.6452403	-5.6462346	-0.0010837
C	-5.9198439	-3.1046244	-0.0014991
C	-5.1197980	4.3011093	-0.0005130
C	-3.1125236	5.9189781	-0.0002913
C	4.3082340	5.1122488	-0.0008032
C	5.9198442	3.1046244	-0.0006040
C	5.1197982	-4.3011094	-0.0000141
C	-4.3082337	-5.1122488	-0.0015084
C	3.1125239	-5.9189783	-0.0002587
C	-5.5443968	-4.4601192	-0.0013003
H	-6.3978052	-5.1451806	-0.0006347
C	-4.4578171	5.5412944	-0.0001619
C	5.5443970	4.4601191	-0.0003860
C	4.4578174	-5.5412946	-0.0000157
H	5.1449684	-6.3938727	0.0005769
H	-0.5316535	6.7334462	-0.0006772
H	1.9643315	6.4686095	-0.0009598

H	6.7485221	0.5302318	-0.0003273
H	6.4729498	-1.9618381	0.0000946
H	6.2128448	-4.3577021	0.0004692
H	0.5316538	-6.7334462	-0.0007387
H	-1.9643312	-6.4686095	-0.0013933
H	-4.3645752	-6.2060187	-0.0011543
H	-7.0005150	-2.9271960	-0.0010095
H	-6.7485216	-0.5302319	-0.0015574
H	-6.4729494	1.9618382	-0.0012190
H	-2.9315603	6.9985091	0.0002539
H	-5.1449681	6.3938724	0.0004834
H	-6.2128446	4.3577019	-0.0002592
H	6.3978054	5.1451806	0.0002053
H	4.3645754	6.2060186	-0.0003126
H	7.0005153	2.9271959	0.0000101
H	2.9315606	-6.9985094	0.0000765

1.2. FeN_4, Pyrrolic-1L

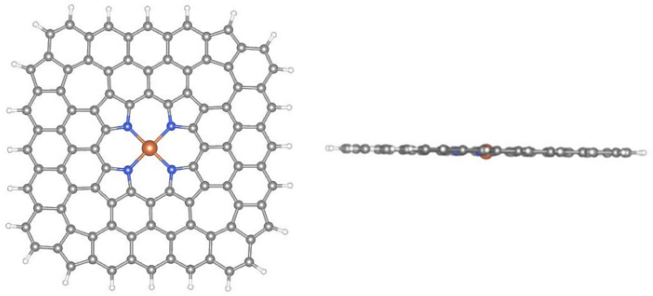

125

Fe	-1.7165572	-0.3805287	-0.0283683
N	-1.4174612	1.5511571	-0.0691798
N	0.2140301	-0.6796669	-0.0945663
N	-2.0154769	-2.3121343	0.0172935
N	-3.6469281	-0.0813031	0.0434283
C	-2.3705986	2.5472151	-0.0440976
C	-1.7924284	3.8440587	-0.0794078
C	-0.3835108	3.6608301	-0.1299881
C	-0.2113828	2.2460284	-0.1217056
C	-4.3351338	1.1174992	0.0551723
C	-4.6502033	-1.0401381	0.1013786
C	-5.7560321	0.9472872	0.1197160
C	-5.9385542	-0.4628085	0.1485736
C	-3.2212136	-3.0068537	0.0788984
C	-1.0619558	-3.3080237	0.0025307
C	-1.6395404	-4.6046120	0.0534156
C	-3.0484718	-4.4213878	0.1035777
C	1.2176397	0.2793161	-0.1436837
C	0.9026705	-1.8782786	-0.0945786
C	2.5066323	-0.2977368	-0.1737370
C	2.3242121	-1.7077848	-0.1419908

C	1.0596083	1.6720125	-0.1581231
C	-3.7653250	2.3931729	0.0148755
C	-4.4920150	-2.4327601	0.1202125
C	0.3330359	-3.1538712	-0.0494748
C	-6.6475276	2.0662079	0.1453146
C	-4.6203919	3.5437940	0.0395066
C	-6.0474942	3.3697918	0.1034322
C	0.7363172	4.5600087	-0.1762566
C	2.2168776	2.5340196	-0.2045490
C	3.6709762	0.5185666	-0.2196382
C	3.5177370	1.9512995	-0.2358209
C	2.0397254	3.9613548	-0.2137998
C	3.2165466	-2.8263314	-0.1448272
C	1.1889581	-4.3041220	-0.0512629
C	-4.1675106	-5.3202203	0.1708514
C	-5.6484805	-3.2944153	0.1880784
C	-5.4708024	-4.7215189	0.2115062
C	-6.9487934	-2.7114588	0.2341365
C	-7.1021361	-1.2787729	0.2150857
C	-0.8222587	-5.7635983	0.0521606
C	0.6049313	-5.6091512	-0.0012632
C	-4.0358502	4.8490432	0.0031836
C	-2.6088882	5.0033962	-0.0562425
C	2.6166531	-4.1298545	-0.0992250
C	-8.1259754	-3.5515175	0.3032400
C	-6.6555699	-5.5485305	0.2806891
C	-7.9349258	-4.9552505	0.3231212
C	-6.4860084	-6.9600452	0.3062051
C	-4.0150749	-6.7643883	0.2002261
C	-5.2331054	-7.5745165	0.2697939
C	-8.3796890	-0.7084602	0.2642845
C	-9.5557455	-1.5527559	0.3325186
C	-9.4179909	-2.9491149	0.3504604
C	-10.7026829	-0.6882158	0.3714767
C	-5.1490945	-9.0196321	0.3030154
C	-8.0962882	1.9168173	0.2125251
C	-8.9029974	3.1405920	0.2324882
C	-8.2841605	4.3918286	0.1896896
C	-6.2772012	5.8370756	0.0890681
C	-4.8759283	6.0230865	0.0290358
C	-2.0340577	6.2880202	-0.0872265
C	-4.2733989	7.3217994	-0.0045294
C	-2.8831251	7.4653478	-0.0608877
C	-6.8729764	4.5555751	0.1266793
C	-10.3456808	3.0618314	0.2983944
C	-2.0230695	8.6210477	-0.1005472
C	4.6958329	2.7917601	-0.2801228
C	3.2253799	4.7887493	-0.2592334
C	0.5847688	6.0045629	-0.1819120
C	1.8036071	6.8150396	-0.2300894
C	3.0564822	6.2005514	-0.2671127
C	4.5050960	4.1956263	-0.2916798
C	4.9494069	-0.0513519	-0.2447040
C	6.1263079	0.7933203	-0.2898608

C	5.9885658	2.1896800	-0.3075561
C	7.2740907	-0.0708323	-0.3053731
C	1.7205728	8.2605775	-0.2373235
C	-1.3962466	-7.0478596	0.1056449
C	1.4459878	-6.7827809	-0.0009632
C	3.4430430	-5.3152360	-0.0979021
C	4.6661722	-2.6765496	-0.1883166
C	5.4736928	-3.8999517	-0.1859796
C	4.8548764	-5.1511871	-0.1429212
C	2.8476388	-6.5965931	-0.0507154
C	-0.5462307	-8.2248009	0.1045253
C	0.8441679	-8.0812051	0.0513840
C	6.9172752	-3.8207786	-0.2269084
C	-2.7746079	-7.4699125	0.1690006
C	-2.7336814	-8.9391855	0.2055248
C	-8.8014400	0.6844220	0.2620954
C	-10.2613971	0.6461907	0.3300414
C	-0.6553716	6.7102201	-0.1419417
C	5.3715698	-1.4440457	-0.2311648
C	6.8325662	-1.4053416	-0.2704301
C	-0.6951775	8.1799651	-0.1486208
C	-11.0121145	1.8629982	0.3462890
H	-12.1108743	1.8285793	0.3970519
C	-3.9513680	-9.6869635	0.2726526
H	-3.9168591	-10.7866108	0.2996762
C	-1.4054550	-9.3801414	0.1663415
C	0.5231851	8.9280403	-0.1978228
H	0.4894909	10.0280322	-0.2030521
C	7.5839717	-2.6218282	-0.2675674
H	8.6834921	-2.5870534	-0.2972417
H	-6.0961313	-9.5783141	0.3553676
H	-7.3842809	-7.5957110	0.3587028
H	-10.3069245	-3.5969874	0.4030288
H	-10.9039373	4.0104526	0.3101801
H	-4.9254526	8.2093622	0.0163034
H	1.4969904	-8.9684460	0.0509295
H	3.5033012	-7.4821034	-0.0509850
H	7.4760690	-4.7691490	-0.2235674
H	5.3893391	4.8521309	-0.3255088
H	6.8781950	2.8378635	-0.3410955
H	2.6681688	8.8194976	-0.2748679
H	-6.9321289	6.7229094	0.1088457
H	8.3223463	0.2537293	-0.3378297
H	3.9554117	6.8364950	-0.3020399
H	-2.3518729	9.6681077	-0.0934024
H	-8.9167047	5.2936859	0.2070283
H	-11.7501694	-1.0124259	0.4252714
H	-8.8184758	-5.6114563	0.3756750
H	-1.0758233	-10.4268590	0.1813008
H	5.4880907	-6.0527406	-0.1419916

1.3. FeN_4, Pyrrolic-2

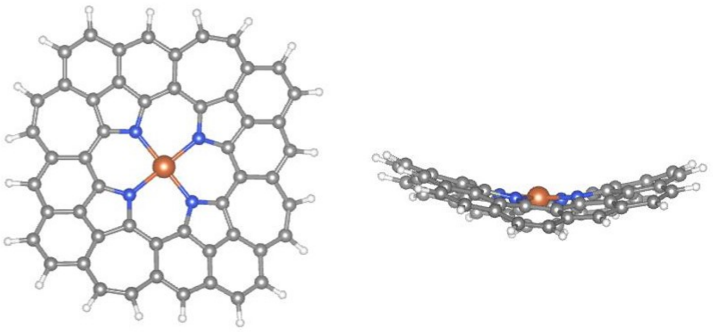

77

N	-1.4424932	1.1490840	-0.1578787
N	0.2436158	-1.0637058	-0.0705514
N	-1.9796272	-2.7511296	-0.1087411
N	-3.6563010	-0.5371636	0.0409493
C	-2.3525524	2.1595097	-0.4729382
C	-1.6798615	3.4441306	-0.4758520
C	-0.3638038	3.1703944	-0.0756899
C	-0.2184267	1.7732114	0.0778423
C	-4.2843407	0.6795957	-0.2204357
C	-4.6635072	-1.4332709	0.4142444
C	-5.6778657	0.5435777	-0.0218799
C	-5.9454363	-0.7567481	0.4277692
C	-3.1833780	-3.3689920	0.2278702
C	-1.0856962	-3.7727011	-0.4403418
C	-1.7532302	-5.0566719	-0.3571715
C	-3.0435860	-4.7704191	0.1123002
C	1.2730561	-0.1585901	0.2069704
C	0.8533231	-2.2812627	-0.3658351
C	2.5548528	-0.8315999	0.1330841
C	2.2586726	-2.1378769	-0.2781311
C	1.0705737	1.2413332	0.3379786
C	-3.7583737	1.9525820	-0.5542491
C	-4.4525890	-2.8303104	0.5614925
C	0.3086084	-3.5646667	-0.6270296
C	-6.6408339	1.5526903	-0.2182732
C	-4.7442818	3.0147040	-0.8497245
C	-2.0238341	4.7840757	-0.7877877
C	-4.4494814	4.3722609	-1.3017746
C	-3.3265577	5.1517923	-1.2691181
H	-3.4388457	6.1925299	-1.6150724
H	-5.3513761	4.8881490	-1.6699060
C	1.2749496	-4.6325563	-0.9673657
C	3.2074947	-3.1490881	-0.5234070
C	-1.4269307	-6.4057826	-0.6484216
C	-1.0023625	5.7702731	-0.6236656
C	0.6522178	4.1309863	0.1031416
C	0.2886949	5.4780670	-0.1749348
C	1.9013118	3.6058795	0.5152833

C	3.9096645	-0.4927638	0.3883538
C	4.5672688	-2.7911287	-0.3038616
C	4.8856455	-1.5104106	0.1562193
H	1.0284345	6.2844975	-0.0580924
H	-1.2614876	6.8132664	-0.8641792
H	5.9394980	-1.2577615	0.3513871
H	5.3653085	-3.5297004	-0.4745458
C	-7.2788827	-1.0874112	0.7847147
C	-7.9817064	1.2021314	0.1057236
C	-8.2672587	-0.0699799	0.6086530
C	-5.5045769	-3.8027173	0.9348386
C	-4.0427911	-5.7258183	0.3879179
C	-5.2640568	-5.1888419	0.8630687
H	-9.3046367	-0.3170280	0.8831208
H	-8.7893941	1.9391158	-0.0205388
H	-6.0770621	-5.8721641	1.1503533
C	-3.6935010	-7.0812019	0.1331069
C	-2.4329098	-7.3867780	-0.3876001
H	-4.4216070	-7.8839260	0.3245344
H	-2.1867796	-8.4367850	-0.6106823
C	-0.1595988	-6.7864328	-1.2077227
C	0.9532537	-6.0050816	-1.3509527
H	-0.0673615	-7.8380260	-1.5256545
C	2.6615876	-4.3907152	-0.9333358
C	4.3016797	0.7974764	0.8794513
C	3.5240126	1.9187669	0.9812161
C	2.1455759	2.2218178	0.6111322
C	-6.1251885	2.7809630	-0.6998777
H	-6.8190196	3.6028881	-0.9313173
C	-7.6380007	-2.3696537	1.3198312
C	-6.8559571	-3.4904412	1.3874207
H	5.3595078	0.9034923	1.1710375
H	4.0592594	2.8123808	1.3417876
H	2.7318966	4.2954252	0.7277488
H	3.3393923	-5.2170565	-1.1945255
H	1.8276377	-6.5308134	-1.7682927
H	-7.3668219	-4.3765997	1.7982056
H	-8.6739349	-2.4693869	1.6833473
Fe	-1.7094886	-0.8018589	-0.0869915

1.4. FeN_4, Pyrrolic-2L

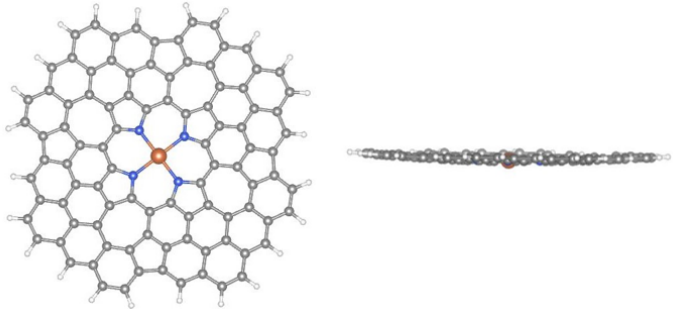

125

N	-1.4098626	1.0821494	-0.3249804
N	0.2940003	-1.1666174	-0.3667392
N	-1.9586762	-2.8718393	-0.2850429
N	-3.6624534	-0.6229377	-0.2456207
C	-2.3246051	2.1370489	-0.2841870
C	-1.6770651	3.4252092	-0.2875510
C	-0.3229570	3.0773366	-0.3445809
C	-0.1551501	1.6834034	-0.3623696
C	-4.2624374	0.6320784	-0.2227780
C	-4.7165299	-1.5379022	-0.1709980
C	-5.6560846	0.4648007	-0.1424853
C	-6.0040464	-0.8881736	-0.0981251
C	-3.2126793	-3.4731124	-0.2277642
C	-1.0419888	-3.9258344	-0.2736428
C	-1.6873286	-5.2134600	-0.2066036
C	-3.0428290	-4.8665208	-0.1900225
C	1.3500420	-0.2511737	-0.3864601
C	0.8946468	-2.4213790	-0.3757407
C	2.6397837	-0.9002485	-0.4013980
C	2.2903702	-2.2536370	-0.4036437
C	1.1593585	1.1448667	-0.3832395
C	-3.7230178	1.9475349	-0.2319279
C	-4.5256981	-2.9340060	-0.1636858
C	0.3566309	-3.7363762	-0.3218708
C	-6.5531570	1.5165702	-0.0691909
C	-4.6351537	3.0505228	-0.1620002
C	-2.0100140	4.8341807	-0.2205045
C	-4.5168655	4.5115495	-0.1128678
C	-3.3585025	5.3450454	-0.1374322
C	1.2722561	-4.8384118	-0.2959985
C	3.1910781	-3.3044871	-0.3748323
C	-1.3492174	-6.6206020	-0.1281028
C	-0.9004562	5.7761738	-0.2180046
C	0.7291926	3.9788538	-0.3399084
C	0.4742340	5.3561403	-0.2745333
C	2.0093351	3.4522759	-0.3631633
C	4.0476465	-0.5642243	-0.3799320
C	4.5689404	-3.0484214	-0.3455240
C	4.9913714	-1.6747841	-0.3539025
C	-7.4067620	-1.2226627	0.0281017
C	-7.9257153	1.2621119	0.0572935
C	-8.3468978	-0.1111784	0.1019820
C	-5.6293365	-3.8483121	-0.0651565
C	-4.0914081	-5.7668681	-0.0904836
C	-5.3705031	-5.2399240	-0.0355995
C	-3.8309837	-7.1420007	-0.0032656
C	-2.4551899	-7.5614618	-0.0279714
C	0.0022796	-7.1303652	-0.1251684
C	1.1588165	-6.2977235	-0.2034373
C	2.6627764	-4.5833343	-0.3262964
C	4.5583337	0.7855510	-0.3638333
C	3.7226223	1.9432001	-0.3681794

C	2.2664504	2.0602505	-0.3832546
C	-6.0239306	2.7957738	-0.0854461
C	-7.9143062	-2.5715830	0.1028960
C	-7.0804037	-3.7296687	0.0576023
C	-6.5298595	-6.0501560	0.1055385
C	-7.6349162	-5.0706581	0.1565051
C	-9.3476557	-2.7828170	0.2429342
C	-9.8582250	-4.1180533	0.3263256
C	-9.0298057	-5.2360294	0.2877006
C	-9.7592744	-0.3442563	0.2429107
C	-10.2245366	-1.6707175	0.3048594
C	3.1751983	4.2647473	-0.3292456
C	4.2818664	3.2856174	-0.3387168
C	-6.3100126	-7.4422911	0.1807646
C	-4.9736646	-8.0028628	0.1295909
C	-4.6690980	-9.4052840	0.2185346
C	-2.2167438	-8.9778100	0.0716198
C	-3.3595773	-9.8552282	0.1868279
C	0.2185980	-8.5687114	-0.0288434
C	2.6695901	-8.2525559	-0.0910753
C	-0.8900528	-9.4453938	0.0634869
C	1.5564194	-9.0815039	-0.0195206
C	4.8716461	-5.5320907	-0.2375754
C	5.4328722	-4.1972173	-0.2820677
C	5.9979029	0.9984151	-0.3323798
C	6.4100041	-1.4400248	-0.3156749
C	6.8384667	-3.8955559	-0.2524601
C	7.2900268	-2.5862248	-0.2721349
C	6.8776689	-0.1129521	-0.3118162
C	5.6825349	3.4523862	-0.3144522
C	6.5122544	2.3346741	-0.3130773
C	2.9598874	5.6586624	-0.2759410
C	1.6226778	6.2190849	-0.2469495
C	-1.1327416	7.1949337	-0.1411579
C	1.3236488	7.6237752	-0.1767756
C	0.0146353	8.0739652	-0.1296813
C	-3.5688790	6.7855531	-0.0625287
C	-2.4573093	7.6634048	-0.0706823
C	-5.8518486	5.0679830	-0.0089329
C	-6.8309484	3.9626582	0.0175761
C	-8.7841284	2.4125499	0.1559171
C	-8.2222796	3.7477469	0.1328409
C	-10.1841227	2.1123573	0.2880562
C	-10.6349366	0.8031440	0.3254246
C	-4.9032766	7.2994050	0.0280753
C	-6.0178386	6.4697202	0.0574164
H	-9.4622693	-6.2453581	0.3614399
H	-10.9464880	-4.2470182	0.4295316
H	-11.3047429	-1.8579731	0.4131295
H	-11.7140870	0.6098708	0.4300728
H	-10.9087380	2.9383186	0.3647389
H	-8.9228385	4.5937362	0.2205334
H	-7.0265971	6.9032194	0.1340092
H	-5.0309580	8.3913700	0.0806591

H	-2.6424611	8.7476990	-0.0112144
H	-0.1785280	9.1567860	-0.0737373
H	2.1497100	8.3520649	-0.1564624
H	3.8055959	6.3644022	-0.2441600
H	6.1186859	4.4626175	-0.2939477
H	7.6050467	2.4648288	-0.2916928
H	7.9627167	0.0754919	-0.2839198
H	8.3737043	-2.3917428	-0.2459198
H	1.6883115	-10.1718720	0.0522212
H	-0.7002583	-10.5278800	0.1389815
H	-3.1618132	-10.9361993	0.2597986
H	-5.4910435	-10.1318256	0.3171708
H	-7.1504811	-8.1459205	0.2938728
H	7.5671185	-4.7204275	-0.2097027
C	3.4758353	-5.7482176	-0.2516360
H	5.5770810	-6.3765374	-0.1789621
C	2.4981740	-6.8528179	-0.1811855
H	3.6815806	-8.6850103	-0.0754893
Fe	-1.6845664	-0.8949813	-0.3136646

1.5. FeN_4, Pyridinic-1

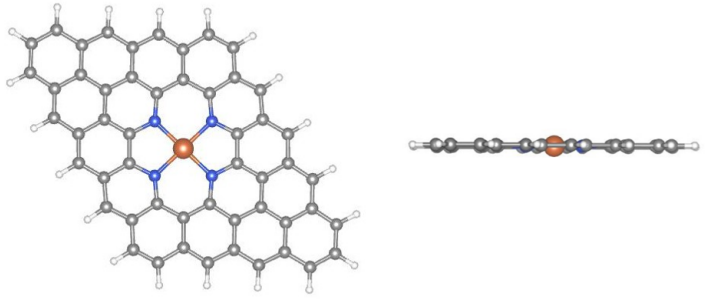

77

C	-2.0120414	2.8995523	0.0113963
C	-2.1485095	1.4871764	-0.0163038
C	-0.7077078	3.4614745	0.0901956
N	0.2739307	1.2626476	0.1123558
C	-0.9828935	0.7259903	0.0361187
C	-1.0670519	-0.6888047	0.0108661
N	0.1175316	-1.3616774	0.0660201
C	0.1592138	-2.7143707	0.0489413
C	-2.3317757	-1.3204351	-0.0678380
C	-2.2988278	-2.7321150	-0.0873302
C	-1.1057822	-3.4251493	-0.0315977
C	-3.4397304	0.8592367	-0.0959233
C	-3.5053401	-0.5419839	-0.1204794
H	-4.4753655	-1.0403077	-0.1810362
H	-3.2356551	-3.2921180	-0.1476518
C	1.7597825	3.2043988	0.2207121
C	2.9899433	2.4645014	0.2773416
N	3.0316151	1.1118049	0.2604592
C	4.2549996	3.1752953	0.3567907

C	5.4480247	2.4822557	0.4128966
C	5.4808697	1.0705489	0.3952840
C	4.2161569	0.4389212	0.3163774
H	6.3848901	3.0422693	0.4725234
C	1.8336257	4.6496547	0.2452413
C	3.1122624	5.3076685	0.3243893
C	4.2649428	4.6117475	0.3775358
H	3.1188024	6.3998396	0.3403836
H	5.2306923	5.1185883	0.4375459
C	-0.5877438	4.8872866	0.1168023
C	0.7072951	5.4436054	0.1952259
H	0.8189039	6.5296532	0.2169190
C	4.1319240	-0.9758931	0.2924779
N	2.8751527	-1.5125376	0.2152832
C	2.6977407	-2.8613933	0.1879627
C	5.2973690	-1.7371218	0.3479889
C	5.1607611	-3.1495309	0.3227890
C	3.8565262	-3.7114285	0.2422004
C	6.6543020	0.2920639	0.4503099
C	6.5885255	-1.1091983	0.4287691
H	7.6243238	0.7903865	0.5109337
C	1.3892918	-3.4542894	0.1070601
C	3.7364590	-5.1372652	0.2174343
C	2.4415630	-5.6935492	0.1364434
C	1.3154098	-4.8995548	0.0832291
H	2.3299040	-6.7796099	0.1156745
C	0.0369083	-5.5575346	0.0016451
C	-1.1156746	-4.8615884	-0.0532540
H	0.0303707	-6.6497052	-0.0143882
H	-2.0813291	-5.3684050	-0.1149774
C	0.4512595	2.6114835	0.1411637
C	7.7242441	-1.9496552	0.4828248
C	-4.5757053	1.6996314	-0.1453735
C	-3.1649082	3.7113390	-0.0397685
C	-4.4642308	3.1026108	-0.1190023
C	-1.7421713	5.6841551	0.0652745
C	-3.0284582	5.1310917	-0.0124349
C	-5.5987383	3.9464706	-0.1685426
C	-4.2072172	5.9281055	-0.0653216
C	-5.4586439	5.3353319	-0.1414236
H	-5.5688064	1.2473768	-0.2059045
H	-6.3509894	5.9646974	-0.1809055
H	-6.5917535	3.4949978	-0.2287966
H	-4.1102658	7.0160871	-0.0448977
H	-1.6301123	6.7710571	0.0867831
C	6.3133694	-3.9613792	0.3785816
C	7.6125703	-3.3526810	0.4600136
C	4.8906297	-5.9341945	0.2735558
C	6.1767622	-5.3811676	0.3540360
H	4.7784695	-7.0211205	0.2538669
H	8.7172802	-1.4974171	0.5445415
C	8.7467437	-4.1966185	0.5155106
C	7.3551969	-6.1782562	0.4126938
C	8.6064651	-5.5855209	0.4916453

```
H      7.2581074   -7.2662687    0.3947102
H      9.7396459   -3.7451733    0.5778043
H      9.4985407   -6.2149490    0.5359348
Fe     1.5745808   -0.1249346    0.1631081
```

1.6. FeN_4, Pyridinic-1L

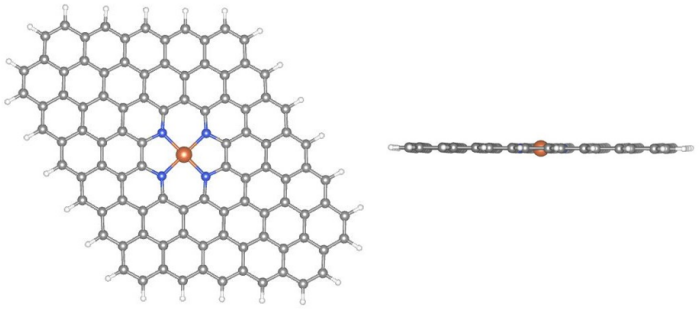

```
129

C     -1.9739928    2.9094251   -0.6223372
C     -2.0881284    1.4938055   -0.6422545
C     -0.6795718    3.4938291   -0.4148923
N      0.3300925    1.2858443   -0.2544260
C     -0.9214254    0.7333147   -0.4559816
C     -0.9992969   -0.6842727   -0.4687852
N      0.1834063   -1.3652755   -0.2772749
C      0.1959098   -2.7429575   -0.2735588
C     -2.2468372   -1.3218820   -0.6696750
C     -2.2727355   -2.7397136   -0.6739675
C     -1.0575008   -3.4522747   -0.4768245
C     -3.3550461    0.8551152   -0.8452821
C     -3.4317228   -0.5590981   -0.8590748
C      1.7778501    3.2817439   -0.0204635
C      2.9991055    2.5268577    0.1778130
N      3.0118126    1.1492279    0.1807542
C      4.2524907    3.2362135    0.3811920
C      5.4672149    2.5236300    0.5812016
C      5.4408752    1.1057977    0.5798892
C      4.1938420    0.4681906    0.3757177
C      1.8510443    4.7330198   -0.0094680
C      3.1106936    5.4094450    0.1924740
C      4.2954250    4.6694342    0.3854520
C     -0.5855737    4.9234521   -0.3992757
C      0.6863101    5.5359338   -0.1964894
C      4.1155542   -0.9494325    0.3653952
N      2.8645525   -1.5019401    0.1604842
C      2.7112685   -2.8758851    0.1391130
C      5.2808919   -1.7099119    0.5601054
C      5.1658854   -3.1255353    0.5457573
C      3.8722431   -3.7099298    0.3334960
C      6.6244893    0.3430119    0.7769771
C      6.5470141   -1.0712084    0.7681057
C      1.4166748   -3.4978585   -0.0724090
```

C	3.7774018	-5.1395671	0.3229855
C	2.5065004	-5.7520419	0.1141587
C	1.3430440	-4.9491277	-0.0808612
C	0.0840619	-5.6255320	-0.2867958
C	-1.1002626	-4.8854853	-0.4822944
C	0.4827901	2.6597346	-0.2291020
C	7.7119761	-1.8615474	0.9642109
C	-4.5219316	1.6454724	-1.0295182
C	-3.1397964	3.6958271	-0.8069513
C	-4.4174492	3.0663191	-1.0105013
C	-1.7595792	5.7240427	-0.5857557
C	-3.0361241	5.1192217	-0.7886585
C	-5.5832423	3.8636979	-1.1929234
C	-4.2061832	5.9177577	-0.9724521
C	-5.4795852	5.2917658	-1.1738495
C	6.3297694	-3.9119236	0.7422270
C	7.6063698	-3.2824085	0.9522536
C	4.9494956	-5.9401320	0.5212619
C	6.2249239	-5.3353188	0.7311589
C	8.7696554	-4.0797649	1.1502068
C	7.3925108	-6.1338210	0.9302062
C	8.6645650	-5.5078259	1.1399747
Fe	1.5977002	-0.1082045	-0.0492879
C	5.5685595	5.3452273	0.5905463
C	6.7363808	3.1909176	0.7875830
C	6.7366189	4.6154090	0.7832115
C	7.8914066	1.0032214	0.9844577
C	7.9037237	2.4280268	0.9819384
C	5.5919369	6.7878902	0.5901659
C	4.4486848	7.5096427	0.4037065
C	3.1751054	6.8614238	0.2002738
H	4.4716876	8.6101957	0.4046615
H	6.5583264	7.2915299	0.7450550
H	7.6864365	5.1508802	0.9368757
H	8.8590907	2.9531266	1.1377383
C	2.0224975	7.6090357	0.0145257
C	-0.3951677	7.7546499	-0.3696027
C	-1.6688576	7.1668702	-0.5709423
C	0.7610720	6.9841495	-0.1856401
H	2.0786975	8.7085487	0.0217249
H	-0.3097244	8.8524655	-0.3566763
C	-2.8360936	7.9432185	-0.7547438
C	-4.1016225	7.3544048	-0.9542882
H	-2.7512834	9.0410783	-0.7407511
C	-5.2952513	8.1270067	-1.1407124
C	-6.5203728	7.5171475	-1.3332682
C	-6.6512408	6.0949681	-1.3562678
H	-5.2175609	9.2249887	-1.1273428
C	-7.9094354	5.4409560	-1.5548360
C	-6.8632343	3.2242934	-1.3955786
C	-5.8003667	0.9979204	-1.2328557
C	-4.6993935	-1.2193073	-1.0618656
C	-3.5421415	-3.4069576	-0.8786528
C	-2.3730536	-5.5612609	-0.6894085

C	-8.0149934	4.0656187	-1.5743866
C	-6.9448985	1.8180503	-1.4115759
C	-5.8527427	-0.4234271	-1.2437690
C	-4.7107629	-2.6440819	-1.0654208
C	-3.5415801	-4.8314348	-0.8792049
H	-8.9941409	3.5867681	-1.7288033
H	-7.9253743	1.3413149	-1.5668685
H	-6.8248671	-0.9172053	-1.3986503
H	-5.6664714	-3.1691787	-1.2188729
H	-4.4913477	-5.3669062	-1.0330538
C	0.0195678	-7.0774988	-0.2942836
C	2.4311556	-7.2002471	0.1066708
C	4.8577741	-7.3829654	0.5124513
C	7.2866565	-7.5704769	0.9199621
C	-1.2530741	-7.7257051	-0.5034606
C	-2.3959257	-7.0039260	-0.6922712
H	-1.2758754	-8.8262630	-0.5057568
H	-3.3617795	-7.5075477	-0.8504883
C	1.1709861	-7.8251193	-0.1011776
C	3.5855313	-7.9707456	0.3022967
C	9.8333240	-6.3110066	1.3403801
C	8.4774535	-8.3430469	1.1238736
C	9.7009991	-7.7331743	1.3262618
H	1.1145821	-8.9246413	-0.1072533
H	3.4995666	-9.0685748	0.2924729
C	6.0226376	-8.1592939	0.7110627
H	5.9369768	-9.2571673	0.7022087
H	8.3987991	-9.4410370	1.1164744
C	11.0901345	-5.6569815	1.5474998
C	11.1972111	-4.2816424	1.5577877
C	10.0483579	-3.4403457	1.3609917
C	8.9893425	-1.2139797	1.1743244
C	9.0429132	0.2073715	1.1777987
H	10.0143725	0.7011727	1.3369860
C	10.1314568	-2.0340995	1.3680677
H	11.1110262	-1.5573395	1.5291320
H	12.1752793	-3.8027905	1.7190520
H	-7.4249445	8.1293398	-1.4736874
H	11.9847652	-6.2805784	1.7009856
H	-8.8063382	6.0645729	-1.6942008
H	10.6031572	-8.3453729	1.4815331

1.7. FeN_4, Pyridinic-2

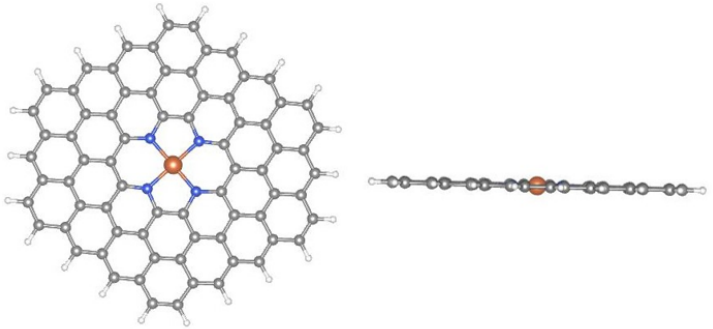

```
101

C    -1.9603273    3.4144163   -0.6477461
C    -2.2071138    2.0203811   -0.6527047
C    -0.6261131    3.8800795   -0.4274082
N     0.1818117    1.5955461   -0.2236130
C    -1.1155422    1.1530374   -0.4382329
C    -1.3169664   -0.2418660   -0.4350429
N    -0.1977285   -1.0323212   -0.2176838
C    -0.3101748   -2.4011539   -0.1996719
C    -2.6095098   -0.7659303   -0.6460397
C    -2.7672242   -2.1727873   -0.6343898
C    -1.6190670   -2.9958722   -0.4114470
C    -3.5197905    1.5000831   -0.8674329
C    -3.7214765    0.1034686   -0.8639907
C     1.8027711    3.4427915    0.0085867
C     2.9475771    2.5823481    0.2321282
N     2.8351003    1.2135174    0.2503029
C     4.2564592    3.1770697    0.4439698
C     5.4045830    2.3539870    0.6671083
C     5.2468317    0.9471329    0.6789598
C     3.9543020    0.4230666    0.4678770
C     2.0104623    4.8809470    0.0050773
C     3.3115235    5.4435718    0.2161326
C     4.4317821    4.5899678    0.4350042
C    -0.3945039    5.2848616   -0.4254087
C     0.9216417    5.7876670   -0.2096751
C     3.7528731   -0.9718366    0.4710841
N     2.4555590   -1.4143499    0.2562410
C     2.1762637   -2.7591522    0.2442118
C     4.8444230   -1.8391769    0.6856748
C     4.5976674   -3.2332142    0.6805312
C     3.2634932   -3.6988805    0.4599716
C     6.3587735    0.0777348    0.8970485
C     6.1570776   -1.3188782    0.9005299
C     0.8346503   -3.2615981    0.0237519
C     3.0319205   -5.1036661    0.4577675
C     1.7158172   -5.6064768    0.2417983
C     0.6269907   -4.6997567    0.0270841
C    -0.6740540   -5.2623834   -0.1840602
```

C	-1.7943516	-4.4087745	-0.4027019
C	0.4611339	2.9403464	-0.2117453
C	7.2566163	-2.2281274	1.1172679
C	7.0088260	-3.6005089	1.1115557
C	5.4299914	-5.5166651	0.8877978
C	4.1350035	-6.0111856	0.6750052
C	5.6984497	-4.1333679	0.8972330
C	3.8799413	-7.4258951	0.6687620
C	2.6182974	-7.9119252	0.4618940
C	1.5028581	-7.0313346	0.2436015
C	0.2161799	-7.5446214	0.0336390
C	-0.8729165	-6.6892711	-0.1793421
C	-2.1920912	-7.2193295	-0.3940645
C	-3.1093296	-4.9681290	-0.6160005
C	-4.0779149	-2.7257382	-0.8471678
C	-5.1842047	-1.8449125	-1.0643814
C	-5.0335245	-0.4585598	-1.0769226
C	-4.6193327	2.4093317	-1.0841646
C	-5.9271473	1.8264151	-1.2961717
C	-3.0611129	4.3145715	-0.8644402
C	-4.3715337	3.7817144	-1.0785124
C	-1.4975912	6.1923822	-0.6426318
C	-2.7926390	5.6978687	-0.8550900
C	1.1346470	7.2125180	-0.2117395
C	0.0192250	8.0931050	-0.4301377
C	3.5104309	6.8704526	0.2111552
C	2.4213514	7.7257998	-0.0019254
C	5.7467688	5.1493213	0.6482621
C	5.9024205	6.5783376	0.6352585
C	4.8296230	7.4005074	0.4257824
C	6.8491396	4.3095943	0.8637413
C	6.7152815	2.9069372	0.8798545
C	7.6708275	0.6397613	1.1099586
C	7.8215278	2.0261132	1.0973147
C	8.7604035	-0.2883440	1.3257649
C	8.5644359	-1.6452145	1.3292520
H	9.7634181	0.1208558	1.4893474
H	9.4106938	-2.3207857	1.4955186
H	7.8356457	-4.3005297	1.2749233
H	6.2497107	-6.2254237	1.0501055
H	4.7220935	-8.1063158	0.8339938
H	2.4302979	-8.9909806	0.4582607
H	0.0597765	-8.6287144	0.0362869
C	-3.2649168	-6.3971550	-0.6033744
H	-2.3167360	-8.3074946	-0.3855239
H	-4.2653513	-6.8121166	-0.7658488
C	-4.2117523	-4.1283961	-0.8311755
H	-5.1987435	-4.5768956	-0.9902681
H	-6.1755653	-2.2830135	-1.2246228
C	-6.1231159	0.4695447	-1.2926506
H	-7.1261554	0.0603477	-1.4560752
H	-6.7733757	2.5019798	-1.4626265
H	-5.1983864	4.4817404	-1.2417169
H	-3.6124226	6.4066390	-1.0170432

```
C     -1.2424748     7.6070841    -0.6366895
H     -2.0846307     8.2875071    -0.8019033
H      0.2073029     9.1721483    -0.4269567
H      2.5777646     8.8098909    -0.0046316
H      6.9029067     6.9932923     0.7974434
H      4.9543013     8.4886672     0.4170498
H      7.8360792     4.7581033     1.0231506
H      8.8128703     2.4642172     1.2576865
Fe     1.3187026     0.0905956     0.0162157
```

1.8. FeN_4, Pyridinic-2L

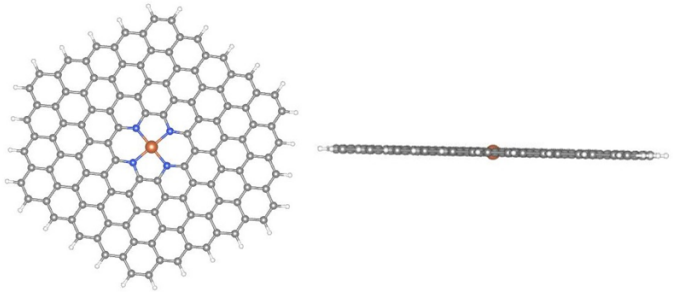

```
157

C     -1.9596506     3.4144013    -0.6539982
C     -2.1984721     2.0204282    -0.6572563
C     -0.6271373     3.8874931    -0.4300876
N      0.1811351     1.6007786    -0.2217840
C     -1.1110908     1.1529651    -0.4392528
C     -1.3137596    -0.2459745    -0.4352455
N     -0.2017426    -1.0408484    -0.2142001
C     -0.3222115    -2.4140166    -0.1953490
C     -2.6028722    -0.7703012    -0.6490497
C     -2.7695443    -2.1746651    -0.6375752
C     -1.6259109    -3.0052126    -0.4101413
C     -3.5083117     1.4984519    -0.8748910
C     -3.7108359     0.1007181    -0.8706949
C      1.7948705     3.4588957     0.0140818
C      2.9356203     2.5938335     0.2429554
N      2.8153255     1.2206048     0.2606072
C      4.2389718     3.1850841     0.4597208
C      5.3823261     2.3545831     0.6887990
C      5.2157286     0.9501978     0.6997538
C      3.9270673     0.4257855     0.4835063
C      2.0030448     4.8965554     0.0106428
C      3.3079885     5.4580311     0.2277510
C      4.4253544     4.6001978     0.4522246
C     -0.4043856     5.2973682    -0.4298669
C      0.9107998     5.8040642    -0.2097614
C      3.7243807    -0.9731490     0.4874726
N      2.4325379    -1.4210306     0.2681377
C      2.1581395    -2.7720165     0.2582493
C      4.8113696    -1.8405390     0.7077659
```

C	4.5725295	-3.2344951	0.7045466
C	3.2402954	-3.7076357	0.4791101
C	6.3232878	0.0792289	0.9237077
C	6.1207604	-1.3185007	0.9278684
C	0.8185808	-3.2790732	0.0333216
C	3.0174788	-5.1174869	0.4792644
C	1.7024438	-5.6241999	0.2583118
C	0.6102669	-4.7166987	0.0375629
C	-0.6948178	-5.2781555	-0.1787489
C	-1.8123774	-4.4203029	-0.4021195
C	0.4553165	2.9518315	-0.2108511
C	7.2143138	-2.2052912	1.1493525
C	6.9877070	-3.6064190	1.1483898
C	5.4400183	-5.5223025	0.9246783
C	4.1201357	-6.0186793	0.7021332
C	5.6701864	-4.1219583	0.9266001
C	3.9013719	-7.4293638	0.7023757
C	2.5941514	-7.9404953	0.4828828
C	1.4963420	-7.0475244	0.2617901
C	0.1950350	-7.5831648	0.0451647
C	-0.9010526	-6.7014588	-0.1746841
C	-2.2074917	-7.2473734	-0.3909014
C	-3.1259652	-4.9726879	-0.6191107
C	-4.0745921	-2.7152712	-0.8529649
C	-5.1922251	-1.8481739	-1.0759973
C	-5.0118211	-0.4403634	-1.0851601
C	-4.6023309	2.3853080	-1.0937868
C	-5.9099662	1.8483650	-1.3096449
C	-3.0577135	4.3019225	-0.8738276
C	-4.3756826	3.7864369	-1.0931185
C	-1.5073107	6.1986009	-0.6512644
C	-2.8275263	5.7022740	-0.8719691
C	1.1168796	7.2273991	-0.2130704
C	0.0189554	8.1203813	-0.4335440
C	3.5141803	6.8813463	0.2239386
C	2.4181948	7.7630349	0.0035045
C	5.7386015	5.1526478	0.6711251
C	5.9290861	6.5674154	0.6640658
C	4.8204100	7.4273011	0.4413276
C	6.8635785	4.3033578	0.8970768
C	6.6869179	2.8952715	0.9067490
C	7.6237750	0.6204016	1.1409623
C	7.8041263	2.0282250	1.1321625
C	8.7248738	-0.2642433	1.3638831
C	8.5214125	-1.6682675	1.3681902
C	-3.3164639	-6.3874446	-0.6119863
C	-4.2512918	-4.1233393	-0.8430486
C	-6.1134273	0.4443422	-1.3052667
C	-1.2885000	7.6092838	-0.6517233
C	-4.6366383	-6.9381006	-0.8296869
C	-4.7951863	-8.3713792	-0.8165993
C	-2.4034923	-8.6788599	-0.3848044
C	-3.7295063	-9.2009260	-0.6044531
H	-5.7968459	-8.7824882	-0.9818571

H	-3.8632571	-10.2880579	-0.5967933
C	-0.0117579	-9.0110211	0.0488097
C	-1.3131645	-9.5221449	-0.1676168
H	-1.4640589	-10.6074036	-0.1632505
C	2.3759954	-9.3687992	0.4839546
C	1.0912715	-9.8692369	0.2692354
C	3.4993140	-10.2443859	0.7088760
C	4.7563637	-9.7501514	0.9196020
C	5.0108869	-8.3307269	0.9259640
H	0.9282929	-10.9527498	0.2711838
H	3.3194383	-11.3248734	0.7070589
H	5.6000363	-10.4278102	1.0888277
C	6.2923061	-7.8193974	1.1412342
C	6.5474998	-6.4231801	1.1483367
H	7.1241355	-8.5124256	1.3091326
C	7.8429430	-5.8928191	1.3660251
C	8.0925605	-4.5064967	1.3718359
H	8.6737338	-6.5868378	1.5348795
C	9.3939852	-3.9504346	1.5895056
C	9.6265781	-2.5742564	1.5921342
H	10.2325884	-4.6352976	1.7589165
C	10.9342056	-1.9918142	1.8097298
C	10.0419619	0.2920987	1.5834667
C	10.2095221	1.6776620	1.5728711
C	9.1192192	2.5790051	1.3512756
C	9.2733356	3.9791064	1.3375503
C	8.1814111	4.8541389	1.1165145
C	8.3328633	6.2653181	1.1020395
C	7.2489406	7.1181113	0.8836301
C	7.4075532	8.5513785	0.8701054
C	6.3421782	9.3808764	0.6562253
C	5.0164289	8.8587851	0.4350649
C	3.9262934	9.7020289	0.2167740
C	2.6249977	9.1908886	-0.0002505
C	1.5219800	10.0490921	-0.2207555
C	0.2371641	9.5486753	-0.4349483
C	-0.8862765	10.4242944	-0.6591275
C	-2.3982327	8.5106990	-0.8740353
C	-2.1435839	9.9301049	-0.8684123
C	-3.9353559	6.6032273	-1.0936467
C	-3.6800209	7.9994260	-1.0872733
C	-5.2313037	6.0729295	-1.3085295
C	-5.4809835	4.6866085	-1.3140044
C	-7.0156435	2.7544505	-1.5306802
C	-6.7829715	4.1306213	-1.5285405
C	-7.4310709	-0.1119284	-1.5216514
C	-8.5203207	0.8165211	-1.7406770
C	-8.3238471	2.1720765	-1.7449926
C	-7.5986406	-1.4974800	-1.5109273
C	-6.5078168	-2.3988834	-1.2921952
C	-5.5695379	-4.6740661	-1.0600578
C	-5.7209524	-6.0852463	-1.0458632
C	-6.6619358	-3.7989737	-1.2784406
C	11.1306726	-0.6362564	1.8055477

```
H     11.7787958    -2.6681431     1.9810450
H     12.1328747    -0.2266712     1.9728886
H     11.2082608     2.0971561     1.7392362
H     10.2672955     4.4095537     1.5026565
H      9.3273742     6.6945966     1.2668341
H      8.4090097     8.9625415     1.0365017
H      6.4759309    10.4680083     0.6487496
H      4.0771421    10.7872916     0.2126038
H      1.6849203    11.1326081    -0.2225361
H     -0.7063331    11.5047716    -0.6576293
H     -2.9874082    10.6077842    -1.0368420
H     -4.5120300     8.6925024    -1.2541661
H     -6.0625388     6.7670268    -1.4749706
H     -7.6219421     4.8155471    -1.6959630
H     -9.1689332     2.8484672    -1.9136314
H     -9.5229044     0.4070057    -1.9058494
H     -7.6562825    -4.2293532    -1.4412629
H     -6.7157244    -6.5144680    -1.2091374
H     -8.5977783    -1.9169112    -1.6749438
Fe     1.3070844     0.0899618     0.0217980
```

1.9. FeN_4, Pyrrolic-UC1

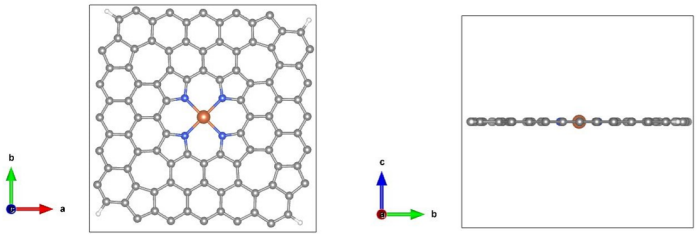


```
1.0
16.8133888245          0.0000000000          0.0000000000
0.0000134330         16.8133697510          0.0000000000
0.0000000000          0.0000000000         15.3348312378
C    N   Fe    H
96    4    1    4
Cartesian
16.335061528         13.535719828          7.667415619
15.537297215         12.307434649          7.667415619
16.178218091         11.028023534          7.667415619
16.155608476          8.553840303          7.667415619
13.369773916         16.039151952          7.667415619
14.291513045         14.875230174          7.667415619
12.081301411         15.479148779          7.667415619
12.116384766         14.068358159          7.667415619
16.147331710          6.097493927          7.667415619
14.097643943         12.358740973          7.667415619
13.495857271         13.649884315          7.667415619
15.450538560          9.798666049          7.667415619
10.903239213         13.371312303          7.667415619
15.976229617          3.614418576          7.667415619
```

11.926122994	11.011365715	7.667415619
9.651310348	14.088372195	7.667415619
10.878247332	11.975389653	7.667415619
9.653335834	15.503582318	7.667415619
15.416207796	4.902840066	7.667415619
14.025165003	7.332800204	7.667415619
13.320789577	8.572395202	7.667415619
10.886732964	16.210389163	7.667415619
13.343834165	11.093473270	7.667415619
14.031703059	9.828908079	7.667415619
15.440331633	7.330820447	7.667415619
8.433753165	11.964000163	7.667415619
7.155231715	14.094945329	7.667415619
5.956044459	16.241346731	7.667415619
10.948473905	5.058046807	7.667415619
13.472996723	0.649101512	7.667415619
12.296003288	2.886501838	7.667415619
9.702081938	5.758512015	7.667415619
5.890641991	13.406879783	7.667415619
4.676681990	15.600226131	7.667415619
7.219140473	11.288541726	7.667415619
11.030714710	3.640360108	7.667415619
12.244676715	1.446881601	7.667415619
13.587152585	3.488171608	7.667415619
8.411752966	13.384106815	7.667415619
7.185464390	15.513780247	7.667415619
11.212481706	7.324674732	7.667415619
11.912405571	6.105972158	7.667415619
11.225498656	9.765041747	7.667415619
14.812508217	2.692502933	7.667415619
9.659489702	11.275588873	7.667415619
13.308255624	6.080753430	7.667415619
11.900785520	8.550415940	7.667415619
8.430287100	16.218867394	7.667415619
14.005379470	4.867690484	7.667415619
5.972759029	11.989104144	7.667415619
4.625281758	14.160593492	7.667415619
10.965305727	0.805871864	7.667415619
3.448408331	16.398026640	7.667415619
5.708397968	9.722450163	7.667415619
8.487482274	5.083223945	7.667415619
9.766141521	2.952416575	7.667415619
7.261715171	5.771667804	7.667415619
3.334161023	13.558705253	7.667415619
5.008679545	10.941199837	7.667415619
8.509515545	3.663189448	7.667415619
9.735867257	1.533527791	7.667415619
2.915712911	12.179204917	7.667415619
6.042985602	5.071800381	7.667415619
7.267935683	1.543635401	7.667415619
3.599994642	8.474549805	7.667415619
6.018005246	3.675824617	7.667415619
4.994999703	6.035758678	7.667415619
3.612725267	10.966098377	7.667415619

```
8.491018490          0.828378197          7.667415619
7.269975701          2.958844146          7.667415619
2.108852492         14.354327077          7.667415619
5.019991934          8.496702440          7.667415619
5.695397052          7.282102188          7.667415619
2.895700140          9.714133279          7.667415619
0.944978201         13.432601092          7.667415619
3.577302060          5.953533369          7.667415619
1.504869929         12.144116466          7.667415619
4.804869213          2.978806320          7.667415619
2.889220209          7.218039434          7.667415619
6.034529533          0.836795109          7.667415619
2.823479505          4.688209546          7.667415619
3.425355620          3.397116813          7.667415619
1.470406630          7.248303511          7.667415619
4.839950564          1.567983506          7.667415619
0.773663399         10.949495676          7.667415619
1.480443441          9.716080466          7.667415619
0.765138475          8.493038562          7.667415619
3.551549212          1.007984655          7.667415619
2.629699846          2.171793002          7.667415619
0.742795872          6.018946527          7.667415619
1.383849032          4.739604561          7.667415619
0.586118041          3.511319883          7.667415619
15.668709919        14.789363535           7.667415619
14.726726566         1.315297030           7.667415619
2.194771188         15.731583589          7.667415619
1.252508734          2.257666906          7.667415619
9.855903189          9.917115752          7.667415619
9.854081046          7.128152149          7.667415619
7.065038618          7.130107354          7.667415619
7.066895837          9.918941678          7.667415619
8.460403759          8.523563199          7.667415619
15.624866365         0.706337085           7.667415619
1.296598944         16.340492925          7.667415619
16.277708853        15.687472737           7.667415619
0.643590787          1.359493315          7.667415619
```

1.10. FeN_4, Pyrrolic-UC1b

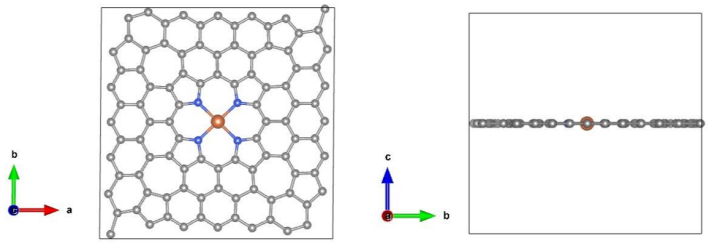


```
1.0
16.7742614746          0.0000000000          0.0000000000
0.1355961282          16.5558946196          0.0000000000
0.0000000000          0.0000000000          15.6096458435
```

```
C    N   Fe
98    4    1
Cartesian
15.736729731        14.946877177         7.804822922
16.380211526        13.570979360         7.804822922
16.216485998        10.949239129         7.804822922
15.596817047        12.261540116         7.804822922
14.349135535        14.722184893         7.804822922
13.409452174        15.765214535         7.804822922
16.191749780         8.424767597         7.804822922
15.502267735         9.689289304         7.804822922
13.576020606        13.472728787         7.804822922
14.166367744        12.209138626         7.804822922
12.125560094        15.215481440         7.804822922
12.183297282        13.833263116         7.804822922
16.183846455         5.929820873         7.804822922
15.491464055         7.179832059         7.804822922
14.091604548         9.680542236         7.804822922
10.961577200        15.940499305         7.804822922
13.404103216        10.942874216         7.804822922
15.478915745         4.718480235         7.804822922
14.088210406         7.166060657         7.804822922
13.396354713         8.417390219         7.804822922
10.961108244        13.151189171         7.804822922
16.029154046         3.399724041         7.804822922
11.988237267        10.842609567         7.804822922
9.721839317        15.253794269         7.804822922
10.925471553        11.777110041         7.804822922
9.709517572        13.856161014         7.804822922
14.087230725         4.674759697         7.804822922
8.517545028        15.968619392         7.804822922
13.382092692         5.900736675         7.804822922
11.983253266         8.399647407         7.804822922
11.296521216         9.598428937         7.804822922
14.926714912         2.441880865         7.804822922
9.708447724        11.080767836         7.804822922
13.696740494         3.270889074         7.804822922
14.931051147         0.979537045         7.804822922
8.462189969        13.171158222         7.804822922
11.985659232         5.965995782         7.804822922
11.295618141         7.190947467         7.804822922
7.257350885        15.286081647         7.804822922
8.479998333        11.761246112         7.804822922
7.209434667        13.884695561         7.804822922
6.038094943        16.013506338         7.804822922
12.357540049         2.780349669         7.804822922
13.523978470         0.557215137         7.804822922
11.008937493         4.953040107         7.804822922
12.293187033         1.369357005         7.804822922
11.097641282         3.548610705         7.804822922
7.253600419        11.119442823         7.804822922
9.765786164         5.666536494         7.804822922
5.921553151        13.237224045         7.804822922
4.726083770        15.416402500         7.804822922
```

6.010262110	11.832876547	7.804822922
4.661692858	14.005421678	7.804822922
3.495365896	16.228614740	7.804822922
10.981133541	0.772335320	7.804822922
9.809756163	2.901126607	7.804822922
8.539409249	5.024672516	7.804822922
5.723736027	9.595163589	7.804822922
9.761846340	1.499788751	7.804822922
8.557095633	3.614760160	7.804822922
5.033523294	10.819972186	7.804822922
7.311110755	5.705385653	7.804822922
3.322534746	13.515015492	7.804822922
2.088337919	15.806379240	7.804822922
5.723097839	7.187796095	7.804822922
5.036271864	8.386462662	7.804822922
2.092603147	14.344033076	7.804822922
3.637062172	10.885149882	7.804822922
8.501688470	0.817285174	7.804822922
7.309746713	2.929840259	7.804822922
2.932032838	12.111153504	7.804822922
6.094069729	5.009079959	7.804822922
7.297372646	1.532166546	7.804822922
5.031312728	5.943606584	7.804822922
6.058228641	3.634948036	7.804822922
3.623062660	8.368625117	7.804822922
2.930968108	9.619844649	7.804822922
0.990231416	13.386225178	7.804822922
1.540402915	12.067506977	7.804822922
3.615415936	5.843116450	7.804822922
6.057668691	0.845392494	7.804822922
2.927855349	7.105446456	7.804822922
4.836066398	2.952727549	7.804822922
1.527688290	9.606052031	7.804822922
0.835498316	10.856188048	7.804822922
4.893748983	1.570495410	7.804822922
2.853067463	4.576826382	7.804822922
3.443333830	3.313170846	7.804822922
1.517165492	7.096601694	7.804822922
0.827487565	8.361087876	7.804822922
3.609928809	1.020630391	7.804822922
2.670217920	2.063625433	7.804822922
1.422585796	4.524455976	7.804822922
0.802897295	5.836719959	7.804822922
1.282596281	1.838832742	7.804822922
0.639165341	3.214889434	7.804822922
0.800618377	0.323990940	7.804822922
16.218771266	16.461766931	7.804822922
9.924521203	9.734095331	7.804822922
9.933976551	7.022797814	7.804822922
7.085341408	9.763225910	7.804822922
7.095092412	7.052075920	7.804822922
8.509770865	8.393030858	7.804822922

1.11. FeN_4, Pyridinic-UC

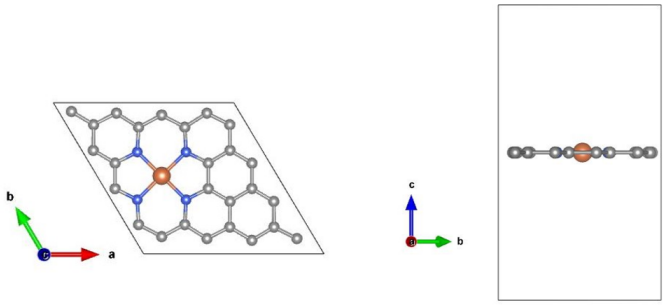


```
1.0
10.0019102097          0.0000000000          0.0000000000
-5.0009534499          8.3605383040          0.0000000000
0.0000000000           0.0000000000         15.1362419128
C    N   Fe
26    4    1
Cartesian
8.494468149          0.851206532          7.568120956
7.213201946          2.904323516          7.568120956
6.001147358          5.022033012          7.568120956
4.774811753          7.151496046          7.568120956
1.000191002          0.957436998          7.568120956
-1.582506684          5.027467765          7.568120956
-2.774427744          7.151496046          7.568120956
3.507824469          0.851206532          7.568120956
-0.279153953          7.015864416          7.568120956
6.001146588          0.755699687          7.568120956
4.789093125          2.904323516          7.568120956
3.582891640          5.027467765          7.568120956
2.279538653          7.015864416          7.568120956
-0.279154424          1.623358481          7.568120956
-1.582506629          3.611754883          7.568120956
-2.788708151          5.734899133          7.568120956
-4.000762136          7.883522837          7.568120956
2.279537437          1.623358481          7.568120956
-1.507440165          7.788015992          7.568120956
4.774811675          1.487726851          7.568120956
3.582890764          3.611754883          7.568120956
1.000193376          7.681785152          7.568120956
7.227481940          1.487726851          7.568120956
6.001146931          3.617189886          7.568120956
4.789091897          5.734899133          7.568120956
3.507825767          7.788015992          7.568120956
-0.350683552          2.999929777          7.568120956
2.351067407          2.999929777          7.568120956
-0.350683029          5.639292622          7.568120956
2.351067781          5.639292622          7.568120956
1.000192114          4.319611324          7.568120956
```

2. Non-planar MN_4 binding

In this section, the top view and side view of non-planar binding motifs discussed in Table 2 are shown. Planar pyrrolic TiN_4 and VN_4 are additionally included for comparison with pyridinic motifs.

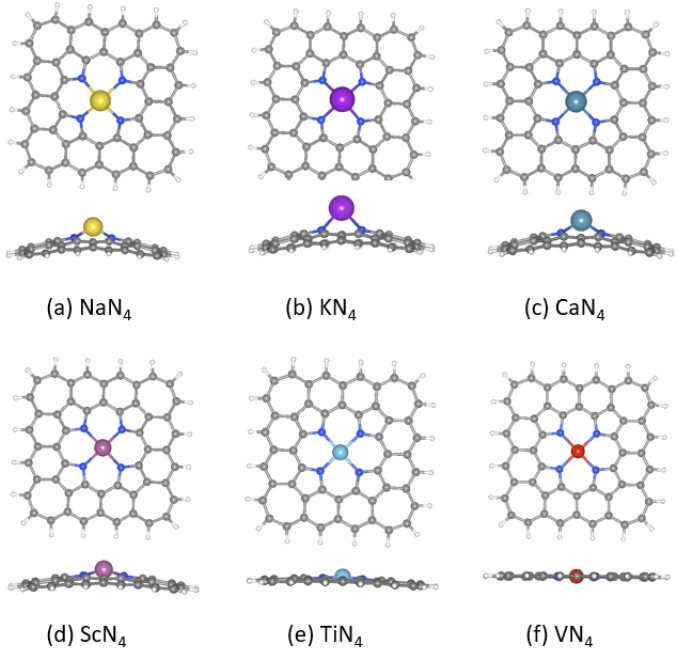

Figure S1. (a-d) Top and side views of pyrrolic-1 MN_4 clusters with non-planar binding geometries. (e,f) Ti and V are included for comparison with pyridinic structures.

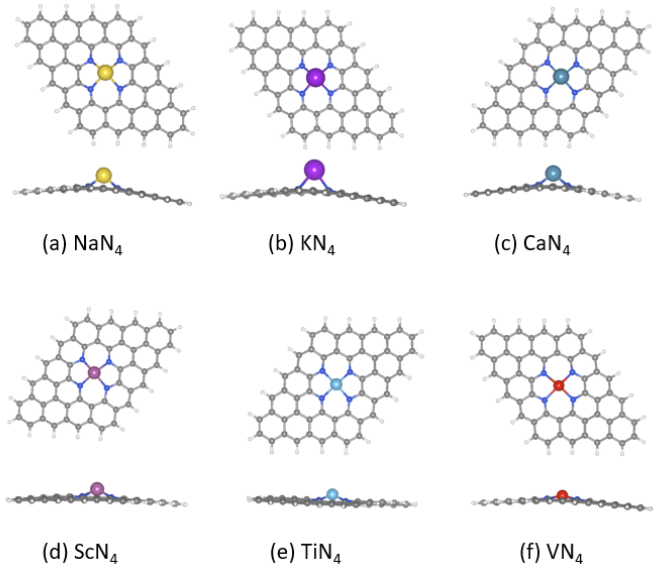

Figure S2. Top and side views of pyridinic-1 MN_4 clusters with non-planar binding geometries.

3. Frontier Molecular Orbitals of Fe and Zn

In this section, the frontier molecular orbitals are plotted to illustrate the differences in binding character between a highly ionic binding character (Zn) and a binding situation involving π-d interaction (Fe). For the pyrrolic-1 FeN_4 cluster, π-d interactions can be observed in all the occupied orbitals shown. In pyridinic-1 FeN_4 cluster, the orbitals illustrating π-d interactions are lower in energy. No significant π-d interaction can be observed for Zn. All orbitals are plotted with Molden.

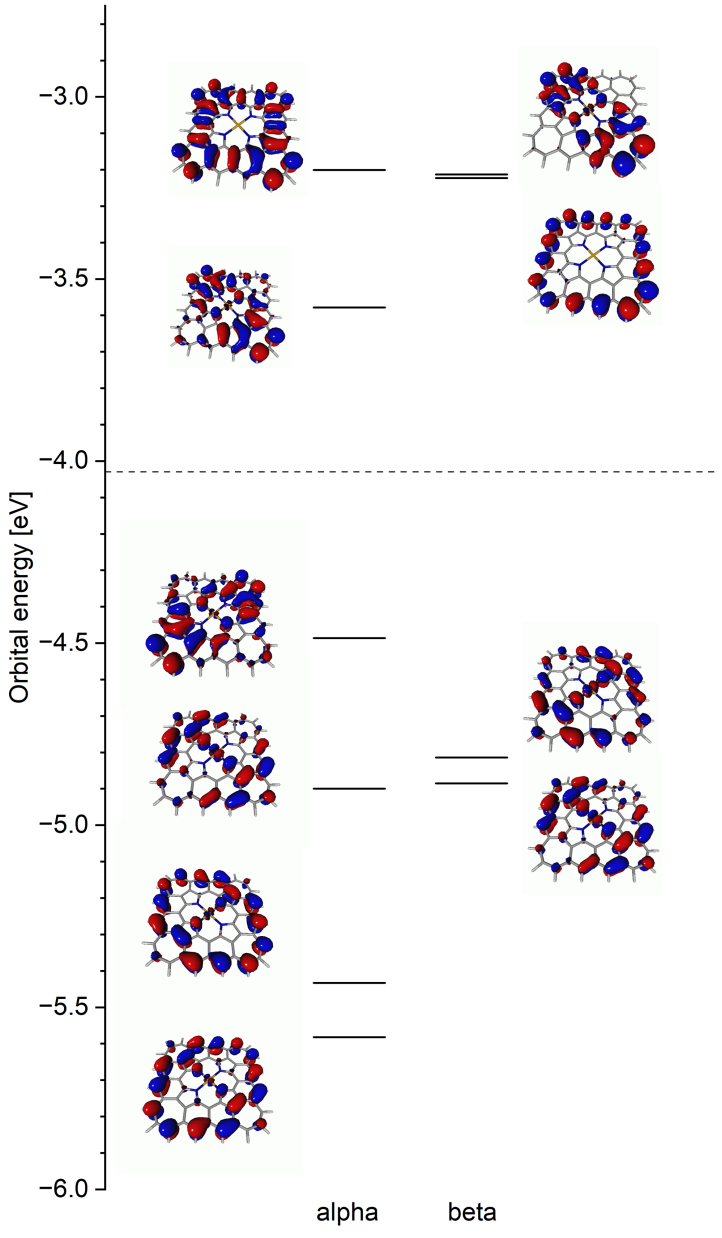

Figure S3. Frontier molecular orbitals of FeN_4 in pyrrolic-1 cluster obtained with PBE0-D3(BJ)/def2-TZVP method. Orbitals below the dashed line are occupied.

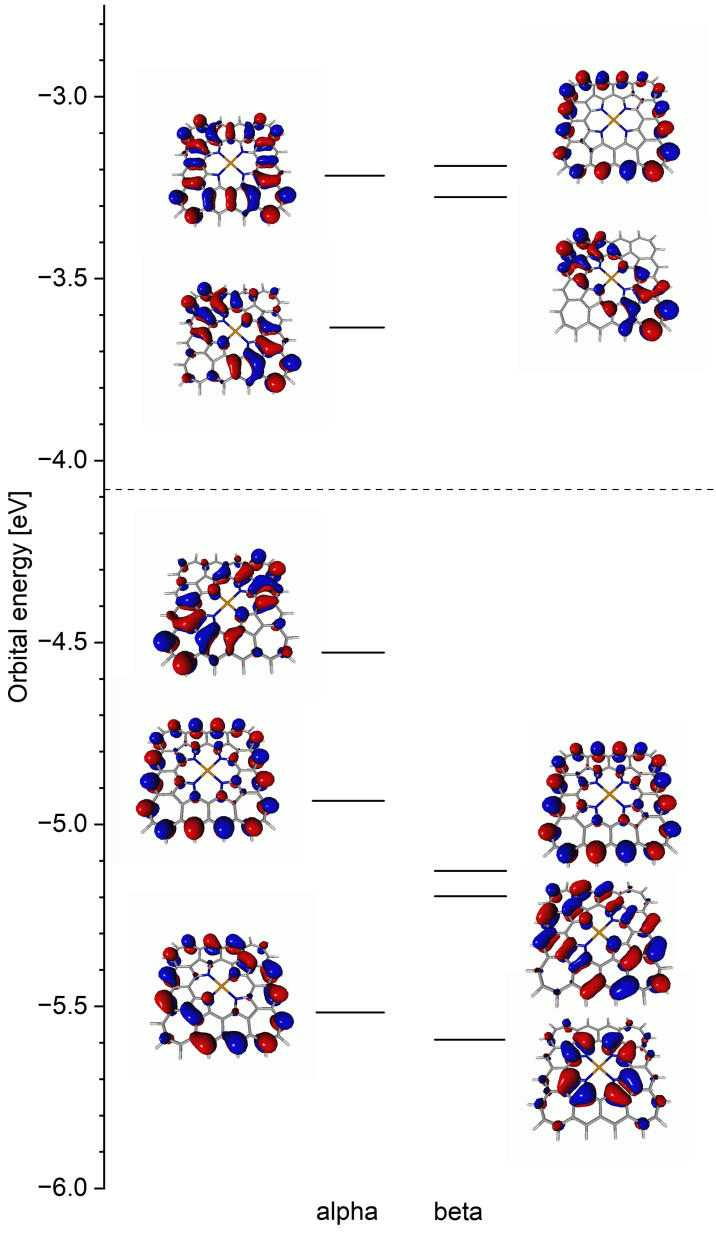

Figure S4. Frontier molecular orbitals of ZnN_4 in pyrrolic-1 cluster obtained with PBE0-D3(BJ)/def2-TZVP method. Orbitals below the dashed line are occupied.

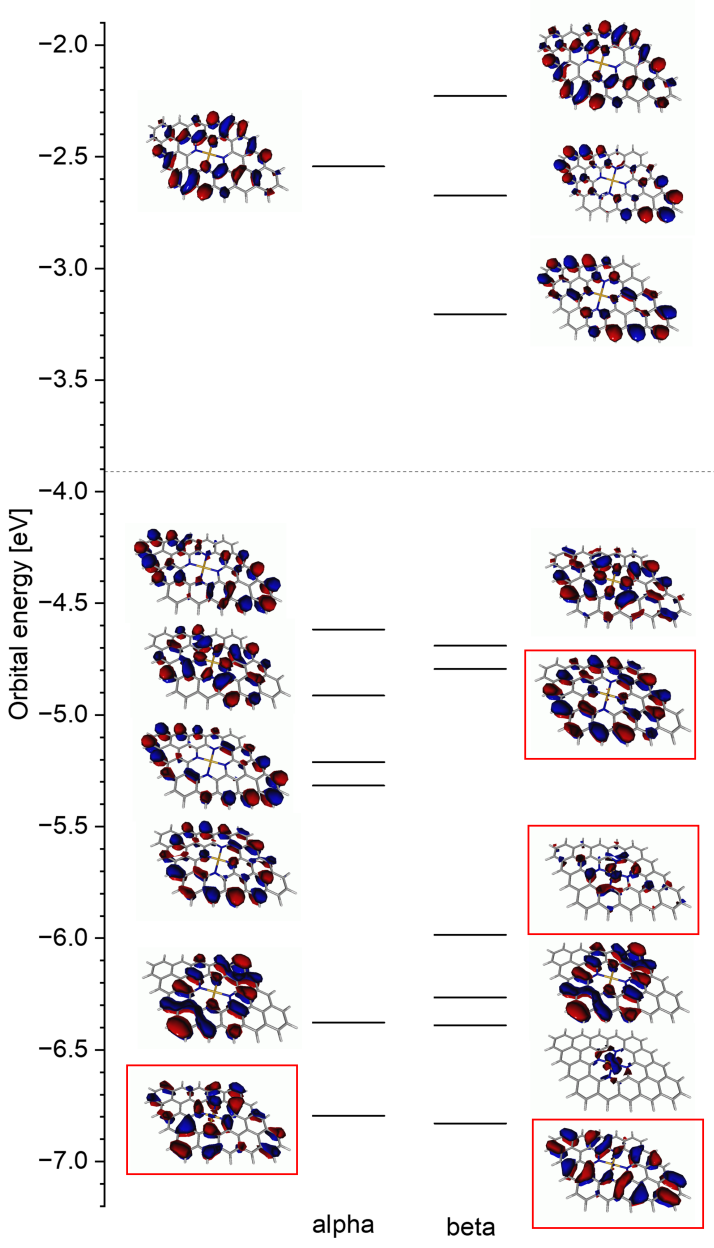

Figure S5. Frontier molecular orbitals of FeN_4 in pyridinic-1 cluster obtained with PBE0-D3(BJ)/def2-TZVP method. Orbitals which indicate π-d interactions are highlighted. Orbitals below the dashed line are occupied.

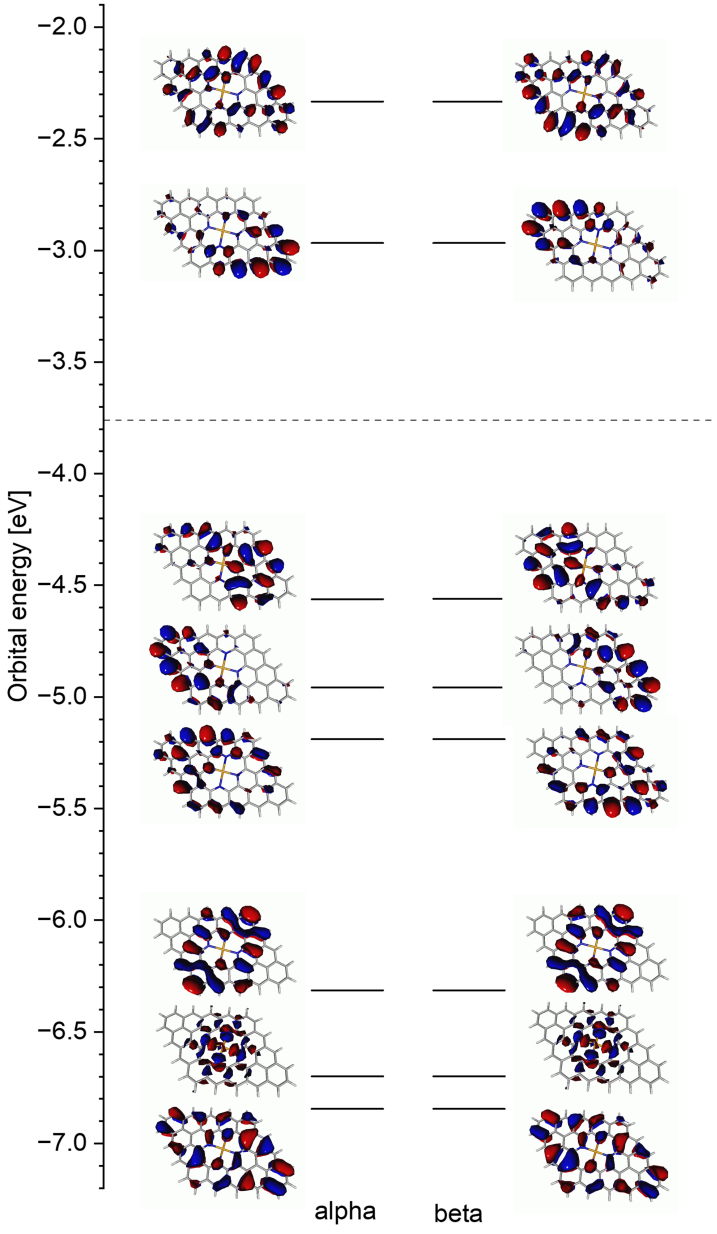

Figure S6. Frontier molecular of ZnN_4 in pyridinic-1 cluster obtained with PBE0-D3(BJ)/def2-TZVP method. Orbitals below the dashed line are occupied.

Paper M3

Elucidating the Intrinsic Activity of Tetrapyrrolic Fe-N-C Electrocatalysts for the Oxygen Reduction Reaction in Alkaline Medium

D. Menga, J. L. Low, A. G. Buzanich, B. Paulus and T.-P. Fellinger, *submitted to Adv. Energy Mater.*

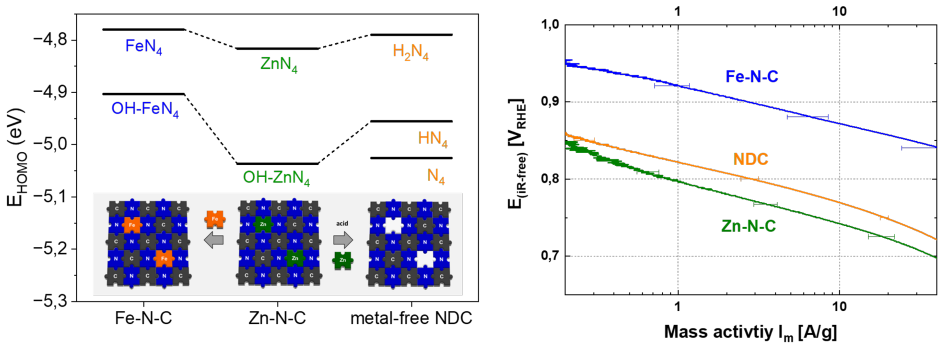

Figure 3.2: Graphical abstract Paper M3.

Computational Highlights

This paper advanced the mechanistic understanding of ORR on M-N-Cs in the alkaline environment. Exploiting the isomorphic nature of transmetallation-synthesized M-N-Cs, the intrinsic activity of three different materials (Zn-N-Cs, Fe-N-Cs and metal-free NDCs) could be compared. The experimental Tafel slope of the three materials were almost identical, despite differing ORR selectivity, suggesting a high likelihood of them sharing the same rate-determining step that is within the transfer of the first two electrons. We observed that the DFT-calculated HOMO energies and Fermi energies of the OH–FeN_4, OH–ZnN_4 and HN_4/N_4 followed the same trend as the experimental onset potential for the corresponding material, allowing us to conclude an alternative outer-sphere mechanism which does not involve inner-sphere adsorption of O_2 during the rate-determining step. In addition, the analysis of the HOMO led to the conclusion that the outer-sphere

electron transfer would not directly involve the metal-atom, correlating to the ability of Fe-N-Cs resist poisoning experiments in other publications.

Author Contributions

Davide Menga and Tim-Patrick Fellinger planned and designed the experiments. Davide Menga synthesized the catalyst and performed the electrochemical measurements. Jian Liang Low designed the computational study and performed the DFT calculations. Jian Liang Low analyzed the DFT results and wrote the computational part of the manuscript under the guidance of Beate Paulus. Ana Guilherme Buzanich performed and analyzed the XAS measurements with structural models from Jian Liang Low. Davide Menga and Tim-Patrick Fellinger and wrote the manuscript. All authors contributed to the final version of the manuscript.

Elucidating the Intrinsic Activity of Tetrapyrrolic Fe-N-C Electrocatalysts for the Oxygen Reduction Reaction in Alkaline Medium

*Davide Menga, Jian Liang Low, Ana Guilherme Buzanich, Beate Paulus and Tim-Patrick Fellinger**

Dr. Davide Menga
Chair of Technical Electrochemistry, Department of Chemistry and Catalysis Research Center, Technische Universität München

Jian Liang Low, Prof. Beate Paulus
Institut für Chemie und Biochemie, Freie Universität Berlin

Dr. Ana Guilherme Buzanich
Division 6.3 Structure Analysis, Bundesanstalt für Material-forschung und -prüfung (BAM)

Dr. Tim-Patrick Fellinger
Division 3.6 Electrochemical Energy Materials, Bundesanstalt für Materialforschung und -prüfung (BAM)
E-mail: tim-patrick.fellinger@bam.de

Keywords: atomically dispersed catalysts, PGM-free, tetrapyrrolic sites, M-N-C catalysts, turnover frequency, oxygen reduction reaction

Abstract:

Carbon-based precious-group metal-free electrocatalysts are gaining momentum in the scientific literature due to their application in many relevant energy conversion processes as well as low cost. However, their development and fundamental understanding are hampered by limitations in the quantification of the intrinsic activity of different catalytic sites as well as understanding the different reaction mechanisms. By complexation of tetrapyrrolic nitrogen doped carbons with iron ions and decomplexation of the corresponding Fe-N-C catalysts, we herein determine intrinsic activities of tetrapyrrolic active sites and gain insights into the reaction mechanism of the oxygen reduction reaction (ORR) in alkaline electrolyte. By comparison of the activity of isomorphic catalysts differing solely in type/amount of complexed metal, TOF values of 0.33 s^{-1} and 1.84 s^{-1} are found at 0.80 V_{RHE} and 0.75 V_{RHE}, respectively, for tetrapyrrolic N_4 sites and TOF values of 0.4 s^{-1} and 4 s^{-1} are reported for tetrapyrrolic Fe-N_4 sites at 0.90 V_{RHE} and 0.85 V_{RHE}, respectively.

1. Introduction

Carbon-based precious-group metal (PGM)-free electrocatalysts are materials that are intensively studied due to their low cost and application in a wide range of relevant electrochemical reactions.[1] Especially regarding the oxygen reduction reaction (ORR) in proton exchange membrane fuel cells (PEMFCs), they have reached promising initial activity, comparable to state-of-the-art Pt-based electrocatalysts.[2] Even though they are approaching system-relevant stability, they still lack the requirements to meet wide-spread practical application in the technologically more mature acid based PEMFCs.[3] On the other hand, they show exceptional activity and stability in anion exchange membrane fuel cells (AEMFCs), even better compared to Pt-based materials.[4] For this reason, the ORR activity of metal- and nitrogen- co-doped carbons (M-N-Cs) as well as the metal-free nitrogen-doped-carbons (NDCs) is widely studied in alkaline electrolyte. Generally, there are several differences in the ORR mechanism when the pH increases.[5] In acidic medium, an inner-sphere-mechanism model is generally employed to explain the reduction of O_2 to H_2O_2 or H_2O, with the initial oxidative addition of O_2 to the active metal centre (generally accompanied by a concerted H^+ transfer to the oxygen molecule) proposed as the rate determining step (RDS) for low polarizations.[6] In alkaline environment, in contrast, it has been proposed that both inner- and outer-sphere mechanisms can occur, both independently or in parallel.[5b, 6c, 7] The RDS is generally attributed to the first electron transfer to O_2[8] or the first proton transfer to $*O_2^-$ to form *OOH (* indicates that the intermediate is adsorbed on the active site).[6a, 9] Moreover, kinetic isotope effect studies suggest the occurrence of two parallel pathways, one of which has a proton independent RDS.[6c] When an inner-sphere mechanism is taken into account, the possible available adsorption sites in M-N-C are not only the metal centres, but the C atoms close to nitrogen dopants as well. This consideration arises from DFT calculations of the O_2 adsorption on metal-free NDCs (in the Japanese community also referred to as “carbon alloys”) completely free from metal sites.[10] While NDCs often show high activity in alkaline medium, high activity in acid is less common for this

materials class, sometimes rising concerns of metal impurities.[11] For Fe-N-Cs, Fe poisoning experiments suppress the activity in acidic but not under alkaline conditions, indicating a non-metal-centred active site in alkaline electrolyte, i.e., that Fe might not be directly involved in the ORR mechanism.[12] In alkaline electrolyte, the one e^- reduction of O_2 to superoxide ($O_2^{\bullet -}$) is generally reported as a long-range electron transfer happening in the outer Helmholtz plane (OHP) and in most cases promotes only a 2 e^- reduction,[7a] unless adsorption of the reaction intermediates to the catalyst surface happens, in which case a further reduction can take place (for a total of 4 e^-).[13] In an outer-sphere mechanism, the key factor determining the catalytic activity would be the electronic band structure.[13] The relationship between density of state (DOS) at the Fermi level and electron transfer kinetics (i.e., catalytic activity) has been intensively studied.[14] However, the electron transfer is typically occurring at defect sites, which renders them as "apparent" active sites in outer sphere reactions.

In order to rationally compare the intrinsic activity of different catalyst via the turnover frequency (TOF), quantifying catalytic parameters such as active-site density (SD) is desirable. For M-N-Cs, these parameters are hard to assess, and different methods have been proposed in the scientific literature. Except for new emerging techniques,[15] the most established methods mostly rely on probe molecules.[16] The use of probe molecules can limit the applicability of the method to ex-situ measurements[16b] or to a certain pH range[16a] and usually requires pre-treatments of the catalytic surface and strict protocols in order to obtain reproducible results.[16] Moreover, so far, no methods are available for NDCs for different N sites, due to the lack of a suitable probe molecule. When assessing SD and intrinsic activity, a catalyst free from inactive side phases is desirable, since these could influence the obtained values by interacting with the probe molecule or by affecting the employed electrochemical method. In our previous work we showed that via an active-site imprinting strategy followed by a transmetalation reaction, Mg-N-C and Zn-N-C containing Mg-N_4 and Zn-N_4 sites respectively can be transformed into active Fe-N-C electrocatalyst without common unfavourable side phases like iron carbide or metallic iron.[17] Moreover, when Zn is employed,

tetrapyrrolic metal-coordination sites and hence very active and selective tetrapyrrolic Fe-N_4 sites can be prepared.[18] This synthetic strategy gives the opportunity to obtain a platform to systematically investigate the intrinsic activity of different catalytic sites as well as the reaction mechanism. Very recently, we exploited this methodology in order to assess SD and TOF of an Fe-N-C catalyst with state-of-the-art activity in acidic electrolyte.[19]

In this work, we employ the aforementioned catalyst both in its Zn-coordinating state and in the Fe-coordinating state. After performing a M-to-H^+ ion exchange reaction, different electrocatalysts that differ solely in the type of metal coordinated to the tetrapyrrolic N_4 sites as well as the amount (including the metal-free state) are obtained. The different materials are then measured in a rotating ring disc electrode (RRDE) setup in order to gain insights into the ORR mechanism and the intrinsic activity of different catalytic sites in alkaline medium.

2. Results and Discussion

The Zn-N-C electrocatalyst is prepared similarly to what previously reported.[19-20] Briefly, Zn-N-C is prepared by carbonizing 1-ethyl-3-methylimidazolium dicyanamide (Emim-dca) in a $ZnCl_2$/NaCl eutectic mixture (T_m = 250 °C) at 900 °C in Ar atmosphere. Besides having a control on the morphology by simply tuning the mixture composition,[21] the presence of the Lewis-acidic Zn^{2+} ions facilitate the formation of tetrapyrrolic N_4 moieties.[18] The Zn-N-C so obtained is employed in the low- and high-temperature Zn-to-Fe ion-exchange reaction as well as in the M-extraction (i.e., Zn-to-H^+ ion-exchange reaction) in order to obtain the Fe-N-C and the metal-free NDC, respectively. The partially Fe-extracted sample is obtained from the Fe-N-C after M-extraction. The M-extraction step is performed using HCl, a non-oxidizing acid, and elevated temperatures of 160 °C for three days. In order to completely remove the Zn from Zn-N-C, this procedure was repeated two times. The metal amount in the final catalysts was determined by inductively coupled plasma-mass spectrometry (ICP-MS).

Extended X-ray absorption fine structure (EXAFS) measurements are employed to confirm the tetrapyrrolic coordination of the M in the Zn-N-C as well as the Fe-N-C and the partially extracted Fe-N-C. No Zn signal was detected for NDC, further confirming the total extraction of Zn. **Figure 1 a-c** shows the magnitude of the Fourier transformed spectrum of the samples, where one main peak at ~ 2 Å is found, typical for M-N/O scattering in M-N-Cs. When comparing the experimental data with the model based on a 2D tetrapyrrolic Zn-N-C and hydroxy-coordinated Fe-N-C (inset of the figures), a very good agreement is found for Zn-N-C (Figure 1a), Fe-N-C (Figure 1b) and Fe-N-C-extr (Figure 1c), respectively, allowing for the quantitative extraction of structural parameters (**Table S1**). Zn cations in Zn-N-C are coordinated to four pyrrolic N at 2.04 Å. In Fe-N-C, Fe cations are coordinated to four pyrrolic N at 2.04 Å and ~ 1 O atoms (from OH groups) at 1.83 Å. Fe-N-C-extr shows similar Fe coordination, indicating the same Fe environment of the remaining Fe atoms after extraction (Table S1). Cryo-Mössbauer spectroscopy was employed on Fe-N-C to further confirm the environment around the Fe atoms.[22] The spectrum measured at T=4.2 K shows two quadrupole doublets, namely D1 and D2, assigned to atomically dispersed Fe-N_4 sites (**Figure 1d**), confirming the results obtained via EXAFS analysis. D1 and D2 have a line width of 0.90 mm s^{-1} and 0.55 mm s^{-1} respectively, which points to a high homogeneity of the Fe-N_4 environment.[19] The Fe content in Fe-N-C-extr is too little to allow for a meaningful deconvolution of the Mössbauer spectrum (**Figure S1**).

RRDE measurements were employed to measure the ORR activity of the four isomorphic catalysts in O_2-saturated 0.1 M NaOH electrolyte. For all the measured catalyst a relatively low loading of 0.145 mg cm^{-2} was employed to minimize the chance for artifacts.[23] **Figure 2 a and b** show the Tafel plots and peroxide yield, respectively, and the mass activity values are reported in **Table 1**. Zn-N-C shows the lowest performance and an increase in activity is observed when Zn is removed from the catalyst. This indicates a negative impact on the activity of Zn^{2+} coordinated to tetrapyrrolic N_4 sites and is in agreement with our previous study by Petek et al.[24] Interestingly, the NDC clearly shows an increased peroxide detection in the ring current (Figure 2b). The detected

peroxide is more than doubled compared to Zn-N-C when comparing the same loading of 0.145 mg cm^{-2} i.e., ≈35 % vs ≈15 %, respectively. This indicates that the Zn^{2+} metal centre supports the peroxide reduction. The comparison of the kinetic current in the two samples, together with the Zn content in the Zn-N-C material, allows for the determination of the intrinsic activity of tetrapyrrolic N_4 sites in alkaline electrolyte. Similar to the nitrite stripping method[16a] and our recent work,[19] it is possible to calculate the TOF using equation 1:

$$TOF\ (s^{-1}) = \frac{\Delta i_{kin}\ (A\ g^{-1})}{F\ (A\ s\ mol^{-1}) \times \Delta SD\ (mol\ g^{-1})} \qquad (1)$$

The ΔSD is calculated from the Zn content (**Table S2**), which is used as probe. The Δi_{kin} is calculated as difference in kinetic current. TOF values of 0.33 s^{-1} and 1.84 s^{-1} are herein reported for the ORR activity of tetrapyrrolic N_4 sites in alkaline media at 0.80 V_{RHE} and 0.75 V_{RHE}, respectively. Intriguingly, both catalysts have an identical Tafel slope (TS) of ~ 50 mV dec^{-1}, pointing to the fact that the RDS of the reaction is similar for both. Fe-N-C presents a mass activity of 2.8 ± 0.8 A g^{-1} and 28 ± 10 A g^{-1} at 0.90 V_{RHE} and 0.85 V_{RHE}, respectively, which places this catalyst among the best ORR catalysts reported so far in alkaline electrolyte.[16b, 25] After partial Fe extraction, the activity decreases. Both catalysts produce a negligible amount of HO_2^- (< 3 %) at this catalyst loading (Figure 2b), pointing to a 4 e^- reduction (either direct or apparent) of the O_2 for Fe-N-C, differently compared to Zn-N-C and NDC, for which the 2 e^- reduction has a strong contribution on the ORR activity.[8, 26] The good activity of Fe-N-C is a consequence of its high TOF value which is calculated using equation 1. The ΔSD is the difference in Fe content between Fe-N-C and Fe-N-C-extr and the Δi_{kin} is the difference in kinetic activity between the two catalysts. The catalyst has a TOF of 0.4 s^{-1} and 4 s^{-1} at 0.90 V_{RHE} and 0.85 V_{RHE}, respectively, which are amongst the highest values reported for Fe-N-C electrocatalysts in alkaline medium.[15b, 16b, 16c] These values are also in line with reported values obtained with well-established methods,[16b] supporting the validity of the described procedure. Intriguingly, Fe-N-C and Fe-N-C-extr show the same TS of ~ 50 mV dec^{-1} like Zn-N-C and NDC, pointing to the fact that the RDS is similar for all the four isomorphic catalysts considered. This

allows for further considerations about the reaction mechanism of these materials in alkaline electrolytes. Due to the high pH, a strong OH^- adsorption is expected on the electrode surface, as well as on the M-N_4 sites, making a double layer effect dominant in the ORR mechanism and promoting the outer-sphere mechanism.[5b] This picture matches very well with the activity of NDC, which produces high amounts of HO_2^-, since the outer-sphere mechanism will promote mostly the 2 e^- reduction.[7a] When a metal is introduced in the N_4 pocket, a lower HO_2^- yield is observed. This effect is particularly pronounced in the Fe-based samples, where even a minute Fe amount is enough to bring the peroxide yield almost to zero. For Fe-N-Cs it has been reported that peroxide reduction in alkaline electrolyte is kinetically favoured and that any peroxide intermediate formed during ORR is immediately reduced further to OH^-.[7a] The adsorption of the HO_2^- produced by the NDC on the M sites with further reduction to OH^- (for a total of 4 e^- involved) requires an inner sphere mechanism. Since the TS are unaffected by the presence and identity of metal M, this means that the RDS is not affected, hence the RDS for all four catalysts is to be found in the first 2 e^- reduction. Like previously shown for poisoning experiments,[12] the majority of the current generated by Fe-N-C in alkaline environment does not originate from Fe-N_4 sites. This is evident when comparing the difference in activity between Fe-N-C and Fe-N-C-extr in acidic electrolyte (**Figure S2** and **Table S3**), where a far larger loss in performance is observed after Fe extraction compared to alkaline electrolyte. The higher efficiency of Fe-N-C and Fe-N-C-extr towards the 4 e^- reduction does not explain the lower overpotential needed for the ORR. Moreover, Zn-N-C shows lower HO_2^- yield compared to NDC but higher overpotential. To explain the difference in activity, we looked at the difference in the valence electronic properties of NDC, Zn-N-C and Fe-N-C (**Table S4**) , since it will affect the first electron transfer to O_2.[13] It has been shown that for outer-sphere electron transfer, the DOS around the Fermi level and the electronic structure relates to the catalytic activity.[14c-e] In the case of NDCs, the nitrogen doping causes the material to behave as a semiconductor and samples with higher carrier concentration and flat band potential were shown to require lower overpotential to start the ORR.[14c] We performed DFT calculation employing models featuring different pyrrolic-type N_4 coordination

sites,[27] namely the metal free H_2N_4, the Zn- and Fe- coordinated M-N_4, resembling NDC, Zn-N-C and Fe-N-C respectively (**Figure S3** and **S4**). Due to the OH^- adsorption on the electrode surface, as well as on the M-N_4 sites, we considered the electronic structures of the OH-adsorbed MN_4 and deprotonated H_2N_4 for the study. For the molecular systems, an analogue to the Fermi level as a descriptor for outer-sphere electron transfer is the energy of the highest occupied molecular orbital (HOMO) depicted in **Figure 3**. From Figure 3a, we observed that the HOMO energies E_{HOMO} of FeN_4, ZnN_4 and H_2N_4 already qualitatively follow the measured reactivity trend in Figure 2a. The trend is retained when the alkaline environment is taken into consideration (OH-FeN_4 vs OH-ZnN_4 vs HN_4), albeit with more pronounced differences in E_{HOMO}. In fact, the shift of 0.13 V in the experimental Tafel plot between Fe-N-C and Zn-N-C (Figure 2a) is in very close agreement with the difference in HOMO energy between OH-FeN_4 (-4.90 eV) and OH-ZnN_4 (-5.04 eV), indicative of an RDS involving a one-electron transfer. For the periodic models shown in Figure S4, a similar but less quantitative trend is observed among the Fermi levels E_f of OH-FeN_4, OH-ZnN_4 and HN_4, in good agreement with the results obtained from the cluster model. For the NDC, the description is complicated by the degree of deprotonation of the H_2N_4 site in the alkaline medium. Studies on molecular porphyrin compounds determined the average pKa of the H_2N_4 to be significantly lower than that of water and could even be doubly deprotonated by weaker bases than hydroxides.[28] Due to the larger extent of electron delocalization in NDC, the protons at the H_2N_4 site are expected to be acidic and thus susceptible to deprotonation in the alkaline environment. Among the cluster models, the calculated HOMO energies of HN_4 (-4.96 eV) and N_4 (-5.03 eV) are both intermediate to OH-FeN_4 and OH-ZnN_4, in good agreement with reactivity trend observed in the reactivity in alkaline ORR (Figure 2a). In particular, the E_{HOMO} of the fully deprotonated N_4 is closer to the expected value based on the shifts in the onset potentials, suggesting that it constitutes most of the metal free N_4 sites. The contour plots of the HOMOs shown in Figure 3b further suggests that the metal in the N_4 site is not likely to be directly involved in the outer-sphere electron transfer, but only influences the

reactivity by shifting the HOMO energy, possibly explaining why Fe-N-Cs are able to resist poisoning experiments in alkaline ORR. [28]

3. Conclusion

In conclusion, the intrinsic activity of M-N-C electrocatalysts with tetrapyrrolic M-N_4 sites was evaluated in alkaline electrolyte using a RRDE setup. Zn, which has been discovered to have a negative impact on the ORR in alkaline medium, was used to probe the TOF of tetrapyrrolic N_4 sites by comparing the difference in kinetic activity between Zn-N-C and NDC and values of 0.33 s^{-1} and 1.84 s^{-1} are reported at 0.80 V_{RHE} and 0.75 V_{RHE}, respectively. Moreover, a clear increase in the 2 e^- reduction of O_2 to HO_2^- takes place when more $N_{pyrrolic}$ sites become available for the ORR. In the same way, the TOF is calculated for the isomorphic Fe-N-C material which has very high values of 0.4 s^{-1} and 4 s^{-1} at 0.90 V_{RHE} and 0.85 V_{RHE}, respectively. The high TOF translates into high mass activity, i.e., 2.8 ± 0.8 A g^{-1} and 28 ± 10 A g^{-1} at 0.90 V_{RHE} and 0.85 V_{RHE}, respectively, ranking this catalyst between the best reported so far in alkaline electrolyte. It was found that the introduction of M in the tetrapyrrolic N_4 pocket reduces the peroxide formation, likely due to HO_2^- coordination to the M sites and further reduction to OH^- (for a total of 4 e^-). Because of the independence of the TS from the metal coordinated to the tetrapyrrolic N_4 sites (including the metal free NDC), the RDS is to be found in the first 2 e^- reduction. Employing DFT, the E_{HOMO} and E_f of cluster and periodic models is calculated respectively, featuring different species in the pyrrolic-type N_4 coordination sites. Mirroring the experimentally measured ORR activity, a correlation between the overpotential needed for the ORR and the E_{HOMO} is found, indicative of an outer-sphere RDS. Proposing a new method for the determination of TOF values in alkaline electrolyte for different catalytic sites and elucidating the ORR mechanism of M-N-C materials with tetrapyrrolic M-N_4 sites, we believe that this work will advance the further development and fundamental understanding of ORR electrocatalysts and, because of its general applicability, it can be employed to shine light to other reactions.

4. Experimental Section

Preparation of Zn-N-C

The catalyst was prepared similarly to what previously reported.[19] 1 g of 1-ethyl-3-methylimidazolium dicyanamide (Emim-dca) were thoroughly mixed with 8.26 g of $ZnCl_2$ and 1.74 g of NaCl inside an Ar-filled glovebox. The mixture was then transferred inside a crucible made of alumina and covered with a quartz lid. This was placed inside a tube furnace under constant Ar flow and heated up to a temperature of 900 °C for 1 hour, employing a heating rate of 2.5 °C/min. The final powder was ground in an agate mortar and washed with 0.1 M HCl overnight. After filtering and washing with deionized water in order to reach neutral pH, the sample was dried at 80 °C.

Preparation of Fe-N-C

As previously reported,[18-19] the Zn-to-Fe ion exchange was carried out at low and high temperature. Firstly, Zn-N-C was degassed at 250 °C under vacuum and transferred inside an Ar-filled glovebox. Here, it was mixed with a $FeCl_3$/LiCl eutectic mixture and placed inside a closed Ar-filled flask. After heating the mixture at 170 °C for 5 hours, the sample was let to cool down to room temperature, opened to air and washed with deionized water to remove the salt mixture. Afterwards, it was stirred in 0.1 M HCl for several hours, filtered, washed with deionized water until neutral pH was reached and dried at 80 °C. The obtained powder was placed again in an alumina crucible and pushed inside a tube furnace pre-heated at 1000 °C under Ar atmosphere. After 15 minutes the furnace was turned off and opened to achieve a quick cool down of the sample.

Preparation of NDC

The metal free sample (NDC) was obtained from Zn-N-C after Zn removal (Zn-to-H^+ ion-exchange reaction). Zn-N-C was placed inside a closed Carius tube and stirred for 3 days in 2.4 M HCl at 160 °C. After filtering, thoroughly washing with deionized water and drying, the powder obtained was placed again inside the Carius tube and the entire procedure was repeated a second time in order to achieve the complete extraction of Zn.

Preparation of Fe-N-C-extr

For the partial Fe extraction, Fe-N-C was placed inside a closed Carius tube and stirred for 3 days in 2.4 M HCl at 160 °C. After filtering, washing with deionized water and drying, the final sample was obtained.

Physical characterizations

X-ray absorption near edge structure (XANES) and extended X-ray absorption fine structure (EXAFS) measurements at the Zn K-edge and at the Fe K-edge were carried out at the BAMline[29] located at BESSY-II (Berlin, Germany), operated by the Helmholtz-Zentrum Berlin für Materialien und Energie. Due to the low metal concentration (< 1 wt. %) the measurements were performed in fluorescence mode. XANES data evaluation and treatment was performed by using ATHENA program from Demeter package.[30] EXAFS curves were Fourier Transformed and fitted with a DFT-optimized model adapted from our previous publications[18-19][27] based on a $MN_4C_{96}H_{24}$ cluster (M = Zn or Fe). The model was used to calculate the scattering paths by FEFF to be able to quantify the coordination number and bond-length. Mössbauer measurements at T = 4.2 K were performed on a standard transmission spectrometer using a sinusoidal velocity waveform with both the source of ^{57}Co in rhodium and the absorber in the liquid He bath of a cryostat. In order to refer the measured isomer shifts to α-Fe at ambient temperature, 0.245 mm s^{-1} was added to the measured values.

Electrochemical measurements

Rotating ring disk electrode (RRDE) measurements in alkaline electrolyte were performed in a Teflon® cell in order to avoid glass dissolution. 0.1 M NaOH was prepared from monohydrate NaOH pellets and deionized ultrapure water. Saturated Ag/AgCl was employed as reference electrode and a Pt wire as counter. Measurements in acidic electrolyte were performed in a three-electrode glass cell using 0.1 M $HClO_4$ as electrolyte, Au wire as the counter electrode and a freshly calibrated RHE as the reference electrode The solution resistance was determined by electrochemical impedance spectroscopy and the reported potentials were corrected accordingly.

The ORR polarization curves were corrected for capacitive contributions by subtracting the curves recorded in Ar-saturated electrolyte from the ones recorded in O_2-saturated electrolyte. Catalyst inks were prepared by dispersing 5 mg of catalyst in 1.68 mL of N,N-dimethylformamide and 50 µL of 5 wt% Nafion suspension, followed by sonication. To obtain a catalyst loading of 145 µg cm^{-2}, 10 µL of ink was drop-cast onto a well-polished glassy carbon electrode and dried under an infrared heater for 60 min. For each curve at least two separate measurements were averaged to give the shown polarization curve, and the standard deviation is illustrated with error bars. Kinetic currents were calculated based on limiting current correction as in reference [31].

Density functional theory (DFT) calculations

Cluster calculations were performed using the program package TURBOMOLE.[32] The active sites were modelled with the finite-sized $MN_4C_{96}H_{24}$ clusters (M = Fe, Zn, H_2) as shown in Figure S3. We applied the hybrid PBE0 functional[33] with Grimme dispersion correction with Becke Johnson damping function D3(BJ).[34] Geometry optimization was performed with def2-SVP basis while a larger def2-TZVP basis was applied for single-point calculations.[35] The conductor-like screening model (COSMO) was applied to describe solvation effects in aqueous environment.[36] Electronic steps were converged to 10^{-7} a.u. in the total energy and 10^{-4} a.u. in the orbital energies, while geometric steps were converged to 10^{-3} a.u. in the maximum norm of the Cartesian gradient. Each cluster was calculated with various preassigned multiplicities and the multiplicity that gave the lowest energy was further analysed. Molecular orbitals were visualized with Molden.[37]

Spin-polarized periodic DFT calculations were performed with the Vienna *ab initio* Simulation Package (VASP) in the framework of the projector-augmented wave (PAW) method with an energy cutoff of 600 eV.[38] The PBE functional was used with Grimme D3(BJ) dispersion correction with Becke-Johnson damping.[34, 39] Hubbard correction for Fe was applied to account for delocalization error associated with the d-electrons (U = 4 eV, J = 1 eV).[40] The RMM-DIIS algorithm was applied for electronic relaxation with a convergence criterion of 10^{-5} eV. The Gaussian smearing approach with smearing width σ = 0.05 eV was applied. Ionic relaxation steps were performed with the

conjugate gradient algorithm with force convergence of 10^{-2} eV/Å. K-points were sampled using a 3x3x1 *Γ*-centered mesh grid during optimization, and a 6x6x1 grid for single point calculations. The pyrrolic model as depicted in in Figure S4 was constructed based on the pyrrolic-D_{4h} model introduced by Menga et al. whereby the carbon lattice is extended to form a periodic 2D lattice with an interlayer vacuum of 15 Å.[18, 27]

Manuscript figures:

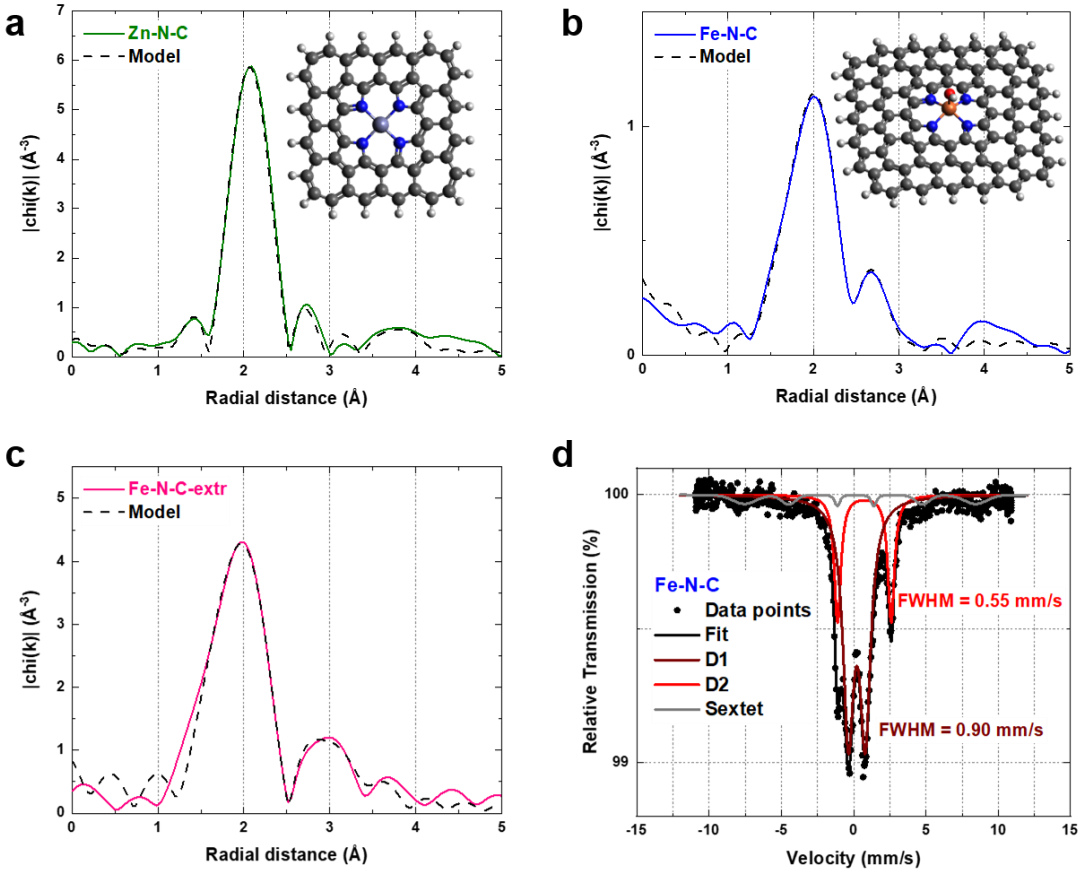

Figure 1. Experimental Fourier transform and best fit EXAFS model of the Zn K-edge EXAFS spectra of Zn-N-C (a) and Fe K-edge EXAFS spectra of Fe-N-C (b) and Fe-N-C-extr (c). The model used for Zn-N-C is displayed in the inset of (a) and the one used for the two Fe-containing samples is shown in the inset of (b) (Light blue = Zn; orange = Fe; blue = N; red = O; gray = C; white = H). Mössbauer spectrum of Fe-N-C measured at 4.2 K (d); FWHM refers to the line width of the indicated quadrupole doublet.

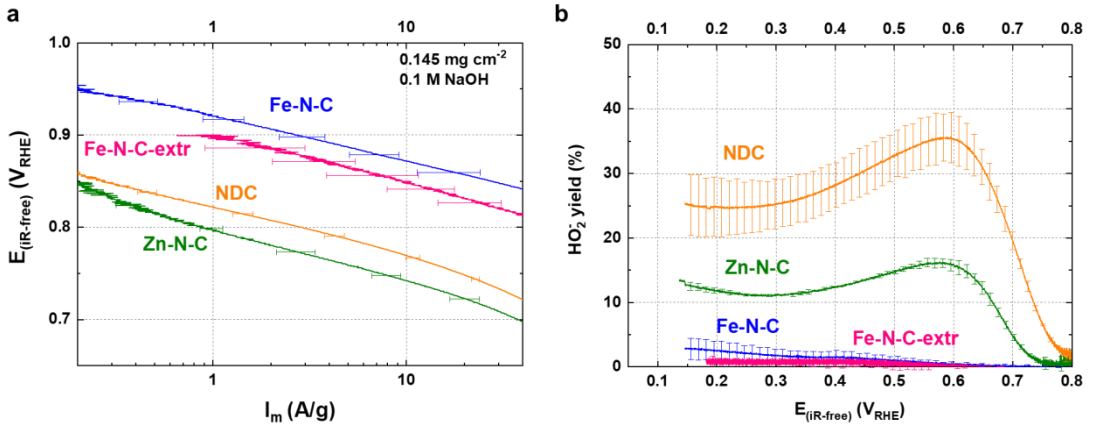

Figure 2. Tafel plots displaying the kinetic mass activity corrected for mass-transport limitation (a). HO_2^- yield obtained via RRDE experiments for the four isomorphic catalysts (b). Measurements were performed at room temperature in O_2-saturated 0.1 M NaOH at 1600 rpm, 10 mV s^{-1} (anodic scans).

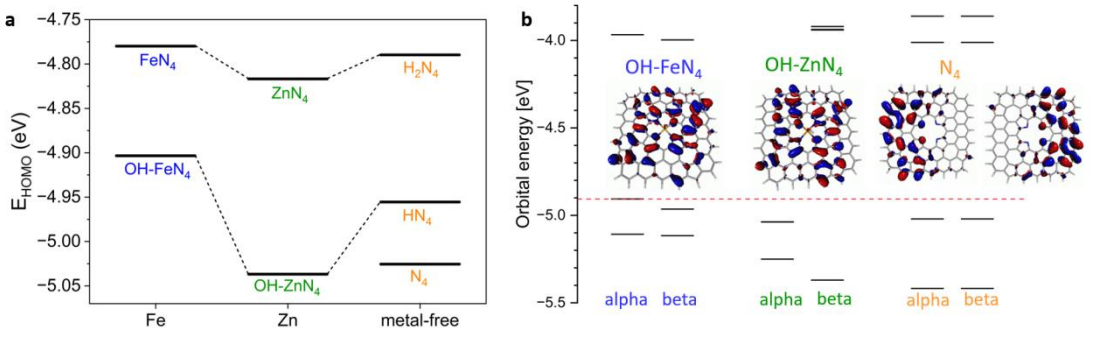

Figure 3. HOMO energies of pristine FeN_4, ZnN_4 and H_2N_4 and corresponding OH-bound/deprotonated structures to account for the alkaline environment (a). Frontier molecular orbital diagram OH-FeN_4, OH-ZnN_4 and doubly deprotonated N_4 and the isocontour plot of the corresponding HOMO(s) (b). The red dashed line indicates the HOMO energy of OH-FeN_4. Electronic structures were obtained with PBE0-D3(BJ)/def2-TZVP and COSMO solvation model.

Table 1. Mass activity (i_{kin}) values at different potentials obtained from RDE measurements in alkaline electrolyte.

Sample	i_{kin} (A g^{-1})		
	0.90 V_{RHE}	**0.85 V_{RHE}**	**0.80 V_{RHE}**
Zn-N-C	-	-	0.9 ± 0.2
NDC	-	-	2.9 ± 0.3
Fe-N-C	2.8 ± 0.8	28 ± 10	153 ± 45
Fe-N-C-extr	1.1 ± 0.7	10 ± 5	67 ± 28

Supporting Information
Supporting Information is available from the Wiley Online Library or from the author.

Acknowledgements
The German Federal Ministry of Economic Affairs and Energy (BMWi) is acknowledged for funding within the Verbundproject innoKA (Project No.: 03ET6096A). Prof. Hubert Gasteiger is acknowledged for hosting the group and for providing an educative and supportive atmosphere. J.L. Low thanks the Elsa-Neumann Scholarship for funding and the Norddeutschen Verbundes für Hoch- und Höchstleistungsrechnen (HLRN) for computational resources. EXAFS experiments were performed at the BAMline at the BESSY-II storage ring (Helmholtz Center Berlin). We thank the Helmholtz-Zentrum Berlin für Materialien und Energie for the allocation of synchrotron radiation beamtime.

Received: ((will be filled in by the editorial staff))
Revised: ((will be filled in by the editorial staff))
Published online: ((will be filled in by the editorial staff))

References

[1] a) Z. Shi, W. Yang, Y. Gu, T. Liao, Z. Sun, *Advanced Science* **2020**, *7*, 2001069; b) T. Asset, F. Maillard, F. Jaouen, in *Supported Metal Single Atom Catalysis*, **2022**, pp. 531-582; c) A. Kumar, V. K. Vashistha, D. K. Das, S. Ibraheem, G. Yasin, R. Iqbal, T. A. Nguyen, R. K. Gupta, M. Rasidul Islam, *Fuel* **2021**, *304*, 121420.

[2] a) S. Liu, C. Li, M. J. Zachman, Y. Zeng, H. Yu, B. Li, M. Wang, J. Braaten, J. Liu, H. M. Meyer, M. Lucero, A. J. Kropf, E. E. Alp, Q. Gong, Q. Shi, Z. Feng, H. Xu, G. Wang, D. J. Myers, J. Xie, D. A. Cullen, S. Litster, G. Wu, *Nature Energy* **2022**, 652–663; b) A. Mehmood, M. Gong, F. Jaouen, A. Roy, A. Zitolo, A. Khan, M.-T. Sougrati, M. Primbs, A. M. Bonastre, D. Fongalland, G. Drazic, P. Strasser, A. Kucernak, *Nature Catalysis* **2022**, *5*, 311-323; c) L. Jiao, J. Li, L. L. Richard, Q. Sun, T. Stracensky, E. Liu, M. T. Sougrati, Z. Zhao, F. Yang, S. Zhong, H. Xu, S. Mukerjee, Y. Huang, D. A. Cullen, J. H. Park, M. Ferrandon, D. J. Myers, F. Jaouen, Q. Jia, *Nature Materials* **2021**, *20*, 1385-1391.

[3] D. Banham, T. Kishimoto, Y. Zhou, T. Sato, K. Bai, J.-i. Ozaki, Y. Imashiro, S. Ye, *Science Advances* **2018**, *4*.

[4] M. M. Hossen, M. S. Hasan, M. R. I. Sardar, J. b. Haider, Mottakin, K. Tammeveski, P. Atanassov, *Applied Catalysis B: Environmental* **2022**, 121733.

[5] a) R. Sgarbi, K. Kumar, F. Jaouen, A. Zitolo, E. A. Ticianelli, F. Maillard, *Journal of Solid State Electrochemistry* **2021**, *25*, 45-56; b) S. Rojas-Carbonell, K. Artyushkova, A. Serov, C. Santoro, I. Matanovic, P. Atanassov, *ACS Catalysis* **2018**, *8*, 3041-3053.

[6] a) J. Wei, D. Xia, Y. Wei, X. Zhu, J. Li, L. Gan, *ACS Catalysis* **2022**, *12*, 7811-7820; b) J. H. Zagal, M. T. M. Koper, *Angewandte Chemie International Edition* **2016**, *55*, 14510-14521; c) D. Malko, A. Kucernak, *Electrochemistry Communications* **2017**, *83*, 67-71.

[7] a) N. Ramaswamy, S. Mukerjee, *The Journal of Physical Chemistry C* **2011**, *115*, 18015-18026; b) N. Ramaswamy, U. Tylus, Q. Jia, S. Mukerjee, *Journal of the American Chemical Society* **2013**, *135*, 15443-15449.

[8] Y. Wu, S. Nagata, Y. Nabae, *Electrochimica Acta* **2019**, *319*, 382-389.

[9] X. Li, C.-S. Cao, S.-F. Hung, Y.-R. Lu, W. Cai, A. I. Rykov, S. Miao, S. Xi, H. Yang, Z. Hu, J. Wang, J. Zhao, E. E. Alp, W. Xu, T.-S. Chan, H. Chen, Q. Xiong, H. Xiao, Y. Huang, J. Li, T. Zhang, B. Liu, *Chem* **2020**, *6*, 3440-3454.

[10] a) W. Yang, T.-P. Fellinger, M. Antonietti, *Journal of the American Chemical Society* **2011**, *133*, 206-209; b) T. Ikeda, M. Boero, S.-F. Huang, K. Terakura, M. Oshima, J.-i. Ozaki, *The Journal of Physical Chemistry C* **2008**, *112*, 14706-14709.

[11] J. Masa, W. Xia, M. Muhler, W. Schuhmann, *Angewandte Chemie International Edition* **2015**, *54*, 10102-10120.

[12] D. Malko, A. Kucernak, T. Lopes, *Journal of the American Chemical Society* **2016**, *138*, 16056-16068.

[13] C. H. Choi, H.-K. Lim, M. W. Chung, J. C. Park, H. Shin, H. Kim, S. I. Woo, *Journal of the American Chemical Society* **2014**, *136*, 9070-9077.

[14] a) H. Gerischer, R. McIntyre, D. Scherson, W. Storck, *The Journal of Physical Chemistry* **1987**, *91*, 1930-1935; b) H. Gerischer, *The Journal of Physical Chemistry* **1985**, *89*, 4249-4251; c) B. Bera, A. Chakraborty, T. Kar, P. Leuaa, M. Neergat, *The Journal of Physical Chemistry C* **2017**, *121*, 20850-20856; d) P. Szroeder, A. Górska, N. Tsierkezos, U. Ritter, W. Strupiński, *Materialwissenschaft und Werkstofftechnik* **2013**, *44*, 226-230; e) K. K. Cline, M. T. McDermott, R. L. McCreery, *The Journal of Physical Chemistry* **1994**, *98*, 5314-5319.

[15] a) R. Z. Snitkoff-Sol, A. Friedman, H. C. Honig, Y. Yurko, A. Kozhushner, M. J. Zachman, P. Zelenay, A. M. Bond, L. Elbaz, *Nature Catalysis* **2022**, *5*, 163-170; b) Z. Jin, P. Li, Y. Meng, Z. Fang, D. Xiao, G. Yu, *Nature Catalysis* **2021**, *4*, 615-622.

[16] a) D. Malko, A. Kucernak, T. Lopes, *Nature Communications* **2016**, *7*, 13285; b) F. Luo, C. H. Choi, M. J. M. Primbs, W. Ju, S. Li, N. D. Leonard, A. Thomas, F. Jaouen, P. Strasser, *ACS Catalysis* **2019**, *9*, 4841-4852; c) G. Bae, H. Kim, H. Choi, P. Jeong, D. H. Kim, H. C. Kwon, K.-S. Lee, M. Choi, H.-S. Oh, F. Jaouen, C. H. Choi, *JACS Au* **2021**, *1*, 586-597.

[17] a) A. Mehmood, J. Pampel, G. Ali, H. Y. Ha, F. Ruiz-Zepeda, T.-P. Fellinger, *Advanced Energy Materials* **2018**, *8*; b) D. Menga, F. Ruiz-Zepeda, L. Moriau, M. Šala, F. Wagner, B. Koyutürk, M. Bele, U. Petek, N. Hodnik, M. Gaberšček, T.-P. Fellinger, *Advanced Energy Materials* **2019**, *9*, 1902412.

[18] D. Menga, J. L. Low, Y.-S. Li, I. Arčon, B. Koyutürk, F. Wagner, F. Ruiz-Zepeda, M. Gaberšček, B. Paulus, T.-P. Fellinger, *Journal of the American Chemical Society* **2021**, *143*, 18010-18019.

[19] D. Menga, A. G. Buzanich, F. Wagner, T.-P. Fellinger, *Angewandte Chemie International Edition* **2022**, 61, e202207089; *Angewandte Chemie* **2022**, 134, e202207089.

[20] K. Elumeeva, N. Fechler, T. P. Fellinger, M. Antonietti, *Materials Horizons* **2014**, *1*, 588-594.

[21] N. Fechler, T.-P. Fellinger, M. Antonietti, *Advanced Materials* **2013**, *25*, 75-79.

[22] a) S. Wagner, H. Auerbach, C. E. Tait, I. Martinaiou, S. C. N. Kumar, C. Kübel, I. Sergeev, H.-C. Wille, J. Behrends, J. A. Wolny, V. Schünemann, U. I. Kramm, *Angewandte Chemie International Edition* **2019**, *58*, 10486-10492; b) M. T. Sougrati, V. Goellner, A. K. Schuppert, L. Stievano, F. Jaouen, *Catalysis Today* **2016**, *262*, 110-120.

[23] M. Bron, S. Fiechter, P. Bogdanoff, H. Tributsch, *Fuel Cells* **2002**, *2*, 137-142.

[24] U. Petek, F. Ruiz-Zepeda, I. Arcon, M. Sala, A. Kopac Lautar, J. Kovac, M. Mozetic, D. Menga, M. Bele, T. P. Fellinger, M. Gaberšček, *Submitted* **2024**.

[25] a) P. G. Santori, F. D. Speck, S. Cherevko, H. A. Firouzjaie, X. Peng, W. E. Mustain, F. Jaouen, *Journal of The Electrochemical Society* **2020**, *167*, 134505; b) L. Huo, B. Liu, G. Zhang, R. Si, J. Liu, J. Zhang, *Journal of Materials Chemistry A* **2017**, *5*, 4868-4878; c) H. Adabi, A. Shakouri, N. Ul Hassan, J. R. Varcoe, B. Zulevi, A. Serov, J. R. Regalbuto, W. E. Mustain, *Nature Energy* **2021**, *6*, 834-843; d) K. Yuan, D. Lützenkirchen-Hecht, L. Li, L. Shuai, Y. Li, R. Cao, M. Qiu, X. Zhuang, M. K. H. Leung, Y. Chen, U. Scherf, *Journal of the American Chemical Society* **2020**, *142*, 2404-2412; e) Z. Jiang, W. Sun, H. Shang, W. Chen, T. Sun, H. Li, J. Dong, J. Zhou, Z.

Li, Y. Wang, R. Cao, R. Sarangi, Z. Yang, D. Wang, J. Zhang, Y. Li, *Energy & Environmental Science* **2019**, *12*, 3508-3514.

[26] Y. Wu, Y. Nabae, *Current Opinion in Electrochemistry* **2021**, *25*, 100633.

[27] J. L. Low, B. Paulus, *Catalysts* **2023**, *13*, 566.

[28] a) S. G. Pukhovskaya, D. T. Nam, Y. B. Ivanova, L. S. Liulkovich, A. S. Semeikin, S. A. Syrbu, M. M. Kruk, *Journal of Inclusion Phenomena and Macrocyclic Chemistry* **2017**, *89*, 325-332; b) A. Farajtabar, F. Gharib, P. Jamaat, N. Safari, *Journal of Chemical & Engineering Data* **2008**, *53*, 350-354.

[29] A. Guilherme Buzanich, M. Radtke, K. V. Yusenko, T. M. Stawski, A. Kulow, C. T. Cakir, B. Röder, C. Naese, R. Britzke, M. Sintschuk, F. Emmerling, *The Journal of Chemical Physics* **2023**, *158*.

[30] B. Ravel, M. Newville, *J Synchrotron Radiat* **2005**, *12*, 537-541.

[31] U. A. Paulus, T. J. Schmidt, H. A. Gasteiger, R. J. Behm, *Journal of Electroanalytical Chemistry* **2001**, *495*, 134-145.

[32] R. Ahlrichs, M. Bär, M. Häser, H. Horn, C. Kölmel, *Chemical Physics Letters* **1989**, *162*, 165-169.

[33] a) J. P. Perdew, M. Ernzerhof, K. Burke, *The Journal of Chemical Physics* **1996**, *105*, 9982-9985; b) M. Ernzerhof, G. E. Scuseria, *The Journal of Chemical Physics* **1999**, *110*, 5029-5036.

[34] a) S. Grimme, J. Antony, S. Ehrlich, H. Krieg, *The Journal of Chemical Physics* **2010**, *132*, 154104; b) S. Grimme, S. Ehrlich, L. Goerigk, *Journal of Computational Chemistry* **2011**, *32*, 1456-1465.

[35] F. Weigend, R. Ahlrichs, *Physical Chemistry Chemical Physics* **2005**, *7*, 3297.

[36] A. Klamt, G. Schüürmann, *J. Chem. Soc., Perkin Trans. 2* **1993**, 799-805.

[37] a) G. Schaftenaar, J. H. Noordik, *Journal of Computer-Aided Molecular Design* **2000**, *14*, 123-134; b) G. Schaftenaar, E. Vlieg, G. Vriend, *Journal of Computer-Aided Molecular Design* **2017**, *31*, 789-800.

[38] a) G. Kresse, J. Hafner, *Physical Review B* **1993**, *47*, 558-561; b) G. Kresse, D. Joubert, *Physical Review B* **1999**, *59*, 1758-1775; c) G. Kresse, J. Furthmüller, *Computational Materials Science* **1996**, *6*, 15-50; dG. Kresse, J. Furthmüller, *Physical Review B* **1996**, *54*, 11169-11186.

[39] J. P. Perdew, K. Burke, M. Ernzerhof, *Physical Review Letters* **1996**, *77*, 3865-3868.

[40] a) S. L. Dudarev, G. A. Botton, S. Y. Savrasov, C. J. Humphreys, A. P. Sutton, *Physical Review B* **1998**, *57*, 1505-1509; b) A. Allerdt, H. Hafiz, B. Barbiellini, A. Bansil, A. E. Feiguin, *Applied Sciences* **2020**, *10*, 2542; c) H. Wende, M. Bernien, J. Luo, C. Sorg, N. Ponpandian, J. Kurde, J. Miguel, M. Piantek, X. Xu, P. Eckhold, W. Kuch, K. Baberschke, P. M. Panchmatia, B. Sanyal, P. M. Oppeneer, O. Eriksson, *Nature Materials* **2007**, *6*, 516-520.

By complexation of tetrapyrrolic nitrogen doped carbons with iron ions and decomplexation of the corresponding Fe-N-C catalysts, we herein determine intrinsic activities of tetrapyrrolic active sites. It turns out that the activity trend follows the HOMO energy of the materials pointing to an outer sphere mechanism at the rate determining step for ORR in alkaline electrolyte.

Davide Menga, Jian Liang Low, Ana Guilherme Buzanich, Beate Paulus and Tim-Patrick Fellinger*

Elucidating the Intrinsic Activity of Tetrapyrrolic Fe-N-C Electrocatalysts for the Oxygen Reduction Reaction in Alkaline Medium

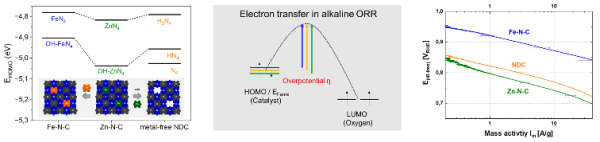

Supporting Information

Elucidating the Intrinsic Activity of Tetrapyrrolic Fe-N-C Electrocatalysts for the Oxygen Reduction Reaction in Alkaline Medium

*Davide Menga, Jian Liang Low, Ana Guilherme Buzanich, Beate Paulus and Tim-Patrick Fellinger**

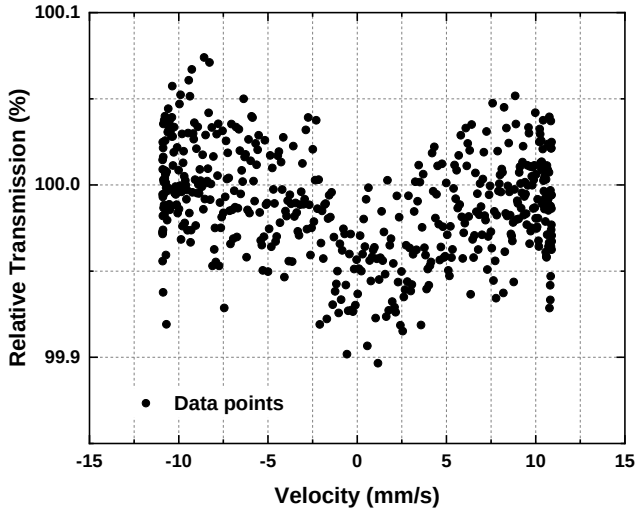

Figure S1. Mössbauer spectrum of Fe-N-C-extr measured at 4.2 K.

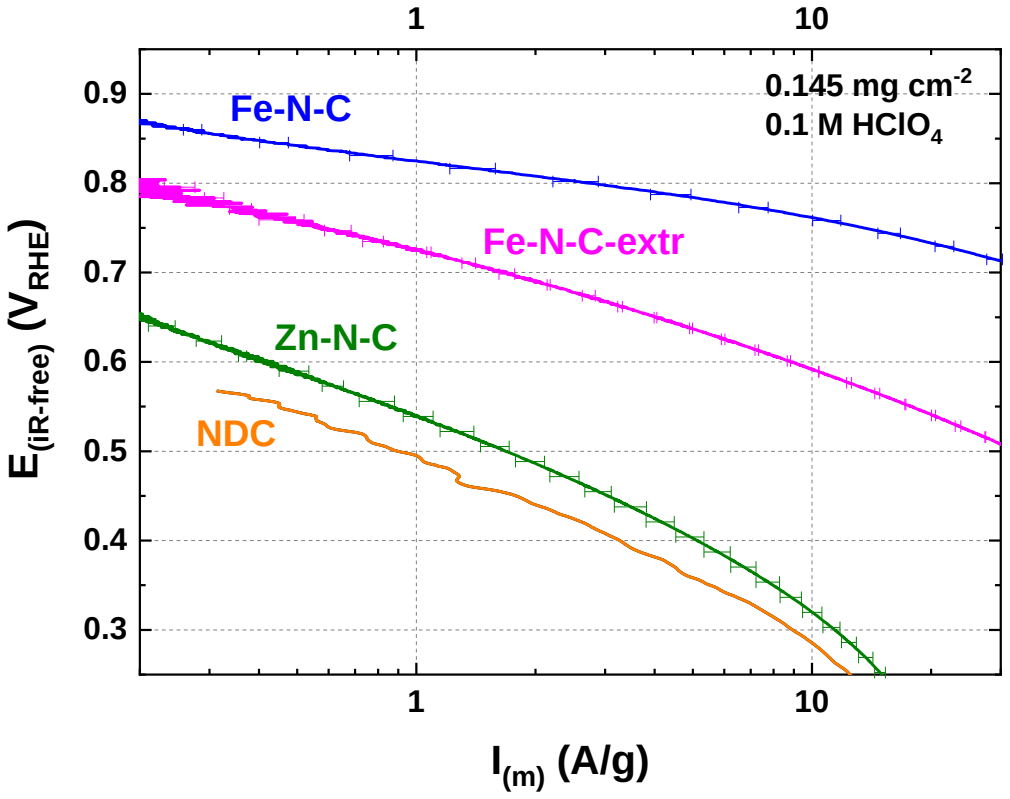

Figure S2. Tafel plots displaying the kinetic mass activity of the catalysts. Measurements were performed with an RDE setup at room temperature in O_2-saturated 0.1 M $HClO_4$ at 1600 rpm, 10 mV s^{-1} (anodic scans).

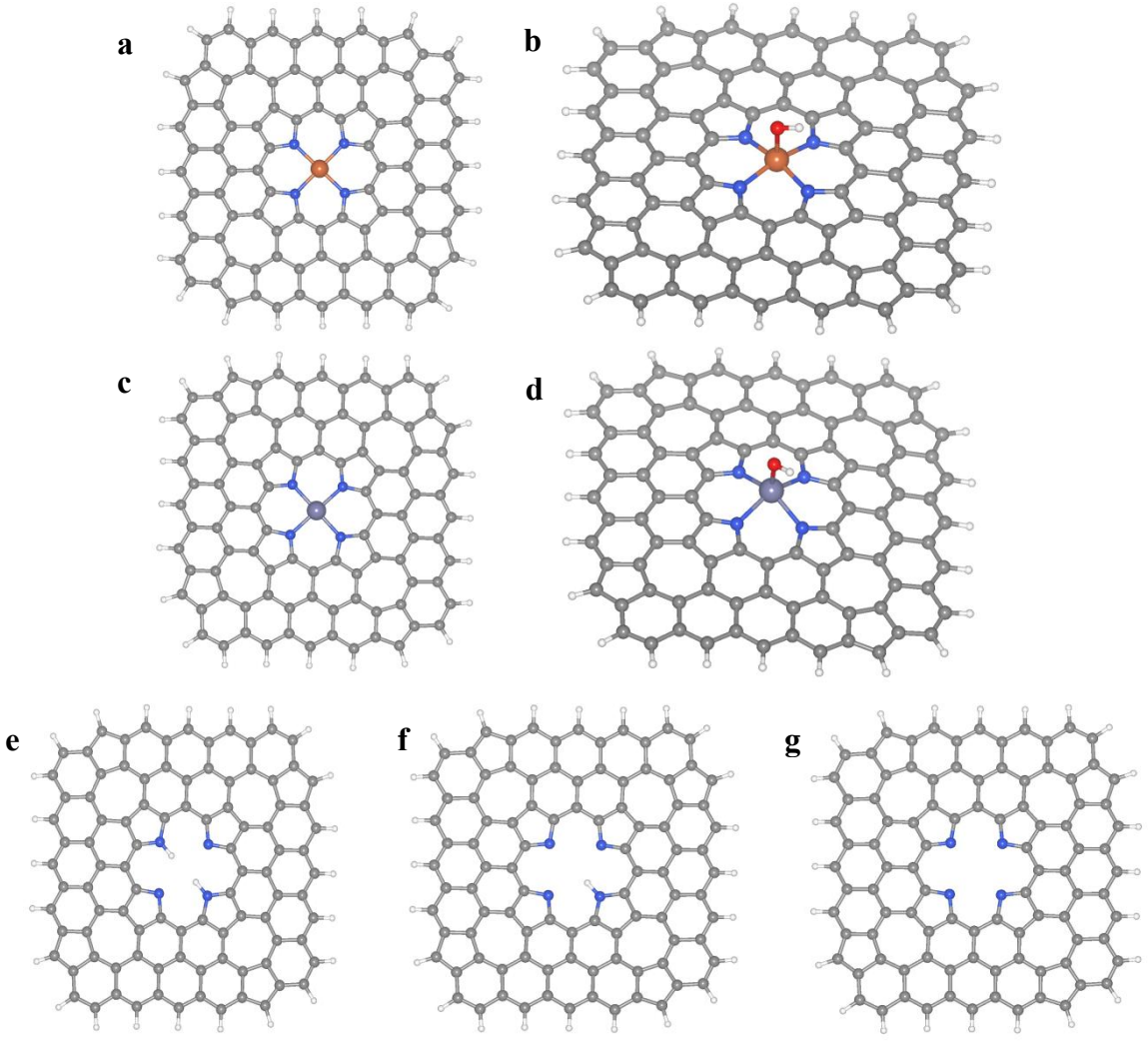

Figure S3. Structure models used for the cluster DFT calculations for (a) FeN_4, (b) OH-FeN_4, (c) ZnN_4, (d) OH-ZnN_4, (e) H_2N_4, (f) HN_4 and (g) N_4 embedded in a $C_{96}H_{24}$ cluster.

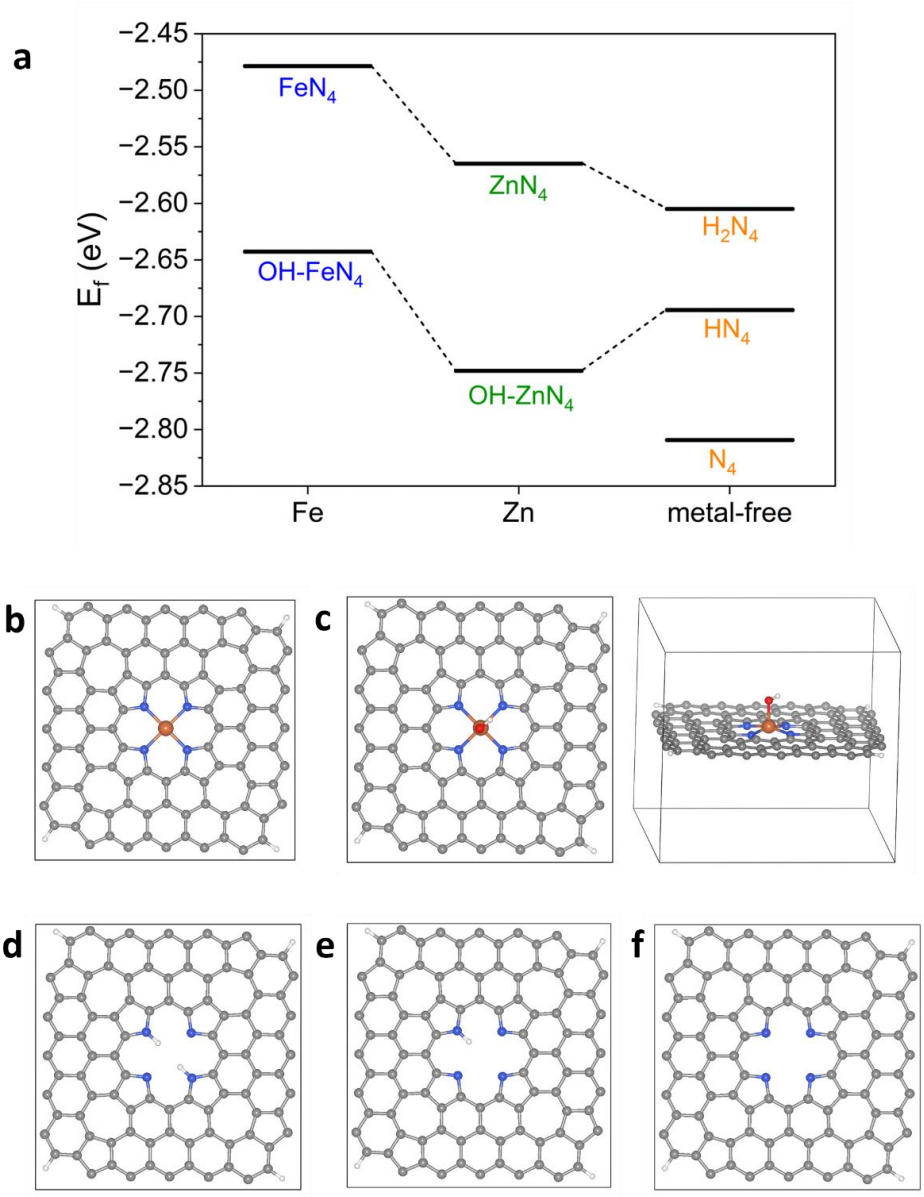

Figure S4. (a) Calculated Fermi level E_f of the MN_4, OH-MN_4, and H_xN_4 (x = 0,1,2) embedded in a periodic carbon lattice. Structure models used for the periodic DFT calculations for (b) FeN_4, (c) OH-FeN_4, (d) H_2N_4, (3) HN_4 and (f) N_4 embedded in a $C_{96}H_4$ unit cell. Geometry optimization and electronic structures are obtained with PBE(+U_{Fe}) functional and plane wave basis using the PAW method.

Table S1. Structural information obtained from EXAFS by fitting the nearest coordination shells around Fe or Zn atoms in the samples with model $ZnN_4C_{96}H_{24}$ or $(OH)FeN_4C_{96}H_{24}$: degeneracy of the scattering path (N), interatomic distance from the fit (R) and from the model (Reff), and Debye-Waller factor (σ^2). The goodness-of-fit parameter is indicated by the R-factor.

Fe-N-C						
Scattering path	N	R (Å)	Reff (Å)	σ^2 (Å^2)	R-factor	
Fe-O	1	1.84	1.81	0.0054	0.013	Single-scattering
Fe-N	4	2.05	2.07	0.0006		Single-scattering
Fe-C	6	3.01	3.08	0.023		Single-scattering
Fe-C	2	3.02	3.10	0.023		Single-scattering
Fe-N-C	16	3.23	3.26	0.022		Triangle scattering
Fe-N-C-N	8	3.40	3.43	0.022		Dog-leg-scattering
Fe-C	4	3.47	3.50	0.022		Single-scattering
Fe-N-C-extr						
Scattering path	N	R (Å)	Reff (Å)	σ^2 (Å^2)	R-factor	
Fe-O	1	1.83	1.81	0.0056	0.013	Single-scattering
Fe-N	4	2.04	2.07	0.0005		Single-scattering
Fe-C	6	3.10	3.08	0.015		Single-scattering
Fe-C	2	3.12	3.10	0.015		Single-scattering
Fe-N-C	16	3.26	3.22	0.003		Triangle scattering
Zn-N-C						
Scattering path	N	R (Å)	Reff (Å)	σ^2 (Å^2)	R-factor	
Zn-N	4	2.04	2.01	0.0052	0.001	Single-scattering
Zn-C	8	3.07	3.04	0.0420		Single-scattering
Zn-N-C	16	3.24	3.21	0.0420		Triangle scattering

Table S2. Elemental composition of the four isomorphic samples. The metal content (M) is obtained from ICP-MS analysis and refers to Zn for Zn-N-C and Fe for Fe-N-C and Fe-N-C-extr. All values are expressed as wt.%.

Sample	C (%)	H (%)	N (%)	M (%)	C/N
Zn-N-C	68.17	1.94	5.89	0.42	11.57
Fe-N-C	75.15	1.00	6.08	0.67	12.36
NDC	72.64	1.09	6.24	-	11.64
Fe-N-C-extr	68.25	1.57	5.16	0.16	13.23

Table S3. Mass activity (i_{kin}) values at different potentials obtained from RDE measurements in acidic electrolyte.

Sample	**i_{kin} (A g^{-1})**			
	0.85 V_{RHE}	**0.80 V_{RHE}**	**0.75 V_{RHE}**	**0.70 V_{RHE}**
Zn-N-C	-	-	-	-
NDC	-	-	-	-
Fe-N-C	0.37 ± 0.02	2.7 ± 0.3	13 ± 1	38 ± 1
Fe-N-C-extr	-	0.12 ± 0.07	0.56 ± 0.03	1.64 ± 0.03

Table S4. HOMO energies (cluster models) and Fermi energies (periodic models) of all the structural motifs. The HOMO energies are obtained with PBE0/def2-TZVP with COSMO solvation model while the Fermi energies are obtained with the PBE(+U_{Fe}) functional with the PAW method. The Hubbard correction is applied for the d-electrons of Fe in the periodic systems with U = 4 eV and J = 1 eV.

	E_{HOMO} (eV)	E_f (eV)
FeN_4	-4.780	-2.479
ZnN_4	-4.817	-2.565
H_2N_4	-4.790	-2.605
OH-FeN_4	-4.904	-2.643
OH-ZnN_4	-5.037	-2.749
HN_4	-4.956	-2.695
N_4	-5.026	-2.810

Paper M4

Exploring the inner- and outer-sphere mechanistic pathways of ORR on M-N-Cs with pyrrolic MN_4 motifs

J. L. Low, C. Roth and B. Paulus, *submitted to J. Phys. Chem. C.*

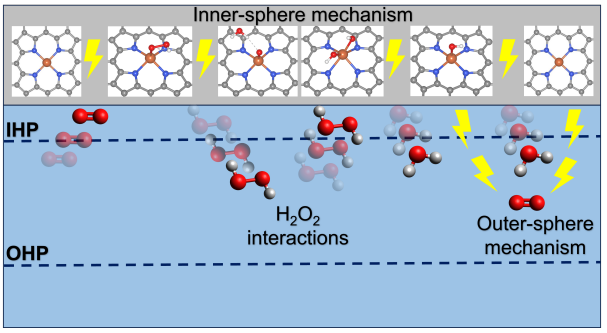

Figure 3.3: Graphical abstract of paper M4.

Computational Highlights

This paper presented a detailed mechanistic study of ORR on pyrrolic MN_4 sites. In addition to the conventional inner-sphere mechanism, we further analyzed trends in the ability to promote outer-sphere electron transfer. For both the inner-sphere and outer-sphere mechanisms, the activity of each MN_4 site is heavily influenced by the metal's oxidation state and its sensitivity to the presence of axial ligands. As the adsorption-free nature of the outer-sphere mechanism inevitably produces free H_2O_2, we further studied the interactions of H_2O_2 with the MN_4 site and identified the $^*(OH)_2$ intermediate whose metal-dependent stability is expected to be critical in subsequent reduction of H_2O_2 to water, allowing us to better understand the 2e-/4e-ORR selectivity as well as the Fenton reactivity of certain M-N-Cs.

Author Contributions

The project was conceived by Jian Liang Low under the guidance of Beate Paulus and inspired by experimental results from Davide Menga and Tim-Patrick Fellinger. Jian Liang Low designed the computational study and performed the DFT calculations. Jian Liang Low analyzed the DFT results under the guidance of Beate Paulus. The manuscript was written by Jian Liang Low with support from Beate Paulus and Christina Roth.

Exploring the inner- and outer-sphere mechanistic pathways of ORR on M-N-Cs with pyrrolic MN_4 motifs

Jian Liang Low,*,† Christina Roth,‡ and Beate Paulus*,†

†*Institute of Chemistry and Biochemistry, Freie Universität Berlin, Arnimallee 22, Berlin 14195, Germany*

‡*Chair of Electrochemical Process Engineering, Universität Bayreuth, Universitätsstraße 30, Bayreuth 95447, Germany*

E-mail: low.jian.liang@fu-berlin.de; b.paulus@fu-berlin.de

Phone: +49 (0)30 838 52051

Abstract

Metal and nitrogen-doped carbon materials (M-N-Cs) have emerged as promising alternatives to costly platinum-group metals (PGMs) for the oxygen reduction reaction (ORR) in renewable energy applications. Notably, there is increasing experimental and theoretical evidence supporting pyrrolic MN_4 coordination over pyridinic MN_4 in these materials, which aligns closer to the MN_4 geometries found in nature. This study utilizes density functional theory (DFT) to elucidate the ability of each metal to catalyze various ORR mechanisms at the pyrrolic MN_4 sites. Among the M-N-Cs of first-row transition metals, pyrrolic CrN_4 and FeN_4 exhibit exceptional 4e-ORR activity, promoting both inner- and outer-sphere mechanisms and H_2O_2 dissociation. Pyrrolic CoN_4 is also promising for 2e-ORR catalysis due to its effective outer-sphere electron-transfer capabilities. These findings offer valuable insights for designing sustainable

electrocatalysts to exploit the full potential of renewable energy sources, advancing the path towards carbon neutrality.

Keywords

single atom catalysis, oxygen reduction reaction, inner- and outer-sphere mechanism, pyrrolic and pyridinic MN_4 motifs

Introduction

With rapidly growing economic and political pressure towards carbon neutrality, there is a crucial need to develop efficient energy storage and conversion technologies in order to exploit the full potential of renewable energy sources. While fuel cells and metal-air batteries are gaining relevance in relatively large-scale energy applications due to their exceptional energy densities, they often face challenges related to energy conversion efficiency.[1,2] In general, the bottleneck for the energy conversion efficiency of fuel cells and metal-air batteries is the sluggish kinetics of the oxygen reduction reaction (ORR) at the cathode, prompting the need for electrocatalysis.[1,3] The state-of-the-art electrocatalysts for ORR are largely derived from scarce and expensive platinum-group metals (PGMs), severely hampering their economic viability.[4,5] In order to achieve sustainability in the large-scale production and application of such energy storage devices, it is thus desirable to design alternative electrocatalysts using more naturally abundant elements such as carbon and non-PGMs.[6]

Recently, metal and nitrogen-doped carbon materials (M-N-Cs) have been widely studied as potential alternatives to PGMs for ORR electrocatalysis, especially with Fe-N-Cs and Co-N-Cs exhibiting ORR currents that are comparable to those of PGMs in alkaline medium.[7–10] Less commonly investigated, yet significant to this study, Cr-N-C and Mn-N-Cs have also been shown to offer promising ORR activity.[11–13] Due to the highly complex structures of these amorphous carbon materials, density functional theory is a crucial tool for extracting

atomic level insights on the single atom sites.[14] While the specific coordination can vary across different materials, there is a general consensus that the nature-inspired MN_4 sites are responsible for the observed electrochemical activities.[7] For the modeling of the MN_4 sites, most studies assume the pyridinic MN_4 coordination embedded in a graphene-like lattice.[7,15–18] However, considering that natural MN_4 complexes exclusively contain the pyrrolic coordination, the existence of such a structure in carbon-based materials cannot be trivialized. In fact, several recent studies independently identified the pyrrolic MN_4 coordination as the active site responsible for ORR activity in Fe-N-Cs and Co-N-Cs,[19–22] prompting the need for more detailed studies on such pyrrolic MN_4 motifs. Synthesis strategies targeting the selective formation of pyrrolic MN_4 sites have also been developed, allowing for intrinsic activity comparison across M-N-Cs with different metal dopants.[8,10,23]

Compared to the pyridinic structures, DFT studies on the pyrrolic MN_4 sites are relatively sparse. Conventionally, periodic boundary conditions are still imposed for the modeling of pyrrolic MN_4 motifs, leading to structures with hole defects relatively close to the active site, high dopant concentrations, or structures with indications of ring strain.[10,24–26] Furthermore, imposing the periodic boundary conditions often entails several technical challenges, namely the high computational cost of hybrid functionals and the influence of lattice strain on the reactivity.[27,28] For transition metal complexes, GGA functionals can produce computational artefacts arising from the self-interaction error and the associated delocalization error.[29–31] In addition, Kirchhoff et al. showed that the self-interaction error of GGA and meta-GGA functionals can manifest even on nitrogen-doped graphene without transition metals, further emphasizing the importance of hybrid functionals for carbon-based catalysis.[32] Unfortunately, as pointed out by Di Liberto et al., this non-trivial source of error is frequently ignored or mishandled, possibly leading to exaggerated results with regards to inner-sphere reactivity.[14,28] For periodic calculations where hybrid functionals are less practical due to computational costs, the Hubbard correction (DFT+U) could be invoked to mitigate the self-interaction error through calibration with an intuitively "similar" reference

material, but can still cause issues pertaining the transferability of Hubbard parameters and reproducibility across systems.[28] In the same publication, it was also reported that even with a reliable GGA+U that matched results from hybrid functionals, the reactivity on periodic systems can be artefacts of suboptimal lattice parameters, which are not typically optimized during the reaction studies. Fortunately, in recent publications, it could be shown that the periodic boundary condition is not really necessary for the description of the chemical properties of the MN_4 site, since the intrinsic properties of MN_4 sites are often only dependent on the local chemical environment.[19,21,26,33] Utilizing a cluster model not only makes the construction of the pyrrolic MN_4 structures more achievable, but also enables a relatively low-cost implementation of the hybrid functionals in place of the GGA or GGA+U methodologies.

For the discussion of ORR activity and selectivity, it is necessary to distinguish between the 2-electron pathway (2e-ORR) in which O_2 is partially reduced to H_2O_2 and the 4-electron pathway (4e-ORR) where the complete reduction to H_2O occurs. While there are certain situations where the 2e-ORR is desired for the H_2O_2 synthesis,[22,34,35] the 4e-ORR pathway is generally preferred for energy conversion applications (e.g. fuel cells) as it maximizes the current densities and minimizes harmful side reactions with the corrosive H_2O_2.[36] Even for the overall 4e-ORR selectivity, the mechanism can be further classified into the direct 4e-ORR or indirect pathways where H_2O_2 is produced and consumed as an intermediate.[18] In a selectivity study using the rotating ring disk electrode (RRDE) measurements, Bonakdapour et al. showed that the macroscopically measured H_2O_2 selectivity is heavily dependent on the catalyst loading, increasing from less than 5% to more than 95% H_2O_2 as the catalyst loading decreases.[37] This implies that even the apparent 4e-ORR selectivity of Fe-N-Cs should be more accurately described as a 2e+2e or a 2e×2e process, which cannot really be explained with an inner-sphere mechanism.[7]

Besides the overall selectivity, the potential-dependent rate-limiting steps can be differentiated into an inner-sphere mechanism, in which the electron is transferred directly

to a strongly bound adsorbate near the inner Helmholtz plane (IHP), or an outer-sphere mechanism where the electron is transferred to species near the outer-Helmholtz plane (OHP).[35,38,39] In alkaline media which generally require lower overpotentials, the outer-sphere mechanism gains relevance due to the presence of adsorbed hydroxyl species.[38,40] Therefore, besides the conventional studies of active site-adsorbate interactions corresponding to the inner-sphere mechanism, we further investigated the intrinsic electronic properties of the active site correlating to its outer-sphere electron-transferring capabilities as well as the respective interactions between the active sites with the inevitably produced H_2O_2.

Computational Method

All calculations were performed with spin-unrestricted Kohn-Sham DFT using the program package TURBOMOLE.[41] For the modeling of the carbon matrix, we used the pyrrolic $MN_4C_{96}H_{24}$ and pyridinic $MN_4C_{98}H_{26}$ clusters terminated by hydrogen atoms. Five- and seven-membered rings were introduced into the pyrrolic clusters to keep the ligand-free structures planar.[26] Excluding the hydrogen atoms, the effective metal concentration is 4.4 $\%_{wt}$, reasonably close to recently achieved dopant concentrations through the templating-transmetallation techniques.[8,9] We applied the hybrid PBE0 functional[42,43] with Grimme's empirical dispersion correction with Becke–Johnson damping function (D3(BJ)).[44,45] Geometry optimizations were performed with the def2-SVP basis while a larger def2-TZVP basis was applied for single-point calculations in combination with the COSMO solvation model.[46,47] Electronic steps were converged to 10^{-7} a.u. in the total energy and 10^{-4} a.u. in the orbital energies, while geometric steps were converged to 10^{-6} a.u. in the total energy and 10^{-3} a.u. in the geometric gradient. Each cluster was calculated with various multiplicities and the one which gave the lowest energy was chosen for further analysis. Atomic charge and spin populations as well as d-orbital occupations were obtained with the natural population analysis.[48] Atomic structures were visualized with VESTA.[49]

For the calculation of potential-dependent intermediate energies for ORR, we applied the computational hydrogen electrode from which the free energy of a proton and electron is defined by

$$G_{\mathrm{H^+ + e^-}} = \frac{1}{2} G_{\mathrm{H_2}} - \mathrm{e}U \tag{1}$$

where U is the applied potential relative to the reversible hydrogen electrode (RHE).[50] The free energies of gaseous species (H_2, O_2) were calculated from their DFT energies along with zero-point energies, the enthalpy of a linear ideal gas ($\frac{7}{2}\mathrm{k}T$) and the tabulated entropies.[51] Due to the complexity of acquiring ab-initio thermodynamic state functions for liquids that truly account for their configurational entropy, we extrapolated the free energy of water from the free energy of combustion of H_2.[51]

$$G_{\mathrm{H_2O}} = G_{\mathrm{H_2}} + \frac{1}{2} G_{\mathrm{O_2}} - 2.46 \text{ eV} \tag{2}$$

Finally, in order to obtain the free energy of each cluster from the DFT energies E_{DFT}, we calculated the zero-point energies and Helmholtz energy at temperature $T = 298$ K from the vibrational frequencies with the harmonic approximation.

$$G_{\mathrm{cluster}} = E_{\mathrm{DFT}} + \sum_i \left[\frac{1}{2} \mathrm{hc}\nu_i + \mathrm{k_B} T \ln \left(1 - \exp \left(-\frac{\mathrm{hc}\nu_i}{\mathrm{k_B} T} \right) \right)^{-1} \right] \tag{3}$$

where h is the Planck's constant, c is the speed of light, $\mathrm{k_B}$ is the Boltzmann's constant and ν_i is the wavenumber corresponding to the vibrational frequency of normal mode i.

Results and discussion

Electronic structure of the ligand-free MN_4 sites

For a preliminary understanding of the site-specific ORR activities, we first analyzed the intrinsic electronic structures of ligand-free MN_4 sites. In a previous publication, it was shown

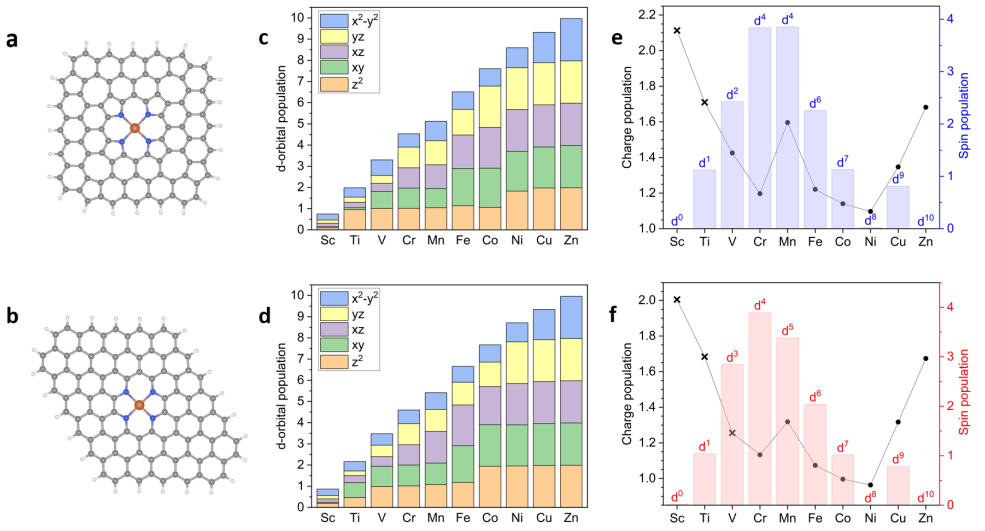

Figure 1: (a,b) Structural model of a planar pyrrolic and pyridinic MN_4 cluster. (c,d) d-orbital population derived from natural population analysis. (e,f) Charge and spin population of transition metal M in the MN_4 site along with the assigned metal-centered d-orbital configuration. The final electronic structures were obtained with PBE0/def2-TZVP with COSMO solvation model. Atoms marked with crosses in (e,f) are significantly displaced from the N_4 plane.

that the popular catalytically active metals in the M-N-Cs (M = Fe, Co) tend to participate heavily in covalent interactions with the π-system of the carbon lattice,[26] thereby decreasing their tendency to form pyrrolic MN_4 sites.[8] However, these metals could still be incorporated into pyrrolic sites upon transmetallation from Zn-N-C and Mg-N-C,[8,52] producing carbon materials with similar overall morphology as well as density and coordination environment of active sites.[23]

For transition metal complexes, the oxidation state of the metal is strongly correlated to its d-orbital occupation and spin population. Figure 1 shows the occupation of the d-orbitals from Sc to Zn and the respective charge and spin population derived from natural population analysis. The corresponding projected density of states (PDOS) for the d-orbitals are shown in Figure S1. With the exception of Cu and Zn, all transition metals exhibit only fractional occupation of the $d_{x^2-y^2}$ orbital resulting from the σ bonding with N atoms. The strength of the σ bond, as measured by the occupation of the $d_{x^2-y^2}$ orbital, increases with

the planarity of the metal binding (Sc < Ti < V) but decreases with the M-N bond length (Fe, Co, Ni > V, Cr) (Geometries in Table S1). As a result of the strong σ-interactions, the anti-bonding $d_{x^2-y^2}$ only starts to fill for Cu and Zn, accompanied by a sharp decrease in the strength of the M-N_4 binding.[26] Based on the projected PDOS (Figure S1) and the visualization of the d-orbitals of pyrrolic ZnN_4 (Figure S2), we observed that the energy of the anti-bonding $d_{x^2-y^2}$ is about 6 eV higher than the other metal-centered orbitals, thereby justifying its unfavorable occupation for transition metals in MN_4 sites.

Besides the σ interactions, π-interactions are also highly relevant in these systems, evident in the fractional occupations of the d_{xz} and d_{yz} orbitals for early transition metals (M = Sc, Ti, V). Due to these π-interactions, the metal-centered anti-bonding d_{xz} and d_{yz} orbitals can be destabilized relative to other orbitals, leading to deviations in the order of orbital occupations from standard ligand field theory. For example, in pyrrolic NiN_4 where d-orbitals except the anti-bonding $d_{x^2-y^2}$ are filled (low spin d^8), the d_{xy} orbital is lower in energy than the molecular orbitals with contributions from the d_{xz} and d_{yz} orbitals (Figure S3).

Neglecting the fractional occupations arising from the ligand-centered σ and π orbitals, we can determine the oxidation state of each transition metal from the d-orbital occupation and spin. The first transition metals (Sc, Ti and V) prefer the oxidation state of +III, largely consistent with the tendency of early transition metals towards higher oxidation states due to lower electronegativities. In contrast, late transition metals (M = Fe, Co, Ni, Cu, Zn) with higher electronegativities have clear preferences for the +II oxidation state, in line with the desired oxidation state for the N_4 site. Cr(II) and Mn(III) are notable outliers in the series, each possessing a different oxidation state from their adjacent metals, but share a common high spin d^4 configuration. Considering the high energy of the anti-bonding $d_{x^2-y^2}$ orbital, the most plausible reason for the anomalies in Cr and Mn is the "half-filled" occupation of the stable d-orbitals in a square-planar complex. For Mn, the occupation of the $d_{x^2-y^2}$ is marginally higher than Cr along with a much higher charge population, indicating that it is indeed more favorable for Mn to lose the additional electron, thereby being oxidized to +III,

than to fully occupy the anti-bonding $d_{x^2-y^2}$ orbital or undergo spin pairing.

For a brief comparison in the electronic structure between the pyrrolic and pyridinic MN_4 motifs in Figure 1, we observed that most transition metals exhibit similar charge and spin populations in either MN_4 cluster. In general, the stronger covalent interactions in pyridinic sites lead to smaller charge populations of the metal atoms in the pyridinic clusters. The most significant differences between the pyrrolic and pyridinic clusters are observed in VN_4 and MnN_4, as the increased d-orbital populations bring the respective metal closer to the +II oxidation state. For MnN_4, the anomalous high-spin d^4 configuration appears to be less favored in the pyridinic motif, evident in the partial spin pairing leading to higher occupation of the d_{xz} orbital.

The inner-sphere mechanism

For an inner-sphere ORR mechanism, the most commonly proposed mechanism is the associative mechanism with step-wise protonation of adsorbed O_2 molecule.

$$\text{free} + O_2 + (H^+ + e^-) \longrightarrow {}^*OOH \tag{4}$$

$${}^*OOH + (H^+ + e^-) \longrightarrow {}^*O + H_2O \tag{5}$$

$${}^*O + (H^+ + e^-) \longrightarrow {}^*OH \tag{6}$$

$${}^*OH + (H^+ + e^-) \longrightarrow \text{free} + H_2O \tag{7}$$

The first and last reaction steps are of particular importance for the inner-sphere ORR activity, as they correspond to the potential dependent adsorption and desorption steps in the ORR cycle. We thus studied the free energies of reductive adsorption to *OOH (ΔG_{ad}) and the reductive desorption from *OH (ΔG_{des}), corresponding to the processes in

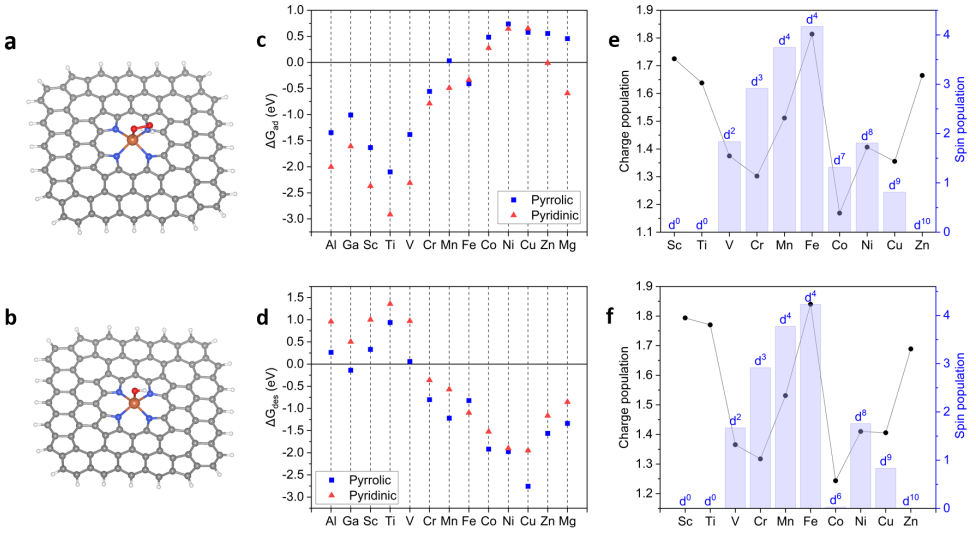

Figure 2: Structural model of a pyrrolic (a) *OOH and (b) *OH cluster. Free energy of potential-dependent (c) adsorption step ΔG_{ad} and (d) desorption step ΔG_{des} at 0 V_{RHE}. Charge and spin population of transition metal M in the pyrrolic (e) *OOH and (b) *OH sites along with the assigned metal-centered d-orbital configuration. The final electronic structures were obtained with PBE0/def2-TZVP with COSMO solvation model.

equations 4 and 7, respectively:

$$\Delta G_{\mathrm{ad}} = G_{*\mathrm{OOH}} - G_{\mathrm{free}} - G_{\mathrm{O_2}} - G_{\mathrm{H^+ + e^-}} \tag{8}$$

$$\Delta G_{\mathrm{des}} = G_{\mathrm{free}} + G_{\mathrm{H_2O}} - G_{*\mathrm{OH}} - G_{\mathrm{H^+ + e^-}} \tag{9}$$

According to Sabatier's principle and its applications in electrocatalysis,[53,54] an ideal ORR catalyst should bind strongly to OOH such that molecular oxygen could be activated, but weakly enough to OH to prevent irreversible oxidation of the active site. Thus, both the adsorption (ΔG_{ad}) and the desorption (ΔG_{des}) steps should be as exergonic as possible. However, due to similarities in the metal-ligand interactions, ΔG_{ad} is negatively correlated to ΔG_{des}, as depicted in the scaling relation shown in Figure S5. Therefore, in accordance with Sabatier's principle, MN_4 sites with intermediate reactivities should be employed for ORR catalysis assuming an inner-sphere mechanism.

Looking closely into the ΔG_{ad} and ΔG_{des} of the individual metals shown in Figure 2d,e

and the resulting free-energy diagrams for ORR on pyrrolic MN_4 motifs in Figure S4 a,b,c, we could identify potential metal dopants for promoting ORR among the pyrrolic MN_4 sites. The early transition metals (M = Sc, Ti and V), along with group 13 metals (M = Al, Ga) bind very strongly to both OOH and OH, resulting in highly negative ΔG_{ad} and positive ΔG_{des}. The exceptionally strong binding can be attributed to destabilization of the MN_4 structure as a result of the initial mismatch between the +III metal oxidation state and the ideal -II oxidation state of the N_4 site. Thus, the reductive desorption step on these MN_4 sites is already endergonic even at 0 V_{RHE} (Figure S4b), implying that the regeneration of the ligand-free active site is thermodynamically unfavorable at higher ORR potentials. The complete opposite to the metals that bind too strongly to ligands are the late transition metals (M = Co, Ni, Cu, Zn) and group 2 metal (Mg) where the ΔG_{ad} are already positive at 0 V_{RHE}. The poor reactivity of these MN_4 sites can be traced to the retention of the +II oxidation state of these metals upon ligand binding, resulting in the formal oxidation of the N_4 site to a less optimal -I oxidation state. Interestingly, for Co, while the binding of OH oxidizes the transition metal to the +III (low spin d^6) oxidation state, the binding of OOH does not. For these relatively inert MN_4 sites, an associative inner-sphere mechanism would be unfeasible without external influences to stabilize the *OOH intermediate.

Among the pyrrolic sites, CrN_4 and FeN_4 have the most promising inner-sphere ORR reactivity as both the adsorption (ΔG_{ad}) and desorption steps (ΔG_{des}) are exergonic at 0 V_{RHE}. In the presence of an axial ligand, Cr is generally oxidized from the +II (high spin d^4) to the +III (high spin d^3) oxidation state. Surprisingly, yet familiar, both Mn and Fe adopt the high-spin d^4 configuration in the pyrrolic MN_4 site upon binding of OOH or OH. As the formal oxidation state of Mn remains unchanged, the reactivity of Mn is relatively poor compared to Cr and Fe. In contrast, the high charge and spin population of Fe in both the *OOH and *OH intermediates indicate an unusually high +IV oxidation state in order to adopt d^4 configuration. Similar to Cr, the ability of Fe to adjust its oxidation state to the presence of an axial ligand confers moderate reactivity to the active site, thus making it

ideal for promoting the inner-sphere ORR mechanism.

Briefly comparing the reactivities of pyrrolic and pyridinic MN_4 sites (Figure 2c,d and Figure S4), we observed that the pyridinic sites generally exhibit higher inner-sphere reactivity with more negative ΔG_{ad} and more positive ΔG_{des}. Universally, the stronger binding of ligands implies destabilization of the ligand-free MN_4 sites, consistent with previous findings that such metals often exhibit poor affinity to pyridinic structures.[26] In this regard, modeling the inner-sphere mechanisms on the pyridinic sites may appear to be more promising at first glance due to the more exergonic first protonation step to *OOH. However, considering the last two data points in Figure 2c, the inner-sphere mechanism on pyridinic sites leads to an erroneous prediction that Zn-N-C and Mg-N-C should be similar, or even higher, in reactivity compared to Fe-N-Cs, contrary to the observed differences in intrinsic activity between isomorphic Zn-N-Cs and Fe-N-Cs.[23,52] We note that apparent reactivity of the pyridinic ZnN_4 site is also implied in a recent work by Karmodak et al.,[55] further substantiating the instability of pyridinic ZnN_4. In addition, even for the pyridinic motifs, the apparently high inner-sphere activity of FeN_4 and CoN_4 reported in previous studies[16,56,57] becomes greatly suppressed once hybrid functionals are applied. This effect corroborates well with a study by Barlocco et al. who reported that the PBE functional overestimated the stability of the H$-CoN_4$ intermediate for hydrogen evolution reaction (HER) by 0.5 eV compared to the PBE0 functional, leading to an exaggeration of its theoretical HER activity.[27,28] Despite the partial success of the conventional inner-sphere mechanism in explaining the reactivity of materials like Fe-N-Cs, it cannot fully account for reactivity trends among of the late transition metals (M = Co – Zn), or even the reactivity differences between the acidic and the alkaline medium. Therefore, we performed an alternative study in order to determine the possible influence of the outer-sphere mechanism on M-N-Cs, noting that its significance has already been highlighted for metal-based and graphene-based catalysts in the alkaline medium.[38,40,58]

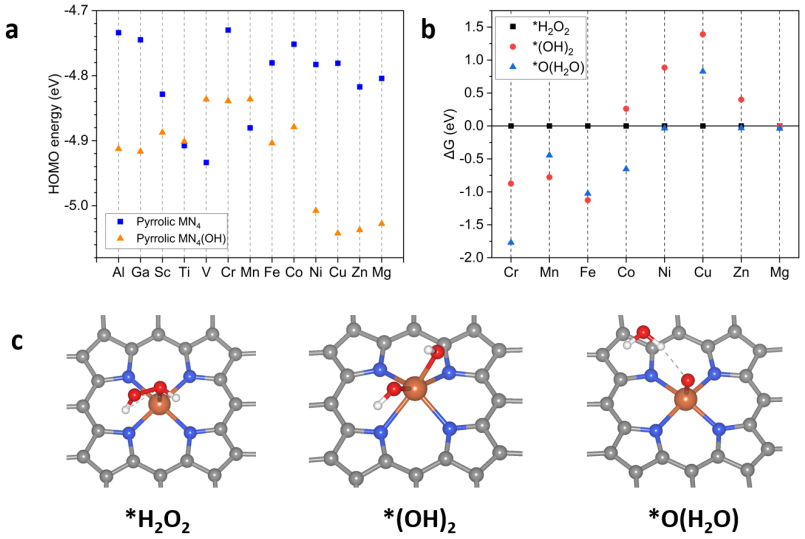

Figure 3: (a) HOMO energy of free and OH-bound pyrrolic motif. (b) Relative free energy between isomeric intermediates $^*H_2O_2$ (defined as zero), $^*(OH)_2$ and $^*O(H_2O)$. (c) Close-up views of three intermediates at the pyrrolic FeN_4 cluster. Geometries were obtained with PBE0/def2-SVP. The final electronic structures were obtained with PBE0/def2-TZVP with COSMO solvation model.

Outer-sphere electron transfer

Although weak interactions with intermediates can be detrimental to the inner-sphere activity, it does not necessarily imply that such M-N-Cs are unsuitable for ORR catalysis. Most notably, Co-N-Cs have been widely shown to exhibit excellent ORR activities, with relatively high 2e-ORR selectivity,[59] despite poor interactions with adsorbates. This somewhat counter-intuitive, Sabatier-defying, ORR activity can be explained by the outer-sphere mechanism, in which a net electron transfer to oxygen in the outer Helmholtz plane occurs without direct adsorption.[38] The outer-sphere mechanism is especially significant in alkaline media, as the metals' interactions with hydroxides can interfere with the adsorption of intermediates. From ab-initio calculations, a descriptor for the ability of M-N-Cs to donate electrons would be the Fermi energy, or in the case of cluster models the energy of the highest occupied molecular orbital (HOMO).[60,61]

Figure 3a shows the HOMO energies of the ligand-free and OH-bound pyrrolic MN_4

clusters. Among the ligand-free sites, transition metals in the +II oxidation state (M = Cr, Fe, Co, Ni, Cu, Zn) generally lead to higher HOMO energies compared to those with the +III oxidation state (M = Sc, Ti, V, Mn). MN_4 sites containing the p-block metals (M = Al, Ga) are outliers to this trend with the ligand-free sites exhibiting relatively high HOMO energies despite their +III oxidation state. Interestingly, the binding of an OH ligand leads to a reversal in the trend in HOMO energies, with metals in the +III/+IV oxidation state (M = Sc, Ti, V, Cr, Mn, Fe, Co, Ga) generally producing higher HOMO energies than those in the +II oxidation state (M = Mg, Ni, Cu, Zn). Considering their relatively high HOMO energies both in the free and ligand bound states, MN_4 sites with M = Al, Ga, Cr, Fe or Co are expected to have significant contributions from the outer-sphere mechanism regardless of the presence of axial ligands. Especially for Cr and Fe where metal-ligand interactions are moderately strong, both the inner- and outer-mechanisms can even occur simultaneously, further boosting their already exceptional ORR activities.

Interactions with H_2O_2

Even though the outer-sphere mechanism can in principle assist in electron transfer and increase the overall ORR currents, its adsorption-free nature would inevitably lead to the production of H_2O_2. As such, the excellent ability of FeN_4 to promote the outer-sphere mechanism partially contradicts the fact that Fe-N-Cs are known to be highly selective towards 4e-ORR, especially in alkaline media. In order to understand the selectivity towards 2e- or 4e-ORR, it is thus necessary to investigate the interactions between the produced H_2O_2 with the MN_4 sites. For that purpose, we studied three different isomeric structures shown in Figure 3c in the pyrrolic MN_4 sites, namely the physisorbed $^*H_2O_2$, the dissociated $^*(OH)_2$ and the $^*O(H_2O)$ structure which would have been produced following the reduction of the $^*OOH$ intermediate (Equation 5). Metals that are irreversibly poisoned by OH at typical ORR potentials are excluded (M = Al, Ga, Sc, Ti, V), as it is unlikely for them to have free MN_4 sites for interaction with H_2O_2 under typical ORR conditions.

Among the remaining metals in pyrrolic MN_4 sites, we further distinguish between metals that are inert towards H_2O_2 from those with at least one stable water-producing intermediate, namely either $^*(OH)_2$ or $^*O(H_2O)$ (Figure 3b). Consistent with their universally weak interactions with the adsorbates, MN_4 sites with M = Mg, Ni, Cu or Zn clearly belong to the former group as the formation of either $^*(OH)_2$ or $^*O(H_2O)$ from $^*H_2O_2$ is determined to be endergonic or reversible at best. It is thus unlikely for these MN_4 sites to be involved in promoting the subsequent H_2O_2 reduction reaction (H_2O_2RR) within the IHP. Meanwhile, metals with intermediate reactivities (M = Cr, Mn, Fe) favor the formation of both the water-producing intermediate due to their abilities to adopt higher oxidation states. In particular, the exergonic formation of the $^*(OH)_2$ intermediate implies a significant driving force towards the dissociation of H_2O_2 at these sites. While such an interaction is consistent with the relatively high H_2O_2RR currents measured on Mn-N-Cs and Fe-N-Cs[62] and the generally high 4e-ORR selectivity of the latter, it can have detrimental effects on the stability of these active sites, one of the key limitations reported in Fe-N-C catalysts.[7,63] In particular, if either of the OH fails to bind to the metal upon dissociation of H_2O_2, OH radicals could be produced in a Fenton-like reaction,[64] inducing oxidative stress on the carbon matrix.[63,65–67] Such a process is especially relevant in acidic media where the H_2O_2 remains in its protonated form.[36,68] Therefore, although the complementary outer-sphere mechanism is theoretically favorable for producing higher currents, it could in fact be detrimental to the corrosion resistance of metals such as Cr and Fe in the pyrrolic MN_4 site due to their strong interactions with H_2O_2. In order to increase the long-term stability of such materials, modifications should be targeted at either decreasing the relative contribution of the outer-sphere mechanism (but potentially leading to smaller currents) or minimizing interactions of FeN_4 sites with H_2O_2, for example by providing alternative active sites for H_2O_2RR which do not produce OH radicals.

Besides Fe-N-Cs, Co-N-Cs are also popular for ORR electrocatalysis, especially towards 2e-ORR. As discussed in the previous section, pyrrolic CoN_4 sites have relatively high HOMO

energies to promote electron donation regardless in both the ligand-free and OH-bound forms (Figure 3a). Additionally, due to its transitional position between two strongly contrasting groups of MN_4 sites (M = Cr, Mn, Fe vs M = Ni, Cu, Zn), CoN_4 is unique among the studied transition metals in its interactions with H_2O_2. While the direct dissociation of $^*H_2O_2$ to form $^*(OH)_2$ is endergonic, the formation of $^*O(H_2O)$ intermediate is relatively stable compared to $^*H_2O_2$ (Figure 3b). The former suggests that pyrrolic CoN_4 would not be able to catalyze the subsequent reduction of H_2O_2 within the IHP, leading to smaller currents but also lower production of destructive OH radicals compared to the more reactive metals (M = Cr, Mn, Fe). Nevertheless, the reduction of an adsorbed $^*OOH$ intermediate is still thermodynamically more likely to form $^*O(H_2O)$ than $^*H_2O_2$. Therefore, depending on the desired application, external means to promote or suppress interactions with axial ligands for the inner sphere mechanism would be crucial in modulating the overall ORR selectivity of Co-N-Cs.

Conclusion

In summary, we performed an extended study of the oxygen reduction reaction on M-N-Cs containing first row transition metals as well as group 2 and group 13 metals, taking into consideration not only the conventional inner-sphere mechanism, but also the possibility of an outer-sphere mechanisms leading to 2e-ORR and 2e+2e-ORR pathways. An overview of each metal's ability to participate in the inner-sphere and outer-sphere mechanism is depicted in Figure 4.

In general, while the conventional inner-sphere mechanism can qualitatively explain the ORR activity for certain materials like Fe-N-Cs, there are instances where the mechanism contradicts experimental observations, especially the reactivity comparison among M-N-Cs in the alkaline media for late transition metals. While all metals can contribute to the outer-sphere mechanisms in their stable form, only those with intermediate reactivities can promote

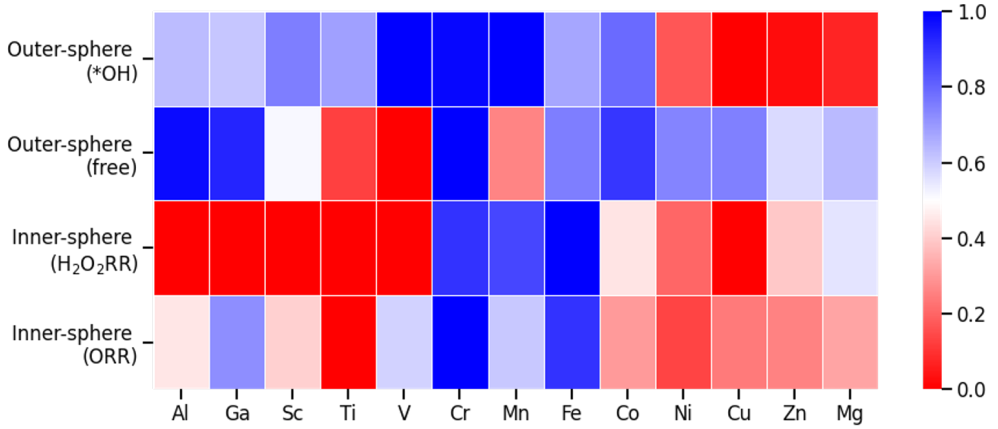

Figure 4: A heatmap illustrating the ratings of various processes based on their respective energies, where a rating of 0 (red) represents the worst performance and a rating of 1 (blue) signifies the best. The processes evaluated include the free energy of the most endergonic step for inner-sphere ORR, the dissociation energy of physisorbed H_2O_2 for H_2O_2RR, and the respective HOMO energies for Outer-sphere electron transfer.

the inner-sphere mechanism and the dissociation of H_2O_2. As a result of the change in metal oxidation state upon the binding of axial ligands, pyrrolic CrN_4 and FeN_4 are exceptional in their ability to promote 4e-ORR as they not only catalyze the inner-sphere mechanism and H_2O_2 dissociation, but are also relatively good electron donors regardless of the presence of axial ligands. However, the H_2O_2 produced from an outer-sphere mechanism could be the Achilles' heel to their long-term stability. In contrast, while CoN_4 does not interact as strongly with axial ligands, it is still able to promote outer-sphere electron transfer in both the ligand-free and OH-adsorbed states, making it suitable for 2e-ORR applications. In addition to showcasing the influence of the oxidation state of metal M on the inner-sphere ORR activity, this study highlights the significance of factoring in contributions from the outer-sphere mechanism as well as interactions with H_2O_2 to justify the overall ORR activity, selectivity and long-term stability. This insight holds promise in catalyst design, as the targeted manipulation of the preferred electron transfer mechanism as well as the interactions with H_2O_2 could be crucial in mitigating the current limitations of various M-N-C catalysts.

Acknowledgement

J.L. Low acknowledges the Elsa-Neumann Scholarship for funding and support. The computations were performed with resources provided by the North-German Supercomputing Alliance (HLRN) and computer facilities of the Freie Universität Berlin (ZEDAT). We would like to thank Dr. Tim-Patrick Fellinger (BAM) and Dr. Davide Menga (MIT) for the experimental characterization of the outer-sphere mechanism which inspired this study.

Supporting Information Available

DFT energies, vibrational free energy correction terms, spin states and geometries of ligand free, *OOH and *OH structures ; projected density of states plots for transition metals ; d-orbital analysis for pyrrolic ZnN_4 and NiN_4 ; scaling relation plot and overall free-energy diagrams for the inner-sphere ORR mechanism ; charge- and spin population of metal M in pyridinic *OOH and *OH

References

(1) Shao, W.; Yan, R.; Zhou, M.; Ma, L.; Roth, C.; Ma, T.; Cao, S.; Cheng, C.; Yin, B.; Li, S. Carbon-Based Electrodes for Advanced Zinc-Air Batteries: Oxygen-Catalytic Site Regulation and Nanostructure Design. *Electrochemical Energy Reviews* **2023**, *6*, 11.

(2) Ning, F.; He, X.; Shen, Y.; Jin, H.; Li, Q.; Li, D.; Li, S.; Zhan, Y.; Du, Y.; Jiang, J.; others Flexible and lightweight fuel cell with high specific power density. *ACS Nano* **2017**, *11*, 5982–5991.

(3) Gasteiger, H.; Yan, S. Dependence of PEM fuel cell performance on catalyst loading. *Journal of Power Sources* **2004**, *127*, 162–171.

(4) Nie, Y.; Li, L.; Wei, Z. Recent advancements in Pt and Pt-free catalysts for oxygen reduction reaction. *Chemical Society Reviews* **2015**, *44*, 2168–2201.

(5) Stacy, J.; Regmi, Y. N.; Leonard, B.; Fan, M. The recent progress and future of oxygen reduction reaction catalysis: A review. *Renewable and Sustainable Energy Reviews* **2017**, *69*, 401–414.

(6) Anastas, P.; Eghbali, N. Green chemistry: principles and practice. *Chemical Society Reviews* **2010**, *39*, 301–312.

(7) Asset, T.; Maillard, F.; Jaouen, F. Electrocatalysis with single-metal atom sites in doped carbon matrices. *Supported metal single atom catalysis* **2022**, 531–582.

(8) Menga, D.; Low, J. L.; Li, Y.-S.; Arčon, I.; Koyutürk, B.; Wagner, F.; Ruiz-Zepeda, F.; Gaberšček, M.; Paulus, B.; Fellinger, T.-P. Resolving the dilemma of Fe–N–C catalysts by the selective synthesis of tetrapyrrolic active sites via an imprinting strategy. *Journal of the American Chemical Society* **2021**, *143*, 18010–18019.

(9) Mehmood, A.; Gong, M.; Jaouen, F.; Roy, A.; Zitolo, A.; Khan, A.; Sougrati, M.-T.; Primbs, M.; Bonastre, A. M.; Fongalland, D.; others High loading of single atomic iron sites in Fe–NC oxygen reduction catalysts for proton exchange membrane fuel cells. *Nature Catalysis* **2022**, *5*, 311–323.

(10) Zhang, N.; Zhou, T.; Chen, M.; Feng, H.; Yuan, R.; Yan, W.; Tian, Y.; Wu, X.; Chu, W.; Wu, C.; others High-purity pyrrole-type FeN 4 sites as a superior oxygen reduction electrocatalyst. *Energy & Environmental Science* **2020**, *13*, 111–118.

(11) Luo, E.; Zhang, H.; Wang, X.; Gao, L.; Gong, L.; Zhao, T.; Jin, Z.; Ge, J.; Jiang, Z.; Liu, C.; others Single-atom Cr- N4 sites designed for durable oxygen reduction catalysis in acid media. *Angewandte Chemie* **2019**, *131*, 12599–12605.

(12) Liu, H.; Zhu, S.; Cui, Z.; Li, Z.; Wu, S.; Liang, Y. Unveiling the roles of multiple active sites during oxygen reduction reaction in Cr2O3@ Cr-NC composite catalyst. *Journal of Catalysis* **2021**, *396*, 402–408.

(13) Parida, S. K.; Barik, T.; Jena, H. A polypyrrole derived nitrogen doped porous carbon support for an atomically dispersed Mn electrocatalyst for the oxygen reduction reaction. *Sustainable Energy & Fuels* **2023**, *7*, 3684–3691.

(14) Di Liberto, G.; Pacchioni, G. Modeling Single-Atom Catalysis. *Advanced Materials* **2023**, 2307150.

(15) Liu, K.; Fu, J.; Lin, Y.; Luo, T.; Ni, G.; Li, H.; Lin, Z.; Liu, M. Insights into the activity of single-atom Fe-NC catalysts for oxygen reduction reaction. *Nature Communications* **2022**, *13*, 2075.

(16) Rao, P.; Wu, D.; Wang, T.-J.; Li, J.; Deng, P.; Chen, Q.; Shen, Y.; Chen, Y.; Tian, X. Single atomic cobalt electrocatalyst for efficient oxygen reduction reaction. *eScience* **2022**, *2*, 399–404.

(17) Xu, H.; Wang, D.; Yang, P.; Liu, A.; Li, R.; Li, Y.; Xiao, L.; Zhang, J.; An, M. A theoretical study of atomically dispersed MN 4/C (M= Fe or Mn) as a high-activity catalyst for the oxygen reduction reaction. *Physical Chemistry Chemical Physics* **2020**, *22*, 28297–28303.

(18) Tylus, U.; Jia, Q.; Strickland, K.; Ramaswamy, N.; Serov, A.; Atanassov, P.; Mukerjee, S. Elucidating oxygen reduction active sites in pyrolyzed metal–nitrogen coordinated non-precious-metal electrocatalyst systems. *The Journal of Physical Chemistry C* **2014**, *118*, 8999–9008.

(19) Zitolo, A.; Goellner, V.; Armel, V.; Sougrati, M.-T.; Mineva, T.; Stievano, L.; Fonda, E.; Jaouen, F. Identification of catalytic sites for oxygen reduction in iron-and nitrogen-doped graphene materials. *Nature Materials* **2015**, *14*, 937–942.

(20) Hu, X.; Chen, S.; Chen, L.; Tian, Y.; Yao, S.; Lu, Z.; Zhang, X.; Zhou, Z. What is the Real Origin of the Activity of Fe–N–C Electrocatalysts in the O2 Reduction Reaction? Critical Roles of Coordinating Pyrrolic N and Axially Adsorbing Species. *Journal of the American Chemical Society* **2022**, *144*, 18144–18152.

(21) Ni, L.; Gallenkamp, C.; Wagner, S.; Bill, E.; Krewald, V.; Kramm, U. I. Identification of the catalytically dominant iron environment in iron-and nitrogen-doped carbon catalysts for the oxygen reduction reaction. *Journal of the American Chemical Society* **2022**, *144*, 16827–16840.

(22) Chen, S.; Luo, T.; Li, X.; Chen, K.; Fu, J.; Liu, K.; Cai, C.; Wang, Q.; Li, H.; Chen, Y.; others Identification of the highly active Co–N4 coordination motif for selective oxygen reduction to hydrogen peroxide. *Journal of the American Chemical Society* **2022**, *144*, 14505–14516.

(23) Menga, D.; Guilherme Buzanich, A.; Wagner, F.; Fellinger, T.-P. Evaluation of the Specific Activity of M- N- Cs and the Intrinsic Activity of Tetrapyrrolic FeN4 Sites for the Oxygen Reduction Reaction. *Angewandte Chemie International Edition* **2022**, e202207089.

(24) Calle-Vallejo, F.; Martínez, J. I.; Rossmeisl, J. Density functional studies of functionalized graphitic materials with late transition metals for oxygen reduction reactions. *Physical Chemistry Chemical Physics* **2011**, *13*, 15639–15643.

(25) Calle-Vallejo, F.; Martínez, J.; García-Lastra, J.; Abad, E.; Koper, M. Oxygen reduction and evolution at single-metal active sites: Comparison between functionalized graphitic materials and protoporphyrins. *Surface science* **2013**, *607*, 47–53.

(26) Low, J. L.; Paulus, B. Computational Modelling of Pyrrolic MN4 Motifs Embedded in Graphene for Catalyst Design. *Catalysts* **2023**, *13*, 566.

(27) Barlocco, I.; Cipriano, L. A.; Di Liberto, G.; Pacchioni, G. Modeling hydrogen and oxygen evolution reactions on single atom catalysts with density functional theory: role of the functional. *Advanced Theory and Simulations* **2023**, *6*, 2200513.

(28) Di Liberto, G.; Cipriano, L. A.; Pacchioni, G. Universal principles for the rational design of single atom electrocatalysts? Handle with care. *ACS Catalysis* **2022**, *12*, 5846–5856.

(29) Zhou, F.; Cococcioni, M.; Marianetti, C. A.; Morgan, D.; Ceder, G. First-principles prediction of redox potentials in transition-metal compounds with LDA+ U. *Physical Review B* **2004**, *70*, 235121.

(30) Wang, L.; Maxisch, T.; Ceder, G. Oxidation energies of transition metal oxides within the GGA+ U framework. *Physical Review B* **2006**, *73*, 195107.

(31) Patel, A. M.; Ringe, S.; Siahrostami, S.; Bajdich, M.; Nørskov, J. K.; Kulkarni, A. R. Theoretical approaches to describing the oxygen reduction reaction activity of single-atom catalysts. *The Journal of Physical Chemistry C* **2018**, *122*, 29307–29318.

(32) Kirchhoff, B.; Ivanov, A.; Skúlason, E.; Jacob, T.; Fantauzzi, D.; Jónsson, H. Assessment of the accuracy of density functionals for calculating oxygen reduction reaction on nitrogen-doped graphene. *Journal of Chemical Theory and Computation* **2021**, *17*, 6405–6415.

(33) Khosravi, A.; Vessally, E.; Oftadeh, M.; Behjatmanesh-Ardakani, R. Ammonia capture by MN4 (M= Fe and Ni) clusters embedded in graphene. *Journal of Coordination Chemistry* **2018**, *71*, 3476–3486.

(34) Wang, K.; Huang, J.; Chen, H.; Wang, Y.; Song, S. Recent advances in electrochemical 2e oxygen reduction reaction for on-site hydrogen peroxide production and beyond. *Chemical Communications* **2020**, *56*, 12109–12121.

(35) Zheng, R.; Meng, Q.; Zhang, L.; Ge, J.; Liu, C.; Xing, W.; Xiao, M. Co-based Catalysts for Selective H2O2 Electroproduction via 2-electron Oxygen Reduction Reaction. *Chemistry–A European Journal* **2023**, *29*, e202203180.

(36) Choi, C. H.; Lim, H.-K.; Chung, M. W.; Chon, G.; Sahraie, N. R.; Altin, A.; Sougrati, M.-T.; Stievano, L.; Oh, H. S.; Park, E. S.; others The Achilles' heel of iron-based catalysts during oxygen reduction in an acidic medium. *Energy & Environmental Science* **2018**, *11*, 3176–3182.

(37) Bonakdarpour, A.; Lefevre, M.; Yang, R.; Jaouen, F.; Dahn, T.; Dodelet, J.-P.; Dahn, J. Impact of loading in RRDE experiments on Fe–N–C catalysts: two-or four-electron oxygen reduction? *Electrochemical and Solid-State Letters* **2008**, *11*, B105.

(38) Ramaswamy, N.; Mukerjee, S. Influence of inner-and outer-sphere electron transfer mechanisms during electrocatalysis of oxygen reduction in alkaline media. *The Journal of Physical Chemistry C* **2011**, *115*, 18015–18026.

(39) Malko, D.; Kucernak, A. Kinetic isotope effect in the oxygen reduction reaction (ORR) over Fe-N/C catalysts under acidic and alkaline conditions. *Electrochemistry Communications* **2017**, *83*, 67–71.

(40) Ramaswamy, N.; Tylus, U.; Jia, Q.; Mukerjee, S. Activity descriptor identification for oxygen reduction on nonprecious electrocatalysts: linking surface science to coordination chemistry. *Journal of the American Chemical Society* **2013**, *135*, 15443–15449.

(41) Ahlrichs, R.; Bär, M.; Häser, M.; Horn, H.; Kölmel, C. Electronic structure calculations on workstation computers: The program system turbomole. *Chemical Physics Letters* **1989**, *162*, 165–169.

(42) Perdew, J. P.; Ernzerhof, M.; Burke, K. Rationale for mixing exact exchange with density functional approximations. *The Journal of Chemical Physics* **1996**, *105*, 9982–9985.

(43) Ernzerhof, M.; Scuseria, G. E. Assessment of the Perdew–Burke–Ernzerhof exchange-correlation functional. *The Journal of Chemical Physics* **1999**, *110*, 5029–5036.

(44) Grimme, S.; Antony, J.; Ehrlich, S.; Krieg, H. A consistent and accurate ab initio parametrization of density functional dispersion correction (DFT-D) for the 94 elements H-Pu. *The Journal of Chemical Physics* **2010**, *132*, 154104.

(45) Grimme, S.; Ehrlich, S.; Goerigk, L. Effect of the damping function in dispersion corrected density functional theory. *Journal of Computational Chemistry* **2011**, *32*, 1456–1465.

(46) Weigend, F.; Ahlrichs, R. Balanced basis sets of split valence, triple zeta valence and quadruple zeta valence quality for H to Rn: Design and assessment of accuracy. *Physical Chemistry Chemical Physics* **2005**, *7*, 3297–3305.

(47) Klamt, A.; Schüürmann, G. COSMO: a new approach to dielectric screening in solvents with explicit expressions for the screening energy and its gradient. *Journal of the Chemical Society, Perkin Transactions 2* **1993**, 799–805.

(48) Reed, A. E.; Weinstock, R. B.; Weinhold, F. Natural population analysis. *The Journal of Chemical Physics* **1985**, *83*, 735–746.

(49) Momma, K.; Izumi, F. VESTA 3 for three-dimensional visualization of crystal, volumetric and morphology data. *Journal of Applied Crystallography* **2011**, *44*, 1272–1276.

(50) Nørskov, J. K.; Rossmeisl, J.; Logadottir, A.; Lindqvist, L.; Kitchin, J. R.; Bligaard, T.; Jonsson, H. Origin of the overpotential for oxygen reduction at a fuel-cell cathode. *The Journal of Physical Chemistry B* **2004**, *108*, 17886–17892.

(51) Chase, M. W.; (US), N. I. S. O. *NIST-JANAF thermochemical tables*; American Chemical Society Washington, DC, 1998; Vol. 9.

(52) Mehmood, A.; Pampel, J.; Ali, G.; Ha, H. Y.; Ruiz-Zepeda, F.; Fellinger, T.-P. Facile metal coordination of active site imprinted nitrogen doped carbons for the conservative preparation of non-noble metal oxygen reduction electrocatalysts. *Advanced Energy Materials* **2018**, *8*, 1701771.

(53) Sabatier, P. *La catalyse en chimie organique*; C. Béranger, 1920; Vol. 3.

(54) Ooka, H.; Huang, J.; Exner, K. S. The sabatier principle in electrocatalysis: Basics, limitations, and extensions. *Frontiers in Energy Research* **2021**, *9*, 654460.

(55) Karmodak, N.; Nørskov, J. K. Activity and Stability of Single-and Di-atom catalysts for O2 reduction reaction. *Angewandte Chemie* **2023**, e202311113.

(56) Tang, C.; Chen, L.; Li, H.; Li, L.; Jiao, Y.; Zheng, Y.; Xu, H.; Davey, K.; Qiao, S.-Z. Tailoring acidic oxygen reduction selectivity on single-atom catalysts via modification of first and second coordination spheres. *Journal of the American Chemical Society* **2021**, *143*, 7819–7827.

(57) Bi, P.; Xiao, T.; Yang, X.; Niu, M.; Wen, Z.; Zhang, K.; Qin, W.; So, S. K.; Lu, G.; Hao, X.; others Regulating the vertical phase distribution by fullerene-derivative in high performance ternary organic solar cells. *Nano Energy* **2018**, *46*, 81–90.

(58) Choi, C. H.; Lim, H.-K.; Chung, M. W.; Park, J. C.; Shin, H.; Kim, H.; Woo, S. I. Long-range electron transfer over graphene-based catalyst for high-performing oxygen reduction reactions: importance of size, N-doping, and metallic impurities. *Journal of the American Chemical Society* **2014**, *136*, 9070–9077.

(59) Jung, E.; Shin, H.; Lee, B.-H.; Efremov, V.; Lee, S.; Lee, H. S.; Kim, J.; Hooch Antink, W.; Park, S.; Lee, K.-S.; others Atomic-level tuning of Co–N–C catalyst for high-performance electrochemical H2O2 production. *Nature Materials* **2020**, *19*, 436–442.

(60) Amiinu, I. S.; Liu, X.; Pu, Z.; Li, W.; Li, Q.; Zhang, J.; Tang, H.; Zhang, H.; Mu, S. From 3D ZIF nanocrystals to Co–Nx/C nanorod array electrocatalysts for ORR, OER, and Zn–air batteries. *Advanced Functional Materials* **2018**, *28*, 1704638.

(61) Xu, H.; Wang, D.; Yang, P.; Liu, A.; Li, R.; Li, Y.; Xiao, L.; Ren, X.; Zhang, J.; An, M. Atomically dispersed M–N–C catalysts for the oxygen reduction reaction. *Journal of Materials Chemistry A* **2020**, *8*, 23187–23201.

(62) Sun, Y.; Silvioli, L.; Sahraie, N. R.; Ju, W.; Li, J.; Zitolo, A.; Li, S.; Bagger, A.; Arnarson, L.; Wang, X.; others Activity–selectivity trends in the electrochemical production of hydrogen peroxide over single-site metal–nitrogen–carbon catalysts. *Journal of the American Chemical Society* **2019**, *141*, 12372–12381.

(63) Ku, Y.-P.; Ehelebe, K.; Hutzler, A.; Bierling, M.; Böhm, T.; Zitolo, A.; Vorokhta, M.; Bibent, N.; Speck, F. D.; Seeberger, D.; others Oxygen reduction reaction in alkaline media causes iron leaching from Fe–N–C electrocatalysts. *Journal of the American Chemical Society* **2022**, *144*, 9753–9763.

(64) Fan, X.; Gao, Y.; Yang, F.; Low, J. L.; Wang, L.; Paulus, B.; Wang, Y.; Trampuz, A.; Cheng, C.; Haag, R. A Copper Single-Atom Cascade Bionanocatalyst for Treating Multidrug-Resistant Bacterial Diabetic Ulcer. *Advanced Functional Materials* **2023**, 2301986.

(65) Jaouen, F.; Charreteur, F.; Dodelet, J. Fe-based catalysts for oxygen reduction in PEMFCs: Importance of the disordered phase of the carbon support. *Journal of the Electrochemical Society* **2006**, *153*, A689.

(66) Lefèvre, M.; Dodelet, J.-P. Fe-based catalysts for the reduction of oxygen in polymer electrolyte membrane fuel cell conditions: determination of the amount of peroxide released during electroreduction and its influence on the stability of the catalysts. *Electrochimica Acta* **2003**, *48*, 2749–2760.

(67) Goellner, V.; Armel, V.; Zitolo, A.; Fonda, E.; Jaouen, F. Degradation by hydrogen peroxide of metal-nitrogen-carbon catalysts for oxygen reduction. *Journal of the Electrochemical Society* **2015**, *162*, H403.

(68) Bae, G.; Chung, M. W.; Ji, S. G.; Jaouen, F.; Choi, C. H. pH effect on the H2O2-induced deactivation of Fe-NC catalysts. *ACS Catalysis* **2020**, *10*, 8485–8495.

For Table of Content Only

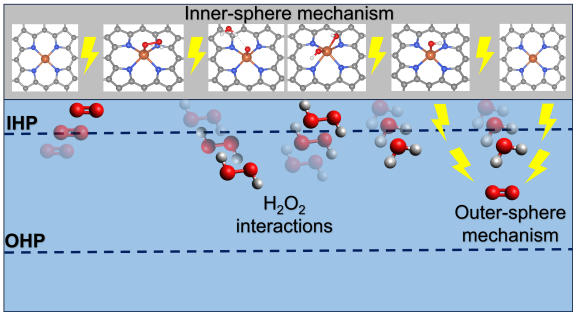

Supporting Information:

Exploring the inner- and outer-sphere mechanistic pathways of ORR on M-N-Cs with the pyrrolic MN_4 motifs

Jian Liang Low,*,† Christina Roth,‡ and Beate Paulus*,†

†*Institute of Chemistry and Biochemistry, Freie Universität Berlin, Arnimallee 22, Berlin 14195, Germany*

‡*Chair of Electrochemical Process Engineering, University of Bayreuth, Universitätsstraße 30, Bayreuth 95447, Germany*

E-mail: low.jian.liang@fu-berlin.de; b.paulus@fu-berlin.de

Phone: +49 (0)30 838 52051

Table S1: Multiplicity $2S+1$, DFT energy E_{DFT} and vibrational free energy correction term F_{vib} of the most stable spin state of **pyrrolic $\mathbf{MN_4}$** along with the average M-N bond lengths $d_{\mathrm{M-N}}$ and the perpendicular distance between metal M and the N_4 site d_{perp}. The perpendicular distance is calculated as a scalar product between an M-N vector and the normal vector to the N-N diagonals.

M	$2S+1$	$E_{\mathrm{DFT}}(\mathrm{E_h})$	$F_{\mathrm{vib}}(\mathrm{E_h})$	$d_{\mathrm{M-N}}$ (Å)	d_{perp} (Å)
Al	2	-4131.7233	0.8612	1.94	0.00
Ga	2	-5813.9351	0.8585	1.97	0.00
Sc	2	-4649.9331	0.8573	2.09	0.45
Ti	3	-4738.6339	0.8573	2.02	0.18
V	2	-4833.1596	0.8564	1.99	0.06
Cr	3	-4933.6389	0.8572	2.00	0.01
Mn	6	-5040.1527	0.8582	1.96	0.00
Fe	3	-5152.8303	0.8595	1.96	0.00
Co	4	-5271.8859	0.8589	1.95	0.00
Ni	3	-5397.4295	0.8583	1.95	0.00
Cu	4	-5529.5796	0.8567	1.98	0.00
Zn	1	-5668.4547	0.8552	2.02	0.05
Mg	1	-4089.3490	0.8573	2.03	0.07

Table S2: Multiplicity $2S+1$, DFT energy E_{DFT} and vibrational free energy correction term F_{vib} of the most stable spin state of **pyridinic $\mathbf{MN_4}$** along with the average M-N bond lengths $d_{\mathrm{M-N}}$ and the perpendicular distance between metal M and the N_4 site d_{perp}. The perpendicular distance is calculated as a scalar product between an M-N vector and the normal vector to the N-N diagonals.

M	$2S+1$	$E_{\mathrm{DFT}}(\mathrm{E_h})$	$F_{\mathrm{vib}}(\mathrm{E_h})$	$d_{\mathrm{M-N}}$ (Å)	d_{perp} (Å)
Al	2	-4209.2796	0.8990	1.89	0.00
Ga	2	-5891.4906	0.8967	1.92	0.00
Sc	2	-4727.4748	0.8948	2.07	0.78
Ti	1	-4816.1693	0.8947	2.01	0.63
V	4	-4910.6947	0.8956	1.98	0.33
Cr	5	-5011.1945	0.8960	1.94	0.00
Mn	4	-5117.7020	0.8966	1.91	0.00
Fe	3	-5230.4021	0.8976	1.90	0.00
Co	2	-5349.4676	0.8977	1.89	0.00
Ni	1	-5475.0217	0.8978	1.88	0.00
Cu	2	-5607.1606	0.8963	1.93	0.00
Zn	1	-5746.0269	0.8941	1.96	0.02
Mg	1	-4166.9125	0.8965	1.97	0.00

Table S3: Multiplicity $2S+1$, DFT energy E_{DFT} and vibrational free energy correction term F_{vib} of the most stable spin state of **pyrrolic *OOH-MN$_4$** along with the average M-N bond lengths $d_{\mathrm{M-N}}$, the shortest M-O bond length $d_{\mathrm{M-O}}$ and the perpendicular distance between metal M and the N_4 site d_{perp}. The perpendicular distance is calculated as a scalar product between an M-N vector and the normal vector to the N-N diagonals.

M	$2S+1$	E_{DFT}(E$_\mathrm{h}$)	F_{vib}(E$_\mathrm{h}$)	$d_{\mathrm{M-N}}$ (Å)	$d_{\mathrm{M-O}}$ (Å)	d_{perp} (Å)
Al	1	-4282.6298	0.8732	2.01	1.78	0.43
Ga	1	-5964.8292	0.8706	2.03	1.85	0.46
Sc	1	-4800.8511	0.8702	2.17	1.96	0.79
Ti	2	-4889.5720	0.8731	2.05	1.84	0.58
V	1	-4984.0697	0.8706	2.03	1.77	0.39
Cr	2	-5084.5194	0.8722	2.01	1.83	0.26
Mn	5	-5191.0081	0.8697	1.99	2.00	0.22
Fe	4	-5303.6994	0.8685	2.07	1.87	0.50
Co	3	-5422.7251	0.8708	1.97	1.95	0.16
Ni	6	-5548.2572	0.8680	2.01	2.04	0.19
Cu	5	-5680.4156	0.8688	1.99	2.46	0.04
Zn	2	-5819.2932	0.8691	2.05	2.23	0.27
Mg	2	-4240.1870	0.8669	2.06	2.10	0.38

Table S4: Multiplicity $2S+1$, DFT energy E_{DFT} and vibrational free energy correction term F_{vib} of the most stable spin state of **pyrrolic *OH-MN$_4$** along with the average M-N bond lengths $d_{\mathrm{M-N}}$, the shortest M-O bond length $d_{\mathrm{M-O}}$ and the perpendicular distance between metal M and the N_4 site d_{perp}. The perpendicular distance is calculated as a scalar product between an M-N vector and the normal vector to the two N-N diagonals.

M	$2S+1$	E_{DFT}(E$_\mathrm{h}$)	F_{vib}(E$_\mathrm{h}$)	$d_{\mathrm{M-N}}$ (Å)	$d_{\mathrm{M-O}}$ (Å)	d_{perp} (Å)
Al	1	-4207.5500	0.8706	2.02	1.74	0.50
Ga	1	-5889.7474	0.8684	2.05	1.81	0.53
Sc	1	-4725.7616	0.8659	2.17	1.84	0.77
Ti	2	-4814.4873	0.8686	2.04	1.75	0.51
V	1	-4908.9837	0.8707	2.02	1.75	0.48
Cr	2	-5009.4288	0.8690	2.01	1.80	0.27
Mn	3	-5115.9239	0.8666	2.01	1.88	0.35
Fe	6	-5228.6148	0.8666	2.07	1.81	0.55
Co	1	-5347.6347	0.8705	1.96	1.80	0.13
Ni	6	-5473.1713	0.8650	2.03	1.86	0.38
Cu	5	-5605.2939	0.8645	1.99	2.19	0.13
Zn	4	-5744.2132	0.8635	2.12	1.88	0.68
Mg	4	-4165.1152	0.8650	2.14	1.87	0.70

Table S5: Multiplicity $2S+1$, DFT energy E_{DFT} and vibrational free energy correction term F_{vib} of the most stable spin state of **pyridinic *OOH-MN$_4$** along with the average M-N bond lengths $d_{\mathrm{M-N}}$, the shortest M-O bond length $d_{\mathrm{M-O}}$ and the perpendicular distance between metal M and the N_4 site d_{perp}. The perpendicular distance is calculated as a scalar product between an M-N vector and the normal vector to the two N-N diagonals.

M	$2S+1$	E_{DFT}(E$_\mathrm{h}$)	F_{vib}(E$_\mathrm{h}$)	$d_{\mathrm{M-N}}$ (Å)	$d_{\mathrm{M-O}}$ (Å)	d_{perp} (Å)
Al	1	-4360.2115	0.9122	1.96	1.78	0.50
Ga	1	-6042.4080	0.9099	2.00	1.85	0.55
Sc	1	-4878.4211	0.9088	2.15	1.97	0.92
Ti	2	-4967.1364	0.9096	2.08	1.88	0.82
V	3	-5061.6379	0.9088	2.01	1.78	0.56
Cr	4	-5162.0832	0.9106	1.97	1.83	0.35
Mn	5	-5268.5780	0.9094	1.97	1.91	0.47
Fe	2	-5381.2745	0.9127	1.91	1.78	0.24
Co	3	-5500.3148	0.9100	1.92	1.93	0.21
Ni	2	-5625.8523	0.9070	1.89	2.31	0.05
Cu	3	-5757.9929	0.9075	1.94	2.52	0.04
Zn	2	-5896.8861	0.9078	2.07	1.91	0.71
Mg	2	-4317.7917	0.9089	2.12	1.93	0.86

Table S6: Multiplicity $2S+1$, DFT energy E_{DFT} and vibrational free energy correction term F_{vib} of the most stable spin state of **pyridinic *OH-MN$_4$** along with the average M-N bond lengths $d_{\mathrm{M-N}}$, the shortest M-O bond length $d_{\mathrm{M-O}}$ and the perpendicular distance between metal M and the N_4 site d_{perp}. The perpendicular distance is calculated as a scalar product between an M-N vector and the normal vector to the two N-N diagonals.

M	$2S+1$	E_{DFT}(E$_\mathrm{h}$)	F_{vib}(E$_\mathrm{h}$)	$d_{\mathrm{M-N}}$ (Å)	$d_{\mathrm{M-O}}$ (Å)	d_{perp} (Å)
Al	1	-4285.1337	0.9102	1.97	1.73	0.54
Ga	1	-5967.3276	0.9076	2.01	1.81	0.59
Sc	1	-4803.3303	0.9058	2.15	1.85	0.93
Ti	2	-4892.0375	0.9054	2.08	1.78	0.81
V	3	-4986.5502	0.9078	2.01	1.78	0.53
Cr	4	-5087.0011	0.9082	1.97	1.80	0.35
Mn	5	-5193.4985	0.9063	1.97	1.87	0.45
Fe	4	-5306.1818	0.9101	1.94	1.83	0.40
Co	1	-5425.2309	0.9093	1.90	1.81	0.15
Ni	2	-5550.7670	0.9053	1.98	1.87	0.38
Cu	3	-5682.9052	0.9048	1.96	1.98	0.32
Zn	2	-5821.8017	0.9041	2.10	1.85	0.81
Mg	2	-4242.6979	0.9057	2.11	1.84	0.84

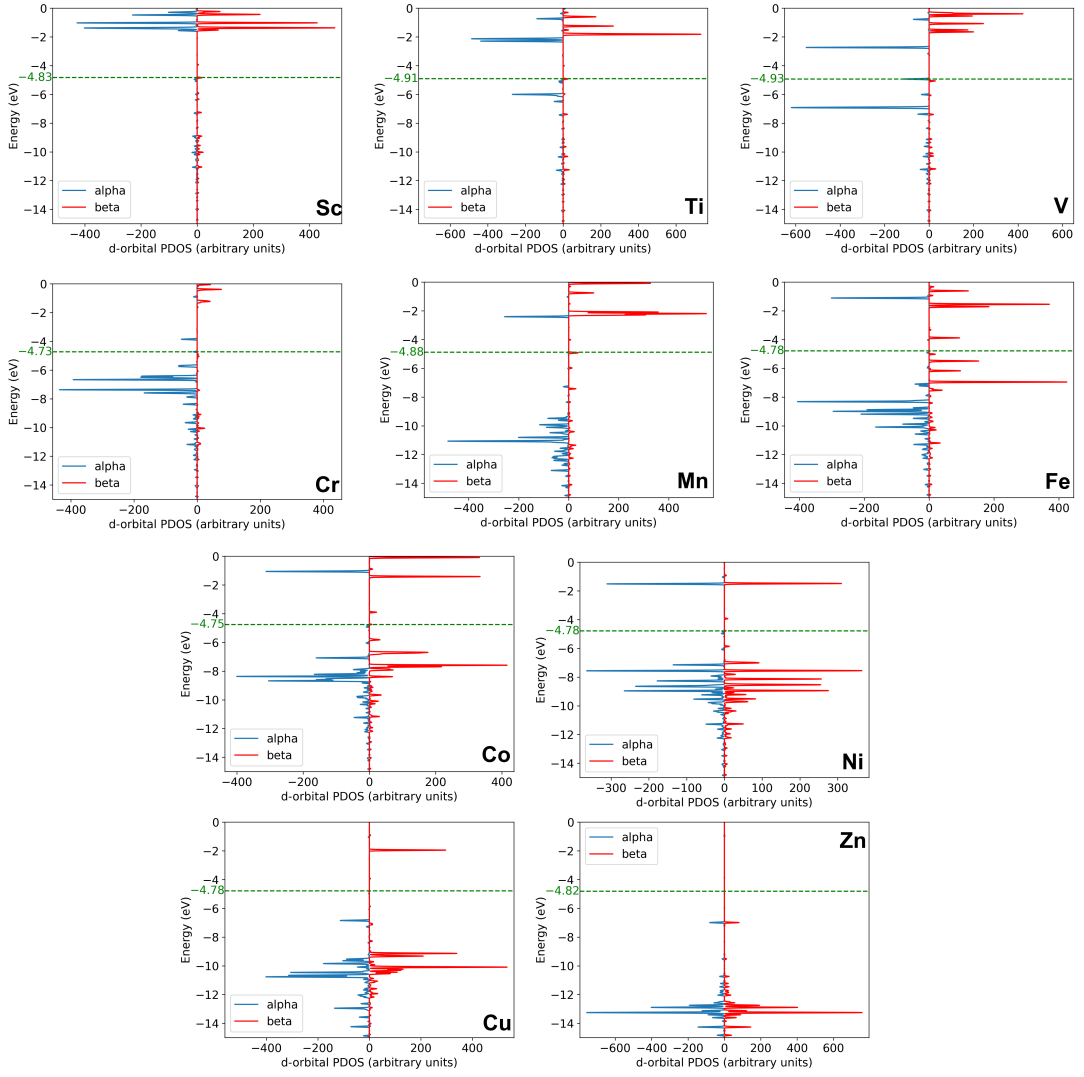

Figure S1: Projected density of state (PDOS) plots of the d-orbital occupations for the **pyrrolic MN_4** site. The PDOS plots are obtained upon Mulliken population analysis of the electronic structure at PBE0-D3(BJ)/def2-TZVP level with COSMO solvation model. The green dotted line displays the energy of the HOMO, which are generally delocalized π-orbitals of the carbon framework.

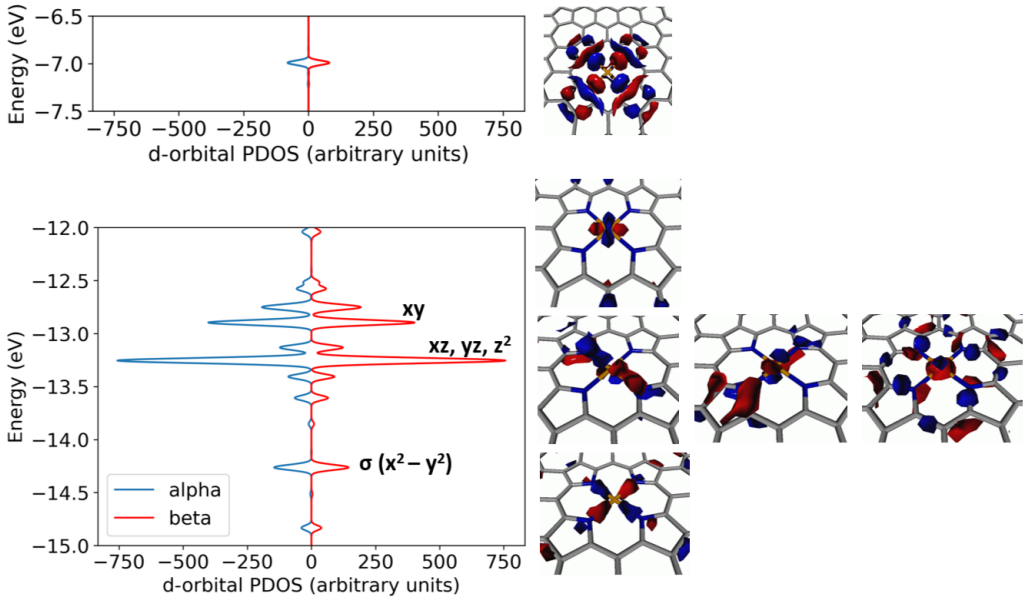

Figure S2: Projected density of state (PDOS) and corresponding d-orbitals for the pyrrolic ZnN_4. The PDOS plots are obtained upon Mulliken population analysis of the electronic structure at PBE0-D3(BJ)/def2-TZVP level with COSMO solvation model. The orbitals are plotted with GMolden with a contour spacing of 0.03.

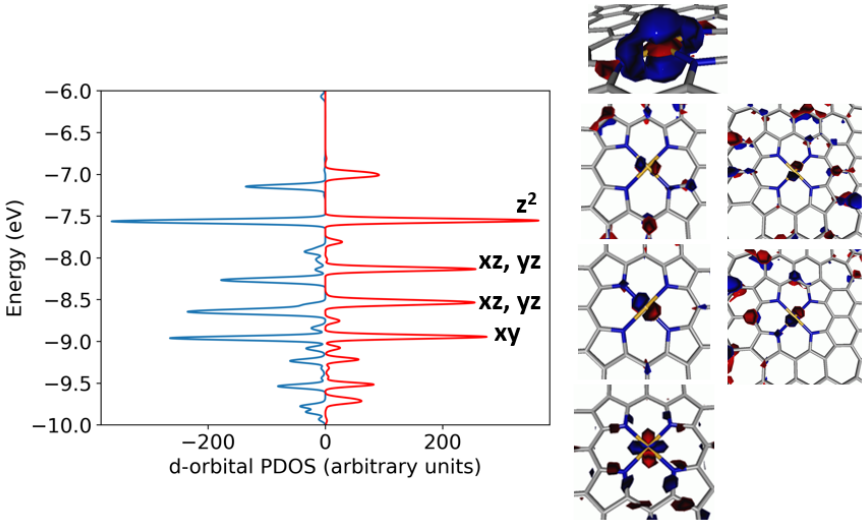

Figure S3: Projected density of state (PDOS) and corresponding d-orbitals for the pyrrolic NiN_4. The PDOS plots are obtained upon Mulliken population analysis of the electronic structure at PBE0-D3(BJ)/def2-TZVP level with COSMO solvation model. The orbitals are plotted with GMolden with a contour spacing of 0.03.

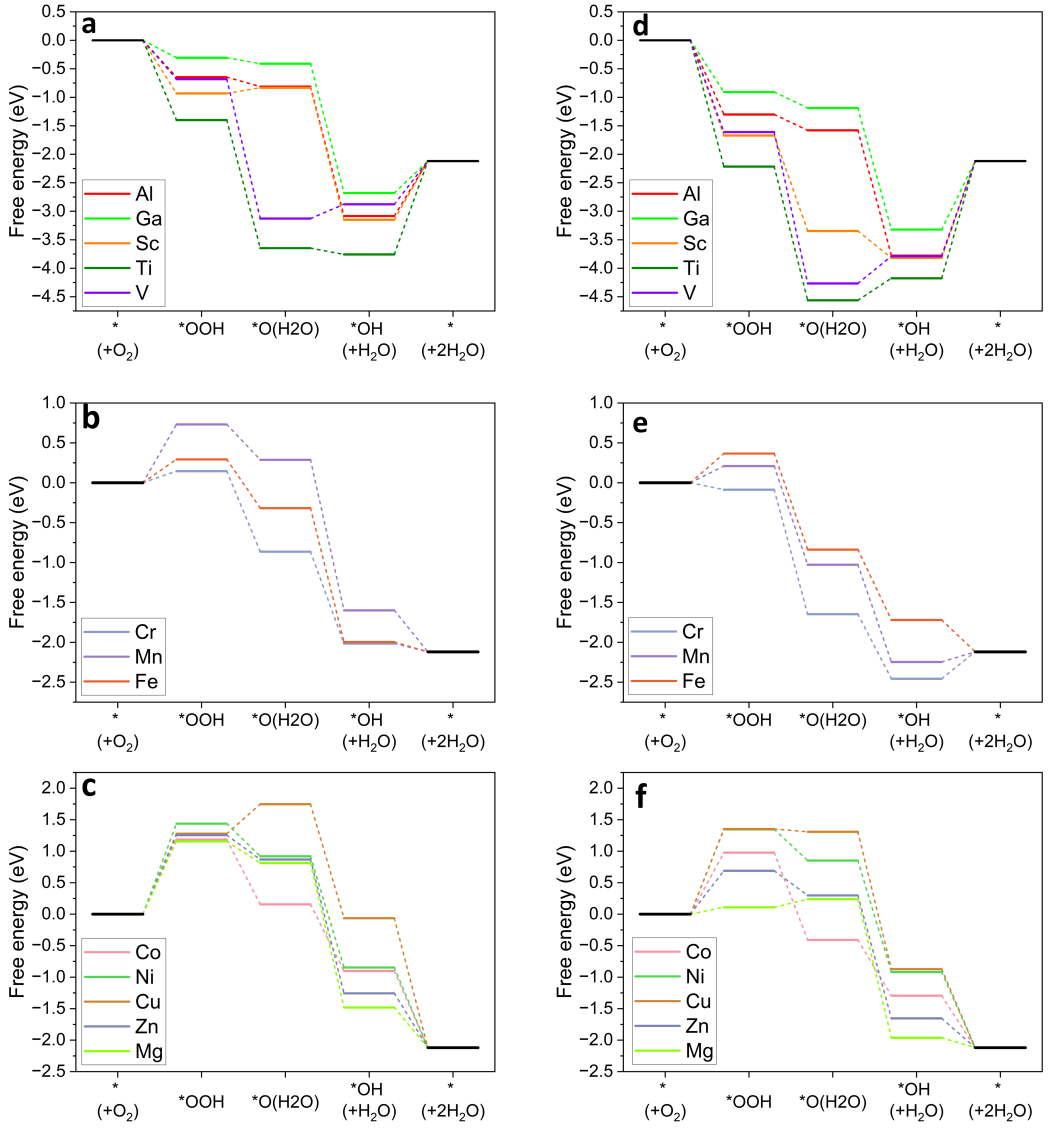

Figure S4: Free energy diagrams for the inner-sphere ORR mechanism on (a,b,c) pyrrolic MN_4 sites as well as (d,e,f) pyridinic MN_4 sites at $U = 0.7$ V_{RHE}.

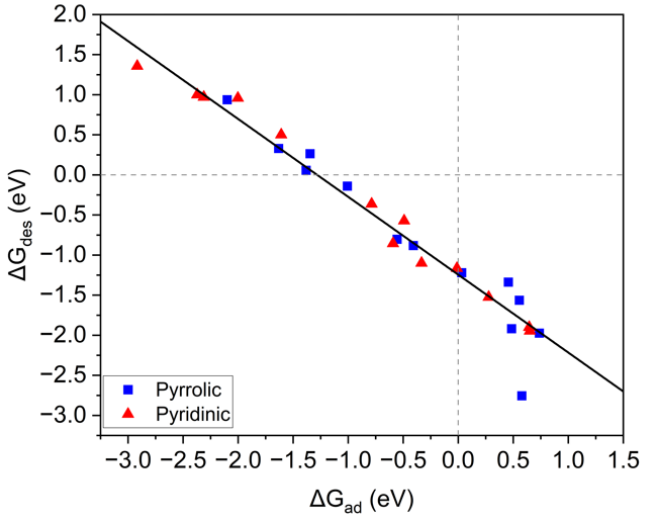

Figure S5: Scaling relations plot between free energy for the potential-dependent desorption step ΔG_{des} and the adsorption step ΔG_{ad}

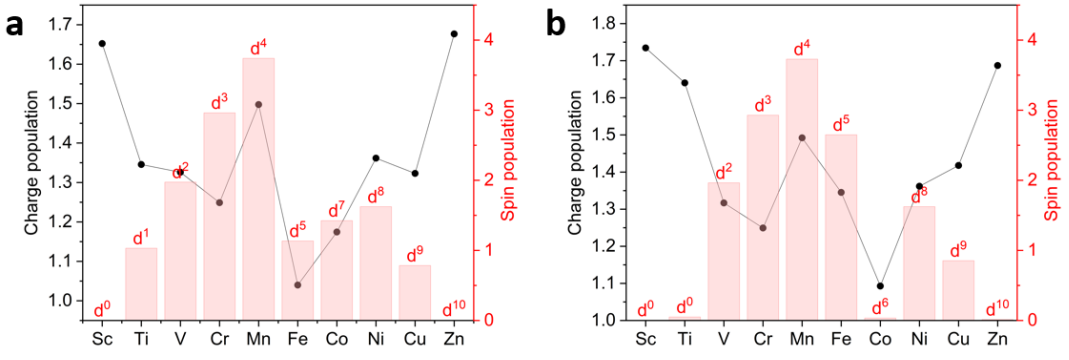

Figure S6: Charge and spin population of transition metal M in the pyridinic (a) *OOH and (b) *OH sites along with the assigned metal-centred d-orbital configuration. The final electronic structures were obtained with PBE0/def2-TZVP with COSMO solvation model.

Paper M5

On the Intrinsic CO_2 Reduction Activity of Atomically-Dispersed Ni-N-C and Co-N-C Electrocatalysts

A. Mehmood, S. A. Abbas, J. L. Low, S. Dietzmann, G. Ali, B. Paulus, K. H. Chae, K. M. Nam, K.-D. Jung and T.-P. Fellinger, *submitted to ACS Catal.*

This is a pre-print which is pending re-submission to another journal.

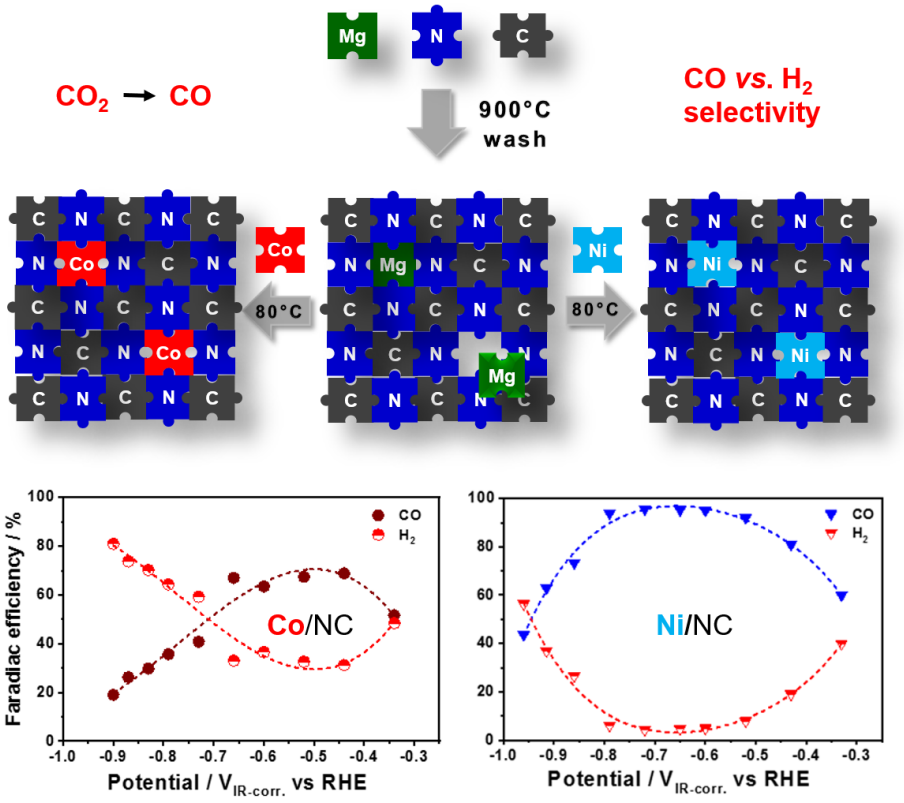

Figure 3.4: Graphical abstract of paper M5.

Computational Highlights

This paper further illustrated the value of the templating-transmetallation strategy using an Mg-salt as templating agent for producing isomorphic Co-N-Cs and Ni-N-Cs. The materials' intrinsic activity and selectivity towards CO_2RR and competing HER were compared. Assisting in the elucidation of local geometry with EXAFS, we optimized geometric models for the incorporation of planar pyrrolic and pyridinic MN_4 motifs with various oxygen ligands. Especially for the Ni-N-Cs, we determined an excellent fit to the pyrrolic MN_4 structure, with the less porous material exhibiting a smaller M-OH coordination number indicating a lower accessibility of active sites. We subsequently studied the reaction

mechanisms on NiN_4 and CoN_4 sites using the computational hydrogen electrode method. Initial results revealed a glaring contradiction that the NiN_4 site is not only catalytically inert, but also unselective towards CO_2RR (vs HER). Nevertheless, using a modification of the computational hydrogen electrode (CHE) to study the potential-dependent adsorption of K^+ ions, we determined that cations are more strongly adsorbed on pyrrolic MN_4 sites than on pyridinic counterparts. Furthermore. their interactions with the reaction intermediates not only reverse the selectivity to favor CO_2RR, but also alleviate the apparent inertness of the NiN_4 sites.

Author Contributions

Asad Mehmood and Syed Asad Abbas are co-first authors. The project was conceptualized by Asad Mehmood and Tim-Patrick Fellinger. Asad Mehmood synthesized and characterized the materials. Syed Asad Abbas conducted the electrochemical tests. Jian Liang Low designed and performed the DFT calculations. Jian Liang Low analyzed the DFT results and wrote the computational parts of the manuscript under the guidance of Beate Paulus. Ghulam Ali and Keun Hwa Chae performed the XAS measurements. Ghulam Ali and Simon Dietzmann performed the XAS data analysis with assistance from Jian Liang Low. Ki Min Nam and Kwang-Deog Jung analyzed the electrochemical data. The overall analysis of results was conducted by Asad Mehmood, Syed Asad Abbas and Tim-Patrick Fellinger. Asad Mehmood and Tim-Patrick Fellinger wrote the manuscript. All authors contributed to the final version of the manuscript.

On the intrinsic CO_2 reduction activity of atomically-dispersed Ni-N-C and Co-N-C electrocatalysts

Asad Mehmood[a]†*, Syed Asad Abbas[b]†, Jian Liang Low[c], Simon Dietzmann[a], Ghulam Ali[d], Beate Paulus[c], Keun Hwa Chae[e], Ki Min Nam[b], Kwang-Deog Jung[f], and Tim-Patrick Fellinger[a]*

[a] Division 3.6 Electrochemical Energy Materials, Bundesanstalt für Materialforschung und -prüfung (BAM), 12203 Berlin, Germany

[b] Department of Chemistry and Chemistry Institute of Functional Materials, Pusan National University, Busan 46241, Republic of Korea.

[c] Institute of Chemistry and Biochemistry, Freie Universität Berlin, Arnimallee 22, 14195 Berlin, Germany.

[d] US-Pakistan Center for Advanced Studies in Energy (USPCASE), National University of Science and Technology (NUST), H-12, Islamabad, 44000, Pakistan.

[e] Advanced Analysis Center, Korea Institute of Science and Technology (KIST), Hwarangno 14-gil 5, Seongbuk-gu, Seoul 02792, Republic of Korea.

[f] Center for Clean Energy and Chemical Engineering, Korea Institute of Science and Technology (KIST), Hwarangno 14-gil 5, Seongbuk-gu, Seoul 02792, Republic of Korea.

*Correspondence to: Asad Mehmood. Email: asad.mehmood@bam.de and Tim-Patrick Fellinger. Email: tim-patrick.fellinger@bam.de

† These authors contributed equally.

Abstract

M-N-C catalysts are a relatively new class of promising electrocatalysts, due to their high atom efficiency and potential to utilize abundant elements to substitute rare element-based catalysts. The chemical and morphological complexity of the materials however still complicates the assessment of their technological potential. We herein use active-site imprinted Mg-N-Cs as platform substrates for ion-exchange reactions towards chemically and morphologically equivalent Ni-N-C and Co-N-C electrocatalysts for the CO_2 reduction reaction. This way, a fair comparison of the intrinsic catalytic activity of both types of catalysts becomes experimentally feasible. We report strong metal-support interactions and consistently higher activity and selectivity to CO at high stability for Ni-N-Cs. The Ni-N-C catalyst shows almost double the specific activity compared to the equivalent Co-N-C and a Faraday efficiency of >80% at a very low overpotential of η= -0.43 V (even 95% at η = -0.5 to -0.8 V). DFT calculations reveal the crucial role of alkali metal ions in stabilizing the

reaction intermediates for enhanced activity and CO selectivity on tetrapyrrolic NiN_4 active sites. The stability of the Ni-N-C at -0.65 V is very high, showing 92.5 % retention of the current density with a 97.6 % retention of the CO selectivity after 100 h of test.

Keywords: Electrochemical carbon dioxide reduction, single atom catalyst, active-stie imprinting, Ni-N_4 sites, Co-N_4 sites

Introduction

The conversion of carbon dioxide has become a topic of intense study because of increasing environmental considerations.[1] By means of electrochemical reduction CO_2 can be converted into a variety of useful products *e.g.* carbon monoxide, methane, methanol, formic acid *etc.*, which can be used as either fuel or a feedstock for producing useful chemicals.[2-4] Since fossil resources are coming without formation costs, the CO_2 conversion pathways must be energetically efficient and as inexpensive as possible so that the green technology benefits can be harnessed with minimal extra cost.[5] These challenges can be addressed by developing innovative catalysts having high product selectivity while operating at low overpotentials with robust performance stability.[6] The use of entirely abundant elements would be desirable to foster stable market prices, exclude costs for recycling and fulfil criteria for green and sustainable technology.[7] For the electrochemical CO_2 reduction reaction (CO2RR) to CO, state-of-the-art catalysts such as gold and silver are not only expensive, but also suffer from sintering and surface modifications that result in considerable loss of CO Faraday efficiency (FE_{CO}) and large overpotentials associated with these catalysts.[8] Single-atom transition metal catalysts have recently emerged as an interesting class of low-cost materials. Therein, the active central metal ion is embedded into nitrogen doped carbons (NCs) by chelate coordination to *e.g.* nitrogen atoms of carbon matrix to form M-N_x structures similar to M-N_4 motif porphyrin and phthalocyanine-type molecular complexes.[9-11] Interestingly, such M-N_x sites hosted in porous carbon frameworks, generally represented as M/N/C or M-N-C catalysts, have shown excellent CO selectivity in the electrochemical reduction of carbon dioxide.[12-14] Of particular interest are iron, cobalt, nickel and more recently zinc based active centers for which high FE_{CO} values have been reported.[15-17] Zhang *et al.* investigated well-defined model catalysts and observed a 99% FE_{CO} for Co-phthalocyanine catalysts with tetrapyrrolic Co-N_4 sites, far outperforming the respective Fe, Ni and Cu counterparts for which FE_{CO} values were well below 50%.[18] Pan *et al.* reported a 93% FE_{CO} for Fe-N-Cs in comparison to 45% for Co-

N-Cs, where the exact structure of the active sites is not well-defined.[19] Similarly, FE_{CO} values over 90% have been reported for Ni-N_4 sites supported on carbon nanotubes (CNTs) or other carbon supports.[20, 21] There is, however, discrepancy in CO selectivity for the same metal-based active centers *e.g.* Ni-N_4 or Co-N_4 reported by different groups. This might be caused by variations in the coordination geometry or by the presence of inconspicuous side phases formed during conventional pyrolytic syntheses. Furthermore, different chemical and morphological features of the carbon backbone, acting as a support and solid-state ligand, may considerably affect the electronic structure of active centers as discussed by Hu *et al*.[11]

For the further development of M-N-C electrocatalysts, it is important to determine the specific activity of active sites with different active metals and evaluate their respective selectivity and stability. The specific catalytic activity for non-ideal, practically relevant materials is convoluted with often complex mass-transport restraints, so that only an apparent catalytic activity is commonly accessible.[22] M-N-Cs with different type of single atoms can hence be compared, only if one can account for mass-transport resistances or if the catalyst morphology is comparable. Furthermore, the situation is complicated due to an expected large effect of the support chemistry (equivalent of metal-support interactions). Different coordination environments will affect the specific activity of the active site and also electronic interaction with the support are comprehensible.[23, 24] M-N-Cs are commonly prepared via carbonization in the presence of compounds of the active metal, which inevitably has a direct and often strong influence on the resulting chemical and physical structure. Therefore, a comparable structure-performance relation is not strictly feasible among pyrolytic M-N-C preparations.

We herein use identical NCs with preformed coordination sites to form comparable Ni-N-Cs and Co-N-Cs with conservation of the support chemistry and morphology. It is shown that, compared to Co-Nx sites, Ni-Nx sites exhibit considerably larger turnover frequencies (TOFs) for CO_2 reduction to CO as well as higher selectivity for CO. Small mass-transport limitations can further be realized with a hierarchical pore structure of the NC support and high specific surface area, resulting in yet unprecedented selectivity for CO formation with FE_{CO} values around 95% at relatively low overpotentials of 480 – 490 mV. The prepared Ni-N-C catalyst shows a high stability with only 7.5% activity loss and 97.6% retained CO-selectivity after 100 h of testing.

Results and Discussion

Structural Characterisation of Catalysts

We recently showed that Lewis-acidic magnesium ions can be utilized to imprint coordination sites into NCs with a pyrolytic method, analogous to the template-ion reaction used in supramolecular chemistry. Such imprinted NCs (essentially being Mg-N-Cs) can be converted into selected M-N-C catalysts by coordination of the desired, catalytically active metal ions at low temperatures. The method decouples the formation of the NC catalyst support from the formation of active-sites.[25-28] Additional thermal treatment further improves the catalysts.[27, 28] Mg-N-Cs were prepared at 800 °C and 1000 °C by an ionothermal salt template-transformation carbonization similar to our earlier report,[25] while the second heat-treatment at 900 °C was equally applied to all catalysts. We herein successfully employed imidazole as an inexpensive C/N-precursor and $MgCl_2 \cdot 6\ H_2O$ as a porogen and source of magnesium ions. Acidic extraction of most of the Mg^{2+} from the as-obtained Mg-N-C was followed by a wet-chemical reaction with Ni or Co ions, respectively resulting in Ni-N-Cs and Co-N-Cs by coordination and ion-exchange. Four catalysts, including Ni-N-C_800, Ni-N-C_1000, Co-N-C_800 and Co-N-C_1000 were scrutinized, where 800 and 1000 represent the pyrolysis temperatures of 800 °C and 1000 °C, at which the Mg-N-C supports were synthesized.

Porosity analysis of the Ni and Co catalysts was carried out using N_2-physisorption. The isotherms of Ni-N-C_800 and Co-N-C_800 catalysts are type II (Figure 1a), indicating a predominantly non-porous nature of carbon sheets.[29] The isotherms are very similar due to the preformed carbon support and resemble the one of Mg-N-C_800 closely (Figure S1). The corresponding pore size distribution (PSD) curves (Figure 2b) also reflect the existence of only few pores. On the other hand, both Ni-N-C_1000 and Co-N-C_1000 catalysts exhibit type IV isotherms with the characteristic hysteresis loops indicative of mesoporous materials (Figure 1a).[30] Sharp N_2 gas uptake at low relative pressure ($p\ p_0^{-1} < 0.02$) is observed for the both samples pointing to a large abundance of micropores. All catalysts closely resemble the morphology of the Mg-N-C supports prepared without coordination of transition metal ions, importantly allowing for fair comparison of Ni with Co catalysts (Figure 1a-b and S1).

Measures of the morphological properties of all catalysts are summarized in Table 1, while a detailed comparison of surface areas and porosities of Ni and Co catalysts with the Mg-N-C_800 and Mg-N-C_1000 matrices (before Ni and Co coordination) is provided in Table S1. The Ni-N-C_800 and Co-N-C_800 catalysts (like Mg-N-C_800) have comparably low surface areas of 287 and 375 $m^2 g^{-1}$, respectively, while the other two catalysts Ni-N-C_1000 and Co-N-C_1000 possess substantially higher surface areas of 1686 and 1591 $m^2 g^{-1}$ like Mg-N-C_1000. High surface areas and hierarchical porosities are beneficial for a facile mass-transport of reacting species to the active centres. The PSD curves of both catalysts in Figure 1b are bimodal with large degree of micro- and small meso-domains. Comparing the surface area and porosity values reveal that these catalysts with their carbon sheet morphology have very low internal porosity, which is advantageous to avoid pore blockage throughout the Ni and Co coordination/transmetalation.

The morphology and elemental distribution of Ni and Co catalysts were examined using scanning electron microscopy (SEM) and TEM imaging coupled with an energy dispersive X-ray detector (EDX). All catalysts consist of crumpled thin carbon sheets as can be seen in SEM (Figure S2) and TEM (Figure 3 and S3) images. The formation of such disordered carbon structures results from the polymerization/carbonization of organic precursors (imidazole in this case) in the eutectic salt mixtures, herein throughout salt template transformation carbonization.[31] Inorganic salts can act as inorganic solvent and/or hard template, while facilitating polymerization/carbonization of organic precursors.[32-36] Formation of extended ionothermal 2D carbon structures were originally reported by Antonietti et al. carbonizing glucose in LiCl-KCl.[37] The distribution of Ni and Co sites embedded in the final catalysts was mapped with the EDX (Figure S4) and it can be clearly observed that the population of Ni sites is significantly higher in Ni-N-C_800 (2.21 wt.%) as compared to the Ni-N-C_1000 (0.57 wt.%), still clearly outmatching the amount of residual Mg. The presence of residual Mg and its distribution in Mg-N-C_800 and Mg-N-C_1000 was also mapped (Figure S5) and the corresponding Mg contents are listed in Table S2. In the cobalt catalysts, the amount of coordinated cobalt in Co-N-C_800 and Co-N-C_1000 catalysts is 1.57 and 0.43 wt.%, respectively. Higher metal contents in both Ni-N-C_800 and Co-N-C_800 catalysts are due to the higher heteroatom content of the Mg-N-C_800 carbon support (Table S2), which was pyrolyzed at lower temperature (T_c = 800 ^oC). Larger amounts of heteroatoms, particularly Lewis-basic sites enable the coordination of larger quantities of Ni and Co single atoms as M-N/O sites to the Mg-N-

C support.[38] More precisely, the higher amount of Ni for Ni-N-C_800 goes along with retaining higher amounts of nitrogen, while Co-N-C_800 has relatively lower nitrogen and metal contents, at the same time increased oxygen contents (Table 1). Both, Ni-N-C_1000 and Co-N-C_1000 have smaller N-contents compared to Mg-N-C_1000, while a relatively strong decrease in the O-content is observed for Co-N-C_1000 compared to Co-N-C_800. The deconvoluted high resolution N 1s XPS spectra of both Mg-N-C_800 and Mg-N-C_1000 show a small M-N_x fraction (~399 eV) confirming the existence of residual imprinted Mg-N_x moieties, which withstood the extraction by acid washing (Figure S6 and Table S2).

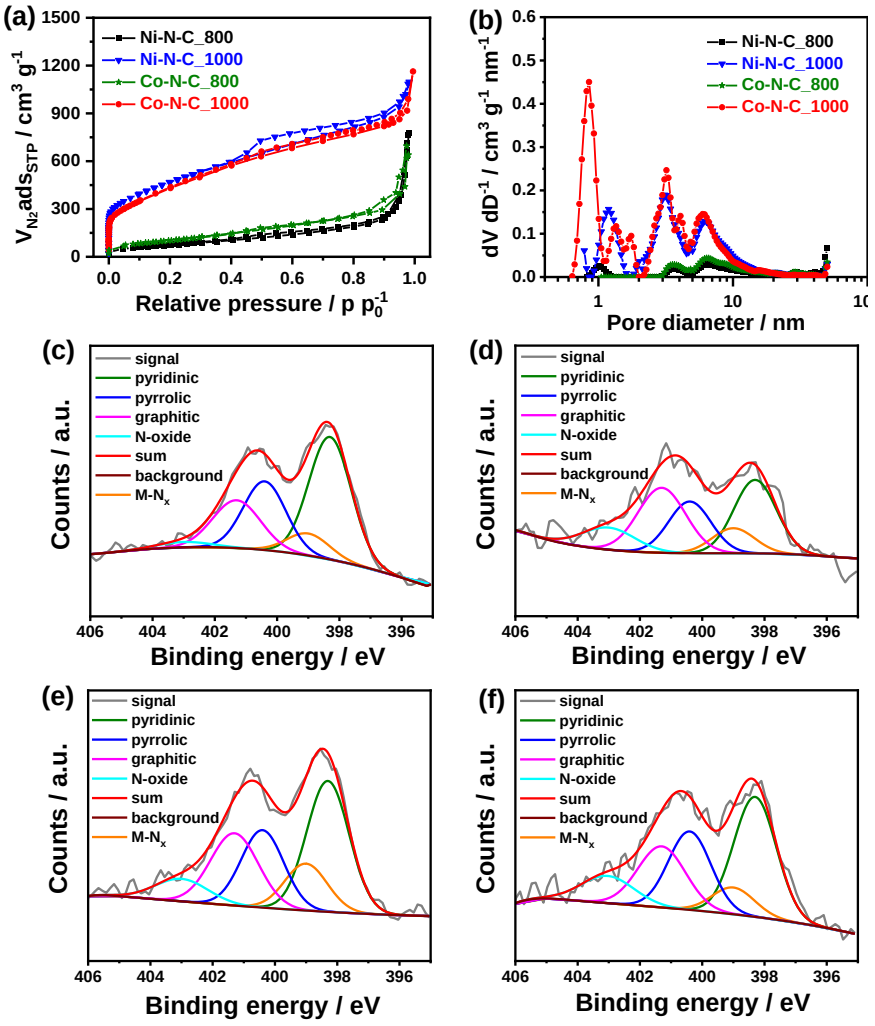

Figure 1. (a) N_2 adsorption-desorption isotherms and (b) corresponding pore size distributions calculated by QSDFT method. (c) Deconvoluted XPS high resolution N1s spectra of Ni-N-C_800, (d) Ni-N-C_1000, (e) Co-N-C_800 and (f) Co-N-C_1000 catalysts.

The amount and chemical nature of doped nitrogen in these catalysts was analyzed by XPS (Figure 1c-f and Table 1). The total nitrogen contents decrease as the pyrolysis temperature increases from 800 to 1000 °C. For Ni-N-C_800 and Co-N-C_800, the total amount of nitrogen is 9.36 and 7.36 at.%, respectively, which dropped to 3.39 at.% for Ni-N-C_1000 and 4.80 at.% for Co-N-C_1000. This trend is consistent with the general observation of an increased overall loss of heteroatoms at higher carbonization temperatures and correlates with reduced metal loadings of the catalysts pyrolyzed at higher temperature.[39] Interestingly, the total heteroatom content of Co and Ni catalysts are in each case similar, while Co-N-C_800 has a strikingly higher O-content. Compared to the transition metal-free reference samples HT900-Mg-N-C_800 (Mg-N-C_800 post-treated at 900 °C) and Mg-N-C_1000 (Table S5), it is apparent that the presence of transition metal results in relatively high heteroatom content at 800 °C, while it is relatively reduced at 1000 °C. Despite the similar concentration of heteroatoms, generally substantially more nickel is bound compared to cobalt.

Table 1. Summary of SSA, TPV, surface O and N contents (by XPS), and Ni and Co metal contents (by EDX).

Catalyst	**SSA_{BET} [m^2g^{-1}]**	**SA_{ext} [m^2g^{-1}]**	**TPV[a)] [cm^3g^{-1}]**	**O-Cont. [at.%]**	**N-Cont. [at.%]**	**Metal Cont.[b)] [wt.%]**
Ni-N-C_800	287	287	0.97	3.01	9.36	Ni ≈2.21
Ni-N-C_1000	1686	1559	1.70	3.94	3.39	Ni ≈0.57
Co-N-C_800	375	375	0.84	5.52	7.36	Co ≈1.57
Co-N-C_1000	1591	1478	1.42	2.46	4.80	Ni ≈0.43

a) TPV was measured at $p \cdot p_0^{-1} = 0.98$.

b) The metal content was determined by EDX.

The qualitative and quantitative analysis of different types of nitrogen sites in these catalysts was done by deconvoluting high resolution N1s peaks (Figure 1c-f). Five different types of nitrogen sites could be discerned that included pyridinic ($N_{pyridinic}$), pyrrolic ($N_{pyrrolic}$), graphitic ($N_{graphitic}$), oxidized nitrogen (N-oxide) and metal-coordinated nitrogen (M-N_x) at the binding energies of 398.3, 400.4, 401.3, 403 and 399 eV, respectively.[40] For the materials originally prepared at 800 °C and post-treated at 900 °C, the Lewis-basic $N_{pyridinic}$, $N_{pyrrolic}$ and N_{M-N} are the major fractions making up about 70 % of the N sites (Figures 1c-d and S6, Tables 2 and S2). The spectra of Ni-N-C_800 and Co-N-C_800 catalysts show an increased relative abundance of M-N and $N_{pyridinic}$

sites compared to the transition metal-free support material HT900_Mg-N-C (Fig. S6). For the materials prepared at 1000 °C, the Lewis-basic N-sites are still dominant, but with a lower relative abundance of low binding energy species. While the spectrum of Co-N-C_1000 resembles well the one of Mg-N-C_1000, Ni-N-C_1000 shows a more pronounced loss of $N_{pyridinic}$ and N_{M-N}.

Altogether, it can be stated that desirable M-N_4 surface complexes were successfully prepared. Consistent with our previous findings, Co^{2+} ions are less prone to coordinate/transmetallate Mg^{2+} ions within imprinted coordination sites, also compared to the herein investigated Ni^{2+} ions, resulting in relatively lower metal loadings. In the case of Co-N-C_800, a larger contribution of O-coordination is apparent, likely since Co-N/O sites or amorphous cobalt oxide is formed due to kinetically limited Mg^{2+} to Co^{2+} ion-exchange. The employment of Mg-N-C_1000 as support has the advantage of desirable morphological characteristics, while the formation of M-N_4 is successful despite a lower metal loading along with reduced heteroatom concentration. Despite the second heat-treatment at 900 °C, the formation of parasitic inorganic side-phases is not observed, and the morphology of the support is retained. This approach results in the unique opportunity to deconvolute morphological restraints to the intrinsic catalytic activity and fairly compare the specific properties of Co- and Ni sites.

Table 2. Total N contents and absolute amounts of different N-sites determined from high-resolution N1s XPS peaks.

Catalyst	**N_{total} [at.%]**	**$N_{pyridinic}$ [at.%]**	**M-N_x [at.%]**	**$N_{pyrrolic}$ [at.%]**	**$N_{graphitic}$ [at.%]**	**N-oxide [at.%]**
Ni-N-C_800	9.36	4.19	0.76	2.35	1.83	0.23
Ni-N-C_1000	3.39	0.99	0.34	0.70	0.99	0.37
Co-N-C_800	7.36	2.64	0.95	1.56	1.64	0.57
Co-N-C_1000	4.80	1.75	0.39	1.15	1.01	0.50

The local coordination environment of the Ni and Co atomic sites was analyzed by synchrotron-based X-ray absorption spectroscopy (XAS). The position of main Ni K-edge peaks of X-ray absorption near edge structure (XANES) of Ni-N-C_800 and Ni-N-C_1000 indicate an average oxidation state of +2 (Figure 2a).[41] When compared with the XANES profile of the nickel (II) phthalocyanine ($Ni^{II}Pc$), the absence of shoulder peak at 8339 eV for both Ni catalysts indicates an additional ligand or a distorted, almost tetrahedral geometry of the

Ni-N_4 sites. The *Fourier*-transformed, extended X-ray absorption fine structure (EXAFS) spectra of both Ni catalysts reveal the radial distribution function related to nearest neighbour atoms (Figure 2c and e). The dominant peak at around 1.8 – 2.0 Å (all radial distances are phase-corrected) is related to the proximal Ni-N/O distance, while the second minor peak at larger distance of around 2.9 – 3.1 Å originates from the Ni-N/C scattering in the second coordination shell. The EXAFS profiles of Ni-N-C_800 (Figure 2c) and Ni-N-C_1000 (Figure 2e) were fitted with DFT-optimized geometric models. For Ni-N-C_800 catalyst, the best fit was obtained using a $(OH)NiN_4$ structure with a tetrapyrrolic coordination i.e. central Ni atom binding one OH group in the axial position and coordinated to four pyrrolic nitrogen atoms embedded in a planar carbon plane. Best EXAFS fit for the Ni-N-C_1000 was obtained with a $(OH)_2NiN_4$ structure with a tetrapyrrolic coordination corresponding to two OH groups bound in the axial positions. Different structural parameters obtained from the EXAFS fitting of both catalysts are provided in Tables S3 and S4. For Ni-N-C_1000 catalyst, a slightly shorter first-shell coordination (Ni-N/O) is observed, which can be attributed to the higher Ni-O coordination number as well as the shorter Ni-O bond lengths in the DFT-optimized geometries of $(OH)_2NiN_4$ (1.85 Å) compared to $(OH)NiN_4$ (1.94 Å). The fitted Ni-N distances are nearly identical. These results are in good agreement with our recent computational study where a relatively high affinity of templating Mg^{2+} ions towards tetrapyrrolic coordination in carbon materials was determined.[42]

Likewise, a comparison of XANES profiles of Co-N-C_800 and Co-N-C_1000 catalysts with those of $Co^{II}Pc$ in Figure 2b reveals distorted square-planar geometry of the Co-N_4 sites. The EXAFS profiles of both Co-N-C_800 and Co-N-C_1000 catalysts were fitted best using a $(OH)_2CoN_4C_{12}$ structure with tetrapyrrolic coordination (Figure 2d and f) corresponding to a central Co atom bound to two OH groups in the axial positions and coordinated to four pyrrolic nitrogen atoms embedded in a planar carbon plane. Details of fitted parameters are provided in Tables S5 and S6.

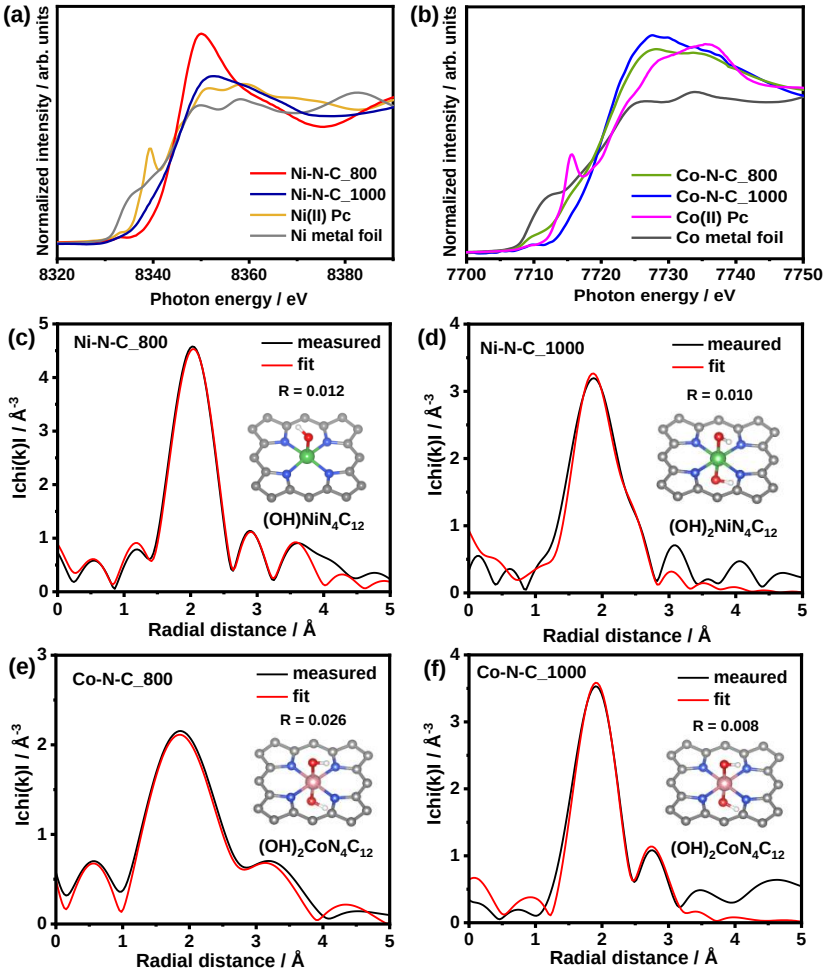

Figure 2. XANES spectra of (a) Ni K-edge of Ni-N-C_800 and Ni-N-C_1000 and (b) Co K-edge of Co-N-C_800 and Co-N-C_1000 catalysts. Fitted EXAFS profiles of (c) Ni-N-C_800 and (d) Ni-N-C_1000, (e) Co-N-C_800 and (f) Co-N-C_1000. Details of EXAFS fitting for Ni and Co catalysts are provide in the supporting information.

Aberration-corrected high-resolution scanning transmission electron microscopy (HR-STEM) imaging also confirmed the atomic dispersion of Ni and Co single atoms/ions in the carbon frameworks of Ni-N-C_1000 and Co-N-C_1000 catalysts (Figure S7). The bright spots in the HR-STEM dark-field images represent Ni and Co single atoms embedded. It is evident that Ni and Co single atoms are dispersed with high uniformity in both catalysts without visible aggregation.

Electrochemical CO_2 reduction activity

The electrochemical activities of these catalysts were evaluated by performing linear sweep voltammetry (LSV) in CO_2-saturated 0.1 M potassium bicarbonate ($KHCO_3$) electrolyte. LSVs were also measured in N_2-saturated electrolyte (Figure S8) where the reductive current was solely due to hydrogen evolution reaction (HER). The active-site-imprinted nitrogen-doped carbon (Mg-N-C_800) shows negligible current, indicating absent catalytic activity towards both CO_2 reduction as well HER of both the N-sites as well as residual Mg-N/O sites. However, after Ni ions are coordinated to form Ni-N-C_800, it starts reducing CO_2 to CO particularly under applied potentials $E_{appl} \leq$ -0.5 V_{RHE}) with high FE_{CO} that reach up to 95% in the potential range of -0.65 – -0.9 V_{RHE} (Figure 3b). These results are consistent with previously reported large overpotentials required for CO_2 reduction on Ni-N_x catalysts due to the weak binding of COOH* compared to respective Fe or Co sites.[15, 43] Despite the high overpotential, a desirable high CO selectivity >90% is possible, as the low affinity towards the adsorption of *H suppresses the competing HER process. Even though Ni-N-C_800 has a relatively high loading of 2.21 wt.%Ni, the obtained current densities are relatively low. For Co-N-C_800, having the equivalent morphology, CO_2 reduction also results in very similar low currents pointing to a limiting porosity, negatively influencing the mass transport. Here, CO_2 reduction starts at even significantly lower potential compared to Ni-N-C_800, resulting in very low CO selectivity dropping below FE_{CO} = 20% at -0.7 V_{RHE} (Figure 3b). The relatively high overpotential, despite an expected stronger binding of COOH* may be due to the previously mentioned contribution of O-binding in Co-N/O sites or even amorphous Co oxide species.

Interestingly, Ni-N-C_1000, with its highly porous carbon microstructure, delivers much improved performance with an onset potential < -0.30 V_{RHE} (Figure 3a and S8), which is over 200 mV up-shifted compared to the Ni-N-C_800, despite an almost four-fold lower Ni-loading. The current densities obtained with Ni-N-C_1000 are 2-3 times higher than those generated with Ni-N-C_800 in the potential range of ≤ -0.8 V_{RHE}, which is attributed to improved mass-transport porosity. While mesopores with diameters of 2.5 – 5 nm (Figure 1b) allow for improved mass-transport of CO_2, the abundant micropores with diameters 0.8 – 0.9 nm (that is 2-3 times larger than the dynamic diameter of CO_2 molecules) can still contribute to CO_2 reduction. Despite the largely improved performance, the similar shape of the polarization curves of both Ni catalysts confirms the identical nature of active sites as characterized by EXAFS. The large effect of the improved mass-transport porosity is confirmed

by the performance of Co-N-C_1000, which shows even higher current densities at low potential than Ni-N-C_1000 (Figure 3a). The FE_{CO} values between 65 to 69% in the potential range of -0.4 – -0.65 V_{RHE} (Figure 3b) are much improved compared to Co-N-C_800, pointing to higher activity of the herein more present Co-N_4 sites. Compared to Ni catalysts the selectivity is very low, due to the strong binding affinity of *H on Co site, which promotes the competing HER process. The amount of dihydrogen gas generated by the two Ni catalysts in -0.50 – -0.80 V_{RHE} range is negligible as compared to their cobalt counterparts, which can be clearly witnessed from the comparative plots of CO and H_2 Faraday efficiencies (Figure S9) and current densities (Figure S10). The observed differences in activity and selectivity can be interpreted as intrinsic properties of tetrapyrrolic Co-N_4 versus tetrapyrrolic Ni-N_4 sites since we are able to exclude the influence of mass transport.

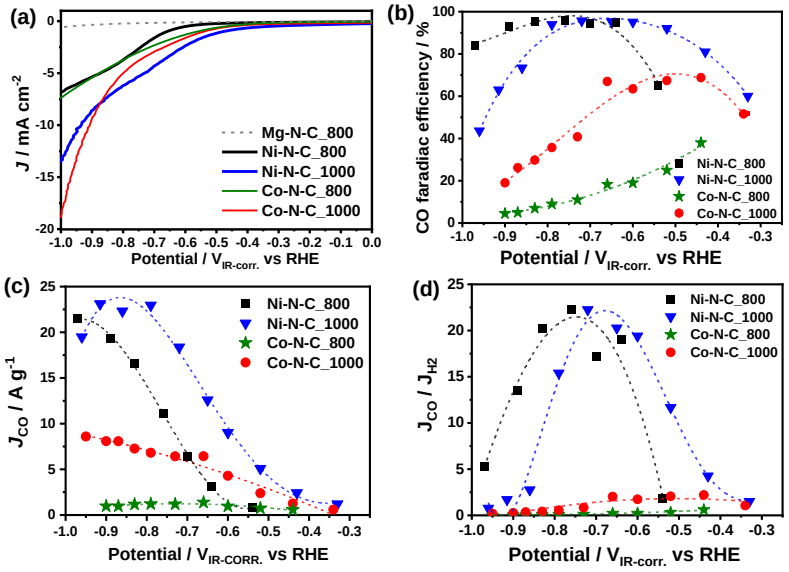

Figure 3. (a) LSVs measured in CO_2-saturated 0.1 M $KHCO_3$ electrolyte at a scan rate of 10 mV s^{-1}. Catalyst loading was 0.25 mg cm^{-2}, (b) CO Faraday efficiencies, (c) mass activities or mass normalized CO partial current densities, and (d) variation of product stoichiometry with applied potential reflected by the ratio of CO and H_2 current densities.

Accordingly, it is reasonable to compare TOFs of Ni-N-C and Co-N-C catalysts with analogous morphology as a measure for the true relation of their intrinsic catalytic properties. Since our approach results in the formation of surface accessible and atomically dispersed active sites, the metal loading determined by EDX (Table 1) can be utilized to calculate the active site density (SD), and subsequently the turnover frequency (TOF) per site. The

respective values for all catalysts are compared in Table 3. The Ni-N-C_800 catalyst possesses high density of Ni atomic sites (2.27 $x10^{20}$ sites g^{-1}), which are very density packed (7.91 x 10^{17} sites m^{-2}) owing to very low specific surface area (287 m^2 g^{-1}). Considering the cross-section of an adsorbed CO_2 molecule (σ=21 $Å^2$), 17% of the total surface is covered with active sites. On the other hand, the Ni-N-C_1000 catalyst has a significantly lower SD value of 0.58 $x10^{20}$ sites g^{-1} and those sites are sparsely distributed all over the carbon matrix ($0.34 \cdot 10^{17}$ sites m^{-2}) due to very high catalyst surface area (1686 $m^2 g^{-1}$). This relates to ≈0.7% of the total surface being covered with active sites. Despite considerably higher density of Ni-N_4 sites, the activity of Ni-N-C_800 catalyst is relatively low. This suggests that most of those sites are apparently inaccessible to CO_2, which is supported by the EXAFS fit with a single OH-ligand, indicating a lower accessibility compared to the other catalysts, being coordinated by two OH-ligands. This is reflected by extremely low TOFs of this catalyst (e.g. at -0.65 and -0.80 V_{RHE}) being far smaller than for Ni-N-C_1000 (Table 3). The similar shape of the polarization curves of the Ni-N-C catalysts is indicative of the identical nature of active sites, being differently utilized. Hence, the microstructure of the carbon framework plays a dominant role in accelerating the rate of reaction by effectively channelling the transport of CO_2 molecules to the active centres. The structural tuning of the carbon matrix can therefore be an effective approach for lowering the overpotential of CO_2 reduction, while maintaining the Faraday efficiency at high levels. Ni-N-C_1000 exceeds FE_{CO} values of 80% at a very low potential of -0.43 V_{RHE}, outperforming most of the reported CO_2 reduction catalysts (Figure 3b).[44, 45] FE_{CO} values of 95% are obtained in the potential range of -0.50 – -0.80 V_{RHE}, which is among the highest reported for the non-precious metal catalysts.[46]

The SD and TOF values of the cobalt catalysts are provided in Table 3. Co-N-C_800 has a considerably higher density of active sites than the 1000 °C counterpart. This trend is consistent with that observed for the two corresponding Ni catalysts. The TOF values of Co-N-C_1000 at -0.65 and -0.80 V_{RHE} are 0.42 and 0.51 s^{-1}, respectively, which are far greater (> 20x) than those obtained for Co-N-C_800. However, TOFs of Co-N-C_1000 are up to two times lower when compared with the corresponding values of 0.68 and 1.16 s^{-1} for Ni-N-C_1000 catalyst, indicating superior intrinsic CO_2 reduction activity of Ni-N-C catalysts compared to Co-N-C, in general. Specific CO current densities (mass activities in A g^{-1}) of all catalysts are plotted in Figure 3c. The most active Ni-N-C_1000 catalyst delivers remarkable mass activities that are 2-5 times higher than those

obtained for the Ni-N-C_800 and Co-N-C_1000 in the potential range of interest i.e. -0.50 – -0.80 V_{RHE} that corresponds to the highest CO selectivity region. As summarized in Table S7, the Ni-N-C_1000 catalyst delivers mass activities of 13 and 23 A g^{-1} at -0.65 and -0.80 V_{RHE}, respectively, which are among highest reported for non-precious metal catalysts measured under similar conditions[47, 48]. The stoichiometric ratio of CO_2 reduction products (CO and H_2 in this case) is an important parameter to be considered for practical systems. As can be seen in Figure 3d, the CO/H_2 stoichiometry for the best Ni-N-C_1000 catalyst is relatively stable (between 19 – 22) in an applied potential range of -0.60 – -0.75 V_{RHE}, which makes it highly relevant for its application in commercial systems.

Table 3. SDs and TOFs of Ni and Co catalysts. a) Surface coverage was calculated based on the cross-section of adsorbed CO_2 molecules of σ=0.21 $Å^2$.

Catalyst	**Gravimetric site density [10^{20} sites g^{-1}]**	**Areal site density/surface coverage[a)] [10^{17} sites m^{-2}/%]**	**TOF @ -0.65 V_{RHE} [s^{-1}]**	**TOF @ -0.80 V_{RHE} [s^{-1}]**
Ni-N-C_800	2.27	7.91/16.6	0.05	0.24
Ni-N-C_1000	0.58	0.34/0.72	0.68	1.16
Co-N-C_800	1.60	4.27/0.09	0.025	0.022
Co-N-C_1000	0.44	0.28/0.006	0.42	0.51

For further mechanistic understanding of CO_2RR and HER in Ni-N-Cs and Co-N-Cs, we performed DFT calculations to study the CO_2RR and HER mechanism of the NiN_4 and CoN_4 sites. Due to the site-retaining nature of the transmetalation strategy, we restrict our calculations to MN_4 sites, although other M-N_x sites were also reported to enhance catalytic activity.[15, 49, 50] For CO_2RR and HER, the respective formation of the *COOH* and *H intermediates are the most endergonic reductive steps and the difference between their energies can be correlated to the CO/H_2 selectivity. For CoN_4 sites, the energies of *COOH* and *H are both relatively low (values), in good agreement with the observed high activity and HER selectivity of Co-N-Cs. However, for NiN_4 sites, the energies of both intermediates COOH* and H* are very high (1.08 eV and 0.95 eV at -0.65 V_{RHE} respectively), in good agreement with several previous DFT studies,[15, 49] but contradicting both the observed high activity and the CO_2RR selectivity of Ni-N-Cs. Inspired by studies which elucidated the influence of alkali-

metal ions on electrochemical reactions,[51-53] we further considered the possible involvement of K^+ ions from the electrolyte at the MN_4 site. For that purpose, we applied a modification of the computational hydrogen electrode to study the potential-dependent adsorption of K^+ ions at the MN_4 sites.[54] From the reaction energy profile for K^+ adsorption in Figure S12, we found that the adsorption of K^+ is thermodynamically more favourable for the tetrapyrrolic sites with the adsorption of up to 2 K^+ ions at a potential of -0.65 V_{RHE}. In contrast, tetrapyridinic site can barely adsorb a single K^+ ion at the same potential.

We further calculated the energies of the *COOH and *H intermediates in the presence of K^+ ion(s) for tetrapyrrolic and tetrapyridinic motifs. From Figure 4a and b, it could be shown that the adsorption of a single K^+ at the NiN_4 site already changes the relative stability of the *COOH and *H intermediate, leading to a reversal in the selectivity compared to pristine NiN_4. The reversal could be traced to the stabilization of the *COOH intermediate which adopts a negative charge in the presence of K^+ (NBO charge -0.64e) unlike the *H intermediate (NBO charge +0.02). For CoN_4 sites, the energy difference between *COOH and *H are also decreased, but the *H intermediate remains slightly more stable than *COOH, further explaining its selectivity towards HER. Nevertheless, the energies of both intermediates on K_1NiN_4 remain relatively high, making either reaction energetically unfeasible. Interestingly, with the inclusion of 2 K^+ ions, the energies of the intermediates are significantly decreased (Figure 4c), while the CO_2RR selectivity is retained. Furthermore, the reactivity on the opposite face of the K_2MN_4 site is almost identical to that of pristine MN_4, implying that the decreased reaction energy barriers are attributed to active interactions between K^+ and the adsorbates. Upon analysis of the net NBO charges of both *COOH (-0.68) and *H (-0.62) on the same face of K_2NiN_4, it is evident that both adsorbates effectively serve as counterions to stabilize the repulsion between K^+ ions, with *COOH affording a better stabilization due to the presence of highly electronegative O atoms. Consistent with the tetrapyrrolic geometry of NiN_4 sites elucidated with EXAFS, the high activity and CO_2RR selectivity of Ni-N-Cs at -0.65 V_{RHE} can be explained by the reaction energy profile of K_2MN_4. Ironically, the apparent inactivity of pristine Ni-N_4 (Figure 4a) proves to be beneficial towards the CO_2RR selectivity, since no reaction would occur in the absence of two K^+ on the same face as the reactants, unlike in Co-N_4 on which reactions are feasible with or without K^+, leading to a lower overall selectivity. Notably, some of the best CO_2RR catalysts exhibiting CO-selectivity are historically inert noble metals like Ag and Au. Qin et. al. recently proposed the involvement of 2

cations in stabilizing the intermediates.[55-57] In support of this mechanism, our study further highlights the role of heteroatoms like N in fixating the cations in order to activate the originally inert site.

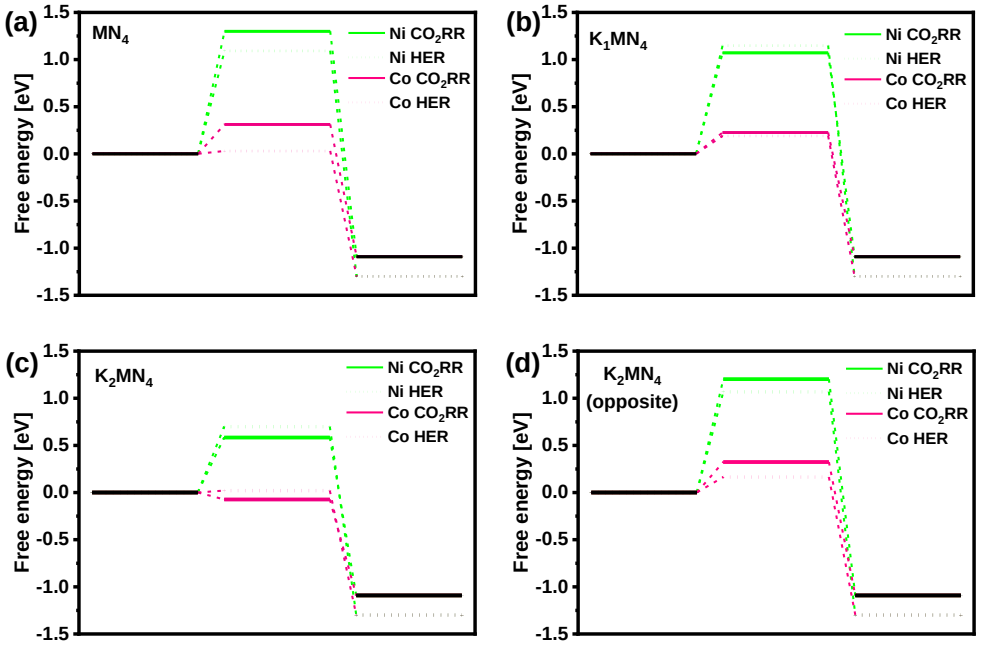

Figure 4. Reaction energy diagram for CO_2RR and HER for tetrapyrrolic (a) pristine MN_4, (b) K_1MN_4 , (c) K_2MN_4 and (d) K_2MN_4 with adsorbates on the opposite face. The intermediates shown are *COOH for CO_2RR and *H for HER.

Lastly, the performance stability of Ni-N-C_1000 and Co-N-C_1000 catalysts was evaluated in a 100 h continuous operation under an applied potential of -0.65 V_{RHE} (Figure 5). The LSVs measured before and after 100 h tests for both catalysts are provided in Figure S15. Both catalysts exhibit excellent performance stability, largely maintaining activity as well as selectivity (Figure 5). The initial current density for Ni-N-C_1000 catalyst is -3.15 mA cm^{-2} with an FE_{CO} of 95%. After 100 h of testing, the current density is still -2.91 mA cm^{-2} at 92.5% Faraday efficiency (Figure 5a), showing 92.5% and 97.6% retentions of current density and FE_{CO} values, respectively, (Figure 5b). These results show a high-performance stability and selectivity of this Ni single atom catalyst. Similarly, Co-N-C_1000 is also found to perform with remarkable stability of current density and product selectivity (Figure 5c and d). The current density remains almost stable with an initial value of -2.69 mA cm^{-2} and only slightly changed -2.65 mA cm^{-2} after 100 h of operation, i.e. showing a very high retention

of 98.5%. The retention of CO Faraday efficiency is also very high (96.5%) with initial and final values of FE_{CO} of 66.5% and 64.2%.

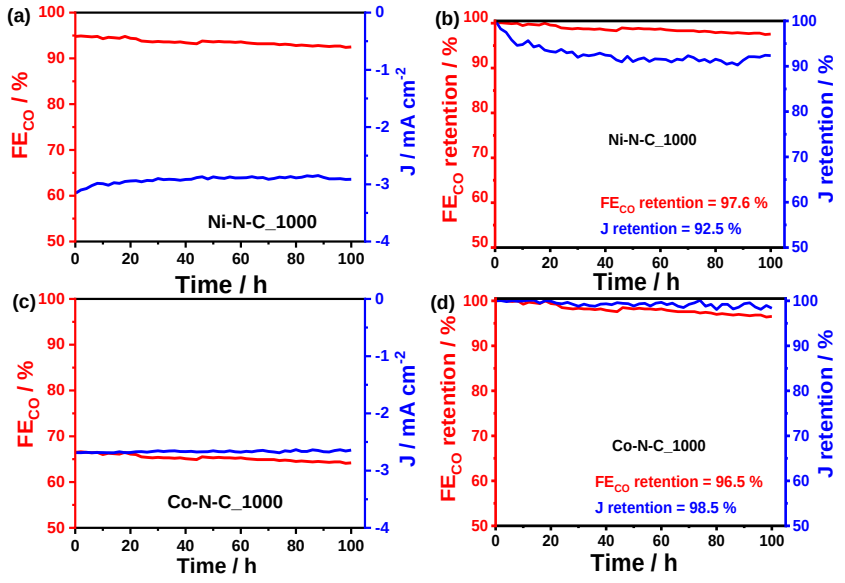

Figure 5. Performance stability tests at an applied potential of -0.65 V_{RHE}. CO Faraday efficiency and current density of (a) Ni-N-C_1000 and (c) Co-N-C_1000. Corresponding retention values of both these parameters for 100 h operation (b) Ni-N-C_1000 and (d) Co-N-C_1000. Catalyst loadings were 0.25 mg cm^{-2}.

Conclusions

The present study allows for 1) a few general statements on the preparation and evaluation of atomically dispersed M-N-C catalysts, and 2) the conclusion that atomically dispersed tetrapyrrolic Ni-N-C catalysts are generally more promising candidates for the selective CO_2 reduction to CO in aqueous media than atomically dispersed tetrapyrrolic Co-N-C catalyst. The employment of identical active site imprinted nitrogen-doped carbons as solid-state ligand leads to a deconvolution of morphological factors from the intrinsic properties of single atom sites with deviating active metals. The active site imprinting/ion-exchange strategy therefore allows for the ranking of intrinsic catalytic properties (activity, selectivity, and stability) within the family of atomically dispersed M-N-C catalysts. Herein, the size of the imprinting metal ion compared to the target metal ions needs to be

considered. Possibly related to the retention of active site geometry upon heat treatment, exchange of Mg^{2+} ions (72 pm) with Ni^{2+} ions (69 pm) is more easily obtained than with Co^{2+} ions (74.5 pm), while coordination sites of carbon supports prepared at higher temperature are more easily coordinated, coming with the costs of lower metal loadings. The composition of the carbon support also has a strong effect on the specific activity of active sites (strong metal-support interactions or more likely limited site accessibility), herein more than compensating the reduced metal loading. Compared to isomorphic Ni-N-Cs, the prepared Co-N-Cs consistently showed an onset of the electrocatalytic hydrogen evolution at lower overpotential, leading to more competition with the targeted CO_2 reduction. Consequently, the CO-selectivity of Co-N-Cs is much smaller than that of Ni-N-Cs. For the best set of catalysts, the Ni-N-C shows almost twice the turnover frequency compared to the isomorphic Co-N-C (1.16 s^{-1} compared to 0.51 s^{-1} at -0.8 V_{RHE}). The high activity and CO_2RR selectivity of Ni-N-Cs are further supported by DFT calculations, from which interactions between adsorbates with metal ions are shown to be crucial for elucidating the catalytic performance for NiN_4 sites. As a result, the Ni-N-C catalyst obtained with the new synthetic strategy is among the most active, selective, and stable ones reported catalysts of it´s class.

Supporting Information

Experimental section including catalyst synthesis, characterisation, and electrochemical tests details. SEM, TEM and elemental mapping, EXAFS fitting parameters, additional XPS, electrochemical CO_2 reduction results, additional DFT results.

Acknowledgement

SAA would like to acknowledge the 2020 Post-Doc. Development Program of Pusan National University. JLL acknowledges the Elsa-Neumann scholarship for financial support and HLRN for high performance computing

resources. Funding by the German Research Foundation (DFG) within the framework of the priority program SPP 2240 (research project FE 1590/1-1) is gratefully acknowledged.

Data availability: The data used in the production of the figures in this paper are available for download [DOI inserted after acceptance].

Table of Contents

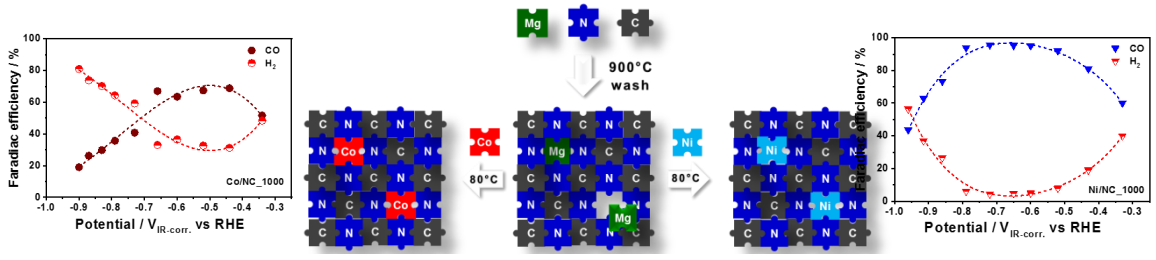

Uncategorized References

(1) Markewitz, P.; Kuckshinrichs, W.; Leitner, W.; Linssen, J.; Zapp, P.; Bongartz, R.; Schreiber, A.; Müller, T. E. Worldwide innovations in the development of carbon capture technologies and the utilization of CO2. *Energy & Environmental Science* **2012**, *5* (6). DOI: 10.1039/c2ee03403d.
(2) Wu, J.; Sharifi, T.; Gao, Y.; Zhang, T.; Ajayan, P. M. Emerging Carbon-Based Heterogeneous Catalysts for Electrochemical Reduction of Carbon Dioxide into Value-Added Chemicals. *Adv Mater* **2019**, *31* (13), e1804257. DOI: 10.1002/adma.201804257.
(3) Qiao, J.; Liu, Y.; Hong, F.; Zhang, J. A review of catalysts for the electroreduction of carbon dioxide to produce low-carbon fuels. *Chem Soc Rev* **2014**, *43* (2), 631-675. DOI: 10.1039/c3cs60323g.
(4) Abbas, S. A.; Kim, S.-H.; Saleem, H.; Ahn, S.-H.; Jung, K.-D. Preparation of Metal Amalgam Electrodes and Their Selective Electrocatalytic CO2 Reduction for Formate Production. *Catalysts* **2019**, *9* (4). DOI: 10.3390/catal9040367.
(5) Zhang, W.; Hu, Y.; Ma, L.; Zhu, G.; Wang, Y.; Xue, X.; Chen, R.; Yang, S.; Jin, Z. Progress and Perspective of Electrocatalytic CO2 Reduction for Renewable Carbonaceous Fuels and Chemicals. *Adv Sci (Weinh)* **2018**, *5* (1), 1700275. DOI: 10.1002/advs.201700275.
(6) Zhu, X.; Li, Y. Review of two-dimensional materials for electrochemical CO2 reduction from a theoretical perspective. *WIREs Computational Molecular Science* **2019**, *9* (6), e1416. DOI: 10.1002/wcms.1416.
(7) United States Environmental Protection Agency. *Green chemistry's 12 principles*. 2017. https://www.epa.gov/greenchemistry/basics-green-chemistry#twelve (accessed 2020 25 May).
(8) Cui, H.; Guo, Y.; Guo, L.; Wang, L.; Zhou, Z.; Peng, Z. Heteroatom-doped carbon materials and their composites as electrocatalysts for CO2 reduction. *Journal of Materials Chemistry A* **2018**, *6* (39), 18782-18793, 10.1039/C8TA07430E. DOI: 10.1039/C8TA07430E.
(9) Yang, X.-F.; Wang, A.; Qiao, B.; Li, J.; Liu, J.; Zhang, T. Single-Atom Catalysts: A New Frontier in Heterogeneous Catalysis. *Accounts of Chemical Research* **2013**, *46* (8), 1740-1748. DOI: 10.1021/ar300361m.
(10) Francke, R.; Schille, B.; Roemelt, M. Homogeneously Catalyzed Electroreduction of Carbon Dioxide-Methods, Mechanisms, and Catalysts. *Chem Rev* **2018**, *118* (9), 4631-4701. DOI: 10.1021/acs.chemrev.7b00459.
(11) Hu, X. M.; Ronne, M. H.; Pedersen, S. U.; Skrydstrup, T.; Daasbjerg, K. Enhanced Catalytic Activity of Cobalt Porphyrin in CO2 Electroreduction upon Immobilization on Carbon Materials. *Angew Chem Int Ed Engl* **2017**, *56* (23), 6468-6472. DOI: 10.1002/anie.201701104.
(12) Su, X.; Yang, X. F.; Huang, Y.; Liu, B.; Zhang, T. Single-Atom Catalysis toward Efficient CO2 Conversion to CO and Formate Products. *Acc Chem Res* **2019**, *52* (3), 656-664. DOI: 10.1021/acs.accounts.8b00478.
(13) Li, J.; Pršlja, P.; Shinagawa, T.; Martin Fernandez, A. J.; Krumeich, F.; Artyushkova, K.; Atanassov, P.; Zitolo, A.; Zhou, Y.; García-Muelas, R. Volcano trend in electrocatalytic CO2 reduction activity over atomically dispersed metal sites on nitrogen-doped carbon. *ACS Catalysis* **2019**, *9* (11), 10426-10439.
(14) Li, J.; Zitolo, A.; Garces-Pineda, F. A.; Asset, T.; Kodali, M.; Tang, P.; Arbiol, J.; Galán-Mascarós, J. R.; Atanassov, P.; Zenyuk, I. V. Metal oxide clusters on nitrogen-doped carbon are highly selective for CO2 electroreduction to CO. *ACS Catalysis* **2021**, *11* (15), 10028-10042.
(15) Varela, A. S.; Ju, W.; Bagger, A.; Franco, P.; Rossmeisl, J.; Strasser, P. Electrochemical Reduction of CO2 on Metal-Nitrogen-Doped Carbon Catalysts. *ACS Catalysis* **2019**, *9* (8), 7270-7284. DOI: 10.1021/acscatal.9b01405.
(16) Yang, F.; Song, P.; Liu, X.; Mei, B.; Xing, W.; Jiang, Z.; Gu, L.; Xu, W. Highly efficient CO2 electroreduction on ZnN4-based single-atom catalyst. *Angewandte Chemie International Edition* **2018**, *57* (38), 12303-12307.
(17) Guo, Y.; Yang, H.; Zhou, X.; Liu, K.; Zhang, C.; Zhou, Z.; Wang, C.; Lin, W. Electrocatalytic reduction of CO 2 to CO with 100% faradaic efficiency by using pyrolyzed zeolitic imidazolate frameworks supported on carbon nanotube networks. *Journal of Materials Chemistry A* **2017**, *5* (47), 24867-24873.
(18) Zhang, Z.; Xiao, J.; Chen, X. J.; Yu, S.; Yu, L.; Si, R.; Wang, Y.; Wang, S.; Meng, X.; Wang, Y.; et al. Reaction Mechanisms of Well-Defined Metal-N4 Sites in Electrocatalytic CO2 Reduction. *Angew Chem Int Ed Engl* **2018**, *57* (50), 16339-16342. DOI: 10.1002/anie.201808593.

(19) Pan, F.; Zhang, H.; Liu, K.; Cullen, D.; More, K.; Wang, M.; Feng, Z.; Wang, G.; Wu, G.; Li, Y. Unveiling active sites of CO2 reduction on nitrogen-coordinated and atomically dispersed iron and cobalt catalysts. *Acs Catalysis* **2018**, *8* (4), 3116-3122.
(20) Cheng, Y.; Zhao, S.; Johannessen, B.; Veder, J. P.; Saunders, M.; Rowles, M. R.; Cheng, M.; Liu, C.; Chisholm, M. F.; De Marco, R.; et al. Atomically Dispersed Transition Metals on Carbon Nanotubes with Ultrahigh Loading for Selective Electrochemical Carbon Dioxide Reduction. *Adv Mater* **2018**, *30* (13), e1706287. DOI: 10.1002/adma.201706287.
(21) Yang, H. B.; Hung, S.-F.; Liu, S.; Yuan, K.; Miao, S.; Zhang, L.; Huang, X.; Wang, H.-Y.; Cai, W.; Chen, R.; et al. Atomically dispersed Ni(i) as the active site for electrochemical CO2 reduction. *Nature Energy* **2018**, *3* (2), 140-147. DOI: 10.1038/s41560-017-0078-8.
(22) Hursan, D.; Samu, A. A.; Janovak, L.; Artyushkova, K.; Asset, T.; Atanassov, P.; Janaky, C. Morphological Attributes Govern Carbon Dioxide Reduction on N-Doped Carbon Electrodes. *Joule* **2019**, *3* (7), 1719-1733. DOI: 10.1016/j.joule.2019.05.007.
(23) Ramaswamy, N.; Tylus, U.; Jia, Q.; Mukerjee, S. Activity descriptor identification for oxygen reduction on nonprecious electrocatalysts: linking surface science to coordination chemistry. *Journal of the American Chemical Society* **2013**, *135* (41), 15443-15449.
(24) Mun, Y.; Lee, S.; Kim, K.; Kim, S.; Lee, S.; Han, J. W.; Lee, J. Versatile strategy for tuning ORR activity of a single Fe-N4 site by controlling electron-withdrawing/donating properties of a carbon plane. *Journal of the American Chemical Society* **2019**, *141* (15), 6254-6262.
(25) Mehmood, A.; Pampel, J.; Ali, G.; Ha, H. Y.; Ruiz‐Zepeda, F.; Fellinger, T. P. Facile Metal Coordination of Active Site Imprinted Nitrogen Doped Carbons for the Conservative Preparation of Non‐Noble Metal Oxygen Reduction Electrocatalysts. *Advanced Energy Materials* **2018**, *8* (9), 1701771.
(26) Menga, D.; Ruiz-Zepeda, F.; Moriau, L.; Sala, M.; Wagner, F.; Koyuturk, B.; Bele, M.; Petek, U.; Hodnik, N.; Gaberscek, M.; et al. Active-Site Imprinting: Preparation of Fe-N-C Catalysts from Zinc Ion-Templated Ionothermal Nitrogen-Doped Carbons. *ADVANCED ENERGY MATERIALS* **2019**, *9* (43). DOI: 10.1002/aenm.201902412.
(27) Menga, D.; Low, J. L.; Li, Y.-S.; Arčon, I.; Koyutürk, B.; Wagner, F.; Ruiz-Zepeda, F.; Gaberšček, M.; Paulus, B.; Fellinger, T.-P. Resolving the Dilemma of Fe–N–C Catalysts by the Selective Synthesis of Tetrapyrrolic Active Sites via an Imprinting Strategy. *Journal of the American Chemical Society* **2021**, *143* (43), 18010-18019. DOI: 10.1021/jacs.1c04884.
(28) Mehmood, A.; Gong, M.; Jaouen, F.; Roy, A.; Zitolo, A.; Khan, A.; Sougrati, M.-T.; Primbs, M.; Bonastre, A. M.; Fongalland, D. High loading of single atomic iron sites in Fe–NC oxygen reduction catalysts for proton exchange membrane fuel cells. *Nature Catalysis* **2022**, *5* (4), 311-323.
(29) Sing, K. S. W. Reporting physisorption data for gas/solid systems with special reference to the determination of surface area and porosity (Recommendations 1984). *Pure and Applied Chemistry* **1985**, *57* (4), 603-619. DOI: https://doi.org/10.1351/pac198557040603.
(30) Abbas, S. A.; Jung, K.-D. Preparation of mesoporous microspheres of NiO with high surface area and analysis on their pseudocapacitive behavior. *Electrochimica Acta* **2016**, *193*, 145-153. DOI: 10.1016/j.electacta.2016.02.054.
(31) Pampel, J.; Mehmood, A.; Antonietti, M.; Fellinger, T. P. Ionothermal template transformations for preparation of tubular porous nitrogen doped carbons. *Materials Horizons* **2017**, *4* (3), 493-501. DOI: 10.1039/c6mh00592f.
(32) Ota, E.; Otani, S. Carbonization of aromatic compounds in molten salt. *Chemistry Letters* **1975**, *4* (3), 241-242.
(33) Fechler, N.; Fellinger, T. P.; Antonietti, M. "Salt templating": a simple and sustainable pathway toward highly porous functional carbons from ionic liquids. *Adv Mater* **2013**, *25* (1), 75-79. DOI: 10.1002/adma.201203422.
(34) Pampel, J.; Mehmood, A.; Antonietti, M.; Fellinger, T.-P. Ionothermal template transformations for preparation of tubular porous nitrogen doped carbons. *Materials Horizons* **2017**, *4* (3), 493-501.

(35) Mehmood, A.; Ali, G.; Koyutürk, B.; Pampel, J.; Chung, K. Y.; Fellinger, T.-P. Ion-Sieving Nanoporous Nitrogen Doped Carbons with Enhanced Capacity for Sodium Ion Battery Anodes. *Energy Storage Materials* **2020**.
(36) Kuhn, P.; Antonietti, M.; Thomas, A. Porous, covalent triazine-based frameworks prepared by ionothermal synthesis. *Angewandte Chemie International Edition* **2008**, *47* (18), 3450-3453.
(37) Liu, X.; Giordano, C.; Antonietti, M. A Facile Molten-Salt Route to Graphene Synthesis. *Small* **2014**, *10* (1), 193-200.
(38) Jeong, H. Y.; Balamurugan, M.; Choutipalli, V. S. K.; Jo, J.; Baik, H.; Subramanian, V.; Kim, M.; Sim, U.; Nam, K. T. Tris(2-benzimidazolylmethyl)amine-Directed Synthesis of Single-Atom Nickel Catalysts for Electrochemical CO Production from CO2. *Chemistry* **2018**, *24* (69), 18444-18454. DOI: 10.1002/chem.201803615.
(39) Li, H.; Xiao, N.; Hao, M.; Song, X.; Wang, Y.; Ji, Y.; Liu, C.; Li, C.; Guo, Z.; Zhang, F.; et al. Efficient CO2 electroreduction over pyridinic-N active sites highly exposed on wrinkled porous carbon nanosheets. *Chemical Engineering Journal* **2018**, *351*, 613-621. DOI: 10.1016/j.cej.2018.06.077.
(40) Lu, C.; Yang, J.; Wei, S.; Bi, S.; Xia, Y.; Chen, M.; Hou, Y.; Qiu, M.; Yuan, C.; Su, Y.; et al. Atomic Ni Anchored Covalent Triazine Framework as High Efficient Electrocatalyst for Carbon Dioxide Conversion. *Advanced Functional Materials* **2019**, *29* (10). DOI: 10.1002/adfm.201806884.
(41) Farges, F.; Brown, G. E.; Petit, P.-E.; Munoz, M. Transition elements in water-bearing silicate glasses/melts. part I. a high-resolution and anharmonic analysis of Ni coordination environments in crystals, glasses, and melts. *Geochimica et Cosmochimica Acta* **2001**, *65* (10), 1665-1678. DOI: https://doi.org/10.1016/S0016-7037(00)00625-6.
(42) Low, J. L.; Paulus, B. Computational Modelling of Pyrrolic MN4 Motifs Embedded in Graphene for Catalyst Design. *Catalysts* **2023**, *13* (3), 566.
(43) Ju, W.; Bagger, A.; Hao, G. P.; Varela, A. S.; Sinev, I.; Bon, V.; Roldan Cuenya, B.; Kaskel, S.; Rossmeisl, J.; Strasser, P. Understanding activity and selectivity of metal-nitrogen-doped carbon catalysts for electrochemical reduction of CO2. *Nat Commun* **2017**, *8* (1), 944. DOI: 10.1038/s41467-017-01035-z.
(44) Pan, F.; Xiang, X.; Li, Y. Nitrogen Coordinated Single Atomic Metals Supported on Nanocarbons: A New Frontier in Electrocatalytic CO2 Reduction. *Engineered Science* **2018**. DOI: 10.30919/es.1804232.
(45) Li, X.; Bi, W.; Chen, M.; Sun, Y.; Ju, H.; Yan, W.; Zhu, J.; Wu, X.; Chu, W.; Wu, C.; et al. Exclusive Ni-N4 Sites Realize Near-Unity CO Selectivity for Electrochemical CO2 Reduction. *J Am Chem Soc* **2017**, *139* (42), 14889-14892. DOI: 10.1021/jacs.7b09074.
(46) Fei, H.; Dong, J.; Chen, D.; Hu, T.; Duan, X.; Shakir, I.; Huang, Y.; Duan, X. Single atom electrocatalysts supported on graphene or graphene-like carbons. *Chem Soc Rev* **2019**, *48* (20), 5207-5241. DOI: 10.1039/c9cs00422j.
(47) Nishihara, H.; Hirota, T.; Matsuura, K.; Ohwada, M.; Hoshino, N.; Akutagawa, T.; Higuchi, T.; Jinnai, H.; Koseki, Y.; Kasai, H.; et al. Synthesis of ordered carbonaceous frameworks from organic crystals. *Nat Commun* **2017**, *8* (1), 109. DOI: 10.1038/s41467-017-00152-z.
(48) Jia, M.; Choi, C.; Wu, T.-S.; Ma, C.; Kang, P.; Tao, H.; Fan, Q.; Hong, S.; Liu, S.; Soo, Y.-L.; et al. Carbon-supported Ni nanoparticles for efficient CO2 electroreduction. *Chemical Science* **2018**, *9* (47), 8775-8780, 10.1039/C8SC03732A. DOI: 10.1039/C8SC03732A.
(49) Yang, J.; Qiu, Z.; Zhao, C.; Wei, W.; Chen, W.; Li, Z.; Qu, Y.; Dong, J.; Luo, J.; Li, Z. In situ thermal atomization to convert supported nickel nanoparticles into surface-bound nickel single-atom catalysts. *Angewandte Chemie International Edition* **2018**, *57* (43), 14095-14100.
(50) Vijay, S.; Ju, W.; Brückner, S.; Tsang, S.-C.; Strasser, P.; Chan, K. Unified mechanistic understanding of CO2 reduction to CO on transition metal and single atom catalysts. *Nature Catalysis* **2021**, *4* (12), 1024-1031.
(51) Resasco, J.; Chen, L. D.; Clark, E.; Tsai, C.; Hahn, C.; Jaramillo, T. F.; Chan, K.; Bell, A. T. Promoter effects of alkali metal cations on the electrochemical reduction of carbon dioxide. *Journal of the American Chemical Society* **2017**, *139* (32), 11277-11287.
(52) Shin, S.-J.; Choi, H.; Ringe, S.; Won, D. H.; Oh, H.-S.; Kim, D. H.; Lee, T.; Nam, D.-H.; Kim, H.; Choi, C. H. A unifying mechanism for cation effect modulating C1 and C2 productions from CO2 electroreduction. *Nature Communications* **2022**, *13* (1), 5482.

(53) Monteiro, M. C.; Dattila, F.; Hagedoorn, B.; García-Muelas, R.; López, N.; Koper, M. T. Absence of CO2 electroreduction on copper, gold and silver electrodes without metal cations in solution. *Nature Catalysis* **2021**, *4* (8), 654-662.
(54) Nørskov, J. K.; Rossmeisl, J.; Logadottir, A.; Lindqvist, L.; Kitchin, J. R.; Bligaard, T.; Jonsson, H. Origin of the overpotential for oxygen reduction at a fuel-cell cathode. *The Journal of Physical Chemistry B* **2004**, *108* (46), 17886-17892.
(55) Qin, X.; Vegge, T.; Hansen, H. A. CO2 activation at Au (110)–water interfaces: An ab initio molecular dynamics study. *The Journal of Chemical Physics* **2021**, *155* (13).
(56) Qin, X.; Vegge, T.; Hansen, H. A. Cation-coordinated inner-sphere CO2 electroreduction at Au–water interfaces. *Journal of the American Chemical Society* **2023**, *145* (3), 1897-1905.
(57) Qin, X.; Hansen, H. A.; Honkala, K.; Melander, M. M. Cation-induced changes in the inner-and outer-sphere mechanisms of electrocatalytic CO2 reduction. *Nature Communications* **2023**, *14* (1), 7607.

Supplementary Information

On the intrinsic CO_2 reduction activity of atomically-dispersed Ni-N-C and Co-N-C electrocatalysts

Asad Mehmood[a†*], Syed Asad Abbas[b†], Jian Liang Low[c], Simon Dietzmann[a], Ghulam Ali[d], Beate Paulus[c], Keun Hwa Chae[e], Ki Min Nam[b], Kwang-Deog Jung[f], and Tim-Patrick Fellinger[a*]

[a] Division 3.6 Electrochemical Energy Materials, Bundesanstalt für Materialforschung und -prüfung (BAM), 12203 Berlin, Germany

[b] Department of Chemistry and Chemistry Institute of Functional Materials, Pusan National University, Busan 46241, Republic of Korea.

[c] Institute of Chemistry and Biochemistry, Freie Universität Berlin, Arnimallee 22, 14195 Berlin, Germany.

[d] US-Pakistan Center for Advanced Studies in Energy (USPCASE), National University of Science and Technology (NUST), H-12, Islamabad, 44000, Pakistan.

[e] Advanced Analysis Center, Korea Institute of Science and Technology (KIST), Hwarangno 14-gil 5, Seongbuk-gu, Seoul 02792, Republic of Korea.

[f] Center for Clean Energy and Chemical Engineering, Korea Institute of Science and Technology (KIST), Hwarangno 14-gil 5, Seongbuk-gu, Seoul 02792, Republic of Korea.

*Correspondence to: Asad Mehmood. Email: asad.mehmood@bam.de and Tim-Patrick Fellinger. Email: tim-patrick.fellinger@bam.de

Table of Contents

19. **Table S7**: Activity comparison of recently reported high performance single atom catalysts in H-Type electrochemical cell for CO_2 reduction reaction.

20. **Figure S12**: Free energy diagram for the reductive adsorption of K^+ ions on tetrapyrrolic (green) and tetrapyridinic (blue) NiN_4 sites calculated with B3LYP-D3(BJ)/def2-TZVP and COSMO solvation model.

21. **Figure S13**: Free energy diagrams for CO_2RR and HER tetrapyridinic MN_4 and K_1MN_4 sites calculated with B3LYP-D3(BJ)/def2-TZVP and COSMO solvation model.

22. **Figure S14**: Structures of *COOH and *H adsorbed on tetrapyrrolic (a) pristine NiN_4, (b) K_1NiN_4, (c) K_2NiN_4 on the same face and (d) K_2NiN_4 on the opposite face. Geometries are obtained with B3LYP-D3(BJ)/def2-SVP with COSMO solvation model.

23. **Figure S15:** LSVs of (a) Ni-N-C_1000 and (b) Co-N-C_1000 catalysts before and after 100 h stability test measured under nitrogen and CO_2 saturation condition in 0.1 M $KHCO_3$ electrolyte.

24. Supporting References

1. Experimental Procedures

1.1. ***Synthesis of electrocatalysts*:** In the first step, carbon nanosheets were prepared by mixing imidazole (99 %, Sigma Aldrich) as combined C/N precursor with $MgCl_2 \cdot 6\ H_2O$ (99-102 %, Sigma Aldrich) and thorough grinding in a glove box. A weight ratio of imidazole and magnesium chloride salt of 1:10 was chosen. In the ionothermal synthesis route, the inorganic salt system (in this case $MgCl_2 \cdot 6\ H_2O$) acts simultaneously as a solvent and porogen, while the Lewis-acidic Mg^{2+} also acts as a coordination-site-imprinting ion. The precursor-salt mixture was then carbonized either at 800 or 1000 ^oC in a furnace under nitrogen environment. The heating rate was 2.5 K min^{-1} and the dwelling time was 1 h. Afterwards, the pyrolyzed product (2-3 g monolith consisting of NC mixed with Mg salt) was stirred in 2 M H_2SO_4 (1 L) overnight and then washed with excess deionized water to remove the salt and dried in a vacuum oven. The as-obtained NC nanosheets with Mg imprinted sites were named as Mg-N-C_X, where X corresponds to the synthesis temperature (800 and 1000 ^oC), e.g. Mg-N-C_800 represents the sample synthesized at 800 ^oC. In the second step, Ni and Co active centers were coordinated to the coordination-site-imprinted Mg-N-C nanosheets. A specified amount of carbon nanosheets (generally 50 mg) was dispersed in 5 mM solution of $NiCl_2 \cdot 6H_2O$ (98 %, Sigma Aldrich) in methanol and refluxed overnight. Subsequently, washing in deionized water was carried out multiple times and finally all the samples were subjected to a second heat-treatment step at 900 ^oC in N_2 environment for 1 h to obtain Ni-N-C_800 and Ni-N-C_1000 catalysts. For preparing Co-N-C catalysts, $CoCl_2 \cdot 6H_2O$ (98 %, Sigma Aldrich) salt was used instead while rest of the procedure was unchanged.

1.2. ***Physicochemical characterization*:** Nitrogen sorption experiments were performed using Belsorp mini II, BEL Japan. All samples were outgassed at 150 ^oC prior to the measurements. Specific surface areas (SSAs) were calculated using Brunauer-Emmett-Teller (BET) method. The values of total pore volumes (TPV) were calculated at p $p_0^{-1} \sim 0.98$. X-ray photoelectron spectroscopy (XPS) was performed using PHI 5000 VersaProbe (Ulvac-PHI) with a background pressure of 2×10^{-7} and a spot size of 100 µm x 100 µm. C 1s peak (284.6 eV) was used for the data calibration. Morphology of carbon sheets was evaluated by scanning electron microscopy (SEM, Zeiss Gemini 1550). Transmission electron microscopy (TEM) and elemental mapping were performed using a Talos TEM (F200X, EFI Co.) with an accelerating voltage of 200 kV. The single atom structures of Ni and Co sites were probed by high-resolution aberration-corrected scanning TEM (ARSTEM) and electron energy loss spectroscopy (EELS) using a Titan TEM (TM 80-300). The local coordination environment of Ni and Co atoms were probed by X-ray absorption spectroscopy (XAS). Ni and Co K-edges were measured at KIST-PAL 1D beamline of Pohang Light Source (PLS-II which operates with an electron beam energy of 3 GeV and a beam current of 400 mA), South Korea. The beamline is equipped with a double crystal monochromator (DCM) consisting of a pair of Si(111) crystal and operates with an X-ray energy range of 4-16 KeV, an energy resolution of 2×10^{-4}, and a beam size of 1×0.5 mm. The XAS data of samples were taken in transmission mode. Ni(II) phthalocyanine, Ni metal foil, Co(II) phthalocyanine and Co metal foil were also measured as reference materials.

1.3. ***Electrochemical measurements and product analysis*:** Electrochemical characterizations such as cyclic voltammetry, impedance analysis, and linear sweep voltammetry experiments were performed in a two compartment three electrode cell in N_2/CO_2 saturated 0.1 M $KHCO_3$ electrolyte. The catalyst inks were prepared by sonicating 5 mg of catalyst powder in a mixture of 50 µL Nafion suspension (5 wt.%, Sigma Aldrich) and 840 µL of ethanol (99.9%) for 30 minutes. The working electrode was prepared by drop casting 44.5 µL of homogenously dispersed catalyst ink on a glassy carbon of 1 x 1 cm^2 size to obtain a loading of 250 µg cm^{-2}. Cathode and anode chambers were separated by a Nafion 115 membrane. Saturated calomel electrode (SCE) was used as reference electrode. High purity CO_2 gas was introduced into the cathode chamber with a flow rate of 10 mL min^{-1}. Pt foil was used a counter electrode. All the electrochemical studies were performed using Ivium stat, Ivium technologies. Electrode potentials measured vs SCE were converted to the reversible hydrogen electrode (RHE) scale using the $E_{RHE} = E_{SCE} + 0.244 + (0.0591 \times pH)$, where pH of CO_2-saturated 0.1 M $KHCO_3$ solution was

pH 6.8 while that of the N_2-saturated 0.1 M $KHCO_3$ solution was pH 8.6. Cyclic voltammetry experiments were performed at the scan rate of 10 mVs^{-1}. Gaseous products from the electrochemical cell were analyzed using Younglin 6500 GC system equipped with RESTEK microsieve (RT-Msieve 5A) and a pulse discharged detector (PDD), helium gas with ultra-high purity was used as carrier gas. Liquid products were analyzed using ion chromatography (ICS-900 Dionex) with a column of Dionex IonPac AS19 RFIC using 0.02 M NaOH as the mobile electrolyte at the rate of 1.0 mL min^{-1}.

1.4. ***EXAFS fitting:*** XANES data evaluation and treatment was performed by using ATHENA program from Demeter package.[1] This includes background removal, energy calibration with Fe metal foil spectrum, and pre- and post-edge normalization. Further information on the local coordination environment was achieved by EXAFS. EXAFS curves were Fourier Transformed between 1.5-8.5 Å with a Hanning-type window, to obtain a radial distribution-like information. These were fitted with a DFT based model consisting of a central atom (Ni or Co) binding one or two OH groups in the axial positions and coordinated to four pyrrolic nitrogen atoms embedded in a planar carbon plane. The model was used to calculate the scattering paths by FEFF to be able to quantify the coordination number and bond-length. The goodness of the fit is determined by evaluating the reduced-χ^2 test and R-factor. The fitting range was kept between 1-3.6 Å that includes all the scattering paths displayed in the tables S1-S4. The degeneracy of the scattering path (which corresponds to the coordination number, N, in the case of single scattering paths) was varied until an amplitude reduction factor (S_0^2) of about 1 was achieved. The best results are displayed in the tables S1-S4.

1.5. ***DFT:*** We performed ab-initio calculations using unrestricted Kohn-Sham DFT as implemented in TURBOMOLE.[2] Calculations were performed using finite-sized graphene clusters with H-termination on boundary carbon atoms to minimize boundary effects.[3] The PBE0 functional[4, 5] was used to obtain EXAFS model structures and the B3LYP functional[6, 7], in combination with the COSMO solvation[8], was used for modelling electrochemical reactions. Grimme's dispersion correction with Becke-Johnson damping function D3(BJ) was applied in all cases.[9, 10] Geometry optimization was performed with the def2-SVP basis[11] with COSMO solvation. Vibrational frequencies were obtained with analytical frequency analysis with the def2-SVP basis without solvation.[12] Single point calculations were performed with the def2-TZVP basis to obtain energies and charges. The self-consistent field (SCF) convergence criteria were 10^{-7} E_h in total energy and 10^{-4} E_h in orbital energies. Convergence criteria for geometry optimization were 10^{-6} E_h in the energy and 10^{-3} a.u. in the maximum norm of the Cartesian gradient. The zero-point energies and Helmholtz free energies ($U - TS$) were approximated using the harmonic vibrational frequencies with a frequency scaling of 0.9614 to compensate the overestimation of vibrational frequencies of the B3LYP functional.[13] For linear gases (H_2, CO_2, CO), the enthalpy of an ideal gas at 298 K, 1 bar is assumed (0.09 eV) and the entropic contributions were obtained from the NIST database. All atomic structures were visualized with VESTA.[14]

1.6. ***Computational electrodes:*** For the modelling of electrochemical CO_2RR and HER, we applied the computational hydrogen electrode developed by Norskov *et al.*[15] In this approach, the free energy $G_{(H^+ + e^-)}$ for a reductive protonation step is defined to be

$$G^0_{(H^+ + e^-)} = \frac{1}{2} G^0_{H_2} - eU$$

where $G^0_{H_2}$ is the free energy of H_2 at standard temperature and pressure and U is the applied potential. For potentials measured against the reversible hydrogen electrode, the concentration of H^+ (*i.e.* pH) does not influence the free energies. For studying the K^+ adsorption, taking into consideration the standard reduction potential for potassium $E^0(K^+/K_s)$, we similarly define the free energy $G^0_{(K^+ + e^-)}$ to be

$$G^0_{(\mathrm{K^+ + e^-})} = G^0_{\mathrm{K_s}} - e\left(U - E^0(\mathrm{K^+/K_s})\right)$$

where U is the applied potential vs SHE. Since molecular DFT calculations cannot describe solids, we approximate the free energy $G_{\mathrm{K_s}}$ with the free energy of K atom, treated as monoatomic ideal gas, in combination with the atomization energy obtained from the NIST database.

$$G^0_{\mathrm{K_s}} = G^0_{\mathrm{K_g}} - \Delta_{atom} G_{\mathrm{K}}$$

Finally, to account for the non-standard concentrations, correction terms for the concentrations $[K^+]$ = 0.1 M and pH ($[H^+] = 10^{-6.8}$ M) were included to simulate the conditions in the electrochemical measurements

$$G_{(\mathrm{K^+ + e^-})} = G^0_{(\mathrm{K^+ + e^-})} + k_{\mathrm{B}} T \ln \frac{[\mathrm{H^+}]}{[\mathrm{K^+}]}$$

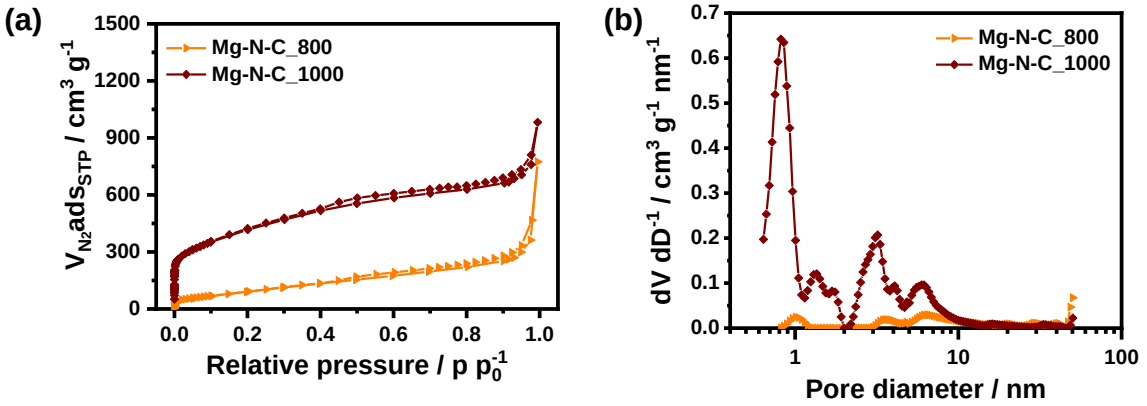

Figure S1: (a) N_2 adsorption-desorption isotherms of the Mg-N-C_800 and Mg-N-C_1000 samples and (b) their corresponding pore size distributions calculated by QSDFT method.

Table S1: Summary of surface areas and porosities of Mg-N-Cs, Ni and Co catalysts.

Sample	**S_{BET}**	**SSA_{QSDFT}**	**SA_{Ext}**	**$V_{micropore}$ (t-plot)**	**$V_{micropore}$ (QSDFT)**	**$V_{mesopore}$ (QSDFT) (calc.)**	**V_{total} (QSDFT, up to 50nm)**	**V_{total} (at p p$_0^{-1}$ ~0.98)**
	m^2 g^{-1}			cm^3 g^{-1}				
Mg-N-C_800	371	276	335	0.019	0.016	0.466	0.485	0.560
Mg-N-C_1000	1506	1343	1415	0.029	0.287	0.774	1.061	1.176
Co-NC_800	375	333	375	0.000	0.015	0.585	0.600	0.841
Co-NC_1000	1591	1329	1478	0.000	0.190	1.113	1.303	1.419
Ni-NC_800	287	235	287	0.000	0.006	0.633	0.639	0.968
Ni-NC_1000	1686	1684	1559	0.038	0.257	1.187	1.444	1.697

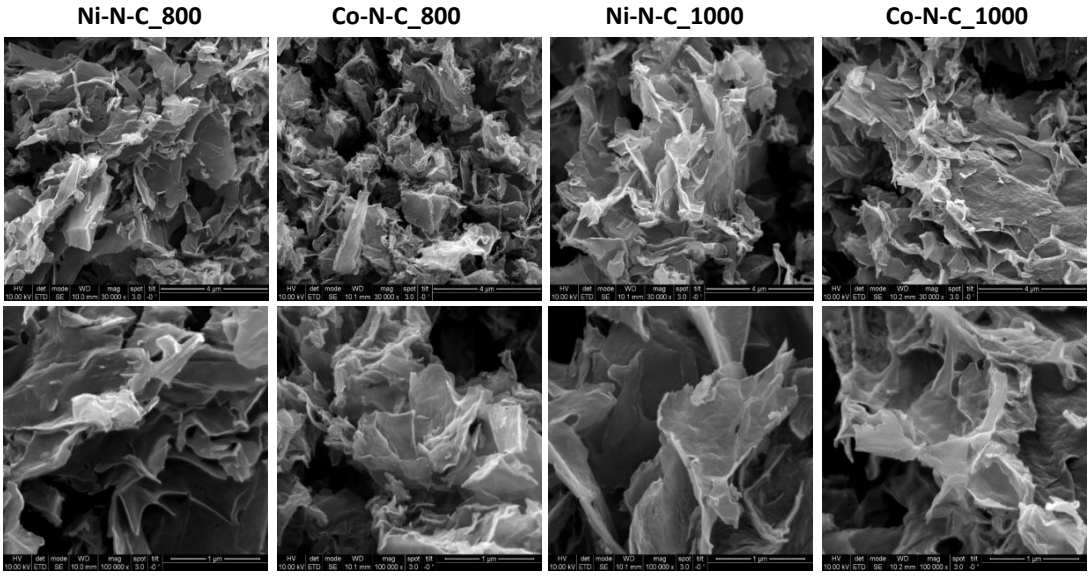

Figure S2: Scanning electron microscopy (SEM) images of Ni and Co catalysts.

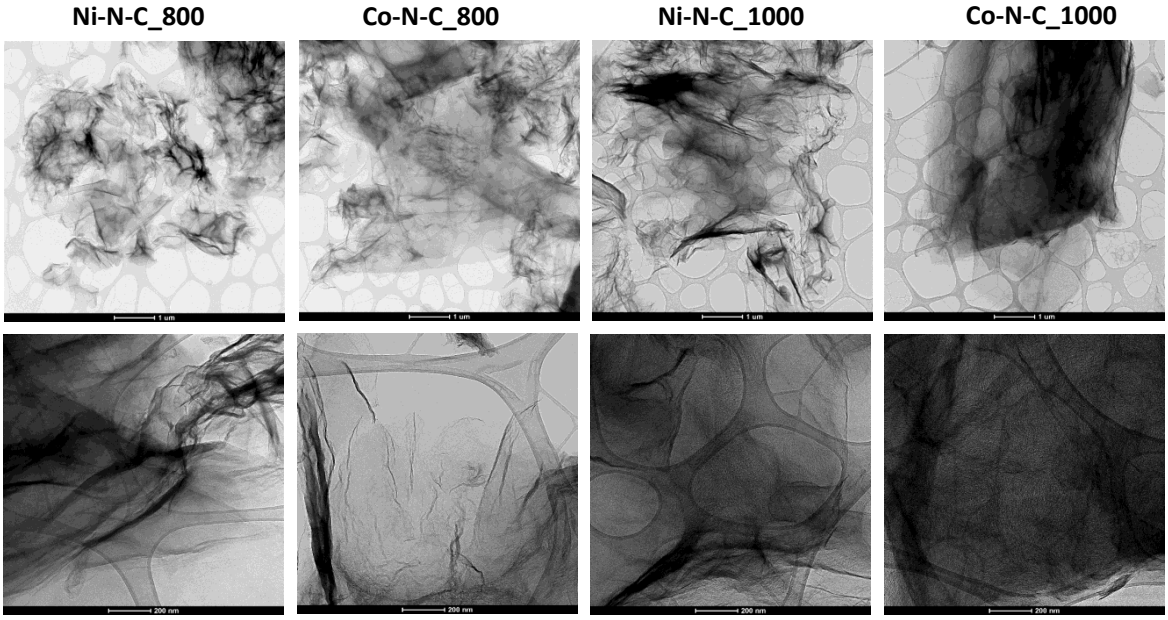

Figure S3: Transmission electron microscopy (TEM) images of Ni and Co catalysts.

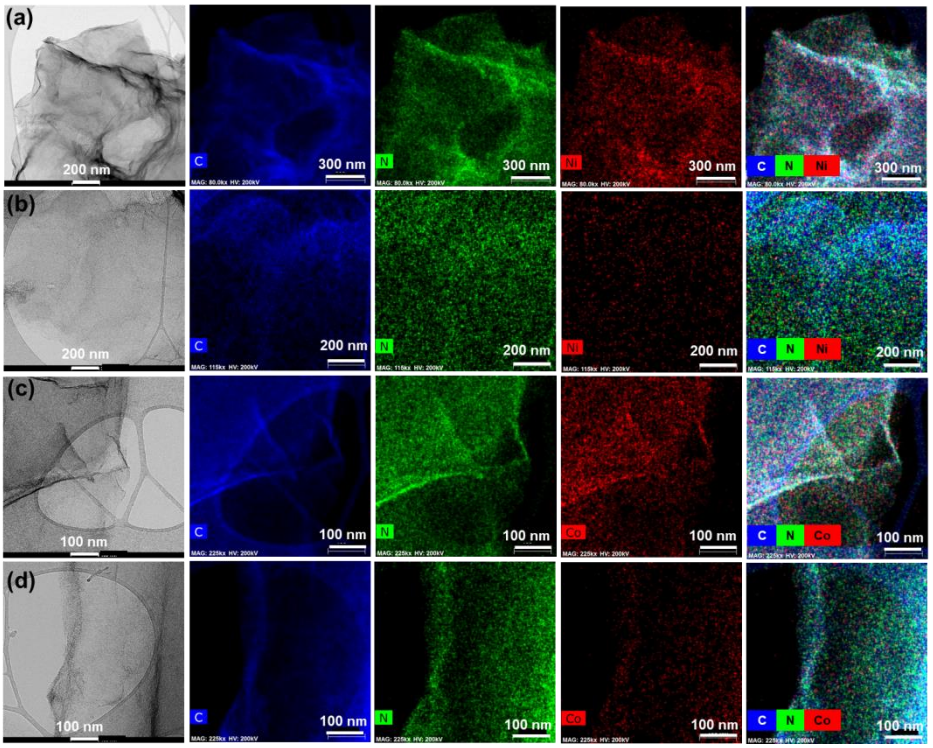

Figure S4: TEM images along with elemental mapping of (a) Ni-N-C_800, (b) Ni-N-C_1000, (c) Co-N-C_800 and (d) Co-N-C_1000 catalysts to visualize the homogeneous distribution of Ni and Co in porous carbon sheets.

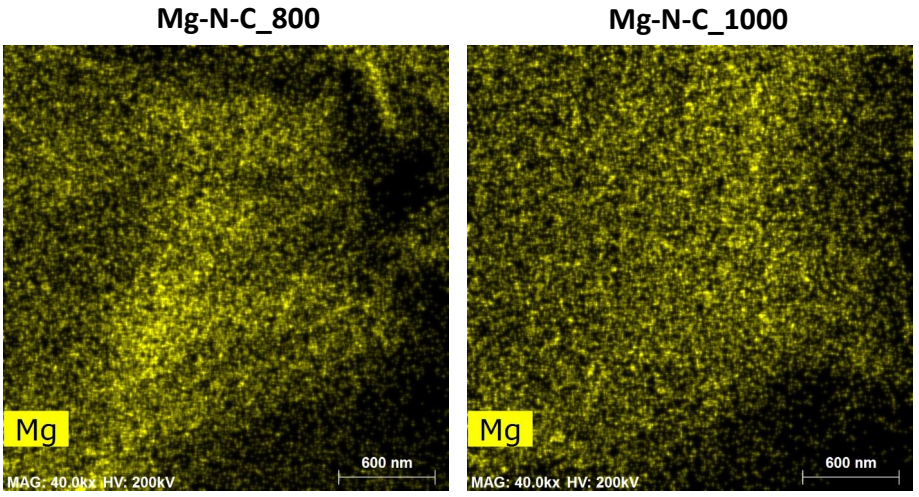

Figure S5: EDX mapping of Mg-N-C_800 and Mg-N-C_1000 before Ni and Co coordination to visualize the presence and distribution of Mg atoms in porous carbon sheets.

Table S2. Surface O and N contents of Mg-N-C scaffolds determined by XPS before Ni and Co coordination and subsequent activation. The absolute amounts of different types of nitrogen sites are calculated the deconvolution of high resolution N 1s XPS peaks. Mg metal contents are determined by EDX.

Sample	XPS		Deconvoluted N sites					EDX
	O-content [at.%]	N-content [at.%]	$N_{pyridinic}$ [at.%]	M-N_x [at.%]	$N_{pyrrolic}$ [at.%]	$N_{graphItic}$ [at.%]	N-oxide [at.%]	Mg-content [wt.%]
Mg-N-C_800	3.66	20.66	10.02	1.60	7.39	1.52	0.12	0.36
HT900-Mg-N-C_800	2.45	8.59	3.40	0.68	2.41	1.45	0.65	-
Mg-N-C_1000	3.70	5.36	1.91	0.20	1.31	1.42	0.52	0.17

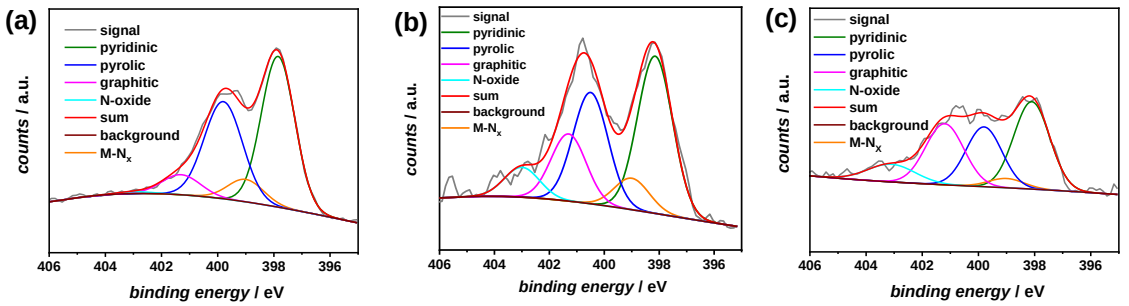

Figure S6: Deconvoluted XPS high resolution N 1s spectra of (a) Mg-N-C_800, (b) HT900- Mg-N-C _800 and (c) Mg-N-C_1000 samples.

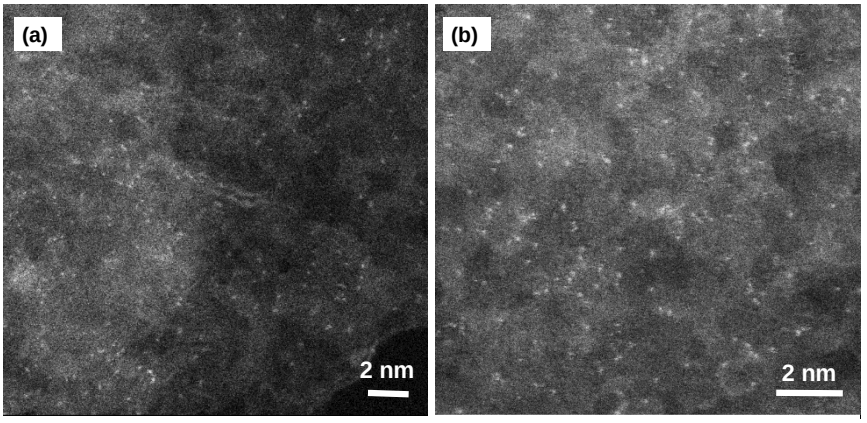

Figure S7: HR-STEM images of (a) Ni-N-C_1000 and (b) Co-N-C_1000.

Table S3. Structural information obtained from EXAFS by fitting the nearest coordination shells around Ni atoms in **Ni-N-C_800** with the pyrrolic model $(OH)NiN_4C_{12}$ consisting of a Ni atom binding one OH group in the axial positions and coordinated to four pyrrolic nitrogen atoms embedded in a planar carbon plane: degeneracy of the scattering path (N), interatomic distance from the fit (R) and from the model (Reff), and Debye-Waller factor (σ^2). The goodness-of-fit parameter is indicated by the R-factor 0.012. The amplitude reduction factor S_0^2 was 1.0 ± 0.2 in the R-range of 1-3.3 Å and k-range of 1.5-7.6 Å.

scattering path	N	R (Å)	Reff(Å)	σ^2 (Å^2)	
Ni-O	1	2.05	1.94	0.00808	single-scattering
Ni-N	4	2.06	1.96	0.00808	single-scattering
Ni-C	6	2.90	2.98	0.04127	single-scattering
Ni-C	2	2.93	3.01	0.04127	single-scattering

Table S4. Structural information obtained from EXAFS by fitting the nearest coordination shells around Ni atoms in **Ni-N-C_1000** with the pyrrolic model $(OH)_2NiN_4C_{12}$ consisting of a Ni atom binding two OH groups in the axial positions and coordinated to four pyrrolic nitrogen atoms embedded in a planar carbon plane: degeneracy of the scattering path (N), interatomic distance from the fit (R) and from the model (Reff), and Debye-Waller factor (σ^2). The goodness-of-fit parameter is indicated by the R-factor 0.010. The amplitude reduction factor S_0^2 was 1.1 ± 0.4 in the R-range of 1-3 Å and k-range of 1.5-8.5 Å.

scattering path	N	R (Å)	Reff(Å)	σ^2 (Å^2)	
Ni-O	2	1.81	1.85	0.01944	single-scattering
Ni-N	4	1.93	1.96	0.01944	single-scattering
Ni-H	2	2.25	2.29	0.01944	single-scattering
Ni-C	7	2.60	2.98	0.02298	single-scattering
Ni-C	1	2.97	3.00	0.01944	single-scattering

Table S5. Structural information obtained from EXAFS by fitting the nearest coordination shells around Ni atoms in **Co-N-C_800** with the pyrrolic model $(OH)_2CoN_4C_{12}$ consisting of a Co atom binding two OH groups in the axial positions and coordinated to four pyrrolic nitrogen atoms embedded in a planar carbon plane: degeneracy of the scattering path (N), interatomic distance from the fit (R) and from the model (Reff), and Debye-Waller factor (σ^2). The goodness-of-fit parameter is indicated by the R-factor 0.026. The amplitude reduction factor S_0^2 was defined to 0.70 in the R-range of 1.15-3.6 Å and k-range of 2.9-5.9 Å. The rbkg-value was set to 1.1.

scattering path	N	R (Å)	Reff(Å)	σ^2 (Å^2)	
Co-O	2	1.86	1.86	0.01143	single-scattering
Co-N	4	1.98	1.98	0.01143	single-scattering
Co-H	2	2.33	2.33	0.01143	single-scattering
Co-C	7	3.00	3.00	0.01143	single-scattering
Co-C	1	3.02	3.03	0.01143	single-scattering

Table S6. Structural information obtained from EXAFS by fitting the nearest coordination shells around Ni atoms in **Co-N-C_1000** with the pyrrolic model $(OH)_2CoN_4C_{12}$ consisting of a Co atom binding two OH groups in the axial positions and coordinated to four pyrrolic nitrogen atoms embedded in a planar carbon plane: degeneracy of the scattering path (N), interatomic distance from the fit (R) and from the model (Reff), and Debye-Waller factor (σ^2). The goodness-of-fit parameter is indicated by the R-factor 0.0080. The amplitude reduction factor S_0^2 was 0.71 ± 0.3 in the R-range of 1-3.3 Å and k-range of 1.5-7.5 Å

scattering path	N	R (Å)	Reff(Å)	σ^2 (Å^2)	
Co-O	2	1.83	1.86	0.00947	single-scattering
Co-N	4	1.95	1.98	0.00947	single-scattering
Co-H	2	2.30	2.33	0.00947	single-scattering
Co-C	7	2.74	3.00	0.05547	single-scattering
Co-C	1	2.77	3.03	0.05547	single-scattering
Co-N-C	16	3.14	3.17	0.00947	triangle-scattering

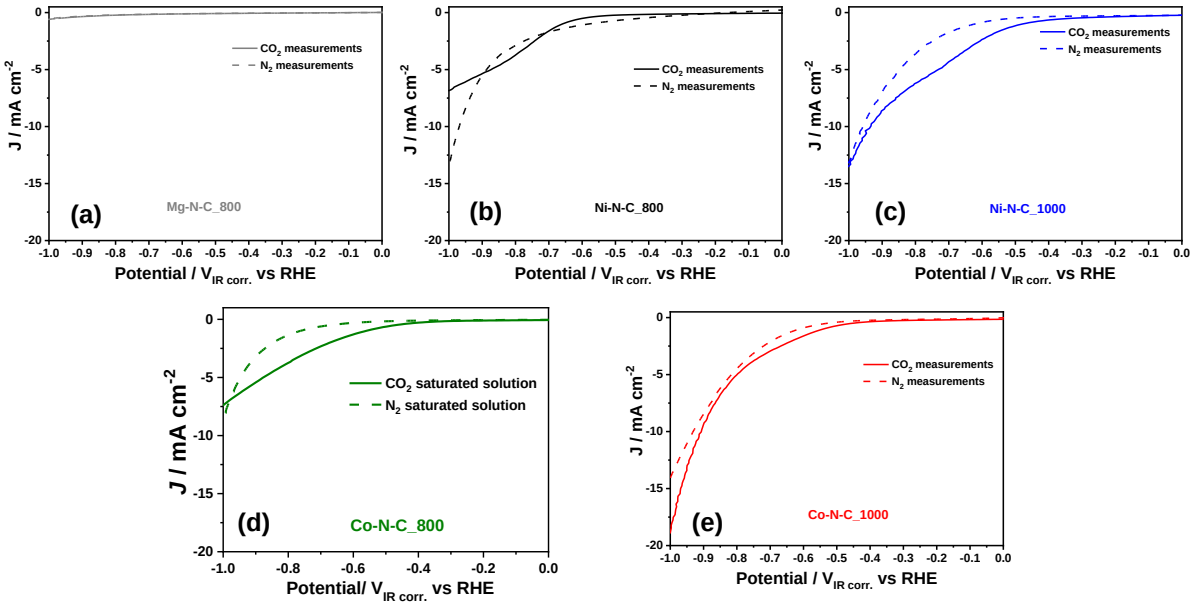

Figure S8: Linear sweep voltammograms (LSV) of (a) Mg-N-C_800, (b) Ni-N-C_800, (c) Ni-N-C_1000, (d) Co-N-C_800 and (e) Co-N-C_1000 catalysts measured under N_2 and CO_2 saturation condition in 0.1 M $KHCO_3$ electrolyte.

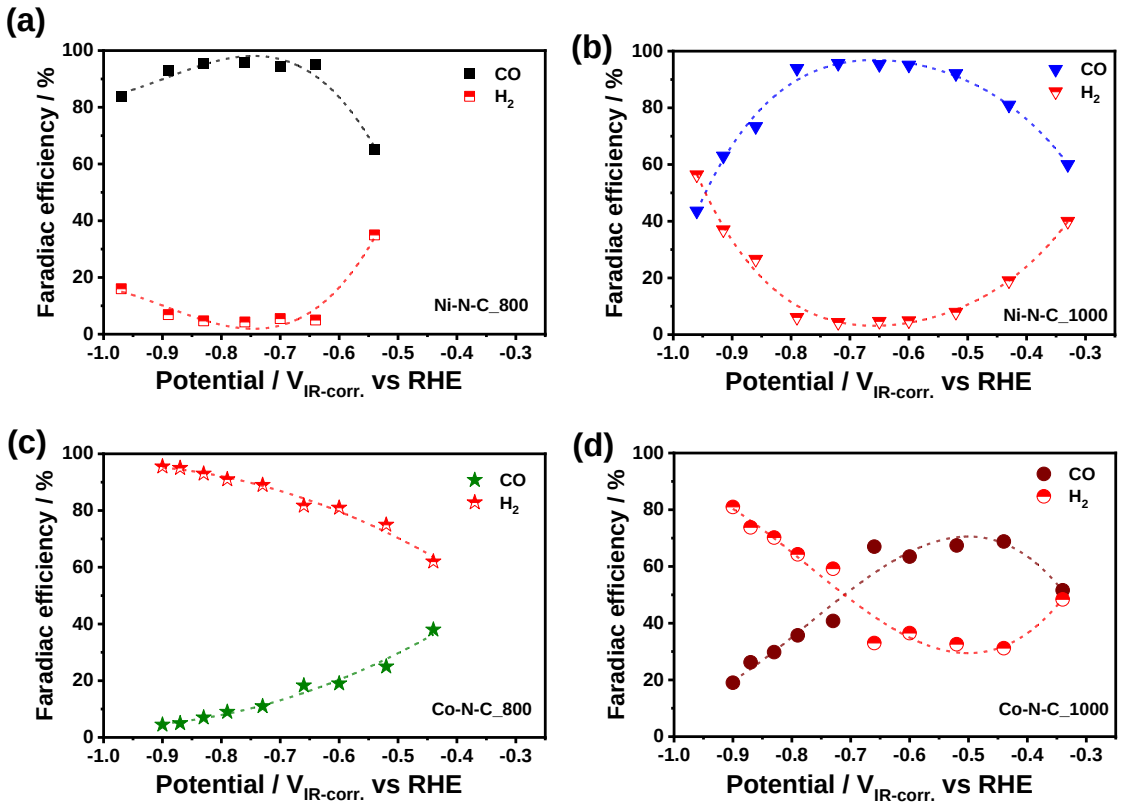

Figure S9: H_2 and CO faradaic efficiencies of (a) Ni-N-C_800, (b) Ni-N-C_1000, (c) Co-N-C_800 and (d) Co-N-C_1000 catalysts over entire applied potential range.

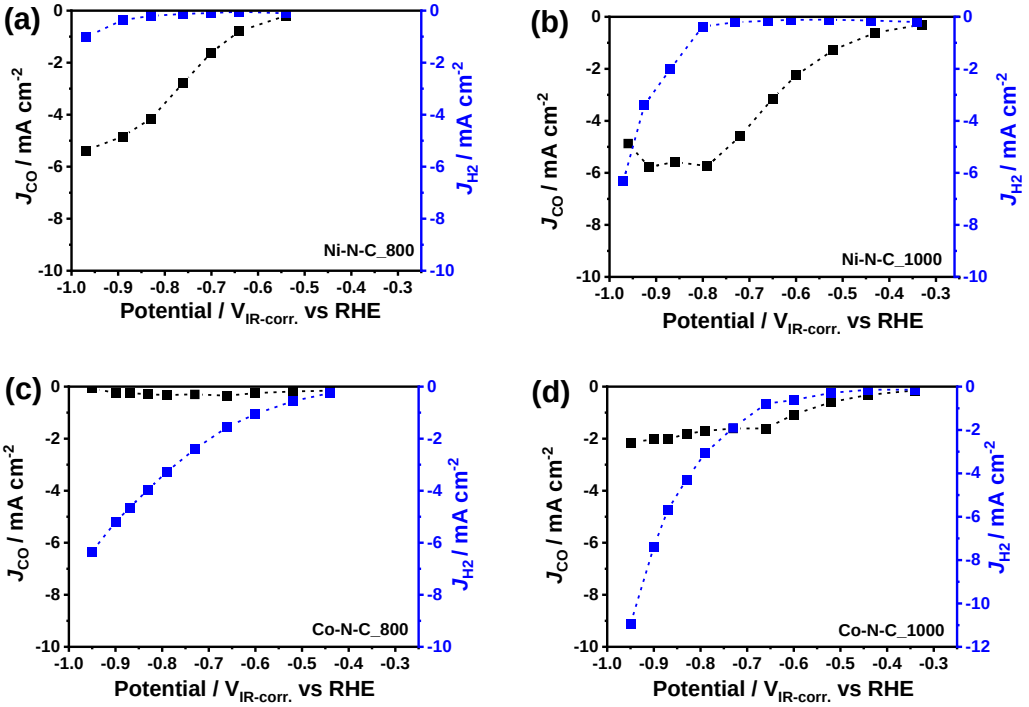

Figure S10: CO and H_2 current densities of (a) Ni-N-C_800, (b) Ni-N-C_1000, (c) Co-N-C_800 and (d) Co-N-C_1000 catalysts.

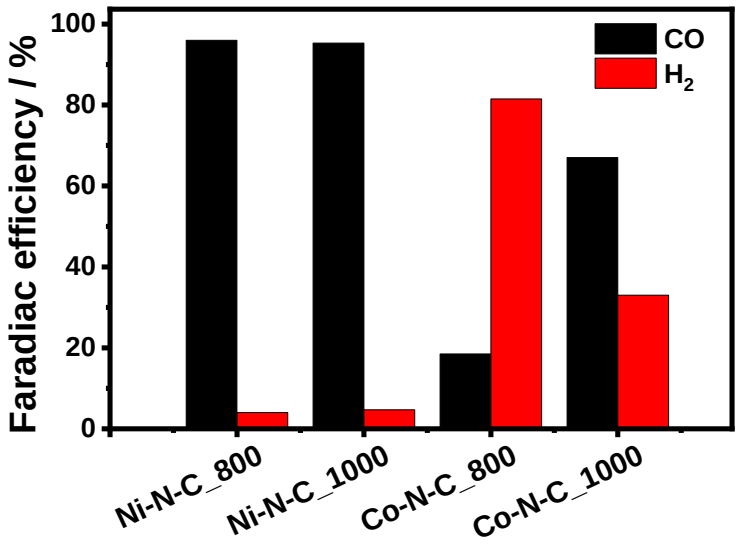

Figure S11: Comparison of CO and H_2 faradaic efficiencies of Ni and Co catalysts at -0.65 V_{RHE}.

Table S7: Activity comparison of recently reported high performance single atom catalysts in H-Type electrochemical cell for CO_2 reduction reaction.

Catalyst	$KHCO_3$ electrolyte conc. (M)	Catalyst loading (mg cm^{-2})	Maximum CO faradic efficiency (%)	CO Current density at 0.80 V_{RHE} (mA cm^{-2})	Mass activity at 0.65 V_{RHE} (A g^{-1})	Mass activity at 0.80 V_{RHE} (A g^{-1})	Ref.
Ni-N-C_1000	**0.1**	**0.25**	**95.7**	**5.8**	**13.0**	**23.0**	**This Work**
Co-N-C_1000	0.1	0.25	67.0	1.8	6.4	7.2	This Work
Ni-N-C	0.1	0.76	85.0	11.0	2.5	14	Ref S[16]
Co-N-C	0.1	0.76	20.0	3.0	2.6	4.5	Ref S[16]
Fe-N-C	0.1	0.76	65.0	3.7	6.9	5.6	Ref S[16]
Ni-N-C	0.1	0.75	85.0	10.6	4.0	14.1	Ref S[17]
Fe-N-C	0.1	0.6	93.0	9.0	8.0	15.0	Ref S [18]
Co-N-C	0.1	0.6	45.0	3.0	1.5	5.0	Ref S [18]
NiN-GS	0.1	0.2	93.2	4.14	2.5	20.7	Ref S[19]
CoPc	0.5	2.0	99.0	8.0	1.5	4.0	Ref S[20]
4-1-0.25-100	0.5	0.5	83.0	2.0	9.0	4.0	Ref S[21]
Ni_2-CPDpy973	0.1	0.055	87	0.55	N/A	10	Ref S[22]
Ni SAs/NC	0.5	0.185	71.9	3.0	N/A	16.2	Ref S[23]
Ni-NC_ATPA@C	0.5 (in RDE setup)	1.4	93.7	13.2	3.9	9.4	Ref S[24]

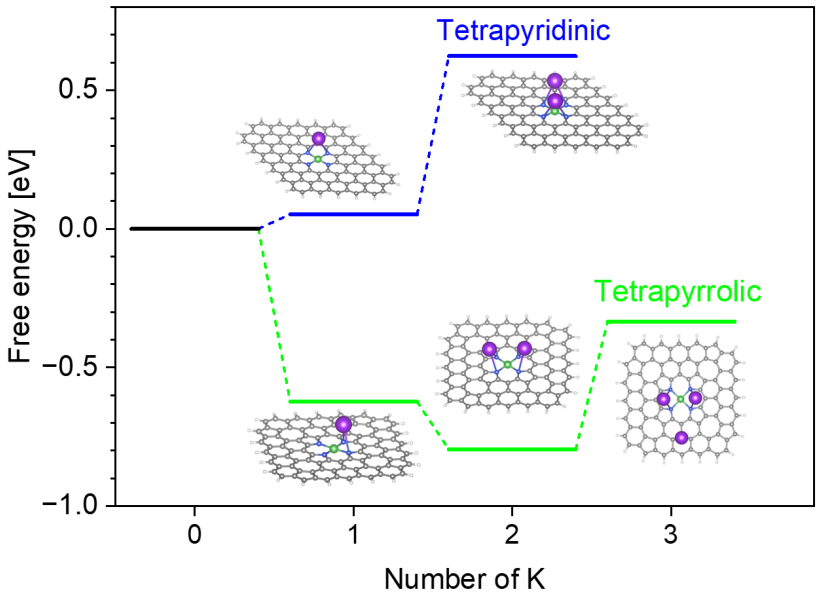

Figure S12: Free energy diagram for the reductive adsorption of K^+ ions on tetrapyrrolic (green) and tetrapyridinic (blue) NiN_4 sites calculated with B3LYP-D3(BJ)/def2-TZVP and COSMO solvation model. Vibrational frequencies for the enthalpic and entropic contributions were obtained with B3LYP-D3(BJ)/def2-SVP without solvation. The adsorption energies for CoN_4 differ by less than 0.1 eV. The structures of the K-adsorbed NiN_4 are shown with Ni (green), N (blue), C (grey) and K (purple).

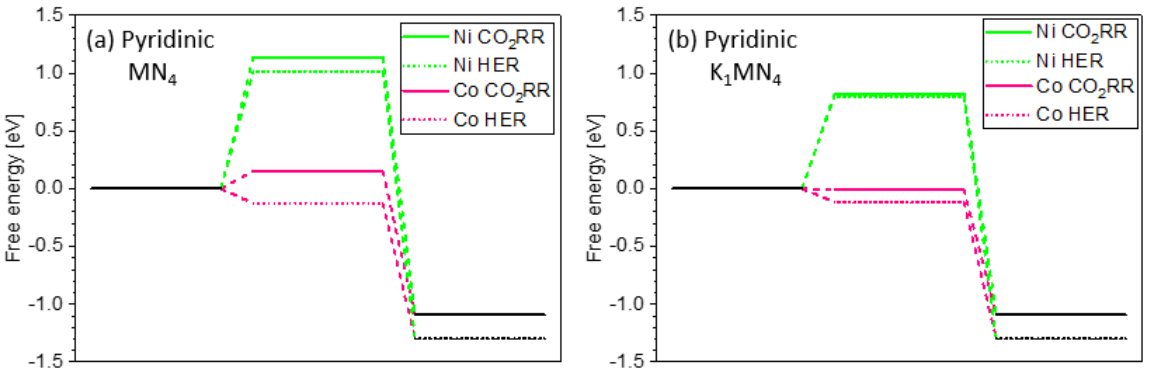

Figure S13: Free energy diagrams for CO_2RR and HER tetrapyridinic MN_4 and K_1MN_4 sites calculated with B3LYP-D3(BJ)/def2-TZVP and COSMO solvation model. Vibrational frequencies for the enthalpic and entropic contributions were obtained with B3LYP-D3(BJ)/def2-SVP without solvation.

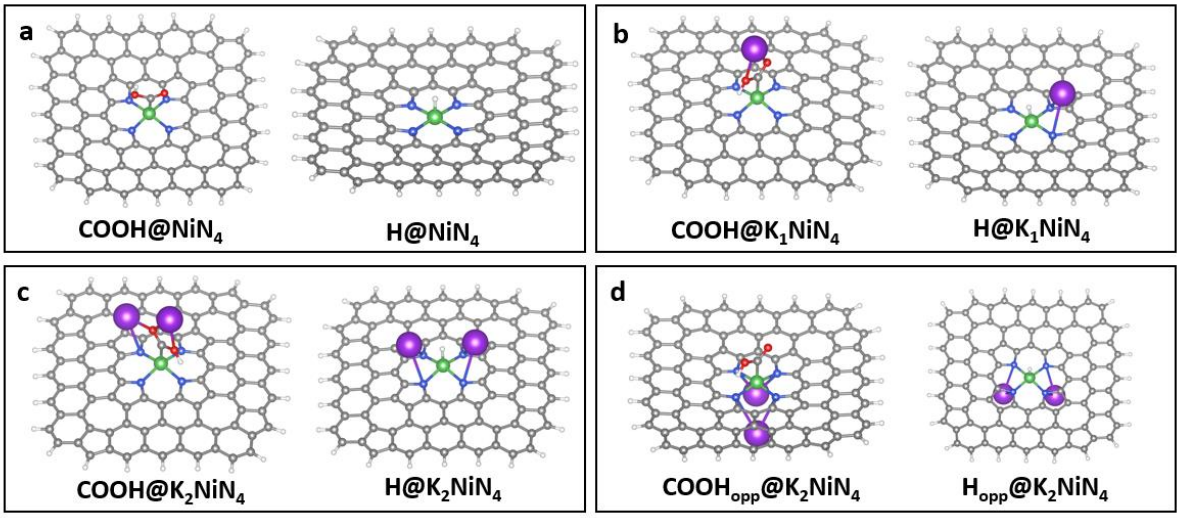

Figure S14: Structures of *COOH and *H adsorbed on tetrapyrrolic (a) pristine NiN_4, (b) K_1NiN_4, (c) K_2NiN_4 on the same face and (d) K_2NiN_4 on the opposite face. Geometries are obtained with B3LYP-D3(BJ)/def2-SVP with COSMO solvation model.

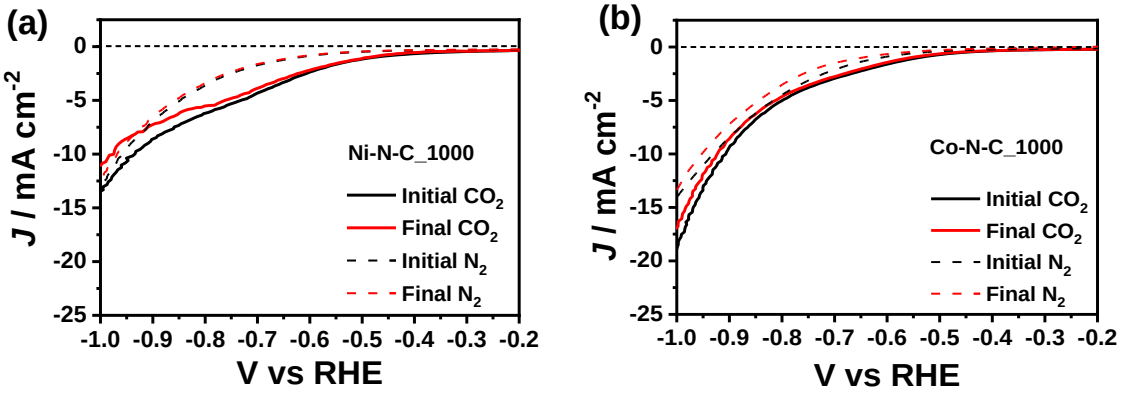

Figure S15: LSVs of (a) Ni-N-C_1000 and (b) Co-N-C_1000 catalysts before and after 100 h stability test measured under nitrogen and CO_2 saturation condition in 0.1 M $KHCO_3$ electrolyte.

Supporting References

(1) Ravel, B.; Newville, M. ATHENA, ARTEMIS, HEPHAESTUS: data analysis for X-ray absorption spectroscopy using IFEFFIT. *Journal of synchrotron radiation* **2005**, *12* (4), 537-541.
(2) Ahlrichs, R.; Bär, M.; Häser, M.; Horn, H.; Kölmel, C. Electronic structure calculations on workstation computers: The program system turbomole. *Chemical Physics Letters* **1989**, *162* (3), 165-169.
(3) Khosravi, A.; Vessally, E.; Oftadeh, M.; Behjatmanesh-Ardakani, R. Ammonia capture by MN4 (M= Fe and Ni) clusters embedded in graphene. *Journal of Coordination Chemistry* **2018**, *71* (21), 3476-3486.
(4) Perdew, J. P.; Ernzerhof, M.; Burke, K. Rationale for mixing exact exchange with density functional approximations. *The Journal of chemical physics* **1996**, *105* (22), 9982-9985.
(5) Ernzerhof, M.; Scuseria, G. E. Assessment of the Perdew–Burke–Ernzerhof exchange-correlation functional. *The Journal of chemical physics* **1999**, *110* (11), 5029-5036.
(6) Lee, C.; Yang, W.; Parr, R. G. Development of the Colle-Salvetti correlation-energy formula into a functional of the electron density. *Physical review B* **1988**, *37* (2), 785.
(7) Becke, A. D. A new mixing of Hartree–Fock and local density-functional theories. *The Journal of chemical physics* **1993**, *98* (2), 1372-1377.
(8) Klamt, A.; Schüürmann, G. COSMO: a new approach to dielectric screening in solvents with explicit expressions for the screening energy and its gradient. *Journal of the Chemical Society, Perkin Transactions 2* **1993**, (5), 799-805.
(9) Grimme, S.; Antony, J.; Ehrlich, S.; Krieg, H. A consistent and accurate ab initio parametrization of density functional dispersion correction (DFT-D) for the 94 elements H-Pu. *The Journal of chemical physics* **2010**, *132* (15).
(10) Grimme, S.; Ehrlich, S.; Goerigk, L. Effect of the damping function in dispersion corrected density functional theory. *Journal of computational chemistry* **2011**, *32* (7), 1456-1465.
(11) Weigend, F.; Ahlrichs, R. Balanced basis sets of split valence, triple zeta valence and quadruple zeta valence quality for H to Rn: Design and assessment of accuracy. *Physical Chemistry Chemical Physics* **2005**, *7* (18), 3297-3305.
(12) Deglmann, P.; Furche, F.; Ahlrichs, R. An efficient implementation of second analytical derivatives for density functional methods. *Chemical physics letters* **2002**, *362* (5-6), 511-518.
(13) Scott, A. P.; Radom, L. Harmonic vibrational frequencies: an evaluation of Hartree− Fock, Møller− Plesset, quadratic configuration interaction, density functional theory, and semiempirical scale factors. *The Journal of Physical Chemistry* **1996**, *100* (41), 16502-16513.
(14) Momma, K.; Izumi, F. VESTA 3 for three-dimensional visualization of crystal, volumetric and morphology data. *Journal of applied crystallography* **2011**, *44* (6), 1272-1276.
(15) Nørskov, J. K.; Rossmeisl, J.; Logadottir, A.; Lindqvist, L.; Kitchin, J. R.; Bligaard, T.; Jonsson, H. Origin of the overpotential for oxygen reduction at a fuel-cell cathode. *The Journal of Physical Chemistry B* **2004**, *108* (46), 17886-17892.
(16) Ju, W.; Bagger, A.; Hao, G.-P.; Varela, A. S.; Sinev, I.; Bon, V.; Roldan Cuenya, B.; Kaskel, S.; Rossmeisl, J.; Strasser, P. Understanding activity and selectivity of metal-nitrogen-doped carbon catalysts for electrochemical reduction of CO2. *Nature communications* **2017**, *8* (1), 944.
(17) Möller, T.; Ju, W.; Bagger, A.; Wang, X.; Luo, F.; Thanh, T. N.; Varela, A. S.; Rossmeisl, J.; Strasser, P. Efficient CO 2 to CO electrolysis on solid Ni–N–C catalysts at industrial current densities. *Energy & Environmental Science* **2019**, *12* (2), 640-647.
(18) Pan, F.; Zhang, H.; Liu, K.; Cullen, D.; More, K.; Wang, M.; Feng, Z.; Wang, G.; Wu, G.; Li, Y. Unveiling active sites of CO2 reduction on nitrogen-coordinated and atomically dispersed iron and cobalt catalysts. *Acs Catalysis* **2018**, *8* (4), 3116-3122.
(19) Jiang, K.; Siahrostami, S.; Akey, A. J.; Li, Y.; Lu, Z.; Lattimer, J.; Hu, Y.; Stokes, C.; Gangishetty, M.; Chen, G. Transition-metal single atoms in a graphene shell as active centers for highly efficient artificial photosynthesis. *Chem* **2017**, *3* (6), 950-960.
(20) Zhang, Z.; Xiao, J.; Chen, X. J.; Yu, S.; Yu, L.; Si, R.; Wang, Y.; Wang, S.; Meng, X.; Wang, Y. Reaction mechanisms of well-defined metal–N4 sites in electrocatalytic CO2 reduction. *Angewandte Chemie International Edition* **2018**, *57* (50), 16339-16342.

(21) Shi, J.-J.; Hu, X.-M.; Madsen, M. R.; Lamagni, P.; Bjerglund, E. T.; Pedersen, S. U.; Skrydstrup, T.; Daasbjerg, K. Facile synthesis of iron-and nitrogen-doped porous carbon for selective CO2 electroreduction. *ACS Applied Nano Materials* **2018**, *1* (7), 3608-3615.
(22) Nishihara, H.; Hirota, T.; Matsuura, K.; Ohwada, M.; Hoshino, N.; Akutagawa, T.; Higuchi, T.; Jinnai, H.; Koseki, Y.; Kasai, H. Synthesis of ordered carbonaceous frameworks from organic crystals. *Nature communications* **2017**, *8* (1), 109.
(23) Zhao, C.; Dai, X.; Yao, T.; Chen, W.; Wang, X.; Wang, J.; Yang, J.; Wei, S.; Wu, Y.; Li, Y. Ionic exchange of metal–organic frameworks to access single nickel sites for efficient electroreduction of CO2. *Journal of the American Chemical Society* **2017**, *139* (24), 8078-8081.
(24) Jia, M.; Choi, C.; Wu, T.-S.; Ma, C.; Kang, P.; Tao, H.; Fan, Q.; Hong, S.; Liu, S.; Soo, Y.-L. Carbon-supported Ni nanoparticles for efficient CO 2 electroreduction. *Chemical Science* **2018**, *9* (47), 8775-8780.

Paper S1

A Copper Single-Atom Cascade Bionanocatalyst for Treating Multidrug-Resistant Bacterial Diabetic Ulcer

X. Fan, Y. Gao, F. Yang, J. L. Low, L. Wang, B. Paulus, Y. Wang, A. Trampuz, C. Cheng, R. Haag, *Adv. Funct. Mater.* **2023**, *33*, 2301986.
DOI: https://doi.org/10.1002/adfm.202301986

Computational Highlights

This paper introduced an abiotic alternative to dual-enzyme-based catalysts that effectively breaks down glucose into ·OH radicals for the treatment of diabetic ulcers. The catalyst exploits the Fenton reactivity of the Cu atom in a specific coordination environment hosted by carbon. Preliminary EXAFS analysis determined a coordination number of 3 at Cu, prompting us to optimize geometric models of various CuN_xO_{3-x} motifs for fitting the EXAFS scattering paths. Among the various trivalent structures, the T-shaped CuN_2O structure fitted best to the EXAFS-measured Cu-N(O) bond lengths. Subsequent DFT studies of the reaction mechanism further highlighted the advantage of such a coordination geometry which confers intermediate Fenton reactivity in comparison to the inert CuN_4 and unstable trigonal CuN_3 sites. The role of water in separating the dissociated ·OH radical from Cu was also elucidated, as both OH would be bound to Cu and unable to desorb as radicals without the water molecule. The elimination of an OH bound to Cu could only occur via reductive protonation with H_2O_2 as the reductant, thereby explaining the experimentally observed oxygen evolution.

Author Contributions

Andrej Trampuz, Chong Cheng, and Rainer Haag conceived and supervised the project. Xin Fan performed the main experiments and wrote the manuscript. Yang Gao performed the animal experimentation. Fan Yang conducted the XAS measurements and assisted the data analysis. Jian Liang Low designed the computational study and performed the DFT calculations. Jian Liang Low analyzed the DFT results and wrote the computational part of the manuscript under the guidance of Beate Paulus. Lei Wang assisted the in-vitro antibacterial experiments. Yi Wang performed the high-resolution TEM measurements. A.T. provided the lab and drug-resistant bacterial strains for supporting the in-vitro antibacterial studies. All authors contributed to the final version of the manuscript.

RESEARCH ARTICLE

ADVANCED FUNCTIONAL MATERIALS
www.afm-journal.de

A Copper Single-Atom Cascade Bionanocatalyst for Treating Multidrug-Resistant Bacterial Diabetic Ulcer

Xin Fan, Yang Gao, Fan Yang, Jian Liang Low, Lei Wang, Beate Paulus, Yi Wang, Andrej Trampuz, Chong Cheng,* and Rainer Haag**

Diabetic ulcers induced by multidrug-resistant (MDR) bacteria have severely endangered diabetic populations. These ulcers are very challenging to treat because the local high glucose concentration can both promote bacterial growth and limit the immune system's bactericidal action. Herein, a glucose oxidase-peroxidase (GOx-POD) dual-enzyme mimetic (DEM) bionanocatalyst, Au@CuBCats is synthesized to simultaneously control glucose concentration and bacteria in diabetic ulcers. Specifically, the AuNPs can serve as GOx mimics and catalyze the oxidation of glucose for the formation of H_2O_2; the H_2O_2 can then be further catalytically converted into OH via the POD-mimetic copper single atoms. Notably, the unique copper single atoms coordinated by one oxygen and two nitrogen atoms (CuN_2O_1) exhibit better POD catalytic performance than natural peroxidase. Further DFT calculations are conducted to study the catalytic mechanism and reveal the advantage of this CuN_2O_1 structure as compared to other copper single-atom sites. Both in vitro and in vivo experiments confirm the outstanding antibacterial therapeutic efficacy of the DEM bionanocatalyst. This new bionanocatalyst will provide essential insights for the next generation of antibiotic-free strategies for combating MDR bacterial diabetic ulcers, and also offer inspiration for designing bionanocatalytic cascading medicines.

1. Introduction

Diabetes and its complications have emerged as one of the major threats to human health, causing a large number of deaths annually.[1,2] Especially, a diabetic ulcer is one of the most serious chronic complications, featured with slow-healing wounds that are very sensitive to bacterial infections.[3] An important factor responsible for this complication is the overabundance of glucose in the wound area, which promotes the proliferation of bacteria and prevents the immune system from killing them, resulting in long-term bacterial colonization and an extremely hard-to-cure lesion.[4] To make matters worse, the emergence of multidrug-resistant (MDR) bacteria, which vitiate antibiotics' bactericidal effects, has now aggravated the situation, further endangering diabetic ulcer patients. It is therefore important to develop new strategies not only for combating MDR

X. Fan, R. Haag
Institute of Chemistry and Biochemistry
Freie Universität Berlin
Takustraße 3, 14195 Berlin, Germany
E-mail: haag@chemie.fu-berlin.de

X. Fan, L. Wang, A. Trampuz
Charité – Universitätsmedizin Berlin
Freie Universität Berlin
Humboldt-Universität zu Berlin, and Berlin Institute of Health
14195 Berlin, Germany
E-mail: andrej.trampuz@charite.de

The ORCID identification number(s) for the author(s) of this article can be found under https://doi.org/10.1002/adfm.202301986

DOI: 10.1002/adfm.202301986

Y. Gao
Department of Ultrasound
West China Hospital
Sichuan University
610041 Chengdu, China

F. Yang
Department of Physics
Freie Universität Berlin
Arnimallee 14, 14195 Berlin, Germany

J. L. Low, B. Paulus
Institute of Chemistry and Biochemistry
Freie Universität Berlin
Arnimallee 22, 14195 Berlin, Germany

Y. Wang
College of Materials Science and Engineering
Nanjing University of Aeronautics and Astronautics
210016 Nanjing, China

C. Cheng
College of Polymer Science and Engineering, State Key Laboratory of Polymer Materials Engineering
Sichuan University
610065 Chengdu, China
E-mail: chong.cheng@scu.edu.cn

bacterial infections but also for controlling the glucose levels in diabetic ulcers.

Glucose oxidase (GOx) is a natural enzyme originally generated by fungi and insects.[5] Recently, it has been explored as a good candidate for treating bacterial diabetic ulcers, since it shows the ability to catalyze the glucose oxidation to generate hydrogen peroxide (H_2O_2), which is toxic to bacteria. Moreover, since glucose is one of the major nutrition sources for bacterial growth, its consumption can also lead to bacterial starvation.[6] Until now, GOx has been encapsulated in diverse matrices like hydrogel,[7–8] metal-organic frameworks,[9–11] covalent organic frameworks,[12–13] and porous silica[14] to fabricate therapeutic platforms. However, to achieve effective antibacterial efficacy, the dosage or concentration of H_2O_2 must be very high, which causes inevitable toxicity and inflammation. Recent studies have innovatively combined GOx and peroxidase (POD) in a single system in which the generated H_2O_2 can be further catalyzed into more efficient bactericidal hydroxyl radicals (•OH), thus achieving a better therapeutic effect with higher biosafety.[15–16] Nevertheless, these natural-enzyme-based therapies still face challenges due to their high synthesis cost, poor stability, and limited mass production.

Inspired by the natural POD with multiple transition metallic active sites coordinated by nitrogen and oxygen, transition-metal-based composites have been constructed and applied for diverse scenarios that require the mass generation of OH. For example, $[FeIII(OH)(tpena)]^+$ complex was synthesized and proven to activate H_2O_2 with the formation of OH under pH 8,[17] Co_3O_4 nanoplates were synthesized as POD mimics for detecting glucose in the presence of GOx,[18] and copper-based nanozymes were designed for phenol degradation.[19] These results confirm that the transition metallic sites serve as high-performance POD mimics. However, their bioapplications are still very limited because of the potential toxicity from ion leaching. This limitation prompted us to develop bionanocatalytic medicines with single metallic atom catalytic centers; here we can not only take maximum advantage of metal, but also minimize the danger of ion leaching, since the overall dosage of metal is significantly reduced and these metallic atoms are fixed by heteroatoms in the matrix. In addition, recent studies have revealed that small gold nanoparticles (AuNPs, approved by the US Food and Drug Administration)[20] of ≈5 nm in diameter can oxidize glucose to generate gluconic acid and H_2O_2, just as GOx does.[21] Due to their high biosafety and easy synthesis, we consider AuNPs an excellent building block for constructing abiotic GOx-POD mimetic cascade catalytic platforms. To the best of our knowledge, such a rational design of dual-enzyme mimetic AuNPs/single metallic atomic bionanocatalysts for treating multidrug-resistant bacterial diabetic ulcer has not been reported until now.

In this work, we synthesized an AuNP-anchored copper single atomic bionanocatalyst (Au@CuBCats) as a novel GOx-POD dual enzyme mimetic treatment platform for bacterial diabetic ulcers. Specifically, the AuNPs can serve as GOx mimics and catalyze the oxidation of glucose for the formation of H_2O_2, the H_2O_2 can then be further catalytically converted into OH via POD-mimetic copper single atoms without extra energy input. Thus, upon the treatment with Au@CuBCats, both glucose concentration and bacterial infection in diabetic ulcers can be effectively controlled. Notably, the unique copper single atoms coordinated by one oxygen and two nitrogen atoms (CuN_2O_1) exhibit better POD catalytic performance than natural horseradish peroxidase (HRP). Further density functional theory (DFT) calculations were conducted to facilitate a fundamental understanding of the catalytic activity and reveal the advantage of the CuN_2O_1 structure compared to other copper single-atom sites. In vitro antibacterial results demonstrate that bionanocatalysts can induce a significant bacteria-killing effect against both gram-positive and gram-negative strains. In vivo study of bacterial diabetic ulcers in a rabbit ear model confirms the outstanding therapeutic efficacy and biosafety of the bionanocatalyst. Therefore, we believe that this novel bionanocatalyst will provide essential perspectives to the next generation of antibiotic-free strategies for combating MDR bacterial infection of diabetic ulcers, and that it will also yield inspiration for designing bionanocatalytic cascading medicines.

2. Results and Discussion

The synthesis of the Au@CuBCats started with the coordination reaction of copper ions and chloranilic acid (CA), and the obtained precursors were termed as CuCA. Then, CuCA was subjected to a dicyandiamide (DCD)-assisted pyrolysis step followed by an acid etching step, producing the bionanocatalysts with abundant single-atomic copper, termed as CuBCats. Finally, the gold nanoparticles were reduced in situ on CuBCats' surface to obtain the final product, Au@CuBCats, as illustrated in **Figure 1**a. We then systematically studied the chemical and physical structures of Au@CuBCats by scanning electron microscopy (SEM), scanning transmission electron microscopy (STEM), X-ray powder diffraction (XRD), X-ray photoelectron spectroscopy (XPS) and X-ray absorption spectroscopy (XAS). Both STEM images (Figure 1b; Figure S1, Supporting Information) and SEM images (Figure S2, Supporting Information) confirmed that the bionanocatalysts had 2D structures before-and-after AuNPs loading. Meanwhile, we observed from the aberration-corrected high-angle annular dark-field scanning transmission electron microscopy images with atomic resolution (Figure 1c; Figure S3a, Supporting Information) that the isolated copper atoms were well-dispersed on the carbon matrix, where no apparent copper particle or cluster was found. Energy dispersive spectroscopy (EDS) mapping (Figure 1d; Figure S3b, Supporting Information) suggested that various elements were uniformly distributed in the bionanocatalysts. Also, the XRD pattern (Figure S4, Supporting Information) showed no copper crystal peaks; instead, the typical peaks for the (111), (200), (220), and (311) facets of AuNPs appeared, confirming the successful synthesis of Au@CuBCats.

The XPS survey scanning of CuCA-C (CuCA-C is the CuBCats without acid etching), CuBCats, and Au@CuBCats shows a clear N peak, whereas no apparent N signal was noticed for CuCA precursors, suggesting that the DCD-assisted pyrolysis facilitates N-doping (Figure S5, Supporting Information). Meanwhile, the atomic ratio of each sample has been summarized based on XPS results in Table S1 (Supporting Information). Based on the atomic ratio, the AuNPs loading rate was calculated to be 21 wt%. To understand the nitrogen atoms' bonding environment, the high-resolution XPS N1s spectra were fitted (Figure S6, Supporting Information). Here we found the highest percentage of pyridinic-N (36.17%), which plays an important role in anchoring atomic metals according to previous studies,[22–24] suggesting the formation of Cu–N_x sites. To further study the oxidation state

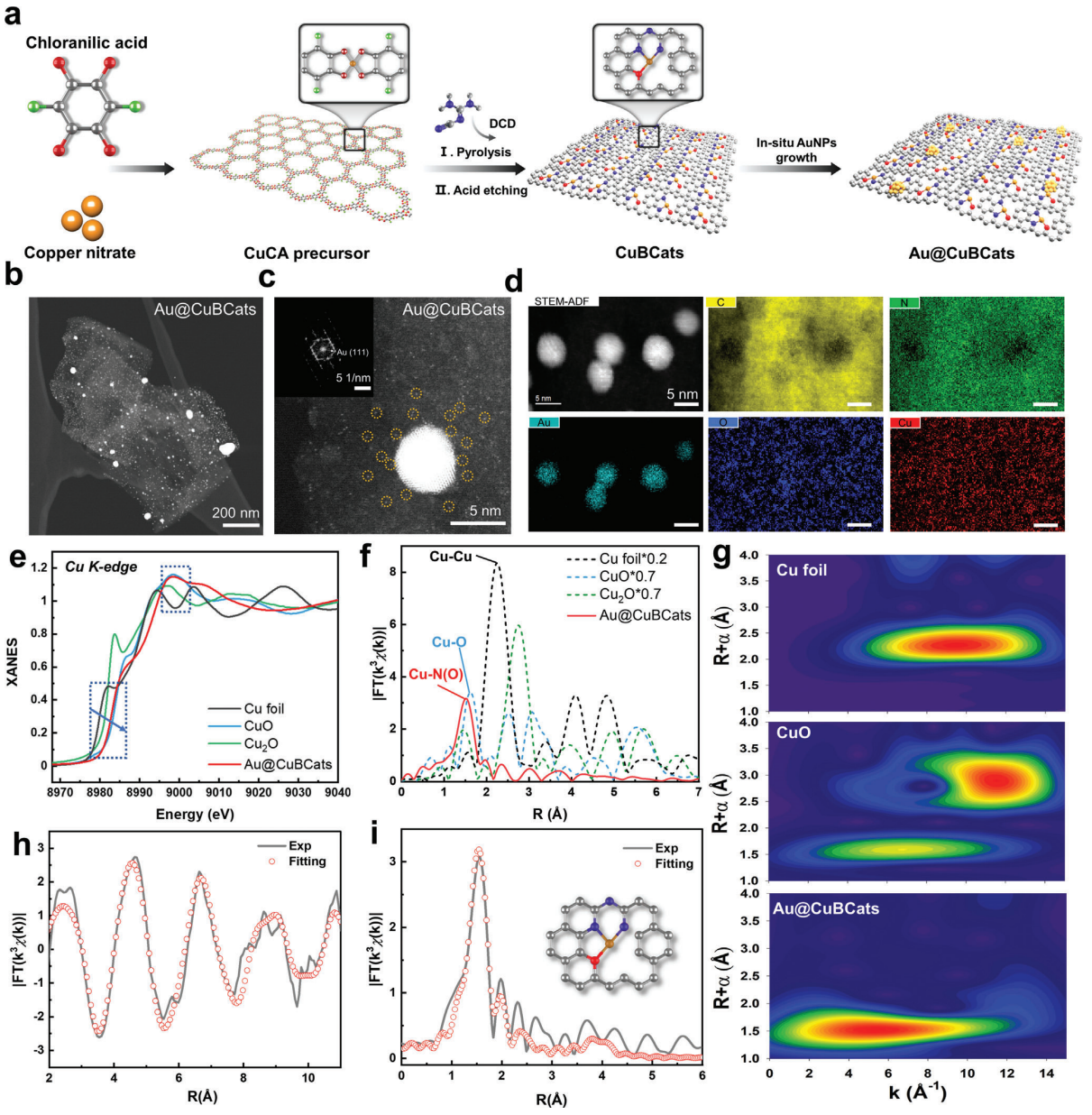

Figure 1. Synthesis and structural characterizations of Au@CuBCats. a) Schematic illustration of the synthesis of Au@CuBCats. b,c) STEM images of Au@CuBCats, on which the copper single-atoms are highlighted by yellow circles. Insert: Fast Fourier transform (FFT) pattern of gold nanoparticle. d) EDS mapping of Au@CuBCats. e,f) XANES and EXAFS spectra at Cu K-edge of Au@CuBCats. g) Wavelet transform of Cu foil, CuO, and Au@CuBCats. h,i) EXAFS fitting result of Au@CuBCats at k and R space, respectively.

of the Cu single atoms in Au@CuBCats, we measured X-ray absorption energy near-edge structure (XANES) of Cu foil, Cu_2O, CuO, and Au@CuBCats (Figure 1e). The results confirmed that the XANES of Au@CuBCats were located between those of Cu_2O and CuO, suggesting the valency of copper single-atoms was between +1 and +2. Subsequently, the extended X-ray absorption fine structure (EXAFS) was investigated to analyze the coordination configurations of the Cu sites. As shown in Figure 1f, the first coordination shell is located at 1.5 Å, suggesting Cu–N or/and Cu–O coordination. Meanwhile, no obvious Cu–Cu scattering at 2.2 Å was noticed in Au@CuBCats. Moreover, wavelet transform based on the EXAFS results was conducted to distinguish the backscattering atoms (Figure 1g). We observed the maximum intensity of Cu foil and CuO at 9.7 and 11.5 $Å^{-1}$, respectively, which

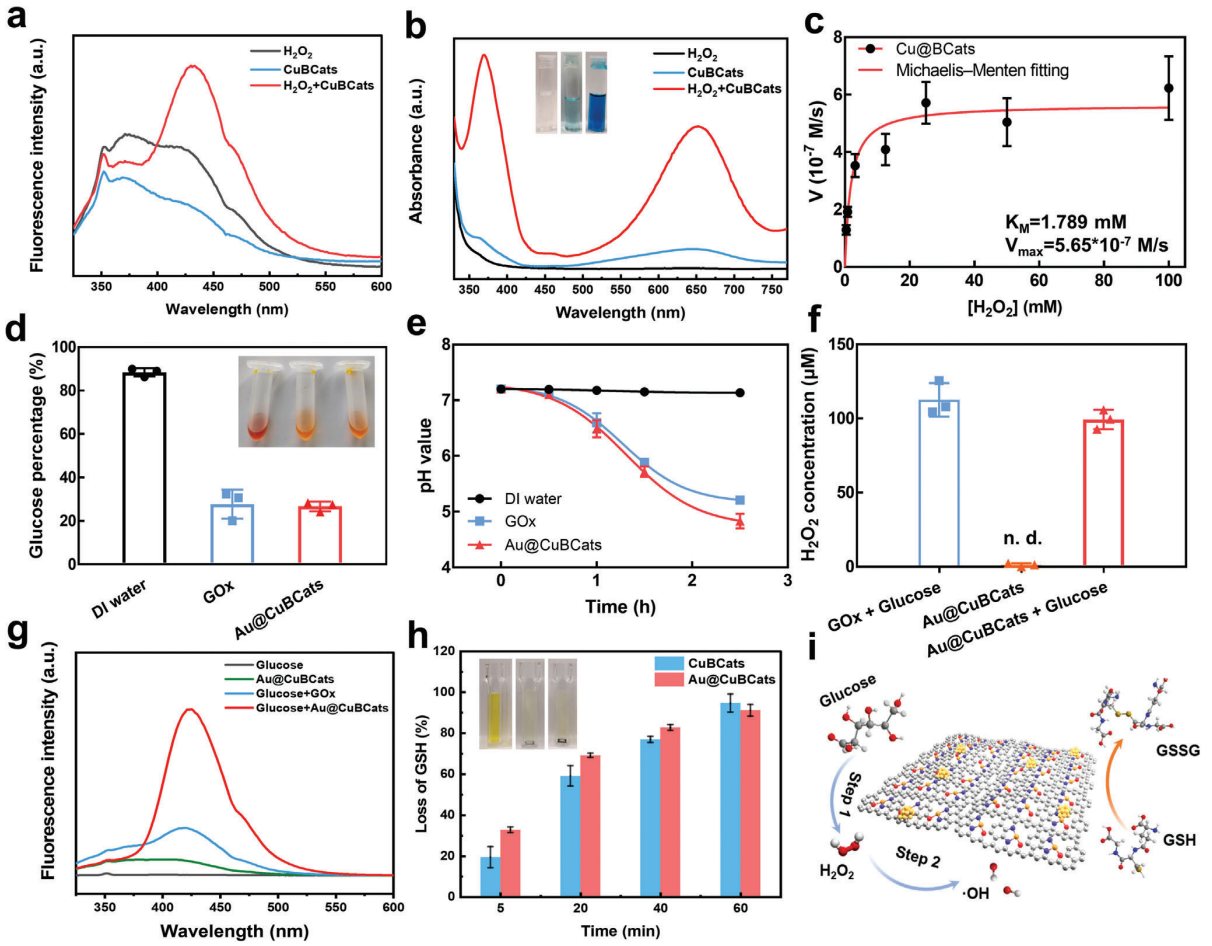

Figure 2. Catalytic performance of Au@CuBCats and CuBCats. a) Fluorescence spectroscopy in the presence of TA for measuring the OH generation property of CuBCats in the presence of H_2O_2, b) UV–Vis spectroscopy in the presence of TMB for characterizing peroxidase-like property, and c) Michaelis–Menten fitting curve of initial oxi-TMB generation velocities against H_2O_2 concentrations. d) Glucose percentage after 2 h incubation. e) The change of pH value with the increasing incubation time. f) H_2O_2 generation after 2 h incubation. n.d. represents non-detectable. g) OH generation property of Au@CuBCats in the presence of glucose. h) GSH consumption caused by Au@CuBCats and CuBCats. i) Schematic illustration of Au@CuBCats as a dual-enzyme-mimetic platform for initiating cascade catalysis and GSH depletion.

can be assigned to the Cu–Cu configuration. In comparison, the Au@CuBCats showed the maximum intensity at 5.2 $Å^{-1}$, which is assigned to Cu–N or/and Cu–O configuration. Although the copper was pre-anchored by oxygen in CuCA precursors, the coordinated O species also reacted with carbon and escaped under high temperatures.[25] Meanwhile, the N species generated from dicyandiamide would take over the vacancies during pyrolysis, thus assisting with anchoring the atomic Cu. Based on the synthesis procedures mentioned above, we speculate that both Cu–N and Cu–O exist in this structure. From the fitting result, we determined the coordination number (CN) of Cu–N(O) to be very close to three. Nevertheless, further unveiling the respective coordination number of N and O could be challenging due to the similar bond lengths of Cu–N and Cu–O. Therefore, in accordance with a previous study,[24] the back-scattering paths of N and O were simultaneously applied to obtain the best-fitting result; the fittings with fixed CN of N and O were also compared (Table S2 and Table S3, Supporting Information). Upon fitting the EXAFS spectra to various structural models optimized with DFT, we confirmed that the best fit was obtained when the Cu center coordinated with one O atom and two N atoms (Figure 1 h,e). Therefore, the atomic Cu structure model of Au@CuBCats can be deduced; it is shown in the inset of Figure 1i.

Next, to study the OH generation property of bionanocatalysts, terephthalic acid (TA) was used as a probe since it can be oxidized by OH to generate the fluorescent compound TAOH, which can be easily detected by fluorescence spectroscopy under excitation at 315 nm. The significant TAOH signal at 430 nm confirms that CuBCats can catalyze H_2O_2 to generate abundant OH (**Figure 2**a). This OH generation can be attributed to the intrinsic POD-like activity of the atomic metal center.[26,27] Thus, a POD substrate, 3,3′,5,5′-tetramethylbenzidine (TMB) was used

to study the POD-like property and steady-state catalytic kinetics. After 5 min of incubation, the TMB + H_2O_2 + CuBCats group became blue, with remarkable absorption peaks reflecting oxidized TMB at both 370 and 652 nm (Figure 2b). Then, we calculated the Michaelis–Menten constant (K_M) and the maximum initial velocity (V_{max}) to assess the catalytic efficacy of CuBCats (Figure 2c). The K_M value of the CuBCats was 1.789 mM for H_2O_2 substrate, indicating the higher affinity of CuBCats for H_2O_2 than that of HRP (3.70 mM for the H_2O_2 substrate).[28] Meanwhile, the V_{max} value of CuBCats showed around a 10-fold increase compared to HRP (V_{max} of HRP against H_2O_2 substrate is 8.71×10^{-8} M s^{-1}), suggesting the advanced POD-like performance of atomic copper sites.

After anchoring the AuNPs on CuBCats' surface, glucose was used to initiate the GOx-POD cascade catalytic process of Au@CuBCats. As shown in Figure 2d, a large amount of glucose consumption was noticed after a 2 h incubation with Au@CuBCats, almost equivalent to that of GOx, revealing the comparable glucose oxidative activity of Au@CuBCats (50 μg mL^{-1}) and GOx (2 U mL^{-1}). The downstream products-gluconic acid, H_2O_2, and OH were also examined by real-time pH meter, H_2O_2 assay kit, and TA measurement, respectively. We noticed a significant decrease in pH value over the incubation period (Figure 2e), revealing the generation of gluconic acid. Subsequently, we confirmed the generation of H_2O_2 in the Au@CuBCats + glucose group by H_2O_2 assay kit (Figure 2f). In agreement with TA measurements of CuBCats, we further demonstrated that Au@CuBCats can not only continuously catalyze the in situ-generated H_2O_2 to OH (Figure 2g), but also lead to the oxidation of TMB in the presence of glucose (Figure S7, Supporting Information). We did not notice a significant difference of DEM catalytic property of Au@CuBCats after exposing to air at room temperature over one month (Figure S8, Supporting Information). Moreover, glutathione (GSH), a common reducing agent in bacteria, was used as a model compound to test the intrinsic oxidative property of the catalysts. It was observed that the depletion rates of GSH were up to 94.66% and 91.11% at 60 min for CuBCats and Au@CuBCats, respectively, suggesting that these catalysts with single atomic copper sites have great power in weakening the bacterial antioxidant system and inducing oxidative stress. All of the above data confirm that the Au@CuBCats can catalyze the decomposition of glucose to OH via a dual-enzyme-mimetic cascade catalysis, and also further improve ROS treatment efficacy by depleting bacterial alternative oxidase (AOX).

The mechanism of how AuNPs catalyzes the oxidation of glucose to H_2O_2 has been studied both experimentally and theoretically.[21,29] For the further mechanistic understanding of the entire reaction, we performed DFT studies on the subsequent generation of OH from H_2O_2. Based on geometric fitting to our XAS data, we built a model of CuN_2O_1 embedded in graphene, as shown in Figure 1i. Upon characterizing the first-shell coordination geometry around Cu, we further considered that the N-containing precursor DCD exhibits the N–C–N–C–N connectivity (Figure S9, Supporting Information), prompting us to include an additional nitrogen dopant two atoms away from the coordination N. In fact, among the three possible arrangements of the CuN_2O_1 motifs, the motif shown is most stable only with the additional nitrogen dopant (Figure S10, Supporting Information). It is thus likely that this particular CuN_2O_1 arrangement, which fits best to the EXAFS data, is a result of bidentate coordination of DCD onto Cu during pyrolysis, while the remaining O originates from the initial coordination to CA. In addition to CuN_2O_1, other kinds of atomic copper sites were also calculated for comparison.

A proposed scheme of the reaction is shown in **Figure 3**a. The reaction starts from the adsorption of an H_2O_2 molecule. In the absence of solvent molecules, the geometry optimization of the H_2O_2-adsorbed led to the dissociation of H_2O_2 to form 2OH bound to CuN_2O_1. Although this already highlights the high catalytic activity of the Cu center, it cannot explain how OH radicals could be generated, since OH bound to Cu is unlikely to dissociate as radicals. Nevertheless, this contradiction is resolved by adding a single H_2O molecule to the calculations, upon which dissociation still occurs but the OH can be stabilized by H_2O in the $^*OH–H_2O–OH$ intermediate. With the assistance of H_2O, the OH is able to diffuse away from the reaction center instead of binding to Cu. For comparison of the dissociation kinetics, we further obtained the transition state for the dissociative step. In this mechanism, the OH that remains bound to the CuN_2O_1 site is unlikely to spontaneously desorb on its own as OH because of its strong binding (Figure S11, Supporting Information). Instead, the catalyst can be regenerated via protonation-reduction of $^*OH$ to form H_2O that finally desorbs. Since the evolution of O_2 was generated during the reaction (Figure S12, Supporting Information), we assumed the electrons originate from other H_2O_2 molecules and simulated the final reductive step at the standard reduction potential $U = E^0(O_2/H_2O_2) = 0.70$ V. Based on both experimental and theoretical results we mentioned above, the possible reaction mechanism of the cascading catalysis of was proposed as Equations (1) and (2):

$$\text{Glucose} \xrightarrow{\text{AuNPs}} \text{Gluconic acid} + H_2O_2 \quad (1)$$

$$H_2O_2 \xrightarrow{CuN_2O_1} {}^{\bullet}OH + H_2O + O_2 \quad (2)$$

A combined free energy diagram, shown in Figure 3b, confirms that the reaction on the CuN_2O_1 site has a significantly lower energy barrier (0.44 eV) than that of CuN_4 (Figure 3b) and is thus more suitable for the H_2O_2 decomposition. In contrast, the dissociation of H_2O_2 on CuN_3 could be considered barrier-free, as the dissociation already occurs upon geometry optimization of the $H_2O_2(H_2O)$ intermediate. However, the instability of CuN_3 is reflected in the final reductive step, where the release of $^*OH$ would be inhibited. Therefore, in contrast to the other two motifs, CuN_2O_1 exhibits the ideal reactivity, one that is favorable for both the dissociation and desorption steps. Bader charge analysis showed the CuN_2O_1 center to be positively charged at +0.72 e, a value between those of CuN_4 (+1.11 e) and CuN_3 (+0.68 e). Generally, a more positively charged center implies a higher oxidation state of Cu and a lower tendency for releasing $^*OH$,[22] consistent with the result for the OH-releasing step in the free energy diagram: the free energy for releasing $^*OH$: $CuN_4 > CuN_2O_1 > CuN_3$. From the above results, we can conclude that the POD-like reaction pathway of atomic copper centers can be much improved by adjusting the copper coordination microenvironment.

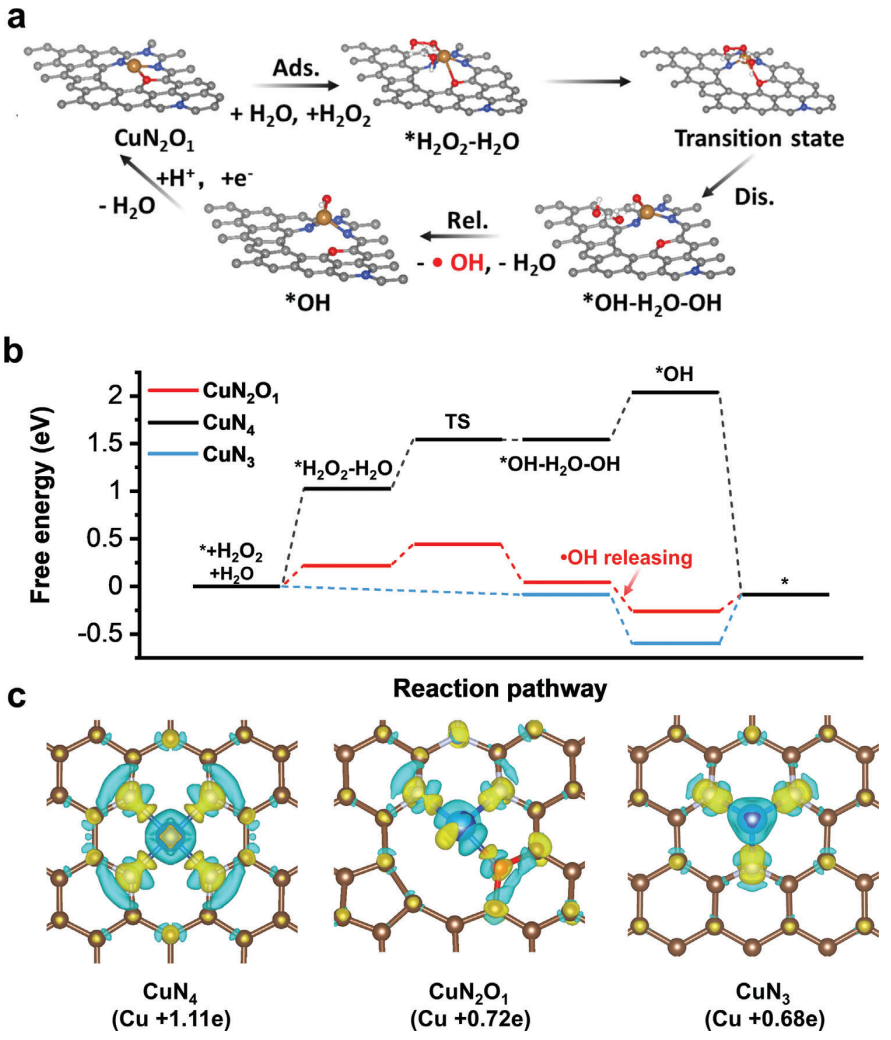

Figure 3. Mechanism of POD-like activity on CuN_2O_1 site. a) Scheme of the proposed reaction mechanism on CuN_2O_1 site. b) Free energy diagram for the reaction process on CuN_2O_1, CuN_4, and CuN_3 sites. c) Charge density difference plot and Bader charge of Cu in CuN_2O_1, CuN_4, and CuN_3 sites.

Encouraged by the above experimental and theoretical studies, we expect that the Au@CuBCats can serve as an ideal bactericidal agent in the presence of glucose via DEM cascade catalysis. To prove this concept, methicillin-resistant *Staphylococcus aureus* (*MRSA*, Gram-positive multidrug-resistant strain) and clinically isolated extended-spectrum β-lactamases producing *E. coli* (ESLP *E. coli*, a gram-negative MDR strain) were selected as presentative bacteria for the in vitro antibacterial study. As shown in **Figure 4**a, the bacterial colonies of both strains after treatment with Au@CuBCats were significantly smaller than those treated by PBS, glucose, glucose+GOx and glucose+CuBCats. Importantly, we noticed a significant difference ($P < 0.0001$) between glucose+GOx and glucose+Au@CuBCats groups (Figure 4c), attributable to the OH, generated by the cascade catalysis, further improving bactericidal performance.

Furthermore, we used SEM and confocal laser scanning microscope (CLSM) to investigate the antibacterial mechanism of Au@CuBCats from morphology and intracellular ROS level aspects, respectively. From SEM images (Figure 4b), we observed that the *MRSA* and ESLP *E. coli* exposed to the PBS, glucose and glucose+CuBCats maintained their original plump structures with intact outer membranes. After being treated with glucose+GOx, we noticed some distorted bacterial structures owing to the oxidative damage from H_2O_2. By contrast, in the group treated with glucose+Au@CuBCats, most of the bacteria suffered significant morphological deformations like collapse, distortion and breakage (highlighted by red arrows), indicating the highest bactericidal efficacy. Apart from the planktonic bacterial model, we also tested the antibiofilm performance. As shown in Figure S13 (Supporting Information), significant

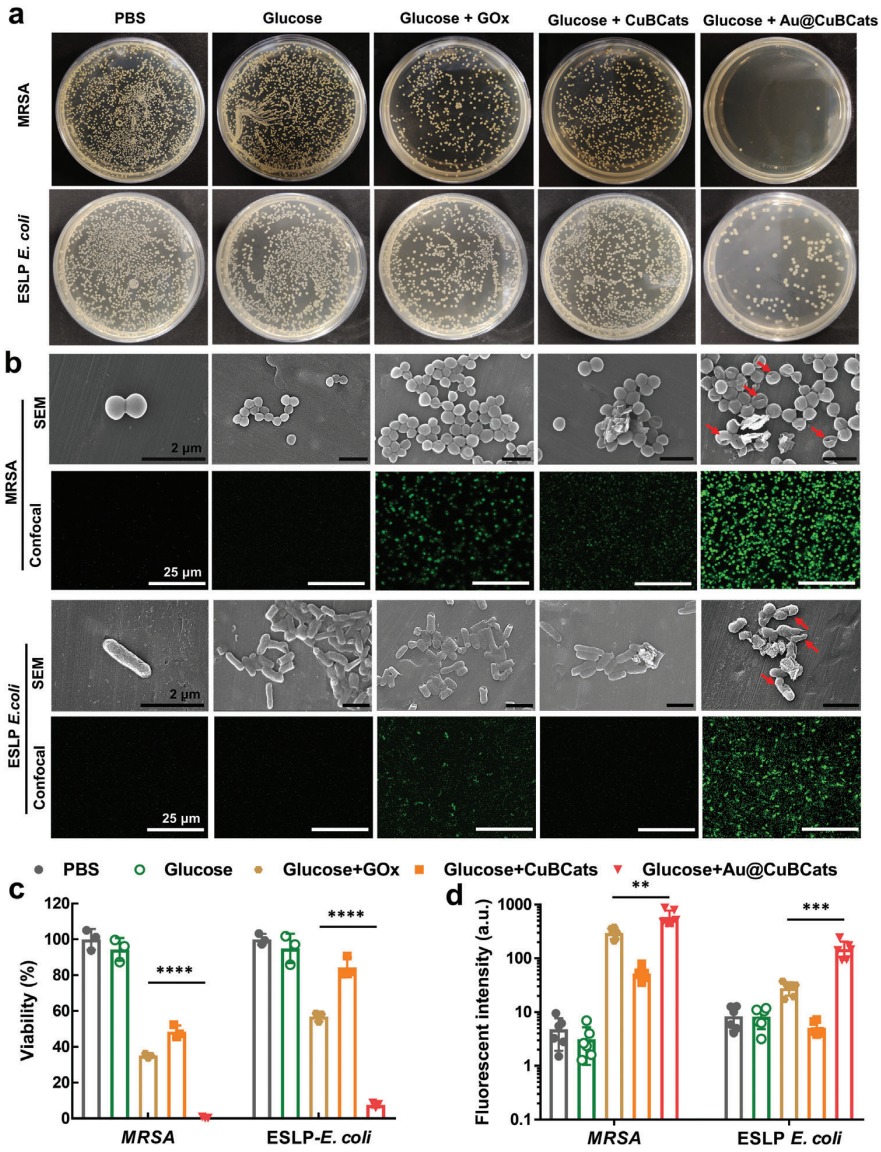

Figure 4. In vitro bacterial killing profile of Au@CuBCats. a) Bacterial colonies after different treatments. b) SEM and CLSM images for bacterial cells after different treatments. Before confocal observation, the bacteria were dye-labelled by 2′,7′-dichlorodihydrofluorescein diacetate (DCF-DA) assay kit, which revealed the intracellular ROS level of bacteria. White scale bar: 25 μm. Black scale bar: 2 μm. c) Bacterial viability calculated from agar plates. The data are normalized to the PBS-treated group as 100% and presented as mean ± SD, n = 3. d) Semiquantitative statistics of intercellular ROS level of bacteria. The data are estimated from six fluorescent images by ImageJ. $^{*}p < 0.05$; $^{**}p < 0.01$; $^{***}p < 0.001$; $^{****}p < 0.0001$ by multiple *t*-tests for data in (c) and (d).

biofilm biomass reduction can be noticed for all Au@CuBCats treated groups. When the concentration was 800 μg mL^{-1}, Au@CuBCats were able to reduce 84.6% of biofilm, suggesting the robust antibiofilm effect. We then applied a fluorescent probe, namely DCF-DA, to further determine the intracellular ROS level of bacteria. Consistently, we found the highest intracellular ROS level for both strains in the glucose+Au@CuBCats treatment group (Figure 4b,d), suggesting that the highest oxidative stress was induced by OH. Interestingly, we also noticed that the Au@CuBCats were able to effectively reduce the intracellular GSH level of MRSA (Figure S14, Supporting Information), leading to the oxidative stress.

Before conducting animal experiments, we first evaluated the biosafety of Au@CuBCats in both cellular and blood level. From CCK-8 results, we noticed the cell viability could fully recover to≈100% at day 3 after treatment by Au@CuBCats below 200 μg mL^{-1} (Figure S15, Supporting Information). Also, the Au@CuBCats exhibited no hemolytic effect even under high

concentration of 800 μg mL^{-1} (Figure S16, Supporting Information). Therefore, we are confident to further investigate the Au@CuBCats' ability for healing infected diabetic ulcers (**Figure 5**a). Wounds (6 mm in diameter) were inflicted on the ear of the diabetic rabbits and subsequently infected by *MRSA* to become ulcers. The formed diabetic ulcers were then randomly divided into four groups (n = 6 for each group) based on the following treatments: i) PBS; ii) CuBCats; iii) Vancomycin; iv) Au@CuBCats. To monitor the ulcer healing process, we photographed the ulcers every 4 days and the ulcer area was calculated from these images. As shown in Figure 5b and Figure S17 (Supporting Information), the vancomycin and Au@CuBCats groups recovered significantly faster and achieved 100% ulcer closure at day 11, when swollen ulcers were still observed in the PBS and CuBCats groups. Also, we found no viable *MRSA* colony for the vancomycin and Au@CuBCats groups (Figure 5c; Figure S18, Supporting Information). Consistent with these results, the bacterial number (BN) in the epidermis was calculated from the Giemsa staining (Figure 5d,e). Almost no bacterial cells were found in the epidermis for the vancomycin and Au@CuBCats groups, revealing that Au@CuBCats' bactericidal efficacy is as robust as that of vancomycin.

To further investigate the epidermis recovery and potential toxicity of Au@CuBCats at the tissue level after treatment, we collected the ulcer area and conducted systematic histological studies (Figure 5d,e). In order to determine inflammation levels in the ulcers after the different treatments, we applied hematoxylin and eosin (H&E) staining and immunofluorescence staining of proinflammatory cytokines including interleukin-1 beta (IL-1β) and tumor necrosis factor-alpha (TNF-α).[30] From H&E staining, we analyzed the inflammatory infiltration area (IIA) in ulcer tissues. Notably, the tissues of the Au@CuBCats and vancomycin groups exhibited well-ordered collagen structures and no apparent inflammation, properties similar to healthy tissues (Figure S19, Supporting Information). The absence of visible lesions demonstrates the good biosafety of Au@CuBCats treatment. By contrast, a great number of neutrophils and large IIA were observed for the tissues in the PBS and CuBCats groups, suggesting severe tissue inflammation originating from the surviving bacterial colonies. Compared to the PBS group, the vancomycin and Au@CuBCats groups showed very limited IL-1β expressions of 14.31% and 10.12%, respectively. In addition, significantly less TNF-α was found in the vancomycin (5.95%) and Au@CuBCats (6.59%) groups than in the PBS group. Besides, we did not find any lesion in major organs' H&E staining images (Figure S20, Supporting Information). These data confirmed the highly efficient therapeutic effect and good biosafety of the Au@CuBCats treatment.

The rebirth of collagen and vessels is an important indicator of tissue recovery.[31,32] Therefore, we used Masson's trichrome staining and cluster of differentiation 31 (CD31) immunofluorescence staining, respectively, to study the ulcer healing status via collagen deposition and neovascularization. The group treated with Au@CuBCats showed the highest collagen deposition area (CDA), suggesting the best collagen recovery. The CD31 expressions in the PBS and CuBCats groups were apparently limited as compared to the Au@CuBCats and vancomycin groups, with tissues still unrecovered from bacterial infection. Meanwhile, the Au@CuBCats and vancomycin groups had more than twice as many new vessels as the PBS group, confirming accelerated tissue healing. Taken together, these results demonstrate that Au@CuBCats can effectively cure bacterial diabetic ulcers in vivo and achieve accelerated regenerative ulcer healing. Also, as a ROS-based antibacterial therapy, the proposed Au@CuBCats have advantages like less possibility to arouse bacterial resistance, higher stability, and wider antibacterial spectrum as comparing to vancomycin. Therefore, we believe the Au@CuBCats show the potential as an antibiotic alternative for treating diabetic bacterial ulcers.

3. Conclusion

In conclusion, we synthesized a GOx-POD DEM bionanocatalyst Au@CuBCats. Via the DEM cascading catalysis by AuNPs and copper single atoms, the glucose can be catalyzed in situ to generate OH without extra energy input. Notably, the unique copper single atoms coordinated by one oxygen and two nitrogen atoms (CuN_2O_1) exhibit better POD catalytic performance than natural HRP. Further DFT calculations were performed to understand the catalytic mechanism and reveal the advantage of the CuN_2O_1 structure over other copper single-atom sites as both the dissociation of H_2O_2 and desorption of *OH are kinetically accessible. In vitro antibacterial results demonstrated that bionanocatalysts could induce significant bacterial reduction against the MDR bacterial strains *MRSA* and ESLP *E. coli*. In our in vivo study of bacterial diabetic ulcers in a rabbit ear model, the Au@CuBCats group exhibited rapid 100% recovery of the ulcer without any remaining inflammation lesion, suggesting the bionanocatalyst's outstanding therapeutic efficacy and biosafety. This work provides a proof of concept of a multi-enzyme mimetic bionanocatalyst serving as an MDR bacterial diabetic ulcer treatment. We also believe that this work will offer inspirations for designing the antibiotic-free bactericidal system and bionanocatalytic cascading medicines.

4. Experimental Section

Reagents: The chemical reagents including the cell culture materials were provided by commercial sources. All the reagents were of analytical grade and were used without further purification. ESLP *E. coli* was clinically isolated from patients in Charité and *MRSA* (ATCC 43 300) was purchased from American Type Culture Collection. Ultrapure water (18.2 MΩ; Millipore Co., USA) was applied in all experiments.

Instruments: STEM and EDX Mapping images were recorded by a JEOL JEM-ARM 200F scanning transmission electron microscope equipped with a cold field emission electron source, a DCOR probe corrector (CEOS GmbH), a 100 mm^2 JEOL Centurio EDX detector microscope. SEM images were obtained by using SU8030 scanning electron microscope (Hitachi). XAS spectra at the copper K-edge were collected at the BESSY synchrotron (Berlin, Germany) at beamlines KMC-3. The UV absorption spectra were recorded by M200 P Infinite PRO microplate reader (Tecan). The fluorescent spectra were measured by Fluorescence Spectrometer FP-6500 (Jasco). The fluorescence images were taken with Leica TCS SP8 CARS fluorescence confocal microscope.

Synthesis of CuBCats: Typically, 145 mg of copper nitrate hydrate and 1.044 g of chloranilic acid were separately dissolved in 50 mL methanol to get metal and ligand solution, respectively. Then, the metal solution was fast poured into the ligand solution under a high-speed magnetic stirring. The reaction was kept overnight. The products (CuCA precursors) were then washed with ethanol for three times by centrifugation and dried in an oven at 65 °C. Afterwards, the CuCA precursors were mixed with the

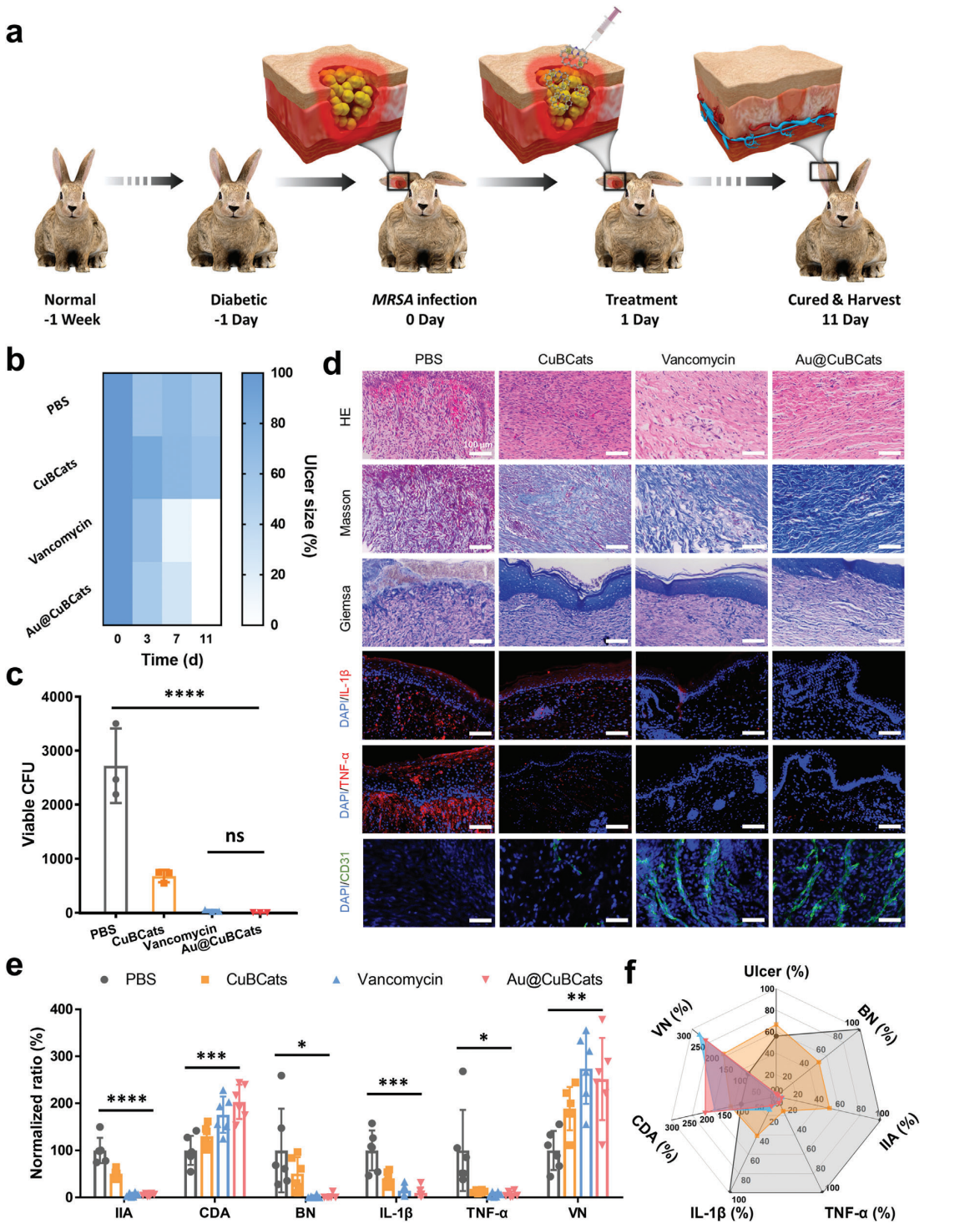

Figure 5. In vivo diabetic ulcer treatment with Au@CuBCats. a) Schematic illustration of the experimental flow. b) Ulcer size ratios with different treatments at days 0, 3, 7, and 11. c) Viable *MRSA* CFU on ulcer after 11 days of treatment. d) Immunohistochemical studies, and e) corresponding statistical analysis (normalized to PBS group) of diabetic ulcer collected from rabbit at day 11. Scale bar: 100 μm. f) Overall performance of PBS, CuBCats, vancomycin, and Au@CuBCats in the in vivo diabetic ulcer treatment. The data are estimated from six fluorescent images by ImageJ. $^{*}p < 0.05$; $^{**}p < 0.01$; $^{***}p < 0.001$; $^{****}p < 0.0001$ by multiple *t* test for data in (c) and (e), ns represents no significant difference.

same mass amount of DCD in corundum boat and then subjected to a 900 °C-pyrolysis step for 3 h in a tube furnace, followed by an acid etching step using 1 M HCl under 90 °C overnight. Finally, the products were washed with water for three times by centrifugation and dried in an oven at 65 °C. We selected 900 °C as the carbonization temperature in order to local adjusting the copper single-atom structures. According to previous studies, when choosing 800 °C or a lower temperature for pyrolysis, metal-N_4 single-atom sites could be easily obtained. While a 900 °C carbonization temperature can facilitate the formation of unsaturated metallic single-atom sites, which possessed higher catalytic activities comparing to the symmetric metal-N_4 single-atom sites.[33–35]

Synthesis of Au@CuBCats: Typically, 1 mg of CuBCats were homogeneously dispersed in 1 mL of chloroauric acid ($HAuCl_4$) aqueous solution (2 mM) under the assistance of sonication. The oxygen-containing group within CuBCats could coordinate with Au ions via static interaction. Then, 62.5 µL of fresh prepared sodium borohydride aqueous solution (100 mM) was introduced to the above CuBCats-$HAuCl_4$ solution under vigorous magnetic stirring. The coordinated Au ions could then be in situ reduced on the CuBCats. After three times of water washing and drying, the final products, Au@CuBCats were obtained.

Computational Details: Spin-polarized DFT calculations were performed with the Vienna ab initio Simulation Package (VASP) in the framework of the projector-augmented wave (PAW) method with energy cutoff E_{cut} = 600 eV.[36,37] Geometry optimizations (including transition states) and frequency analyses were performed with the PBE functional, followed by single-point calculations with the PBE0 functional.[38] Grimme D3(BJ) dispersion correction with Becke-Johnson damping was applied to account for Van der Waals interactions.[39]

The RMM-DIIS algorithm was applied for electronic relaxation during geometry optimization while the conjugate gradient algorithm was applied, starting from the PBE wave function, for the single point calculation. The electronic convergence criterion was set to 10^{-5} eV. The Gaussian smearing approach with smearing width $\sigma = 0.05$ eV was applied. K-points were sampled using a 3 × 3 × 1 Γ-centered mesh grid. Ionic relaxation steps were performed with the conjugate gradient algorithm with force convergence of 10^{-2} eV Å^{-1}. During geometry optimization, all atomic positions and the unit cell shape were optimized at constant unit cell volume (ISIF = 4). Transition states were obtained using the climbing image nudged elastic band (CI-NEB) method using nine images.[40]

Supporting Information

Supporting Information is available from the Wiley Online Library or from the author.

Acknowledgements

X.F. and Y.G. contributed equally to this work. This work was financially supported by the National Key R&D Program of China (2019YFA0110600), and Deutsche Forschungsgemeinschaft (DFG) of Germany through grants from the Collaborative Research Centers (SFB) 765 and 1449. The authors are grateful for the support of Benjamin Allen in polishing the language of the manuscript. X.F., F.Y., and L.W. acknowledge the support from China Scholarship Council (CSC). J.L.L. acknowledged support from the Elsa-Neumann Scholarship and the computing resources of Norddeutscher Verbund für Hoch- und Höchstleistungsrechnung (HLRN). Prof. C.C. thanks the support from the National Natural Science Foundation of China (Nos. 52161145402 and 52173133), the Sichuan Science and Technology Program (No. 2021YFH0087), the 1·3·5 Project for Disciplines of Excellence, West China Hospital, Sichuan University (No. ZYJC21047), the innovation project of Med-X Center for Materials, Sichuan University (No. MCM202102), the State Key Laboratory of Polymer Materials Engineering (No. sklpme2021-4-02). The authors thank Li Li, Fei Chen, and Chunjuan Bao of the Institute of Clinical Pathology, Sichuan University, for processing histological staining and BiosupraMol for providing SEM and CLSM. All animal experiments were performed by following the animal ethical standard from Animal Ethics Committee in West China Hospital, Sichuan University, Chengdu, China, with approval number 2021024A.

Open access funding enabled and organized by Projekt DEAL.

Conflict of Interest

The authors declare no conflict of interest.

Data Availability Statement

The data that support the findings of this study are available from the corresponding author upon reasonable request.

Keywords

cascade catalysis, copper single-atom catalysts, diabetic ulcers, enzyme-mimetic bionanocatalysts, multi-drug resistant bacteria

Received: February 20, 2023
Revised: April 3, 2023
Published online: May 13, 2023

[1] Y. Zheng, S. H. Ley, F. B. Hu, *Nat Rev Endocrinol* **2018**, *14*, 88.
[2] P. Zimmet, K. G. Alberti, D. J. Magliano, P. H. Bennett, *Nat Rev Endocrinol* **2016**, *12*, 616.
[3] T. Wang, Y. Li, E. J. Cornel, C. Li, J. Du, *ACS Nano* **2021**, *15*, 9027.
[4] Y. Liang, M. Li, Y. Yang, L. Qiao, H. Xu, B. Guo, *ACS Nano* **2022**, *16*, 3194.
[5] C. M. Wong, K. H. Wong, X. D. Chen, *Appl. Microbiol. Biotechnol.* **2008**, *78*, 927.
[6] Y. Deng, X. Ouyang, J. Sun, X. Shi, Y. Li, Y. K. Chan, W. Yang, S. Peng, *Bioact Mater* **2022**, *25*, 748.
[7] T. Huang, B. Yuan, W. Jiang, Y. Ding, L. Jiang, H. Ren, J. Tang, *J. Mater. Chem. B* **2021**, *9*, 6190.
[8] Y. Zhu, J. Zhang, J. Song, J. Yang, Z. Du, W. Zhao, H. Guo, C. Wen, Q. Li, X. Sui, L. Zhang, *Adv. Funct. Mater.* **2020**, *30*, 1905493.
[9] C. Zhang, L. Zhang, W. Wu, F. Gao, R.-Q. Li, W. Song, Z.-N. Zhuang, C.-J. Liu, X.-Z. Zhang, *Adv. Mater.* **2019**, *31*, 1901179.
[10] C. Fang, Z. Deng, G. Cao, Q. Chu, Y. Wu, X. Li, X. Peng, G. Han, *Adv. Funct. Mater.* **2020**, *30*, 1910085.
[11] W. Xu, L. Jiao, Y. Wu, L. Hu, W. Gu, C. Zhu, *Adv. Mater.* **2021**, *33*, 2005172.
[12] G. Zhang, Y. Ji, X. Li, X. Wang, M. Song, H. Gou, S. Gao, X. Jia, *Adv Healthc Mater* **2020**, *9*, 2000221.
[13] X. Wan, H. Zhang, W. Pan, N. Li, B. Tang, *Chem. Commun.* **2021**, *57*, 5402.
[14] Y. Hu, S. Bai, X. Fan, F. Zhou, B. Chen, S. Tan, H. Xu, A. Pan, S. Liang, Y. He, *Biomater. Sci.* **2022**, *10*, 2358.
[15] C. Wu, K. Schwibbert, K. Achazi, P. Landsberger, A. Gorbushina, R. Haag, *Biomacromolecules* **2017**, *18*, 210.
[16] Y. Zhu, J. Zhang, J. Song, J. Yang, Z. Du, W. Zhao, H. Guo, C. Wen, Q. Li, X. Sui, *Adv. Funct. Mater.* **2020**, *30*, 1905493.
[17] C. J. Miller, Y. Chang, C. Wegeberg, C. J. McKenzie, T. D. Waite, *ACS Catal.* **2021**, *11*, 787.
[18] Q. Wang, J. Chen, H. Zhang, W. Wu, Z. Zhang, S. Dong, *Nanoscale* **2018**, *10*, 19140.
[19] J. Wang, R. Huang, W. Qi, R. Su, B. P. Binks, Z. He, *Appl. Catal., B* **2019**, *254*, 452.
[20] D. Bobo, K. J. Robinson, J. Islam, K. J. Thurecht, S. R. Corrie, *Pharm. Res.* **2016**, *33*, 2373.

[21] Y. Lin, Z. Li, Z. Chen, J. Ren, X. Qu, *Biomaterials* **2013**, *34*, 2600.
[22] X. Lu, S. Gao, H. Lin, L. Yu, Y. Han, P. Zhu, W. Bao, H. Yao, Y. Chen, J. Shi, *Adv. Mater.* **2020**, *32*, 2002246.
[23] Y. Sun, S. Mu, Z. Xing, J. Guo, Z. Wu, F. Yu, M. Bai, X. Han, C. Cheng, L. Ye, *Adv. Mater.* **2022**, *34*, 2206208.
[24] Y. Cai, J. Fu, Y. Zhou, Y.-C. Chang, Q. Min, J.-J. Zhu, Y. Lin, W. Zhu, *Nat. Commun.* **2021**, *12*, 586.
[25] H. Luo, L. Lari, H. Kim, S. Hérou, L. C. Tanase, V. K. Lazarov, M.-M. Titirici, *Nanoscale* **2022**, *14*, 910.
[26] B. Xu, H. Wang, W. Wang, L. Gao, S. Li, X. Pan, H. Wang, H. Yang, X. Meng, Q. Wu, L. Zheng, S. Chen, X. Shi, K. Fan, X. Yan, H. Liu, *Angew. Chem., Int. Ed.* **2019**, *58*, 4911.
[27] M. Huo, L. Wang, H. Zhang, L. Zhang, Y. Chen, J. Shi, *Small* **2019**, *15*, 1901834.
[28] L. Gao, J. Zhuang, L. Nie, J. Zhang, Y. Zhang, N. Gu, T. Wang, J. Feng, D. Yang, S. Perrett, X. Yan, *Nat. Nanotechnol.* **2007**, *2*, 577.
[29] P. Cheng, H. Wang, X. Shi, *Nanoscale* **2020**, *12*, 3050.
[30] C. Mao, W. Jin, Y. Xiang, Y. Zhu, J. Wu, X. Liu, S. Wu, Y. Zheng, K. M. C. Cheung, K. W. K. Yeung, *Adv. Funct. Mater.* **2022**, *32*, 2202887.
[31] X. Fan, X. Wu, F. Yang, L. Wang, K. Ludwig, L. Ma, A. Trampuz, C. Cheng, R. Haag, *Angew. Chem., Int. Ed.* **2022**, *61*, e202113833.
[32] L. Li, S. Cao, Z. Wu, R. Guo, L. Xie, L. Wang, Y. Tang, Q. Li, X. Luo, L. Ma, C. Cheng, L. Qiu, *Adv. Mater.* **2022**, *34*, 2108646.
[33] S. Ma, Z. Han, K. Leng, X. Liu, Y. Wang, Y. Qu, J. Bai, *Small* **2020**, *16*, 2001384.
[34] C. Yan, H. Li, Y. Ye, H. Wu, F. Cai, R. Si, J. Xiao, S. Miao, S. Xie, F. Yang, *Energy Environ. Sci.* **2018**, *11*, 1204.
[35] W. Zheng, J. Yang, H. Chen, Y. Hou, Q. Wang, M. Gu, F. He, Y. Xia, Z. Xia, Z. Li, *Adv. Funct. Mater.* **2020**, *30*, 1907658.
[36] G. Kresse, J. Hafner, *Phys. Rev. B* **1993**, *47*, 558.
[37] G. Kresse, J. Furthmüller, *Comput. Mater. Sci.* **1996**, *6*, 15.
[38] J. P. Perdew, K. Burke, M. Ernzerhof, *Phys. Rev. Lett.* **1996**, *77*, 3865.
[39] S. Grimme, S. Ehrlich, L. Goerigk, *J. Comput. Chem.* **2011**, *32*, 1456.
[40] G. Henkelman, B. P. Uberuaga, H. Jónsson, *Chem. Phys.* **2000**, *113*, 9901.

ADVANCED FUNCTIONAL MATERIALS

Supporting Information

for *Adv. Funct. Mater.*, DOI 10.1002/adfm.202301986

A Copper Single-Atom Cascade Bionanocatalyst for Treating Multidrug-Resistant Bacterial Diabetic Ulcer

Xin Fan, Yang Gao, Fan Yang, Jian Liang Low, Lei Wang, Beate Paulus, Yi Wang, Andrej Trampuz, Chong Cheng* and Rainer Haag**

Supporting Information

69451 Weinheim, Germany

A Copper Single-Atom Cascade Bionanocatalyst for Treating Multidrug-Resistant Bacterial Diabetic Ulcer

Xin Fan, Yang Gao, Fan Yang, Jian Liang Low, Lei Wang, Beate Paulus, Yi Wang, Andrej Trampuz*, Chong Cheng*, and Rainer Haag*

Supporting Information

XAFS measurements and simulations. X-ray absorption spectroscopy (XAS) at the Cu K-edge were performed at beamline KMC-3 at the BESSY-II synchrotron (Helmholtz Center Berlin, Germany) using a set-up including a Si[111] double-crystal monochromator, a 13-element energy-resolving Si-drift detector (RaySpec) for X-ray fluorescence monitoring, and DXP-XMAP pulse-processing electronics (XIA). Samples were held at 20 K in a liquid-helium cryostat (Oxford). The energy axis of the monochromator was calibrated (accuracy ±0.1 eV) using the K-edge spectrum of copper foil (fitted reference energy of 8979eV in the first derivative spectrum). The spot size on the samples was ca. 1.5 x 2.0 mm (vertical x horizontal) as set by a focusing mirror and slits. X-ray fluorescence spectra were collected using a continuous scan mode of the monochromator (scan duration ~10 min). 3 scans were averaged (1-2 scans per sample spot) for signal-to-noise ratio improvement. XAS data were processed (dead-time correction, background subtraction, normalization, self-absorption correction) to yield XANES and Cu-EXAFS spectra using our earlier described procedures and in-house software.[1] k^3-weighted EXAFS spectra were simulated with in-house software and phase functions from FEFF9. The range of the fits was 2.3-10.3 Å, and the amplitude reduction factor (S_0^2) was 0.89. The errors represent the 68% confidence interval of the respective fit parameter in all EXAFS fit tables. The obtained R_f value of the fits are given for the distance range of interest (1-5 Å of reduced distance).

GOx-mimetic activity of Au@CuBCats. To evaluate the GOx-mimetic activity of Au@CuBCats, we tested the glucose consumption, the pH changing and the H_2O_2 generation after certain time of incubation.

For the glucose consumption experiment, typically, 100 μL of Au@CuBCats aqueous dispersion (1 mg/mL) was mixed with 100 μL of glucose solution (1 mg/mL), and 3,5-dinitrosalicylic acid (DNS) method was used to evaluate the glucose concentration. In brief, after a 2.5-hour incubation, 0.6 mL of DNS reagent was added to above solution, which was then heated at 100 ℃ for 5 minutes and quickly transferred to cool water for 20 minutes. The free GOx (2U/mL) and DI water groups served as comparison.

For pH changing monitoring, Au@CuBCats aqueous dispersion was added into glucose solution, which was dissolved in PBS (0.5 mM, initial pH=7.2). The final concentrations of Au@CuBCats and glucose were 50 μg/mL and 100 mM, respectively. pH value was recorded with a real-time pH meter.

For H_2O_2 generation experiment, a H_2O_2 assay kit (Pierce™) was employed, which is based on the oxidation of ferrous ions (Fe^{2+}) to ferric ions (Fe^{3+}) by peroxides and the Fe^{3+} then combine a xylenol orange to form a purple-colored complex with the maximum absorbance at 560 nm. In brief, the reaction solution was centrifuged at 14,800 r.p.m. for 5 min and the supernatants were collected. Finally, the supernatants and detection solution were mixed for 30 min at room temperature and then measured using a microplate reader. The level of H_2O_2 in products was calculated according to a standard concentration curve with triplicate experiments.

•OH generation activity of the bionanocatalysts. Terephthalic acid (TA) was used as a fluorescent probe that easily reacts with •OH to form a highly fluorescent product, 2-hydroxy terephthalic acid (HA). In a typical procedure, 150 μg of the bionanocatalyts were dispersed in 1.5 mL of PBS (0.5 mM, pH~7.2). Then, the dispersions were mixed with 1.5 mL of 6 mM TA solution containing 200 μM H_2O_2 (or 2 mM glucose) for 12 h in the dark, and finally, the changes in the 435 nm fluorescence emission peak were recorded using a Fluorescence Spectrometer.

Peroxidase-mimetic activity. To monitor the peroxidase-like property of the bionanocatalysts, the 3,3,5,5-tetramethylbenzidine (TMB) molecular probe was utilized, and reactions were carried out in 0.1 mL acetate buffer solution (0.1 M, pH = 4.0), and the final concentrations of TMB, H_2O_2, and CuBCats were 1 mM, 100 μM, and 50 μg/mL, respectively. After 5 min reaction time, photos were taken, and the UV-vis absorption spectra were measured by a microplate reader.

For the measurement of Au@CuBCats with dual-enzyme mimetic cascading catalytic performance, the Au@CuBCats were dispersed in PBS (0.5 mM, initial pH=7.2) that containing glucose. Then, the TMB was firstly dissolved in DMSO and then diluted to Au@CuBCats-PBS solution. The final

concentrations for Au@CuBCats, glucose and TMB were fixed to 50 μg/mL, 1 mM and 0.1 mM, respectively. Finally, the absorption at 652 nm was measured by a microplate reader at different incubation times.

The steady-state kinetic assay was performed at room temperature. For kinetic parameters, the experiments were carried out in 100 μL NaAc buffer containing 50 μg/mL CuBCats, 832 μM TMB, and a series of concentrations of H_2O_2 ranging from 0 to 1000 mM. The absorbances of all reactions were monitored in a time-scan mode at 652 nm through a microplate reader, and the Michaelis–Menten constant was calculated according to the Michaelis–Menten saturation curve by GraphPad Prism 7.0 (GraphPad Software).

GSH depletion test. The consumption of GSH was detected with a 5,5'-Dithiobis-(2-nitrobenzoic acid) (DTNB) probe by UV–vis spectroscopy. The bionanocatalysts were mixed with GSH and DTNB in PBS (pH 7.2) at room temperature in the cuvette. The final concentrations of bionanocatalysts, GSH and DTNB were fixed to 50 μg/mL, 0.1 mM and 0.1 mM, respectively. At different points, the absorbance at 410 nm of the mixed solution was recorded by UV–vis spectrophotometer. In this experiment, PBS served as negative control and H_2O_2 served as the positive control and the consumption of GSH was calculated as the following equation, where A(t), A(Pos), and A(Neg) represent the absorbance at 410 nm of bionanocatalysts group, positive control group and negative control group at time t, respectively.

$$Loss\ of\ GSH(\%) = (1 - \frac{A(t) - A(Pos)}{A(Neg) - A(Pos)}) \bullet 100\%$$

For the intracellular GSH consumption, we used an assay kit (ab112132, abcam) to evaluate the intracellular GSH levels. Briefly, we diluted the overnight *MRSA* culture by PBS to 10^7 CFU/mL. Then, we introduced the Au@CuBCats with a final concentration of 50 μg/mL to the bacterial solution and incubated them in a 37 ºC oven for 4 h. Afterwards, we strictly followed the instructions of the assay kit to label the bacterial cell by a thiol-dye. The bacterial solution without dye-labeling served as a negative control and the bacterial solution without materials served as positive control. Finally, a flow cytometer was used to evaluate the fluorescence intensity of bacterial solution.

***In vitro* planktonic bacterial killing tests.** Typically, the Au@CuBCats were firstly dispersed in LB media. Then, 100 μL of sample dispersions with a series of dilution times and glucose with the final

concentration of 1 mg/mL were introduced into 100 μL of ~10^5 CFU/mL bacterial suspensions. The suspensions were incubated at 37 ºC for 4 h. The experimental groups of PBS, glucose, glucose + GOx (2U/mL as a final concentration), and glucose + CuBCats served as a comparison. At last, the bactericidal ratio for the samples under different conditions was studied via agar plate counting. The bacterial suspensions were diluted and cultured on agar plates for 12 h to count the bacterial colonies. Meanwhile, SEM was utilized to observe the morphologies of bacteria after different treatment.

***In vitro* antibiofilm tests.** Typically, we introduced 200 μL of *MRSA* solution (10^6 CFU/mL) to each well in 96-well plate and cultured them in 37ºC oven for 48 hours to obtain biofilms attaching on the bottoms of well. Afterwards, for each well, 100 μL of Au@CuBCats-PBS solution with different concentrations and glucose with final concentration of 1 mg/mL were placed and incubated in 37ºC oven overnight. The biofilms without Au@CuBCats were considered as control group. Next, to remove the Au@CuBCats, the biofilms were gently washed 3 times by PBS and stained by 0.1% crystal violet for 15 minutes in room temperature. Again, the biofilms were gently washed by RO water to remove the excess dye. After drying in room temperature, the crystal violet in the bottom of each well was redissolved by 100 μL of ethanol, and finally the optical density of each well at 595 nm was analyzed by microplate reader.

Bacterial intracellular ROS level. We used 2′,7′-Dichlorofluorescein diacetate (DCF-DA, Sigma-Aldrich) to study the bacterial intracellular ROS level induced by bionanocatalysts. The bacterial cells with final concentration of 10^8 CFU/mL were treated with different groups for 4 h. Afterwards, the treated bacterial cells were washed with PBS for 3 times by centrifugation, followed by being stained with 10 μM of DCF-DA for 30 min in the dark. The fluorescent bacterial cells were observed with confocal microscope and the fluorescent intensity was quantified by the Image J software.

Hemolytic experiment. Typically, the PBS-diluted red blood cells (RBCs) were mixed with different concentrations of Au@CuBCats in centrifuge tubes. 1% Triton X-100-treated RBCs were considered as the positive control, and PBS-dispersed RBCs were considered as the negative control. All the experimental groups were incubated at 37 ºC with shaking for 3 h and then centrifuged at 6000 rpm for 5 min. The absorbance of supernatant was measured at 545 nm by microplate reader.

Cytotoxicity test. Human skin keratinocyte cell line HaCaT was chosen as model cell line to investigate the cells toxicity of the bionanocatalysts. HaCaT cells were grown in Eagle's minimal essential medium (DMEM) supplemented with 10% fetal bovine serum, 4.5 g/L glucose, 2 mM L-

glutamine, 100 mg/ml streptomycin, and 100 units/ml penicillin) in a 96-well plate at 37 °C and 5% CO_2. The cytotoxicity was then measured via CCK-8 assay according to the manufacturer's instruction. Briefly, we seeded the cells in 96-well plates (~ 10^4 cells/well) and cultured them for 24 hours in oven. Then, different concentrations of Au@CuBCats diluted by DMEM were introduced to wells and cultured with cells for 24 hours in oven. Afterwards, we gently washed the cells by PBS for 2 times to remove the Au@CuBCats and refilled the wells by 100 μL of DMEM. Next, 10 μL of CCK-8 reagent was introduced to each well and the cells were cultured for 2 hours before their optical density being measured by a microplate reader at OD 460 nm. Also, the cell regrowth after exposing to materials for the next two days was recorded by same CCK-8 assay. The cells without adding materials at day 1 were considered as control.

***In vivo* rabbit's ear bacterial diabetic ulcer model.** To assess the therapeutic effects of the bionanocatalysts, we established a diabetic ulcer model. All the studies on these animals were performed by following the animal ethical standard from Animal Ethics Committee in West China Hospital, Sichuan University, Chengdu, China with approval number 2021024A. Male New Zealand white rabbits (3.5-4 kg) were used in the study. The animals were 3-4 months of age. Rabbits were housed in individual cages, with a 12-h light/dark cycle and controlled temperature and humidity. Rabbits were fed a standard chow and water ad libitum. Typically, to establish the diabetic rabbit model, the rabbits were firstly anesthetized after adaptive feeding, and hair was shaved off the back of the ears. Then, Alloxan (150 mg/kg) (Sigma-Aldrich) was made up in 30 mL of saline and administered via an ear vein using an intravenous cannula at a rate of 1.5 mL/min. After treatment, water containing glucose was provided for 24 h to prevent hypoglycemia. Blood glucose levels were measured daily with a glucose strip after the injection and were considered diabetes when blood glucose levels stabilized above 300 mg/dL (16.67 mol/L). Insulin therapy was administered if the animal lost weight and had "high" (> 33 mmol/L) glucose readings using insulin glargine.

To create bacterial diabetic ulcer, the diabetic rabbits were anesthetized after 4 weeks of hyperglycemia. Three wounds were then created on each ear using sterile, disposable 6 mm punch biopsies. The wounds were created and the dermis was exposed to bare cartilage. Then 0.5 mL MRSA bacterial suspension (1×10^8 CFU/mL) was dropped on the wounds. After being infected for 1 day, the ulcers formed with festering.

The typical treatment procedure was as follows: 100 μL of Au@CuBCats (10 mg/mL) was added to

the ulcers. PBS and vancomycin (16 μg/mL) were also used as a contrast. After 11 days of treatment, the ulcers were cut off and fixed with 10% formaldehyde solution for histological analysis including H&E, Masson, Giemsa, TNF-α, IL-1β, and CD31 staining. Fluorescence images were observed by automatic microscope (Olympus, IX83).

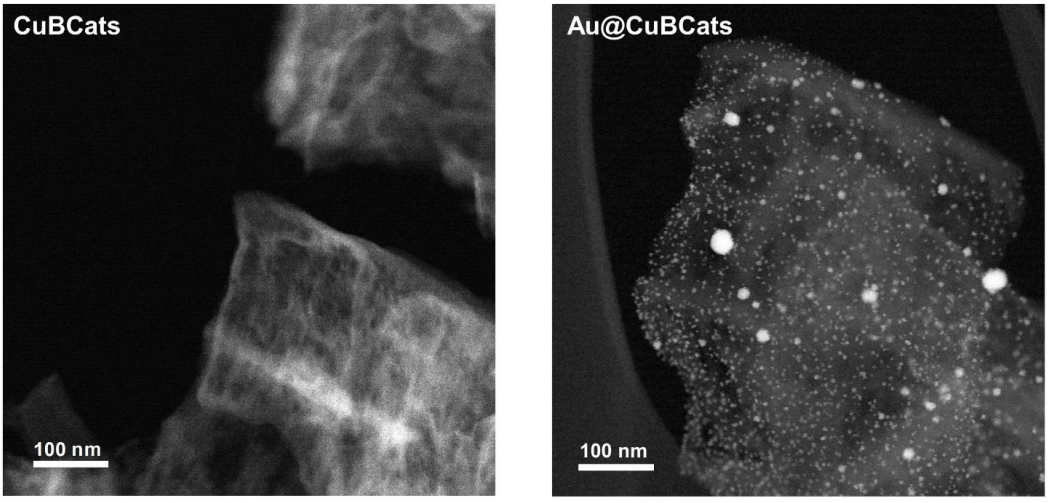

Figure S1. STEM images of CuBCats and Au@CuBCats.

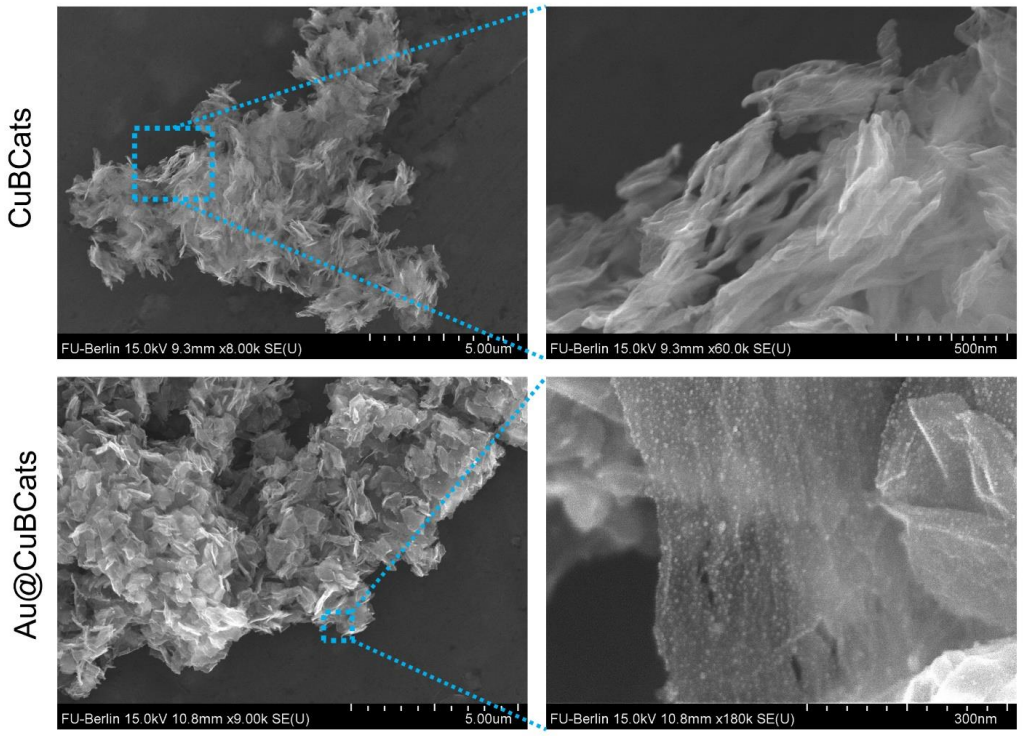

Figure S2. SEM images of CuBCats and Au@CuBCats.

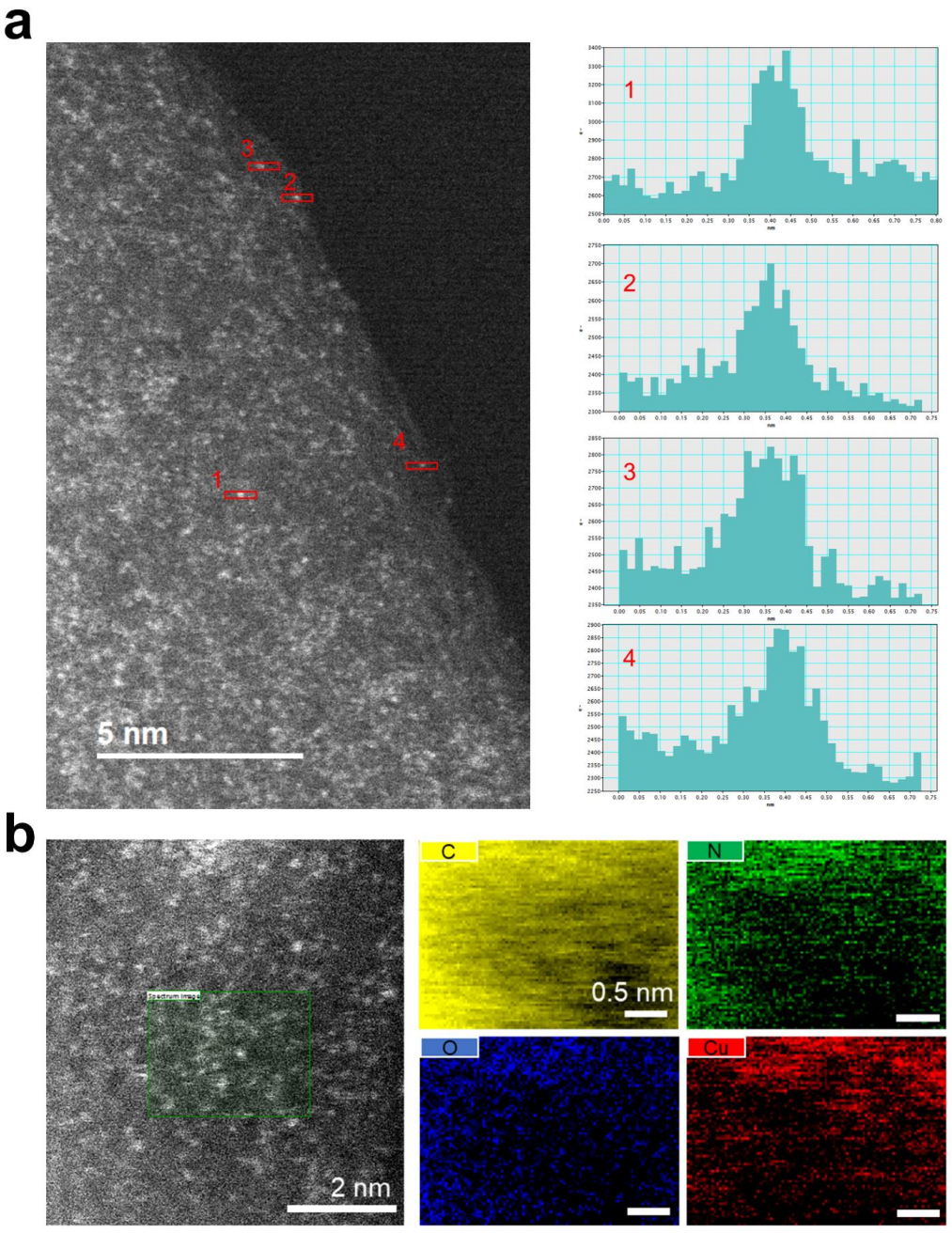

Figure S3. (a) High-resolution STEM image of CuBCats with highlighted copper single atoms and corresponding intensity profiles. (b) EDS mapping of CuBCats.

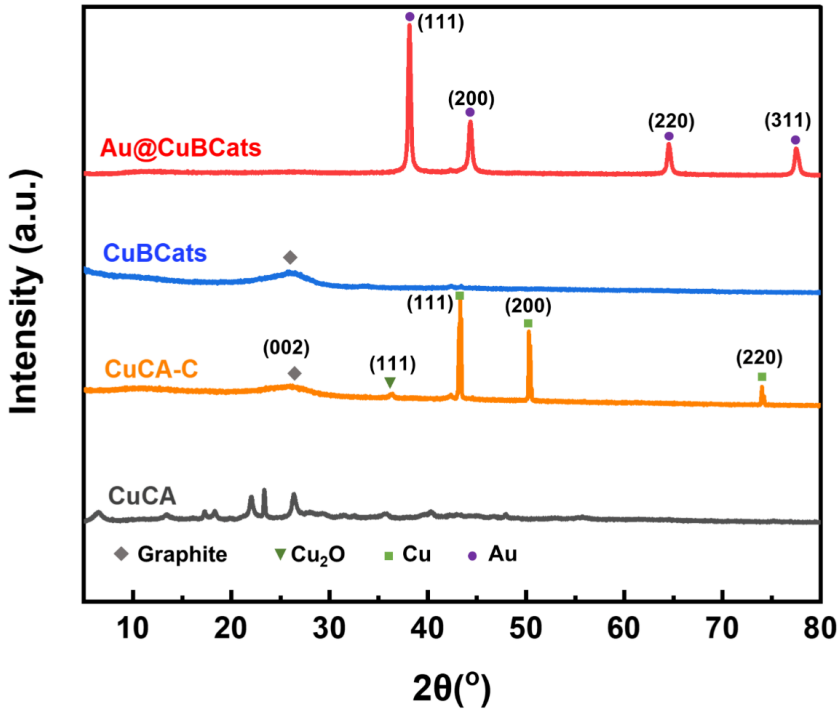

Figure S4. XRD patterns of CuCA, CuCA-C, CuBCats, and Au@CuBCats. CuCA-C is the CuBCats without acid etching.

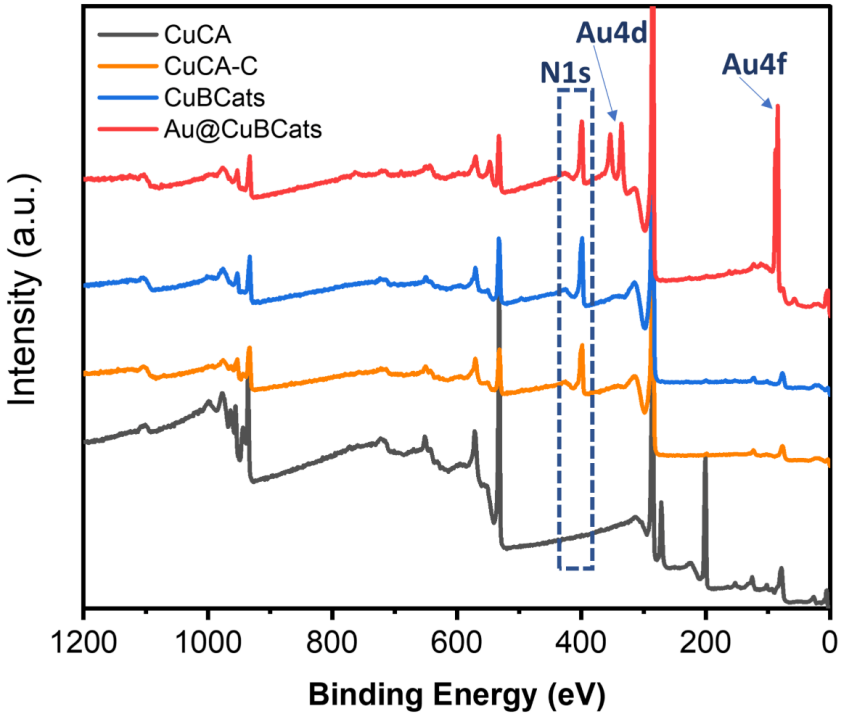

Figure S5. XPS survey of CuCA, CuCA-C, CuBCats and Au@CuBCats.

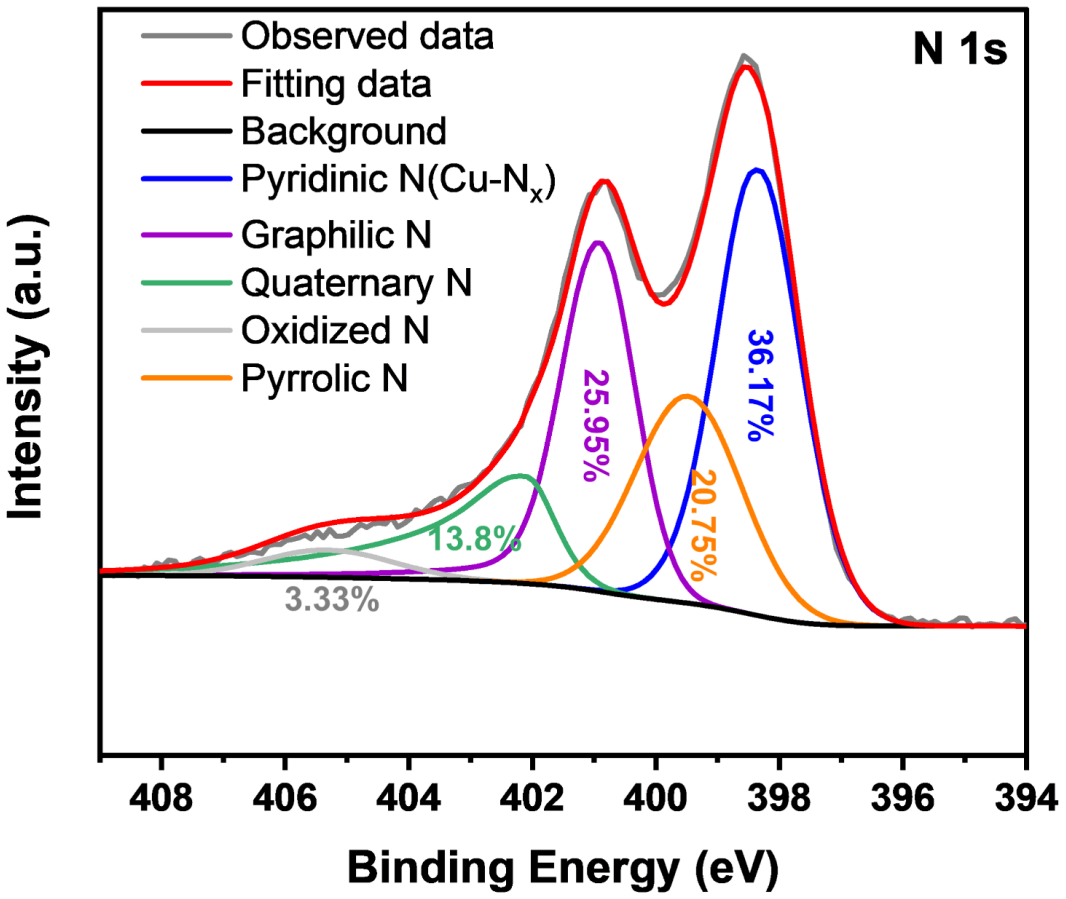

Figure S6. High-resolution XPS N1s spectra of Au@CuBCats.

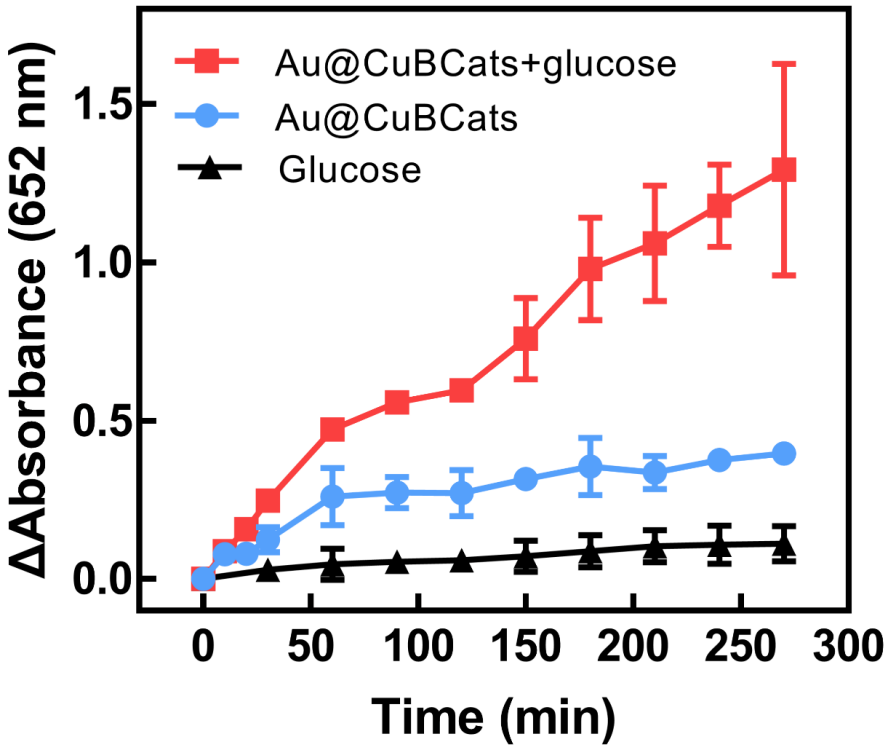

Figure S7. Time-dependent absorbance changes at 652 nm as a result of the catalyzed oxidation of TMB.

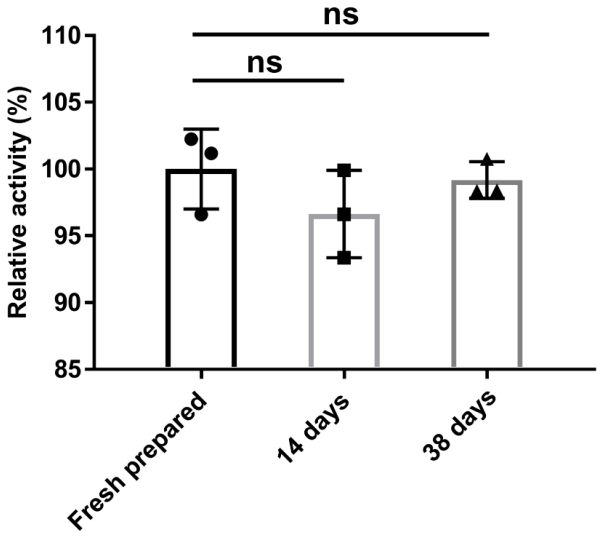

Figure S8. Relative catalytic activities of fresh prepared Au@CuBCats, 14-day-aged and 38-day-aged

room-temperature stored Au@CuBCats. The activities were determined by the absorbance at 652 nm (oxidized TMB peak) with the presence of Au@CuBCats and glucose. The final concentrations of Au@CuBCats, TMB, and glucose were fixed to 50 μg/mL, 0.1 mM and 1 mM, respectively. ns represents no significant difference.

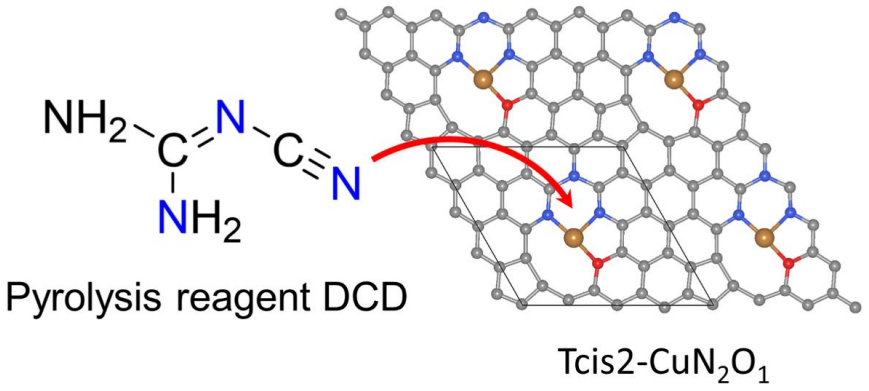

Figure S9. Schematic illustration of how DCD may play a role in facilitating the formation of N-C-N-C-N structure.

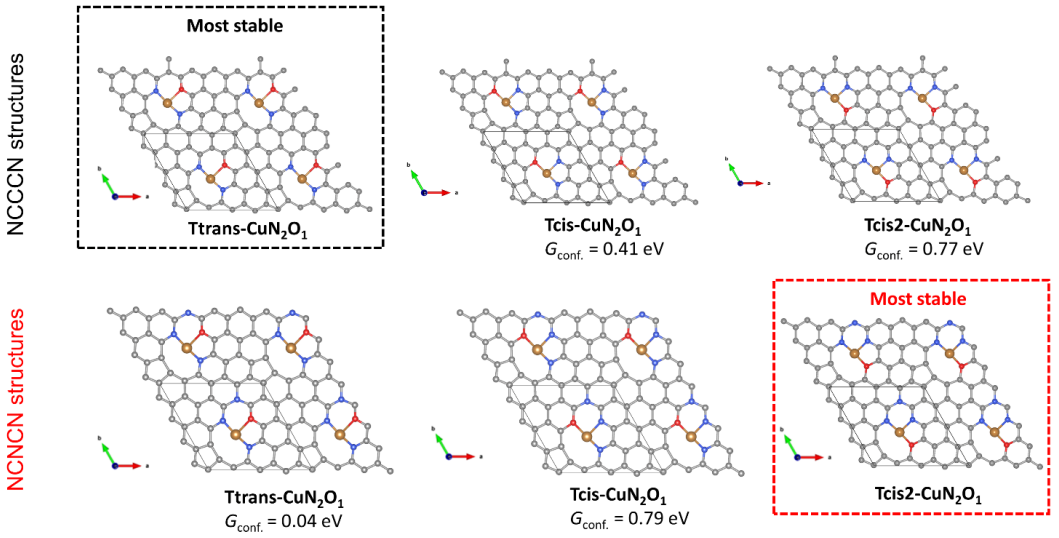

Figure S10. Possible arrangements of CuN_2O_1 motifs derived from a hexagonal 4x4 supercell of graphene with addition N dopant (bottom) and without (top). The conformational free energy of each

motif $G_{conf.}$ is shown with reference to the respective most stable structure.

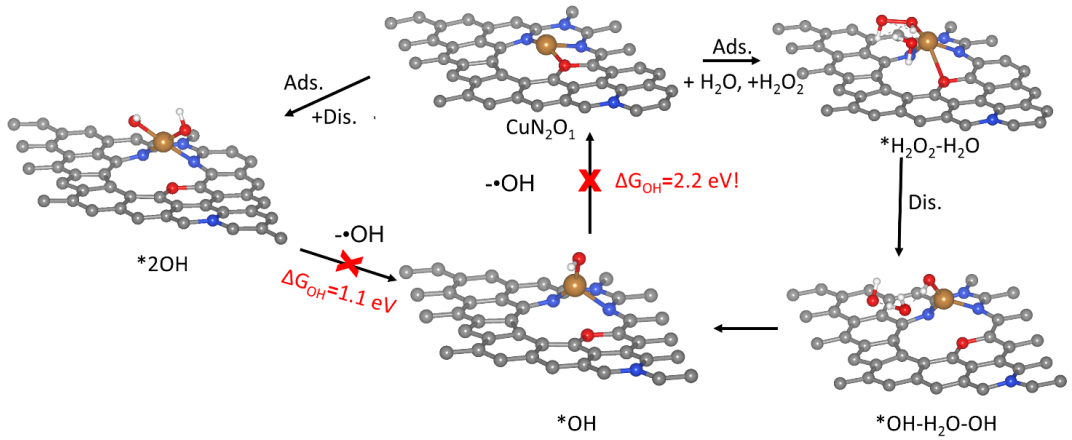

Figure S11. Scheme of alternative reaction mechanisms involving the unfeasible desorption of OH radical from the Cu center. The proposed mechanism differs from the mechanism on the right in the final desorption step of OH.

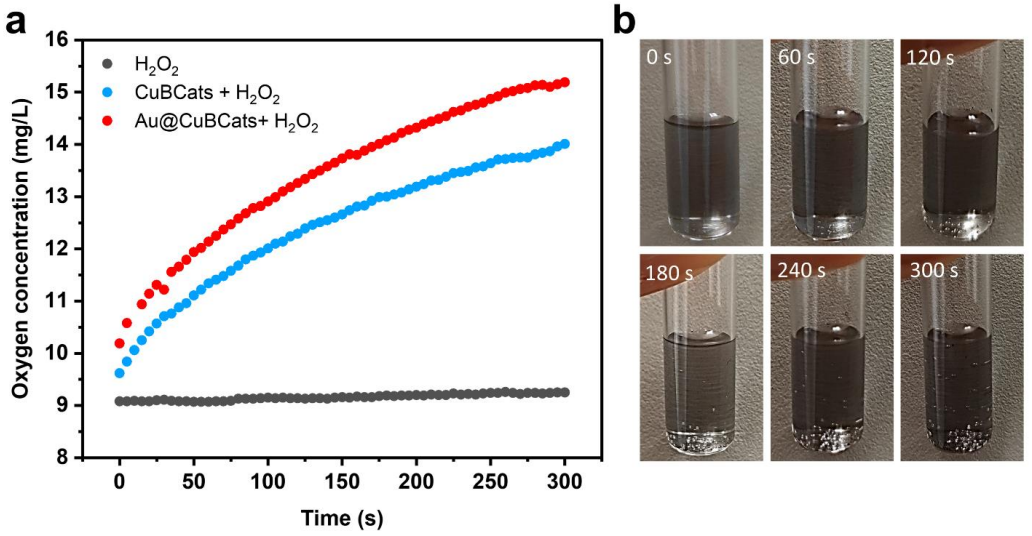

Figure S12. (a) The variation of dissolved oxygen concentrations of H_2O_2, CuBCats + H_2O_2 and Au@CuBCats + H_2O_2 in NaAC/HAc buffer. The final concentration of H_2O_2, CuBCats and Au@CuBCats were fixed to 100 mM, 50 μg/mL and 50 μg/mL, respectively. (b) The typical images of oxygen generation of Au@CuBCats + H_2O_2 group over 300 seconds.

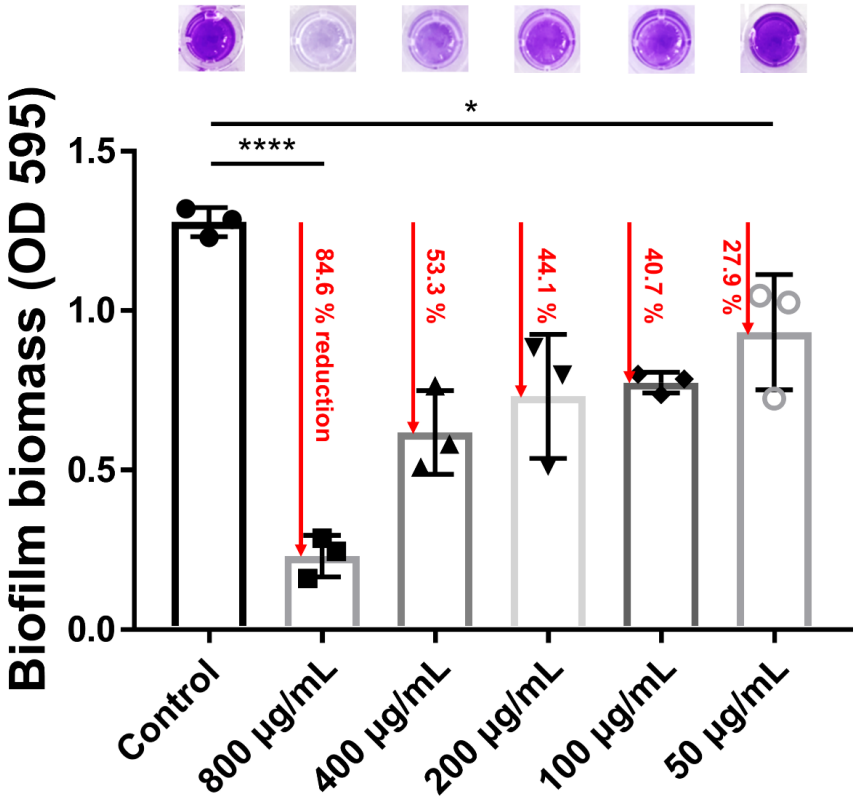

Figure S13. Biofilm biomass after treatment of different concentrations of Au@CuBCats in the presence of glucose with the final concentration of 1 mg/mL. *P < 0.05; ****P < 0.0001 by multiple t tests for data.

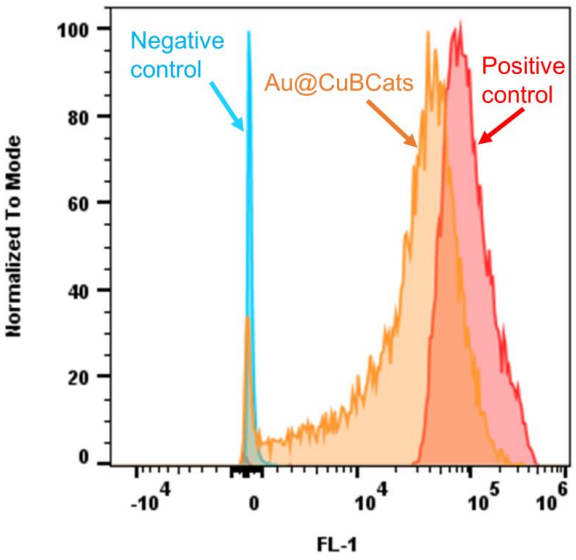

Figure S14. *MRSA*'s intracellular GSH changes before-and-after being treated by Au@CuBCats. Samples were analyzed by flow cytometer at Ex/Em=490/520 nm (FL-1 Channel). The final concentration of Au@CuBCats was fixed to 50 μg/mL.

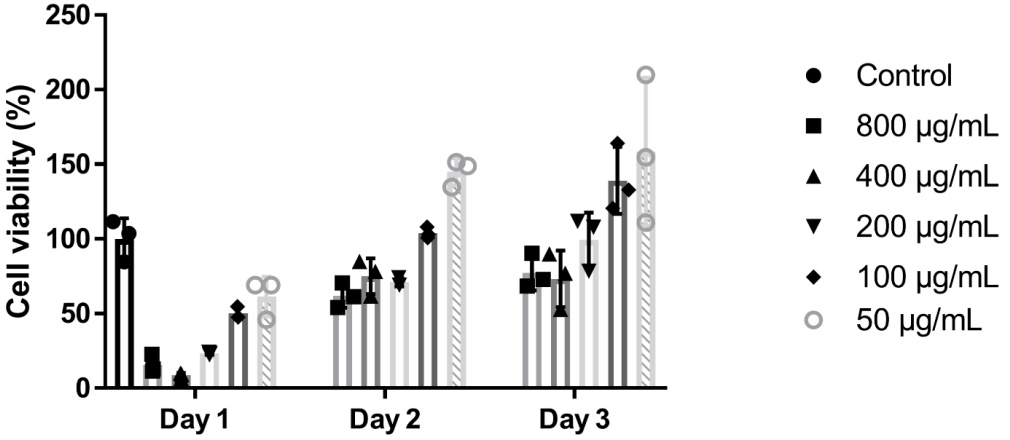

Figure S15. CCK-8 assay to reveal the HaCaT cells viability after being treated by different concentrations of Au@CuBCats. The cells without adding materials at 1 day were considered as control.

As a result, the decreases of cell viability were noticed after incubation with Au@CuBCats for 1 day, attributable to ROS generation from Au@CuBCats under the high glucose concentration (~4.5 g/L) in DMEM that we used. While after the Au@CuBCats being washed away, the significant cell regrowth

was noticed at day 2 and day 3, providing the evidence that the cells could recover soon after treatment. The full recovery (~100% cell viability) can be noticed when the materials' concentration below 200 μg/mL at day 3.

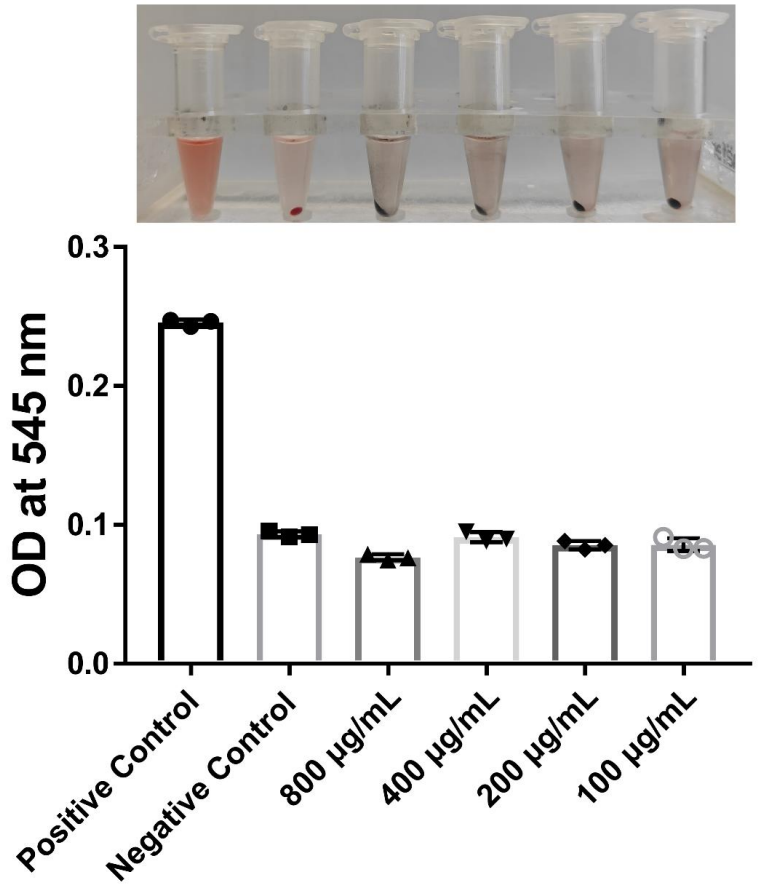

Figure S16. Hemolysis effect of Au@CuBCats under different concentrations. Triton X-100-treated red blood cells (RBCs) served as positive control and PBS-treated RBCs served as negative control.

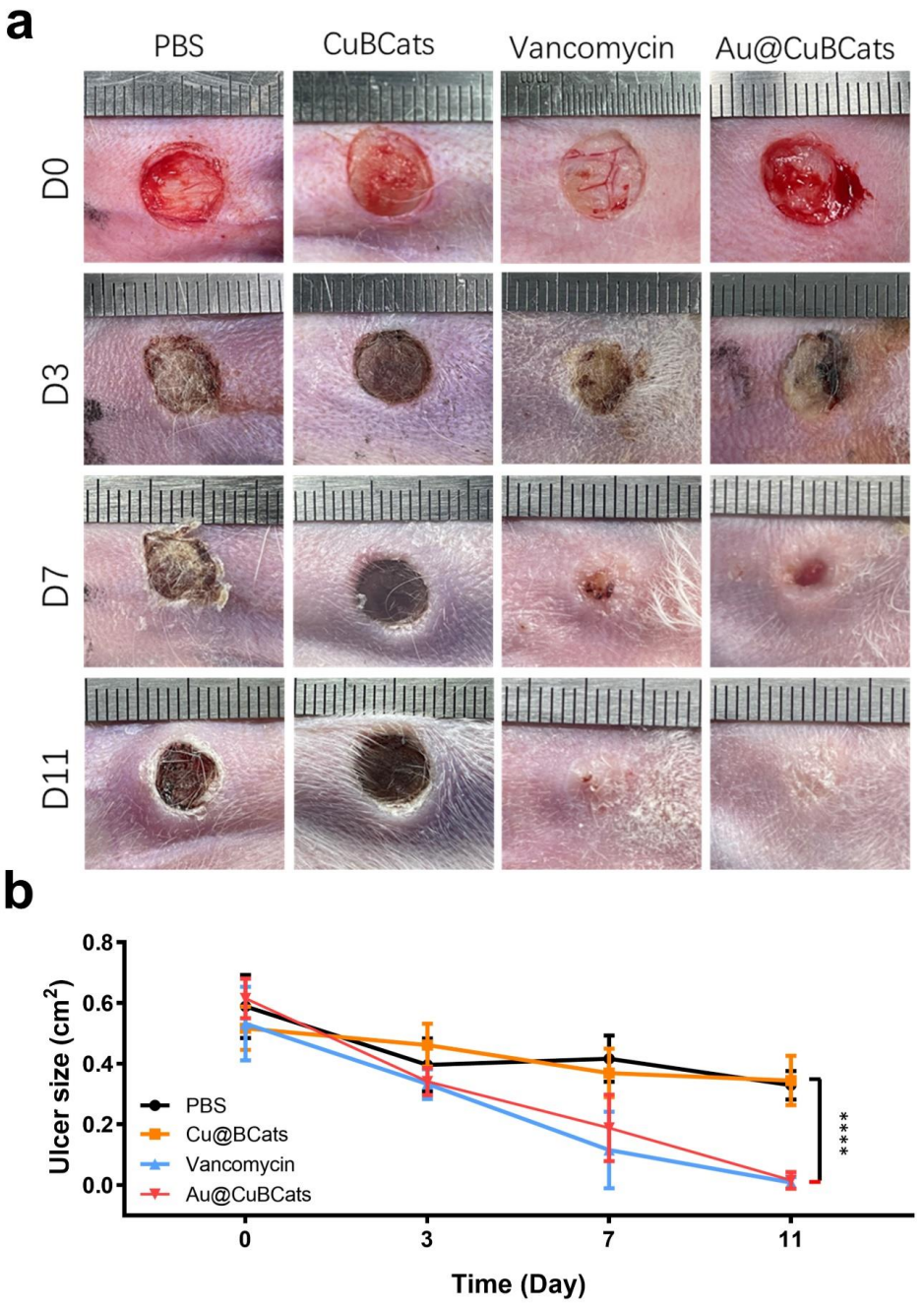

Figure S17. (a) Typical ulcer photos and (b) wound size curves at different day after treatment. The data are presented as mean ± SD, n=6. *P < 0.05; **P < 0.01; ***P< 0.001; ****P < 0.0001 by multiple t tests.

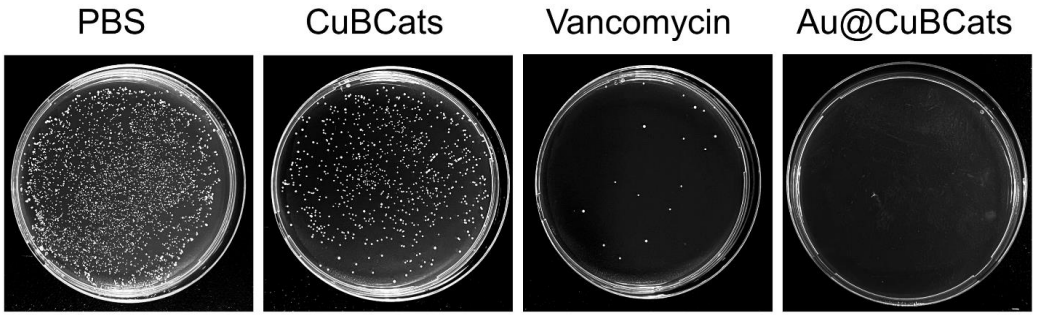

Figure S18. Typical agar plate photos for the remaining *MRSA* colonies in the ulcer after different treatment on day 11.

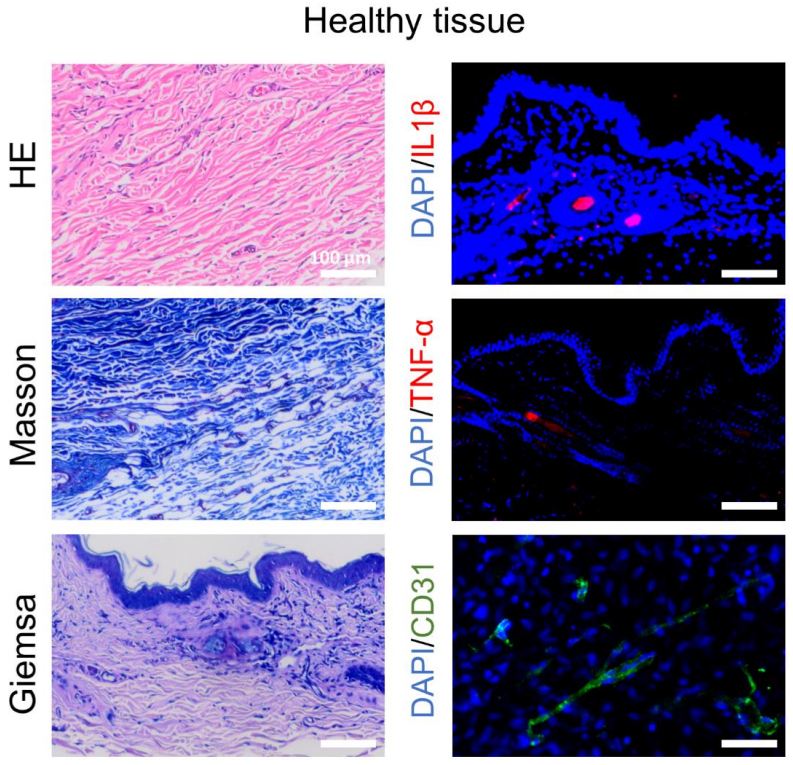

Figure S19. Histological staining of healthy rabbit ear's tissue. Scale bar: 100 μm.

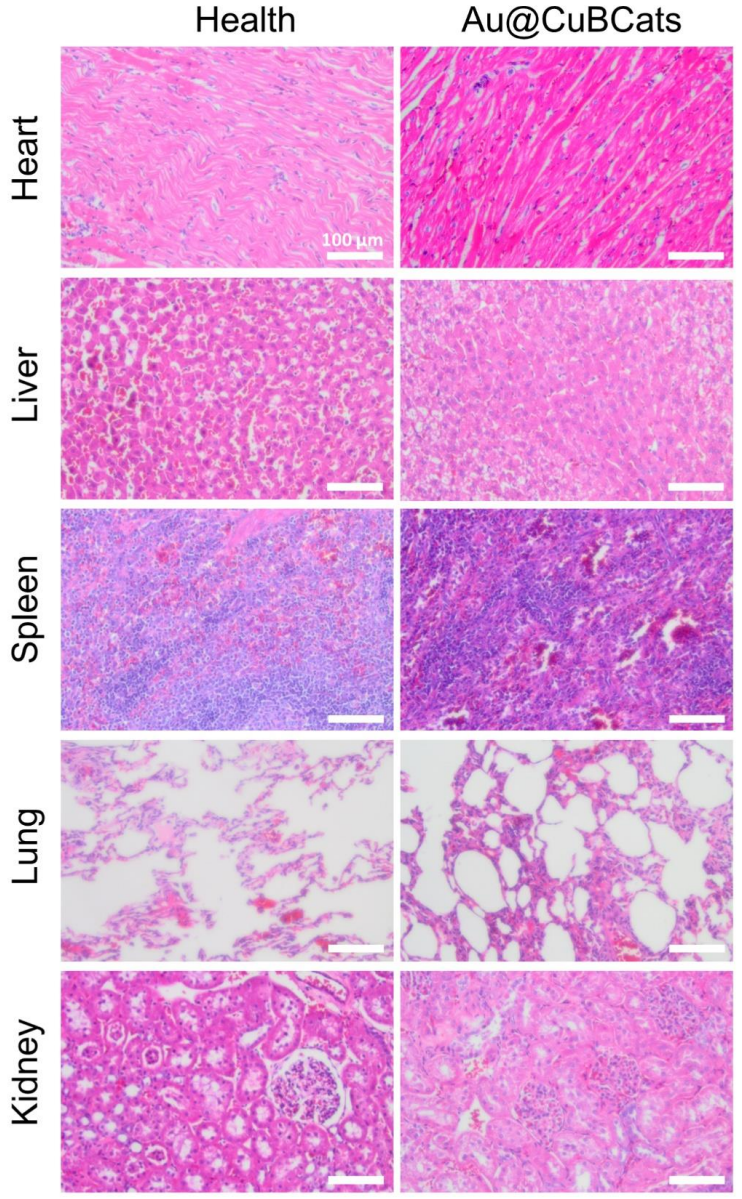

Figure S20. Typical H&E staining images of major organs for healthy rabbits and Au@CuBCats treated rabbits. Scale bar: 100 μm.

Table S1. Atomic ratio of samples

Sample	Atomic ratio (%)					
	Carbon	Nitrogen	Oxygen	Copper	Chlorine	Gold
CuCA	56.45	-	25.65	4.57	11.76	-

CuCA-C	83.55	10.36	4.71	1.38	-	-
CuBCats	82.73	10.96	5.44	0.87	-	-
Au@CuBCats	82.48	10.41	4.60	0.83	-	1.68

Table S2. Best EXAFS fitting parameters at the Cu K-edge.

Sample	path	CN	R(Å)	σ^2(Å^2)	ΔE_0 (eV)	R_f
Au@CuBCats	Cu-N	2.07	1.889	0.004	9.4	23.9
	Cu-O	0.91	1.908	0.004		

CN: coordination numbers; ***R:*** bond distance; $\boldsymbol{\sigma^2}$***:*** Debye-Waller factors; $\boldsymbol{\Delta E_0}$***:*** the inner potential correction; $\boldsymbol{R_f}$***:*** goodness of fit.

Table S3. EXAFS fitting data with fixed coordination number of Cu-N and Cu-O at the Cu K-edge.

Structure	path	CN	R(Å)	σ^2(Å^2)	ΔE_0 (eV)	R_f
CuN_1O_2	Cu-N	1*	1.802	0.010	9.1	41.8
	Cu-O	2*	1.928	0.010		
CuN_3	Cu-N	3*	1.923	0.009	11.0	26.5
CuO_3	Cu-O	3*	1.901	0.009	9.5	26.2

CN: coordination numbers; ***R:*** bond distance; $\boldsymbol{\sigma^2}$***:*** Debye-Waller factors; $\boldsymbol{\Delta E_0}$***:*** the inner potential correction; $\boldsymbol{R_f}$***:*** goodness of fit. * The coordination number is fixed during the fitting.

Compared to the best-fitting result (Table S1), CuN_1O_2, CuN_3 and CuO_3 model fits not that well with experimental spectrum of Au@CuBCats (judging from R_f).

References

[1] H. Dau, P. Liebisch, M. Haumann, *Anal. Bioanal. Chem.* **2003**, 376, 562.

4 Summary

"The greatest enemy of knowledge is not ignorance, it is the illusion of knowledge."
-Stephen Hawking

In this chapter, I summarize the key computational findings of the publications and explain their relevance in the broader context of M-N-C catalysis. The publications covered multiple aspects of M-N-Cs, including their synthesis, (electro)catalytic applications and degradation. A very brief description of my contributions for each paper was given in Chapter 3, which will be explained in greater detail in this chapter.

4.1 Modeling of MN_4 Sites

Owing to their inherent structural disorder, the modeling of M-N-Cs demands careful calibration in order to determine specific influences that could arise from the structure and the size of the carbon host. For computational studies of the MN_4 sites, the most popular choice of model is the periodic model containing the pyridinic MN_4 site (Figure 2.5a), possibly due to its relative ease of construction from graphene. However, the majority of the computational results in the main publications were obtained using molecular DFT methods instead of periodic DFT. The justification for using the molecular model was made in **Paper M2**, where the binding energy

$$E_{\mathrm{b}} = E_{\mathrm{MN_4}} - E_{\mathrm{M}} - E_{\mathrm{N_4}} \tag{4.1}$$

and the atomic structure at the MN_4 site were compared among various cluster and periodic models illustrated in Figure 4.1. In general, it could be shown that models with similar local atomic structure at the MN_4 site exhibit similar binding characteristics. For example, as the carbon lattice in the pyrrolic-1 cluster (Figure 4.1) is already planar, its binding energy ($E_{\mathrm{b,Fe}} = -9.6$ eV) did not change significantly when the carbon backbone was extended to the pyrrolic-1L cluster ($E_{\mathrm{b,Fe}} = -9.9$ eV) or the pyrrolic-UC1 periodic model ($E_{\mathrm{b,Fe}} = -9.9$ eV). In contrast, the alternative pyrrolic-2 cluster, which differs in the arrangement of the

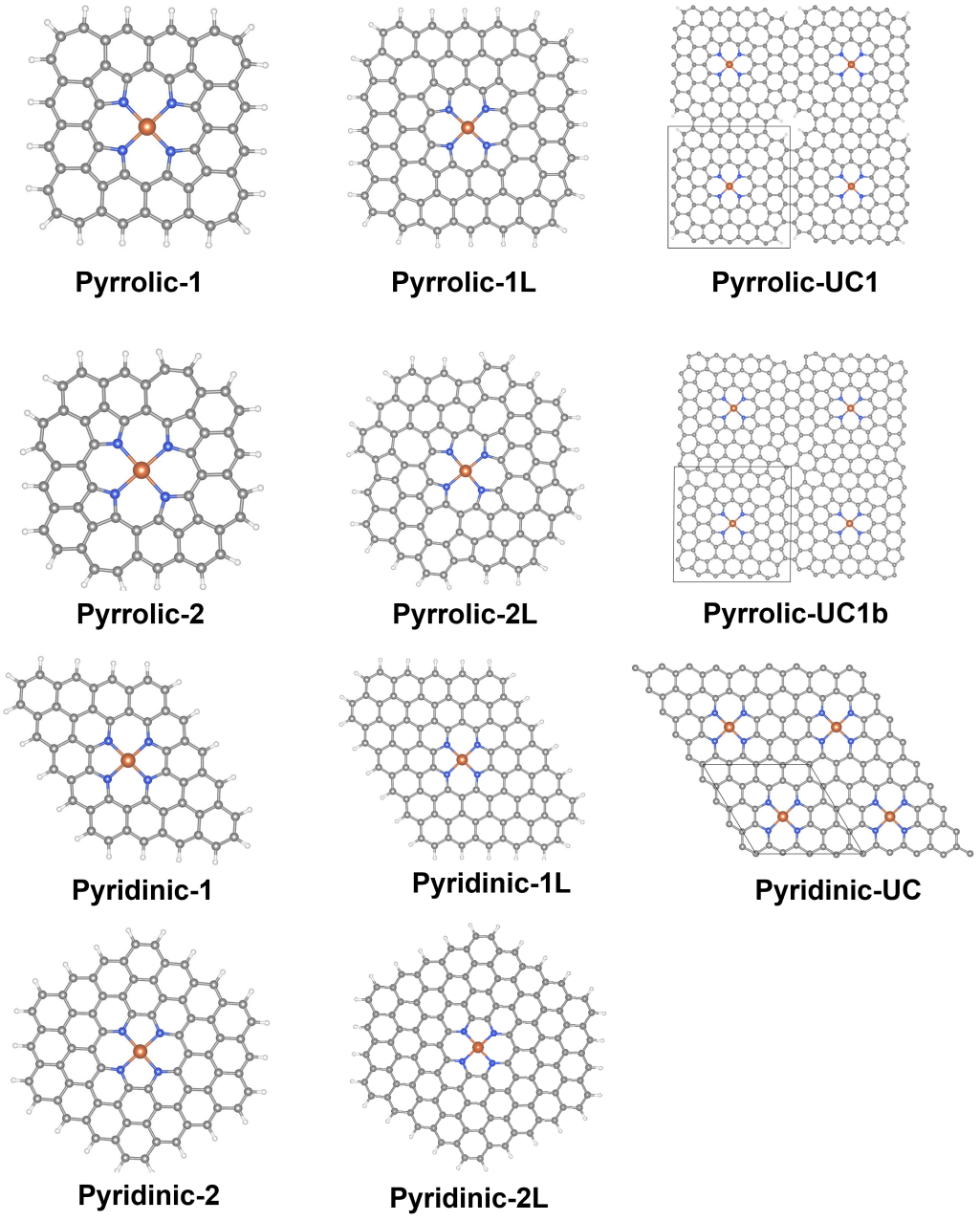

Figure 4.1: From **Paper M2**: (a) Structural models used for the DFT calculations. The isomeric pyrrolic-1 and pyridinic-1 cluster models were used for the templating studies in **Paper M1** and **Paper M2**. The larger pyrrolic-1L and pyridinic-1L models were used for reaction studies in **Paper M3**, **Paper M4** and **Paper M5**. The pyrrolic-UC1 periodic model was used for the Fermi-level calculations in **Paper M3**.

outermost carbon ring compared to pyrrolic-1, possesses a saddle-like curvature, leading significant differences in the binding energy ($E_{b,Fe} = -8.5$ eV) compared to the planar models. However, extending its carbon lattice to the pyrrolic-2L cluster resulted in an increased planarity, recovering a significant portion of the difference in binding energy ($E_{b,Fe} = -9.5$ eV). A similar comparison among the pyridinic models led to the same conclusion that the binding is mainly determined by the local atomic structure at the MN_4 site, suggesting that both the molecular and the periodic DFT could describe the chemistry of the planar pyrrolic MN_4 motif equally well, despite their inherent methodological differences (Section 2.1.5). A slight exception to this is the pyridinic ZnN_4 coordination, for which a Jahn-Teller distortion [164] was predicted for the pyridinic-1 and pyridinic-1L clusters ($d_{Zn-N} = 1.96, 1.99$ Å; $E_{b,Zn} = -4.1$ eV), leading to higher stability compared to the pyridinic-UC periodic model without the distortion ($d_{Zn-N} = 1.96$ Å; $E_{b,Zn} = -3.8$ eV). This behavior not only highlighted the poor geometric affinity of Zn towards the smaller pyridinic N_4 site, which will be further discussed in the following section, but also illustrated how geometric constraints like the periodic boundary conditions can influence the chemical properties at the active sites. Notably, Di Liberto *et al.* previously reported that sub-optimal or unrelaxed lattice parameters could lead to exaggerated reactivity of the MN_4 sites [134]. Switching to the molecular DFT not only simplified the construction and relaxation of the geometric models without artificial constraints, especially for the structurally irregular pyrrolic MN_4 motifs, but also dramatically reduced the computational cost of hybrid DFT functionals which are necessary for handling the self-interaction errors in TMs (Section 2.1.6) [133, 134].

4.2 Templating-transmetallation Synthesis

The overarching motivation behind all the main publications was the templating-transmetallation strategy for the synthesis of M-N-Cs, originally proposed by the group of Dr. Tim-Patrick Fellinger [25, 30] and subsequently refined in later publications [8, 24], including **Paper M1** and **Paper M5**. In brief, the synthesis involves using a sacrificial metal ion such as Zn^{2+} (**Paper M1**, **Paper M3**) or Mg^{2+} (**Paper M5**) for templating the MN_4 site, followed by a heat-assisted transmetallation with the desired catalytically active TM. Despite being more labor-intensive, this strategy holds several advantages in comparison to conventional synthesis approaches involving a direct pyrolysis. In **Paper M1**, it could be experimentally shown that using Zn in place of Fe prevented the carbothermal reduction of the

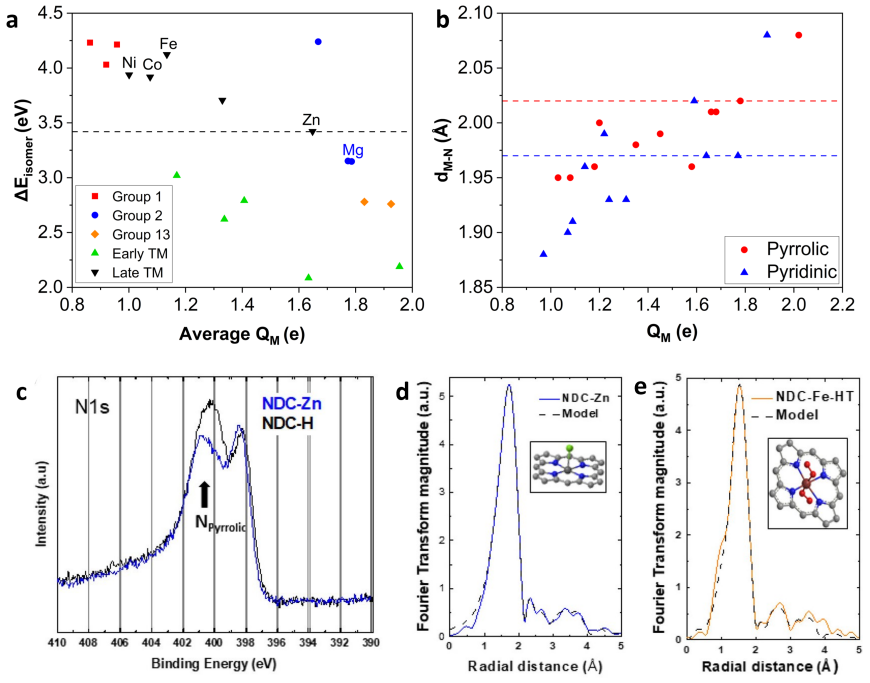

Figure 4.2: From **Paper M2**: (a) Plot of energy difference between the isomeric pyrrolic-1 and pyridinic-1 clusters against the average NBO charge of metal. (b) Plot of M-N bond length against the NBO charge for the pyrrolic-1 and pyridinic-1 clusters. The dotted lines represent the longest bond length in a planar structure. From **Paper M1**: (c) XPS spectrum of the N_{1s} for as prepared Zn-N-C (blue) and after acid-washing (black). (d-e) Fourier transformed magnitude of the EXAFS profile for the Zn-N-C and Fe-N-C after transmetallation, fitted to the pyrrolic $Cl{-}ZnN_4$ and $(O_2)_2{-}FeN_4$ models (insets) respectively.

catalytic material during pyrolysis, suppressing the formation of undesirable side phases such as iron-nanoparticles, iron carbides and iron nitrides [27–29] while simultaneously increasing the dopant concentration. In addition, M-N-Cs obtained upon transmetallation from the same pyrolyzed material exhibited very similar morphological properties as well as active site geometries and concentrations [20], allowing for a fair comparison of intrinsic activity among single atom metal sites as illustrated in **Paper M3** and **Paper M5**.

In **Paper M1**, **Paper M3** and **Paper M5**, the fitting of DFT-optimized MN_4 geometries to experimentally measured extended X-ray absorption fine structure (EXAFS) profiles facilitated the identification of the pyrrolic MN_4 coordination motif as well as the type and quantity of additional ligands at the metal sites. For example, in **Paper M1**, the EXAFS profiles (Figure 4.2d,e) exhibited excellent fitting to the DFT-optimized pyrrolic-1 cluster even beyond the first nitrogen

coordination shell, leading to the confirmation of the pyrrolic Cl–ZnN_4C_{12} and $(O_2)_2$–FeN_4C_{12} local structures for the corresponding materials (insets of Figure 4.2d,e). Analogously, the EXAFS profiles of materials transmetallated from Zn-N-Cs and Mg-N-Cs in **Paper M3** and **Paper M5**, respectively, could be fitted to the local atomic structure at the pyrrolic-1L MN_4 clusters. A further experimental proof of the pyrrolic MN_4 coordination was given by the N_{1s} XPS data shown in Figure 4.2c, where the demetallation of Zn-N-C through acid leaching led to an increase in the intensity for the (metal-free) pyrrolic nitrogen signal. Since the metals used for templating (M = Zn, Mg) almost exclusively formed the pyrrolic MN_4 sites, we conducted a DFT study on their relative affinity towards the pyrrolic motifs in comparison to catalytically active TMs like Fe. This was illustrated in **Paper M1** and **Paper M2**, featuring energetic, electronic and structural comparisons among isomeric pyrrolic-1 and pyridinic-1 models (Figure 4.2) with a common chemical formula of $MN_4C_{52}H_{20}$. The models were first introduced in **Paper M1**, where Zn was shown to exhibit a higher affinity to the pyrrolic motif than Fe, and later extended to other TMs in **Paper M2**.

Drawing insights from the NBO charge population of each metal M in the MN_4 site, we derived and compared the ionic/covalent nature of the chemical bonds at the respective MN_4 sites and determined how they could influence the templating of the MN_4 site, specifically the binding of metals within the N_4 site (Equation 4.1) and their affinity towards either the pyrrolic or pyridinic MN_4 motifs, defined by

$$\Delta E_{\text{isomer}} = E_{\text{pyrrolic}-1} - E_{\text{pyridinic}-1} \tag{4.2}$$

where $E_{\text{pyrrolic}-1}$ and $E_{\text{pyridinic}-1}$ are the electronic energies (DFT) of the respective clusters. The ΔE_{isomer} values served as a descriptor for the metals' relative affinity towards either motif, and could be correlated to the NBO charges of the metals and the M-N bond lengths (Figure 4.2a,b). Notably, all ΔE_{isomer} were positive, confirming the thermodynamic stability of the pyridinic site. However, it will be illustrated later that this is not necessarily an advantage for M-N-C synthesis. Focusing on metals used in the templating procedures, Zn and Mg generally exhibited highly positive NBO charges ($Q_{\text{Zn}} = +1.6$, $Q_{\text{Mg}} = +1.8$), close to the expected charge reflecting their +II oxidation states. The highly positive charges are indicative of significant ionic contributions in the binding, and correlate to lower ΔE_{isomer} values in Figure 4.2a, and longer M-N bond lengths in Figure 4.2b. In fact, the Zn-N and Mg-N bond lengths tend to approach the

respective planarity limits for both the pyrrolic and pyridinic motifs (dotted lines in Figure 4.2b), above which the metal could no longer be bound in plane with the nitrogen atoms, thereby illustrating their common tendency to maximize the space provided by the N_4 cavity. In contrast to these metals, catalytically active TMs (M = Fe, Co, Ni) generally exhibited more positive $\Delta E_{\mathrm{isomer}}$ values, correlating to a higher preference towards the pyridinic motifs. This behavior is a result of the covalent contributions arising from π-d orbital hybridization, based on frontier molecular orbital analysis in **Paper M2**, leading to smaller NBO charges and shorter M-N bond lengths (Figure 4.2a,b). Coincidentally, these metals, especially Fe, are often responsible for the graphitization of the material during pyrolysis [26], leading to their expulsion from the carbon lattice in the form of metal nanoparticles, metal carbides and metal nitrides [27–29]. Based on the pyrrolic vs pyridinic affinity studies in **Paper M1** and **Paper M2**, it could be deduced that the graphitization behaviors of these TMs could be linked to their higher tendency to form the pyridinic motif, which also explained why Zn and Mg with a lower preference to the pyridinic motif could achieve relatively high dopant concentrations [8]. Rather ironically, the structural resemblance between the pyridinic MN_4 site and graphene/graphite, which was believed to confer thermodynamic stability, could in fact be the stimulant for its premature degradation at the pyrolysis stage.

Upon elucidation of the templating effects of the metal ions, we further studied the subsequent transmetallation aspect of the synthesis based on the binding energies of the metals at the pyrrolic MN_4 sites in **Paper M1** and **Paper M2**. In **Paper M1** where the PBE functional was used, it could be shown that the binding of Zn was relatively weak ($E_{\mathrm{b,Zn}} = -6.1$ eV) compared to Fe ($E_{\mathrm{b,Zn}} = -9.7$ eV). Admittedly, the difference was overestimated due to the use of the GGA-type PBE functional in **Paper M1**. The difference became partially reduced upon switching to the hybrid PBE0 functional in **Paper M2** ($E_{\mathrm{b,Zn}} = -7.2$ eV, $E_{\mathrm{b,Fe}} = -9.1$ eV), showcasing the effects of the self-interaction error which favors covalent delocalization. However, the difference in E_{b} was still significant enough that the conclusions in **Paper M1** remained solid. In fact, the binding of Zn was determined to be the weakest among the first row TMs in **Paper M2**, making it an ideal starting material for transmetallation. The exceptionally weak binding of Zn could be attributed to the occupation of the energetically high anti-bonding $d_{x^2-y^2}$ orbital in a square planar complex (Section 2.1.6) as well as its inability to accept π-electrons with fully occupied d-orbitals. In **Paper M1**, we further determined a small activation barrier of 0.4 eV for Zn-Fe ion exchange at the MN_4 site, implying

that the elevated temperature during transmetallation was only necessary to facilitate the diffusion of Fe-ions towards the ZnN_4 sites. As a result of its exceptionally weak binding in the N_4 site, Zn is probably the best candidate as the sacrificial ion, illustrated by the success of several templating-transmetallation strategies involving sacrificial Zn [8, 24, 25, 31]. In comparison, the stronger binding of Mg ($E_{b,Mg} = -9.1$ eV) is rather close to those of the catalytically active TMs ($E_{b,Fe} = -9.1$ eV, $E_{b,Co} = -9.6$ eV), potentially complicating the transmetallation procedure in reference [30] as well as in **Paper M5**.

4.3 Electrochemical Mechanisms

Following the successful identification of the pyrrolic MN_4 coordination motifs, we proceeded to study the electrocatalytic mechanisms of ORR (**Paper M3** and **Paper M4**) and CO_2RR (**Paper M5**) at these active sites. Some of the most significant conclusions in these papers were inspired by initial contradictions between theory and experiment. However, our approach for resolving the contradictions was rather unconventional, mainly because the site-retaining nature of the transmetallation step confined our analysis to the pyrrolic MN_4 motifs. As a result, instead of identifying and sampling various possibilities for the MN_x active sites, our focus shifted towards deriving novel mechanistic insights pertaining to the Faradaic and non-Faradaic processes that could occur at each part of the electric double layer (Section 2.2.5).

4.3.1 Oxygen Reduction Reaction

The design of M-N-Cs for ORR, especially Fe-N-Cs and Co-N-Cs, is possibly the most widely studied among other electrocatalytic applications. Computational studies based on DFT typically involved the pyridinic MN_4 motifs in a periodic setup, often with the use of GGA functionals. As discussed in Section 4.1, each of these methodological choices can artificially enhance the reactivity, making it advantageous to switch to a cluster model and apply the hybrid functionals instead, especially for the structurally irregular pyrrolic MN_4 motifs.

Applying the CHE method in **Paper M4**, we first investigated the commonly proposed inner-sphere mechanism of ORR at the pyrrolic MN_4 clusters (selected examples in Figure 4.3d), in relation to the oxidation states of the TMs deduced with a NBO population analysis (Figure 4.3e). Consistent with the chemistry of natural porphyrin complexes, the majority of the TMs exhibited the +II oxidation

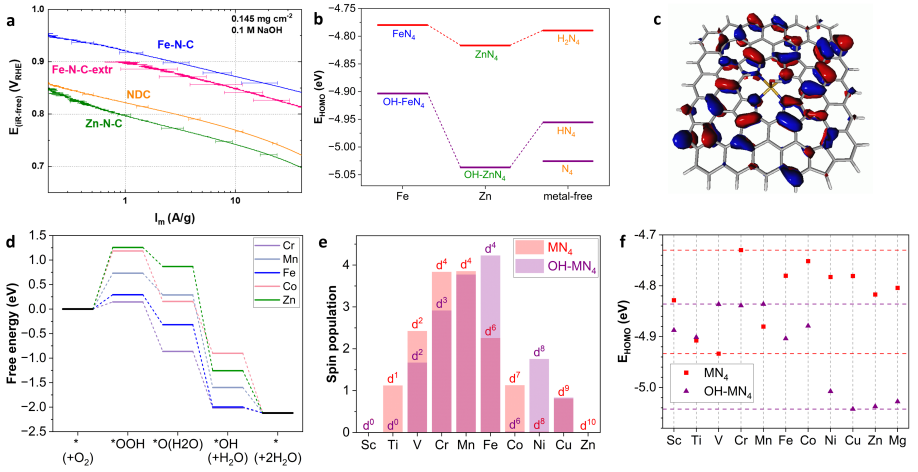

Figure 4.3: From **Paper M3**: (a) Tafel plot of Zn-N-C (green), Fe-N-C after Zn-Fe transmetallation (blue), NDC after acid leaching of Zn-N-C (orange) and partially demetallated Fe-N-C after acid leaching (pink). (b) Plot of E_{HOMO} on the pyrrolic FeN_4, ZnN_4, and H_2N_4 (red lines) in the pyrrolic-1L clusters and corresponding OH-bound/deprotonated clusters (purple lines). (c) Contour plot of the HOMO for the OH–FeN_4 motif. From **Paper M4**: (d) Reaction energy diagram for the inner-sphere ORR at the MN_4 for various metals simulated at $U = 0.7\ \mathrm{V_{RHE}}$ with the CHE method (Equation 2.99). (e) Plot of spin population and corresponding metal-centered d-orbital occupations. (f) Plot of E_{HOMO} of MN_4 (red) and OH–MN_4 (purple).

state at the pristine MN_4 site, except for the less electronegative early TMs (Sc, Ti, V) and Mn with the +III oxidation states (Figure 4.3e). The exception of Mn was particularly surprising since both the Cr and Fe atoms exhibited the +II oxidation state. Nevertheless, the anomaly could be explained by the stability of the high spin d^4 configuration in a square planar ligand field (Section 2.1.6), corresponding to the half-filling of d-orbitals except the unstable $d_{x^2-y^2}$ orbital. Surprisingly, the deviation towards the high spin d^4 configuration was also exhibited by the penta-coordinated OH–FeN_4 motif, resulting in relatively high charge and spin populations and possibly suggesting a +IV oxidation state for Fe (Figure 4.3e). Among all the metals studied, only Fe and Cr displayed potential for inner-sphere ORR activity at the pyrrolic MN_4 site (Figure 4.3d), with relatively low *OOH free energies of +0.29 eV and +0.13 eV respectively, relative to the initial state at $U = +0.7\ \mathrm{V_{RHE}}$. In contrast to Fe and Cr, late TMs from Co to Zn generally exhibited poor inner-sphere activities at the MN_4 site, with highly unstable *OOH intermediates of about +1.2 eV at the same potential. At this point, the reader may have noticed that I have already contradicted myself, as I previously mentioned that Co-N-Cs are widely popular for (alkaline) ORR. Before attempting to resolve

this contradiction, I will introduce a theory-experiment collaborative study to derive a crucial mechanistic insight for the alkaline ORR.

Paper M3 featured a comparison of the intrinsic alkaline ORR activities and selectivities among the isomorphic Zn-N-C, Fe-N-C (transmetallated from Zn-N-C) and metal-free nitrogen-doped carbon (NDC, acid-leached Zn-N-C) (Figure 4.3a). In the alkaline medium, all three materials exhibited the same Tafel slope despite differing ORR selectivities, suggesting a common rate-determining step (RDS) based on Butler-Volmer kinetics (Section 2.2.4) which was independent of the selectivity (*i.e.* within the transfer of the first two electrons in $O_2 \rightarrow H_2O_2$). In addition, the potential offsets in the parallel Tafel plots, equivalent to the differences in exchange current density i_{eq} (Equation 2.130), quantified the influence of the metals (or lack thereof) on this common RDS. Relative to the Fe-N-C, the Tafel plots for Zn-N-C and NDC were shifted by ca. 0.13 V and 0.10 V respectively. However, if we were to assume a common RDS derived from the inner-sphere mechanism, the ZnN_4 site would theoretically require a much higher overpotential by 0.90 V compared to FeN_4, based on the $^*OOH$ energies in Figure 4.3d. In principle, the adsorption of any intermediates should be even more challenging on the metal free NDC, inconsistent with its observed higher activity than Zn-N-C for alkaline ORR. Therefore, we had to conclude that the common RDS, characterized by Tafel analysis, could not possibly be derived from the inner-sphere mechanism.

Since the inner-sphere mechanism failed to reproduce the trends for alkaline ORR, we further considered an alternative mechanism involving the outer-sphere electron transfer, inspired by previous studies on metal-based catalysts and NDCs [47, 49]. In **Paper M3**, we studied the influence of metal dopants on the valence electronic properties of the carbon host, exploiting the HOMO energies E_{HOMO} of the cluster models and the Fermi levels E_f of the periodic models as descriptors for electron transfers. Notably, both the trends in the E_{HOMO} and the E_f could be correlated to the potential offsets for alkaline ORR (Fe-N-C > NDC > Zn-N-C), especially with the alkaline environment taken into consideration. The cluster model employing the hybrid PBE0 functional was slightly more successful (Figure 4.3b), as the difference in E_{HOMO} between the $OH{-}MN_4$ motifs could be correlated almost quantitatively to the shift in the Tafel plots between Fe-N-C ($E_{HOMO} = -4.90$ eV) and Zn-N-C ($E_{HOMO} = -5.04$ eV) in alkaline ORR, indicating that the common RDS should involve a one-electron transfer from the HOMO of the $OH{-}MN_4$ motif. For the metal free NDC, a HOMO energy of $E_{HOMO} \approx -5.00$ eV would be expected based on the potential

shifts in the Tafel plots, intermediate to that of HN_4 ($E_{HOMO} = -4.96$ eV) and N_4 ($E_{HOMO} = -5.03$ eV), suggesting that the original H_2N_4 sites were deprotonated to various extents in the alkaline medium, consistent with the acidity observed in porphyrin complexes [165, 166].

Inspired by the conclusions of **Paper M3**, we extended the study of E_{HOMO} to other first-row TMs in **Paper M4** (Figure 4.3f). Interestingly, just as in the inner-sphere mechanism, the oxidation state of the metal (Figure 4.3e) could also be correlated to the trends in E_{HOMO} (Figure 4.3f). In general, relatively high E_{HOMO} values could be determined for metals that exhibit the oxidation states of +II oxidation state in MN_4 and +III/+IV in $OH{-}MN_4$. Cr, Fe and Co are the most noteworthy candidates, having relatively high E_{HOMO} in both cases due to the formal oxidation of the metal upon OH-binding. Therefore, we concluded in **Paper M4** that the high ORR activity of Co-N-Cs was likely a result of the outer-sphere electron transfer, consistent with its excellent 2e-ORR selectivities which will be discussed Section 4.3.2. In **Paper M3** and **Paper M4**, it was further determined that, despite the metals' delicate influence on the E_{HOMO}, the HOMOs (*e.g.* of $OH{-}FeN_4$ in Figure 4.3c) did not contain significant contributions from the metal's atomic orbitals, thus explaining the Fe-N-Cs' ability to retain its alkaline ORR activity even in the presence of poisoning ligands [50].

4.3.2 Hydrogen Peroxide Reduction and Fenton Reaction

Although the identification of the outer-sphere RDS in **Paper M1** could explain the activity differences among various M-N-Cs, it raised further questions pertaining to the ORR selectivity. Since the outer-sphere electron transfer inherently did not involve the specific adsorption of ORR intermediates, the formation of mobile H_2O_2 intermediates should be inevitable during alkaline ORR. In **Paper M3**, the in-situ measurements of the H_2O_2 (in alkaline HO_2^-) yield using the RRDE technique elucidated significant differences in ORR selectivities, ranging from a negligible H_2O_2 yield for the Fe-N-C to about 30% in the metal free N-C (Figure 4.4a). While an outer-sphere electron transfer to the H_2O_2 intermediate could in principle occur, especially for the metal-free NDC, a fully outer-sphere mechanism could not explain the differences in selectivity. The most obvious contradiction was depicted in Figure 4.4a, with the Zn-N-C producing a lower yield of HO_2^- than the metal-free NDC despite having poorer outer-sphere activity (Figure 4.3a,b). These observations indicated the existence of a mechanistic

pathway that promotes the inner-sphere reduction of H_2O_2 at the MN_4 sites, likely in parallel to the outer-sphere processes.

In **Paper M4**, we studied the specific interactions between the MN_4 sites and H_2O_2, based on the relative stability among three isomeric intermediates $^*H_2O_2$, $^*(OH)_2$ and $^*O(H_2O)$ (Figure 4.4b). It should be noted that any of the 3 intermediates could in principle lead to the subsequent reduction to $^*OH$ and finally to water, already illustrating the advantage of M-N-Cs (including Zn-N-C in **Paper M3**) in promoting inner-sphere H_2O_2RR compared to metal-free NDCs. However, a further examination of the relative stability of the $^*(OH)_2$ intermediate could shed light on the intrinsic selectivity differences among metals in the MN_4 site. Consistent with the trends in inner-sphere activity (Section 4.3.1), the dissociation of $^*H_2O_2$ into the $^*(OH)_2$ intermediate was predicted to be exergonic for the mid TMs (M = Cr, Mn, Fe), but endergonic or reversible for the late TMs and Mg (Figure 4.4b). The distinction in the dissociation behavior of H_2O_2 coincided with generally reported selectivity differences, with mid TMs like Fe generally exhibiting overall 4e-selectivity [3, 7, 52–55] and late TMs like Co favoring the 2e-ORR [55, 56], providing further support for the 2e+2e-ORR in the former. However, although the strong dissociation tendency of H_2O_2 on mid TMs would be favorable for the overall current production, it could also come at the cost of long-term stability. Materials that interact strongly with H_2O_2, especially Fe-N-Cs, were frequently reported to promote the Fenton reaction, producing reactive oxygen species (ROS) like •OH radicals that would gradually destroy the catalyst [18, 59–61, 167] and the membrane [168, 169].

Paper S1 featured a side study of the Fenton reaction for biomedical applications, utilizing a dual-component catalyst containing Au-nanoparticles (AuNPs) embedded on a Cu-N-C for breaking down glucose into ROS. Our DFT investigation focused on the role of the single atom Cu-site for catalyzing the Fenton reaction. Consistent with the behavior of pyrrolic CuN_4 in Figure 4.4b, the pyridinic CuN_4 site was also determined to be inert towards H_2O_2 in Figure 4.4c. However, the EXAFS profile of the material indicated a coordination number of 3 for the Cu atom, fitting best to the DFT-optimized T-shaped CuN_2O motif (compared to CuN_4, trigonal pyramidal CuN_xO_{3-x} and other T-shaped CuN_xO_{3-x} motifs). The T-shaped motifs were derived upon the removal of a N atom from a pyridinic CuN_4 site. During the initial testing of the Fenton mechanism, a geometry optimization was performed with a $^*H_2O_2$ intermediate at the CuN_2O site, which resulted in the barrier-free dissociation of H_2O_2 to form the $^*(OH)_2$ intermediate, similar to the one shown in Figure 4.4b. Due to the strength of

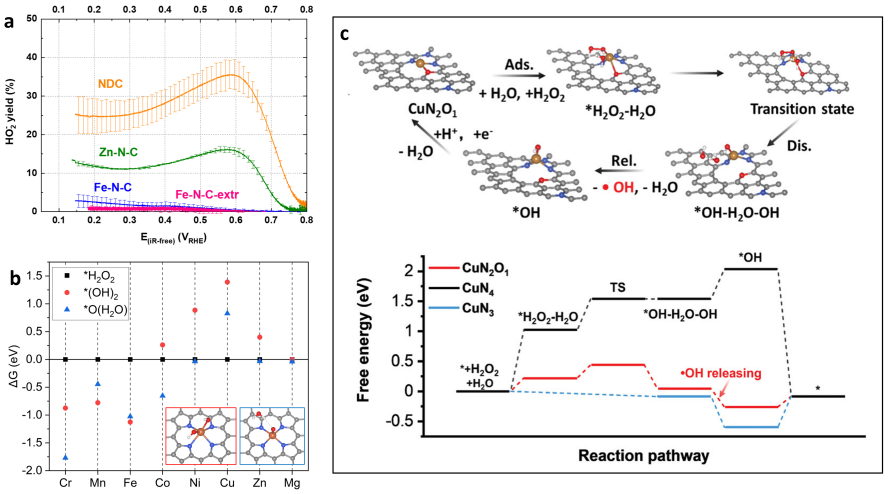

Figure 4.4: From **Paper M1**: (a) Yield of HO_2^- measured with RRDE for (a) Tafel plot of Zn-N-C (green), Fe-N-C after Zn-Fe transmetallation (blue), metal-free N-C after acid leaching of Zn-N-C (orange) and partially demetallated Fe-N-C after acid leaching (pink). From **Paper M4**: (b) Free energy plot and structures (inset) of the $^*(OH)_2$ (red) and $^*O(H_2O)$ (blue) relative to $^*H_2O_2$. From **Paper S1**: (c) Simulated reaction mechanism for the Fenton r eaction on a trivalent T-shaped CuN_2O_1 (top) and the corresponding free energy profile for the reaction (bottom).

the Cu-OH bond, the metal-bound OH would be highly unlikely to desorb as a •OH radical ($\Delta E_{\mathrm{des}} > 2$ eV), making the Fenton reaction theoretically unfeasible starting from a $^*(OH)_2$ motif. However, a closer inspection of the optimization trajectory indicated that the H_2O_2 dissociation initially occurred with only one OH bound to Cu, followed by a rearrangement of the second OH to form a bond with Cu. With this in mind, I proceeded to determine whether the rearrangement could be intercepted by a solvent molecule (water). As shown in the reaction mechanism in Figure 4.4c, the explicit water molecule was indeed able to separate the second OH from the Cu-site, introducing a small dissociation barrier of $E_{\mathrm{a}} = 0.44$ eV for the CuN_2O motif determined with the NEB method. As the $^*OH{-}H_2O{-}OH$ intermediate featured an •OH that was not bound to the metal, the latter could potentially diffuse away from the catalyst, for example towards bacterial cells for the diabetic ulcer treatment in **Paper S1**. In the final step of the mechanism in Figure 4.4c, the regeneration of the free active site was thermodynamically feasible only with a reductive protonation of the $^*OH$ intermediate using the CHE method [143]. In this case, the reaction was simulated at the potential of $U = E^0(O_2/H_2O_2) = +0.70$ V, inspired by the experimentally observed oxygen evolution during the reaction.

Although **Paper S1** did not strictly involve an electrochemical cell, the mechanistic insights for the Fenton reaction are expected to be relevant to ORR catalysis, especially since both the pyrrolic FeN_4 motif in **Paper M4** and the T-shaped CuN_2O motif in **Paper S1** are highly reactive towards dissociating H_2O_2. In addition to providing mechanistic insights on the Fenton reaction, particularly the influence of the aqueous environment in altering the dissociation pathway, **Paper S1** aptly demonstrated the chemical equivalent of the German saying "Des einen Freud, des anderen Leid[11]", showcasing the utilization of the electrochemically catastrophic Fenton reaction for an entirely different realm of applications.

4.3.3 Carbon Dioxide Reduction Reaction

The last part of this chapter is dedicated to a discussion on the electrochemical CO_2RR, an energy-consuming process that converts the greenhouse gas CO_2 into valuable chemical products. Due to its negative standard reduction potential $E^0(CO_2/CO) = -0.10\ V_{RHE}$, the CO_2RR is typically plagued by the competing HER defined by the RHE potential of $E^0(H^+/H_2) = 0\ V$. In fact, the scale is tilted even further towards HER if we account for the huge abundance of hydrogen (H^+ or H_2O) in the aqueous medium and the electrochemical interface compared to CO_2. As a result, a high CO_2RR selectivity is in principle only feasible in the low overpotential (kinetic) region, away from mass-transport limitations, and would further require an electrocatalyst that could invert the thermodynamic selectivity towards HER.

Paper M5 featured a study of the intrinsic CO_2RR behavior on the isomorphic Co-N-C and Ni-N-C, each transmetallated from Mg-N-C which was pyrolyzed at either 800 ℃ or 1000 ℃. Consistent with previous studies, the Ni-N-Cs were generally much more selective towards CO_2RR than the corresponding Co-N-Cs [9, 78–80], with the former achieving CO Faradaic efficiencies of $FE_{CO} > 96\,\%$ at the potential $U \approx -0.65\ V_{RHE}$ (Figure 4.5a). However, the high activity and selectivity of the former posed a major dilemma in its quantum chemical modeling. Figure 4.5c displays the free energy profiles for the CO_2RR and the competing HER, based on the energies of the $^*COOH$ and $^*H$ intermediates which are necessary to form CO or H_2 respectively. At both the pyrrolic NiN_4 and CoN_4 sites, the $^*H$ intermediates were 0.2 – 0.3 eV more stable than the $^*COOH$ intermediates, reflecting the thermodynamic selectivity and the thermodynamic-kinetic relations of the Bell-Evans-Polanyi principle [170, 171], but contradicting the experimental

11 One man's joy is another man's sorrow

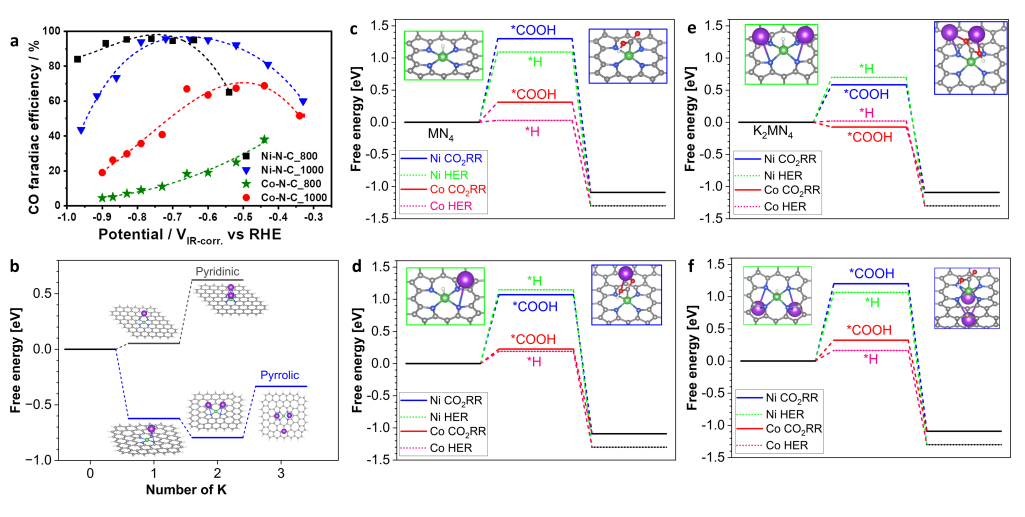

Figure 4.5: From **Paper M5**: (a) CO Faradaic efficiency for Ni-N-Cs and Co-N-Cs, each obtained upon transmetallation from Mg-N-Cs. The numbers in the names (800, 1000) refer to the pyrolysis temperatures for the synthesis of Mg-N-C. (b) Free energy diagram for the potential-dependent adsorption of K^+ ions, simulated at $U = -0.65\ V_{RHE}$ with the modified CHE method (Equation 2.104). (c-f) Free energies diagrams for CO_2RR and HER on pyrrolic NiN_4 and CoN_4 (c) without K^+, (d) with 1 K^+, (e) with 2 K^+ on the same face and (f) opposite side face of the intermediates, simulated at $U = -0.65\ V_{RHE}$ with the CHE method (Equation 2.99).

observations in Figure 4.5a. Even more puzzling was the apparent reactivity of the Ni-N-C, since both intermediates were determined to be highly unstable ($\Delta G_{*COOH} = 1.30$ eV, $\Delta G_{*H} = 1.09$ eV) at $U = -0.65\ V_{RHE}$ (Figure 4.5c). The inertness of the NiN_4 site even has solid theoretical justification, as all d-orbitals except the anti-bonding $d_{x^2-y^2}$ are fully occupied in a square planar low spin d^8 complex (Figure 4.3e), a common behavior among group 10 (d^8) transition metals. In fact, from a recent study by Hursán *et al.*, the NiN_4 site was so stable that it was the only metal (among Fe, Sn, Cu, Co, Ni and Zn) whose M-N-C did not form metallic clusters during CO_2RR [172]. The CO_2RR activity and selectivity of the Ni-N-C was high despite the absence of metallic clusters, further confirming the NiN_4 site as the active site for the reaction.

While excellent numbers for CO_2RR activities and selectivities on Ni-N-Cs were reported in **Paper M5**, the true novelty of the publication lies in the fact that the materials were obtained via transmetallation and thus isomorphic, allowing for a fair comparison of intrinsic CO_2RR properties. Conventionally, the puzzling reactivity of Ni-N-Cs was explained with alternative NiN_x sites instead of the NiN_4 sites, such as the unsaturated NiN_xC_{4-x} [84, 85] or the trivalent NiN_3 sites [81,

82]. However, as mentioned repeatedly, the transmetallation step generally retained the atomic structure of the active site, making it questionable to introduce modified active sites to our simulations. Recent studies of CO_2RR elucidated the role of cations in enabling the reaction on noble metals like Cu and Au [93–97], prompting a similar investigation for Ni-N-Cs. However, these studies typically applied the computationally demanding AIMD calculations. With the large unit cell size required for the pyrrolic MN_4 motif (*e.g.* pyrrolic-UC1 in Figure 4.2) and the complexity of TMs' chemistry (Section 2.1.6), an AIMD simulation would not be feasible without major sacrifices in accuracy. Therefore, we proposed a simpler approach in **Paper M5**, based on standard DFT with a modification of the CHE (Equation 2.104), in order to study the potential-dependent involvement of cations at the active site. Comparing the thermodynamics for the K^+ adsorption in Figure 4.5b, it became evident that the pyrrolic MN_4 sites were inherently better at adsorbing the cations than the pyridinic ones. At the simulated potential of $U = -0.65\,V_{RHE}$, the adsorption of the first two K^+ ions were predicted to be exergonic, while the adsorption of a single K^+ was already slightly endergonic at the pyridinic site. It should be mentioned that similar energy profiles were obtained with the CoN_4 sites or the Na^+ ions. Considering the exergonic adsorption of cations at the pyrrolic MN_4 sites, we extended the study of CO_2RR and HER in Figure 4.5c to the pyrrolic NiN_4 motifs with the adsorbed K^+ ion(s) (Figure 4.5d-f).

For the K_1MN_4 motif in Figure 4.5d, we observed that a single K^+ had a slight influence in the intermediates' energies. For both metals, the *COOH intermediate was stabilized by up to 0.2 eV, while the *H intermediate was destabilized by up to 0.1 eV. The stabilizing and destabilizing influences could be explained by electrostatic interactions between the adsorbates and the K^+ ions, with the COOH adopting a combined NBO charge of -0.64 e while the H atom in *H remained neutral at +0.02 e on K_1NiN_4. As a result of these interactions, the K_1NiN_4 site already exhibited a reversal in the selectivity, although the electrochemical barriers were still high ($\Delta G_{*\mathrm{COOH}} = 1.07\,\mathrm{eV}$, $\Delta G_{*\mathrm{H}} = 1.15\,\mathrm{eV}$). Fortunately, upon the introduction of the second K^+ ions in Figure 4.5e, this barrier became significantly smaller ($\Delta G_{*\mathrm{COOH}} = 0.58\,\mathrm{eV}$, $\Delta G_{*\mathrm{H}} = 0.70\,\mathrm{eV}$), making the reactions finally feasible, and still CO_2RR-selective, at the originally inert NiN_4 site. Based on the Arrhenius relation [146], a Faradaic efficiency of $\mathrm{FE_{CO}}$= 98.8 % could be predicted, very close to the observed 96 %.

In order to elucidate the chemistry behind the enhanced stability of the intermediates on K_2NiN_4, we conducted an additional reaction study at the same K_2NiN_4 site, but with the intermediates adsorbing on the opposite face of the

MN_4 site instead (Figure 4.5f). In this case, the K^+ ions did not have a significant influence on the reactivity, recovering the reaction profile of the cation-free site shown Figure 4.5c. With this, we were able to exclude electronic effects due to electron donation from K to the MN_4 clusters. However, it is acknowledged that the reduction of the Ni(II) to Ni(I) reported in some studies [76, 80] could still be relevant for further decreasing the electrochemical barriers, requiring excited state simulations for theoretical justification which lies beyond the scope of my work. Amusingly, the computational results of **Paper M5** resolved the initial contradiction in the reactivity of the NiN_4 site by introducing an irony to the electrochemical mechanism. The inertness of the original NiN_4 site ultimately proved to be beneficial to the CO_2RR selectivity, as no (HER-selective) reaction would occur in the absence of cations on the same face of the reactants. In contrast, although the pyrrolic CoN_4 site could also favor CO_2RR with 2 cations on the same face, the site is still reactive and HER-selective otherwise, correlating to its diminished CO-selectivity (FE_{CO}< 60 %) in **Paper M5**. Notably, the involvement of 2 cations in the CO_2RR mechanism on Au, arguably the most noble among the noble metals, was also reported in recent studies by Qin *et al.* [95–97], although the cations were mainly transient in the simulations due to their unfavorable adsorption on the Au surface. Thus, the computational results in **Paper M5** not only extended the possibility of the cations' participation in CO_2RR to M-N-Cs, but also showcased the commonly neglected role of the neighboring heteroatoms in localizing them for the reaction.

4.4 Conclusions and Outlook

In brief, my work harnessed the strengths of DFT to close some knowledge gaps regarding the synthesis of M-N-Cs (Section 4.1 and Section 4.2) and their electrochemical applications (Section 4.3), allowing for a more targeted optimization of these materials in the future. It should be emphasized that most, if not all, of the conclusions drawn in these works are results of synergistic collaborative efforts between computational and experimental groups, illustrating the significance of interdisciplinary research for the understanding of catalytic mechanisms and the knowledge-based optimization of catalysts. The interdisciplinary research proved to be especially fruitful when contradictions between theory and experiment were identified and scrutinized, leading to the derivation of novel, sometimes ironical, insights that could advance our understanding on M-N-Cs and electrocatalytic mechanisms.

In the first part of my work, I performed computational studies on the templating-transmetallation strategy for the synthesis of M-N-Cs with dense active sites and comparable morphological properties. The combined efforts from both theoretical simulations and experimental measurements provided abundant evidence for the nature-inspired pyrrolic MN_4 structures, either directly through the spectroscopic techniques and templating studies in **Paper M1** and **Paper M2** (Figure 4.2) or indirectly from mechanistic studies in **Paper M3** (Figure 4.3a,b) and **Paper M5** (Figure 4.5b). The templating-transmetallation strategy opens up the possibility of introducing other metals or even non-metals into the M-N-C, including but not limited to those studied in **Paper M2** and **Paper M4**. For example, in addition to CrN_4 sites which was shown to behave similarly to FeN_4 sites for ORR (**Paper M4**), those containing the post-transition metals may also be significant for ORR (**Paper M4**) and HCOOH-selective CO_2RR electrocatalysis [77].

Focusing on the elucidation of electrochemical mechanisms, the second part of my work universally emphasized the active role of deceptively inconspicuous species at the interface for the respective reactions. These include hydroxides for the alkaline ORR (**Paper M3**, **Paper M4**), water for the Fenton reaction (**Paper S1**), and cations for the CO_2RR (**Paper M5**). The results collectively illustrated the need to consider environmental influences in order to bridge computational simulations to the physical reality, especially at the species-diverse electrochemical interface. From the ORR studies in **Paper M3** and **Paper M4**, the outer-sphere electron transfer mechanism could be identified to have a significant influence on the rate-determining step, especially in the alkaline medium, potentially motivating the development and refinement of electron dynamic methodologies and in-situ spectroscopic techniques to support the discovery and development of materials that promote these long-range electron transfers. With the inevitable production of H_2O_2 through the outer-sphere mechanism, the study of its dissociation behaviors at the MN_4 sites in **Paper M4** provided a distinguishing factor, namely the stability of the $^*(OH)_2$ motif, for comparing the overall ORR selectivity and stability among the M-N-Cs. The ability of H_2O_2 to produce the ·OH radicals at inner-sphere-active sites was further supported by the mechanistic study of the Fenton reaction in **Paper S1**, which elucidated the involvement of water in intercepting the binding of the dissociated ·OH to the active site. Therefore, for electrochemical applications, it would be necessary to find ways to prevent the Fenton reaction, or at least reduce its impact on the catalytic stability, possibly requiring a precise control on the inner- and outer-sphere activity of the active sites.

For the mechanistic study of the CO_2RR, the results of **Paper M5** illustrated that up to two cations could be adsorbed at the pyrrolic N atoms of the seemingly inert NiN_4 site, subsequently playing a crucial role in tuning the activity and selectivity for CO_2RR. Considering that most CO_2RR catalysts are chemically noble, much like the NiN_4 site, the conclusions drawn in **Paper M5** are probably not exclusive to M-N-Cs. With the possibility of modeling the MN_4 site with both the molecular and periodic DFT (**Paper M2**), the study of potential-dependent cation adsorption and its subsequent influence on CO_2RR could be extended to periodic DFT calculations in order to calibrate the method for heterogeneous catalysts in general. In particular, for the noble metal catalysts, the existence of oxide phases during CO_2RR have been reported to enhance CO_2RR selectivity [173–176], prompting the need to investigate the possibility of the cations' adsorption on surface O-atoms for CO_2RR.

Overall, the significance of my work lies in challenging several common assumptions in the modeling of active sites in M-N-Cs and their respective electrocatalytic mechanisms. Since my computational studies were heavily inspired by experimental data and observations, the collaboratively derived results are expected to be relevant for future theoretical and experimental work, illustrating the value of a theory-experiment synergy in the knowledge-based development of an inherently disordered material.

Bibliography

[1] S. K. Tiwari, V. Kumar, A. Huczko, R. Oraon, A. D. Adhikari, G. C. Nayak, *Critical Reviews in Solid State and Materials Sciences* **2016**, *41*, 257–317.

[2] H. Jung, A. Karmakar, A. Adhikari, R. Patel, S. Kundu, *Sustainable Energy & Fuels* **2022**, *6*, 640–663.

[3] T. Asset, F. Maillard, F. Jaouen in *Supported Metal Single Atom Catalysis*, (Eds.: P. Serp, D. Pham Minh), Wiley-VCH, Weinheim, Germany, **2022**, pp. 531–582.

[4] M. Titirici, S. G. Baird, T. D. Sparks, S. M. Yang, A. Brandt-Talbot, O. Hosseinaei, D. P. Harper, R. M. Parker, S. Vignolini, L. A. Berglund, Y. Li, H.-L. Gao, L.-B. Mao, S.-H. Yu, N. Díez, G. A. Ferrero, M. Sevilla, P. Á. Szilágyi, C. J. Stubbs, J. C. Worch, Y. Huang, C. K. Luscombe, K.-Y. Lee, H. Luo, M. J. Platts, D. Tiwari, D. Kovalevskiy, D. J. Fermin, H. Au, H. Alptekin, M. Crespo-Ribadeneyra, V. P. Ting, T.-P. Fellinger, J. Barrio, O. Westhead, C. Roy, I. E. L. Stephens, S. A. Nicolae, S. C. Sarma, R. P. Oates, C.-G. Wang, Z. Li, X. J. Loh, R. J. Myers, N. Heeren, A. Grégoire, C. Périssé, X. Zhao, Y. Vodovotz, B. Earley, G. Finnveden, A. Björklund, G. D. J. Harper, A. Walton, P. A. Anderson, *Journal of Physics: Materials* **2022**, *5*, 032001.

[5] G. Di Liberto, G. Pacchioni, *Advanced Materials* **2023**, *35*, e2307150.

[6] H. A. Gasteiger, S. S. Kocha, B. Sompalli, F. T. Wagner, *Applied Catalysis B: Environmental* **2005**, *56*, 9–35.

[7] M. Lefèvre, E. Proietti, F. Jaouen, J.-P. Dodelet, *Science* **2009**, *324*, 71–74.

[8] A. Mehmood, M. Gong, F. Jaouen, A. Roy, A. Zitolo, A. Khan, M.-T. Sougrati, M. Primbs, A. M. Bonastre, D. Fongalland, G. Drazic, P. Strasser, A. Kucernak, *Nature Catalysis* **2022**, *5*, 311–323.

[9] A. S. Varela, N. Ranjbar Sahraie, J. Steinberg, W. Ju, H.-S. Oh, P. Strasser, *Angewandte Chemie International Edition* **2015**, *54*, 10758–10762.

[10] W. Ju, A. Bagger, G.-P. Hao, A. S. Varela, I. Sinev, V. Bon, B. Roldan Cuenya, S. Kaskel, J. Rossmeisl, P. Strasser, *Nature Communications* **2017**, *8*, 944.

[11] J. Pei, R. Zhao, X. Mu, J. Wang, C. Liu, X.-D. Zhang, *Biomaterials Science* **2020**, *8*, 6428–6441.

[12] R. Jasinski, *Nature* **1964**, *201*, 1212–1213.

[13] R. Jasinski, *Journal of The Electrochemical Society* **1965**, *112*, 526.

[14] H. Jahnke, M. Schönborn, G. Zimmermann, *Topics in Current Chemistry* **1976**, *61*, 133–181.

[15] S. Gupta, D. Tryk, I. Bae, W. Aldred, E. Yeager, *Journal of Applied Electrochemistry* **1989**, *19*, 19–27.

[16] C. Wang, X. Hu, X. Hu, X. Liu, Q. Guan, R. Hao, Y. Liu, W. Li, *Applied Catalysis B: Environmental* **2021**, *296*, 120331.

[17] G. Wu, K. Artyushkova, M. Ferrandon, A. J. Kropf, D. Myers, P. Zelenay, *ECS Transactions* **2009**, *25*, 1299–1311.

[18] M. Ferrandon, X. Wang, A. J. Kropf, D. J. Myers, G. Wu, C. M. Johnston, P. Zelenay, *Electrochimica Acta* **2013**, *110*, 282–291.

[19] Z. Li, G. Li, L. Jiang, J. Li, G. Sun, C. Xia, F. Li, *Angewandte Chemie International Edition* **2015**, *54*, 1494–1498.

[20] D. Menga, A. Guilherme Buzanich, F. Wagner, T.-P. Fellinger, *Angewandte Chemie International Edition* **2022**, e202207089.

[21] E. Proietti, F. Jaouen, M. Lefèvre, N. Larouche, J. Tian, J. Herranz, J.-P. Dodelet, *Nature Communications* **2011**, *2*, 416.

[22] S. Ma, G. A. Goenaga, A. V. Call, D.-J. Liu, *Chemistry: A European Journal* **2011**, *17*, 2063–2067.

[23] B. Hou, C. C. Wang, R. Tang, Q. Zhang, X. Cui, *Materials Research Express* **2020**, *7*, 025506.

[24] L. Jiao, J. Li, L. L. Richard, Q. Sun, T. Stracensky, E. Liu, M. T. Sougrati, Z. Zhao, F. Yang, S. Zhong, H. Xu, S. Mukerjee, Y. Huang, D. A. Cullen, J. H. Park, M. Ferrandon, D. J. Myers, F. Jaouen, Q. Jia, *Nature Materials* **2021**, *20*, 1385–1391.

[25] D. Menga, F. Ruiz–Zepeda, L. Moriau, M. Šala, F. Wagner, B. Koyutürk, M. Bele, U. Petek, N. Hodnik, M. Gaberšček, T.-.-P. Fellinger, *Advanced Energy Materials* **2019**, *9*, 1902412.

[26] Harold Johann Thomas Ellingham, *Journal of the Society of Chemical Industry* **1944**, *63*, 125–160.

[27] A. Zitolo, V. Goellner, V. Armel, M.-T. Sougrati, T. Mineva, L. Stievano, E. Fonda, F. Jaouen, *Nature Materials* **2015**, *14*, 937–942.

[28] U. I. Kramm, M. Lefèvre, N. Larouche, D. Schmeisser, J.-P. Dodelet, *Journal of the American Chemical Society* **2014**, *136*, 978–985.

[29] U. I. Kramm, I. Herrmann-Geppert, S. Fiechter, G. Zehl, I. Zizak, I. Dorbandt, D. Schmeißer, P. Bogdanoff, *Journal of Materials Chemistry A* **2014**, *2*, 2663–2670.

[30] A. Mehmood, J. Pampel, G. Ali, H. Y. Ha, F. Ruiz-Zepeda, T.-P. Fellinger, *Advanced Energy Materials* **2018**, *8*, 1701771.

[31] S. Liu, M. Wang, X. Yang, Q. Shi, Z. Qiao, M. Lucero, Q. Ma, K. L. More, D. A. Cullen, Z. Feng, G. Wu, *Angewandte Chemie International Edition* **2020**, *59*, 21698–21705.

[32] H. T. Chung, D. A. Cullen, D. Higgins, B. T. Sneed, E. F. Holby, K. L. More, P. Zelenay, *Science* **2017**, *357*, 479–484.

[33] T. Marshall-Roth, N. J. Libretto, A. T. Wrobel, K. J. Anderton, M. L. Pegis, N. D. Ricke, T. van Voorhis, J. T. Miller, Y. Surendranath, *Nature Communications* **2020**, *11*, 5283.

[34] L. Li, Y. Wen, G. Han, Y. Liu, Y. Song, W. Zhang, J. Sun, L. Du, F. Kong, Y. Ma, Y. Gao, J. Wang, C. Du, G. Yin, *Chemical Engineering Journal* **2022**, *437*, 135320.

[35] X. Hu, S. Chen, L. Chen, Y. Tian, S. Yao, Z. Lu, X. Zhang, Z. Zhou, *Journal of the American Chemical Society* **2022**, *144*, 18144–18152.

[36] N. Zhang, T. Zhou, M. Chen, H. Feng, R. Yuan, C. Zhong, W. Yan, Y. Tian, X. Wu, W. Chu, C. Wu, Y. Xie, *Energy & Environmental Science* **2020**, *13*, 111–118.

[37] S. Chen, T. Luo, X. Li, K. Chen, J. Fu, K. Liu, C. Cai, Q. Wang, H. Li, Y. Chen, C. Ma, L. Zhu, Y.-R. Lu, T.-S. Chan, M. Zhu, E. Cortés, M. Liu, *Journal of the American Chemical Society* **2022**, *144*, 14505–14516.

[38] D. M. Koshy, S. Chen, D. U. Lee, M. B. Stevens, A. M. Abdellah, S. M. Dull, G. Chen, D. Nordlund, A. Gallo, C. Hahn, et al., *Angewandte Chemie International Edition* **2020**, *59*, 4043–4050.

[39] W. Shao, R. Yan, M. Zhou, L. Ma, C. Roth, T. Ma, S. Cao, C. Cheng, B. Yin, S. Li, *Electrochemical Energy Reviews* **2023**, *6*, 11.

[40] H.-.-F. Wang, C. Tang, Q. Zhang, *Advanced Functional Materials* **2018**, *28*, 1770123.

[41] Z. Cao, H. Hu, M. Wu, K. Tang, T. Jiang, *Journal of Materials Chemistry A* **2019**, *7*, 17581–17593.

[42] A. Baroutaji, T. Wilberforce, M. Ramadan, A. G. Olabi, *Renewable and Sustainable Energy Reviews* **2019**, *106*, 31–40.

[43] T. Kadyk, C. Winnefeld, R. Hanke-Rauschenbach, U. Krewer, *Energies* **2018**, *11*, 375.

[44] T. J. Leo, J. A. Durango, E. Navarro, *Energy* **2010**, *35*, 1164–1171.

[45] L. van Biert, M. Godjevac, K. Visser, P. V. Aravind, *Journal of Power Sources* **2016**, *327*, 345–364.

[46] H. A. Gasteiger, J. E. Panels, S. G. Yan, *Journal of Power Sources* **2004**, *127*, 162–171.

[47] N. Ramaswamy, S. Mukerjee, *The Journal of Physical Chemistry C* **2011**, *115*, 18015–18026.

[48] N. Ramaswamy, U. Tylus, Q. Jia, S. Mukerjee, *Journal of the American Chemical Society* **2013**, *135*, 15443–15449.

[49] C. H. Choi, H.-K. Lim, M. W. Chung, J. C. Park, H. Shin, H. Kim, S. I. Woo, *Journal of the American Chemical Society* **2014**, *136*, 9070–9077.

[50] D. Malko, A. Kucernak, T. Lopes, *Journal of the American Chemical Society* **2016**, *138*, 16056–16068.

[51] D. Malko, A. Kucernak, *Electrochemistry Communications* **2017**, *83*, 67–71.

[52] E. Luo, H. Zhang, X. Wang, L. Gao, L. Gong, T. Zhao, Z. Jin, J. Ge, Z. Jiang, C. Liu, et al., *Angewandte Chemie International Edition* **2019**, *131*, 12599–12605.

[53] H. Liu, S. Zhu, Z. Cui, Z. Li, S. Wu, Y. Liang, *Journal of Catalysis* **2021**, *396*, 402–408.

[54] S. K. Parida, T. Barik, H. Jena, *Sustainable Energy & Fuels* **2023**, *7*, 3684–3691.

[55] Y. Sun, L. Silvioli, N. R. Sahraie, W. Ju, J. Li, A. Zitolo, S. Li, A. Bagger, L. Arnarson, X. Wang, T. Moeller, D. Bernsmeier, J. Rossmeisl, F. Jaouen, P. Strasser, *Journal of the American Chemical Society* **2019**, *141*, 12372–12381.

[56] R. Zheng, Q. Meng, L. Zhang, J. Ge, C. Liu, W. Xing, M. Xiao, *Chemistry: A European Journal* **2023**, *29*, e202203180.

[57] M. Bron, S. Fiechter, P. Bogdanoff, H. Tributsch, *Fuel Cells* **2002**, *2*, 137–142.

[58] A. Bonakdarpour, M. Lefevre, R. Yang, F. Jaouen, T. Dahn, J.-P. Dodelet, J. R. Dahn, *Electrochemical and Solid-State Letters* **2008**, *11*, B105.

[59] R. Chenitz, U. I. Kramm, M. Lefèvre, V. Glibin, G. Zhang, S. Sun, J.-P. Dodelet, *Energy & Environmental Science* **2018**, *11*, 365–382.

[60] C. H. Choi, C. Baldizzone, J.-P. Grote, A. K. Schuppert, F. Jaouen, K. J. J. Mayrhofer, *Angewandte Chemie International Edition* **2015**, *54*, 12753–12757.

[61] C. H. Choi, H.-K. Lim, M. W. Chung, G. Chon, N. Ranjbar Sahraie, A. Altin, M.-T. Sougrati, L. Stievano, H. S. Oh, E. S. Park, F. Luo, P. Strasser, G. Dražić, K. J. J. Mayrhofer, H. Kim, F. Jaouen, *Energy & Environmental Science* **2018**, *11*, 3176–3182.

[62] D. Banham, T. Kishimoto, Y. Zhou, T. Sato, K. Bai, J.-I. Ozaki, Y. Imashiro, S. Ye, *Science advances* **2018**, *4*, eaar7180.

[63] H. J. H. Fenton, *Journal of the Chemical Society Transactions* **1894**, *65*, 899–910.

[64] Y. Hu, Q. Cao, C. Neumann, T. Lehnert, F. Börrnert, Y. Wang, U. Kaiser, A. Turchanin, S. Eigler, *Carbon* **2021**, *185*, 568–577.

[65] C. M. Wong, K. H. Wong, X. D. Chen, *Applied Microbiology and Biotechnology* **2008**, *78*, 927–938.

[66] Y. Zhu, J. Zhang, J. Song, J. Yang, Z. Du, W. Zhao, H. Guo, C. Wen, Q. Li, X. Sui, L. Zhang, *Advanced Functional Materials* **2020**, *30*, 1905493.

[67] S. Thangudu, C.-H. Su, *Biomolecules* **2021**, *11*, 1015.

[68] M. Huo, L. Wang, Y. Wang, Y. Chen, J. Shi, *ACS Nano* **2019**, *13*, 2643–2653.

[69] X. Lu, S. Gao, H. Lin, L. Yu, Y. Han, P. Zhu, W. Bao, H. Yao, Y. Chen, J. Shi, *Advanced Materials* **2020**, *32*, e2002246.

[70] X. Lu, S. Gao, H. Lin, J. Shi, *Small* **2021**, *17*, e2004467.

[71] B. Xu, H. Wang, W. Wang, L. Gao, S. Li, X. Pan, H. Wang, H. Yang, X. Meng, Q. Wu, L. Zheng, S. Chen, X. Shi, K. Fan, X. Yan, H. Liu, *Angewandte Chemie International Edition* **2019**, *131*, 4965–4970.

[72] M. Huo, L. Wang, H. Zhang, L. Zhang, Y. Chen, J. Shi, *Small* **2019**, *15*, e1901834.

[73] X. Wang, Q. Shi, Z. Zha, D. Zhu, L. Zheng, L. Shi, X. Wei, L. Lian, K. Wu, L. Cheng, *Bioactive Materials* **2021**, *6*, 4389–4401.

[74] A. M. Appel, J. E. Bercaw, A. B. Bocarsly, H. Dobbek, D. L. DuBois, M. Dupuis, J. G. Ferry, E. Fujita, R. Hille, P. J. A. Kenis, C. A. Kerfeld, R. H. Morris, C. H. F. Peden, A. R. Portis, S. W. Ragsdale, T. B. Rauchfuss, J. N. H. Reek, L. C. Seefeldt, R. K. Thauer, G. L. Waldrop, *Chemical Reviews* **2013**, *113*, 6621–6658.

[75] T. Asset, S. T. Garcia, S. Herrera, N. Andersen, Y. Chen, E. J. Peterson, I. Matanovic, K. Artyushkova, J. Lee, S. D. Minteer, S. Dai, X. Pan, K. Chavan, S. Calabrese Barton, P. Atanassov, *ACS Catalysis* **2019**, *9*, 7668–7678.

[76] J. Li, P. Pršlja, T. Shinagawa, A. J. Martín Fernández, F. Krumeich, K. Artyushkova, P. Atanassov, A. Zitolo, Y. Zhou, R. García-Muelas, N. López, J. Pérez-Ramírez, F. Jaouen, *ACS Catalysis* **2019**, *9*, 10426–10439.

[77] S. Lambie, J. L. Low, N. Gaston, B. Paulus, *ChemPhysChem* **2022**, *23*, e202200024.

[78] T. Möller, W. Ju, A. Bagger, X. Wang, F. Luo, T. Ngo Thanh, A. S. Varela, J. Rossmeisl, P. Strasser, *Energy & Environmental Science* **2019**, *12*, 640–647.

[79] C.-Z. Yuan, K. Liang, X.-M. Xia, Z. K. Yang, Y.-F. Jiang, T. Zhao, C. Lin, T.-Y. Cheang, S.-L. Zhong, A.-W. Xu, *Catalysis Science & Technology* **2019**, *9*, 3669–3674.

[80] H. B. Yang, S.-F. Hung, S. Liu, K. Yuan, S. Miao, L. Zhang, X. Huang, H.-Y. Wang, W. Cai, R. Chen, J. Gao, X. Yang, W. Chen, Y. Huang, H. M. Chen, C. M. Li, T. Zhang, B. Liu, *Nature Energy* **2018**, *3*, 140–147.

[81] J. Yang, Z. Qiu, C. Zhao, W. Wei, W. Chen, Z. Li, Y. Qu, J. Dong, J. Luo, Z. Li, Y. Wu, *Angewandte Chemie International Edition* **2018**, *130*, 14291–14296.

[82] K. Jiang, S. Siahrostami, A. J. Akey, Y. Li, Z. Lu, J. Lattimer, Y. Hu, C. Stokes, M. Gangishetty, G. Chen, Y. Zhou, W. Hill, W.-B. Cai, D. Bell, K. Chan, J. K. Nørskov, Y. Cui, H. Wang, *Chem* **2017**, *3*, 950–960.

[83] H. Kim, D. Shin, W. Yang, H. Da Won, H.-S. Oh, M. W. Chung, D. Jeong, S. H. Kim, K. H. Chae, J. Y. Ryu, J. Lee, S. J. Cho, J. Seo, H. Kim, C. H. Choi, *Journal of the American Chemical Society* **2021**, *143*, 925–933.

[84] C. Yan, H. Li, Y. Ye, H. Wu, F. Cai, R. Si, J. Xiao, S. Miao, S. Xie, F. Yang, Y. Li, G. Wang, X. Bao, *Energy & Environmental Science* **2018**, *11*, 1204–1210.

[85] S. Vijay, W. Ju, S. Brückner, S.-C. Tsang, P. Strasser, K. Chan, *Nature Catalysis* **2021**, *4*, 1024–1031.

[86] K. P. Kuhl, E. R. Cave, D. N. Abram, T. F. Jaramillo, *Energy & Environmental Science* **2012**, *5*, 7050.

[87] A. R. Woldu, Z. Huang, P. Zhao, L. Hu, D. Astruc, *Coordination Chemistry Reviews* **2022**, *454*, 214340.

[88] E. L. Clark, S. Ringe, M. Tang, A. Walton, C. Hahn, T. F. Jaramillo, K. Chan, A. T. Bell, *ACS Catalysis* **2019**, *9*, 4006–4014.

[89] Y. Hori, A. Murata, K. Kikuchi, S. Suzuki, *Journal of the Chemical Society Chemical Communications* **1987**, 728.

[90] M. R. Thorson, K. I. Siil, P. J. A. Kenis, *Journal of The Electrochemical Society* **2013**, *160*, F69–F74.

[91] S. Ringe, E. L. Clark, J. Resasco, A. Walton, B. Seger, A. T. Bell, K. Chan, *Energy & Environmental Science* **2019**, *12*, 3001–3014.

[92] T. Ludwig, J. A. Gauthier, C. F. Dickens, K. S. Brown, S. Ringe, K. Chan, J. K. Nørskov, *The Journal of Physical Chemistry C* **2020**, *124*, 24765–24775.

[93] M. C. O. Monteiro, F. Dattila, B. Hagedoorn, R. García-Muelas, N. López, M. T. M. Koper, *Nature Catalysis* **2021**, *4*, 654–662.

[94] M. C. O. Monteiro, F. Dattila, N. López, M. T. M. Koper, *Journal of the American Chemical Society* **2022**, *144*, 1589–1602.

[95] X. Qin, T. Vegge, H. A. Hansen, *The Journal of Chemical Physics* **2021**, *155*, 134703.

[96] X. Qin, T. Vegge, H. A. Hansen, *Journal of the American Chemical Society* **2023**, *145*, 1897–1905.

[97] X. Qin, H. A. Hansen, K. Honkala, M. M. Melander, *Nature Communications* **2023**, *14*, 7607.

[98] A. Szabo, N. S. Ostlund, *Modern quantum chemistry: Introduction to advanced electronic structure theory*, Dover Publications, Mineola N.Y., **1996**.

[99] W. Koch, M. C. Holthausen, *A chemist's guide to density functional theory*, 2nd ed., repr, Wiley-VCH, Weinheim, **2010**.

[100] C. Kittel, *Introduction to solid state physics*, 8. ed., [Nachdr.], Wiley, Hoboken, NJ, **2011**.

[101] D. R. Hartree, *Mathematical Proceedings of the Cambridge Philosophical Society* **1928**, *24*, 89–110.

[102] E. Schrödinger, *Physical Review* **1926**, *28*, 1049–1070.

[103] M. Born, R. Oppenheimer, *Annalen der Physik* **1927**, *389*, 457–484.

[104] J. C. Slater, *Physical Review* **1929**, *34*, 1293–1322.

[105] J. C. Slater, *Physical Review* **1930**, *35*, 210–211.

[106] W. Pauli, *Zeitschrift für Physik* **1925**, *31*, 765–783.

[107] C. C. J. Roothaan, *Reviews of Modern Physics* **1951**, *23*, 69–89.

[108] G. G. Hall, *Proceedings of the Royal Society of London. Series A. Mathematical and Physical Sciences* **1951**, *205*, 541–552.

[109] C. Møller, M. S. Plesset, *Physical Review* **1934**, *46*, 618–622.

[110] L. H. Thomas, *Mathematical Proceedings of the Cambridge Philosophical Society* **1927**, *23*, 542–548.

[111] E. Fermi, *Zeitschrift für Physik* **1928**, *48*, 73–79.

[112] P. Hohenberg, W. Kohn, *Physical Review* **1964**, *136*, B864–B871.

[113] W. Kohn, L. J. Sham, *Physical Review* **1965**, *140*, A1133–A1138.

[114] J. C. Slater, *Physical Review* **1951**, *81*, 385–390.

[115] S. H. Vosko, L. Wilk, M. Nusair, *Canadian Journal of Physics* **1980**, *58*, 1200–1211.

[116] J. P. Perdew, Y. Wang, *Physical Review B* **1992**, *45*, 13244–13249.

[117] J. Tao, J. P. Perdew, V. N. Staroverov, G. E. Scuseria, *Physical Review Letters* **2003**, *91*, 146401.

[118] A. D. Becke, *Physical review. A* **1988**, *38*, 3098–3100.

[119] C. Lee, W. Yang, R. G. Parr, *Physical Review B* **1988**, *37*, 785–789.

[120] J. P. Perdew, *Physical Review B* **1986**, *33*, 8822–8824.

[121] J. P. Perdew, M. Ernzerhof, K. Burke, *The Journal of Chemical Physics* **1996**, *105*, 9982–9985.

[122] A. D. Becke, *The Journal of Chemical Physics* **1993**, *98*, 5648–5652.

[123] P. J. Stephens, F. J. Devlin, C. F. Chabalowski, M. J. Frisch, *The Journal of Physical Chemistry* **1994**, *98*, 11623–11627.

[124] F. Bloch, *Zeitschrift für Physik* **1929**, *52*, 555–600.

[125] Samuel Francis Boys, *Proceedings of the Royal Society of London. Series A. Mathematical and Physical Sciences* **1950**, *200*, 542–554.

[126] A. Schäfer, H. Horn, R. Ahlrichs, *The Journal of Chemical Physics* **1992**, *97*, 2571–2577.

[127] F. Weigend, M. Häser, H. Patzelt, R. Ahlrichs, *Chemical Physics Letters* **1998**, *294*, 143–152.

[128] F. Weigend, R. Ahlrichs, *Physical Chemistry Chemical Physics* **2005**, *7*, 3297–3305.

[129] P. E. Blöchl, *Physical Review B* **1994**, *50*, 17953–17979.

[130] H. Bethe, *Annalen der Physik* **1929**, *395*, 133–208.

[131] J. S. Griffith, L. E. Orgel, *Quarterly Reviews Chemical Society* **1957**, *11*, 381.

[132] J. Börgel, M. G. Campbell, T. Ritter, *Journal of Chemical Education* **2016**, *93*, 118–121.

[133] A. M. Patel, S. Ringe, S. Siahrostami, M. Bajdich, J. K. Nørskov, A. R. Kulkarni, *The Journal of Physical Chemistry C* **2018**, *122*, 29307–29318.

[134] G. Di Liberto, L. A. Cipriano, G. Pacchioni, *ACS Catalysis* **2022**, *12*, 5846–5856.

[135] A. Klamt, G. Schüürmann, *Journal of the Chemical Society Perkin Transactions 2* **1993**, 799–805.

[136] A. E. Reed, R. B. Weinstock, F. Weinhold, *The Journal of Chemical Physics* **1985**, *83*, 735–746.

[137] T. Engel, P. Reid, *Physical chemistry: Thermodynamics, statistical thermodynamics, and kinetics*, Global edition, Pearson, Upper Saddle River, **2020**.

[138] A. J. Bard, L. R. Faulkner, *Electrochemical methods: Fundamentals and applications*, 2nd ed., Wiley, New York, **2001**.

[139] L. Boltzmann, *Studien über das Gleichgewicht der lebendigen Kraft zwischen bewegten materiellen Punkten: vorgelegt in der Sitzung am 8. October 1868*, k. und k. Hof- und Staatsdr, **1868**.

[140] S. N. Bose, *Zeitschrift für Physik* **1924**, *26*, 178–181.

[141] E. Fermi, *Zeitschrift für Physik* **1926**, *36*, 902–912.

[142] J. W. Gibbs, *Transactions of the Connecticut Academy of Arts and Sciences* **1873**, *2*, 382–404.

[143] J. K. Nørskov, J. Rossmeisl, A. Logadottir, L. Lindqvist, J. R. Kitchin, T. Bligaard, H. Jónsson, *The Journal of Physical Chemistry B* **2004**, *108*, 17886–17892.

[144] H. A. Hansen, I. C. Man, F. Studt, F. Abild-Pedersen, T. Bligaard, J. Rossmeisl, *Physical Chemistry Chemical Physics* **2010**, *12*, 283–290.

[145] X. Chen, L. P. Granda-Marulanda, I. T. McCrum, M. T. M. Koper, *Chemical Science* **2020**, *11*, 1703–1713.

[146] S. Arrhenius, *Zeitschrift für Physikalische Chemie* **1889**, *4U*, 96–116.

[147] H. Eyring, *The Journal of Chemical Physics* **1935**, *3*, 107–115.

[148] M. G. Evans, M. Polanyi, *Transactions of the Faraday Society* **1935**, *31*, 875.

[149] D. Sheppard, R. Terrell, G. Henkelman, *The Journal of Chemical Physics* **2008**, *128*, 134106.

[150] G. Henkelman, H. Jónsson, *The Journal of Chemical Physics* **1999**, *111*, 7010–7022.

[151] A. Heyden, A. T. Bell, F. J. Keil, *The Journal of Chemical Physics* **2005**, *123*, 224101.

[152] G. Mills, H. Jónsson, G. K. Schenter, *Surface Science* **1995**, *324*, 305–337.

[153] H. Jónsson, G. Mills, K. W. Jacobsen, **1995**, 385–404.

[154] J. A. V. Butler, *Transactions of the Faraday Society* **1924**, *19*, 729–733.

[155] J. A. V. Butler, *Transactions of the Faraday Society* **1924**, *19*, 734.

[156] T. Erdey-Grúz, M. Volmer, *Zeitschrift für Physikalische Chemie* **1930**, *150A*, 203–213.

[157] J. A. V. Butler, *Transactions of the Faraday Society* **1932**, *28*, 379.

[158] J. Tafel, *Zeitschrift für Physikalische Chemie* **1905**, *50U*, 641–712.

[159] H. Helmholtz, *Annalen der Physik und Chemie* **1879**, *243*, 337–382.

[160] M. Gouy, *Journal de Physique Théorique et Appliquée* **1910**, *9*, 457–468.

[161] D. L. Chapman, *The London Edinburgh and Dublin Philosophical Magazine and Journal of Science* **1913**, *25*, 475–481.

[162] O. Stern, *Zeitschrift für Elektrochemie und Angewandte Physikalische Chemie* **1924**, *30*, 508–516.

[163] D. C. Grahame, *Chemical Reviews* **1947**, *41*, 441–501.

[164] H. A. Jahn, E. Teller, *Proceedings of the Royal Society of London. Series A. Mathematical and Physical Sciences* **1937**, *161*, 220–235.

[165] S. G. Pukhovskaya, D. T. Nam, Y. B. Ivanova, L. S. Liulkovich, A. S. Semeikin, S. A. Syrbu, M. M. Kruk, *Journal of Inclusion Phenomena and Macrocyclic Chemistry* **2017**, *89*, 325–332.

[166] A. Farajtabar, F. Gharib, P. Jamaat, N. Safari, *Journal of Chemical & Engineering Data* **2008**, *53*, 350–354.

[167] H. Xie, X. Xie, G. Hu, V. Prabhakaran, S. Saha, L. Gonzalez-Lopez, A. H. Phakatkar, M. Hong, M. Wu, R. Shahbazian-Yassar, V. Ramani, M. I. Al-Sheikhly, D.-e. Jiang, Y. Shao, L. Hu, *Nature Energy* **2022**, *7*, 281–289.

[168] K. H. Wong, E. Kjeang, *ChemSusChem* **2015**, *8*, 1072–1082.

[169] J. Chen, X. Yan, C. Fu, Y. Feng, C. Lin, X. Li, S. Shen, C. Ke, J. Zhang, *ACS Applied Materials & Interfaces* **2019**, *11*, 37779–37786.

[170] Ronald Percy Bell, *Proceedings of the Royal Society of London. Series A. Mathematical and Physical Sciences* **1936**, *154*, 414–429.

[171] M. G. Evans, M. Polanyi, *Transactions of the Faraday Society* **1936**, *32*, 1333.

[172] D. Hursán, J. Timoshenko, E. Ortega, H. S. Jeon, M. Rüscher, A. Herzog, C. Rettenmaier, S. W. Chee, A. Martini, D. Koshy, B. Roldán Cuenya, *Advanced Materials* **2024**, *36*, e2307809.

[173] R. M. Arán-Ais, F. Scholten, S. Kunze, R. Rizo, B. Roldan Cuenya, *Nature Energy* **2020**, *5*, 317–325.

[174] L. Yuan, S.-F. Hung, Z.-R. Tang, H. M. Chen, Y. Xiong, Y.-J. Xu, *ACS Catalysis* **2019**, *9*, 4824–4833.

[175] P. Grosse, A. Yoon, C. Rettenmaier, A. Herzog, S. W. Chee, B. Roldan Cuenya, *Nature Communications* **2021**, *12*, 6736.

[176] K. Jiang, P. Kharel, Y. Peng, M. K. Gangishetty, H.-Y. G. Lin, E. Stavitski, K. Attenkofer, H. Wang, *ACS Sustainable Chemistry & Engineering* **2017**, *5*, 8529–8534.

Acknowledgments

First and foremost, I am deeply grateful to Prof. Dr. Beate Paulus for giving me the opportunity to conduct research in her group, especially during the turbulent COVID-19 pandemic. Beate has been an extremely understanding and insightful supervisor who has provided valuable support in navigating the scientific, administrative, financial, and even political aspects of my doctoral journey. It is truly a blessing to have her as my Doktormutter.

I am also thankful to my second supervisor, Prof. Dr.-Ing. Christina Roth, for her willingness to share her profound expertise in electrochemistry and for her assistance in proofreading my work, even on short notice. Additionally, I appreciate the opportunities for collaborations and knowledge exchange with Christina's very hospitable Lehrstuhl that further developed my understanding of electrochemical concepts, measurements and engineering.

I am further thankful to Dr. Tim-Patrick Fellinger and his team, especially Dr. Davide Menga and Dr. Asad Mehmood, for the pleasant collaborative efforts that greatly influenced my work and inspired my endeavor in a previously unfamiliar realm of electrochemistry. I am also grateful to Prof. Dr. Rainer Haag and Dr. Fan Xin for facilitating the interdisciplinary project in the biomedical sciences. Theory-focused collaborations with the teams of Prof. Nicola Gaston and Prof. Dr. Vera Krewald are also appreciated.

I would like to acknowledge various sources of funding throughout my doctoral studies, including the Elsa-Neumann Scholarship, the Dahlem Research School Molecular Science, and the Collaborative Research Center 1349. Computational resources and support from the university (Curta) as well as the Norddeutsche Verbund zur Förderung des Hoch- und Höchstleistungsrechnens (HLRN, now NHR) are also appreciated. Additionally, I am grateful for the assistance provided by language models such as ChatGPT, which helped refine certain sections of this thesis.

Next, I would like to thank my lovely colleagues in the theoretical chemistry department for the pleasant working environment, especially Jingjing, Kangli, Jiajun and Luca who were often engaged in my distracting chatters at the office. I am also thankful to those who have provided valuable sustenance, including

Jennifer (bread), Stephanie and Joana (coffee), Simon and the Feierabendbierchen gang (beer), as well as everyone else who have occasionally contributed delicious cakes and food. I would also like to thank Julija for her assistance in navigating administrative tasks during my studies.

Finally, I would like to thank my friends and family for enriching my personal life. Special mentions go to Amber, Yingshen and Dongwei for the encouragement and advice in navigating the doctoral studies, Nicole for helping with my German abstract, and my KTV pengyous for making my life in Berlin much more enjoyable. Last but not least, I am most grateful to my sister Huizhi for inspiring and supporting me in various ways to pursue and complete my studies in Germany.